Computational and Mathematical Methods in Medicine

Mathematical Modeling and Models for Optimal Decision-Making in Health Care

Lead Guest Editor: Giedrius Vanagas
Guest Editors: Tomas Krilavičius and Ka L. Man

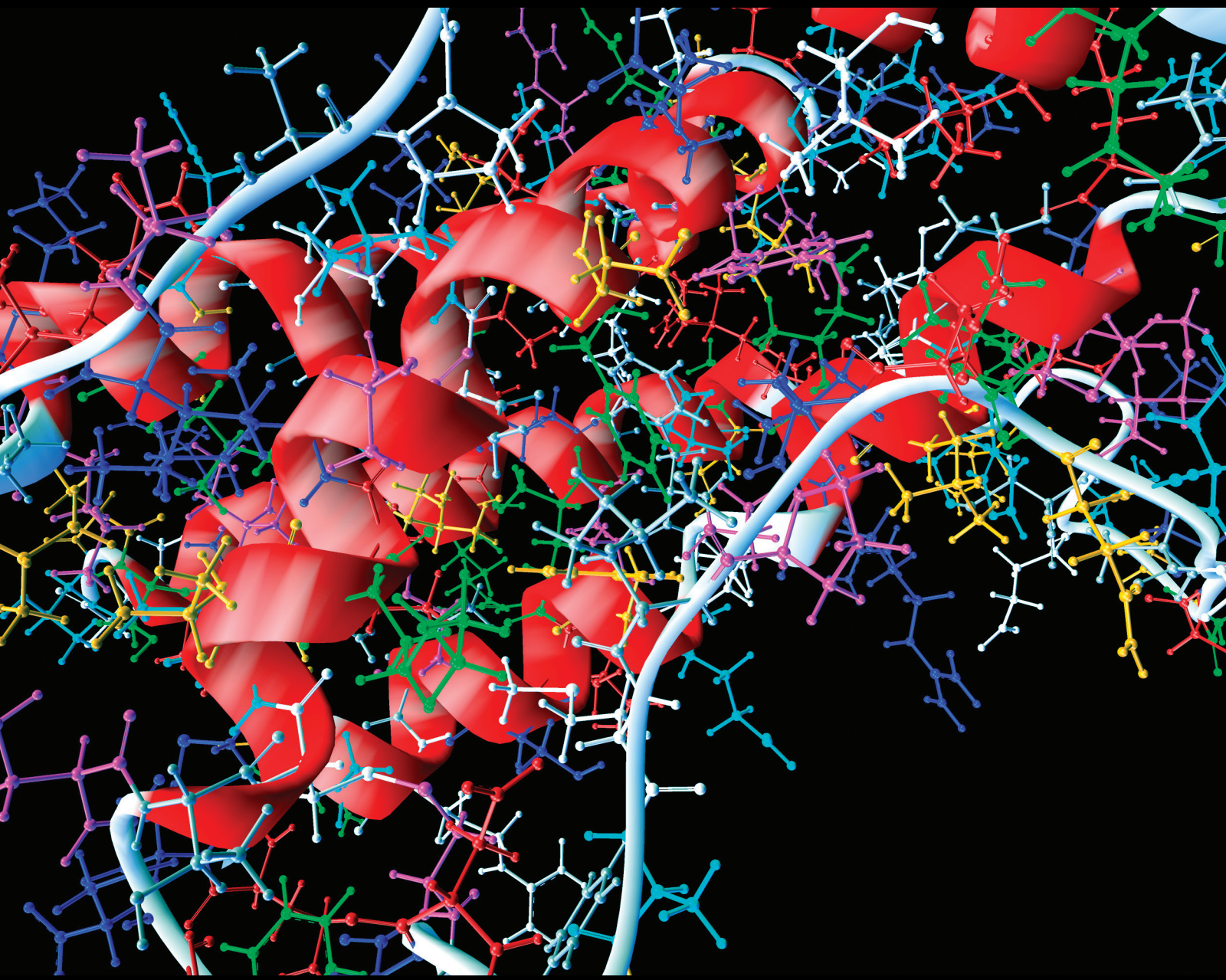

Mathematical Modeling and Models for Optimal Decision-Making in Health Care

Computational and Mathematical Methods in Medicine

Mathematical Modeling and Models for Optimal Decision-Making in Health Care

Lead Guest Editor: Giedrius Vanagas
Guest Editors: Tomas Krilavicius and Ka L. Man

Editorial Board

Contents

Hindawi
Computational and Mathematical Methods in Medicine
Volume 2019, Article ID 2945021, 4 pages
https://doi.org/10.1155/2019/2945021

Editorial

Mathematical Modeling and Models for Optimal Decision-Making in Health Care

Giedrius Vanagas,[1] **Tomas Krilavičius**,[2,3] **and Ka Lok Man**[4,5]

[1]*Institute of Pharmacoeconomics, LT-51052 Kaunas, Lithuania*
[2]*Vytautas Magnus University, Kaunas, Lithuania*
[3]*Lithuania and Baltic Institute of Advanced Technology, Vilnius, Lithuania*
[4]*Xi'an Jiaotong-Liverpool University, Suzhou 215123, China*
[5]*Swinburne University of Technology Sarawak, Kuching, Malaysia*

Correspondence should be addressed to Giedrius Vanagas; g.vanagas@gmail.com

Received 31 July 2019; Accepted 1 August 2019; Published 14 August 2019

Many aspects in the management of healthcare systems are quantitative, the amount of data within the health care increases by the minute, and, in reality, it makes difficult for healthcare systems to identify the insights into what is most valuable for the patients. Data-driven approach to health (or health economic) outcome assessment, artificial intelligence, and mathematical, computational, methodological, and technological advances are the core of effective healthcare system management [1–3].

Modeling in medicine is a valuable tool in the planning and evaluation of interventions, especially when a clinical trial is ethically or logistically impossible [4, 5]. The development of such mathematical models used to simulate medical outcomes is a growing area in medicine. The mathematical modeling is known by various names like predictive modeling, simulation, or decision analysis. In general, modeling techniques are used for health service planning, effectiveness and outcome assessment, healthcare financing and budget impact assessment, health economic assessments, infectious disease surveillance, health service outcomes predicting purposes, and other applications in health care. Mathematical modeling is also helpful when limitations like a rare event prohibit implementing RCT and similar studies or expanding research on actual patients due to time, ethical, legal, financial, technical, and other limitations [6, 7].

With this special issue, we add to the literature by providing case studies and practical examples of mathematical modeling and models for optimal decision-making in health care. We aim to address questions from data analytics, solving problems in predicting outcomes for clinical medicine and public health.

Blood pressure (BP) is one of the indispensable elements of physiological health characteristics and a significant indicator for predicting and diagnosing hypertension and cardiovascular diseases. Q. Wang et al. proposed a two-domain fusion model to estimate BP continuously from pulse wave acquired with a pressure sensor. In more detail, the optimal external pressure applied on the pressure sensor was first determined in order to capture pulse wave in the radial artery. The captured pulse wave was then processed in both the time and frequency domains via filtering and fast Fourier transform. A set of features were extracted from these two domains and input into a neural network along with blood pressure values measured by a commercial sphygmomanometer for training. Finally, the model was tested on new data for accuracy evaluation, and the proposed two-domain fusion method achieved a high degree of accuracy in measuring blood pressure.

H. Shang et al. proposed an improvement for ECG analysis, namely, improved sliding window area method for T wave detection. It allows better detection of T wave onset and offset, which allows improving clinical diagnosis as well as daily heart monitoring.

A. K. Heikhmakhtiar and K. M. Lim proposed computational prediction of the combined effect of CRT and

LVAD on cardiac electromechanical delay in the failing ventricle with left bundle branch blocked (LBBB) and right bundle branch blocked (RBBB) conditions. The subjects were normal sinus rhythm, LBBB, RBBB, LBBB with CRT-only, RBBB with CRT-only, LBBB with CRT + LVAD, and RBBB with CRT + LVAD. The results showed that the CRT-only shortened the total electrical activation time (EAT) in the LBBB and RBBB conditions by 20.2% and 17.1%, respectively. The CRT-only reduced the total mechanical activation time (MAT) and electromechanical delay (EMD) of the ventricle under LBBB by 21.3% and 10.1%, respectively. Furthermore, the CRT-only reduced the contractile adenosine triphosphate (ATP) consumption by 5%, increased left ventricular (LV) pressure by 6%, and enhanced cardiac output (CO) by 0.2 L/min under LBBB condition. However, CRT-only barely affected the ventricle under RBBB condition. Under the LBBB condition, CRT + LVAD increased LV pressure and CO by 10.5% and 0.9 L/min, respectively. CRT + LVAD reduced ATP consumption by 15%, shortened the MAT by 23.4%, and shortened the EMD by 15.2%. In conclusion, they computationally predicted and quantified that the CRT + LVAD implementation is superior to CRT-only implementation particularly in HF with LBBB condition.

Magnetic resonance imaging has been widely used in diagnostic imaging for general checkup in clinical practice, especially in detection and diagnosis of brain diseases. However, brain MR imaging has some lacks such as noise, intensity inhomogeneity, low contrast, and partial volume effect , which brings serious obstacles to segment the brain MR images. The study of J. Song and Z. Zhang presented a novel and more robust method to noise in the brain magnetic resonance imaging, together with a more effective estimation method of the bias field.

Automatic segmentation of different images is one of the most important topics in medicine. L. Cao et al. discuss application of Random Forests Stacks for automatic segmentation of pathological glomerular basement membranes in TEM images. It allows faster observation of morphological changes, reducing manual and laborious work of specialists. Another exercise in image processing is discussed in J. Song and Z. Zhang. Improvements for brain tissue segmentation and bias field correction of MR images are proposed and evaluated. The results are promising and potentially can deal with noise in brain MR images.

In conventional radiotracer and drug development, poor bench-to-bedside translation often results due to the differences between in vitro and in vivo conditions [8]. The study by Y.-H. Nai and H. Watabe evaluated the feasibility of extending the amyloid-validated screening methodology to support the development of tau PET radiotracers, where more challenges like off-target binding exist. This is the first in silico method investigated, which uses the physicochemical and pharmacological properties of the compounds to support tau PET radiotracers developments. 22 PET radiotracers reported to bind to tau proteins were investigated, including 9 clinically applied and tau-focused radiotracers. The study supported the use of the screening methodology in radiotracer development by allowing comparison of candidate radiotracers with clinically applied radiotracers based on SUVR, with respect to binding to a single target, and provides some insights to guide the development of in silico models in supporting the development of tau radiotracers.

Automatic identification of relevant biomarkers is one of the important steps towards personalized treatment. B. Haller et al. evaluate applicability of a number of methods, for example, Cox regression with linear interaction, Multivariable Fractional Polynomials for Interaction (MFPI), Local Partial Likelihood Bootstrap (LPLB), and the Subpopulation Treatment Effect Pattern Plot (STEPP), for biomarker identification. Experiments on randomized clinical trials show that the Cox regression works best when interactions are monotonous and the number of events is low. When complexity increases, MFPI and LPLB outperform other methods. The authors recommend application of statistical methods developed for assessment of interactions between continuous biomarkers and treatment instead of arbitrary or data-driven categorization of continuous covariates.

The study of D. Liu et al. applies similarity measures of single and interval valued neutrosophic sets based on Euclidean distance for diagnostics. Novel theoretical model is developed in the paper, and its effectiveness is demonstrated on generalized diagnosis, showing that it performs well in solving a multiple criteria decision process. The proposed similarity measures were applied to medical diagnosis decision problems, and a number of examples were used to illustrate the feasibility and effectiveness of the proposed similarity measure.

Coreference resolution is a challenging part of natural language processing (NLP) with applications in machine translation, semantic search, and other information retrieval and decision support systems. V. Žitkus et al. presented a method for coreference resolution in the Lithuanian language and its application for processing e-health records from a hospital reception. The novelty of their proposed method is the ability to process coreferences with minimal linguistic resources, which is important in linguistic applications for rare and endangered languages. Their experimental results have shown that coreference resolution is applicable to the development of NLP-powered online healthcare services in Lithuania.

Computer-aided models for mammographic breast cancer diagnosis (MBCD) have been explored for over thirty years [9]. The study of L. Zou et al. dedicated to the technique of CNN applied in a specific application of MBCD, and it aims to provide clues on how to use CNN in intelligent diagnosis. This study is restricted to peer-reviewed journal publications, and consequently, technical details and pros and cons of each model can be delivered. Furthermore, based on how to use CNN techniques, the MBCD models are broadly categorized into three groups. One is to design shallow models or to modify existing models for decreased time cost and medical instances for training; another is to make the best use of a pretrained CNN model by transfer learning and parameter fine-tuning; and the third is to take advantage of CNN models for feature extraction, while the differentiation between malignant and benign lesions is based on machine learning classifiers. At last, findings,

challenges, and limitations are summarized, and some clues on the future work are also given. At present, the design and use of CNN-based MBCD is at its early stage and result-oriented. The ultimate goal of using deep learning tools is to facilitate clinical practice. This review provides benefits to scientific researchers, industrial engineers, and those who are devoted to intelligent cancer diagnosis.

The past application of mathematical models in medicine also has been proven useful in cardiovascular diseases (CVDs). The study of O. Saidi et al. aimed to describe a comprehensive Markov model based on both a probabilistic multivariate approach and simple linear regression meta-modeling using the model to evaluate the effects of increases in uptake of stroke treatments, lifestyle changes, and primary prevention among the Tunisian population aged 35–94 years in 2025. It examined three interventions: improved medical treatments in the acute phase, secondary prevention of stroke by increasing the prescribing of statins, and primary prevention aiming to reduce salt intake.

Type-1 diabetes is a condition caused by the lack of insulin hormone, which leads to an excessive increase in blood glucose level. The glucose kinetics process is difficult to control due to its complex and nonlinear nature and with state variables that are difficult to measure. P. D. Ngo et al. proposed a method for automatically calculating the basal and bolus insulin doses for patients with type-1 diabetes using reinforcement learning with a feedforward controller. The proposed controller also improved the blood glucose responses and prevented hypoglycemia condition. Simulation of the control system in different uncertain conditions provided insights on how the inaccuracies of carbohydrate counting and meal-time reporting affect the performance of the control system. As a conclusion, the proposed controller is an effective tool for reducing postmeal blood glucose rise and for countering the effects of external known events such as meal intake and maintaining blood glucose at a healthy level under uncertainties.

In the paper of B. H. Lichae et al., the fractional-order differential model of HIV-1 infection of CD4+ T-cells with the effect of drug therapy has been introduced. There are three components: uninfected CD4+ T-cells, x, infected CD4+ T-cells, y, and density of virions in plasma, z. The aim is to gain numerical solution of this fractional-order HIV-1 model by the Laplace Adomian decomposition method (LADM). The solution of the proposed model has been achieved in a series form. Moreover, to illustrate the ability and efficiency of the proposed approach, the solution has been compared with the solutions of some other numerical methods. The Caputo sense has been used for fractional derivatives.

Beds are key, scarce medical resources in hospitals. The study of L. Luo et al. aimed to balance the utilization of existing beds in a large tertiary hospital in China. The author developed a data-driven hybrid three-stage framework incorporating data analysis, simulation, and mixed integer programming to minimize the gaps in bed occupancy rates (BOR) among different departments. The first stage is to calculate the length of stay (LOS) and BOR of each department and identify the departments that need to allocate beds. In the second stage were used a fitted arrival distribution and median LOS as the input to a generic simulation model. In the third stage was built a mixed integer programming model using the results obtained in the first two stages to generate the optimal bed allocation strategy for different departments. The case study demonstrated the effectiveness of the proposed data-driven hybrid three-stage framework and provides hospital bed policy makers with a feasible solution for bed allocation.

Mathematical models are often used and prove their applicability for optimal decision-making. They are also useful to derive estimates of rare or future events from recorded intermediate points. When developing models, decisions are needed about the appropriate level of complexity to be represented and about model structure and assumptions.

Conflicts of Interest

The editors declare no conflicts of interest.

Acknowledgments

We would like to express our gratefulness to Prof. Katarzyna Kolasa for participation in the preparation of the call materials and participation in guest editing some manuscripts. Also, we would like to thank all researchers who submitted their research work and reviewers who made very important comments and suggestions for authors to improve their manuscripts.

Giedrius Vanagas
Tomas Krilavičius
Ka Lok Man

References

[1] A. X. Costa, S. A. Ridley, A. K. Shahani, P. R. Harper, V. De Senna, and M. S. Nielsen, "Mathematical modelling and simulation for planning critical care capacity," *Anaesthesia*, vol. 58, no. 4, pp. 320–327, 2003.

[2] R. B. Chambers, "The role of mathematical modeling in medical research: "research without patients?"," *The Ochsner Journal*, vol. 2, no. 4, pp. 218–223, 2000.

[3] M. Calder, C. Craig, D. Culley et al., "Computational modelling for decision-making: where, why, what, who and how," *Royal Society Open Science*, vol. 5, no. 6, article 172096, 2018.

[4] G. P. Garnett, S. Cousens, T. B. Hallett, R. Steketee, and N. Walker, "Mathematical models in the evaluation of health programmes," *The Lancet*, vol. 378, no. 9790, pp. 515–525, 2011.

[5] W. Crown, N. Buyukkaramikli, M. Y. Sir et al., "Application of constrained optimization methods in health services research: report 2 of the ISPOR Optimization Methods Emerging Good Practices Task Force," *Value in Health*, vol. 21, no. 9, pp. 1019–1028, 2018.

[6] Y. Zheng, F. Pan, and S. Sorensen, "Modeling treatment sequences in pharmacoeconomic models," *PharmacoEconomics*, vol. 35, no. 1, pp. 15–24, 2017.

[7] L. Echazu and D. Nocetti, "Priority setting in health care: disentangling risk aversion from inequality aversion," *Health Economics*, vol. 22, no. 6, pp. 730–740, 2013.

[8] Y.-H. Nai, M. Shidahara, C. Seki, and H. Watabe, "Biomathematical screening of amyloid radiotracers with clinical usefulness index," *Alzheimer's & Dementia: Translational Research & Clinical Interventions*, vol. 3, no. 4, pp. 542–552, 2017.

[9] N. I. R. Yassin, S. Omran, E. M. F. El Houby, and H. Allam, "Machine learning techniques for breast cancer computer aided diagnosis using different image modalities: a systematic review," *Computer Methods and Programs in Biomedicine*, vol. 156, pp. 25–45, 2018.

Hindawi
Computational and Mathematical Methods in Medicine
Volume 2019, Article ID 7037230, 15 pages
https://doi.org/10.1155/2019/7037230

Research Article

A Simulation Study Comparing Different Statistical Approaches for the Identification of Predictive Biomarkers

Bernhard Haller, Kurt Ulm, and Alexander Hapfelmeier

Technical University of Munich, School of Medicine, Institute of Medical Informatics, Statistics and Epidemiology, Ismaninger Str. 22, 81675 Munich, Germany

Correspondence should be addressed to Bernhard Haller; bernhard.haller@tum.de

Received 1 February 2019; Accepted 22 May 2019; Published 13 June 2019

Guest Editor: Tomas Krilavičius

Identification of relevant biomarkers that are associated with a treatment effect is one requirement for adequate treatment stratification and consequently to improve health care by administering the best available treatment to an individual patient. Various statistical approaches were proposed that allow assessing the interaction between a continuous covariate and treatment. Nevertheless, categorization of a continuous covariate, e.g., by splitting the data at the observed median value, appears to be very prevalent in practice. In this article, we present a simulation study considering data as observed in a randomized clinical trial with a time-to-event outcome performed to compare properties of such approaches, namely, Cox regression with linear interaction, Multivariable Fractional Polynomials for Interaction (MFPI), Local Partial-Likelihood Bootstrap (LPLB), and the Subpopulation Treatment Effect Pattern Plot (STEPP) method, and of strategies based on categorization of continuous covariates (splitting the covariate at the median, splitting at quartiles, and using an "optimal" split by maximizing a corresponding test statistic). In different scenarios with no interactions, linear interactions or nonlinear interactions, type I error probability and the power for detection of a true covariate-treatment interaction were estimated. The Cox regression approach was more efficient than the other methods for scenarios with monotonous interactions, especially when the number of observed events was small to moderate. When patterns of the biomarker-treatment interaction effect were more complex, MFPI and LPLB performed well compared to the other approaches. Categorization of data generally led to a loss of power, but for very complex patterns, splitting the data into multiple categories might help to explore the nature of the interaction effect. Consequently, we recommend application of statistical methods developed for assessment of interactions between continuous biomarkers and treatment instead of arbitrary or data-driven categorization of continuous covariates.

1. Introduction

For medical decision making, predictive biomarkers play an important role for various diseases [1–4]. A biomarker is called "predictive," if the difference between the effectiveness of two or more treatment options depends on the value of that biomarker [5, 6]. In the presence of a qualitative biomarker-treatment interaction [7], i.e., when the choice of the "optimal" treatment for a given patient depends on the patient's value of a certain biomarker, the biomarker can be used for treatment stratification [8]. Biomarkers used in clinical practice for treatment stratification are, e.g., the human epidermal growth factor receptor 2 (HER-2) status for breast cancer patients [9, 10] or presence of epidermal growth factor receptor (EGFR) mutation in non-small cell lung cancers (NSCLC) [11]. Consequently, the identification of biomarkers that allow prediction of the treatment effect when different treatment options are available is essential to increase clinical decision making in the sense of a stratified or personalized medicine [12].

In practice, investigation of such treatment effect heterogeneity over the range of a certain biomarker in data obtained from a randomized clinical trial is often performed by subgroup analyses [13], where the difference in outcome between the study groups, quantified, e.g., by a hazard ratio, an odds ratio, or a mean difference, is estimated for patient subgroups with similar characteristics [14] and compared using a statistical test for interaction, which can be

performed by including the product of the biomarker and the variable indicating treatment allocation in an appropriate regression model [15, 16]. While this procedure is intuitive and straightforward for categorical variables, e.g., gender or presence of comorbidities as diabetes, investigation of treatment effect heterogeneity with respect to continuous variables, e.g., age or continuously measured blood parameters, requires categorization of the variable, when subgroup analyses are to be performed. Such categorization of continuous variables was criticized due to loss of information leading to a loss of power for detection of true interactions, implication of biological implausible effects, and lack of comparability of results from different studies [17, 18]. Therefore, various approaches were proposed in the literature that allow to model and test for treatment effect heterogeneity over the range of a continuous variable that do not require categorization of the variable [19–21].

In this article, we describe a simulation study comparing different approaches for detection of an interaction between one (predefined) continuous covariate and treatment. We simulated data as they would be expected to be collected in a randomized clinical trial intended to compare efficacy of two treatment groups or of treatment versus placebo. Consequently, patients are allocated randomly into one of two treatment arms and the distribution of the variable of interest (often referred to as a biomarker [22]) is expected to be the same for both treatment groups. As most predictive biomarkers were identified for treatment of cancer [23], a time-to-event outcome is considered, as typically overall survival or progression-free survival is considered as primary endpoint in randomized phase III oncological trials [24]. Results obtained by methods relying on categorization of the continuous variable as well as methods that do not use such categorization were investigated. We considered a method splitting the continuous biomarker at its median to determine two subgroups for further analysis, the use of four subgroups determined by splitting data at the quartiles, and use of an "optimal" cutoff value found by maximization of the Wald statistics of the interaction term in a Cox regression model. Additionally, we applied the Subpopulation Treatment Effect Pattern Plot (STEPP) approach that incorporates overlapping subgroups [25], the Cox regression model [26] assuming a linear covariate-treatment interaction term, the Multivariable Fractional Polynomials for Interaction (MFPI) approach that incorporates nonlinear transformations for the interaction term [19], and the Local Partial-Likelihood Bootstrap (LPLB) that uses local estimates of the treatment effect at different values of the variable of interest [27]. Different scenarios with absence and presence of biomarker-treatment interactions were investigated in order to estimate and compare type I error probability and statistical power of the different approaches under the given scenarios. Sample size and censoring distribution are varying to investigate the impact of these characteristics on the outcome.

The article is organized as follows. In Section 2, the simulation study is described. The different methods used for identification of a biomarker-treatment interaction are shortly introduced in Section 2.1, and references to original articles and further articles including more detailed descriptions of the considered methods are given. The setting of the simulation study and the relevant aspects that were varied are described in Section 2.2. Results of the simulation study, namely, observed type I error probabilities for scenarios with no true biomarker-treatment interactions and estimates for statistical power for scenarios with truly present biomarker-treatment interactions, are presented in Section 3. A discussion of the results with concluding remarks and strengths and limitations of our simulation study is given in Section 4.

2. Methods

The methods investigated in the simulation study are described in Section 2.1. Details on the settings used in the simulation study and the data generating process are given in Section 2.2. Data were generated and analysed using the statistical software R [28]. Cox regression was performed using the function *coxph* provided in the R library *survival* [29, 30]. For convenience, the continuous covariate of interest will be called "biomarker" and denoted as Z throughout the section. Treatment allocation will be represented by a binary treatment variable T with $T = \{0, 1\}$, where $T = 1$ represents, e.g., an experimental treatment and $T = 0$ a placebo control or standard treatment. As it appears to be the most relevant effect size in practice, homogeneity of the hazard ratio between the study groups in regard to the biomarker of interest was investigated. For all statistical tests, a significance level of $\alpha = 5\%$ was used. Exact 95% confidence intervals for rejection probabilities were calculated.

2.1. Methods Used to Test for a Biomarker-Treatment Interaction

2.1.1. Median Split. In many applications investigating treatment-effect heterogeneity in regard to a continuous biomarker, individuals are divided into two subgroups of equal size. This is achieved by splitting the data at the median of the biomarker Z. This procedure will be denoted as "Median split" in this article. A binary indicator variable that is assigned the value of one if the biomarker value is above or equal to the observed median and zero else is derived. To test for biomarker-treatment interaction, a Cox regression model with this indicator variable, the binary treatment indicator, and their product (the interaction term) is fitted to the data. The p value of the Wald test for the interaction term was used to decide whether the null hypothesis of no biomarker-treatment interaction can be rejected on the prespecified significance level of $\alpha = 5\%$.

2.1.2. Quartile Split. As an alternative approach, individuals were divided into four subgroups with splits at the corresponding quartiles of the biomarker of interest ("Quartile split"). The categorical variable indicating the corresponding subgroup was used as a dummy coded nominal independent variable in a Cox regression model. Additionally, the binary

treatment indicator and an interaction term between the dummy coded categorical variable indicating the biomarker quartile and treatment were included. A likelihood ratio test with three degrees of freedom provided in the R library *car* [31] was performed to test for presence of a biomarker-treatment interaction.

2.1.3. "Optimal" Split. For this approach, henceforth called "Optimal split", an "optimal" cutoff value for splitting the continuous variable into two subgroups was determined in a first step. Of all possible cutoff values (restricted to a minimum subgroup size of 10% of the overall sample size), the one leading to the largest value of the Wald statistic for the interaction term between the dichotomized biomarker and treatment in a Cox regression model also including the corresponding main effects as independent variables was used to define the subgroups for assessment of treatment effect heterogeneity. In a second step, these subgroups were treated as if they were predefined subgroups, and assessment of a biomarker-treatment interaction was performed as described for the Median split procedure in Section 2.1.1.

2.1.4. Subpopulation Treatment Effect Pattern Plot (STEPP) Method. The Subpopulation Treatment Effect Pattern Plot ("STEPP") method was proposed by Bonetti and Gelber [25]. In the STEPP procedure, heterogeneity of the treatment effect over the range of a biomarker of interest is assessed by estimating the effect in multiple overlapping subgroups. Additionally, methods for estimation of simultaneous confidence intervals and for testing the null hypothesis of no biomarker-treatment interaction were developed [25, 32]. Two different versions, a "tail-oriented" and a "sliding window" approach, were proposed initially. In our simulation study, we used the "sliding window" approach, where the number of individuals within two consecutive subgroups is held (approximately) constant by adding and eliminating the same number of observations and the number of observations overlapping between two consecutive subgroups is chosen a priori. For our analysis, the number of individuals within each subgroup was chosen to be $n/5$ and the number of overlapping individuals to be $n/10$. So, the subgroup sizes were 50, 100, and 200 for scenarios with 250, 500, and 1000 observations, and the number of overlapping observations was 25, 50, and 100, respectively. This led to a total number of nine subgroups considered irrespective of the sample size. A test on homogeneity of the hazard ratio over all subgroups was performed to test for a biomarker-treatment interaction. A permutation test as recommended in [32] was conducted using 500 permutations for each simulated dataset. Further details on the STEPP procedure can be found in [33, 34]. For application of STEPP, the R library *stepp* [35] was used.

2.1.5. Cox Regression Model with Linear Interaction. To avoid categorization of the continuous biomarker of interest Z, a Cox regression model [26] assuming a linear interaction between Z and treatment T was considered. This procedure implies that the log-hazard ratio between the study groups is linearly associated with the biomarker value. The main effects of the biomarker Z, the treatment group T, and their product $Z \times T$ were used as independent variables in a Cox regression model. The p value of the Wald test for the interaction term was considered to decide on rejection of the null hypothesis of no biomarker-treatment interaction. This procedure will be called "Cox model with linear interaction" or shortly "Cox (linear Int.)" throughout the article.

2.1.6. Multivariable Fractional Polynomials for Interaction (MFPI). To allow for nonlinear interaction terms, Royston and Sauerbrei proposed the Multivariable Fractional Polynomials for Interaction ("MFPI") approach [19], which is based on the Multivariable Fractional Polynomials (MFP) approach presented by Royston and Altman [36]. A nonlinear transformation is considered for the biomarker of interest, and a model including main effects of treatment and the transformed biomarker as well as their interaction is compared to a model including only the corresponding main effects. In the original publication, a model with two polynomial transformations p_1 and p_2 (FP2) out of the set $p \in \{-2, -1, -0.5, 0, 0.5, 1, 2, 3\}$, where $p = 0$ indicates a logarithmic transformation, was described. Identification of the best transformation was proposed to be determined in the model without an interaction term by finding the combination of transformations providing the highest (log-) likelihood value (later called flex1 approach). Based on the results of a simulation study [37, 38] considering a continuous outcome, an alternative approach with only one polynomial transformation (FP1) and separate determination of the best transformation in the model with and without interaction (flex3, potentially leading to non-nested models) was recommended. We applied both approaches, the FP2-flex1 and the FP1-flex3 approach, to our simulated data. To test for presence of a biomarker-treatment interaction, likelihood ratio tests comparing the models with and without interaction terms were performed for both strategies.

2.1.7. Local Partial-Likelihood Bootstrap (LPLB). Another method proposed in the literature for modelling nonlinear interaction effects between a continuous biomarker and treatment is the Local Partial-Likelihood Estimation proposed by Fan et al. [21]. Liu et al. developed a bootstrapping method, called Local Partial-Likelihood Bootstrap ("LPLB"), that allows to test for the presence of an overall treatment effect and to test whether the treatment effect is heterogeneous over the range of a continuous biomarker [27]. In the LPLB approach, linear approximations of the treatment effect estimate at a given biomarker value are obtained by first-order Taylor approximations using weighted data in the local neighbourhood of the biomarker value of interest. The proposed bootstrap test makes use of the residual bootstrap [39]. The obtained local estimates of the log-hazard ratio are compared to the estimate obtained from a standard Cox regression model assuming a constant treatment effect over the biomarker range. The maximum observed standardized

difference of the local estimates to the constant log-hazard ratio is considered as test statistic. For our simulation study, we used the R library *lplb* [40] to apply the LPLB procedure. Local estimates were obtained for every decile of the empirical biomarker distribution. A bandwidth, indicating the amount of observations in the neighbourhood used for local estimation, of 0.2 was used and an Epanechnikov kernel was considered for weighting. Five hundred bootstrap samples were drawn for each generated dataset.

2.2. Simulation Settings. Data were generated to mimic data observed in a randomized clinical trial primarily intended for comparison of two different treatment options. Consequently, simulated individuals were randomly allocated to one of two treatment groups ($T = \{0, 1\}$) with equal probability for each group. The covariate of interest was randomly generated from a uniform distribution with a minimum value of zero and a maximum value of one. Event times were drawn from an exponential distribution with the individual hazard rate depending on the allocated treatment group and the drawn covariate value as described in Section 2.2.1. Censoring times were drawn from exponential distributions with rates as described in Section 2.2.3. The lower value of the two time variables was allocated as observed time and an observed event was indicated, if the drawn event time was smaller than the corresponding censoring time, and a censored observation was indicated else.

2.2.1. Functional Form. In order to estimate the type I error probability and the statistical power for detection of truly present interaction effects associated with the different approaches, different scenarios were investigated. Overall, six different functional forms were considered, two without presence of an interaction effect (Scenarios 1 and 2) and four scenarios considering different shapes of interaction terms (Scenarios 3 to 6). All scenarios are visualized in Figure 1, showing the hazard rates used for simulation of the event times in dependence of the biomarker value (dashed black and solid grey line and black scale/axis) and the resulting hazard ratios (using a logarithmic scale) between the treatment groups (red line and scale/axis).

Scenario 1. No associations between treatment and risk for an event and between the biomarker of interest and risk for an event are present; the hazard rate for each individual was set to 1, irrespective of treatment group and biomarker value (Figure 1(a)).

$$\lambda(x \mid z, T = 0) = \lambda(x \mid z, T = 1) = 1, \tag{1}$$

where $\lambda(x)$ indicates the hazard rate as a function of time. Consequently, the hazard ratio between the groups is 1 for all covariate values, indicating no biomarker-treatment interaction.

$$\mathrm{HR}(z) = 1. \tag{2}$$

Scenario 2. In the second scenario, the hazard rate depends on the value of the biomarker Z for both treatment groups, but the hazard ratio between the treatment groups is the same for all biomarker values, so no biomarker-treatment interaction is present (Figure 1(b)).

$$\begin{aligned} \lambda(x \mid z, T = 0) &= 0.5 \exp\left((2z - 1)^2\right), \\ \lambda(x \mid z, T = 1) &= \exp\left((2z - 1)^2\right), \end{aligned} \tag{3}$$

leading to a hazard ratio of two for all values of Z.

$$\mathrm{HR}(z) = 2. \tag{4}$$

Scenario 3. In the third scenario, a true linear interaction (on the log-hazard scale) between the biomarker of interest and treatment is present, leading to a hazard ratio between the treatment groups of one for a biomarker value of $Z = 0$ and to a hazard ratio of $\exp(0.75) = 2.12$ for a value of $Z = 1$.

$$\begin{aligned} &\lambda(x \mid z, T = 0) = 0.7 \exp(0.5z), \\ &\lambda(x \mid z, T = 1) = 0.7 \exp(0.5z + 0.75z) = 0.7 \exp(1.25z). \end{aligned} \tag{5}$$

The hazard ratio increases linearly on a logarithmic scale.

$$\mathrm{HR}(z) = \exp(0.75z). \tag{6}$$

The scenario is displayed in Figure 1(c)).

Scenario 4. In the fourth scenario, a true qualitative biomarker-treatment interaction, with a higher risk for an event under treatment $T = 0$ as compared to treatment $T = 1$ for patients with a small value of Z and a higher risk for an event under $T = 1$ for individuals with a large value of Z, is considered (Figure 1(d)). The hazard ratio is monotonically, but not linearly increasing over the biomarker range.

$$\begin{aligned} \lambda(x \mid z, T = 0) &= 0.9, \\ \lambda(x \mid z, T = 1) &= 0.35 \exp\left(1.7\sqrt{z} - 0.2z^2 - 0.3z\right). \end{aligned} \tag{7}$$

The qualitative interaction is indicated by a hazard ratio being smaller than one for values of $Z < 0.424$ and larger than one for $Z > 0.424$.

$$\begin{aligned} \mathrm{HR}(z) &= \frac{0.35 \exp\left(1.7\sqrt{z} - 0.2z^2 - 0.3z\right)}{0.9} \\ &= 0.389 \exp\left(1.7\sqrt{z} - 0.2z^2 - 0.3z\right). \end{aligned} \tag{8}$$

Scenario 5. In Scenario 5, the risk for an event is similar under both treatments for most of the individuals, but the risk increases under treatment $T = 1$ for large values of Z (Figure 1(e)).

$$\begin{aligned} \lambda(x \mid z, T = 0) &= 0.9, \\ \lambda(x \mid z, T = 1) &= 0.9 + 1.75z^8. \end{aligned} \tag{9}$$

Consequently, the hazard ratio is close to one for small and moderate values of Z but increases for large values. For $Z = 1$, the hazard ratio reaches a value of 2.94.

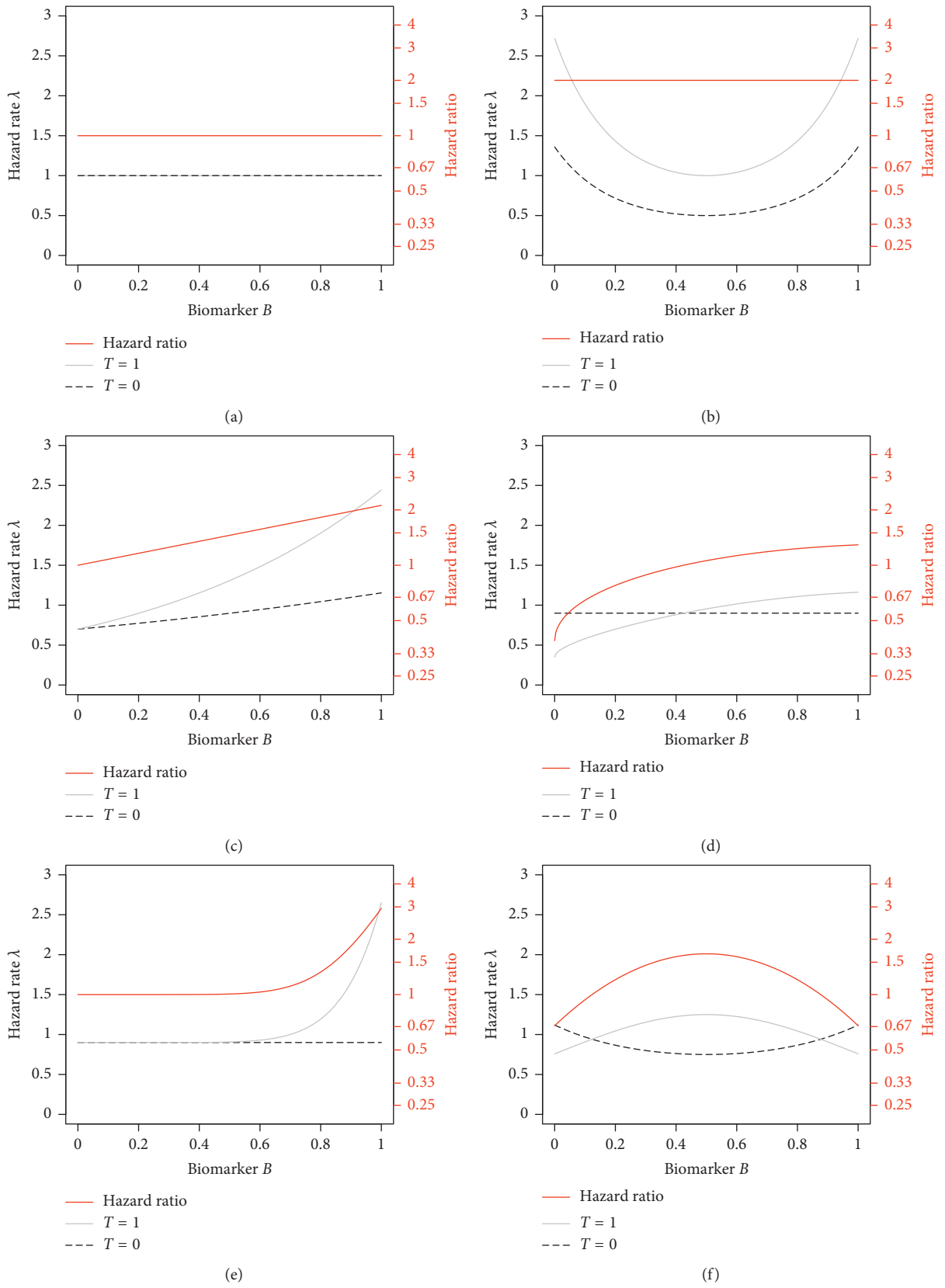

FIGURE 1: Scenarios used in the simulation study for comparison of statistical methods. In scenarios 1 and 2 (a, b), data are generated under the null hypothesis of no biomarker-treatment interaction. In scenarios 3 to 6, which are illustrated in (c) to (f), the hazard ratio (illustrated on a log-scale by the red line) depends on the biomarker value, so biomarker-treatment interactions are present.

$$\mathrm{HR}(z) = 1 + \frac{1.75z^8}{0.9}. \quad (10)$$

Scenario 6. In the sixth scenario, the hazard ratio for group $T = 0$ depending on Z follows a U-shape, while the hazard ratio for $T = 1$ is inversely U-shaped (Figure 1(f)).

$$\lambda(x \mid z, T = 0) = 0.75 \exp\left(0.4(2z-1)^2\right),$$
$$\lambda(x \mid z, T = 1) = 1.25 \exp\left(-0.5(2z-1)^2\right). \quad (11)$$

This setting leads to a qualitative biomarker-treatment interaction with lower risks for an event under $T = 1$ for small and large values of Z and lower risks under $T = 0$, else indicated by an inversely U-shaped hazard ratio over the range of Z.

$$\mathrm{HR}(z) = \frac{5}{3} \exp\left(-0.9(2z-1)^2\right). \quad (12)$$

2.2.2. Sample Size. In order to evaluate whether properties of the methods under consideration are related to the sample size of the trial, three different settings for sample sizes were chosen. The generated datasets included 250, 500, or 1000 individuals, which appear to be typical sample sizes for randomized clinical trials.

2.2.3. Censoring Distribution. In addition to the sample size, censoring distributions were varied to produce scenarios with different numbers of observed events. Censoring times were drawn from exponential distributions with hazard rates of $\lambda_{\mathrm{cens}} = 0.3$ or $\lambda_{\mathrm{cens}} = 2$, respectively, to produce scenarios with censoring proportions of about 25% and about 67%, leading to numbers of about 188, 375, and 750 expected events for scenarios with low amount of censored observations and of 83, 167, and 333 expected events for scenarios with high amount of censored observations.

3. Results

For each of the 36 scenarios described in Section 2.2, 1000 datasets were generated and the methods presented in Section 2.1 were applied. The p value of the corresponding statistical test on biomarker-treatment interaction was saved and compared to the conventional significance level of $\alpha = 5\%$. Resulting frequencies of type I errors, i.e., proportions of simulated datasets for which a statistically significant biomarker-treatment interaction was found, although it is not present in the corresponding scenario (Scenarios 1 and 2), are shown in Figure 2 for all considered methods and are also tabulated with 95% confidence intervals in Table 1. It can be seen that for the method using the "optimal" cutpoint to define two subgroups to be compared, the probability for a false-positive result was about 50% for both scenarios simulating data under the null hypothesis, irrespective of sample size and amount of censored observations. The Multivariable Fractional Polynomial for Interaction (MFPI) procedure with the FP1-flex3 strategy also provided an increased type I error probability of about 10%. This was mainly caused by those datasets for which different polynomial transformations for the biomarker were selected for models with and without consideration of a biomarker-treatment interaction, leading to a comparison of nonnested regression models. When only simulated datasets were considered, in which the same transformations were used for the models with and without interaction term and consequently two nested models were compared, the estimated type I error probabilities ranged from 3.8% to 6.6%. Contrarily, for datasets with different chosen transformations, the null hypothesis was falsely rejected in 14.1% to 23.8% of the corresponding simulation runs. For the simulations under Scenario 2 with a low sample size of 250 observations and a high amount of censored observations, leading to an expected number of about 83 events, type I error frequencies exceeding the nominal significance level were observed for all methods.

In Figures 3 (Scenarios 3 and 4) and 4 (Scenarios 5 and 6) and in Tables 2 (Scenarios 3 and 4) and 3 (Scenarios 5 and 6), the results of the scenarios with true biomarker-treatment interaction are presented. Consequently, the frequency of rejected null hypotheses can be interpreted as an estimate for the statistical power of the methods under the corresponding settings. As the procedure using two subgroups defined by an optimal, data-driven cutpoint (Optimal split) and the MFPI (FP1-flex3) approach provided type I error probabilities relevantly exceeding the nominal level of $\alpha = 5\%$, these procedures are not considered in the comparison of statistical power and are consequently not displayed in Figures 3 and 4. Nevertheless, the results are presented in Tables 2 and 3 in italics for completeness.

For the scenario fulfilling the assumption of the standard Cox regression model with a linear interaction term (Scenario 3), the Cox model with linear interaction outperformed all the other investigated methods by achieving the highest observed statistical power (Figures 3(a) and 3(b) and Table 2). The MFPI (FP2-flex1) approach performed slightly better than the approach using two subgroups defined by a split at the median of the variable when the number of expected events was large, but for the scenario with 1000 observations and a low amount of censored observations, the observed power was about 10 percentage points lower for these methods as compared to the Cox regression model with an interaction term considering the biomarker as continuous variable (Cox model with linear interaction: 83.8%; MFPI (FP2-flex1): 74.7%; Median split: 70.2%). The method splitting the data into four subgroups (Quartile split), the STEPP, and the LPLB performed worse than the other approaches.

In Scenario 4, considering a situation with a slightly nonlinear interaction, the Cox regression model considering the continuous biomarker performed best again, followed (at least for scenarios with a large number of events) by the MFPI (FP2-flex1) approach. For small to moderate event numbers, the methods relying on categorization of the data (Median split and Quartile split) performed similarly to MFPI (FP2-flex1). With the chosen

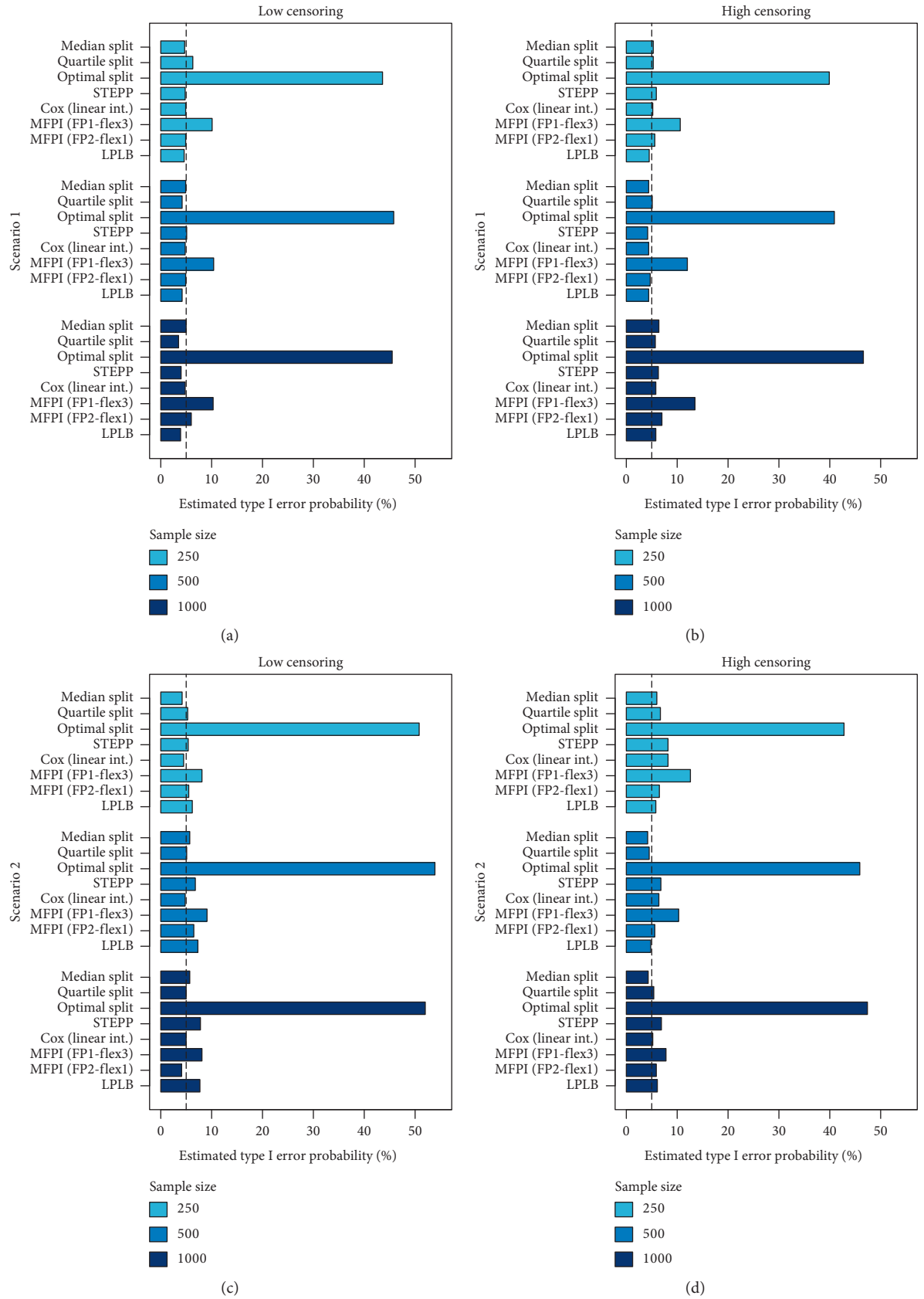

Figure 2: Results of scenarios simulated under the null hypothesis of no biomarker-treatment interaction. Bars represent relative frequencies of falsely rejected null hypotheses.

Table 1: Estimated type I error probabilities with exact 95% confidence intervals (in brackets) for Scenarios 1 and 2 for all investigated methods.

		$n = 250$		$n = 500$		$n = 1000$	
		Low cens.	High cens.	Low cens.	High cens.	Low cens.	High cens.
Scenario 1	Median split	4.7% (3.5–6.2%)	5.3% (4.0–6.9%)	4.9% (3.6–6.4%)	4.4% (3.2–5.9%)	5.0% (3.7–6.5%)	6.4% (5.0–8.1%)
	Quartile split	6.3% (4.9–8.0%)	5.3% (4.0–6.9%)	4.2% (3.0–5.6%)	5.1% (3.8–6.7%)	3.5% (2.4–4.8%)	5.7% (4.3–7.3%)
	Optimal split	43.6% (40.5–46.7%)	39.9% (36.8–43.0%)	45.8% (42.7–48.9%)	40.9% (37.8–44.0%)	45.5% (42.4–48.6%)	46.6% (43.5–49.7%)
	STEPP	4.8% (3.6–6.3%)	5.9% (4.5–7.5%)	5.1% (3.8–6.7%)	4.2% (3.0–5.6%)	4.0% (2.9–5.4%)	6.3% (4.9–8.0%)
	Cox (linear int.)	4.9% (3.6–6.4%)	5.2% (3.9–6.8%)	4.8% (3.6–6.3%)	4.4% (3.2–5.9%)	4.8% (3.6–6.3%)	5.8% (4.4–7.4%)
	MFPI (FP1-flex3)	10.1% (8.3–12.1%)	10.6% (8.8–12.7%)	10.4% (8.6–12.5%)	12.0% (10.1–14.2%)	10.3% (8.5–12.4%)	13.5% (11.4–15.8%)
	MFPI (FP2-flex1)	4.9% (3.6–6.4%)	5.6% (4.3–7.2%)	4.9% (3.6–6.4%)	4.7% (3.5–6.2%)	6.0% (4.6–7.7%)	7.0% (5.5–8.8%)
	LPLB	4.6% (3.4–6.1%)	4.5% (3.3–6.0%)	4.2% (3.0–5.6%)	4.4% (3.2–5.9%)	3.9% (2.8–5.3%)	5.8% (4.4–7.4%)
Scenario 2	Median split	4.2% (3.0–5.6%)	6.0% (4.6–7.7%)	5.7% (4.3–7.3%)	4.2% (3.0–5.6%)	5.7% (4.3–7.3%)	4.3% (3.1–5.7%)
	Quartile split	5.3% (4.0–6.9%)	6.7% (5.2–8.4%)	5.1% (3.8–6.7%)	4.5% (3.3–6.0%)	5.0% (3.7–6.5%)	5.4% (4.1–7.0%)
	Optimal split	50.8% (47.7–53.9%)	42.8% (39.7–45.9%)	53.9% (50.8–57.0%)	45.9% (42.8–49.0%)	52.0% (48.9–55.1%)	47.4% (44.3–50.5%)
	STEPP	5.4% (4.1–7.0%)	8.2% (6.6–10.1%)	6.8% (5.3–8.5%)	6.8% (5.3–8.5%)	7.8% (6.2–9.6%)	6.9% (5.4–8.7%)
	Cox (linear int.)	4.5% (3.3–6.0%)	8.2% (6.6–10.1%)	4.8% (3.6–6.3%)	6.4% (5.0–8.1%)	5.0% (3.7–6.5%)	5.2% (3.9–6.8%)
	MFPI (FP1-flex3)	8.1% (6.5–10.0%)	12.6% (10.6–14.8%)	9.1% (7.4–11.1%)	10.3% (8.5–12.4%)	8.1% (6.5–10.0%)	7.8% (6.2–9.6%)
	MFPI (FP2-flex1)	5.5% (4.2–7.1%)	6.5% (5.1–8.2%)	6.5% (5.1–8.2%)	5.6% (4.3–7.2%)	4.1% (3.0–5.5%)	5.9% (4.5–7.5%)
	LPLB	6.2% (4.8–7.9%)	5.8% (4.4–7.4%)	7.3% (5.8–9.1%)	4.8% (3.6–6.3%)	7.7% (6.1–9.5%)	6.1% (4.7–7.8%)

settings, the estimated power for LPLB and STEPP was smaller than for the other investigated methods (Figures 3(c) and 3(d) and Table 2).

In the rather complex Scenario 5 with an almost identical risk for an event under both treatments for most patients and an increasing difference between treatments for large values of the biomarker, the MFPI (FP2-flex1) approach performed best in scenarios with a large number of observed events. In scenarios with a high amount of censored observations, the Cox model with linear interaction performed slightly better (small to moderate sample size) or very similar (large sample size) to MFPI (FP2-flex1) (Figures 4(a) and 4(b) and Table 3). When censoring was low and sample size was large, the LPLB approach reached an observed power that was close to MFPI (FP2-flex1) and slightly better than the Cox regression model. While categorization using a Median split was much worse than the other methods for most settings under Scenario 5 (e.g., with an observed power for $n = 1000$ and low amount of censored observations of 46.6%), splitting the study population in four subgroups (Quartile split) provided results that were relevantly better than Median split (estimated power for the mentioned settings of 70.9%), but worse than MFPI (FP2-flex1) (87.5%), Cox regression with linear interaction (76.2%), or LPLB (83.4%).

In Scenario 6, the only investigated scenario with nonmonotonous hazard ratio over the range of the biomarker of interest, the Cox model with linear interaction and the procedure defining subgroups at the observed median (Median split) were not able to identify the present biomarker-treatment interaction (estimated power between 4.6% and 6.2% for Cox model with linear interaction and between 3.9% and 6.4% for Median split). The highest empirical power was observed for LPLB and the method defining four subgroups at the observed quartiles (Quartile split). STEPP and MFPI were able to identify the association between biomarker and treatment effect in a relevant amount of generated datasets but performed worse than LPLB and Quartile split (Figures 4(c) and 4(d) and Table 3).

4. Discussion

It is well known and accepted that different patients react differently to the same treatment. Consequently, for making a treatment decision, characteristics of the patient or of the disease, e.g., of a tumour, should be considered. Predictive

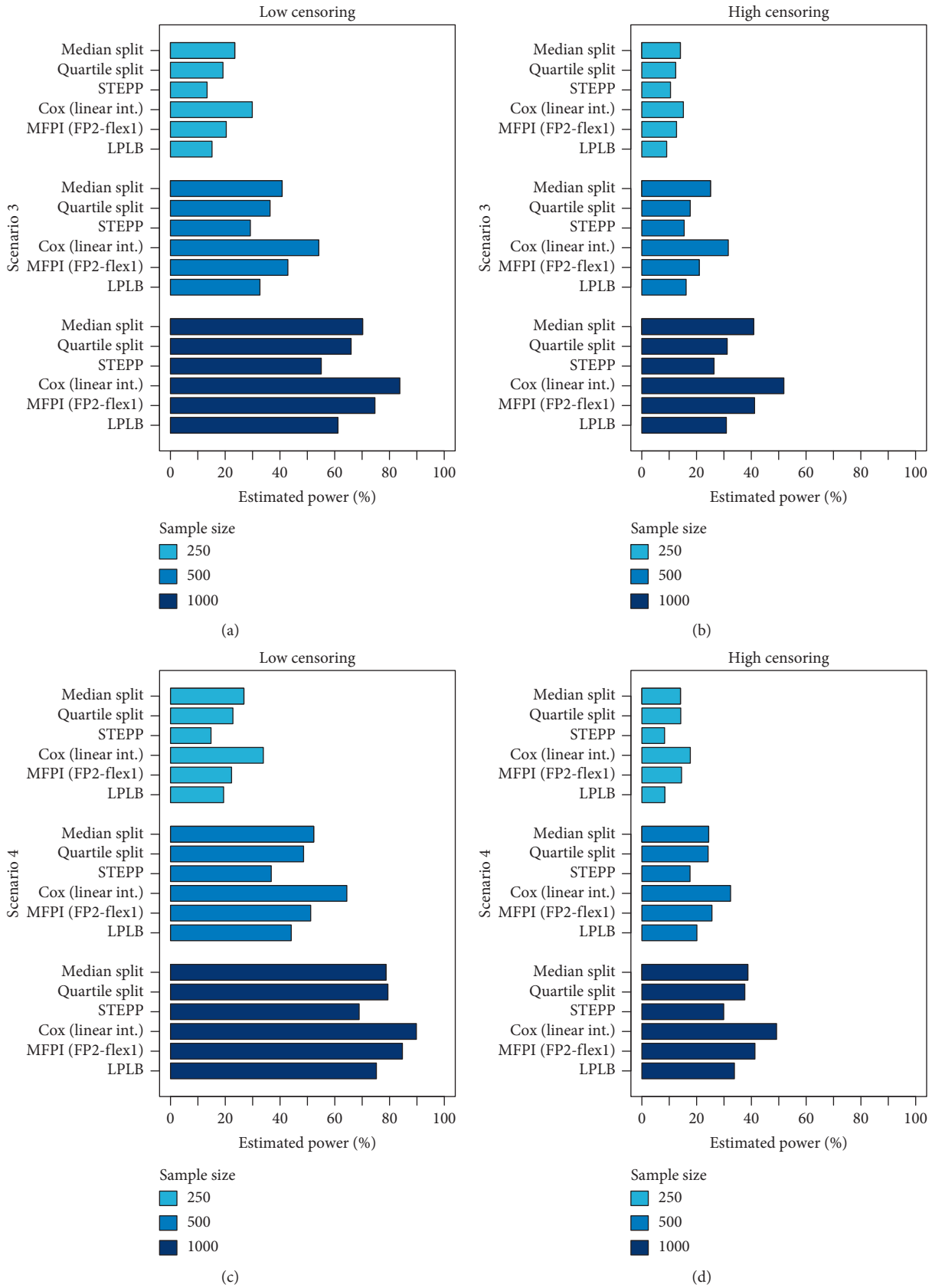

Figure 3: Results of scenarios simulated under the alternative hypothesis of a truly present biomarker-treatment interaction. Bars represent relative frequencies of correctly rejected null hypotheses.

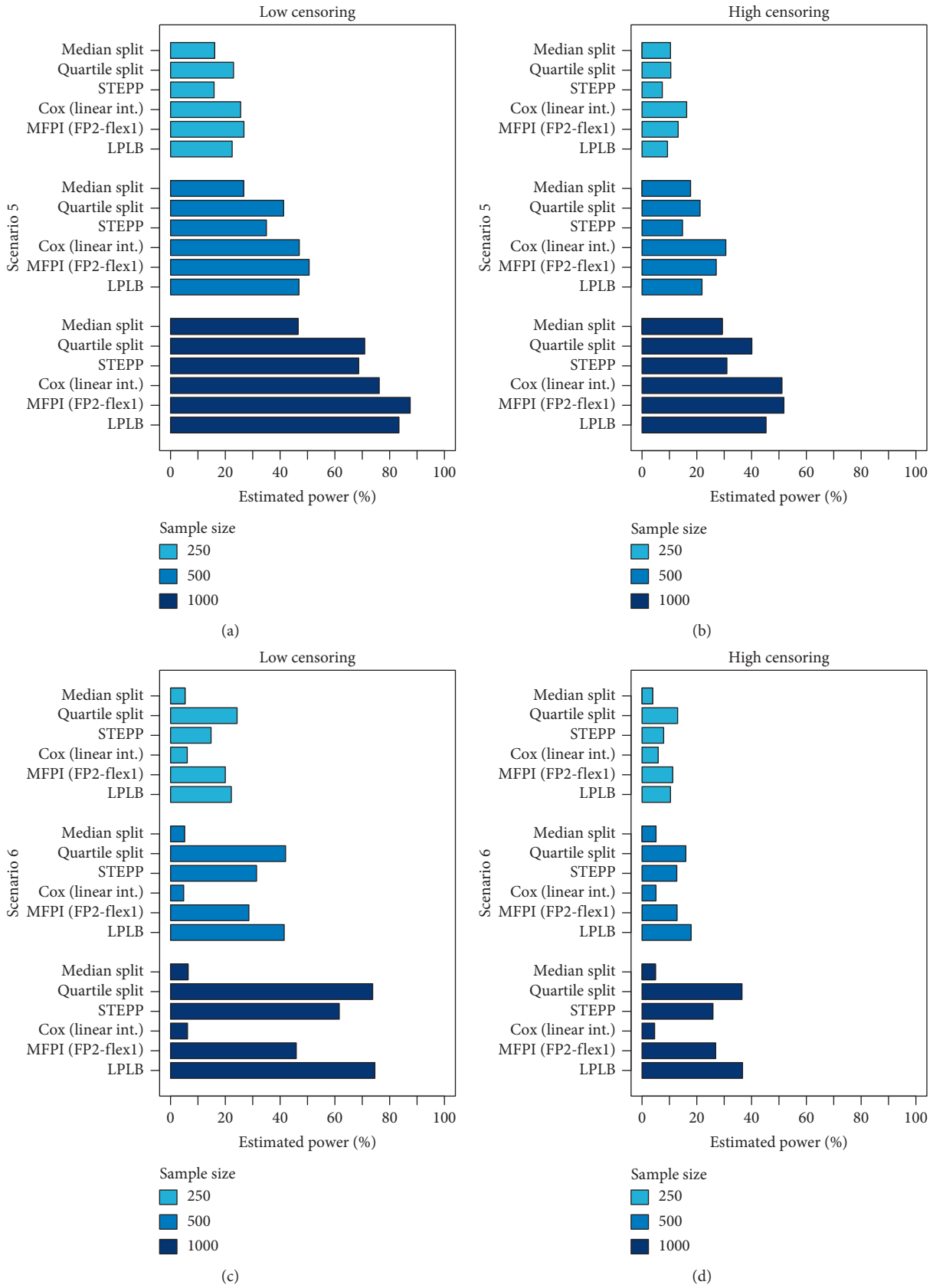

Figure 4: Results of scenarios simulated under the alternative hypothesis of a truly present biomarker-treatment interaction. Bars represented relative frequencies of correctly rejected null hypotheses.

Table 2: Estimated power with exact 95% confidence intervals (in brackets) for Scenarios 3 and 4 for all investigated methods.

		$n = 250$		$n = 500$		$n = 1000$	
		Low cens.	High cens.	Low cens.	High cens.	Low cens.	High cens.
Scenario 3	Median split	23.5% (20.9–26.3%)	14.1% (12.0–16.4%)	40.8% (37.7–43.9%)	25.1% (22.4–27.9%)	70.2% (67.3–73.0%)	40.9% (37.8–44.0%)
	Quartile split	19.2% (16.8–21.8%)	12.4% (10.4–14.6%)	36.4% (33.4–39.5%)	17.7% (15.4–20.2%)	66.0% (63.0–68.9%)	31.2% (28.3–34.2%)
	Optimal split	*71.4% (68.5–74.2%)*	*57.6% (54.5–60.7%)*	*86.4% (84.1–88.5%)*	*71.7% (68.8–74.5%)*	*97.1% (95.9–98.0%)*	*84.6% (82.2–86.8%)*
	STEPP	13.4% (11.3–15.7%)	10.5% (8.7–12.6%)	29.2% (26.4–32.1%)	15.5% (13.3–17.9%)	55.1% (52.0–58.2%)	26.4% (23.7–29.2%)
	Cox (linear int.)	29.9% (27.1–32.8%)	15.2% (13–17.6%)	54.2% (51.1–57.3%)	31.6% (28.7–34.6%)	83.8% (81.4–86.0%)	51.9% (48.8–55.0%)
	MFPI (FP1-flex3)	*30.2% (27.4–33.2%)*	*18.2% (15.9–20.7%)*	*54.2% (51.1–57.3%)*	*32.5% (29.6–35.5%)*	*82.8% (80.3–85.1%)*	*51.1% (48–54.2%)*
	MFPI (FP2-flex1)	20.4% (17.9–23.0%)	12.7% (10.7–14.9%)	42.9% (39.8–46.0%)	21.0% (18.5–23.7%)	74.7% (71.9–77.4%)	41.2% (38.1–44.3%)
	LPLB	15.2% (13.0–17.6%)	9.1% (7.4–11.1%)	32.7% (29.8–35.7%)	16.2% (14.0–18.6%)	61.2% (58.1–64.2%)	30.9% (28.0–33.9%)
Scenario 4	Median split	26.8% (24.1–29.7%)	14.1% (12.0–16.4%)	52.3% (49.2–55.4%)	24.4% (21.8–27.2%)	78.7% (76–81.2%)	38.7% (35.7–41.8%)
	Quartile split	22.8% (20.2–25.5%)	14.2% (12.1–16.5%)	48.6% (45.5–51.7%)	24.2% (21.6–27.0%)	79.4% (76.8–81.9%)	37.6% (34.6–40.7%)
	Optimal split	*77.6% (74.9–80.1%)*	*57.8% (54.7–60.9%)*	*92.3% (90.5–93.9%)*	*72.6% (69.7–75.3%)*	*99.1% (98.3–99.6%)*	*88.8% (86.7–90.7%)*
	STEPP	14.8% (12.7–17.2%)	8.3% (6.7–10.2%)	36.8% (33.8–39.9%)	17.6% (15.3–20.1%)	68.9% (65.9–71.8%)	29.9% (27.1–32.8%)
	Cox (linear int.)	33.9% (31.0–36.9%)	17.7% (15.4–20.2%)	64.4% (61.3–67.4%)	32.4% (29.5–35.4%)	89.8% (87.8–91.6%)	49.2% (46.1–52.3%)
	MFPI (FP1-flex3)	*40.4% (37.3–43.5%)*	*25.8% (23.1–28.6%)*	*72.0% (69.1–74.8%)*	*38.8% (35.8–41.9%)*	*92.4% (90.6–94.0%)*	*56.3% (53.2–59.4%)*
	MFPI (FP2-flex1)	22.3% (19.8–25.0%)	14.5% (12.4–16.8%)	51.2% (48.1–54.3%)	25.6% (22.9–28.4%)	84.7% (82.3–86.9%)	41.3% (38.2–44.4%)
	LPLB	19.4% (17.0–22.0%)	8.4% (6.8–10.3%)	44.1% (41.0–47.2%)	20.1% (17.7–22.7%)	75.2% (72.4–77.8%)	33.8% (30.9–36.8%)

Due to increased type I error probabilities, results for Optimal split and MFPI (FP1-flex3) are presented in italics.

biomarkers, i.e., variables that are associated with the treatment effect, e.g., a hazard ratio between two treatment groups, play an important role for treatment selection. Evidence, whether a biomarker is truly predictive, can only be derived from randomized trials involving patients with different values of the biomarker of interest [8]. In practice, treatment effect heterogeneity over different factors of a categorical variable or over the range of a continuous variable in data collected in a randomized clinical trial is often analysed by the means of subgroup analyses, estimating the treatment effect within patients with similar characteristics and comparing treatment effects between subgroups using a test on interaction [14]. While this procedure is straightforward for categorical variables, it relies on categorization of continuous variables. It was shown for different research questions that categorization leads to a loss of power for detection of true associations [41, 42], and the interpretation of subgroup analyses based on categorized continuous variables was often criticized due to its lack of biological plausibility and its increased chance of spurious findings [17, 18, 43]. One common approach to investigate such interactions between continuous biomarkers and treatment without categorization is the inclusion of the product of the biomarker and the treatment indicator as independent variable in a regression model assuming a linear interaction term. To allow a more flexible modelling of relationships between treatment effects and biomarker values, various methods relaxing the linearity assumption for the interaction term, e.g., the Subpopulation Treatment Effect Pattern Plot (STEPP), the Multivariable Fractional Polynomials for Interaction (MFPI) [19], or the Local Partial-Likelihood Bootstrap (LPLB) [27] approach, were developed.

Comparisons between those methods rarely exist in the literature. Royston and Sauerbrei applied the MFPI and the STEPP method to different datasets [44]. Recently, we investigated the interaction between age and treatment in a randomized trial comparing carotid artery stenting (CAS) to carotid endarterectomy (CEA) for patients with symptomatic, severe carotid artery stenosis (SPACE trial [45, 46]). In this analysis, very similar results were obtained from different methods including Cox regression with linear interaction, STEPP, MFPI, and LPLB [47]. To our best knowledge, only a small number of simulation studies were performed to compare the properties of the different procedures under known scenarios. Royston and Sauerbrei

Table 3: Estimated power with exact 95% confidence intervals (in brackets) for Scenarios 5 and 6 for all investigated methods.

		$n = 250$		$n = 500$		$n = 1000$	
		Low cens.	High cens.	Low cens.	High cens.	Low cens.	High cens.
Scenario 5	Median split	16.1% (13.9–18.5%)	10.4% (8.6–12.5%)	26.7% (24.0–29.6%)	17.7% (15.4–20.2%)	46.6% (43.5–49.7%)	29.3% (26.5–32.2%)
	Quartile split	23.0% (20.4–25.7%)	10.5% (8.7–12.6%)	41.3% (38.2–44.4%)	21.2% (18.7–23.9%)	70.9% (68.0–73.7%)	40.1% (37.0–43.2%)
	Optimal split	*79.7% (77.1–82.2%)*	*60.2% (57.1–63.2%)*	*93.8% (92.1–95.2%)*	*78.3% (75.6–80.8%)*	*99.4% (98.7–99.8%)*	*91.9% (90.0–93.5%)*
	STEPP	15.9% (13.7–18.3%)	7.4% (5.9–9.2%)	35.0% (32.0–38.0%)	14.8% (12.7–17.2%)	68.7% (65.7–71.6%)	31.0% (28.1–34.0%)
	Cox (linear int.)	25.6% (22.9–28.4%)	16.3% (14.1–18.7%)	47.0% (43.9–50.1%)	30.6% (27.8–33.6%)	76.2% (73.4–78.8%)	51.1% (48.0–54.2%)
	MFPI (FP1-flex3)	*39.7% (36.7–42.8%)*	*22.6% (20.0–25.3%)*	*67.3% (64.3–70.2%)*	*39.7% (36.7–42.8%)*	*93.8% (92.1–95.2%)*	*66.5% (63.5–69.4%)*
	MFPI (FP2-flex1)	26.8% (24.1–29.7%)	13.2% (11.2–15.5%)	50.6% (47.5–53.7%)	27.1% (24.4–30.0%)	87.5% (85.3–89.5%)	51.8% (48.7–54.9%)
	LPLB	22.5% (19.9–25.2%)	9.3% (7.6–11.3%)	46.9% (43.8–50.0%)	21.9% (19.4–24.6%)	83.4% (80.9–85.7%)	45.3% (42.2–48.4%)
Scenario 6	Median split	5.3% (4.0–6.9%)	3.9% (2.8–5.3%)	5.1% (3.8–6.7%)	5.1% (3.8–6.7%)	6.4% (5.0–8.1%)	4.9% (3.6–6.4%)
	Quartile split	24.3% (21.7–27.1%)	13.0% (11.0–15.2%)	42.0% (38.9–45.1%)	16.0% (13.8–18.4%)	73.8% (71.0–76.5%)	36.5% (33.5–39.6%)
	Optimal split	*73.8% (71.0–76.5%)*	*56.5% (53.4–59.6%)*	*88.1% (85.9–90.0%)*	*67.1% (64.1–70.0%)*	*97.6% (96.4–98.5%)*	*86.3% (84.0–88.4%)*
	STEPP	14.8% (12.7–17.2%)	7.9% (6.3–9.7%)	31.4% (28.5–34.4%)	12.7% (10.7–14.9%)	61.6% (58.5–64.6%)	25.9% (23.2–28.7%)
	Cox (linear int.)	6.1% (4.7–7.8%)	5.9% (4.5–7.5%)	4.8% (3.6–6.3%)	5.1% (3.8–6.7%)	6.2% (4.8–7.9%)	4.6% (3.4–6.1%)
	MFPI (FP1-flex3)	*23.0% (20.4–25.7%)*	*16.5% (14.3–18.9%)*	*30.6% (27.8–33.6%)*	*18.5% (16.1–21.0%)*	*50.9% (47.8–54.0%)*	*27.3% (24.6–30.2%)*
	MFPI (FP2-flex1)	20.0% (17.6–22.6%)	11.2% (9.3–13.3%)	28.6% (25.8–31.5%)	12.8% (10.8–15.0%)	45.9% (42.8–49.0%)	26.9% (24.2–29.8%)
	LPLB	22.2% (19.7–24.9%)	10.4% (8.6–12.5%)	41.5% (38.4–44.6%)	17.9% (15.6–20.4%)	74.6% (71.8–77.3%)	36.7% (33.7–39.8%)

Due to increased type I error probabilities, results for Optimal split and MFPI (FP1-flex3) are presented in italics.

performed a simulation study to compare different MFPI strategies to other regression models and approaches relying on categorization of continuous variables in settings with a continuous outcome [37, 38]. Under all the different MFPI strategies investigated there, the MFPI (FP1-flex3) approach, using one polynomial transformation and allowing for different functional forms in the models with and without considering a covariate-treatment interaction, was identified as the "best" MFPI approach. Bonetti et al. performed a simulation study to evaluate the impact of the parameter settings of the STEPP approach on type I error and statistical power and compared the results to those of a Cox regression model with linear interaction term [32]. Liu et al. also compared performance of their proposed LPLB approach to the Cox regression model with a linear interaction term [27]. Due to the lack of information on the properties of different available methods proposed in the literature for identification of a biomarker-treatment interaction, we performed a simulation study comparing estimates for type I error probability and statistical power of relevant methods under various scenarios. Our aim was to perform a study in the sense of a "neutral" simulation study as described in [48] as we do not favour any of the investigated methods and were not involved in the development or publication of any of them.

As to be expected, we observed that the procedure using an optimal cutoff value determined by maximizing the Wald statistic of the interaction term between the dichotomized biomarker of interest and treatment in a Cox regression model for definition of the subgroups leads to a tremendously increased type I error probability of about 50%. This was observed similarly in simulations presented by Altman et al. who investigated the naïve use of minimum p value categorization of a potentially prognostic variable [49]. Interestingly, an increased type I error probability of about 10% in both scenarios with data simulated under the null hypothesis was also observed for the MFPI (FP1-flex3) approach irrespective of sample size and censoring distribution. This was caused by datasets for which different transformations were selected for the models with and without an interaction term. In the simulation study by Royston and Sauerbrei [37], no relevant increase in the probability of false-positive findings was identified for the MFPI (FP1-flex3) approach for most of their investigated scenarios with observed relative frequencies of type one errors ranging from 5% to 7%. Only for scenarios with

complex functional forms and a covariate of interest following a skewed distribution (called "badly behaved distribution of x" in [37]), an increased type I error probability of up to 20% was found. Maybe this problem is less pronounced in a linear regression setting with quantitative outcome than for our investigated time-to-event endpoint. The originally proposed MFPI (FP2-flex1) approach did not lead to an increased probability of false-positive results and performed generally well for all scenarios. While it was superior to all other methods in a scenario with a hazard ratio constant over a wide range of the biomarker and increasing for individuals with large values when the number of events was large, it was slightly less efficient than a Cox regression model with a linear interaction term in the presence of a truly linear or close to linear biomarker-treatment interaction. Generally, the Cox regression model with a linear interaction term performed better than the other investigated methods for many scenarios. It provided an acceptable probability of false-positive results and higher statistical power than all other methods in the scenario with a truly linear interaction. For small to moderate event numbers, the Cox regression model also outperformed the other methods in scenarios with nonlinear monotonous interaction effects. In one scenario with data generated to provide a nonmonotonous interaction effect over the range of the biomarker of interest, the Cox regression model assuming a linear interaction term was not able to detect this association. For the LPLB procedure, type I error frequencies did not exceed the nominal significance level relevantly and adequate statistical power as compared to the other methods was observed for scenarios with complex functional form of the hazard ratio over the biomarker range. The procedure splitting the data into two subgroups (Median split) led to decreased power for most scenarios, which was also described for other research questions dealing with categorization of continuous covariates [41, 42]. For complex associations, the split into a small number of subgroups might be an adequate first step for data exploration, which was also recommended in the EMA guideline on subgroup analyses [14], or might be used for verification of nonlinear associations found by a corresponding method as also recommended in [38].

Our simulation study has several limitations. Due to limited time and space, only a small number of different scenarios could be investigated. We considered two scenarios in which data were generated under the null hypothesis of no biomarker-treatment interaction and four settings with true biomarker-treatment interactions of different shapes. Additionally, we varied the sample size and used two different amounts of censored observations. We did not vary further aspects of the data generating process as the distribution of the covariate of interest or the influence of further covariates. While some of the methods as fitting a Cox regression model with linear interaction to the data or application of the MFPI approach do not rely on the specification of tuning parameters, other methods such as STEPP or LPLB allow a greater level of user involvement by letting the applicant choose, e.g., the size of the subgroups or the number of overlapping individuals in STEPP or the number of points used for local estimation and the bandwidth in LPLB. As we only used one setting for each of the methods as described in Section 2.1, our findings are only valid for these specific choices, but might not transfer to the methods in general. Further simulation studies are needed to investigate the role of the different tuning parameters on the performance of these methods. In practical applications, subject knowledge could allow more adequate specifications, which might improve performance of the methods compared to our fixed settings. Additionally, we only investigated one potential predictive biomarker and treated it as if investigation of interaction of that biomarker with treatment was the prespecified primary research question. In practice, these kinds of analyses will often be performed as exploratory secondary or add-on analyses, potentially involving multiple biomarkers of interest, and multiplicity issues typically evolving in these situations will have to be addressed adequately. If testing the interaction between a predefined biomarker and treatment is of major interest, this has to be considered in the planning phase of a clinical trial and consequently in the sample size calculation, as often a large sample size is necessary to detect biomarker-treatment interactions [50].

It has to be considered that our simulation study only aims at detection of biomarker-treatment interactions. According to Chen et al., three steps are needed to establish a predictive biomarker in clinical practice: identification of a biomarker, selection of adequate subgroups for treatment stratification, and assessment of clinical utility. Consequently, after identification of a predictive biomarker, subgroups that should be treated by different treatment options have to be identified. For continuous biomarkers, this could be achieved by either application of classification techniques [51] or by exploring the pattern of the treatment effect estimate over the range of the biomarker value. Intuitive visualization as provided by STEPP or by the "treatment effect plot" [52] of the MFPI procedure can be helpful. Additionally, further aspects such as potential risks, patient acceptance, and costs have to be taken into account. Clinical utility might be investigated by randomized clinical trials using biomarker-stratified or biomarker-strategy designs as described by Ondra et al. [53].

As a conclusion of our simulation study, we recommend to perform more detailed and sophisticated analyses for detection of biomarker-treatment interactions than the commonly performed subgroup analyses involving dichotomization of continuous variables. Cox regression models considering linear interaction terms will increase the probability for detection of true interactions as compared to the use of dichotomized variables in many applications. Methods developed for detection of nonlinear interactions can help to identify predictive biomarkers in the presence of complex patterns. We believe that better use of available statistical methods will help to identify and establish predictive biomarkers and increase the number, up to now limited [54], of biomarkers used in clinical practice for treatment stratification and consequently help to improve health care for individual patients.

Data Availability

All findings are based on simulated data. R code for data generation can be obtained from the corresponding author upon reasonable request.

Conflicts of Interest

The authors declare that there are no conflicts of interest regarding the publication of this article.

Acknowledgments

This work was supported by the German Research Foundation (DFG) and the Technical University of Munich within the funding programme Open Access Publishing.

References

[1] E. Thunnissen, K. van der Oord, and M. Den Bakker, "Prognostic and predictive biomarkers in lung cancer. a review," *Virchows Archiv*, vol. 464, no. 3, pp. 347–358, 2014.

[2] W. H. Robinson and R. Mao, "Biomarkers to guide clinical therapeutics in rheumatology?," *Current Opinion in Rheumatology*, vol. 28, no. 2, pp. 168–175, 2016.

[3] R. Hoefflin, A.-L. Geißler, R. Fritsch et al., "Personalized clinical decision making through implementation of a molecular tumor board: a German single-center experience," *JCO Precision Oncology*, vol. 2, no. 2, pp. 1–16, 2018.

[4] T. Ahmadzada, S. Kao, G. Reid, M. Boyer, A. Mahar, and W. Cooper, "An update on predictive biomarkers for treatment selection in non-small cell lung cancer," *Journal of Clinical Medicine*, vol. 7, no. 6, p. 153, 2018.

[5] K. V. Ballman, "Biomarker: predictive or prognostic?," *Journal of Clinical Oncology*, vol. 33, no. 33, pp. 3968–3971, 2015.

[6] K. P. Pritzker, "Predictive and prognostic cancer biomarkers revisited," *Expert Review of Molecular Diagnostics*, vol. 15, no. 8, pp. 971–974, 2015.

[7] M.-Y. C. Polley, B. Freidlin, E. L. Korn, B. A. Conley, J. S. Abrams, and L. M. McShane, "Statistical and practical considerations for clinical evaluation of predictive biomarkers," *JNCI Journal of the National Cancer Institute*, vol. 105, no. 22, pp. 1677–1683, 2013.

[8] A. D. Hingorani, D. A. v. d. Windt, R. D. Riley et al., "Prognosis research strategy (progress) 4: stratified medicine research," *BMJ*, vol. 346, p. e5793, 2013.

[9] E. Senkus, S. Kyriakides, S. Ohno et al., "Primary breast cancer: ESMO Clinical Practice Guidelines for diagnosis, treatment and follow-up," *Annals of Oncology*, vol. 26, no. S5, pp. v8–v30, 2015.

[10] F. Cardoso, E. Senkus, A. Costa et al., "4th ESO-ESMO international consensus guidelines for advanced breast cancer (ABC 4)," *Annals of Oncology*, vol. 29, no. 8, pp. 1634–1657, 2018.

[11] B. Besse, A. Adjei, P. Baas et al., "2nd ESMO Consensus Conference on Lung Cancer: non-small-cell lung cancer first-line/second and further lines of treatment in advanced disease," *Annals of Oncology*, vol. 25, no. 8, pp. 1475–1484, 2014.

[12] J. J. Chen, T.-P. Lu, Y.-C. Chen, and W.-J. Lin, "Predictive biomarkers for treatment selection: statistical considerations," *Biomarkers in Medicine*, vol. 9, no. 11, pp. 1121–1135, 2015.

[13] R. Wang, S. W. Lagakos, J. H. Ware, D. J. Hunter, and J. M. Drazen, "Statistics in medicine-reporting of subgroup analyses in clinical trials," *New England Journal of Medicine*, vol. 357, no. 21, pp. 2189–2194, 2007.

[14] EMA/CHMP, *Guideline on the Investigation of Subgroups in Confirmatory Trial (Draft)*, EMA/CHMP/539146/2013, Committee for Medicinal Products for Human Use, London, UK, 2014.

[15] W. Vach, *Regression Models as a Tool in Medical Research*, Boca Raton, FL, USA, CRC Press, 2012.

[16] P. Royston and W. Sauerbrei, *Multivariable Model-Building: A Pragmatic Approach to Regression Analysis Based on Fractional Polynomials for Modelling Continuous Variables*, John Wiley & Sons, Chichester, UK, 2008.

[17] S. F. Assmann, S. J. Pocock, L. E. Enos, and L. E. Kasten, "Subgroup analysis and other (mis)uses of baseline data in clinical trials," *The Lancet*, vol. 355, no. 9209, pp. 1064–1069, 2000.

[18] S. J. Pocock, S. E. Assmann, L. E. Enos, and L. E. Kasten, "Subgroup analysis, covariate adjustment and baseline comparisons in clinical trial reporting: current practice and problems," *Statistics in Medicine*, vol. 21, no. 19, pp. 2917–2930, 2002.

[19] P. Royston and W. Sauerbrei, "A new approach to modelling interactions between treatment and continuous covariates in clinical trials by using fractional polynomials," *Statistics in Medicine*, vol. 23, no. 16, pp. 2509–2525, 2004.

[20] L. Tian, A. A. Alizadeh, A. J. Gentles, and R. Tibshirani, "A simple method for estimating interactions between a treatment and a large number of covariates," *Journal of the American Statistical Association*, vol. 109, no. 508, pp. 1517–1532, 2014.

[21] J. Fan, H. Lin, and Y. Zhou, "Local partial-likelihood estimation for lifetime data," *The Annals of Statistics*, vol. 34, no. 1, pp. 290–325, 2006.

[22] K. Strimbu and J. A. Tavel, "What are biomarkers?," *Current Opinion in HIV and AIDS*, vol. 5, no. 6, pp. 463–466, 2010.

[23] Personalized Medicine Coalition, "Personalized medicine at FDA: 2017 progress report," January 2019, http://www.personalizedmedicinecoalition.org/Userfiles/PMC-Corporate/file/PM_at_FDA_2017_Progress_Report.pdf.

[24] M. K. Wilson, D. Collyar, D. T. Chingos et al., "Outcomes and endpoints in cancer trials: bridging the divide," *The Lancet Oncology*, vol. 16, no. 1, pp. e43–e52, 2015.

[25] M. Bonetti and R. D. Gelber, "A graphical method to assess treatment-covariate interactions using the Cox model on subsets of the data," *Statistics in Medicine*, vol. 19, no. 19, pp. 2595–2609, 2000.

[26] D. R. Cox, "Regression models and life-tables," *Journal of the Royal Statistical Society: Series B (Methodological)*, vol. 34, no. 2, pp. 187–202, 1972.

[27] Y. Liu, W. Jiang, and B. E. Chen, "Testing for treatment-biomarker interaction based on local partial-likelihood," *Statistics in Medicine*, vol. 34, no. 27, pp. 3516–3530, 2015.

[28] R Core Team, *R: A Language and Environment for Statistical Computing*, R Foundation for Statistical Computing, Vienna, Austria, 2016.

[29] T. M. Therneau, *A Package for Survival Analysis in S*, Mayo Foundation, Rochester, MN, USA, 2015.

[30] T. M. Therneau and P. M. Grambsch, *Modeling Survival Data: Extending the Cox Model*, Springer Science & Business Media, New York, NY, USA, 2000.

[31] J. Fox and S. Weisberg, *An R Companion to Applied Regression*, Sage, Thousand Oaks, CA, USA, 2nd edition, 2011.

[32] M. Bonetti, D. Zahrieh, B. F. Cole, and R. D. Gelber, "A small sample study of the STEPP approach to assessing treatment-covariate interactions in survival data," *Statistics in Medicine*, vol. 28, no. 8, pp. 1255–1268, 2009.

[33] W.-K. Yip, M. Bonetti, B. F. Cole et al., "Subpopulation treatment effect pattern plot (STEPP) analysis for continuous, binary, and count outcomes," *Clinical Trials: Journal of the Society for Clinical Trials*, vol. 13, no. 4, pp. 382–390, 2016.

[34] A. A. Lazar, M. Bonetti, B. F. Cole, W.-K. Yip, and R. D. Gelber, "Identifying treatment effect heterogeneity in clinical trials using subpopulations of events: STEPP," *Clinical Trials*, vol. 13, no. 2, pp. 169–179, 2016.

[35] W.-K. Yip, A. Lazar, D. Zahrieh et al., STEPP: Subpopulation Treatment Effect Pattern Plot (STEPP), R package version 3.2.0.0, 2018, https://CRAN.R-project.org/package=stepp.

[36] P. Royston and D. G. Altman, "Regression using fractional polynomials of continuous covariates: parsimonious parametric modelling," *Applied Statistics*, vol. 43, no. 3, pp. 429–467, 1994.

[37] P. Royston and W. Sauerbrei, "Interaction of treatment with a continuous variable: simulation study of significance level for several methods of analysis," *Statistics in Medicine*, vol. 32, no. 22, pp. 3788–3803, 2013.

[38] P. Royston and W. Sauerbrei, "Interaction of treatment with a continuous variable: simulation study of power for several methods of analysis," *Statistics in Medicine*, vol. 33, no. 27, pp. 4695–4708, 2014.

[39] T. M. Loughin, "A residual bootstrap for regression parameters in proportional hazards models," *Journal of Statistical Computation and Simulation*, vol. 52, no. 4, pp. 367–384, 1995.

[40] S. Zhang and B. Chen, *lplb: Local Partial Likelihood Bootstrap (LPLB) Test, R Package Version 0.1*, 2016, https://github.com/statapps/lplb.

[41] J. Cohen, "The cost of dichotomization," *Applied Psychological Measurement*, vol. 7, no. 3, pp. 249–253, 1983.

[42] R. C. MacCallum, S. Zhang, K. J. Preacher, and D. D. Rucker, "On the practice of dichotomization of quantitative variables," *Psychological Methods*, vol. 7, no. 1, pp. 19–40, 2002.

[43] O. Naggara, J. Raymond, F. Guilbert, D. Roy, A. Weill, and D. G. Altman, "Analysis by categorizing or dichotomizing continuous variables is inadvisable: an example from the natural history of unruptured aneurysms," *American Journal of Neuroradiology*, vol. 32, no. 3, pp. 437–440, 2011.

[44] P. Royston and W. Sauerbrei, "Two techniques for investigating interactions between treatment and continuous covariates in clinical trials," *The Stata Journal: Promoting communications on statistics and Stata*, vol. 9, no. 2, pp. 230–251, 2009.

[45] P. Ringleb, J. Allenberg, J. Berger et al., "30 day results from the SPACE trial of stent-protected angioplasty versus carotid endarterectomy in symptomatic patients: a randomised non-inferiority trial," *The Lancet*, vol. 368, no. 9543, pp. 1239–1247, 2006.

[46] H.-H. Eckstein, P. Ringleb, J.-R. Allenberg et al., "Results of the stent-protected angioplasty versus carotid endarterectomy (SPACE) study to treat symptomatic stenoses at 2 years: a multinational, prospective, randomised trial," *The Lancet Neurology*, vol. 7, no. 10, pp. 893–902, 2008.

[47] B. Haller, H.-H. Eckstein, P. A. Ringleb, and K. Ulm, "Investigation of age–treatment interaction in the space trial using different statistical approaches," *Journal of Applied Statistics*, vol. 46, no. 9, pp. 1689–1701, 2019.

[48] A.-L. Boulesteix, S. Lauer, and M. Eugster, "A plea for neutral comparison studies in computational sciences," *PLoS One*, vol. 8, no. 4, pp. 1–11, 2013.

[49] D. G. Altman, B. Lausen, W. Sauerbrei, and M. Schumacher, "Dangers of using "optimal" cutpoints in the evaluation of prognostic factors," *JNCI Journal of the National Cancer Institute*, vol. 86, no. 11, pp. 829–835, 1994.

[50] M. Bonetti, B. F. Cole, and R. D. Gelber, "Another STEPP in the right direction," *Journal of Clinical Oncology*, vol. 26, no. 22, pp. 3813-3814, 2008.

[51] I. Lipkovich, A. Dmitrienko, and B. Ralph, "Tutorial in biostatistics: data-driven subgroupidentification and analysis in clinical trials," *Statistics in Medicine*, vol. 36, no. 1, pp. 136–196, 2017.

[52] P. Royston and W. Sauerbrei, "Interactions between treatment and continuous covariates: a step toward individualizing therapy," *Journal of Clinical Oncology*, vol. 26, no. 9, pp. 1397–1399, 2008.

[53] T. Ondra, A. Dmitrienko, T. Friede et al., "Methods for identification and confirmation of targeted subgroups in clinical trials: a systematic review," *Journal of Biopharmaceutical Statistics*, vol. 26, no. 1, pp. 99–119, 2016.

[54] M. J. Selleck, M. Senthil, and N. R. Wall, "Making meaningful clinical use of biomarkers," *Biomarker Insights*, vol. 12, pp. 1–7, 2017.

Hindawi
Computational and Mathematical Methods in Medicine
Volume 2019, Article ID 7370231, 12 pages
https://doi.org/10.1155/2019/7370231

Research Article

A Data-Driven Hybrid Three-Stage Framework for Hospital Bed Allocation: A Case Study in a Large Tertiary Hospital in China

Li Luo,[1] **Jialing Li**,[1] **Xueru Xu**,[1] **Wenwu Shen**,[2] **and Lin Xiao**[1]

[1]*Business School of Sichuan University, No. 24 South Section 1, Yihuan Road, Chengdu, China*
[2]*West China Hospital of Sichuan University, No. 17 People's South Road, Chengdu, China*

Correspondence should be addressed to Xueru Xu; 18200291987@163.com and Wenwu Shen; wenwu_shen@163.com

Received 24 December 2018; Revised 6 March 2019; Accepted 2 April 2019; Published 2 May 2019

Guest Editor: Giedrius Vanagas

Beds are key, scarce medical resources in hospitals. The bed occupancy rate (BOR) amongst different departments within large tertiary hospitals is very imbalanced, a situation which has led to problems between the supply of and the demand for bed resources. This study aims to balance the utilization of existing beds in a large tertiary hospital in China. We developed a data-driven hybrid three-stage framework incorporating data analysis, simulation, and mixed integer programming to minimize the gaps in BOR among different departments. The first stage is to calculate the length of stay (LOS) and BOR of each department and identify the departments that need to be allocated beds. In the second stage, we used a fitted arrival distribution and median LOS as the input to a generic simulation model. In the third stage, we built a mixed integer programming model using the results obtained in the first two stages to generate the optimal bed allocation strategy for different departments. The value of the objective function, Z, represents the severity of the imbalance in BOR. Our case study demonstrated the effectiveness of the proposed data-driven hybrid three-stage framework. The results show that Z decreases from 0.7344 to 0.0409 after re-allocation, which means that the internal imbalance has eased. Our framework provides hospital bed policy makers with a feasible solution for bed allocation.

1. Introduction

The inherent difference between limited resources for healthcare and steadily increasing demands occurs all over the world and is particularly serious in developing countries. According to a research report from the World Health Organization (WHO) and World Bank Groups, at least 400 million people worldwide cannot receive one or more basic health services [1].

This differential is particularly apparent with respect to bed resources. Although hospital bed numbers have increased greatly in recent years, this increase cannot cope with the growth rate of admission demand in China. According to the report "Statistical Communique on the Development of China's Health and Family Planning Program 2016" [2], the number of hospitalizations across the nation's medical and health institutions was 227.28 million and the annual hospitalization rate was 16.5%. There were 7.410 million beds in medical institutions across the country. Amongst all of the medical institutions, China's large tertiary hospitals, classed as Class III according to the classification standards (Appendix), are facing the most serious imbalance between admissions and bed resources (Table 1). The number of hospital beds and individuals hospitalized in Class III hospitals increased to 2,213,718 and 76,860,000, respectively. Bed occupancy rates (BORs) reached 98.8% in 2016.

We found that the imbalance between supply and demand in large tertiary (Class III) hospitals is greater than that in the other two classes of hospitals. Hospital managers urgently need to find solutions to alleviate bed shortages. Hospital administrators typically address this issue in two ways: by improving utilization of existing beds or by expanding capacity. The first involves the complex task of strategically allocating the proper amount of beds for each set of care types. A hospital that is unable to find an optimal allocation may acquire additional beds. However, an expansion, which is desirable for one hospital, may not be

Table 1: Hospital beds, hospitalization, and BOR of China's large tertiary hospitals in 2015 and 2016.

Hospital level	Hospital beds		Hospitalization		BOR	
	2015	2016	2015	2016	2015 (%)	2016 (%)
Class III	2,047,819	2,213,718	68,290,000	76,860,000	98.80	98.80
Class II	2,196,748	2,302,887	71,210,000	75,700,000	84.10	84.20
Class I	481,876	517,837	9,650,000	10,390,000	58.80	58

advantageous from the perspective of the public planner [3] and may even have some negative consequences, such as doctor and nurse work overloads, decreases in medical care quality, and aggravation of medical conflicts [4]. Therefore, from the perspective of the sustainability of medical resources, the best option is to improve the utilization of bed resources.

The BOR of the Class III hospitals is usually as high as 98%. However, the utilization rate of beds in different departments of a Class III hospital can be very different. West China Hospital (WCH) is typical of such hospitals (see Section 3.1 for more details). The availability of beds for patient hospitalization services is excessive in some units and scarce in others. This discrepancy between bed availability in different departments leads to the overcrowding of some departments and the idleness of other departments. This internal imbalance has further worsened the shortage of hospital resources.

A possible solution to this problem is to allocate the number of beds among different departments in such a way as to increase the utilization rate of beds and alleviate the shortage of bed resources as much as possible. There has been considerable research into the allocation of bed resources. The study of bed resource allocation can be divided into two main approaches.

One approach is to assign the optimal number of beds in a single department or care units, such as surgery units [5], intensive care units [6, 7], and obstetrics departments [8]. For instance, Akkerman and Knip [5] planned the optimal number of beds for cardiac surgery with the goal of reducing patient waiting time. Oerlemans et al. [9] sent an online questionnaire to all ICU physician members in 90 hospitals of the Dutch Society for Intensive Care, the results of which can be used to improve decision-making regarding allocation of ICU resources. Devapriya et al. [10] proposed the strategic bed analysis model, which is a discrete-event simulation model created after a thorough analysis of patient flow and data from Geisinger Health Systems (GHS). Ridge et al. [11] investigated the problem of hospital bed planning in the intensive care unit. Romanin-Jacur and Facchin [12] studied the ward planning of the intensive surgical department and the pediatric semiintensive care unit.

Another approach to the problem focuses on the number of hospital beds throughout the whole hospital. For example, Akcali et al. [13] planned the best use of hospital beds in the entire hospital with the goal of minimizing the total cost. Utley et al. [14] determined the reasonable number of beds for elective patients in the whole hospital in the case of a very low rate of patient cancellation. However, there is little research on the allocation of beds among different departments or wards.

A range of operational research (OR) methods have been developed and applied to problems of healthcare resource allocation [15], especially bed resources. These methods include queuing theory [16, 17], simulation [18, 19], goal programming [20, 21], and mathematical programming [22–24]. Most of the current research uses a single method for each study. However, the premise of queuing theory is based on very strong assumptions, and it is difficult to apply. Mathematical programming can flexibly add constraints and change the objective function according to specific conditions, and it is more popular. Therefore, a hybrid of different methods is more conducive to solving the problem. Simulation and mathematical programming have become increasingly popular approaches to allocate resources in health care. Tontarski [25] utilized simulation-based optimization and mathematical programming for solving complex nurse-scheduling problems. Studies on the bed allocation problem using mathematical programming, especially combined with simulation, are relatively few.

In short, research into bed allocation mostly focuses on the study of the number of beds in a single department. The problem of how to allocate beds in different departments has not been fully studied. Furthermore, most of the current research on bed allocation is based on a single method such as queuing theory [26] or simulation [27]. There are few hybrid models which integrate data analysis, simulation, and mathematical programming. We propose a solution to the bed allocation problem at an operational level. We develop a data-driven hybrid three-stage framework incorporating data analysis, simulation, and mixed integer programming (MIP) to determine the optimal bed allocation strategy. The first stage is to select departments for allocation according to the relationship between the number of beds and the BOR and have this result approved by hospital management. In the second stage, we used a simulation model to calculate the BOR for different numbers of hospital beds. We thus derive the functional relationship between the two variables. The third stage is to find the best number of beds in five departments using a MIP model. Our study aims to alleviate shortage of beds by balancing the utilization of existing beds without increasing the number of beds in a large hospital in China. Overall, the contributions of this study are as follows:

(1) Our framework is data driven, making the allocation strategy more rational. (i) Using real data from the hospital, data analysis is used to determine the optimal department needs to allocate beds; (ii) the simulation model is used to simulate the

corresponding BOR under different bed allocation scenarios. The relationship between the hospital beds and the BOR is derived from the data, thereby providing data-driven personalized constraints for each department.

(2) The objective function of the MIP model is tailored to Chinese needs. Because the beds in large hospitals in China have been overloaded, we are not blindly reducing the BOR of beds but are keeping the number of beds in a reasonable range.

(3) This paper provides a general framework for the allocation of beds in the Chinese context. Different hospitals can modify the objective function of the model and appropriately add or reduce constraints according to their needs. Our model provides a reference for hospital management to effectively manage hospital bed resources.

The rest of the paper is organized as follows. In Section 2, we briefly introduced the background of the case hospital (WCH) and the process of the data-driven hybrid three-stage framework. Taking WCH as a case study, we applied the framework proposed in Section 2 to WCH, and these analyses of the framework are shown in Section 3. In Section 4, we discuss the results of the paper. Finally, Section 5 concludes the paper and indicates some directions for future research.

2. Materials and Methods

2.1. Study Hospital. From a macro perspective, the overall BOR in China's tertiary hospitals is very high. However, at an individual level, the availability of hospital beds in different departments in individual hospitals is uneven. This phenomenon exists in almost all of the tertiary hospitals in China. It is particularly serious in WCH, a tertiary hospital which is located in Chengdu, Sichuan province. In order to rationally manage beds, the Admission Service Center (ASC), a bed planning organization, was established in 2011. It manages 2956 beds and 28 specialized care departments. After our survey and data analysis (Figure 1), we found that the allocation of beds among the 28 departments is not balanced. For example, the BOR of W3 is as high as 122%, while others, such as W12, are only 64.70%. The reason why the BOR is over 100% is that the extra beds are involved in the calculation process. When the number of inpatients exceeds the number of fixed beds, the hospital will add additional beds to meet the demand, and these beds are often arranged in the corridor. This imbalance further leads to inefficiency and waste of hospital bed space, which in turn exacerbates the shortage of hospital beds.

We focus on balancing the BOR of departments by redistributing beds to improve the utilization rate of resources. This study takes WCH as an example to provide a feasible solution for the shortage of hospital beds in large hospitals.

2.2. Data Collection. This study used data from the Hospital Information System of the ASC for the period from January 1 to December 31, 2013. It includes the time of each patient admission and discharge, demographic information, and department information and has a total of 243,685 admission registrations and 167,843 discharge records.

2.3. Methods. The aim of this research is to balance the BOR of each department by allocating the hospital beds to departments, using a fixed number of existing beds, and keeping the bed utilization rate of each department at a reasonable level. Hence, we proposed a data-driven hybrid three-stage framework to solve this problem. The overall approach is shown in Figure 2.

(1) Stage I (data preliminaries): we selected the key departments by analyzing their current BOR and number of beds.

(2) Stage II (construction of constraint conditions): Simio software [28] was used to establish a simulation model to obtain the different scenarios of the beds and corresponding BOR. We then determined the relationship between the BOR and the number of beds through data fitting, which is one of the constraints of the Stage III.

(3) Stage III (construction of model): we established a MIP model to minimize the gap in BOR among different departments. We applied the genetic algorithm (GA) to solve this model, since GA is one of the best tools for satisfactory solution with advantages like good convergence, low computational complexity, high robustness, and so forth [29].

2.3.1. Stage I: Data Preliminaries

(1) Calculation of Length of Hospital Stay. Length of hospital stay (LOS) indicates the number of days the patient spent in a hospital bed. We made the assumption that the LOS can be considered as a constant [30]. We have got 243,685 admission records and 167,843 discharge records form ASC. The LOS is calculated as the discharge date for each patient minus the date of admission registration in the ASC. The sum of the days of all hospitalized patients is an important parameter for calculating the BOR. This paper uses the data from 2013 1/1 to 2013/12/31. We divided the patients into three types by the discharge date as follows and calculated the LOS in 2013 for each group.

(i) Type I: patients discharged during 2013. Those patients registered in the ASC during or before 2013. Their actual LOS during the 2013 is called LOS1. For example, the actual LOS of the patient who registered before 2013 is discharge date minus January 1, 2013.

(ii) Type II: those patients who left the hospital in 2014, who registered before 2013 or during 2013. Their LOS equals to December 1, 2013, minus registered date or December 31, 2013, minus January 1, 2013, which is named LOS2.

(iii) Type III: because some discharge data are missing, there are patients who are recorded as having been

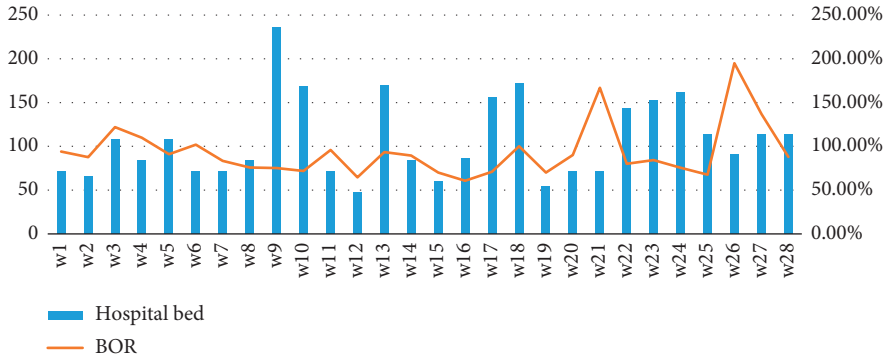

Figure 1: Hospital beds and BOR of 28 departments in West China Hospital.

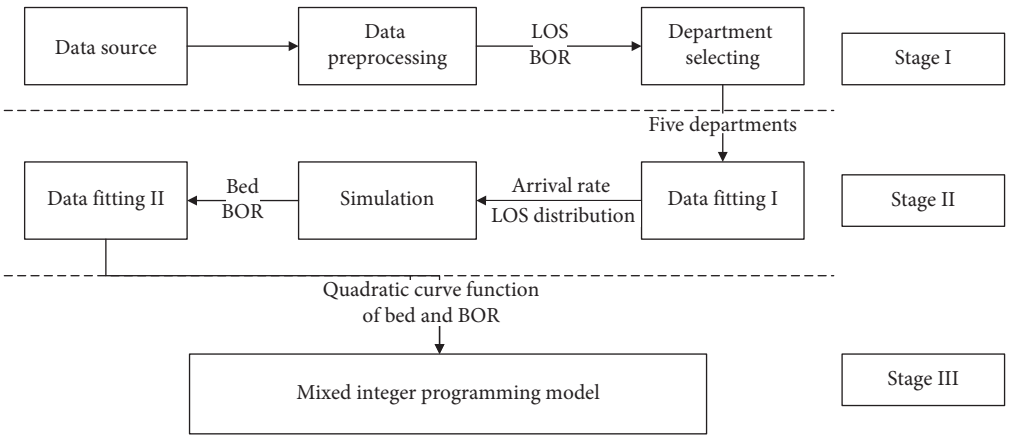

Figure 2: Methodology: process of the data-driven hybrid three-stage framework.

discharged from hospital in 2013 but had no admission records. These patients cannot be ignored. Hence, the number of Type III patients is the total number of discharged patients in one department in 2013 minus the number of Type I. We cannot directly calculate the LOS of Type III patients, so in this study, we used the median of the LOS of Type I patients as the value for the LOS of Type III patients, which we called LOS3.

(2) The Calculation of BOR. We calculated each department's BOR according to the following formulas:

$$\text{all patients' LOS} = \text{LOS1} + \text{LOS2} + \text{LOS3}, \quad (1)$$

$$\text{BOR} = \frac{\text{all patients' LOS}}{\text{LOS that all beds can provide}}. \quad (2)$$

2.3.2. Stage II: Construction of Constraint Conditions. The Simio software was used to build simulation models using data from different departments. Changes in the number of beds, the number of hospitalized patients, and the LOS of patients with different bed numbers were simulated and used to calculate different BOR indexes. The relationship between hospital bed numbers and BOR was an important constraint condition in building the mixed integer programming model in Stage III. It proceeds in three steps:

(1) We used the EASY-FIT [31], a professional data fitting software, to fit the patient's arrival distribution and LOS distribution of each department

(2) The fitted arrival distribution and LOS distribution were used as the input to the simulation model, which identified the relationship between the number of beds and the BOR

(3) We fitted the relationship between the number of beds and the BOR via IBM SPSS Statistics V21 and obtained their functional relationship

2.3.3. Stage III: Construction of the Model. In order to thoroughly understand the hospital bed allocation problem, it is necessary to describe the characteristics of the problem in order to implement them in an appropriate mathematical model. We define parameters and variables of the model:

(1) Parameters

K_{ij}: the ward type j for department i. There are three inpatient ward types.

K_{i1}: the number of single-bed wards in department i.
K_{i2}: the number of double-bed wards in department i.

K_{i3}: the number of three-bed wards in department i

L_i: lower bound of number of beds in department i.

U_i: upper bound of number of beds in department i.

C_t: the total number of beds of all the departments.

$\mathrm{BOR}_i(C_i)$: the BOR of department i, when the number of beds of department i is C_i. The relationship functions between $\mathrm{BOR}_i(C_i)$ and C_i of department i can be obtained from the results of Stage II. Here, we assume that the two variables are quadratic functions.

(2) Variable

C_i: the number of beds of department i and $C_i = K_{i1} + 2K_{i2} + 3K_{i3}$; C_i is a positive integer.

There are n departments in WCH, but i departments ($i \in 1, 2, \ldots, n$) need to be allocated beds. Our main decision variable is C_i, which represents the number of beds for department i. Our goal was to balance the BOR of each department; hence, our objective function is to minimize the total gap between BOR of each department and their average BOR. We developed a MIP model as follows:

(3) Objective function

$$\min(Z) = \sum_{i=1}^{n} \left| \mathrm{BOR}_i(C_i) - \left(\sum_{i=1}^{n} \frac{\mathrm{BOR}_i(C_i)}{\mathrm{n}} \right) \right|. \quad (3)$$

(4) Constraints

$$\mathrm{BOR}_i(C_i) = \beta_i + a_i C_i + b_i C_i^2, \quad i = 1, 2, \ldots n, \quad (4)$$

$$\sum_{i=1}^{n} C_i = C_t, \quad i = 1, 2, \ldots n, \quad (5)$$

$$L_i \leq \mathrm{Ci} \leq U_i, \quad i = 1, 2, \ldots, n, \quad (6)$$

$$C_i = K_{i1} + 2K_{i2} + 3K_{i3}, \quad i = 1, 2, \ldots, n, \quad (7)$$

$$K_{ij} \geq 2, \quad i = 1, 2, \ldots, n, \; j = 1, 2, 3. \quad (8)$$

Because of the imbalance between different specialty care departments, we aimed to balance the BOR of various departments without adding extra beds. In objective function (3), $(\sum_{i=1}^{n} \mathrm{BOR}_i(C_i))/n$ is the average BOR of n departments and Z is the sum of the gap between the BOR of the n departments and the average of their BOR. The purpose of function (3) is to minimize the total gap in BOR between different departments and average BOR.

The constraint described by function (4) means the functional relationship between BOR and the number of beds, which is calculated in Stage II. Here, we assume that the two are quadratic functions: $\mathrm{BOR}_i(C_i) = \beta_i + a_i C_i + b_i C_i^2$, where β_i is a constant and a_i and b_i are coefficients (for more details, see Section 3.2); function (5) means that the total number of beds of the n departments is constant. Function (6) ensures that there will be an upper limit and a lower limit for the beds in each department. Functions (7) and (8) impose restrictions on the ward type and patient gender. Each ward has either one, two, or three beds. The distinction between male and female wards, and the number of ward types in each department should not be less than two. For example, a single-bed ward has at least two wards so that a male patient can live in one room and a female patient can live in another single room. The other two ward types have the same conditions. Both male and female patients can decide which type of ward to live in, ensuring the fair treatment of patients.

3. Results

3.1. Stage I: Data Preliminaries. The LOS of 28 departments can be calculated by function (1), and the BOR of the 28 departments can be calculated by function (2). Table 2 shows the number of beds and BOR in 28 departments of the current WCH. The BOR varies from 60.7% to 195% among the 28 departments. Some literature indicates [32, 33] that the optimal range for BOR is between 85% and 90%. Based on this estimation, we divided these departments into three groups:

(1) Group A: BOR is less than 85%. For example, W9 owns 236 beds, but its BOR is only 75.2%.

(2) Group B: BOR is greater than 90%. For example, the BOR of W6 reaches as high as 102%, but it only has 72 beds.

(3) Group C: BOR is between 85% and 90%. Their bed numbers and BOR are within the normal range, compared to groups A and B.

It is clear that there are serious imbalances in BOR between departments. To solve this problem, we interviewed a hospital manager, three other managerial assistants, and medical physicians of the ASC. We choose five departments (W9, W10, W19, W6, and W27) from groups A and B to solve the problem of bed allocation by applying the framework mentioned in Section 2.3.

3.2. Stage II: Construction of Constraint Conditions. After perprocessing the data and selecting the departments, we fitted the distribution of the patient arrival rate and LOS of the five departments using EASY-FIT, and the results are shown in Table 3.

We obtained the distribution of arrival rates for all five departments. The fitting of LOS is not ideal. Five departments do not display any distribution. We took the median of the LOS as their distribution. We used W9 as the example from which we can build the simulation model. Figure 3 describes the simulation model of W9 in Simio.

We set up a patient entity, called Patients, and a patient source called Source1, in the Simio software. We let Source1 associate with Patients and set the arrival rate to obey the Johnson distribution (0.025, 0.803, −8.16, 85.98).

We built a Server1 to represent beds. Its Service capacity was set to the current number of beds (236), and service time

Table 2: Department information summary.

A	Department	W7	W8	W9	W10	W12	W15	W16	W17	W19
	Beds	72	84	236	168	48	60	86	156	54
	BOR (%)	83.4	75.7	75.2	71.8	64.7	70	60.7	71.1	70
	Department	W24	W23	W25						
	Beds	162	153	114						
	BOR (%)	75.60	84.40	67.60						
B	Department	W1	W3	W4	W5	W6	W11	W13	W18	W21
	Beds	72	108	84	108	72	72	170	172	72
	BOR (%)	94.0	122	110	91	102	95.8	93.5	100	167
	Department	W26	W27	W26						
	Beds	91	114	91						
	BOR (%)	195	137	195						
C	Department	W1	W2	W20	W28					
	Beds	84	66	72	114					
	BOR (%)	89.6	87.7	90	88.1					

Table 3: Results of arrival rate distribution and LOS.

Departments	Department type	Arrival rate	LOS
W6	B	Johnson SB (0.289, 0.983, −3.34, 35.11)	Median = 9
W9	A	Johnson SB (0.025, 0.803, −8.16, 85.98)	Median = 10
W10	A	Uniform (−0.72, 43.75)	Median = 12
W19	A	Uniform (−3.2, 92.36)	Median = 10
W27	B	Uniform (−3.2, 92.36)	Median = 5

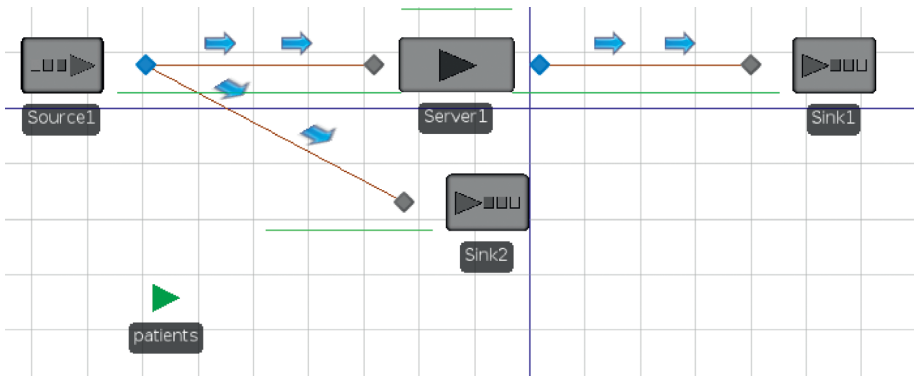

Figure 3: Simulation model of the W9.

was set to 10 days. We calculated the proportion of hospitalizations (43%) based on the number of hospital admissions (12712) and discharges (5478).

There are two leaving routes in the simulation model, namely, Sink1 and Sink2. Sink1 represents the event that a patient leaves the hospital after being served by Server1. The weight from Source1 to Server1 is 43%. Sink2 indicates that a patient who was not admitted to the hospital left the hospital directly through Sink2; the weight from Source1 to Sink2 is 57%.

In order to validate the model, we run the model for a simulated year. The result was that the total number of discharges was 5984, and the BOR was 69.5%. Compared with real data, the difference is 9.2% and 7.5%, respectively. The error was acceptable. Then, we set different parameters for the Server1 and calculated the BOR for different scenarios.

Because W9 belongs to group A, we needed to reduce the number of beds and increase the BOR. We should therefore reduce the number of beds in Server1. In Table 4, we list the number of beds and the corresponding BOR situation for W9. The results of the other four departments are presented in Tables 5–8.

We used the number of beds as an independent variable and the BOR as the dependent variable based on the results in Table 4. The graph of BOR changing with the number of beds is shown in Figure 4. It is difficult to intuitively obtain the relationship equation between the two from the graph, so we selected eight kinds of curve functions—linear, logarithm, quadratic, composite, power, growth, exponential,

Table 4: Beds and corresponding BOR of W9 in the simulation model.

Beds	Discharge	BOR (%)
92	3266	97.3
110	3896	97
123	4351	96.9
135	4771	96.8
148	5226	96.7
160	5646	96.68
172	5926	94.4
180	5982	91.1
185	5984	88.6
198	5984	82.8
210	5984	78.1
223	5984	73.5
236*	5984	69.5
250	5984	65.6

*The current number of hospital beds of W9.

Table 5: Beds and corresponding BOR of W10.

Beds	Discharge	BOR (%)
68	2011	97.2
78	2301	97
88	2585	96.6
98	2865	96.1
108	3145	95.7
113	3201	93.1
118	3216	89.6
128	3246	83.4
138	3276	78
148	3299	73.3
158	3306	68.8
168	3306	64.7
178	3306	61.1

Table 6: Beds and corresponding BOR of W6.

Beds	Discharge	BOR (%)
57	2279	98.6
62	2474	98.4
72	2864	98.1
82	3254	97.8
95	3756	97.4
100	3931	96.9
105	4106	96.4
110	4281	96
115	4438	95.1
120	4516	92.8
125	4538	89.5
130	4538	86.1
140	4538	80

and logistic—with which we can attempt to fit their functional relationships. We used the value of R^2 to determine which relationship function between bed and BOR of W9 had the best fit (Table 9). Since the R^2 value of the quadratic function was the best, at 0.977, we decided that the quadratic function best describes the relationship between the bed numbers and the BOR in W9. We can derive the functional

Table 7: Beds and corresponding BOR of W27.

Beds	Discharge	BOR (%)
114	8196	98.50
130	9332	98.30
145	10345	97.70
149	10482	96.37
152	10527	94.90
160	10640	91.10
168	10674	87
175	10681	83.60
182	10688	80.40
190	10696	77.10
205	10711	71.60
220	10726	66.80

Table 8: Beds and corresponding BOR of W19.

Beds	Discharge	BOR (%)
30	995	97.2
35	1153	97
36	1189	96.8
39	1225	93
38	1165	90.3
40	1258	92.2
45	1246	80.9
47	1230	77.4
50	1246	73.05
52	1252	70.6
54	1274	68.9

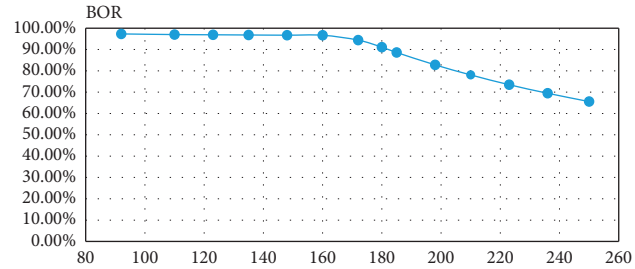

Figure 4: BOR curve for different numbers of beds. The abscissa is the number of beds, and the ordinate is BOR.

relationship between $\mathrm{BOR}_1(C_1)$ and the bed C_1 from Table 9; the equation is: $\mathrm{BOR}_1(C_1) = 0.721 + 0.004C_1 - 0.0000195C_1^2$.

Similar to the analysis process of W9, we obtained the quadratic functional relationships between the BOR and the bed number of the other four departments (Tables 10–13). Hence, the relationship function between beds and BOR of department i is expressed as follows:

$$\mathrm{BOR}_i(C_i) = \beta_i + a_i C_i + b_i C_i^2, \quad (9)$$

where $\mathrm{BOR}_i(C_i)$ represents the bed occupancy rate of department i, C_i is the number of beds in department i, β_i is a constant, and a_i and b_i are coefficients. We have obtained five equations, respectively, for five departments. They are

Table 9: Relationship between bed numbers and BOR in W9.

Function	Model					Parameters			
	R^2	F	df1	df2	Sig.	Constant	b1	b2	b3
Linear	0.836	61.326	1	12	0.000	1.253	−0.002		
Logarithm	0.724	31.538	1	12	0.000	2.550	−0.328		
Quadratic	0.977	230.860	2	11	0.000	0.721	0.004	0.0000195	
Composite	0.820	54.831	1	12	0.000	1.367	0.997		
Power	0.704	28.548	1	12	0.000	6.455	−0.392		
Growth	0.820	54.831	1	12	0.000	0.313	−0.003		
Exponential	0.820	54.831	1	12	0.000	1.367	−0.003		
Logistic	0.820	54.831	1	12	0.000	0.732	1.003		

Table 10: Relationship between bed numbers and BOR in W10.

Function	Model					Parameters			
	R^2	F	df1	df2	Sig.	Constant	b1	b2	b3
Linear	0.919	125.130	1	11	0.000	1.298	−0.004		
Logarithm	0.837	56.598	1	11	0.000	2.813	−0.413		
Quadratic	0.973	181.654	2	10	0.000	0.895	0.003	$-2.854E-5$	
Composite	0.907	107.562	1	11	0.000	1.468	0.995		
Power	0.817	49.021	1	11	0.000	9.578	−0.513		
Growth	0.907	107.562	1	11	0.000	0.384	−0.005		
Exponential	0.907	107.562	1	11	0.000	1.468	−0.005		
Logistic	0.907	107.562	1	11	0.000	0.681	1.005		

Note. The higher the R^2, the better the function model. In the W10 model fitting, the fitting degree of the quadratic curve is the best, and the quadratic curve is directly selected. The bed number of W10 is C_2, and the bed utilization rate is BOR_2 (C_2). According to the estimated value of the parameter, $\mathrm{BOR}_2(C_2) = 0.895 + 0.003C_2 - 0.00002854C_2^2$.

Table 11: Relationship between beds and BOR in W6.

Function	Model					Parameters			
	R^2	F	df1	df2	Sig.	Constant	b1	b2	b3
Linear	0.664	21.741	1	11	0.001	1.118	−0.002		
Logarithm	0.558	13.883	1	11	0.003	1.616	−0.147		
Quadratic	0.956	107.465	2	10	0.000	0.687	0.008	$-4.932E-5$	
Composite	0.645	19.978	1	11	0.001	1.140	0.998		
Power	0.539	12.849	1	11	0.004	1.966	−0.161		
Growth	0.645	19.978	1	11	0.001	0.131	−0.002		
Exponential	0.645	19.978	1	11	0.001	1.140	−0.002		
Logistic	0.645	19.978	1	11	0.001	0.877	1.002		

Note. The higher the R^2, the better the function model. When the W6 model is fitted, it has the same outcome as W9. The quadratic curve is also selected. The bed number of W6 is C_3, and the bed rate is BOR_3 (C_3). According to the estimated value of the parameter, $\mathrm{BOR}_3(C_3) = 0.687 + 0.008C_3 - 0.000049323C_3^2$.

Table 12: Relationship between beds and BOR in W27.

Function	Model					Parameters			
	R^2	F	df1	df2	Sig.	Constant	b1	b2	b3
Linear	0.932	137.447	1	10	0.000	1.446	−0.003		
Logarithm	0.882	74.410	1	10	0.000	3.673	−0.550		
Quadratic	0.967	131.496	2	9	0.000	0.901	0.003	$-2.007E-5$	
Composite	0.964	119.131	2	9	0.000	1.094	0.000	$-2.585E-6$	$-3.039E-8$
Power	0.924	121.995	1	10	0.000	1.720	0.996		
Growth	0.866	64.725	1	10	0.000	24.281	−0.655		
Exponential	0.924	121.995	1	10	0.000	0.542	−0.004		
Logistic	0.924	121.995	1	10	0.000	1.720	−0.004		

Note. The higher the R^2, the better the function model. In the W27 model fitting, the fitting of the quadratic curve is the best, and the quadratic curve is selected. The bed number of W27 is C_4, and the bed utilization rate is BOR_4 (C_4). According to the estimated value of the parameter, $\mathrm{BOR}_4(C_4) = 0.901 + 0.003C_4 - 0.000020066C_4^2$.

Table 13: Relationship between beds and BOR in W19.

Function	Model					Parameters			
	R^2	F	df1	df2	Sig.	Constant	b1	b2	b3
Linear	0.947	159.652	1	9	0.000	1.450	−0.014		
Logarithm	0.915	96.619	1	9	0.000	3.011	−0.579		
Quadratic	0.966	114.721	2	8	0.000	0.911	0.012	$-3.054E-5$	
Composite	0.964	108.277	2	8	0.000	1.095	0.000	$-5.576E-5$	$-1.687E-6$
Power	0.944	151.827	1	9	0.000	1.736	0.983		
Growth	0.908	88.465	1	9	0.000	11.291	−0.695		
Exponential	0.944	151.827	1	9	0.000	0.552	−0.017		
Logistic	0.944	151.827	1	9	0.000	1.736	−0.017		

Note. The higher the R^2, the better the function model. In the W19 model fitting, the fitting of the quadratic curve is the best, and the quadratic curve is selected. The bed number of W19 is C_5, and the bed utilization rate is $\mathrm{BOR}_5(C_5)$. According to the estimated value of the parameter, $\mathrm{BOR}_5(C_5) = 0.911 + 0.012C_5 - 0.0003054C_5^2$.

used as constraints for the mixed integer programming model in Stage III.

3.3. Stage III: A Mixed Integer Programming Model. After data analysis and simulation in the first two stages, we obtained the parameter values in equations (3)–(8), including the five selected departments and established the quadratic function relationship between the bed numbers and the BOR. We then applied these parameters to equations (3)–(8) to solve the model. The specific MIP model is as follows:

Objective function

$$\min(Z) = \sum_{i=1}^{5} \left| \mathrm{BOR}_i(C_i) - \left(\sum_{i=1}^{5} \frac{\mathrm{BOR}_i(C_i)}{5} \right) \right|. \tag{10}$$

Constraints

$$\mathrm{BOR}_1(C_1) = 0.721 + 0.004C_1 - 0.0000195C_1^2, \tag{11}$$

$$\mathrm{BOR}_2(C_2) = 0.895 + 0.003C_2 - 0.00002854C_2^2, \tag{12}$$

$$\mathrm{BOR}_3(C_3) = 0.687 + 0.008C_3 - 0.000049323C_3^2, \tag{13}$$

$$\mathrm{BOR}_4(C_4) = 0.901 + 0.003C_4 - 0.000020066C_4^2, \tag{14}$$

$$\mathrm{BOR}_5(C_5) = 0.911 + 0.012C_5 - 0.0003054C_5^2, \tag{15}$$

$$\sum_{i=1}^{5} C_i = 644, \tag{16}$$

$$92 \le C_1 \le 210, \tag{17}$$

$$68 \le C_2 \le 138, \tag{18}$$

$$57 \le C_3 \le 140, \tag{19}$$

$$114 \le C_4 \le 182, \tag{20}$$

$$30 \le C_5 \le 182, \tag{21}$$

$$C_i = K_{i1} + 2K_{i2} + 3K_{i3}, \quad i = 1, 2, 3, 4, 5, \tag{22}$$

$$K_{ij} \ge 2, \quad i = 1, 2, 3, 4, 5,\ j = 1, 2, 3. \tag{23}$$

Constraints (11)–(15) are quadratic functions of the number of beds and the BOR of the five departments. After we obtain the number of beds in each department, we can calculate their BOR by formulas (11)–(15). Constraint (16) states the total number of beds in five departments. Constraints (17)–(21) limit the upper bound and lower bound on bed numbers of each department. Constraints (22) and (23) restrict the ward type and patient gender. There are three ward types for each department in WCH. So, the number of beds in department i is the sum of the total number of beds from those three types. In order to distinguish the male and female wards, the number of each department type must be a positive integer and should not be less than two. We used the genetic algorithm [34] to solve the MIP model. The genetic algorithm is run on a personal computer with an Intel® Core™ i7-7700 CPU, a 3.60 GHz z Intel processor, and 8.0 GB RAM. The elapsed time is 77.652611 seconds.

We analyzed the results from three aspects:

(1) Initial bed allocations and optimal bed allocations based on our model: as shown in Figure 5, the blue histograms represent the Initial bed allocation, which is the current hospital bed number. The optimal bed allocations from our model are represented by the yellow histograms. Figure 5 shows the optimal bed allocation strategy: the bed of the W9 reduces from 236 to 166, W10 from 168 to 121, and W19 from 54 to 44; W6 increases from 72 to 135 and W27 from 114 to 178.

(2) Initial BOR and optimal BOR: Figure 6 shows the corresponding BOR after optimization. The W9 increases from 69.5% to 84.76%, W10 from 64.7% to 84.01%, W19 from 68.9% to 84.78%; on the contrary, W6 decreases from 98.1% to 86.81% and W27 from 98.5% to 83.48%. Blue lines represent the original

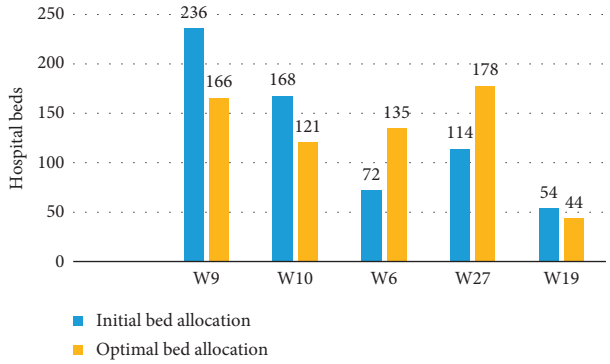

Figure 5: Initial bed allocation strategy and optimal bed allocation strategy.

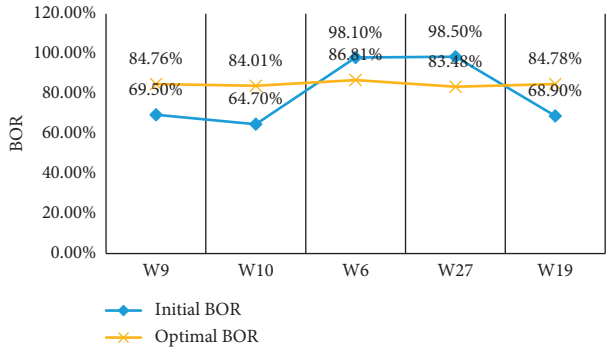

Figure 6: Results of initial BOR and optimal BOR.

BOR, and yellow lines represent the optimal BOR. We found that the maximum and minimum BORs are 98.1% and 64.7%. The maximum difference of BOR is 33.8% but change to 2.80% after optimization.

(3) Objective function value: our objective value, Z, represents the imbalance degree of bed utilization between various departments. For baseline bed allocation, the initial value of the objective function Z is as high as 0.7344. After optimization, the optimal value of Z is 0.0409, indicating that our optimization reduced the severity of the imbalance.

Finally, we can get a combination of beds in different wards based on the number of optimal beds (Table 14). In formula (22), C_i depends on the value of K_{ij}, that is to say, the combinations of K_{ij} produce different C_i values. For example, the optimal number of beds for W9 determined by our model is 166 (C_1 = 166); there are many combinations for single-bed wards (K_{11}), double-bed wards (K_{12}), and triple-bed wards (K_{13}), such as (26, 40, 20), (22, 42, 20), and (36, 20, 30). This means that W9 can provide 26 single-bed wards, 40 double-bed wards, and 20 triple-bed wards; 22 single-bed wards, 42 double-bed wards, and 20 triple-bed wards; or 36 single-bed wards, 20 double-bed wards, and 30 triple-bed wards; and so on.

4. Discussion

Many tertiary hospitals in China are facing the same problem as WCH, with respect to the imbalance in the utilization of bed resources in different departments. The availability of beds for hospital care is excessive in some cases and scarce in others. This phenomenon has caused many problems for hospitals. For example, some hospital wards are always overcrowded, while others are underloaded. Some scheduled patient admissions are delayed or even transferred to other hospitals, and some patients are hospitalized in inappropriate wards which are unsuited to their pathologies, with the risk of a lower quality care and a greater chance of infection [35].

Table 14: Optimal number of beds and different combinations of departments.

Department	Optimal number of beds	Different feasible combinations of K_{ij} : (K_{i1}, K_{i2}, K_{i3})
W9	166	(K_{11}, K_{12}, K_{13}) : (26, 40, 20), (22, 42, 20), (36, 20, 30), ...
W10	121	(K_{21}, K_{22}, K_{23}) : (21, 20, 20), (21, 35, 10), (31, 30, 10), ...
W6	135	(K_{31}, K_{32}, K_{33}) : (35, 20, 20), (20, 40, 7), (25, 10, 30), ...
W27	178	(K_{41}, K_{42}, K_{43}) : (78, 20, 20), (10, 39, 30), (40, 39, 20), ...
W19	44	(K_{51}, K_{52}, K_{53}) : (14, 6, 6), (4, 5, 10), (19, 5, 5), ...

To relieve this imbalance, we propose a data-driven hybrid three-stage framework combining multiple methods to produce a feasible bed allocation strategy since it is difficult to allocate beds among all 28 departments in the whole WCH. We selected five departments (W9, W10, W6, W27, and W19) through data analysis and survey interview. W9, W10, and W19 are departments that have many beds with a low BOR while W6 and W27 have few beds with high BOR. For Stage II, we developed a generic discrete-event simulation model. We fitted the relationship function between BOR and beds of each wards via the simulation model. In Stage III, we developed a MIP model to minimize the imbalance in BOR. The results of Stage II are incorporated into the MIP model as one of the key constraints. We also considered other constraints, such as ward types (single, double, and three-bed wards) and upper and lower bounds on the number of beds.

Our data-driven hybrid three-stage framework produces a flexible allocation strategy for hospital bed management. Our research helps to improve the utilization of medical resources and the quality of medical services by balancing bed numbers and BOR between different departments. Our model may be applied in two ways. Firstly, it can be extended to other wards with different arrival rates and LOS distribution. Secondly, our study can provide a reference for dealing with the problem of hospital bed capacity to other large general hospitals in China. Our research provides a common framework for hospital bed allocation, so other departments or hospitals can follow our three-stages framework to realize their allocation of beds. Because the data of each hospital and the actual situation are different from those of WCH, different constraints or objective functions may be generated. For example, other hospitals

can use data analysis to screen the departments that need to allocate beds; then, they can follow the method described in Stage II to fit the functional relationship between BOR and bed. Different hospitals may have different functional relationships because of their different data. Finally, hospitals can redesign the model with more personalized objective functions and constraints according to their own actual situation.

5. Conclusions

We focused upon the problem of allocating beds among different departments in a hospital. We took a large public hospital in China, WCH, as a case study. To relieve imbalances in BOR between departments, we proposed a three-stage framework. In the first stage, we collected data and identified departments of interest. In the second stage, we identified the functional relationship between the number of beds and the BOR. The third-stage MIP model provides the best number of bed allocations for different departments. It has proven to be a feasible method to ease the shortage of beds.

Our research is based on real data, and hospital managers can draw upon the results of this study to solve the bed occupancy and capacity problem. The three-stage framework can help bed managers adjust the allocation of beds in a timely and dynamic manner. This approach can be applied to the majority of other hospitals and may serve as a starting point for the development of allocation models for other service industries with similar conditions, such as the allocation of beds or room types in hotels.

Future study can consider the following two aspects: since this is the initial stage of bed allocation, the strategy can be extended to more departments. In addition, the practice will be a good reference for other large general hospitals in China. More factors may be considered for inclusion in the MIP model such as other ward resources (nurses and doctors), infectious patients, and the undesirability of mixed-sex rooms.

Appendix

General hospitals have been divided into three levels in China, according to the hospital's functions, tasks, facilities, technology, medical services, and scientific management.

Class I hospitals (the number of beds is 100 or fewer): primary hospitals and health centers that provide prevention, medical care, health care, and rehabilitation services directly to communities in a specific population.

Class II hospitals (101 to 500 beds): regional hospitals that provide comprehensive medical and health services to multiple communities and undertake certain teaching and research tasks.

Class III hospitals (also called tertiary hospitals; authors' hospital; more than 501 beds): regional or higher hospitals that provide high-level specialized medical and health services and perform higher education and scientific research tasks in several areas. Tertiary hospitals are further subdivided into three grades based upon the technical strength of the hospital, management levels, equipment conditions, scientific research capabilities, and more. The West China Hospital is one of the highest-grade hospitals among the tertiary hospitals.

Data Availability

The data used to support the findings of this study are restricted by the West China Hospital in order to protect patient privacy. Data are available from West China Hospital for researchers who meet the criteria for access to confidential data.

Conflicts of Interest

The authors declare that there are no conflicts of interest regarding the publication of this paper.

Acknowledgments

The authors gratefully acknowledge the support from the Admission Service Center of West China Hospital. This research was supported in part by the National Natural Science Foundation of China (Nos. 71532007 and 71131006) and Sichuan Province Science and Technology Support Project Plan (No. 2016FZ0080).

References

[1] World Health Organization, *Tracking Universal Health Coverage: First Global Monitoring Report*, World Health Organization, Geneva, Switzerland, 2015, http://www.who.int/healthinfo/universal_health_coverage/report/2015/en/.

[2] Beijing: China Union Medical University Press. 2016, http://www.nhfpc.gov.cn/guihuaxxs/s10748/201708/d82fa7141696407abb4ef764f3edf095.shtml?from=groupmessage&isappinstalled=1.

[3] T. J. Best, *Hospital Bed Capacity Management*, Dissertations & Theses-Gradworks, Chicago, IL, USA, June 2015.

[4] D. J. Worthington, "Queueing models for hospital waiting lists," *Journal of the Operational Research Society*, vol. 38, no. 5, pp. 413–422, 1987.

[5] R. Akkerman and M. Knip, "Reallocation of beds to reduce waiting time for cardiac surgery," *Health Care Management Science*, vol. 7, no. 2, pp. 119–126, 2004.

[6] K. Seung-Chul, H. Ira, Y. Karl K, and B. Thomas A, "Flexible bed allocation and performance in the intensive care unit," *Journal of Operations Management*, vol. 18, no. 4, pp. 427–443, 2000.

[7] D. Kleinloog, F. B. Houckgeest, and D. Sierink, "Triage after drug overdose: effect of the introduction of a medical psychiatry unit on the allocation of ICU beds," *Critical Care*, vol. 19, no. 1, p. P513, 2015.

[8] L. V. Green, "How many hospital beds?," *British Medical Journal*, vol. 39, pp. 400–412, 2003.

[9] A. J. M. Oerlemans, H. Wollersheim, N. V. Sluisveld, J. G. V. D. Hoeven, W. J. M. Dekkers, and M. Zegers, "Rationing in the intensive care unit in case of full bed occupancy: a survey among intensive care unit physicians," *BMC Anesthesiology*, vol. 16, no. 1, p. 25, 2015.

[10] P. Devapriya, C. T. Strömblad, M. D Bailey et al., "StratBAM: a discrete-event simulation model to support strategic hospital bed capacity decisions," *Journal of Medical Systems*, vol. 39, no. 10, p. 130, 2015.

[11] J. C. Ridge, S. K. Jones, M. S. Nielsen, and A. K. Shahani, "Capacity planning for intensive care units," *European Journal of Operational Research*, vol. 105, no. 2, pp. 346–355, 1998.

[12] G. Romanin-Jacur and P. Facchin, "Optimal planning of a pediatric semi-intensive care unit via simulation," *European Journal of Operational Research*, vol. 29, no. 2, pp. 192–198, 1987.

[13] E. Akcali, M. J. Côté, and C. Lin, "A network flow approach to optimizing hospital bed capacity decisions," *Health Care Management Science*, vol. 9, no. 4, pp. 391–404, 2006.

[14] M. Utley, S. Gallivan, T. Treasure, and O. Valencia, "Analytical methods for calculating the capacity required to operate an effective booked admissions policy for elective inpatient services," *Health Care Management Science*, vol. 6, no. 2, pp. 97–104, 2003.

[15] C. Lakshmi and S. A. Iyer, "Application of queueing theory in health care: a literature review," *Operations Research for Health Care*, vol. 2, no. 1-2, pp. 25–39, 2013.

[16] U. Uzunoglu Kocer and S. Ozkar, "M/C_2/c/K queuing model and optimization for a geriatric care center," *Applied Stochastic Models in Business and Industry*, vol. 31, no. 6, pp. 892–911, 2015.

[17] S. Belciug and F. Gorunescu, "A hybrid genetic algorithm-queuing multi-compartment model for optimizing inpatient bed occupancy and associated costs," *Artificial Intelligence in Medicine*, vol. 68, pp. 59–69, 2016.

[18] T. P. Roh, T. R. Huschka, M. J. Brown, and Y. N. Marmor, "Data-driven simulation use to determine bed resource requirements for the redesign of pre- and post-operative care areas," in *Proceedings of the Winter Simulation Conference*, vol. 1, pp. 1168–1176, Washington, DC, USA, 2014.

[19] E. W. Hans and A. G. Leeftink, "Integral planning of operating rooms and wards: tactical allocation of beds to reduce fluctuations in bed utilization for Medisch Spectrum Twente," in *Enschede*, F. C. Smit, Ed., pp. 1–114, General Books LLC, Memphis, TN, USA, 2015.

[20] J. T. Blake and M. W. Carter, "A goal programming approach to strategic resource allocation in acute care hospitals," *European Journal of Operational Research*, vol. 140, no. 3, pp. 541–561, 2002.

[21] M. M. Hossein, K. Sajad, and T. Mahya, "Reallocation of shafa hospital beds in kerman using goal programming model," *Electronic Physician*, vol. 8, no. 8, pp. 2733–2737, 2016.

[22] I. Marques, M. E. Captivo, and M. Vaz Pato, "An integer programming approach to elective surgery scheduling," *OR Spectrum*, vol. 34, no. 2, pp. 407–427, 2012.

[23] S. Y. Shin, Y. Brun, H. Balasubramanian, P. L. Henneman, and L. J. Osterweil, "Discrete-event simulation and integer linear programming for constraint-aware resource scheduling," *IEEE Transactions on Systems, Man, and Cybernetics: Systems*, vol. 48, no. 9, pp. 1578–1593, 2018.

[24] R. B. Bachouch, A. Guinet, and S. Hajri-Gabouj, "An integer linear model for hospital bed planning," *International Journal of Production Economics*, vol. 140, no. 2, pp. 833–843, 2012.

[25] C. Tontarski, "Modeling and analysis of OR nurse scheduling using mathematical programming and simulation," Dissertations & Theses—Gradworks, 2015.

[26] E. P. C. Kao and G. G. Tung, "Bed allocation in a public health care delivery system," *Management Science*, vol. 27, no. 5, pp. 507–520, 1981.

[27] M. B. Dumas, "Simulation modeling for hospital bed planning," *Simulation*, vol. 43, no. 2, pp. 69–78, 1984.

[28] J. A. Joines and S. D. Roberts, *Simulation Modeling with Simio: A Workbook*, Simio LLC, Sewickley, PA, USA, 2013.

[29] Q. Xiao, L. Luo, S.-Z. Zhao, X.-B. Ran, and Y.-B. Feng, "Online appointment scheduling for a nuclear medicine department in a Chinese hospital," *Computational and Mathematical Methods in Medicine*, vol. 2018, no. 10, pp. 1–13, 2018.

[30] L. B. Holm, H. Lurås, and F. A. Dahl, "Improving hospital bed utilisation through simulation and optimisation: with application to a 40% increase in patient volume in a Norwegian general hospital," *International Journal of Medical Informatics*, vol. 82, no. 2, pp. 80–89, 2013.

[31] K. Schittkowski, "EASY-FIT: a software system for data fitting in dynamical systems," *Structural and Multidisciplinary Optimization*, vol. 23, no. 2, pp. 153–169, 2002.

[32] S. Belciug and F. Gorunescu, "Improving hospital bed occupancy and resource utilization through queuing modeling and evolutionary computation," *Journal of Biomedical Informatics*, vol. 53, pp. 261–269, 2015.

[33] J. K. Cochran and A. Bharti, "Stochastic bed balancing of an obstetrics hospital," *Health Care Management Science*, vol. 9, no. 1, pp. 31–45, 2006.

[34] D. Whitley, "A genetic algorithm tutorial," *Statistics and Computing*, vol. 4, no. 2, pp. 65–85, 1994.

[35] J. Orendi, "Health-care organisation, hospital-bed occupancy, and MRSA," *The Lancet*, vol. 371, no. 9622, pp. 1401-1402, 2008.

Hindawi
Computational and Mathematical Methods in Medicine
Volume 2019, Article ID 3130527, 11 pages
https://doi.org/10.1155/2019/3130527

Research Article

An Improved Sliding Window Area Method for *T* Wave Detection

Haixia Shang,[1] Shoushui Wei,[1] Feifei Liu,[2] Dingwen Wei,[3] Lei Chen,[4] and Chengyu Liu[2]

[1]*School of Control Science and Engineering, Shandong University, Jinan 250061, China*
[2]*School of Instrument Science and Engineering, Southeast University, Nanjing 210096, China*
[3]*Department of Electronic & Electrical Engineering, Bath University, Bath BA27AY, UK*
[4]*School of Science and Technology, Shandong University of Traditional Chinese Medicine, Jinan 250355, China*

Correspondence should be addressed to Shoushui Wei; sswei@sdu.edu.cn and Chengyu Liu; chengyu@seu.edu.cn

Received 4 December 2018; Accepted 5 March 2019; Published 1 April 2019

Guest Editor: Tomas Krilavičius

Background. The *T* wave represents ECG repolarization, whose detection is required during myocardial ischemia, and the first significant change in the ECG signal is being observed in the ST segment followed by changes in other waves like *P* wave and QRS complex. To offer guidance in clinical diagnosis, decision-making, and daily mobile ECG monitoring, the *T* wave needs to be detected firstly. Recently, the sliding area-based method has received an increasing amount of attention due to its robustness and low computational burden. However, the parameter setting of the search window's boundaries in this method is not adaptive. Therefore, in this study, we proposed an improved sliding window area method with more adaptive parameter setting for *T* wave detection. *Methods*. Firstly, *k*-means clustering was used in the annotated MIT QT database to generate three piecewise functions for delineating the relationship between the RR interval and the interval from the *R* peak to the *T* wave onset and that between the RR interval and the interval from the *R* peak to the *T* wave offset. Then, the grid search technique combined with 5-fold cross validation was used to select the suitable parameters' combination for the sliding window area method. *Results*. With respect to onset detection in the QT database, *F*1 improved from 54.70% to 70.46% and 54.05% to 72.94% for the first and second electrocardiogram (ECG) channels, respectively. For offset detection, *F*1 also improved in both channels as it did in the European ST-T database. *Conclusions*. *F*1 results from the improved algorithm version were higher than those from the traditional method, indicating a potentially useful application for the proposed method in ECG monitoring.

1. Introduction

Nowadays, an increase in the number of people suffering from heart diseases has been seen. Characterized by several waveforms such as the *P* wave, QRS complex, and *T* wave, electrocardiogram (ECG) becomes the most intuitive and basic tool to diagnose heart diseases in clinical applications which can provide essential physiological/pathological information for clinical diagnoses and decision-making [1], including important time interval information between the onset and offset of different waves [2]. Besides, many wearable monitoring devices have appeared in recent years, which makes it possible to monitor ECG signals throughout an individual's daily life. Meanwhile, a large amount of ECG data are generated daily, which is impossible for physicians to view/diagnose each ECG signal manually [3]. Therefore, developing accurate automatic analysis algorithms for ECG signals is critical, especially with respect to mobile ECG monitoring [4]. Furthermore, QRS complex have been widely investigated because of its highest amplitude over the past decades. Up to now, there are many classical methods for detecting QRS complex and most of the methods have been listed in [5], and the classical widely-used methods are parabolic fitting [6], neural-network-based method [7], and convolutional neural network [8]. In addition, those methods for detecting the QRS complex have shown high sensitivity with positive predictivity (>99%) on the MIT-BIH arrhythmia database [9], which can provide powerful support for other waves' detections.

As one of three main waves of ECG, the *T* wave represents ECG repolarization, and its absence or unusual shapes may signify disruption in repolarization or another segment of the

heartbeat [10]. Additionally, *T* wave abnormalities are associated with some heart diseases such as inverted *T* waves found in other leads (other than the V1 to V4 leads), which is related to an increase in cardiac deaths, and a tall or wide QRS complex with an upright *T* wave is further suggestive of a posterior infarction. Furthermore, during myocardial ischemia, the first significant change in ECG signal is being observed in ST-segment followed by changes in other waves like *P* wave and QRS complex of ECG signal. Hence, detection of the *T* wave is significant in clinical applications [11].

However, accurate/robust *T* wave detection still presents challenges due to its low amplitude (usually 0.1 to 0.3 mV) as well as great variations in *T* waves' morphologies [12], like positive *T* wave, negative *T* wave, and biphasic *T* wave. Besides, most of the ischemic cases suffering from earlier STEMI (ST-elevation myocardial infarction) have a prominent ST elimination or depression, which significantly affects the detection of the *T* onsets. Nowadays, various approaches based on different techniques have been proposed for *T* wave detection, and those typical techniques are wavelet [13, 14], mathematical model [15], support vector machine (SVM) [16], artificial neural network (ANN) [17–19], low-pass differentiation (LPD) [20], hidden Markov model (HMM) [21, 22], partially collapsed Gibbs sample and Bayesian (PCGS) [23], "wings" function [24], derivative curve [25], adaptive technique [26], computing the Trapezium's area [27], TU complex analyses [28], correlation analysis [29], *k*-nearest neighbor [30], and sliding window area (SWA) [31]. In these aforementioned methods, the wavelet-based method is robust to waveform morphological variations but is sensitive to noise [13, 14]. The mathematical model method needs to build robust ECG templates, but when the waveform variations are large, building universal templates becomes difficult [15]. The SVM-based method is efficient but constructing efficient features is tough [16], and the ANN-based method faces the drawback of high computational complexity [17]. As a comparison, the SWA method has low computational complexity which is also robust to noise and waveform morphological variations [31].

In 2006, Zhang et al. first proposed the SWA method for detecting *T* wave offsets and confirmed its efficiency in the QT database [31]. Subsequently, Song et al. improved this method for detecting *T* wave onsets [32]. Afterwards, our team combined onsets and offsets detection for classifying the morphology of the ST segment [33]. In 2017, our team analyzed its efficiency in the QT database with a different evaluation index (*F*1 measure), and we found that there is still some space for further improvement since the parameter settings in the transitional SWA method are not adaptive [34], and the parameters given by Zhang et al. [31] and Song et al. [32] are empiric values and there is no optimization step included.

Hence, in this study, an improved SWA method for both onset and offset detections of *T* wave with more adaptive parameter settings is proposed. The performance of the improved method was compared with the traditional method, and both methods were validated in two common ECG databases: (1) the QT database (training and testing) and (2) another independent European ST-T database (only testing).

2. Methods

2.1. Data. Records from two datasets are used. The first is the QT database, which contains 105 15-minute two-channel ECG recordings with the sample rate of 250 Hz, and we chose it as the training and testing sets because multiple-type records from different databases are contained in this database. Besides, totally 43 recordings have manually annotated *T* wave onsets and 103 recordings have manually annotated *T* wave offsets. All records with annotations are selected, and for each record, a 0.05–45 Hz low-pass zero-phase filter was applied for denoising before importing to our algorithm. Furthermore, there are usually 30 to 100 representatively manually annotated discrete beats in each annotated recording. Thus, an RR interval adjustment is also needed before using these records because we used the manually annotated *R* peak locations. Table 1 shows the summarized annotated information of the QT database. More detailed information about the annotations of this database can be found in the study by Laguna et al. [35].

The second database is the European ST-T database, which consists 90 2-hour two-channel ECG recordings sampled at 250 Hz, and records of this database are only used to test the robustness of our improved method. The European ST-T database is chosen because of its widely usages in evaluation of algorithms for analysis of ST and *T* wave changes [36, 37]. In this study, 23 recordings (only the first 5 minutes in each recording) were selected and were manually annotated for *T* wave onsets and offsets by a trained staff member because of loss of *T* wave international annotations. Table 1 also shows the detailed annotation information of this database. Besides, when choosing records, if there were serious signal quality problems within the first 5-minute episode, the following 5-minute episode was used and a 0.05–45 Hz bandpass filter was applied for denoising for each record we chose before importing into the algorithm. We do not implement RR interval adjustment because *R* peaks were detected by *jqrs* method [21].

To verify the consistency of the annotations between the two databases, we analyzed the time interval information between the *T* wave onset/offset and the corresponding *R* peak position for the two databases. Figure 1 shows the probability density distributions of the time interval information from the two databases. As shown in Figure 1, we found that our manual annotations of the onset/offset of *T* wave in the European ST-T database had similar probability density distributions with the annotations in the QT database, which indicated the effectiveness of our annotations.

2.2. Sliding Window Area (SWA) Method

2.2.1. SWA Method. SWA is an algorithm for detecting *T* wave onset and offset (T_{on} and T_{end}, respectively) by analyzing the waveform area of ECG within a sliding window [31]. Onset/offset is detected when the area of the sliding window reaches its maximum in a prefixed searching range. Then, we show an example for explaining the method in Figures 2 and 3.

Table 1: Summary of the annotative information of the QT and the European ST-T databases.

Variable	QT database		European ST-T database	
	Onset	Offset	Onset	Offset
No. of recordings	43	105	23	23
No. of annotated beats	1371	3542	14337	14337
Min. Dis_qrs (ms)	52	228	60	220
Max. Dis_qrs (ms)	412	784	264	612
Mean of Dis_qrs (ms)	164	360	160	380
SD of Dis_qrs (ms)	60	71	29	47

Dis_qrs: the time interval between the *T* wave onset/offset and the *R* wave position within the current beat; SD: standard deviation. The annotations of the QT database are taken from the database website https://www.physionet.org/physiobank/database/qtdb/doc/index.shtml.

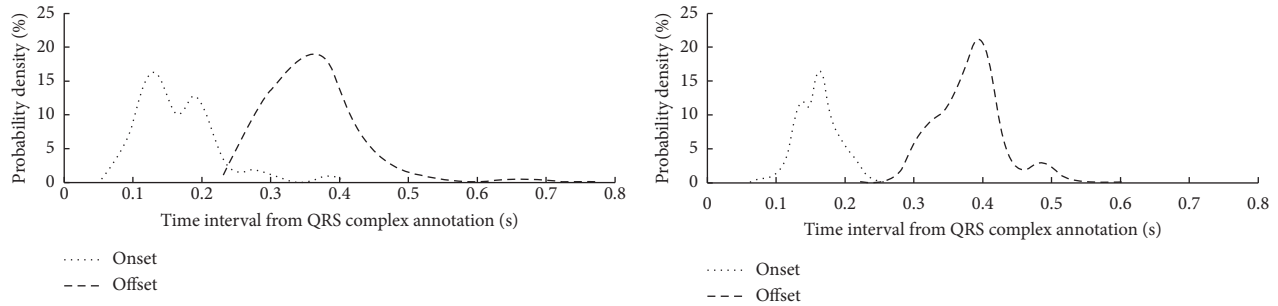

Figure 1: Probability density distribution of the time interval information between *T* wave onset/offset and *R* wave peak by analyzing the annotations from the two databases: (a) QT database and (b) European ST-T database.

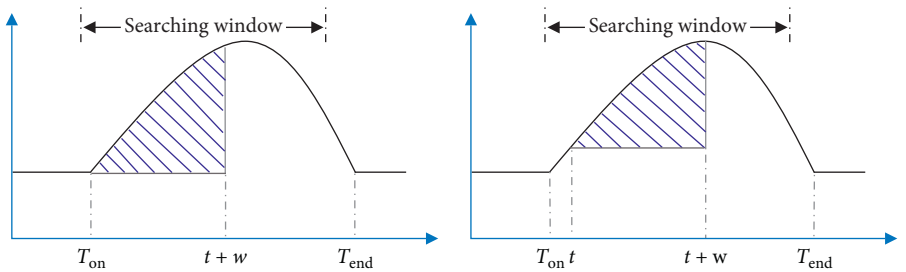

Figure 2: Demonstration of the SWA method for *T* wave onset detection.

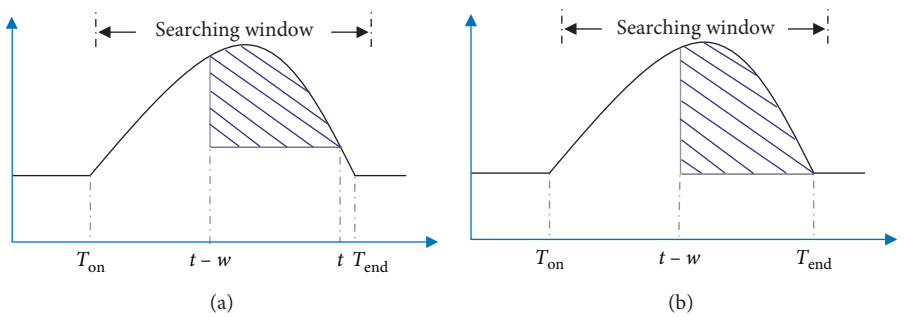

Figure 3: Demonstration of the SWA method for detecting offsets of the *T* wave.

Figure 2 illustrates the detection for T_{on}. Firstly, with the location of R peak, the left and right boundaries (t_1 and t_2, respectively) of search window are determined based on the current RR interval as suggested in the study by Song et al. [32]:

$$\begin{cases} t_1 = \left(\lceil 0.5 \times \sqrt{\text{RR}_i}\,\rceil + R_i + 0.08\right)\text{s}, \\ t_2 = \left(\lfloor 0.15 \times (\text{RR}_i)\rfloor + R_i + 0.12\right)\text{s}, & \text{if RR}_i < 0.88\ \text{s}, \\ t_1 = \left(\lceil 0.5 \times \sqrt{\text{RR}_i}\,\rceil + R_i + 0.1\right)\text{s}, \\ t_2 = \left(R_i + 0.32\right)\text{s}, & \text{if RR}_i \geq 0.88\ \text{s}, \end{cases} \tag{1}$$

where RR_i is the i_{th} RR interval and R_i is the i_{th} position of R peak.

The waveform area (area of onset denoted as: Ao) within the fixed sliding window $[\,t \;\; t+w\,]$ was calculated using the following formula:

$$\text{Ao} = \sum_{j=t}^{t+w} \left(s_j - \overline{s}_k\right), \tag{2}$$

where $w = 0.12$ s (by default), which is the window width, t stretches from t_1 to t_2, s_j is the waveform amplitude at the j_{th} sample point, and $\overline{s}_k$ is the local average amplitude (using a smoothing window of $p = 0.016$ s by default), which is defined according to the following equation:

$$\overline{S}_k = \frac{1}{2p+1} \sum_{j=t-p}^{t+p} S_j. \tag{3}$$

As shown in Figure 2, when $t = T_{\text{on}}$, Ao reaches its maximum value.

Figure 3 illustrates the T_{end} detection. At first, with the location of the R peak, the left and right boundaries (t_3 and t_4, respectively) of the search window are determined based on the current RR interval as suggested in a study by Zhang et al. [31]:

$$\begin{cases} t_3 = \left(\lfloor 0.15 \times \text{RR}_i\rfloor + R_i + 0.148\right)\text{s}, \\ t_4 = \left(\lceil 0.7 \times \text{RR}_i\rceil + R_i - 0.036\right)\text{s}, & \text{if RR}_i < 0.88\ \text{s}, \\ t_3 = \left(R_i + 0.28\right)\text{s}, \\ t_4 = \left(\lceil 0.2 \times \text{RR}_i\rceil + R_i + 0.404\right)\text{s}, & \text{if RR}_i \geq 0.88\ \text{s}. \end{cases} \tag{4}$$

The waveform area (area of ends denoted as: Ae) within the fixed sliding window $[\,t-w \;\; t\,]$ was then calculated according to the following formula:

$$\text{Ae} = \sum_{j=t-w}^{t} \left(s_j - \overline{s}_k\right), \tag{5}$$

where $w = 0.128$ s (by default), t is from t_3 to t_4, and s_j and $\overline{s}_k$ have been defined in equation (2). As shown in Figure 3, when $t = T_{\text{end}}$, Ae reaches its maximum value. As for the difference between Figures 2 and 3 is the direction to calculate the sliding area.

In addition, Algorithm 1 shows the description of the traditional SWA algorithm and more details to which the algorithm proof can refer [31].

2.2.2. Improved SWA Method. One key issue with respect to the SWA method is to accurately determine the search boundaries, but the search boundaries are closely related to the RR interval. As shown in Figures 2 and 3, if the interval of the searching window's boundaries was set too small which means that two boundary points are near the current R peak, the maximum of sliding area could not be found or the detected onset/offset of T wave are nearer to the R peak. These issues affect detection accuracy, which results in detection error and vice versa.

In the traditional SWA method, there are two piecewise functions with predefined parameter settings. In order to more accurately model the relationships between RR interval and the searching boundaries in this study, we performed a k-means clustering analysis between RR intervals and RT_{on} (RT_{on} denotes the time interval between the R peak and T wave onset) as well as the relationship between the RR intervals and RT_{off} (RT_{off} the time interval between the R peak and T wave offset), which is implemented by means of the k-means function in Matlab. The scatter plots with the optimal k-means clustering ($k = 3$) are shown in Figure 4 [38], and k is determined by combining the results of clustering and the computational complexity of parameters' settings as well as the adaptiveness of the algorithm. Then, the two relationships (between RR intervals and RT_{on}, and between RR intervals and RT_{off}) are obtained using the following equations:

$$\begin{aligned} &\text{case 1}: \text{RR} < 0.76\ \text{s}, && 0.05\ \text{s} < \text{RT}_{\text{on}} < 0.25\ \text{s}, \\ &\text{case 2}: 0.76\ \text{s} \leq \text{RR} < 1.13\ \text{s}, && 0.05\ \text{s} < \text{RT}_{\text{on}} < 0.35\ \text{s}, \\ &\text{case 3}: \text{RR} \geq 1.13\ \text{s}, && 0.05\ \text{s} < \text{RT}_{\text{on}} < 0.45\ \text{s}, \\ &\text{case 1}: \text{RR} < 0.72\ \text{s}, && 0.2\ \text{s} < \text{RT}_{\text{off}} < 0.45\ \text{s}, \\ &\text{case 2}: 0.72\ \text{s} \leq \text{RR} < 1.1\ \text{s}, && 0.2\ \text{s} < \text{RT}_{\text{off}} < 0.6\ \text{s}, \\ &\text{case 3}: \text{RR} \geq 1.1\ \text{s}, && 0.2\ \text{s} < \text{RT}_{\text{off}} < 0.8\ \text{s}. \end{aligned} \tag{6}$$

Thus, the three piecewise functions for determining the search boundaries for T wave onset and offset detections were obtained with the parameters presented in Table 2:

$$\begin{cases} t_1 = \left(R_i + \lceil \text{ald} \times \sqrt{\text{RR}_i}\,\rceil + 0.02\right)\text{s}, \\ t_2 = \left(R_i + \lceil \text{alu} \times \sqrt{\text{RR}_i}\,\rceil + 0.16\right)\text{s}, & \text{if RR}_i < 0.76\ \text{s}, \\ t_1 = \left(R_i + \lfloor \text{ard} \times \sqrt{\text{RR}_i}\,\rfloor + 0.04\right)\text{s}, \\ t_2 = \left(R_i + \lfloor \text{aru} \times \sqrt{\text{RR}_i}\,\rfloor + 0.24\right)\text{s}, & \text{if } 0.76\ \text{s} \leq \text{RR}_i < 1.13\ \text{s}, \\ t_1 = \left(R_i + \lceil \text{amd} \times \sqrt{\text{RR}_i}\,\rceil + 0.04\right)\text{s}, \\ t_2 = \left(R_i + \lceil \text{amu} \times \sqrt{\text{RR}_i}\,\rceil + 0.4\right)\text{s}, & \text{if RR}_i \geq 1.13\ \text{s}, \end{cases} \tag{7}$$

$$\begin{cases} t_3 = \left(R_i + \lceil \text{ald} \times \text{RR}_i\rceil + 0.18\right)\text{s}, \\ t_4 = \left(R_i + \lceil \text{alu} \times \text{RR}_i\rceil + 0.3\right)\text{s}, & \text{if RR}_i < 0.72\ \text{s}, \\ t_3 = \left(R_i + \lfloor \text{ard} \times \text{RR}_i\rfloor + 0.18\right)\text{s}, \\ t_4 = \left(R_i + \lfloor \text{aru} \times \text{RR}_i\rfloor + 0.4\right)\text{s}, & \text{if } 0.72\ \text{s} \leq \text{RR}_i < 1.1\ \text{s}, \\ t_3 = \left(R_i + \lceil \text{amd} \times \text{RR}_i\rceil + 0.18\right)\text{s}, \\ t_4 = \left(R_i + \lceil \text{amu} \times \text{RR}_i\rceil + 0.48\right), \text{s} & \text{if RR}_i \geq 1.1\ \text{s}. \end{cases} \tag{8}$$

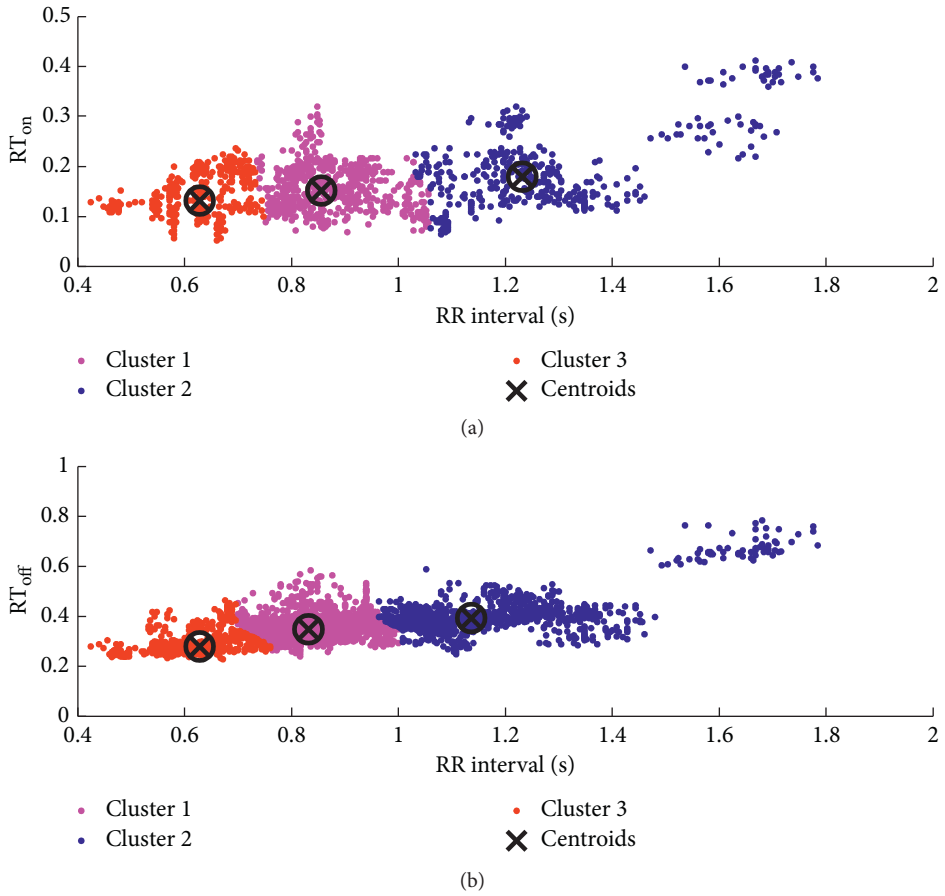

Figure 4: Clustering results for T wave feature points: (a) clustering information of T wave onsets; (b) clustering information of T wave offsets.

Input: ECG signal $S(t)$, R peak locations, R peak numbers N, sliding window width w, smoothing factor p, and morphology predefined factor r
Output: T wave onset locations
Calculation:
(1) Calculate t_1 and t_2 and construct sliding window
window $= S(t_1 : t_2)$
(2) Smooth signal and calculate sliding area for each point i inside $[t_1, t_2]$
$\text{Area}(i) = \text{sum}(S(i : (i + w)) - \text{sum}(S((i - p) : (i + p)))/(p * 2 + 1))$
(3) T wave morphology classification
if $r =$ "p"$\|r =$ "pn"$\|r =$ "bm"$\|r =$ ""
calculate $[k_1, l_1] = \max(\text{Area})$
end if
if $r =$ "n"$\|r =$ "np"$\|r =$ ""
calculate $[k_2, l_2] = \max(-\text{Area})$
end if
(4) Get k
$k = \min(k_1, k_2)$
Output: T wave onset $= R$ peak $+ k$.

Algorithm 1: Traditional SWA algorithm (T wave onset detection).

Then, the *grid search* was used to determine the best combination of parameters in equations (7) and (8), which was implemented by for loop. In a loop, we changed the value of one parameter at a time, kept the other parameters unchanged, and applied the algorithm in the QT database as well as using a 5-fold cross-validation. Then, we stored the $F1$ measure of one loop and started another loop. Through all loops, we traversed all of the combinations of parameters referred to in Table 2. After comparing the results, the combinations of parameters with the highest $F1$ measure

were chosen. The best parameters' combinations for T wave onsets are listed: ald = 0.4, alu = 0.2, ard = 0.4, aru = 0.4, amd = 0.3, and amu = 0.0 and for T wave ends are listed: ald = 0.2, alu = 0.1, ard = 0.2, ard = 0.1, aru = 0.0, amd = 0.0, and amu = 0.1. The improved SWA method can be summarized as a block diagram in Figure 5.

2.3. Evaluation Method. Detections for true and false positives (TP and FP, respectively) and false negative (FN) were determined with a threshold of 100 ms. In this study, indices like sensitivity (Se), positive precision ($P+$), and $F1$ measurement were selected as evaluation indices [39, 40] with the following definitions: $\mathrm{Se} = \mathrm{TP}/(\mathrm{TP} + \mathrm{FN})$, $P+ = \mathrm{TP}/(\mathrm{TP} + \mathrm{FN})$, and $F1 = (\mathrm{TP} \times 2)/(\mathrm{TP} \times 2 + \mathrm{FN} + \mathrm{FP})$. $F1$ measure is selected other than accuracy since $F1$ measure is the weighted average of precision and recall which satisfies our asymmetric datasets where values of false positive and false negatives are not the same.

3. Results

Figure 6 shows the detection examples of the proposed method, compared with the traditional methods, Zhang's method for T wave offset detection [31] and Song's method for T wave onset detection [32]. Figure 6(a) shows the inverted T wave detections, Figure 6(b) shows the biphasic T wave detections, and Figure 6(c) shows the normal T wave detections. From Figure 6, T wave offset detections get better results than T wave onset detections. And, our method got obviously better results when it is applied in T wave onsets detections.

3.1. Results from the QT Database. We firstly tested the performance of the improved SWA method on the QT database. The traditional SWA methods (Song's method [32] and Zhang's method [31]) were used as comparators.

Table 3 shows the results of onset and offset detections in the QT database. Both of the two channels signals (first and second channels) were tested. From Table 3, we found the improved SWA method significantly enhanced detection accuracies for both onset and offset detections. For onset detection, $F1$ improved from 54.70% to 70.46% and 54.05% to 72.94% for two ECG channels, respectively. For offset detection, $F1$ improved from 87.83% to 93.73% and 86.73% to 94.75% for two ECG channels, respectively. In addition, detection errors were also analyzed. As expected, the improved SWA method indicated smaller detection errors than the traditional method except for a slight increase in the offset detection from the second channel (traditional 0.027 ± 31.85 ms versus improved 2.45 ± 33.98 ms). However, it is worthwhile to note that all Se, $P+$, and $F1$ indices increased from ~86% to ~94%.

3.2. Results from the European ST-T Database. Table 4 shows the results of onset and offset detections in the European ST-T database. The improvements after using the improved method were more significant when performing T wave onset detection. $F1$ improved from 41.02% to 84.13% and 44.33% to 87.62% for two ECG channels, respectively. The mean detection errors significantly decreased from 19.52 ms to 7.04 ms and 36.27 ms to 6.35 ms for two ECG channels, respectively. Performance improvements in offset detection were small but convincing $F1$ improved from 98.83% to 99.57% and 91.76% to 98.29% for two ECG channels, respectively. However, the mean detection errors for T wave offset detection slightly increased (not significant) when performing the improved method.

4. Discussion

As seen from Tables 3 and 4, both T wave onset and offset detection of the new proposed method reported better performances ($F1$ measure) than the traditional method, suggesting that applying the clustering technique in the SWA method for deciding searching boundaries is helpful to enhance detection accuracy. In addition, clustering is a statistical-based technique, which can be used to determine whether the independent part of a population belongs to different groups by comparing quantitative multiple features [38]. Besides, we noted that, for the T wave offset detections, neither the traditional SWA nor the improved version reported the better performance than the detection of T wave onsets. One possible explanation is that Zhang proposed this method originally to detect T wave offsets not T wave onsets and proved its mathematical rationality for T wave offsets. Another possible explanation is that the clustering method for determining the search boundaries is a statistical-based technique. Therefore, the accuracy of the clustering results is related to the data amount. However, the annotated T wave onsets in the QT database are far less than the annotated T wave offsets (1371 versus 3452). Thus, the relationship found by clustering analysis between the RR interval and $\mathrm{RT}_{\mathrm{on}}$ is not that strong (Figure 4(a)) compared to the relationship between the RR interval and $\mathrm{RT}_{\mathrm{off}}$ (Figure 4(b)). Moreover, the significant difference between the improved and traditional SWAs indicates that the improved version can more extensively and adaptively determine the search window's boundaries by using the k-means clustering based on the QT database and grid search strategy. However, the traditional SWA only used predefined parameters and did not give out any detailed explanations.

Another difference between Zhang's [31] and our results was observed when using the QT database for validation, Zhang's study chose the better result from the outputs of the two ECG channels [31]. In order to compare our results with those from Zhang, we also calculated smaller errors from the results of two ECG channels. The comparable results are summarized in Table 5. The mean detection errors are similar between Zhang's and our results. We also noted that the standard deviation of detection errors was 25.82 ms for our method and 21.19 ms for the traditional SWA. Both of them were smaller than the acceptable threshold (30.6 ms) proposed by the common standards in Electrocardiography Working Party [41].

Table 5 also summarizes comparable results from other studies. The wavelet-based method reported a mean error of

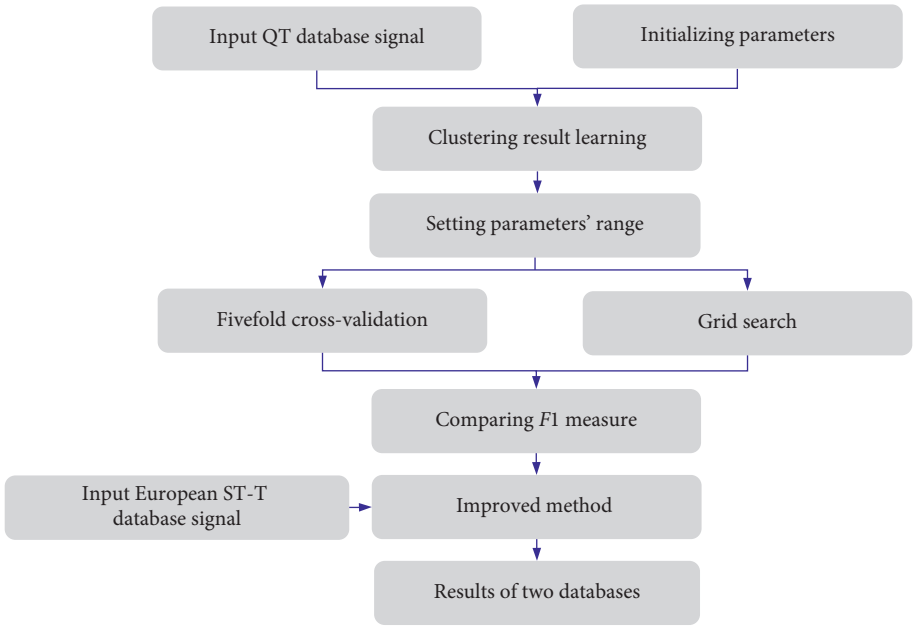

Figure 5: The block diagram of the proposed method for delineating the *T* wave onset/offset.

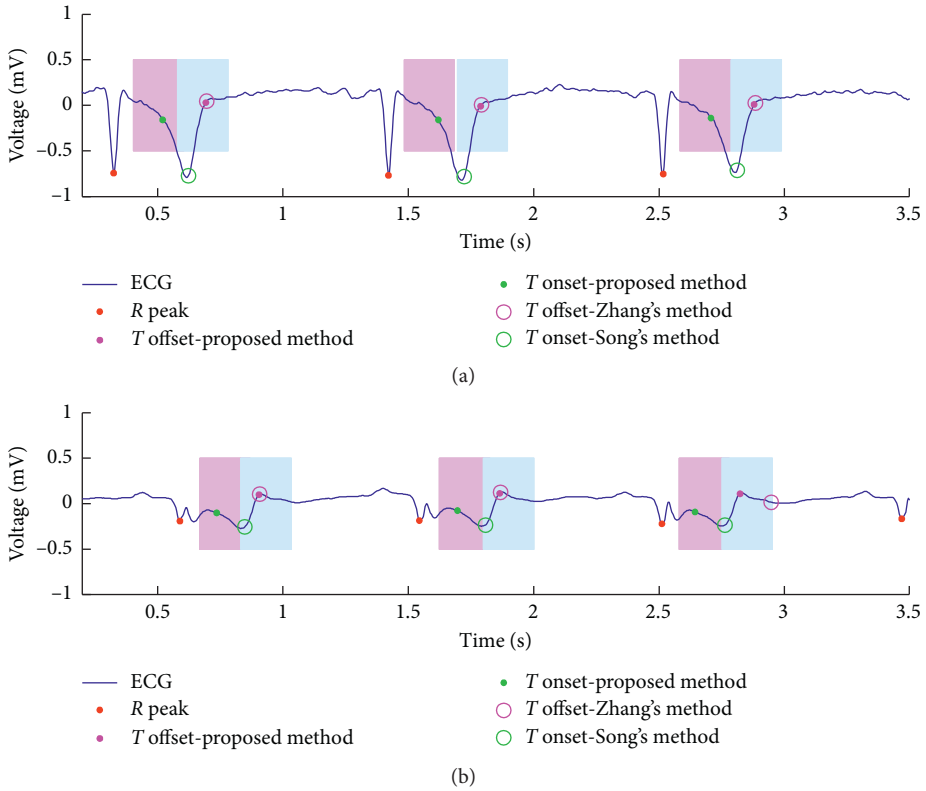

Figure 6: Continued.

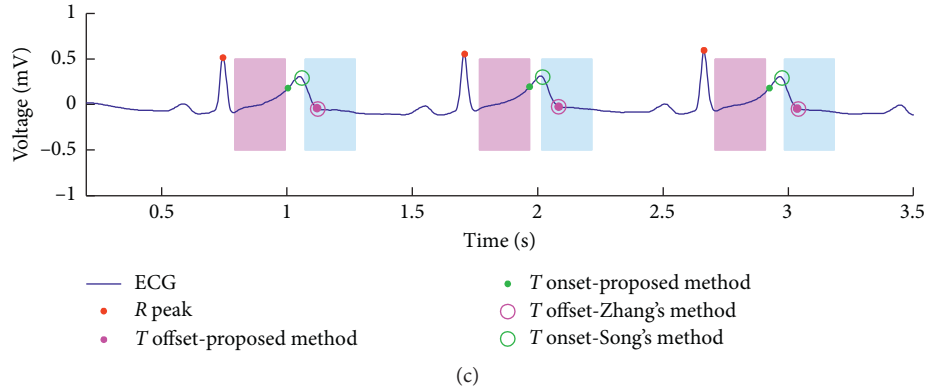

(c)

Figure 6: *T* wave detection examples. The solid points marked (•) are *R* peaks; the solid points marked (• and •) are results of our method; the hollow circles marked (○ and ○) are results of the traditional method; the shadow areas are accepted as TP cases. (a) e0107; (b) e0111; (c) e0118.

Table 2: Information of parameters when detecting the *T* wave.

Parameters	*T* onset			*T* offset		
	IV	CS	CR	IV	CS	CR
ald/alu/ard aru/amd	0.1	0.1	0.1~0.4	0.1	0.1	0.1~0.4
amu	0.0		0.0~0.4	0.0		0.0~0.4

IV: initialized value; CS: change step; CR: change range.

Table 3: Results of *T* wave detection in the QT database.

Detection	Channel	Method	Se (%)	*P*+ (%)	*F*1 (%)	Error mean ± SD (ms)
Onset	First	Traditional SWA [32]	54.70	54.70	54.70	−30.2 ± 40.75
		Improved SWA	70.46	70.46	**70.46**	**7.3 ± 53.12**
	Second	Traditional SWA [32]	54.05	54.05	54.05	−36.27 ± 43.29
		Improved SWA	72.94	72.94	**72.94**	**6.35 ± 53.78**
Offset	First	Traditional SWA [31]	87.83	87.83	87.83	−2.57 ± 30.08
		Improved SWA	93.93	93.93	**93.93**	**1.19 ± 33.59**
	Second	Traditional SWA [31]	86.73	86.73	86.73	0.027 ± 31.85
		Improved SWA	94.75	94.75	**94.75**	**2.45 ± 33.98**

Table 4: Results of *T* wave detection in the European ST-T database.

Detection	Channel	Method	Se (%)	*P*+ (%)	*F*1 (%)	Error mean ± SD (ms)
Onset	First	Traditional SWA [32]	41.02	41.02	41.02	19.52 ± 31.89
		Improved SWA	84.13	84.13	**84.13**	**−7.87 ± 44.22**
	Second	Traditional SWA [32]	44.33	44.32	44.33	−36.27 ± 43.29
		Improved SWA	87.62	87.61	**87.62**	**−15.20 ± 33.54**
Offset	First	Traditional SWA [31]	98.80	98.86	98.83	22.2 ± 22.70
		Improved SWA	99.50	99.65	**99.57**	**26.94 ± 20.98**
	Second	Traditional SWA [31]	91.80	91.71	91.76	21.07 ± 26.31
		Improved SWA	98.29	98.28	**98.29**	**24.54 ± 25.52**

1.6 ms [13, 14]; the low-pass differentiation-based method gave a relative large mean error of 13.5 ms [20], while the hidden Markov model-based method reported a mean error of 5 ms [21, 22]. Furthermore, the partially collapsed Gibbs sample reported 4.3 ms [23], and the *k*-nearest neighbor-based method reported 2.8 ms [20]. The TU complex analysis gave a minimum detection mean error of 0.8 ms but did not include the corresponding Se and *P*+ results [28]. In addition, methods proposed by Mahsa with linear and nonlinear phase observation to detect fiducial points are also

Table 5: Comparable detection results of T wave offset in the QT database.

Methods	Annotations	Se (%)	$P+$ (%)	Mean ± SD (ms)
Improved SWA	3542	**98.5**	**98.5**	**1.21 ± 25.82**
Traditional SWA [31]	3542	95.5	95.5	−1.12 ± 21.19
Wavelet-based [13, 14]	3542	99.77	97.79	−1.6 ± 18.1
Low-pass differentiation-based [20]	3542	99.00	97.74	13.5 ± 27.0
Hidden Markov model-based [21, 22]	3542	NA	NA	−5 ± 14
Partially collapsed Gibbs sample [23]	3403	99.81	98.97	4.3 ± 20.8
k-nearest neighbor-based [30]	30 records	NA	NA	2.8 ± 18.6
TU complex analysis [28]	3528	92.60	NA	0.8 ± 30.3
Neural network and fixed-size least-squares SVM [19]	3542	NA	NA	−3.0 ± 16.9
L.EKF25 [42]	10 records	NA	NA	11 ± 39
N.L.EKF25 [42]				4 ± 23
L.EKF25 [42]	15 records	NA	NA	−17 ± 30
N.L.EKF25 [42]				−21 ± 19

NA: not available; L.EKF25: linear Kalman filter; N.L.EKF25: nonlinear Kalman filter.

listed as comparative method [42], and two parts of QT database including normal sinus rhythm and arrhythmia database are used when evaluating extraction of fiducial points and the nonlinear observation has more smaller deviations 23 ms for the first database and 19 ms for the second database.

The potential issues existing in the above studies consist of two main points: (1) the time tolerance for determining true positive detection was not clear and (2) training and testing were both performed in the QT database, but we used the European ST-T database as the independent testing dataset.

Besides, as deep-learning technology improves, more and more methods based on this technique have been proposed to detect ECG feature points; for instance, a recently proposed method using neural network and fixed-size least-squares SVM to detect T wave end reported it is a minimum detection mean error of −3 ms in the QT database; a QRS complex detection by using two-level convolutional neural network [8] reported its sensitivity of 99.77% in the MIT-BIH AR database. When using deep-learning technique, a great amount of data is needed, and in T wave detection, the annotated T wave ends are limited but a meaningful strategy was proposed in [19], which is to use different strategies for selecting different training sets such as random selection and k-means. But, we just proposed an idea that is to use one independent database (QT dataset) as the training set and testing set and another independent database (records from the European ST-T database annotated by a trained staff) as the testing set.

In order to illustrate difference between error and $F1$ measure, we did statistical analysis of error. And, Figure 7 gives the cumulative line chart of error (denoted as CLCE) of T wave offsets in the QT database which explains our method got more true positive beats than the traditional method inside our time tolerance. The CLCE of T wave onsets in the QT database and CLCE of T wave in the European ST-T database also have the same regularities of distribution as it did in the T wave offsets in the QT database.

Moreover, the limitation of our study is that the annotations of the European ST-T database are only done by a trained staff member which may result in nonauthoritative annotations. Besides, we only combine the data statistic and data mining technique to changing the parameters of traditional SWA method. In our following work, more records with authoritative annotations will be used to test the robustness of the combination of parameters we obtained in this study.

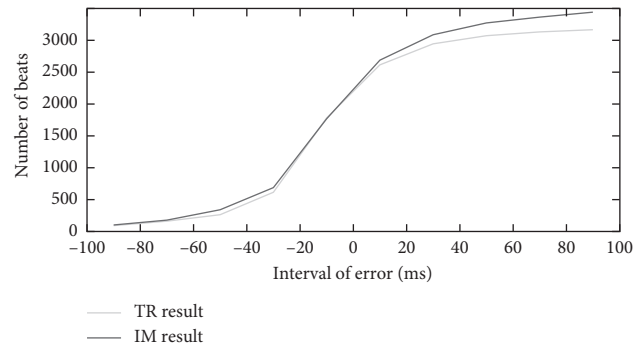

Figure 7: The cumulative line chart of error (T offsets in the QT database). TR result represents the traditional SWA method result, and IM result represents the improved SWA method result.

5. Conclusion

In this paper, an improved sliding window area method for detecting T wave onset and offset was proposed. The main contribution/novelty was for application of the data statistic and data mining technique: (1) *k-means clustering* for the setting of search boundaries and (2) *grid search strategy* to optimize the parameters. Experiments performed in the QT database and the European ST-T database demonstrated the improved method's better performance.

Data Availability

The data used to support the findings of this study are available from the corresponding author upon request.

Conflicts of Interest

The authors declare no conflicts of interest regarding the publication of this work.

Acknowledgments

This work was supported by the National Natural Science Foundation of China under Grant no. 81871444, Shandong Province Key Research and Development Plan under Grant no. 2018GSF118133, and Jiangsu Province Primary Research and Development Plan under Grant no. BE2017735. The authors thank the support from the Southeast-Lenovo Wearable Heart-Sleep-Emotion Intelligent Monitoring Lab.

References

[1] J. H. O'Keefe, S. C. Hammill, and M. Freed, *The Complete Guide to ECGs*, Physicians' Press, Boston, MA, USA, 1997.

[2] J. P. V. Madeiro, P. C. Cortez, J. A. L. Marques, C. R. V. Seisdedos, and C. R. M. R. Sobrinho, "An innovative approach of QRS segmentation based on first-derivative, Hilbert and Wavelet Transforms," *Medical Engineering & Physics*, vol. 34, no. 9, pp. 1236–1246, 2012.

[3] E. J. Topol, "The big medical data miss: challenges in establishing an open medical resource," *Nature Reviews Genetics*, vol. 16, no. 5, pp. 253-254, 2015.

[4] A. Page, O. Kocabas, T. Soyata, M. Aktas, and J.-P. Couderc, "Cloud-based privacy-preserving remote ECG monitoring and surveillance," *Annals of Noninvasive Electrocardiology*, vol. 20, no. 4, pp. 328–337, 2015.

[5] B.-U. Kohler, C. Hennig, and R. Orglmeister, "The principles of software QRS detection," *IEEE Engineering in Medicine and Biology Magazine*, vol. 21, no. 1, pp. 42–57, 2002.

[6] A. I. Manriquez and Q. Zhang, "An algorithm for QRS onset and offset detection in single lead electrocardiogram records," in *Proceedings of the 2007 29th Annual International Conference of the IEEE Engineering in Medicine and Biology Society*, Lyon, France, August 2007.

[7] Q. Xue, Y. H. Hu, and W. J. Tompkins, "Neural-network-based adaptive matched filtering for QRS detection," *IEEE Transactions on Biomedical Engineering*, vol. 39, no. 4, pp. 317–329, 1992.

[8] Y. Xiang, Z. Lin, and J. Meng, "Automatic QRS complex detection using two-level convolutional neural network," *BioMedical Engineering OnLine*, vol. 17, no. 1, p. 13, 2018.

[9] F. Liu, C. Liu, X. Jiang et al., "Performance analysis of ten common QRS detectors on different ECG application cases," *Journal of Healthcare Engineering*, vol. 2018, Article ID 9050812, 8 pages, 2018.

[10] E. B. Hanna and D. L. Glancy, "ST-segment depression and T-wave inversion: classification, differential diagnosis, and caveats," *Cleveland Clinic Journal of Medicine*, vol. 78, no. 6, pp. 404–414, 2011.

[11] J. Tikkanen, T. Kenttä, K. Porthan, H. V. Huikuri, and M. J. Junttila, "Electrocardiographic T wave abnormalities and the risk of sudden cardiac death: the Finnish perspective," *Annals of Noninvasive Electrocardiology*, vol. 20, no. 6, pp. 526–533, 2015.

[12] S. A. Immanuel, A. Sadrieh, M. Baumert et al., "T-wave morphology can distinguish healthy controls from LQTS patients," *Physiological Measurement*, vol. 37, no. 9, pp. 1456–1473, 2016.

[13] A. Ghaffari, M. R. Homaeinezhad, M. Akraminia, M. Atarod, and M. Daevaeiha, "A robust wavelet-based multi-lead Electrocardiogram delineation algorithm," *Medical Engineering & Physics*, vol. 31, no. 10, pp. 1219–1227, 2009.

[14] J. P. Martinez, R. Almeida, S. Olmos, A. P. Rocha, and P. Laguna, "A wavelet-based ECG delineator: evaluation on standard databases," *IEEE Transactions on Biomedical Engineering*, vol. 51, no. 4, pp. 570–581, 2004.

[15] J. P. V. Madeiro, W. B. Nicolson, P. C. Cortez et al., "New approach for T-wave peak detection and T-wave end location in 12-lead paced ECG signals based on a mathematical model," *Medical Engineering & Physics*, vol. 35, no. 8, pp. 1105–1115, 2013.

[16] S. Mehta, N. Lingayat, and S. Sanghvi, "Detection and delineation of P and T waves in 12-lead electrocardiograms," *Expert Systems*, vol. 26, no. 1, pp. 125–143, 2009.

[17] G. Vijaya, V. Kumar, and H. K. Verma, "Artificial neural network based wave complex detection in electrocardiograms," *International Journal of Systems Science*, vol. 28, no. 2, pp. 125–132, 1997.

[18] A. A. S. León et al., "Neural network approach for T-wave end detection: a comparison of architectures," in *Proceedings of the Computing in Cardiology Conference*, Vancouver, BC, Canada, September 2016.

[19] A. A. Suárez-León, C. Varon, R. Willems, S. Van Huffel, and C. R. Vázquez-Seisdedos, "T-wave end detection using neural networks and Support Vector Machines," *Computers in Biology and Medicine*, vol. 96, pp. 116–127, 2018.

[20] P. Laguna, R. Jané, and P. Caminal, "Automatic detection of wave boundaries in multilead ECG signals: validation with the CSE database," *Computers and Biomedical Research*, vol. 27, no. 1, pp. 45–60, 1994.

[21] M. Akhbari, M. B. Shamsollahi, O. Sayadi, A. A. Armoundas, and C. Jutten, "ECG segmentation and fiducial point extraction using multi hidden Markov model," *Computers in Biology and Medicine*, vol. 79, pp. 21–29, 2016.

[22] D. A. Coast, R. M. Stern, G. G. Cano, and S. A. Briller, "An approach to cardiac arrhythmia analysis using hidden Markov models," *IEEE Transactions on Biomedical Engineering*, vol. 37, no. 9, pp. 826–836, 1990.

[23] C. Lin, C. Mailhes, and J. Y. Tourneret, "P- and T-wave delineation in ECG signals using a Bayesian approach and a partially collapsed Gibbs sampler," *IEEE Transactions on Biomedical Engineering*, vol. 57, no. 12, pp. 2840–2849, 2010.

[24] M. Zarrini and A. Sadr, "A real-time algorithm to detect inverted and symmetrical T-wave," in *Proceedings of the International Conference on Computer and Electrical Engineering (ICCEE 2009)*, Dubai, UAE, December 2009.

[25] Y. N. Singh and P. Gupta, "An efficient and robust technique of T wave delineation in electrocardiogram," in *Proceedings of the International Conference on Bio-Inspired Systems and Signal Processing (Biosignals 2009)*, Porto, Portugal, January 2009.

[26] N. Bayasi et al., "Adaptive technique for P and T wave delineation in electrocardiogram signals," in *Proceedings of the 2014 36th Annual International Conference of the IEEE Engineering in Medicine and Biology Society*, Chicago, IL, USA, August 2014.

[27] C. R. Vázquez-Seisdedos, J. Neto, E. J. Marañón Reyes, A. Klautau, and R. C. Limão de Oliveira, "New approach for T-wave end detection on electrocardiogram: performance in noisy conditions," *BioMedical Engineering OnLine*, vol. 10, no. 1, p. 77, 2011.

[28] J. A. Vila, Y. Gang, J. M. R. Presedo, M. Fernandez-Delgado, S. Barro, and M. Malik, "A new approach for TU complex characterization," *IEEE Transactions on Biomedical Engineering*, vol. 47, no. 6, pp. 764–772, 2000.

[29] M. R. Homaeinezhad, M. Erfanianmoshiri-Nejad, and H. Naseri, "A correlation analysis-based detection and delineation of ECG characteristic events using template waveforms extracted by ensemble averaging of clustered heart cycles," *Computers in Biology and Medicine*, vol. 44, no. 1, pp. 66–75, 2014.

[30] I. Saini, D. Singh, and A. Khosla, "K-nearest neighbour-based algorithm for P- and T-waves detection and delineation," *Journal of Medical Engineering & Technology*, vol. 38, no. 3, pp. 115–124, 2014.

[31] Q. Zhang, A. I Manriquez, C Médigue, Y Papelier, and M Sorine, "An algorithm for robust and efficient location of T-wave ends in electrocardiograms," *IEEE Transactions on Biomedical Engineering*, vol. 53, no. 1, pp. 2544–52, 2006.

[32] J. Song, H. Yan, Z. Xiao, X. Yang, and X. Zhang, "A robust and efficient algorithm for st-t complex detection in electrocardiograms," *Journal of Mechanics in Medicine and Biology*, vol. 11, no. 5, pp. 1103–1111, 2011.

[33] M. Xu, S. Wei, X. Qin, Y. Zhang, and C. Liu, "Rule-based method for morphological classification of ST segment in ECG signals," *Journal of Medical and Biological Engineering*, vol. 35, no. 6, pp. 816–823, 2015.

[34] H. Shang et al., "Performance evaluation for the sliding area-based T wave detection method on the QT database," in *Proceedings of the Chinese Automation Congress*, Jinan, China, October 2017.

[35] P. Laguna et al., "A database for evaluation of algorithms for measurement of QT and other waveform intervals in the ECG," in *Proceedings of the Computers in Cardiology, 1997*, Lund, Sweden, September 1997.

[36] G. B. Moody and PhysioNet, "Research resource for complex physiologic signals," *Electrocardiology*, vol. 29, pp. 1–88, 2009.

[37] A. Taddei, G. Distante, M. Emdin et al., "The European ST-T database: standard for evaluating systems for the analysis of ST-T changes in ambulatory electrocardiography," *European Heart Journal*, vol. 13, no. 9, pp. 1164–1172, 1992.

[38] A. K. Jain, "Data clustering: 50 years beyond K-means ☆," *Pattern Recognition Letters*, vol. 31, no. 8, pp. 651–666, 2008.

[39] S. Daskalaki, I. Kopanas, and N. Avouris, "Evaluation of classifiers for an uneven class distribution problem," *Applied Artificial Intelligence*, vol. 20, no. 5, pp. 381–417, 2006.

[40] C. Liu, P. Li, C. Di Maria, L. Zhao, H. Zhang, and Z. Chen, "A multi-step method with signal quality assessment and fine-tuning procedure to locate maternal and fetal QRS complexes from abdominal ECG recordings," *Physiological Measurement*, vol. 35, no. 8, pp. 1665–1683, 2014.

[41] J. Willems, "Recommendations for measurement standards in quantitative electrocardiography," *European Heart Journal*, vol. 6, no. 10, pp. 815–825, 1985.

[42] M. Akhbari, M. B. Shamsollahi, C. Jutten, A. A. Armoundas, and O. Sayadi, "ECG denoising and fiducial point extraction using an extended Kalman filtering framework with linear and nonlinear phase observations," *Physiological Measurement*, vol. 37, no. 2, pp. 203–226, 2016.

Hindawi
Computational and Mathematical Methods in Medicine
Volume 2019, Article ID 6509357, 16 pages
https://doi.org/10.1155/2019/6509357

Review Article

A Technical Review of Convolutional Neural Network-Based Mammographic Breast Cancer Diagnosis

Lian Zou,[1,2,3] Shaode Yu,[1,4] Tiebao Meng,[5] Zhicheng Zhang,[1,2] Xiaokun Liang,[1,2,6] and Yaoqin Xie[1]

[1]*Shenzhen Institutes of Advanced Technology, Chinese Academy of Sciences, Shenzhen, China*
[2]*Shenzhen College of Advanced Technology, University of Chinese Academy of Sciences, Shenzhen, China*
[3]*Cancer Center of Sichuan Provincial People's Hospital, Chengdu, China*
[4]*Department of Radiation Oncology, The University of Texas Southwestern Medical Center, Dallas, TX, USA*
[5]*Department of Medical Imaging, Sun Yat-sen University Cancer Center, Guangzhou, China*
[6]*Medical Physics Division in the Department of Radiation Oncology, Stanford University, Palo Alto, CA, USA*

Correspondence should be addressed to Yaoqin Xie; yq.xie@siat.ac.cn

Received 14 January 2019; Accepted 25 February 2019; Published 25 March 2019

Guest Editor: Giedrius Vanagas

This study reviews the technique of convolutional neural network (CNN) applied in a specific field of mammographic breast cancer diagnosis (MBCD). It aims to provide several clues on how to use CNN for related tasks. MBCD is a long-standing problem, and massive computer-aided diagnosis models have been proposed. The models of CNN-based MBCD can be broadly categorized into three groups. One is to design shallow or to modify existing models to decrease the time cost as well as the number of instances for training; another is to make the best use of a pretrained CNN by transfer learning and fine-tuning; the third is to take advantage of CNN models for feature extraction, and the differentiation of malignant lesions from benign ones is fulfilled by using machine learning classifiers. This study enrolls peer-reviewed journal publications and presents technical details and pros and cons of each model. Furthermore, the findings, challenges and limitations are summarized and some clues on the future work are also given. Conclusively, CNN-based MBCD is at its early stage, and there is still a long way ahead in achieving the ultimate goal of using deep learning tools to facilitate clinical practice. This review benefits scientific researchers, industrial engineers, and those who are devoted to intelligent cancer diagnosis.

1. Introduction

Breast cancer threatens women's life worldwide. In the United States, it might cause an estimation of 0.25 million new cases of invasive breast cancer, 0.06 million new cases of noninvasive breast cancer, and 0.04 million deaths in 2016 [1]. This disease dramatically increases the health burden on those developing and underdeveloped countries [2]. Substantial clinical trial indicates that early detection and diagnosis of breast cancer can provide patients with more flexible treatment options and improved life quality and survivability [3]. Therefore, more and more attention is being paid to related fields, such as novel imaging modalities of ultrasound tomography [4] and breast tomography [5].

Mammography performs as a routine tool for breast cancer screening. It enables high-resolution perception of the internal anatomy of breast and helps the diagnosis of suspicious lesions [6]. Screening mammography scans the breast from the craniocaudal view and mediolateral oblique view, while diagnostic mammography acquires more images when symptoms, such as architecture changes and abnormal findings, are found on screening mammographic images. To date, screen film mammography (FM) has been the reference standard for use in breast cancer screening programs, while due to the demands of higher spatial resolution, digital mammography (DM) has been widely accepted. General rules exist for mammographic image interpretation. However, errors are unavoidable in clinic, and reasons are

manifold. Above all, the difference of perceived visual appearance between malignant and benign lesions is unclear and consequently, how to quantify breast lesions with discriminative features is full of challenges. Moreover, it is still difficult to estimate the disease risk because of limited information and thus, healthy people might be turned into patients. Besides, work overload and fatigue further cause misinterpretation and overdiagnosis. Unfortunately, it is found that more than 70% of suggested biopsies are with benign outcomes during the diagnosis phase [7].

Computer-aided models for mammographic breast cancer diagnosis (MBCD) have been explored for over thirty years [8, 9]. It supports the decision making and helps the differentiation between malignant and benign lesions by providing additional information. Due to the facilitation of MBCD models, the diagnostic performance is enhanced regarding both sensitivity and specificity [10] and unnecessary examinations can be reduced in a cost-effective manner. It further benefits biopsy recommendations, follow-up treatments, and prognosis analysis. From a technical perspective, major MBCD models are consisted of feature extraction and lesion malignancy prediction. The former quantifies lesions with discriminative features and the latter builds the relationship between the features and its label, benign or malignant. Massive studies have devoted to the investigation of breast cancer diagnosis, ranging from using different modalities [11–13], to the analysis of subtle signs [14, 15] and to various technique exploration [16, 17]. Because of the easy accessibility of high-performance computing resources, millions of labeled data, and advanced artificial intelligence methods, convolutional neural network (CNN) has revolutionized image representation and benefited a broad range of applications [18], including but not limited to object recognition [19], visual understanding [20], and numerical regression [21, 22]. Quite different from conventional MBCD techniques, CNN attempts to integrate the feature extraction and lesion classification into a supervised learning procedure. The input of the CNN architectures is image patches of outlined lesion regions, and its output corresponds to the predicted lesion malignancy and intuitively, time and labor can be reduced in feature engineering. Meanwhile, CNN is pushing forward the technique upgrading in the field of medical imaging [23], medical physics [24, 25], medical image analysis [26–28] and radiotherapy [29, 30]. The research toward developing effective and efficient CNN-based MCBD models is still ongoing.

To the best of our knowledge, three review papers have been published regarding deep learning based breast cancer diagnosis. One concerns lesion detection and malignancy prediction using mammography, ultrasound, magnetic resonance imaging and digital tomosynthesis [31]. One focuses on mammography and histology image processing and analysis [32]. Meanwhile, it attempts to map the features/phenotypes between mammographic abnormalities and histological representation. The last one overviews deep learning in the detection and diagnosis of various kinds of cancers by using different imaging modalities [33]. In general, technical details in these review papers are not well delivered.

This paper also presents a review. It is dedicated to the technique of CNN applied in a specific application of MBCD, and it aims to provide clues on how to use CNN in intelligent diagnosis. The contributions of this review are summarized as follows. At first, this study is restricted to peer-reviewed journal publications and consequently, technical details and pros and cons of each model can be delivered. Furthermore, based on how to use CNN techniques, the MBCD models are broadly categorized into three groups. One is to design shallow models or to modify existing models for decreased time cost and medical instances for training; another is to make the best use of a pretrained CNN model by transfer learning and parameter fine-tuning; and the third is to take advantage of CNN models for feature extraction, while the differentiation between malignant and benign lesions is based on machine learning classifiers. At last, findings, challenges, and limitations are summarized, and some clues on the future work are also given.

The remainder of this paper is structured as follows. Section 2 describes basic concepts regarding computer-aided diagnosis (CAD) and transfer learning. Section 3 reviews CNN-based MBCD techniques, including the search strategy of the literature and technical details of involved models. And then, findings, challenges, and future focus are summarized in Section 4. In the end, Section 5 concludes this review.

2. Basic Concept of CAD Models

This section briefly describes the basic concepts of computer-aided diagnosis (CAD) and transfer learning. Specifically, Figure 1 shows the flow chart of machine learning- (ML-) based CAD and major architectures of CNN-based CAD. It should be noted that for diagnosis, a CAD model assumes the suspicious lesion regions have been accurately delineated and its purpose is to predict the malignancy of the input lesions.

2.1. Computer-Aided Diagnosis (CAD). A CAD model can be used to provide additional information and support the decision making on disease diagnosis and cancer staging. It is different from a computer-aided detection model which aims to detect, localize, or segment suspicious regions. However, it should be noticed that a computer-aided detection model can be placed ahead of a diagnosis model for comprehensive analysis from the detection and localization to the diagnosis of suspicious regions.

2.1.1. ML-Based CAD. A ML-based CAD model consists of feature extraction and machine learning-based classification as shown in the left of Figure 1, and feature selection is optional. Widely used features come from image descriptors that quantify the intensity, shape, and texture of a suspicious region [34]. Preferred machine learning classifiers are not limited to artificial neural network (ANN), support vector machine (SVM), k-nearest neighbors, naive Bayesian, and random forest (RF) [35]. Due to the emergency of radiomics

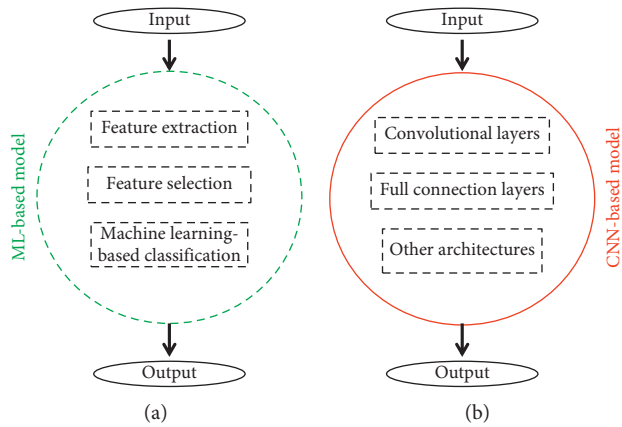

Figure 1: The diagram of the main flow chart of ML-based CAD (a) and major architectures of CNN-based CAD (b). The black dashed line indicates the blocks are modifiable. The green dashed line denotes each step in the ML-based model is interpretable, and the red solid line indicates the CNN-based model is data-driven when the architecture is fixed.

[36–38], it should be noted that feature selection becomes more and more important and it aims to retrieve intrinsic features of suspicious lesions.

Mathematically, the procedure of using a pretrained ML-based CAD model to predict the malignancy of a lesion can be described as follows. First, an outlined suspicious region (I_x) as the input is quantified with scalar variables ($E(I_x)$) by using feature extraction (E). Then, feature selection (S) is employed to decrease the feature dimension and to retrieve informative features ($S(E(I_x))$). In the end, the output of the label (y) of the lesion (I_x) is predicted using machine learning classifiers can be formulated as $y = F(S(E(I_x)))$. For comprehensive understanding, overviews regarding machine learning and breast cancer diagnosis can be referred to [8, 9].

2.1.2. CNN-Based CAD. CNN models are computational models that are composed of multiple processing layers to retrieve features from raw data with multilevel representations and hierarchical abstraction [19]. As shown in the right of Figure 1, a general architecture of CNN models is made up of convolutional layers, full-connection layers, and pooling layers in addition to the input and output layers. Specifically, Figure 2 shows the architecture of VGG16 which consists of 13 convolutional layers, 3 full-connection layers, 5 pooling layers, and 1 softmax layer [39]. For further improvement in object classification, many techniques can be embedded, including nonlinear filtering, data augmentation, local response normalization, hyperparameter optimization, and multiscale representation [31, 32]. At present, widely used deep learning models include, but are not limited to, VGG [39], LeNet [40], AlexNet [41], GoogLeNet [42, 43], ResNet [44], YOLO [45], faster R-CNN [46] and LSTM [47].

Mathematically, the procedure of using a pretrained CNN-based CAD model for the prediction of lesion malignancy can be described as following. Given a suspicious region (I_x), the output of a CNN-based model can be formalized as $y = F(I_x) = f_n(f_{n-1}(\cdots(f(I_x))))$ where n stands for the number of hidden layers and f_i denotes the activation function in the corresponding layer i. Furthermore, how to design the architecture of deep learning models in addition to the comprehensive analysis and systematic methodologies of learning representation can be referred from [18, 19, 48].

It should be noted that CNN models are data-driven and can be trained end-to-end. The models enable the integration of feature extraction, feature selection, and malignancy prediction into an optimization procedure. Therefore, these retrieved features are not designed by human engineers but learned from the input data [19]. In general, remarkable performance of CNN-based CAD models comes from advanced computing hardware resource (i.e., graphic processing units and distributed computing system), open-source software, such as TensorFlow (https://www.tensorflow.org/), and open challenges based on millions of high-quality labeled images, such as ImageNet (http://www.image-net.org/). Its success also benefits from the novel design of architectures for deep learning, such as inception [43] and identity mapping [44].

2.2. Transfer Learning. Transfer learning, or knowledge transfer, is more a machine learning strategy. It aims to reuse a model pretrained in the source domain as a starting point in a different but related target domain [49]. In the field of machine learning, an algorithm is typically designed to address one isolated task, while through transfer learning, the algorithm can be further adapted to a new task (Figure 3). It has several benefits using knowledge transfer. Above all, knowledge transfer enables the quality of the starting point in the target domain and thereby, promising results can be expected. Moreover, how to make use of a pretrained model is flexible. The model can be employed as a feature extractor for high-level representation of images and its parameters can be fine-tuned with target data. In addition, both time and cost can be reduced dramatically. Depending on computing resources, it takes about days to months training a deep model, while the time drops to hours when transferring this model for target applications. Thanks to the accessibility

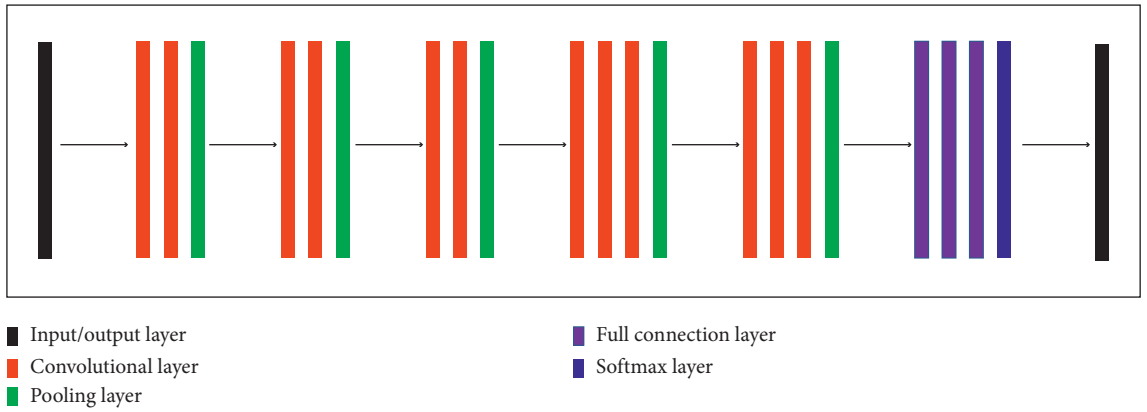

Figure 2: The architecture of VGG16. It consists of 13 convolutional layers, 3 full-connection layers, 5 pooling layers, and 1 softmax layer in addition to the input and output layers.

of pretrained deep models online, high-cost hardware seems unnecessary. Most importantly, transfer learning relieves the requirement of huge amount of instances for model training, which is critically helpful in medical imaging field. At present, the most popular object classification is based on the ImageNet [50] and without additional comments, pretrained CNN models are all denoted an initialization on the ImageNet in this study.

3. CNN-Based MBCD

This section firstly introduces the search strategy of literatures, involved databases and performance metrics. In the end, CNN-based MBCD methods are categorized into three groups based on the design and use of CNN models. This overview concentrates on peer-reviewed journal publications, and it provides technical details and pros and cons of CNN models.

3.1. Search Strategy for Literature Review. For the literature survey, IEEEXplore, Pubmed, ScienceDirect, and Google Scholar were used to search publications relating to CNN-based MBCD. The last update was at December 20, 2018. Keywords are "convolutional neural network," "deep learning," "mammography," "breast cancer," and "diagnosis". Specifically, only papers published on peer-reviewed journals were selected, and our search yielded 18 research articles. Table 1 summarizes the literature from the used databases, the number (no.) of medical images in lesion classification and the diagnosis performance (AUC, the area under the curve; ACC, accuracy; SEN, sensitivity; SPE, specificity). Note that in each literature, only the model which achieves the best classification performance is reported.

3.2. Involved Databases. Table 1 indicates that mostly used mammography databases come from in-house collection (7/18), followed by public databases of BCDR-F03 (5/18), DDSM (4/18), INbreast (3/18), MIAS (1/18), and IRMA (1/18), and the last one comes from the DREAM challenge (1/18). The number of medical images in databases ranges mainly from several hundreds to thousands. Notably, the DREAM challenge is consisted of 82,000 images. Moreover, among the public databases, BCDR-F03 is the only one consisted of FM images, while among in-house collections, [55] is the one study that makes use of FM images (1655 FM images and 799 DM images), and all other databases and in-house collections are made up of DM images.

Three public databases of DDSM (http://marathon.csee.usf.edu/Mammography/Database.html), BCDR-F03 (http://bcdr.inegi.up.pt), INbreast (http://medicalresearch.inescporto.pt/breastresearch/index.php), and MIAS (http://peipa.essex.ac.uk/info/mias.html) are accessible online, while the DREAM challenge (https://www.synapse.org/#Synapse:syn4224222) is devoted to online competition and aims at improving the predictive accuracy of mammographic images for early detection and diagnosis of breast cancer. The IRMA [69] contains image patches selected from the DDSM, MIAS, and other two data sets. Among the public databases, DDSM ("Digital Database for Screening Mammography") remains the largest available resource for mammographic image analysis [70]. It consists of 14 volumes of benign lesion cases and 15 volumes of malignant lesion cases in addition to 2 volumes of benign lesion cases without callback. It also contains 12 volumes of normal cases. The images in DDSM are in an outdated image format with a bit depth of 12 or 16 bits per pixel, and image resolution is larger than [4000, 3000], both depending on scanners.

The database BCDR-F03 ("Film Mammography Dataset Number 3") is a subset of Breast Cancer Digital Repository (BCDR) that collects patient cases from the northern region of Portugal. It was made available for the development and comparison of algorithms [52]. The BCDR-F03 contains 344 patient cases, 736 FM images, and 406 breast lesions. Among the lesions, 230 are benign (426 images) and 176 malignant (310 images). Notably, BCDR-F03 contains FM images in the gray-level digitized TIFF (Tagged Image File Format) with a bit depth of 8 bits per pixel, and image resolution is [720, 1168].

The database INbreast is made up of 115 breast lesion cases and 410 digital images [71]. However, only 56 cases are histologically verified (11 benign and 45 malignant lesions). The mammographic images are saved in DICOM (Digital

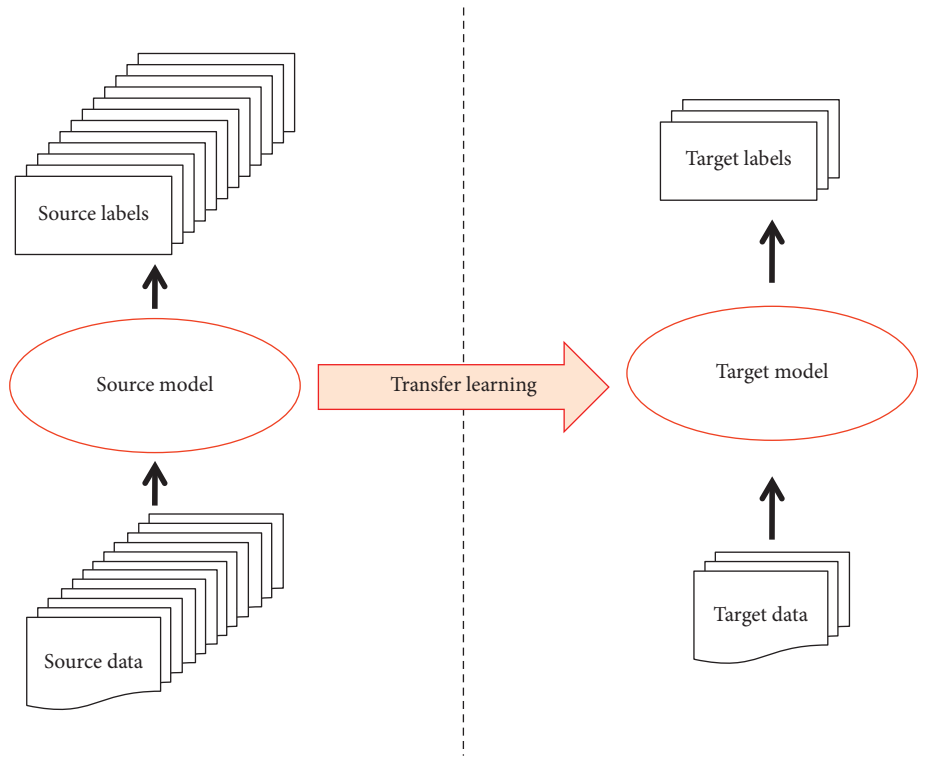

Figure 3: The diagram of knowledge transferred from the source domain to a different but related target domain. In the source domain, a model is trained with sufficient high-quality instances (data and labels) and transfer learning enables the model used in a related target domain. It relieves the requirement of huge amount of instances for the training of deep models in the target domain which is critically helpful in medical imaging field.

Table 1: A summary of CNN based MBCD methods.

	Year	Database	No. of images	AUC	ACC	SPE	SEN
[51]	2016	DDSM	600		0.967		
[52]	2016	BCDR-F03	736	0.82 ± 0.03			
[53]	2016	In-house	607	0.86			
[54]	2017	In-house	3158	0.88	0.82	0.72	0.81
[55]	2017	In-house	2454	0.82 ± 0.02			
[56]	2017	In-house	245	0.86 ± 0.01			
[57]	2017	INbreast	115	0.91 ± 0.12	0.95 ± 0.05		
[58]	2017	In-house	560	0.79 ± 0.02			
[59]	2017	IRMA	2796	0.839	0.837	0.854	0.797
[60]	2018	In-house	78	0.81 ± 0.05			
[61]	2018	In-house	3290	0.7274			
[62]	2018	DDSM	600		0.974		
		MIAS	120		0.967		
[63]	2018	BCDR-F03	736	0.813			
[64]	2018	DDSM	5316	0.98	0.9735		
		BCDR-F03	600	0.96	0.9667		
		INbreast	200	0.97	0.9550		
[65]	2018	DDSM	600		0.97		
[66]	2018	DREAM	82,000	0.85			
		INbreast	115	0.95			
[67]	2018	BCDR-F03	736	0.891	0.852		
[68]	2018	BCDR-F03	736	0.88	0.81		

Imaging and Communications in Medicine) format with 14-bit contrast resolution. The image matrix is [2560, 2238] or [3328, 4084] depending on imaging scanners.

The MIAS database ("Mammographic Image Analysis Society") contains 322 digital images among which 67 lesions are benign and 53 lesions are malignant [72]. Quite

different from above-mentioned databases, MIAS provides the image coordinates of center of each abnormality and the approximate radius (in pixels) of a circle to enclose the abnormality, but not the coordinates of points localized on the boundary of lesions. Images are stored 8 bits per pixel in the PGM (Probabilistic graphical model) format. The database has been reduced to a 200 micron pixel edge and padded/clipped so that the image matrix is [1024, 1024].

3.3. Performance Metrics. To quantify the classification performance of CAD models, widely used metrics are AUC and ACC, followed by SEN and SPE (Table 1). Specifically, ACC, SEN, and SPE are computed based on the confusion matrix. As shown in Table 2, TP is the case which is histologically verified positive and correctly predicted as "positive", while FN represents the case histologically verified positive but misclassified as "negative". Furthermore, TN is the true negative case predicted correctly, and FP is the true negative case but predicted as "positive" [73]. Generally, benign lesions are labeled with "negative" and malignant lesions are labeled "positive".

Given the labels and corresponding prediction results, ACC, SEN, and SPE can be, respectively, formulated as $(TP + TN)/(TP + FN + FP + TN)$, $TP/(TP + FN)$, and $TN/(TN + FP)$. As to AUC, it is quantified based on the receiver operating characteristics (ROC) curve. ROC is a curve of probability and AUC presents a model's capacity of lesion differentiation. To these 4 performance metrics, higher values indicate better performance.

3.4. CNN-Based MBCD Models. In general, CNN-based models can be divided into dedicated models and transferred models. The former include the proposal of new architectures, the modification or integration of existing CNN models, while the latter make the most use of pretrained models and further fine-tune them by using medical instances. Furthermore, it is found that some models just use CNN for feature extraction and lesion diagnosis is fulfilled by using machine learning classifiers. In particular, handcrafted features are taken into consideration. Therefore, in this study, CNN-based MBCD models are broadly categorized into three groups of dedicated models, transferred models, and hybrid models. Table 3 summarizes the CNN-based models from the model building to its pros and cons analysis. Note that the pros of "parameter initialization" indicate the model is pretrained with ImageNet.

3.4.1. Dedicated MBCD Models. To enhance the diagnosis with unlabeled data, [54] proposes a graph-based semi-supervised learning scheme, which is consisted of iterative data weighting, feature selection, and data labeling before using the modified LeNet for lesion diagnosis. Experimental results indicate that the scheme requires quite a small portion of labeled data (100 lesions) for training and achieves promising performance on the unlabeled data (3058 lesions). In addition, the scheme seems less sensitive to the initial labeled data. Reference [55] adds 2 fully connected layers at the last full-connection layer of the frozen AlexNet. The parameters in the AlexNet are initialized on the ImageNet and keep unchanged, while the whole model is trained on medical instances. Reference [58] proposes a four-layered model (3 convolutional layers and 1 full-connection layer) and a 4-fold cross-validation strategy is performed on 560 lesions (280 benign and 280 malignant). Reference [62] designs a CNN architecture (5 convolutional layers and 2 full-connection layers), while it pretrains the model on the ImageNet. Notably, parasitic metric learning is embedded that makes the best use of misclassified medical instances and improves the diagnosis performance. Reference [65] employs YOLO for lesion detection and localization followed by a tensor structure for the malignancy prediction. And consequently, automatic detection and classification of suspicious lesions is achieved simultaneously. Similarly, [66] uses the faster R-CNN for lesion detection and localization and the VGG for cancer diagnosis. The model is first trained on the DDSM and further validated on the INbreast and the DREAM challenge. It performs as one of the best approaches in mammographic image analysis. Reference [67] develops a hybrid model. It first uses the pretrained GoogLeNet for feature extraction, and 3072 features are obtained. And then, an attention mechanism is proposed for feature selection. At last, it uses LSTM to integrate both contexture information from multiview image features and information of clinical data for the lesion classification.

Figure 4 demonstrates the flow chart and an example of dedicated MBCD models. The flow chart highlights that the CNN is a newly designed or modified network and the example describes the architecture of the CNN model from [58]. It should be noted that parameters of dedicated models are with random initialization followed by iterative optimization with medical instances.

Although [55, 62, 66, 67] make use of the ImageNet for parameter initialization, it should be highlighted that one develops a new architecture [62], one modifies the existing architecture and introduces a new learning strategy [55], and the others emphasize on the integration of two kinds of network architectures for simultaneous detection and localization and final lesion diagnosis [66, 67]. Therefore, [55, 62, 66, 67] are categorized into the group of dedicated models.

3.4.2. Transferred CNN Models. Due to insufficient medical instances, deep CNN models pretrained on a large-scale of labeled natural images (such as ImageNet) are transferred and also fine-tuned with medical instances before the application in breast cancer diagnosis. Reference [61] gives out a systematic comparison of one shallow network (3 convolutional layers and 2 full-connection layers) and the AlexNet. Transfer learning is concerned, and experiment results indicate that CNN models with transfer learning outperform the models without transfer learning. Reference [63] investigates three kinds of implementation of an 8-layered CNN architecture. Parameters, such as the number of convolutional filters in each layer, are fine-tuned with mammographic lesion instances. Experimental comparison

Table 2: Confusion matrix.

	Predicted positive	Predicted negative
Histologically verified positive	True positive (TP)	False negative (FN)
Histologically verified negative	False positive (FP)	True negative (TN)

Table 3: Summary of CNN-based MBCD models from the model building to its pros and cons analysis.

Publication (year)	Approach	Pros (+)/cons (−)
[51] (2016)	(1) An 8-layered CNN (2) SVM-based decision mechanism (3) Compared to ML- and CNN-based models	+parameter initialization +decision mechanism −256 mid- and 2048 high-level features
[52] (2016)	(1) A 3-layered CNN (2) SVM-based classification (3) Compared to ML- and CNN-based models	+medical instances for training −17 low- and 400 high-level features −a shallow CNN model
[53] (2016)	(1) Transferred AlexNet (2) SVM-based classification (3) Classifier-based soft voting	+parameter initialization +soft-voting-based decision mechanism −29 low- and 3795 high-level features
[54] (2017)	(1) Modified LeNet (2) Graph based semisupervised learning (3) Feature dimension reduction (4) Using unlabeled data	+semisupervised learning +a few labeled data used for training +less sensitive to initial labeled data
[55] (2017)	(1) Modified AlexNet (2) Multitask transfer learning	+parameter initialization +improved generalizability
[56] (2017)	(1) Transferred the VGG (2) SVM-based classification (3) Compared to ML- and CNN-based models	+parameter initialization +decision mechanism −38 low- and 1472 high-level features
[57] (2017)	(1) R-CNN for detection and diagnosis (2) Feature regression (3) RF-based classification	+minimal user intervention in image analysis −781 low-level features for CNN feature regression
[58] (2017)	(1) A 4-layered CNN	+medical instances for training −a shallow CNN model
[59] (2017)	(1) A 3-layered CNN (2) SVM-based classification (3) Data augmentation	+medical instances for training +image analysis in transformed domain −a shallow CNN model
[60] (2018)	(1) VGG for feature extraction (2) Stepwise feature selection (3) SVM-based classification	+2 features selected for diagnosis
[61] (2018)	(1) Transferred AlexNet (2) Data augmentation (3) Compared to CNN models	+parameter initialization
[62] (2018)	(1) A 7-layered CNN (2) Parasitic metric learning	+parameter initialization +parasitic metric learning
[63] (2018)	(1) Transferred VGG (2) Compared to CNN-based models	+parameter initialization
[64] (2018)	(1) Transferred VGG/ResNet/Inception (2) Comparison on 3 databases	+parameter initialization +systematic comparison −time consuming
[65] (2018)	(1) YOLO and tensor structure (2) Data augmentation	+medical instances for training +simultaneous detection and classification
[66] (2018)	(1) Faster R-CNN and VGG (2) Pretrained with the DDSM	+medical instances for training +both detection and diagnosis +evaluated on a large-scale screening dataset
[67] (2018)	(1) GoogLeNet for feature extraction (2) Attention mechanism for feature selection (3) LSTM for feature fusion	+medical instances for training +multiview and clinical information fusion
[68] (2018)	(1) Transferred AlexNet/GoogLeNet (2) Data augmentation (3) Compared to ML- and CNN-based models	+parameter initialization

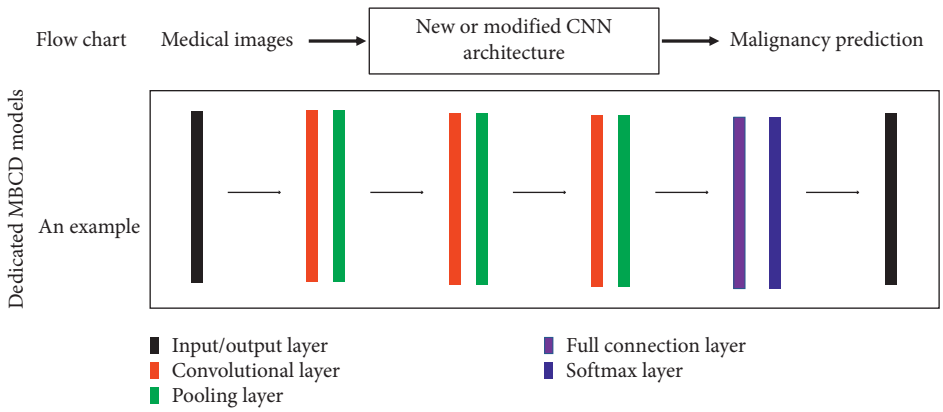

Figure 4: The flow chart and an example of dedicated MBCD models. The flow chart highlights the CNN is a newly designed or modified network, and the example describes the architecture of a CNN model in [58]. It should be noted that parameters of dedicated models are with random initialization followed by iterative optimization with medical instances.

further indicates that incorporating handcrafted features increases the classification performance. Reference [64] concentrates the study on three deep learning models (VGG, RestNet, and GoogLeNet) and knowledge transfer is explored. Experiments are conducted to compare the random initialization and parameter initialization and to figure out how to fine-tune the models. Notably, three public databases (DDSM, INbreast and MIAS) are analyzed. Reference [68] compares two deep networks (AlexNet and GoogLeNet) which are pretrained on the ImageNet, two shallow CNN models, and two ML-based MBCD models. Experimental results suggest that knowledge transfer is helpful in breast lesion diagnosis.

Figure 5 shows the flow chart and an example of transferred MBCD models. The flow chart highlights the offline training of a CNN model on nonmedical images, and moreover, it emphasizes fine-tuning the pretrained model with medical instances. A representative example using VGG as the diagnosis model comes from [64]. It should be noted that parameters of CNN architectures are predetermined in the task of object recognition, and their values are further optimized toward mammographic breast lesion differentiation.

Existing deep architectures are made the most use of, and these models [61, 63, 64, 68] are pretrained on the ImageNet and parameters are initialized. And then, mammographic lesion instances are used to fine-tune the deep models. While to further improve the diagnosis performance, additional techniques, such as data augmentation, are embedded in the training procedure. It should be noted that [61] has designed shallow networks, while its purpose is to verify whether transfer learning could improve the cancer diagnosis, and thereby it is grouped into the transferred CNN models.

3.4.3. CNN Models as Feature Extractors. Among the CNN-based MBCD models, 7 out of 18 take CNN to retrieve high-level features for lesion representation. Reference [51] develops an 8-layered network (5 convolutional layers and 3 full-connection layers). The model is pretrained on the ImageNet to overcome the issue of limited medical instances. And then, SVM performs as the classifier and a decision mechanism is provided. After that, the MBCD model integrates 256 midlevel and 2048 high-level features for lesion classification. Reference [52] designs two shallow networks and experimental results indicate the 3-layered network (2 convolutional layers and 1 full-connection layer) obtains better performance. While for higher accuracy, SVM is further employed which takes these CNN features as its input. Experiment results show the diagnosis performance achieves slight but significant improvement when 17 low-level and 400 high-level features are pooled for lesion quantification. Reference [53] takes advantage of the pretrained AlexNet for the lesion differentiation. More specially, one SVM-based model uses 3795 high-level features as its input and the other SVM-based model uses 29 low-level features for the lesion classification. The outputs are fused by soft voting and significant improvements are achieved in malignancy prediction. Reference [56] investigates different methodologies for feature fusion. It concerns 38 handcrafted features and 1472 CNN learned features, and SVM is as the classifier for each kind of feature. Then, the results from each SVM are fused for final decision making. The results show that the integration of low- and high-level features significantly improves cancer diagnosis. Reference [57] proposes a hybrid framework for mammographic image analysis. With minimal user intervention, it is capable of mass detection, lesion segmentation, and malignancy prediction. Specifically, for lesion differentiation, it regresses the output of the CNN model to 781 handcrafted features and then, a full-connection layer is added for feature abstraction. Finally, RF is utilized to improve the diagnosis accuracy. Reference [59] introduces a shallow network (2 convolutional layers and 1 full-connection layer). It alternatively cooperates with discrete wavelet transform and curvelet transform for image preprocessing. At last, a total of 784 features are handcrafted. Moreover, both softmax and SVM are compared, and SVM outperforms softmax with slight increase. Reference [60] takes advantage of 1472 high-level features from the pretrained VGG with frozen parameters. Its novelty comes from the proposal of step-wise feature selection and the 2 most frequently selected features are used for SVM-based breast lesion classification.

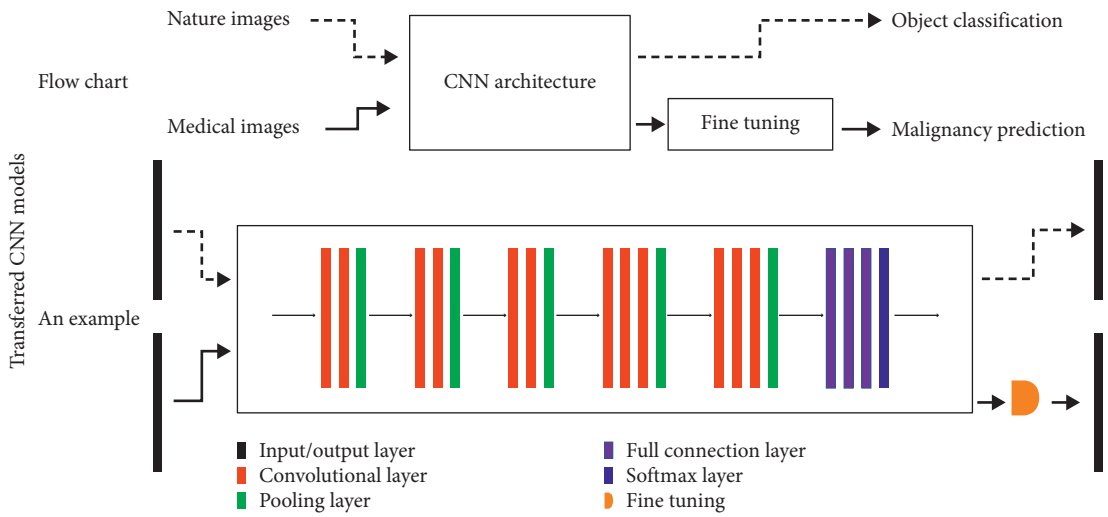

Figure 5: The flow chart and an example of transferred MBCD models. The flow chart emphasizes transfer learning (dashed arrows) and fine-tuning, and the example comes from [64] which makes use of pretrained VGG16 for malignancy prediction. It should be noted that parameters of pretrained models are well-determined in the source domain, while fine-tuning attempts to use medical instances for further optimization of these parameters toward the target task.

Figure 6 shows the flow chart and an example of CNN models as feature extractors. The flow chart highlights information fusion. In other words, whether a CNN model is newly designed or pretrained becomes not important and using low-level feature is optional. Information fusion can be divided into two approaches. One is feature fusion followed by a classifier, and the other is decision fusion of lesion malignancy predicted by using one or more classifiers. The example comes from [51] which develops a new CNN model and the model is pretrained on ImageNet. At last, the model fuses the prediction results (decision fusion) from SVM classifiers which separately use 384 midlevel features and 2048 high-level features as the input.

Prior studies have proved the benefits of low-level features in mammographic image analysis. And at present, how to select the informative CNN features [60] and how to fuse low-, mid-, and high-level features and clinical information have become important [52, 53, 56]. It should be mentioned that even if some MBCD models concern handcrafted features [53, 56], the ultimate purpose is to construct a hybrid framework for improved diagnosis and thereby, these publications [53, 56] are categorized into the third group.

3.4.4. Technical Highlights among CNN-Based MBCD Models. Table 4 summarizes the technical highlights that can distinguish each kind of CNN-based MBCD models. In the Table, "✓" indicates the distinct component in the model, "✖" denotes the component is not included in the models, while "—" means the component is not important in this kind of CNN-based models.

4. Discussion

A total of 18 peer-reviewed journal publications (Table 1) are found with regard to the "convolutional neural network" or "deep learning" based "breast cancer diagnosis" using "mammography" images. The models are generally divided into three groups (Table 4): one highlights the design of new architectures or the modification or integration of existing networks (Figure 4); one concentrates on the use of transfer learning and fine-tuning in breast cancer diagnosis (Figure 5); and the last one concerns a hybrid model in which CNN performs for feature extraction and information fusion becomes indispensable in decision making (Figure 6). In addition, Table 3 summarizes these models from the model building to its pros and cons analysis.

4.1. Our Findings. To overcome the issue of limited medical instances, there are 10 publications that employ transfer learning [51, 53, 55, 56, 61–64, 66, 68], with or without fine-tuning. Transfer learning is able to alleviate this issue to some extent, since deep models have been optimized using massive amount of data in the source domain; and consequently, the time and labor can be considerably reduced in the target domain. In particular, it has been verified that transfer learning benefits the differentiation of breast lesions seen in mammographic images. Besides, to increase the number of medical instances, data augmentation is used [59, 61, 65, 68]. It makes sense in lesion malignancy prediction, since a lesion might be presented in any particular orientation in screening and thus, the MBCD model should be able to learn and recognize the lesion malignancy. For data augmentation, besides image rotation and flipping, other techniques can be adapted, such as image quality degrading (https://github.com/aleju/imgaug) and image deformation [74–76].

To improve the diagnosis performance, 11 out of 18 publications develop shallow architectures or modify existing networks [51, 52, 54, 57–60, 62, 65–67]. Shallow architectures decrease the number of medical instances for training, while machine learning classifiers should be utilized when modified deep networks with frozen or fine-

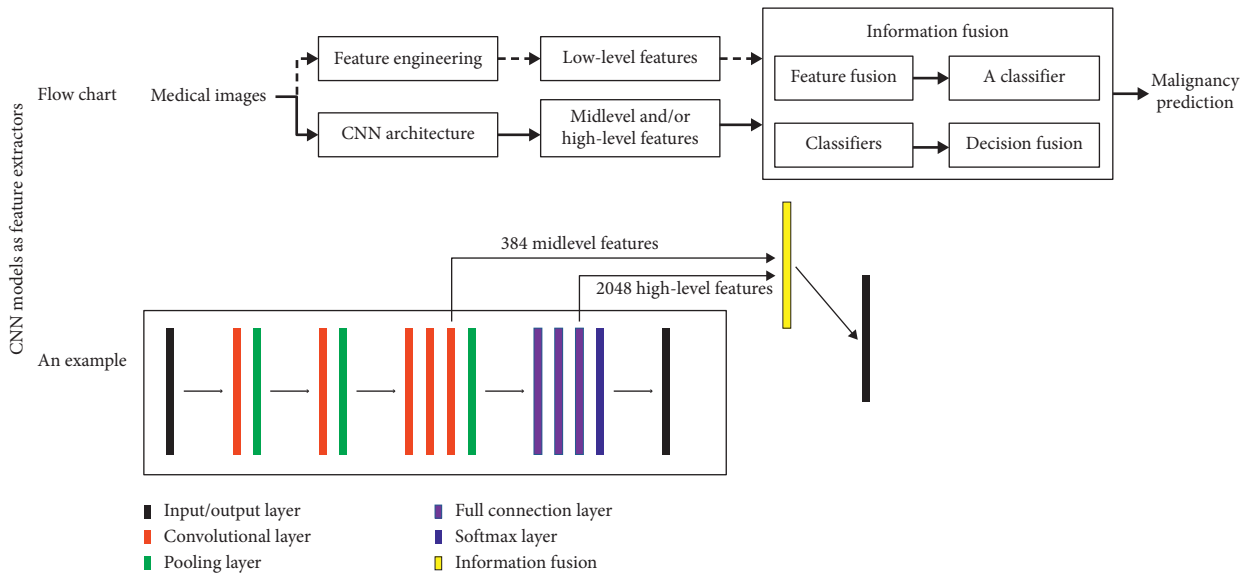

Figure 6: The flow chart and an example of CNN performing as feature extractors. The flow chart highlights the information fusion which can be further divided into two approaches, feature fusion followed by a classifier or decision fusion of lesion malignancy predicted by using one or more classifiers. The example comes from [51] which develops a new CNN model and the model is pretrained on ImageNet. At last, the model fuses the prediction results from SVM classifiers which separately use 384 midlevel features and 2014 high-level features as its input.

Table 4: Technical highlights.

	New architecture	Transfer learning	Fine-tuning	Information fusion
Dedicated CNN models	✓	✖	✖	✖
Transferred CNN models	—	✓	✓	✖
CNN models as feature extractors	—	—	—	✓

tuned parameters perform as feature extractors. However, problems occur. The first problem concerns which classifier to be applied for the differentiation of benign and malignant lesions. It is found that 9 out of 11 publications select SVM [51, 52, 54, 58–60, 62, 65, 66], and 1 uses RF [57] and 1 chooses LSTM [67] for malignancy prediction. The second one is how to choose informative and predictive features among hundreds to thousands of variables. Most publications address this question by comprehensive experiments to make a trade-off between the diagnosis efficiency and effectiveness, while only [56] proposes using the frequency of the CNN feature selected in the training stage as the weighting of the feature importance. Last but not the least, it is time-consuming and troublesome. In general, it takes days to weeks to develop new architectures and to modify or to integrate deep models due to the requirements of model training, parameter optimization, feature selection, and algorithm comparison.

It is also found that 7 publications consider low-level and/or clinical features [51–54, 56, 59, 67]. Low-level features are mainly derived from intensity statistics, shape description, and texture analysis [34]. Specifically, these features can be further analyzed with multiscale decomposition or in transform spaces. Clinical information includes breast density, patients' age, and other symptoms, such as microcalcification. In addition, 4 publications provide the comparison between CNN- and ML-based models [51, 52, 56, 68] and ML-based models are treated as the baseline. It should be noted that ML-based models benefit from the prior knowledge and clinical experience in feature crafting, feature selection, and the use of machine learning classifiers. In particular, it is feasible to build a ML-based model on a very small database [36]. Besides, ML-based models are relatively lightweight computing and require no specific hardware and thus, these models can be easily deployed and managed in daily work.

Integrating multiple representation of mammographic lesions can enhance the performance of breast cancer diagnosis, while how to incorporate low-, mid-, and high-level features or multiview data is quite difficult. There are 4 publications [51, 53, 56, 67] which provide mechanism for information fusion or decision fusion. Reference [51] proposes a decision mechanism by evaluating the consistency of the results from the midlevel features and the high-level features. If not consistent, gray information would be added to assess the similarity and support the decision making. Both [53, 56] build ensemble classifiers by averaging the results from two SVM classifiers among which one makes use the pretrained CNN features and the other analyzes handcrafted features. Reference [67] utilizes LSTM cells to integrate the features from multiview data. Since multiview data contain contextual information, the variations among

multiview images may contribute additional information in lesion interpretation.

4.2. Technical Challenges. Several technical challenges remain. The first challenge comes from how to use the pretrained deep CNN models which is closely related to the MBCD performance [77, 78]. However, there is no definitive answer on how to fine-tune the network and how many medical instances is sufficient for the fine-tuning, even good practice is available [79]. The simplest way is to take the parameters of the whole network or some layers of the network tunable. Some studies suggest layer-wise fine-tuning, while the time consumption will be dramatically increased [80]. On the other hand, when using deep models as feature extractors, other technical issues arise, including how to select high-level features, how to integrate multi-perspective information, and which machine learning classifier is employed. It is pitiful that no tutorial or practical guidelines are repeatable. In clinic, to improve the performance of breast cancer diagnosis, various imaging modalities and clinical data are taken into account that further imposes difficulties on information fusion [9]. Since no one-size-fits-all solution is available, prior knowledge, previous studies, and empirical experience become more and more important to address these technical issues [78–83].

It is also challenging on how to avoid overfitting in the optimization of deep networks. Dropout is proposed to address the problem [84] which aims to randomly drop units (along with connections) from the network in the training stage. It can prevent units from coadapting too much, and a practical guide is provided for the training of a Dropout network [84]. It is full of potential to avoid overfitting by increasing the number of medical instances for training. At last, if there is no possibility to reduce the architecture complexity and no way to increase the number of training instances, the mainstream is to manipulate parameters, such as the learning rate, and to monitor the drop of performance metrics between the training phase and the validation phase [58, 60, 61, 68]. It also should be mentioned that the threshold of the drop is subjective, and thus, comprehensive experiments become necessary.

The third challenge is the curse of dimensionality [85]. It is known that the primary purpose of deep learning is for recognizing the target from thousands of object categories. However, MBCD is a binary classification problem, and the lesions seen in mammographic images are to be labeled as benign or malignant. Thus, it seems not convincing to use thousands of features for a binary classification problem regarding hundreds of medical instances [51–53, 56]. Some studies take recourse to feature selection [60] and feature dimension reduction [54]. As to deep networks, the frequency of features selected in the training phase as a weighting factor of feature importance is meaningful [60].

In practice, challenges exist in each step of the building of CNN-based MBCD models. First, a number of factors influence the quality of mammographic imaging, such as the imaging scanner and reconstruction methods, and both breast compression and motion artifacts during image acquisition further degrade the imaging quality. Therefore, quantitative image quality assessment may be necessary [86]. Moreover, due to different shapes and margin of suspicious lesions and also ambiguous boundaries between lesions and surrounding tissues, the quality of lesion delineation is unstable, and thereby, the techniques for automatic mammographic breast lesion detection and segmentation are still in need of improvement [87]. In addition, evolutionary pruning of knowledge transfer of deep models that are pretrained on sufficient medical images is promising for mammographic breast lesion diagnosis because of the similar feature space [88]. Last but not the least, it is always desirable to build a seamless system to localize the suspicious lesions and give out the malignancy prediction simultaneously [65, 66].

4.3. Future Focus. Except for the technical challenges aforementioned, another three topics should be focused on in the future work. The first one is to collect sufficient high-quality mammographic instances. Due to the limited funding, scarce medical expertise, and privacy issues, there is no big leap in data sharing, in particular, the mammographic lesion images. At present, the DDSM remains the largest publicly available database as well as the first choice in large-scale mammographic image analysis [89]. While based on the fact that over 150 million mammographic examinations are performed worldwide per year, there is significant room for improvement in data collection and sharing. In particular, lack of imaging data restricts the development and upgrading of intelligent systems for personalized diagnosis, including but not limited to the design of deeper architectures, hyperparameter optimization, and the evaluation of generalization capacity. Fortunately, rapid progress is seen in the era of big data and many public databases have been released online, such as TCIA (http://www.cancerimagingarchive.net/), and various challenges are open, such as the DREAM challenge. With such a standardization, it will become easier to compare different approaches on the same problem of the same database and thereby pushing forward the techniques of CNN-based MBCD.

Another topic is about the interpretation of the learned CNN features. In contrast to handcrafted features with mathematical formalization and clear explanation, the interpretation of retrieved CNN features is quite poor. One way to tackle this issue is from qualitative understanding [55, 58] based on visualization. Reference [90] provides a technique for layer-wise feature visualization. In object recognition, the technique indicates that shallow layers typically represent the presence of edges, middle layers mainly detects motifs by spotting particular arrangements of fine structures, while deep layers attempt to assemble these motifs into a larger cluster to be a part of or the whole object [19, 58]. It should be admitted that the layer-wise visualization technique facilitates the visual perception and further understanding of what the networks have learned. Reference [91] analyzed the predicted results in two-dimensional space using t-distributed stochastic neighbor embedding (t-SNE).

The t-SNE represents each object by a point in a scatter plot where nearby points denote similar objects and distant points indicate dissimilar objects. Therefore, a clear insight is provided into the underlying structure of malignancy prediction [55]. Quantitative interpretation of deep learning is ongoing. Reference [92] gives a geometric view to understand the success of deep learning. They claim that the fundamental principle attributing to the success is the manifold structure in data, and deep learning can learn the manifold and the probability distribution on it. Reference [93] provides theory on how to interpret the concept learned and the decision made by a deep model. It further discusses a number of questions in interpretability, technical challenges, and possible applications. The third topic is the translation of the clinical research of CNN-based MBCD into the decision supporting in clinical practice. There is no doubt that deep learning tools can provide valuable and accurate information for cancer diagnosis, while it is impossible to take the role and responsibility of clinicians. The fundamental role of a clinician in routine work is to collaborate with other team members, including physicians, technologists, nurses, therapists, and even patients [94]. Thus, before accepting these decision-supporting systems for daily use, it should provide profound understanding and visual interpretation of deep learning tools, not only the surpassing human-level performance.

Furthermore, one big step to use CNN-based MBCD models for clinical applications comes from the review and approval from the Food and Drug Administration (FDA). To date, several FDA-approved CAD systems have been in the market, such as the QVCAD system (QView Medical Inc, Los Altos, CA) that uses deep learning for automated 3D breast ultrasound analysis. With the increasing use of deep learning algorithms, more and more CNN-based CAD systems will be approved by the FDA. Basically, compelling properties, such as expert-level performance, robustness, and generalizability, should be guaranteed on different imaging devices. While from the perspective of long-term evolution, a global real-life application accounting for widespread geographic, ethic, and genetic variations should be considered. Therefore, there is still a long way ahead of the translation of deep learning tools from scientific research to clinical practice.

4.4. Limitations. There are several limitations. First, this review focuses on CNN for automated MBCD. For computer-aided MBCD, it can also be well tackled by using other CAD techniques, such as case retrieval [95–97] and breast density estimation [98, 99]. Moreover, this study concerns only mammography. For comprehensive disease analysis, other imaging modalities, such as ultrasound and magnetic resonance, should be taken into consideration [31]. Besides, this review is limited to two-dimensional image analysis, and many other medical tasks use CNN models to tackle volumetric images [100–102]. In particular, this study concerns only peer-reviewed journal publications that considerably reduces the number of publications for analysis and consequently, it might omit some high-quality CNN-based MBCD models [103–105]. In addition, some technical details, such as how to prepare medical instances for training, are not delivered in this review, while it should be kept in mind that each step is related to mammographic image analysis.

5. Conclusion

This study presents a technical review of the recent progress of CNN-based MBCD. It categorizes the techniques into three groups based on how to use CNN models. Furthermore, the findings from the model building to the pros and cons of each model are summarized. In addition, technical challenges, future focus, and limitations are pointed out. At present, the design and use of CNN-based MBCD is at its early stage and result-oriented. To the ultimate goal of using deep learning tools to facilitate clinical practice, there is still a long way ahead. This review benefits scientific researcher, industrial engineers, and those who are devoted to intelligent cancer diagnosis.

Conflicts of Interest

The authors declare that they have no conflicts of interest regarding the publication of this paper.

Authors' Contributions

Lian Zou and Shaode Yu contributed equally to this work.

Acknowledgments

The authors would like to thank the editor and reviewers for their constructive comments that have helped to improve the paper quality. Thanks are also given to those researchers who share datasets and codes for fair comparison. This work is supported in part by grants from the National Key Research and Develop Program of China (2016YFC0105102), the Leading Talent of Special Support Project in Guangdong (2016TX03R139), Fundamental Research Program of Shenzhen (JCYJ20170413162458312), the Science Foundation of Guangdong (2017B020229002, 2015B020233011, 2014A030312006) and the Beijing Center for Mathematics and Information Interdisciplinary Sciences, and the National Natural Science Foundation of China (61871374).

References

[1] R. L. Siegel, K. D. Miller, and A. Jemal, "Cancer statistics, 2016," *CA: A Cancer Journal for Clinicians*, vol. 66, no. 1, pp. 7–30, 2016.

[2] L. Fan, K. Strasser-Weippl, J.-J. Li et al., "Breast cancer in China," *Lancet Oncology*, vol. 15, no. 7, pp. e279–e289, 2014.

[3] L. Tabár, A. Gad, L. H. Holmberg et al., "Reduction in mortality from breast cancer after mass screening with mammography," *The Lancet*, vol. 325, no. 8433, pp. 829–832, 1985.

[4] S. Yu, S. Wu, L. Zhuang et al., "Efficient segmentation of a breast in B-mode ultrasound tomography using three-dimensional GrabCut (GC3D)," *Sensors*, vol. 17, no. 8, p. 1827, 2017.

[5] R. Longo, F. Arfelli, R. Bellazzini et al., "Towards breast tomography with synchrotron radiation at Elettra: first images," *Physics in Medicine and Biology*, vol. 61, no. 4, pp. 1634–1649, 2016.

[6] M. J. Michell, A. Iqbal, R. K. Wasan et al., "A comparison of the accuracy of film-screen mammography, full-field digital mammography, and digital breast tomosynthesis," *Clinical Radiology*, vol. 67, no. 10, pp. 976–981, 2012.

[7] F. M. Hall, J. M. Storella, D. Z. Silverstone, and G. Wyshak, "Nonpalpable breast lesions: recommendations for biopsy based on suspicion of carcinoma at mammography," *Radiology*, vol. 167, no. 2, pp. 353–358, 1988.

[8] J. Tang, R. M. Rangayyan, J. Xu, I. El Naqa, and Y. Yang, "Computer-aided detection and diagnosis of breast cancer with mammography: recent advances," *IEEE Transactions on Information Technology in Biomedicine*, vol. 13, no. 2, pp. 236–251, 2009.

[9] N. I. R. Yassin, S. Omran, E. M. F. El Houby, and H. Allam, "Machine learning techniques for breast cancer computer aided diagnosis using different image modalities: a systematic review," *Computer Methods and Programs in Biomedicine*, vol. 156, pp. 25–45, 2018.

[10] Y. Jiang, R. M. Nishikawa, R. A. Schmidt, C. E. Metz, M. L. Giger, and K. Doi, "Improving breast cancer diagnosis with computer-aided diagnosis," *Academic radiology*, vol. 6, no. 1, pp. 22–33, 1999.

[11] H. D. Cheng, J. Shan, W. Ju, Y. Guo, and L. Zhang, "Automated breast cancer detection and classification using ultrasound images: a survey," *Pattern Recognition*, vol. 43, no. 1, pp. 299–317, 2010.

[12] A. Jalalian, S. B. T. Mashohor, H. R. Mahmud, M. I. B. Saripan, A. R. B. Ramli, and B. Karasfi, "Computer-aided detection/diagnosis of breast cancer in mammography and ultrasound: a review," *Clinical Imaging*, vol. 37, no. 3, pp. 420–426, 2013.

[13] S. Mambou, P. Maresova, O. Krejcar, A. Selamat, and K. Kuca, "Breast cancer detection using infrared thermal imaging and a deep learning model," *Sensors*, vol. 18, no. 9, p. 2799, 2018.

[14] H. D. Cheng, X. Cai, X. Chen, L. Hu, and X. Lou, "Computer-aided detection and classification of microcalcifications in mammograms: a survey," *Pattern Recognition*, vol. 36, no. 12, pp. 2967–2991, 2003.

[15] R. M. Rangayyan, F. J. Ayres, and J. E. Leo Desautels, "A review of computer-aided diagnosis of breast cancer: toward the detection of subtle signs," *Journal of the Franklin Institute*, vol. 344, no. 3-4, pp. 312–348, 2007.

[16] I. Christoyianni, A. Koutras, E. Dermatas, and G. Kokkinakis, "Computer aided diagnosis of breast cancer in digitized mammograms," *Computerized Medical Imaging and Graphics*, vol. 26, no. 5, pp. 309–319, 2002.

[17] L. Wei, Y. Yang, R. M. Nishikawa, and Y. Jiang, "A study on several machine-learning methods for classification of malignant and benign clustered microcalcifications," *IEEE Transactions on Medical Imaging*, vol. 24, no. 3, pp. 371–380, 2005.

[18] Y. Bengio, A. Courville, and P. Vincent, "Representation learning: a review and new perspectives," *IEEE Transactions on Pattern Analysis and Machine Intelligence*, vol. 35, no. 8, pp. 1798–1828, 2013.

[19] Y. LeCun, Y. Bengio, and G. Hinton, "Deep learning," *Nature*, vol. 521, no. 7553, pp. 436–444, 2015.

[20] Y. Guo, Y. Liu, A. Oerlemans, S. Lao, S. Wu, and M. S. Lew, "Deep learning for visual understanding: a review," *Neurocomputing*, vol. 187, pp. 27–48, 2016.

[21] S. Yu, S. Wu, L. Wang, F. Jiang, Y. Xie, and L. Li, "A shallow convolutional neural network for blind image sharpness assessment," *PloS one*, vol. 12, no. 5, Article ID e0176632, 2017.

[22] Y. Li, Z. Wang, G. Dai, S. Wu, S. Yu, and Y. Xie, "Evaluation of realistic blurring image quality by using a shallow convolutional neural network," in *Proceedings of the 2017 IEEE International Conference on Information and Automation (ICIA)*, vol. 1, pp. 853–857, Macau, China, July 2017.

[23] Z. Zhang, X. Liang, X. Dong, Y. Xie, and G. Cao, "A sparse-view CT reconstruction method based on combination of DenseNet and deconvolution," *IEEE Transactions on Medical Imaging*, vol. 37, no. 6, pp. 1407–1417, 2018.

[24] Y. Liu, S. Stojadinovic, B. Hrycushko et al., "A deep convolutional neural network-based automatic delineation strategy for multiple brain metastases stereotactic radiosurgery," *PloS One*, vol. 12, no. 10, Article ID e0185844, 2017.

[25] R. Wang, X. Liang, X. Zhu, and Y. Xie, "A feasibility of respiration prediction based on deep Bi-LSTM for real-time tumor tracking," *IEEE Access*, vol. 6, pp. 51262–51268, 2018.

[26] D. Shen, G. Wu, and H.-I. Suk, "Deep learning in medical image analysis," *Annual Review of Biomedical Engineering*, vol. 19, no. 1, pp. 221–248, 2017.

[27] W. Qin, J. Wu, F. Han et al., "Superpixel-based and boundary-sensitive convolutional neural network for automated liver segmentation," *Physics in Medicine & Biology*, vol. 63, no. 9, article 095017, 2018.

[28] T. Xiao, L. Liu, K. Li, W. Qin, S. Yu, and Z. Li, "Comparison of transferred deep neural networks in ultrasonic breast masses discrimination," *BioMed Research International*, vol. 2018, Article ID 4605191, 9 pages, 2018.

[29] P. Meyer, V. Noblet, C. Mazzara, and A. Lallement, "Survey on deep learning for radiotherapy," *Computers in Biology and Medicine*, vol. 98, pp. 126–146, 2018.

[30] X. Zhen, J. Chen, Z. Zhong et al., "Deep convolutional neural network with transfer learning for rectum toxicity prediction in cervical cancer radiotherapy: a feasibility study," *Physics in Medicine & Biology*, vol. 62, no. 21, pp. 8246–8263, 2017.

[31] J. R. Burt, N. Torosdagli, N. Khosravan et al., "Deep learning beyond cats and dogs: recent advances in diagnosing breast cancer with deep neural networks," *British Journal of Radiology*, vol. 91, article 20170545, 2018.

[32] A. Hamidinekoo, E. Denton, A. Rampun, K. Honnor, and R. Zwiggelaar, "Deep learning in mammography and breast histology, an overview and future trends," *Medical Image Analysis*, vol. 47, pp. 45–67, 2018.

[33] Z. Hu, J. Tang, Z. Wang, K. Zhang, L. Zhang, and Q. Sun, "Deep learning for image-based cancer detection and diagnosis–a survey," *Pattern Recognition*, vol. 83, pp. 134–149, 2018.

[34] D. C. Moura and M. A. Guevara López, "An evaluation of image descriptors combined with clinical data for breast cancer diagnosis," *International Journal of Computer Assisted Radiology and Surgery*, vol. 8, no. 4, pp. 561–574, 2013.

[35] G. An, K. Omodaka, S. Tsuda et al., "Comparison of machine-learning classification models for glaucoma management," *Journal of Healthcare Engineering*, vol. 2018, Article ID 6874765, 8 pages, 2018.

[36] R. J. Gillies, P. E. Kinahan, and H. Hricak, "Radiomics: images are more than pictures, they are data," *Radiology*, vol. 278, no. 2, pp. 563–577, 2016.

[37] S. S. F. Yip and H. J. W. L. Aerts, "Applications and limitations of radiomics," *Physics in Medicine and Biology*, vol. 61, no. 13, pp. R150–R166, 2016.

[38] X. Xu, X. Zhang, Q. Tian et al., "Quantitative identification of nonmuscle-invasive and muscle-invasive bladder carcinomas: a multiparametric MRI radiomics analysis," *Journal of Magnetic Resonance Imaging*, vol. 278, no. 2, pp. 563–577, 2018.

[39] K. Simonyan and A. Zisserman, "Very deep convolutional networks for large-scale image recognition," 2014, https://arxiv.org/abs/1409.1556.

[40] Y. LeCun, B. Boser, J. S. Denker et al., "Backpropagation applied to handwritten zip code recognition," *Neural Computation*, vol. 1, no. 4, pp. 541–551, 1989.

[41] A. Krizhevsky, I. Sutskever, and G. E. Hinton, "ImageNet classification with deep convolutional neural networks," in *Proceedings of the Advances in Neural Information Processing Systems*, pp. 1097–1105, Lake Tahoe, NV, USA, December 2012.

[42] C. Szegedy, W. Liu, Y. Jia et al., "Going deeper with convolutions," in *Proceedings of the 2015 IEEE Conference on Computer Vision and Pattern Recognition (CVPR)*, pp. 1–9, Boston, MA, USA, June 2015.

[43] C. Szegedy, V. Vanhoucke, S. Ioffe et al., "Rethinking the inception architecture for computer vision," in *Proceedings of the IEEE Conference on Computer Vision and Pattern Recognition*, pp. 2818–2826, Las Vegas, NV, USA, June 2016.

[44] K. He, X. Zhang, S. Ren, and J. Sun, "Deep residual learning for image recognition," in *Proceedings of the 2016 IEEE Conference on Computer Vision and Pattern Recognition (CVPR)*, pp. 770–778, Las Vegas Valley, NV, USA, June 2016.

[45] J. Redmon, S. Divvala, R. Girshick, and A. Farhadi, "You only look once: Unified, real-time object detection," in *Proceedings of the 2016 IEEE Conference on Computer Vision and Pattern Recognition (CVPR)*, pp. 779–788, Las Vegas Valley, NV, USA, June 2016.

[46] S. Ren, K. He, R. Girshick, and J. Sun, "Faster R-CNN: towards real-time object detection with region proposal networks," in *Proceedings of the Advances in Neural Information Processing Systems*, pp. 91–99, Montreal, Canada, December 2015.

[47] I. Sutskever, O. Vinyals, and Q. V. Le, "Sequence to sequence learning with neural networks," in *Proceedings of the Advances in Neural Information Processing Systems*, pp. 3104–3112, Montreal, Canada, December 2014.

[48] J. Schmidhuber, "Deep learning in neural networks: an overview," *Neural Networks*, vol. 61, pp. 85–117, 2015.

[49] S. J. Pan and Q. Yang, "A survey on transfer learning," *IEEE Transactions on Knowledge and Data Engineering*, vol. 22, no. 10, pp. 1345–1359, 2010.

[50] O. Russakovsky, J. Deng, H. Su et al., "ImageNet large scale visual recognition challenge," *International Journal of Computer Vision*, vol. 115, no. 3, pp. 211–252, 2015.

[51] Z. Jiao, X. Gao, Y. Wang, and J. Li, "A deep feature based framework for breast masses classification," *Neurocomputing*, vol. 197, pp. 221–231, 2016.

[52] J. Arevalo, F. A. González, R. Ramos-Pollán, J. L. Oliveira, and M. A. Guevara Lopez, "Representation learning for mammography mass lesion classification with convolutional neural networks," *Computer Methods and Programs in Biomedicine*, vol. 127, pp. 248–257, 2016.

[53] B. Q. Huynh, H. Li, and M. L. Giger, "Digital mammographic tumor classification using transfer learning from deep convolutional neural networks," *Journal of Medical Imaging*, vol. 3, no. 3, article 034501, 2016.

[54] W. Sun, T.-L. Tseng, J. Zhang, and W. Qian, "Enhancing deep convolutional neural network scheme for breast cancer diagnosis with unlabeled data," *Computerized Medical Imaging and Graphics*, vol. 57, pp. 4–9, 2017.

[55] R. K. Samala, H.-P. Chan, L. M. Hadjiiski, M. A. Helvie, K. Cha, and C. Richter, "Multi-task transfer learning deep convolutional neural network: application to computer-aided diagnosis of breast cancer on mammograms," *Physics in Medicine & Biology*, vol. 62, no. 23, p. 8894, 2017.

[56] N. Antropova, B. Q. Huynh, and M. L. Giger, "A deep feature fusion methodology for breast cancer diagnosis demonstrated on three imaging modality datasets," *Medical Physics*, vol. 44, no. 10, pp. 5162–5171, 2017.

[57] N. Dhungel, G. Carneiro, and A. P. Bradley, "A deep learning approach for the analysis of masses in mammograms with minimal user intervention," *Medical Image Analysis*, vol. 37, pp. 114–128, 2017.

[58] Y. Qiu, S. Yan, R. R. Gundreddy et al., "A new approach to develop computer-aided diagnosis scheme of breast mass classification using deep learning technology," *Journal of X-Ray Science and Technology*, vol. 25, no. 5, pp. 751–763, 2017.

[59] M. M. Jadoon, Q. Zhang, I. Ul Haq, S. Butt, and A. Jadoon, "Three-class mammogram classification based on descriptive CNN features," *BioMed Research International*, vol. 2017, Article ID 3640901, 11 pages, 2017.

[60] K. Mendel, H. Li, D. Sheth, and M. Giger, "Transfer learning from convolutional neural networks for computer-aided diagnosis: a comparison of digital breast tomosynthesis and full-field digital mammography," *Academic Radiology*, 2018, In press.

[61] X. Zhang, Y. Zhang, E. Y. Han et al., "Classification of whole mammogram and tomosynthesis images using deep convolutional neural networks," *IEEE Transactions on Nanobioscience*, vol. 17, no. 3, pp. 237–242, 2018.

[62] Z. Jiao, X. Gao, Y. Wang, and J. Li, "A parasitic metric learning net for breast mass classification based on mammography," *Pattern Recognition*, vol. 75, pp. 292–301, 2018.

[63] A. C. Perre, L. A. Alexandre, and L. C. Freire, "Lesion classification in mammograms using convolutional neural networks and transfer learning," *Computer Methods in Biomechanics and Biomedical Engineering: Imaging & Visualization*, pp. 1–7, 2018.

[64] H. Chougrad, H. Zouaki, and O. Alheyane, "Deep convolutional neural networks for breast cancer screening," *Computer Methods and Programs in Biomedicine*, vol. 157, pp. 19–30, 2018.

[65] M. A. Al-masni, M. A. Al-antari, J.-M. Park et al., "Simultaneous detection and classification of breast masses in digital mammograms via a deep learning YOLO-based CAD system," *Computer Methods and Programs in Biomedicine*, vol. 157, pp. 85–94, 2018.

[66] D. Ribli, A. Horváth, Z. Unger, P. Pollner, and I. Csabai, "Detecting and classifying lesions in mammograms with deep learning," *Scientific Reports*, vol. 8, no. 1, pp. 85–94, 2018.

[67] H. Wang, J. Feng, Z. Zhang et al., "Breast mass classification via deeply integrating the contextual information from multi-view data," *Pattern Recognition*, vol. 80, pp. 42–52, 2018.

[68] S. Yu, L. L. Liu, Z. Y. Wang, G. Z. Dai, and Y. Q. Xie, "Transferring deep neural networks for the differentiation of mammographic breast lesions," *China Technological Sciences*, vol. 62, no. 3, pp. 441–447, 2018.

[69] J. E. Oliveira, M. O. Gueld, A. d. A. Araújo, B. Ott, and T. M. Deserno, "Toward a standard reference database for computer-aided mammography," in *Proceedings of the Medical Imaging 2008: Computer-Aided Diagnosis*, vol. 6915, p. 69151Y, San Diego, CA, USA, March 2008.

[70] M. Heath, K. Bowyer, D. Kopans et al., "The digital database for screening mammography," in *Proceedings of the International Workshop on Digital Mammography*, vol. 6915, pp. 212–218, Toronto, Canada, June 2000.

[71] I. C. Moreira, I. Amaral, I. Domingues, A. Cardoso, M. J. Cardoso, and J. S. Cardoso, "INbreast," *Academic Radiology*, vol. 19, no. 2, pp. 236–248, 2012.

[72] J. Suckling, J. Parker, D. R. Dance et al., "The mammographic image analysis society digital mammogram database," in *Proceedings of the International Workshop on Digital Mammography, Excerpta Medica International Congress Series*, pp. 375–378, York, England, July 1994.

[73] N. Liu, J. Shen, M. Xu, D. Gan, E.-S. Qi, and B. Gao, "Improved cost-sensitive support vector machine classifier for breast cancer diagnosis," *Mathematical Problems in Engineering*, vol. 2018, Article ID 3875082, 13 pages, 2018.

[74] X. Liang, Z. Zhang, T. Niu et al., "Iterative image-domain ring artifact removal in cone-beam CT," *Physics in Medicine & Biology*, vol. 62, no. 13, pp. 5276–5292, 2017.

[75] R. Zhang, W. Zhou, Y. Li, S. Yu, and Y. Xie, "Nonrigid registration of lung CT images based on tissue features," *Computational and Mathematical Methods in Medicine*, vol. 2013, Article ID 834192, 7 pages, 2013.

[76] H. Zhou, Y. Kuang, Z. Yu et al., "Image deformation with vector-field interpolation based on MRLS-TPS," *IEEE Access*, vol. 6, pp. 75886–75898, 2018.

[77] H. Greenspan, B. van Ginneken, and R. M. Summers, "Guest editorial deep learning in medical imaging: overview and future promise of an exciting new technique," *IEEE Transactions on Medical Imaging*, vol. 35, no. 5, pp. 1153–1159, 2016.

[78] H.-C. Shin, H. R. Roth, M. Gao et al., "Deep convolutional neural networks for computer-aided detection: CNN architectures, dataset characteristics and transfer learning," *IEEE Transactions on Medical Imaging*, vol. 35, no. 5, pp. 1285–1298, 2016.

[79] L. Zheng, Y. Zhao, S. Wang, J. Wang, and Q. Tian, "Good practice in CNN feature transfer," 2016, https://arxiv.org/abs/1604.00133.

[80] N. Tajbakhsh, J. Y. Shin, S. R. Gurudu et al., "Convolutional neural networks for medical image analysis: full training or fine tuning?," *IEEE Transactions on Medical Imaging*, vol. 35, no. 5, pp. 1299–1312, 2016.

[81] B. J. Erickson, P. Korfiatis, T. L. Kline, Z. Akkus, K. Philbrick, and A. D. Weston, "Deep learning in radiology: does one size fit all?," *Journal of the American College of Radiology*, vol. 15, no. 3, pp. 521–526, 2018.

[82] S. B. Kotsiantis, I. D. Zaharakis, and P. E. Pintelas, "Machine learning: a review of classification and combining techniques," *Artificial Intelligence Review*, vol. 26, no. 3, pp. 159–190, 2006.

[83] J. Yosinski, J. Clune, Y. Bengio, and H. Lipson, "How transferable are features in deep neural networks," in *Proceedings of the Advances in Neural Information Processing Systems*, pp. 3320–3328, Montréal, Canada, December 2014.

[84] N. Srivastava, G. Hinton, A. Krizhevsky, I. Sutskever, and R. Salakhutdinov, "Dropout: a simple way to prevent neural networks from overfitting," *Journal of Machine Learning Research*, vol. 15, no. 1, pp. 1929–1958, 2014.

[85] K. Chatfield, K. Simonyan, A. Vedaldi, and A. Zisserman, "Return of the devil in the details: delving deep into convolutional nets," 2014, https://arxiv.org/abs/1405.3531.

[86] Z. Zhang, G. Dai, X. Liang, S. Yu, L. Li, and Y. Xie, "Can signal-to-noise ratio perform as a baseline indicator for medical image quality assessment," *IEEE Access*, vol. 6, pp. 11534–11543, 2018.

[87] A. Oliver, J. Freixenet, J. Martí et al., "A review of automatic mass detection and segmentation in mammographic images," *Medical Image Analysis*, vol. 14, no. 2, pp. 87–110, 2018.

[88] R. K. Samala, H.-P. Chan, L. M. Hadjiiski, M. A. Helvie, C. Richter, and K. Cha, "Evolutionary pruning of transfer learned deep convolutional neural network for breast cancer diagnosis in digital breast tomosynthesis," *Physics in Medicine & Biology*, vol. 63, no. 9, article 095005, 2018.

[89] M. Benndorf, C. Herda, M. Langer, and E. Kotter, "Provision of the DDSM mammography metadata in an accessible format," *Medical Physics*, vol. 41, no. 5, article 051902, 2014.

[90] M. D. Zeiler and R. Fergus, "Visualizing and understanding convolutional networks," in *Proceedings of the European Conference on Computer Vision*, vol. 1, pp. 818–833, Zurich, Switzerland, September 2014.

[91] L. V. D. Maaten and G. Hinton, "Visualizing data using t-SNE," *Journal of Machine Learning Research*, vol. 9, pp. 2579–2605, 2008.

[92] N. Lei, Z. Luo, S.-T. Yau, and D. X. Gu, "Geometric understanding of deep learning," 2018, https://arxiv.org/abs/1805.10451.

[93] G. Montavon, W. Samek, and K.-R. Müller, "Methods for interpreting and understanding deep neural networks," *Digital Signal Processing*, vol. 73, pp. 1–15, 2018.

[94] L. Xing, E. A. Krupinski, and J. Cai, "Artificial intelligence will soon change the landscape of medical physics research and practice," *Medical Physics*, vol. 45, no. 5, pp. 1791–1793, 2018.

[95] Q. Huang, X. Huang, L. Liu, Y. Lin, X. Long, and X. Li, "A case-oriented web-based training system for breast cancer diagnosis," *Computer Methods and Programs in Biomedicine*, vol. 156, pp. 73–83, 2018.

[96] D. Gu, C. Liang, and H. Zhao, "A case-based reasoning system based on weighted heterogeneous value distance metric for breast cancer diagnosis," *Artificial Intelligence in Medicine*, vol. 77, pp. 31–47, 2017.

[97] M. Jiang, S. Zhang, H. Li, and D. N. Metaxas, "Computer-aided diagnosis of mammographic masses using scalable image retrieval," *IEEE Transactions on Biomedical Engineering*, vol. 62, no. 2, pp. 783–792, 2015.

[98] K. Holland, A. Gubern-Mérida, R. M. Mann, and N. Karssemeijer, "Optimization of volumetric breast density estimation in digital mammograms," *Physics in Medicine and Biology*, vol. 62, no. 9, pp. 3779–3797, 2017.

[99] J. Lee and R. M. Nishikawa, "Automated mammographic breast density estimation using a fully convolutional network," *Medical Physics*, vol. 45, no. 3, pp. 1178–1190, 2018.

[100] R. Miotto, F. Wang, S. Wang, X. Jiang, and J. T. Dudley, "Deep learning for healthcare: review, opportunities and challenges," *Briefings in Bioinformatics*, vol. 19, no. 6, pp. 1236–1246, 2017.

[101] Q. Dou, L. Yu, H. Chen et al., "3D deeply supervised network for automated segmentation of volumetric medical images," *Medical Image Analysis*, vol. 41, pp. 40–54, 2017.

[102] J. Yun, J. Park, D. Yu et al., "Improvement of fully automated airway segmentation on volumetric computed tomographic images using a 2.5 dimensional convolutional neural net," *Medical Image Analysis*, vol. 51, pp. 13–20, 2019.

[103] G. Carneiro, J. Nascimento, and A. P. Bradley, "Unregistered multiview mammogram analysis with pre-trained deep learning models," in *Proceedings of the International Conference on Medical Image Computing and Computer-Assisted Intervention (MICCAI)*, pp. 652–660, Munich, Germany, October 2015.

[104] N. Dhungel, G. Carneiro, and A. P. Bradley, "Fully automated classification of mammograms using deep residual neural networks," in *Proceedings of the 2017 IEEE 14th International Symposium on Biomedical Imaging (ISBI 2017)*, pp. 310–314, Melbourne, Australia, April 2017.

[105] M. A. Al-masni, M. A. Al-antari, J. M. Park et al., "Detection and classification of the breast abnormalities in digital mammograms via regional convolutional neural network," in *Proceedings of the Annual International Conference of the IEEE Engineering in Medicine and Biology Society (EMBC)*, pp. 1230–1233, Jeju Island, South Korea, July 2017.

Hindawi
Computational and Mathematical Methods in Medicine
Volume 2019, Article ID 1684218, 11 pages
https://doi.org/10.1155/2019/1684218

Research Article

Automatic Segmentation of Pathological Glomerular Basement Membrane in Transmission Electron Microscopy Images with Random Forest Stacks

Lei Cao,[1] **YanMeng Lu**,[2] **ChuangQuan Li**,[1] **and Wei Yang**[1]

[1]*School of Biomedical Engineering, Southern Medical University, GuangZhou 510515, China*
[2]*Central Laboratory, Southern Medical University, GuangZhou 510515, China*

Correspondence should be addressed to Lei Cao; caolei@smu.edu.cn

Received 8 November 2018; Revised 2 February 2019; Accepted 24 February 2019; Published 25 March 2019

Guest Editor: Tomas Krilavičius

Pathological classification through transmission electron microscopy (TEM) is essential for the diagnosis of certain nephropathy, and the changes of thickness in glomerular basement membrane (GBM) and presence of immune complex deposits in GBM are often used as diagnostic criteria. The automatic segmentation of the GBM on TEM images by computerized technology can provide clinicians with clear information about glomerular ultrastructural lesions. The GBM region on the TEM image is not only complicated and changeable in shape but also has a low contrast and wide distribution of grayscale. Consequently, extracting image features and obtaining excellent segmentation results are difficult. To address this problem, we introduce a random forest- (RF-) based machine learning method, namely, RF stacks (RFS), to realize automatic segmentation. Specifically, this work proposes a two-level integrated RFS that is more complicated than a one-level integrated RF to improve accuracy and generalization performance. The integrated strategies include training integration and testing integration. Training integration can derive a full-view RFS_1 by simultaneously sampling several images of different grayscale ranges in the train phase. Testing integration can derive a zoom-view RFS_2 by separately sampling the images of different grayscale ranges and integrating the results in the test phase. Experimental results illustrate that the proposed RFS can be used to automatically segment different morphologies and gray-level basement membranes. Future study on GBM thickness measurement and deposit identification will be based on this work.

1. Introduction

Primary glomerular disease is the most common renal disease in China [1]. The diagnosis of renal diseases is largely dependent on renal biopsy, which is regarded as the gold standard. Transmission electron microscopy (TEM) combined with optical microscopy and immunofluorescence examination constitutes a continuum of pathological diagnosis of renal diseases [2]. TEM allows the observation of pathological changes in the microstructure of various glomerular cells that cannot be resolved under an optical microscope. Thus observations from light and immune pathology can be verified at an ultrastructure level [3]. Studies have found that ultrastructural study provided fundamental or important diagnostic information for 44.3% of renal biopsies [4]. Therefore, TEM is essential for the diagnosis of certain nephropathy. Considering the complexity of the TEM image of the glomerulus and related lesions, it is time consuming and labor intensive for a pathologist to visually recognize subtle pathological changes, resulting in a huge workload. Nevertheless, after the initial screening of the computer, the diagnostic efficiency and accuracy of glomerular diseases can be improved with the help of automatic image-processing technology.

The diagnosis of many renal diseases is closely related to the glomerular basement membrane (GBM) [5]. The basement membrane, along with the lining of the endotheliocytes and the lining of the podocytes on the outside, forms the filtration barrier, allowing the blood to filter out and form the urine, as shown in Figure 1. The changes of

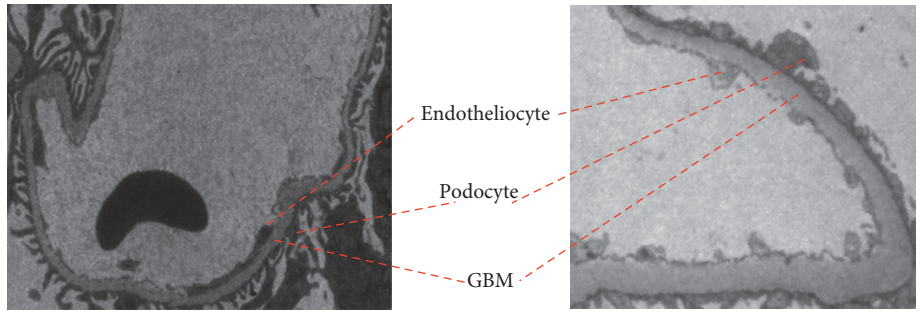

Figure 1: Interimage shape variations and intraimage grayscale inconsistency of GBM (GV: gray value).

thickness in GBM and presence of immune complex deposits in GBM are often used as diagnostic criteria for certain nephropathy, such as membranous nephropathy with extensive membranous thickening and varying amounts of immune complexes, Alport syndrome with diffuse membranous thickening, and familial recurrent hematuria syndrome (thin basement membrane nephropathy) with diffuse thinning of GBM [6, 7]. Manual measurement of the thickness of GBM is an early auxiliary [8, 9], but the workload is very expensive. Then, some semiautomatic software tools [10, 11] are used to obtain the thickness of GBM more quickly and conveniently but still need manual intervention. In terms of morphological complexity, the autoidentification difficulty of deposits is the same as or even greater than GBM and literatures on this have not been found. In practicality, the thickness measurement and deposit identification can be realized subsequently and automatically on condition that the GBM region is completely autorecognized or is segmented.

Early in 1993, Ong et al. [12] applied adaptive window-based tracking to segment glomerular TEM images. Since then, a few semiautomatic or fully automatic methods have been proposed. Kamenetsky et al. [13] and Rangayyan et al. [14] achieved GBM segmentation and measurement through region division and dynamic contour modeling. Wu et al. [15] and Wu and Dikman [16] also proposed two methods. One is to obtain the center line of the GBM by interpolating manual mark points and then autosegment GBM through distance mapping and low-pass filtering [15]. Another method involves the use of threshold and morphological method with no manual mark [16]. Liu et al. not only segmented the GBM but also measured its length and counted the number of slits [17]. Most existing methods mentioned above have made some contribution, but there are still many problems unresolved. These methods either require tedious manual initialization that involves extra work for pathologists and introduces possible subjective errors, or they can only be used to segment truncated GBM fragments with increased contrast and single direction as showed in their experimental results. Therefore, ensuring segmentation quality for the whole complex GBM images remains challenging.

Two common difficulties associated with GBM segmentation are interimage shape variations and intraimage grayscale inconsistency. Figure 1 shows that the low contrast between the GBM segment and surrounding tissues, such as endotheliocytes and podocytes, and variations in the form and width of GBM segments cause difficulty in autoextracting features. In addition to the complex structure of a pathological section, the grayscale distribution of TEM images is very wide because of the uncertainty of sample prefabrication and the illumination inhomogeneity of transmission imaging.

To address the first challenge of autoextracting features, we employ a pixel-wise classifier, namely, random forest (RF) [18], based on machine learning to avoid relying on hand-crafted features. RF is a committee of weak learners (e.g., decision tree) to solve classification and regression problems without manually specifying some features through the construction and combination of multiple decision trees and random selection of attributes [19, 20], which can be used to cope with the complex structural characteristics of biological images. RF has been widely explored from medical image-processing fields, especially detection tasks, including early identification or prediction of Alzheimer's disease [21], adrenal gland abnormality detection [22], and automatic cardiac segmentation [23].

An enhanced generalization effect based on a single RF classifier is hardly obtained because of the grayscale inconsistency intraimage. To address this second challenge, we propose an RF stack (RFS) model based on a wider grayscale range of images. After assigning TEM images to different grayscale groups, we sample from all these groups and train a full-view RF classifier as RFS_1 and multiple RF zoom-view classifiers as RFS_2. In the segmentation phase, each pixel of the new GBM image is classified automatically through full-view and zoom-view RFS and the candidate segment results are combined and optimized. Thus, the segmentation accuracy is improved by using this two-level integrated machine learning method.

The remaining sections of this paper are organized as follows. In Section 2, information regarding GBM image selection and preprocessing is described and the details of the proposed RFS model for GBM segmentation is introduced. In Section 3, experimental results are reported and discussed. In Section 4, the conclusion is presented.

2. Materials and Methods

2.1. Data and Materials

2.1.1. Image Data. Renal biopsy specimens were immediately fixed with 2.5% cold glutaraldehyde with 0.1 M phosphate buffer at pH 7.3 for 4 h, washed with phosphate buffer, postfixed with 1% osmium tetroxide in the same buffer, dehydrated with a graded series of ethanol, and embedded in Spurr resin. Ultrathin sections (70 nm) were contrast enhanced with uranyl acetate and lead citrate and examined using a Hitachi H-7500 electron microscope (Tokyo, Japan) at 60 kV. All of the sections were imaged with MORADA G3 (EMSIS Corporation of Japan) at 5000x magnification. In the field of vision, a whole glomerulus, including the glomerular capillaries and the basement membrane, was selected. Continuous filming was conducted using the attached digital imaging system and controlled by the Pathological Image Workstation of the NanFang Hospital in Guangzhou, China.

2.1.2. Preprocessing of TEM Images. The pathologists collected 351 images from the obtained glomerular TEM images to build a GBM image database. Of these 351 images, 330 were used as a training set and divided into different groups ($N = 37$) according to the range of GBM's intensity. In the test set, 21 images with different sizes and various basement membrane types, such as stripe-, closed-, and compound-type, were used. The image pixels were divided into GBM and background. Figure 2(a) shows the original TEM image, and Figure 2(b) illustrates its corresponding GBM binary mask manually labeled by the pathologist.

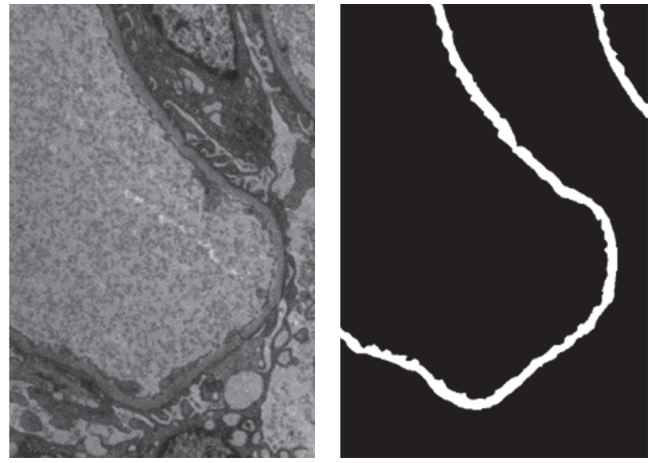

(a) (b)

Figure 2: TEM image (a) and the corresponding binary mask image of GBM (b).

2.2. Method Overview

2.2.1. Workflow Diagram. RF is an ensemble machine learning method, which can be applied to image segmentation by classifying pixels into target or background. The proposed RFS is a RF-based multilevel integrated structure that mainly involves two phases: hierarchical training and refinement testing. The implementation process of RFS is shown in Figure 3.

Train phase: from the prebuilt GBM database, an image is randomly selected from each image group with different GBM grayscale ranges. Hence, N images, namely, Img_1 to Img_N, needed for one training session are ready. The simultaneous sampling of N images and follow-up training yield RFS_1 called the full-view RFS. Then, N RF classifiers, RF_i ($i = 1, \ldots, N$), are generated by sampling and training each image individually, and RFS_2, which is called zoom-view RFS, covering different grayscale ranges is constructed.

Test phase: each pixel of the test image is classified by RFS_1 and constitutes a candidate segmentation R_1. Each pixel of the test image is classified by each RF_i in RFS_2 and got N coarse segmentation results, namely, CR_1 to CR_N. Then, another candidate segmentation R_2 is obtained after an iterative refinement scheme. The final segmentation is selected from R_1 and R_2 by a human expert.

2.2.2. Software Tools. The image-processing and analysis software FIJI (ImageJ) is developed by the US National Health Administration, and FIJI-based secondary development is well known. In this paper, we selected a FIJI plug-in named Trainable Weka Segmentation (TWS) (http://imagej.net/Trainable_Weka_Segmentation) [24], which is based on the free open-source software Weka [25]. TWS combines a series of machine learning algorithms to perform pixel-based image segmentation. Figure 4 shows that TWS is modified and integrated with some image-processing functions provided by Matlab to meet the needs of GBM image segmentation.

2.3. Training

2.3.1. Random Forest. RF [23] is a common method for ensemble learning whose training algorithm relies on bagging integration and random attribute selection in the construction of the decision tree. The training of one RF is shown in a blue arrow line in Figure 3. Bootstrap sampling technology is used to generate T training subsets from the original training set, and T decision tree models are established to form one RF. An RF segmentation is illustrated in an orange arrow line in Figure 3. The test image is separately classified by the T decision trees in the RF, and the result of each decision tree is aggregated to the final output by voting. In this paper, we refer this to level 1 integration.

2.3.2. RFS Classifiers. Considering that the intensities of GBM in various TEM images are significantly different, a single RF classifier cannot extract different grayscale features of all TEM images and the segmentation performance is

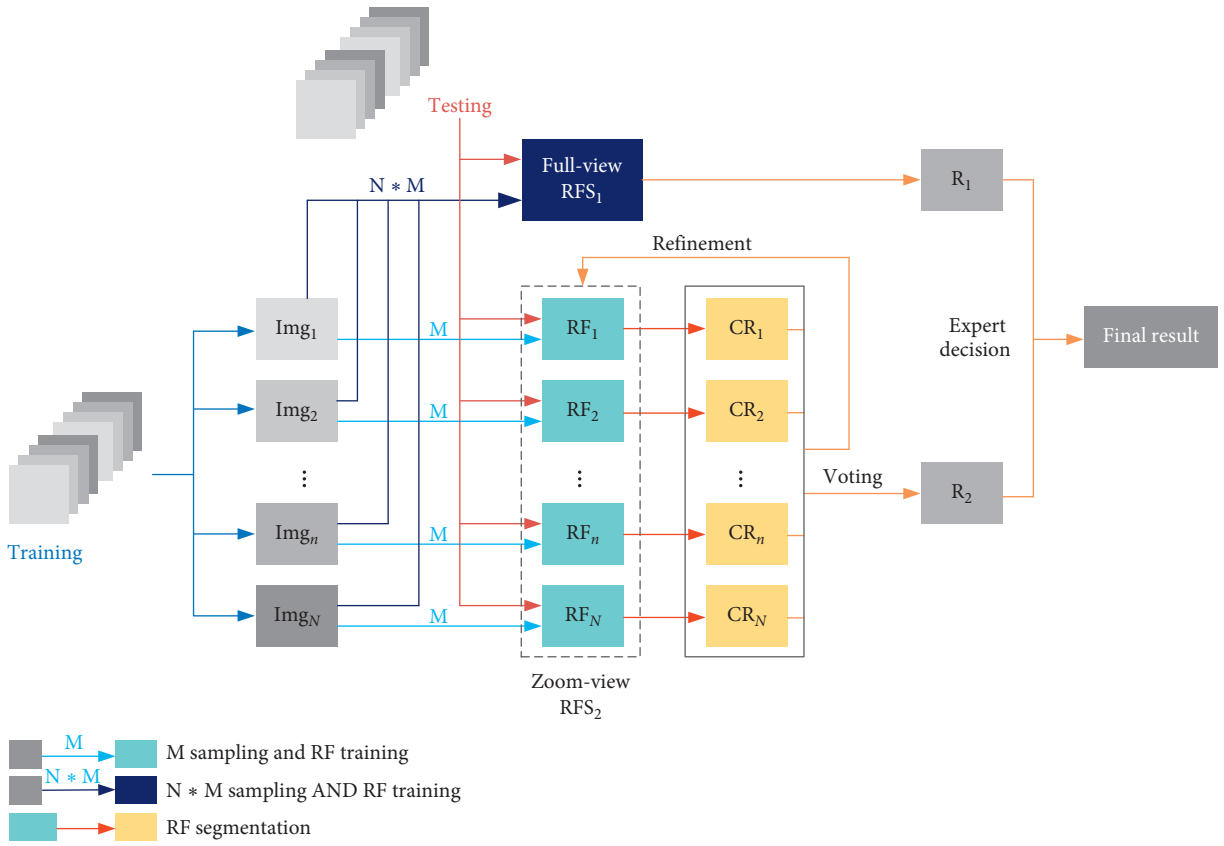

Figure 3: Flowchart of the proposed RFS method.

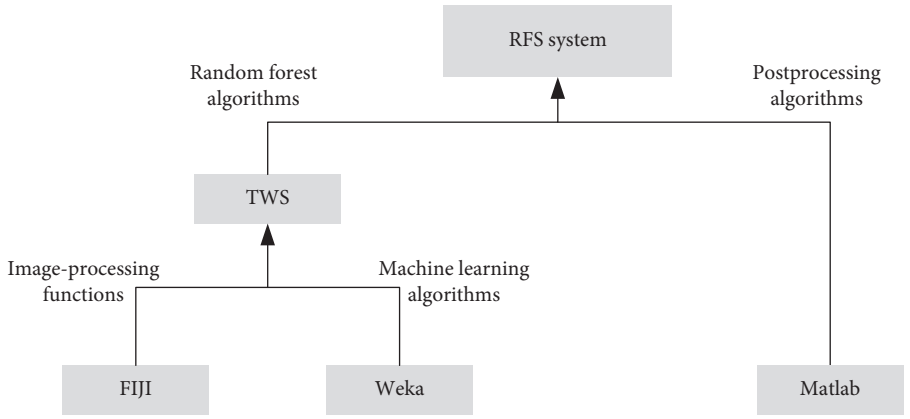

Figure 4: Software tools.

unstable. For example, given an RF classifier sampled and trained from Figure 2, the membrane illustrated in Figure 5(a) can be well segmented as shown in Figure 5(b) because of the similar grayscale of the GBM in Figure 5(a) and the classifier. A poor result is obtained by using the same classifier to segment the membrane in Figure 5(c), and the entire membrane fragment is almost not segmented as shown in Figure 5(d).

To address this problem, we introduced level 2 integration. We first assigned all training images to N groups according to the average intensity in the GBM regions. Then, RFSs were constructed. Full-view and zoom-view methods were proposed. The full-view method simultaneously takes samples from N different grayscale range images. As M pixels are sampled in each image, $M \times N$ pixels are sampled at the same time for training and RFS_1 is obtained. RFS_1 is a large file in the same logic form of an RF. Due to the large number of sampled pixels and the limited depth of the tree, we can assume that leaf nodes form stacks.

The zoom-view method separately takes samples from N grayscale range images for training and obtains a series of RFs ranging from RF_1 to RF_N, thereby forming RFS_2. Since the sampling points of each forest in RFS_2 are well targeted

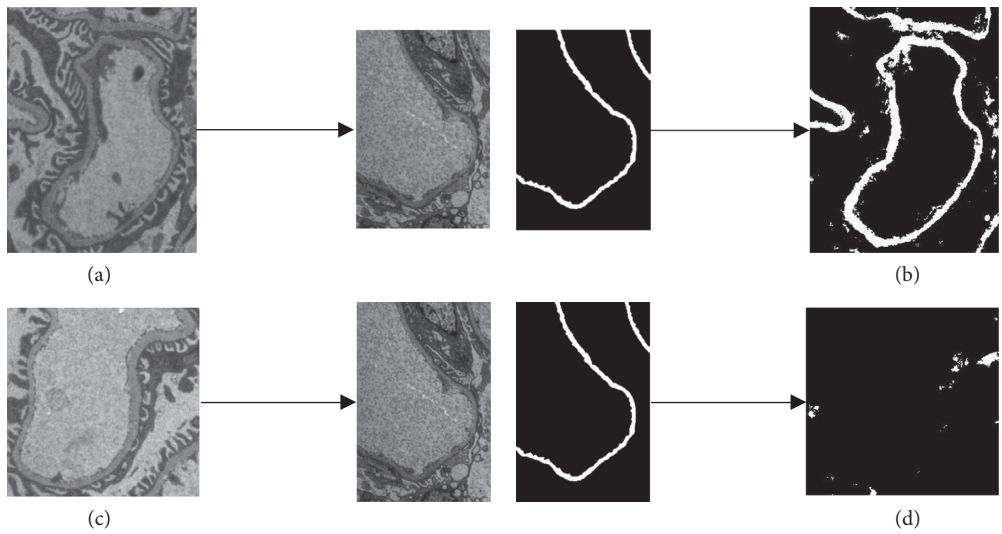

Figure 5: Segmentation results of TEM images with different grayscale ranges by using the same RF classifier.

to images with the similar range, the generalization performance of a single forest is limited and the results need to be integrated and refined at the test or segment phase.

2.3.3. Implementation Details. In the prebuilt GBM database, the TEM images in the training set were divided into $N = 37$ groups according to the average intensity of GBM. The average intensities of the GBM begin from about 73 Hounsfield units with an intensity step of 3 Hounsfield units.

TWS has 15 applicable features, and 14 of them were selected as the inputs of the decision tree in this paper: common grayscale features (mean, minimum, maximum, median, and variance), boundary features (Sobel filter, Hessian, and difference of Gaussians), texture features (Gaussian blur, entropy, and Kuwahara filter), and other features (membrane projections, Lipschitz filter, and neighbors).

Other RF training parameters include the number of decision trees ($T = 100$), the depth of decision trees ($D = 9$), and the number of sampling points per image ($M = 2000$). The selection of some parameters is discussed in Section 4.

2.4. Segmentation. Given an image to be segmented or tested, two candidate segmentation results can be separately obtained by RFS_1 and RFS_2. Pixel-by-pixel classification through full-view RFS_1 yields a candidate segmentation R_1. The process of getting candidate R_2 is more complicated. After the preparation of a series of coarse results, namely, CR_1 to CR_N, dealt by zoom-view RFS_2, the probability map are reconstructed and the candidate R_2 can be obtained after postprocessing and iterative refinement is completed. Finally, R_1 and R_2 are evaluated by experts to determine an enhanced segmentation.

2.4.1. Probability Map. For each image pixel to be segmented, equation (1) is used to reconstruct the probability map with the N coarse segmentation results, namely, CR_1 to CR_N:

$$p(i, j) = \frac{n(i.j)}{N}, \tag{1}$$

where $N = 37$ is the total number of coarse segmentation results, $n(i, j)$ is the frequency of the pixel of ith row, jth column is marked as GBM by each CR, and $p(i, j)$ is the probability of the pixel (i, j) as GBM.

2.4.2. Postprocessing. In the probability map, a large gray value of a pixel corresponds to a high probability to become GBM. Therefore, by maximizing the similarity belonging to the same category or avoiding it to reach the minimum, the fuzzy C-means (FCM) [26] algorithm is utilized for postprocessing to divide the image into the GBM regions and the background. Then, after some false positives are removed through a morphological operation, the GBM regions can be extracted.

2.4.3. Iterative Refinement. Not every coarse segmentation results $CR_i (i = 1, \ldots, N)$ obtained from RFS_2 provides useful information on the construction of the probability graph. In some extreme cases, some coarse segmentation results are counterproductive to the probability map. Therefore, a refinement process is described in Algorithm 1.

Figure 6 shows the whole segmentation process of RFS_2, including (1) 37 RF classifiers, (2) probability map, (3) postprocessing, and (4) iterative refinement.

2.4.4. Manual Interaction for Final Decision. For a test image, the candidate segmentation results R_1 and R_2 are compared with a gold standard labeled by a pathologist. For new images without gold standard, a user can compare R_1 with R_2 and make the final decision based on the following aspects:

(1) Coarse segmentation results with an obvious error GBM area are eliminated on the basis of the preset threshold w_1.
(2) The remaining K_1 coarse segmentation results $\mathrm{CR}_i\,(i = 1, \ldots, K_1)$ are used to obtain the probability map P_1 and the binary mask B_1 as shown in Sections 2.4.1 and 2.4.2.
(3) The Jaccard similarity $S_i\,(i = 1, \ldots, K_1)$ of B_1 and each $\mathrm{CR}_i\,(i = 1, \ldots, K_1)$ are calculated. If the similarity S_i is less than a preset threshold w_2, the corresponding CR_i is abandoned. The remaining K_2 segmentation results are used to obtain a new probability map P_2 and the binary mask B_2.
(4) The Jaccard similarity (J) of B_1 and B_2 is calculated. If $J \leq 98\%$, let $P_1 = P_2$ and $B_1 = B_2$, and step (3) is repeated until $J > 98\%$ before they exit the loop.
(5) After the loop ends, the candidate result R_2 equal to B_2 is obtained.

Algorithm 1

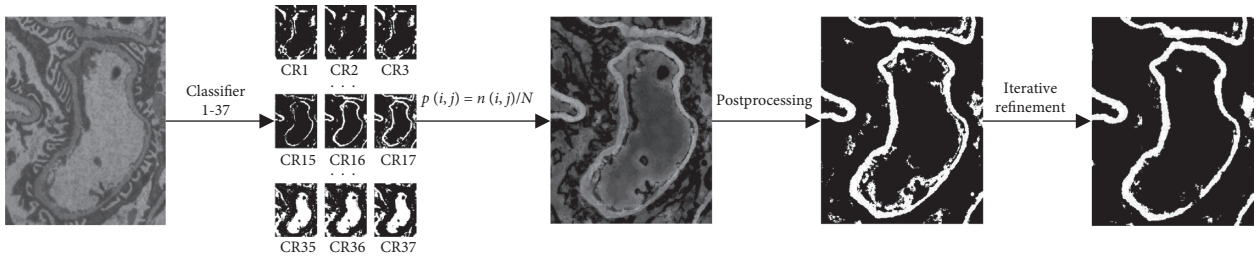

Figure 6: Segmentation process of RFS_2.

(1) Whether the foot process of the epithelial cell or the cytoplasm of the endothelial cell is inappropriately contained in the region of the basement membrane because its electron density is similar to that of the basement membrane
(2) Whether the subepithelial immune deposit is erroneously excluded from the basement membrane because its electron density is higher than that of basement membrane
(3) The continuity of the basement membrane should be cautiously analyzed because pathological fracture defects of the basement membrane are few

2.5. Evaluation Metrics. The accuracy of the proposed method is evaluated by Jaccard coefficient, which is widely utilized to evaluate the performance of segmentation methods [27–29]. It is a measure of geometric similarity defined by

$$\mathrm{Jaccard}\,(A, B) = \frac{A \cap B}{A \cup B}, \tag{2}$$

where A and B are the results of manual segmentation by human experts and the proposed method. The range of Jaccard value is [0, 1]. A large coefficient value corresponds to an accurate segmentation result.

3. Experiments and Results

In this study, 21 TEM images with different grayscale ranges, sizes, and basement membrane morphologies are used for evaluation. These images are manually segmented by pathologists as the gold standard.

3.1. Validation. The RFS method provides robust segmentation results of GBMs with different morphologies and grayscale ranges. RFS_1 and RFS_2 are trained with $M = 2000$ and $N = 37$. Figure 7 shows the segmented images obtained from the strip-, closed-, and compound-type basement membranes by using the RFS method. The top line shows original images, and the bottom line shows the corresponding segmentation results. As can be seen from the figure, although the orientation, width, and other morphologies of the GBM vary greatly, the results of the segmentation are relatively accurate. For the three test images shown, the Jaccard values are higher than 0.75.

Figure 8 shows the segmented images from different grayscale range basement membranes. It can be seen that most of the GBM is accurately segmented. Compared with RF, the segmentation results of RFS are better. For example, the original TEM image shown in Figure 5(c) fails with RF segmentation, but it can be well segmented by RFS, as shown in column 1 of Figure 8.

As shown in Figures 7 and 8, although the morphology and grayscale range of the basement membrane vary greatly, the results of the RFS segmentation are stable, indicating a good generalization performance of the RFS method. Future study on GBM thickness measurement and deposit identification will be based on this.

3.2. Influence of the RF Classifiers of Different Grayscale Ranges. A multilevel integrated RFS classifier is constructed to address the generalization problem of GBM segmentation. This is based on the hypothesis that, for an RF classifier, the closer the grayscale range of the image to be segmented is to the training image, the better the segmentation effect will be. The experimental results from the heat map in Figure 9

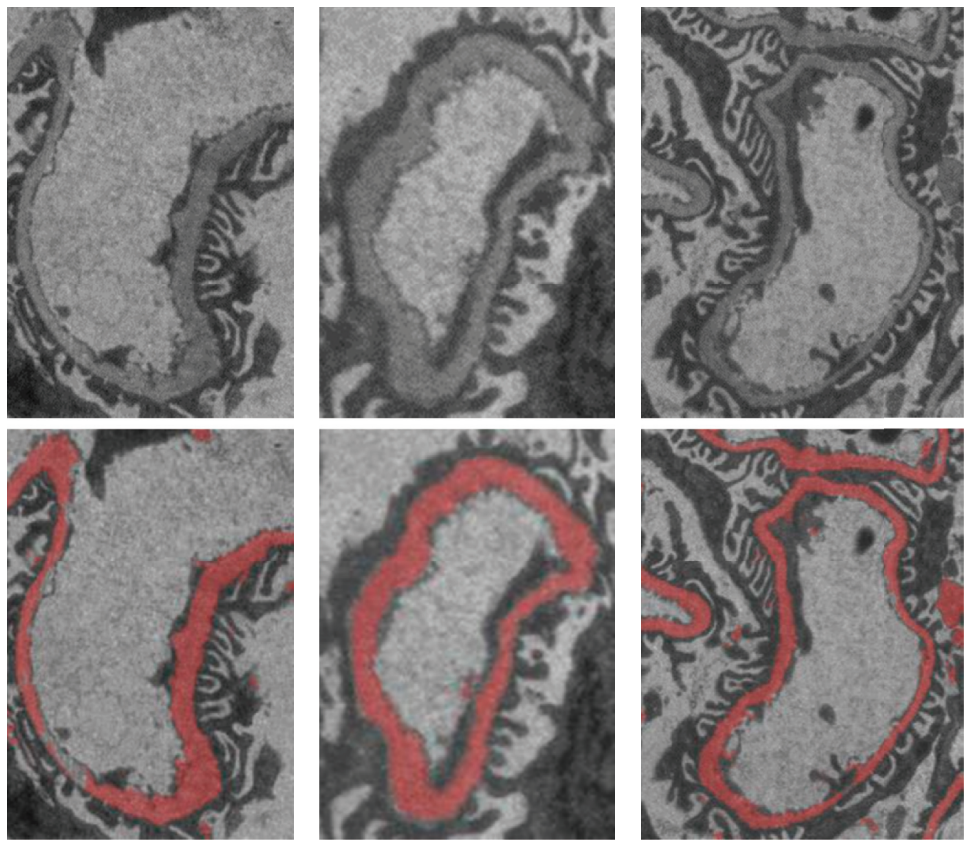

(a) (b) (c)

Figure 7: Segmentation results of RFS with different morphologies of GBM. (a) Strip type: size, 217∗307; Jaccard, 0.75. (b) Close type: size, 150∗206; Jaccard, 0.84. (c) Compound type: size, 282∗367; Jaccard, 0.76.

confirm this hypothesis. The horizontal axis from low to high represents 37 RF classifiers corresponding to 37 grayscale ranges of the training images. The range of the 1st grayscale is [73.5, 75.5], and the range of the 37th grayscale is [145.5, 147.5]. The vertical axis represents the grayscale mean value of the GBM of the 21 test images. The grayscale mean value of test image 1 is 78, which is close to the grayscale range of levels 1 and 2. The 21st test image has an average grayscale of 145, which is higher than the grayscale range of level 37.

In this experiment, each test image is separately segmented by these 37 RF classifiers of different grayscale ranges, and the corresponding Jaccard value is shown in different colors. An accurate segmentation result corresponds to a high Jaccard value, and its color turns to bright yellow. It can be seen from the color distribution in Figure 9 that most RF classifiers are only sensitive to test images with a close grayscale range. However, as shown in Figures 7 and 8, the RFS can accurately segment test images with different grayscale ranges that means the generalization performance of RF is not good as proposed RFS.

3.3. Differences between Full-View RFS_1 and Zoom-View RFS_2. The multilevel RFS is constructed in full view and zoom view as shown in Figure 3. The refinement details of zoom-view RFS_2 are given in Algorithm1, involving the setting of thresholds w_1 and w_2. The Jaccard values of the segmentation result for each test image (the pink dots) by using RFS_2 with three different parameter combinations are shown in columns 1, 2, and 3 of Figure 10, where $w_1 = 1$ indicates that all $N = 37$ coarse segmentation results are included in the steps of iterative optimization without filtering. The Jaccard values of the segmentation result by using full-view RFS_1 are shown in column 4 of Figure 10.

Figure 10 shows that the full-view RFS_1 is more robust than the zoom-view RFS_2. Regardless of how thresholds w_1 and w_2 are set, the mean value of RFS_2 is lower than RFS_1. However, when $w_2 = 0.3$, the segmentation result of some test images of RFS_2 is better than that of RFS_1. In the experimental data, the maximum segmentation accuracy is 0.85 but the minimum value is almost 0 and all these values are obtained through RFS_2.

The stability of RFS_1 is mainly caused by a large sample training of the classifier, involving 2000×37 sample points. However, the disadvantage of this method is its high-intensity computation. Some low accuracy of RFS_2 is caused by the effect of N course segmentation results on refinement process. If the similarity of most results with the gold standard is insufficient, a poor optimized image is obtained. Otherwise, the result is enhanced or even exceed that of RFS_1. Therefore, the final step of this method involves

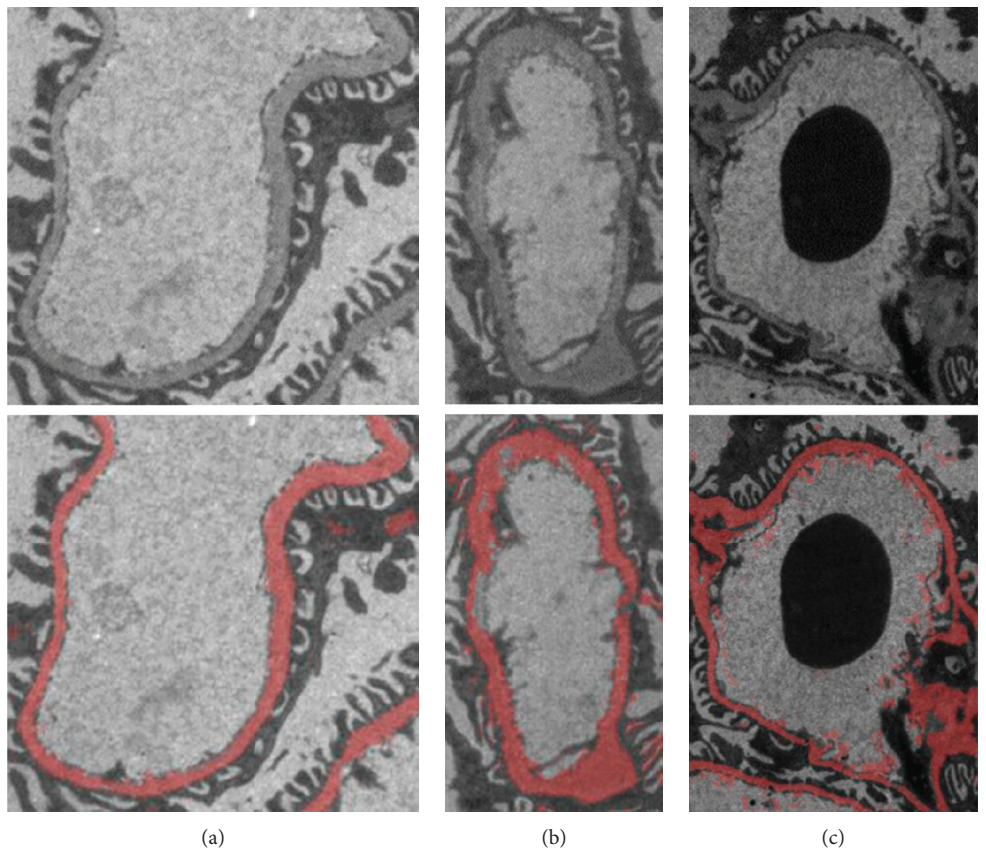

Figure 8: Segmentation results of RFS with various grayscale ranges of GBM (RoGV: range of gray value). (a) RoGV: 54–255; size: 282∗274; Jaccard: 0.70. (b) RoGV: 43–187; size: 168∗308; Jaccard: 0.71. (c) RoGV: 12–167; size: 297∗408; Jaccard: 0.65.

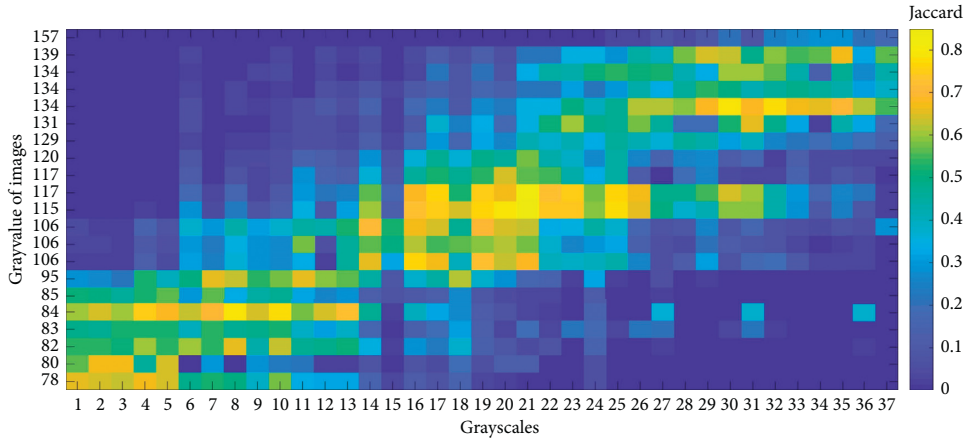

Figure 9: Heat map of segmentation results of different grayscale ranges of RF classifiers.

the selection between the two candidate segmentation results of RFS_1 and RFS_2.

3.4. Effects of Postprocessing and Refinement. The following methods are adopted to validate the effect of postprocessing and iterative refinement on RFS_2: (1) voting method (V), (2) additional postprocessing with FCM on the voting result ($V+F$), (3) additional iterative refinement on the voting result ($V+I$), and (4) additional iterative refinement on method 2 ($V+F+I$), namely, RFS_2. Figure 11 shows the mean and variance of methods (1)–(4), full-view RFS_1 (5), and the final result (6). The mean accuracy of V is the lowest among them. V increases after FCM postprocessing and further improves after iterative refinement is completed. The final result includes the maximum mean and a relatively small variance.

4. Discussion

4.1. Methods for Constructing Ensembles. Ensemble methods construct a set of classifiers and then classify new data

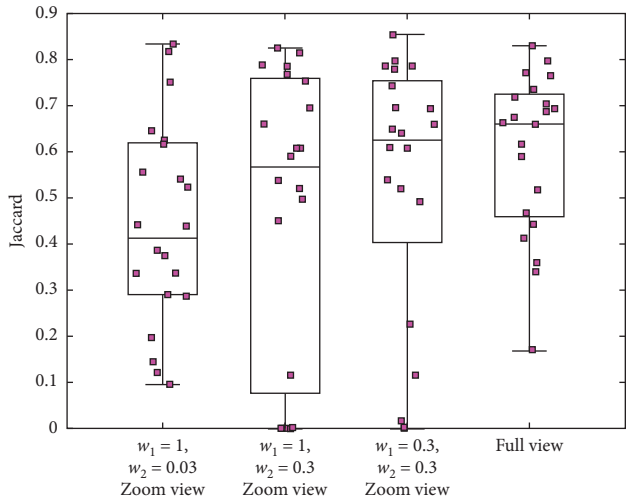

Figure 10: Jaccard values of zoom-view RFS_2 at three different parameter combinations and full-view RFS_1.

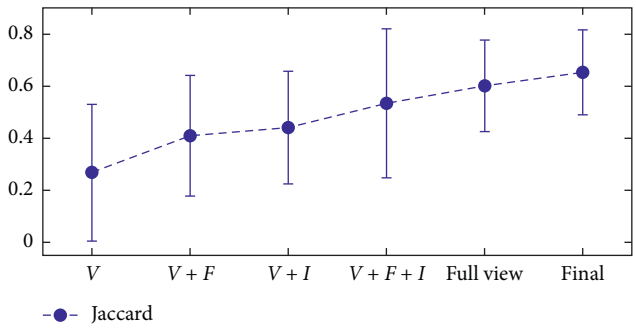

Figure 11: Effects of postprocessing and refinement methods.

points by taking a weighted vote of their predictions. Dietterich [30] assumed that five general purpose ensemble methods exist: enumeration of hypotheses, manipulation of training examples, manipulation of input features, manipulation of output targets, and injection of randomness. We adopted two of them and developed their corresponding RFS methods. Full-view RFS_2 manipulates the training examples to generate multiple hypotheses. Considering the complicated GBM images, we sample multiple grayscale images to further increase the diversity of the hypotheses. Zoom-view RFS_1 manipulates the output probability graph to achieve integration. The iterative refinement step is addressed to reduce the adverse effect of the rough segmentation result, further improving the accuracy of segmentation.

4.2. Selection of the Parameters. The number of decision trees is among the most important parameter in the application of RF algorithm in medical image segmentation [31]. Theoretically, with the increasing number of decision trees, the classification accuracy of the algorithm gradually increases as computational cost rapidly increases. The optimal number of trees should obtain a good balance between evaluation metric, processing time, and memory usage. In this study, the number of decision trees is experimentally set to 100.

The number of sampling points is another critical parameter in the RFS method. In our experiment, as the number of sampling points increases from 200 to 2000 per training image, the accuracy rate of the RFS classifier increases by approximately 10%, whereas the accuracy is not improved greatly if the number of sampling points continuously increases. Thus, the total sampling point is set to 74,000, where $M = 2000$ and $N = 37$, to obtain the best result.

In TWS, 15 available image feature attributes are provided in the decision tree construction. In our experiment, the application of most features can improve the accuracy of segmentation, but entropy (E) and anisotropic diffusion (A) are time consuming. Let $13F$ indicates 13 other features aside from E and A; Figure 12 shows that the application of feature A not only costs more time but also reduces the accuracy of segmentation whether by using classifier RFS_1 or RFS_2. Therefore, only 14 features other than anisotropic diffusion are used to construct the decision tree in the proposed RFS method.

4.3. Limitations of the Proposed Method. Our experiment results reveal that the proposed RFS method obtains poor performance for some cases. For example, for a low-contrast image, the accuracy rate of voting is almost 0. Only the accuracy rate of $V + I$ reaches 23%, whereas the accuracy rates of the other methods are below 20%, even that of RFS_1. Such bad results greatly reduce the average accuracy of the RFS method. RF can be combined with other pattern recognition methods for better performance. Lu et al. [32] applied incomplete RF with a robust vector machine for the early identification of mild cognitive impairment. This method outperforms two other semi-supervised learning methods. Therefore, to improve the segmentation accuracy of low-contrast GBM images, the combination of RF methods with other methods will be our future work.

5. Conclusion

The segmentation of the whole GBM region in TEM pathological images can provide more rapid and intuitionistic observation for the morphological change and can reduce the tedious and expensive manual workload of the pathologist. This work proposed a two-level integrated RFS method involving training integration and testing integration to autosegment a GBM image. A total of 351 clinical images were included in the experiment. The accuracy and generalization ability of the RFS method were validated. Experimental results illustrated that the proposed method could be used for the automatic segmentation of GBM with different morphological characteristics and grayscale ranges. Further study is underway to improve segmentation accuracy of the automated CAD system and to implement GBM thickness measurement

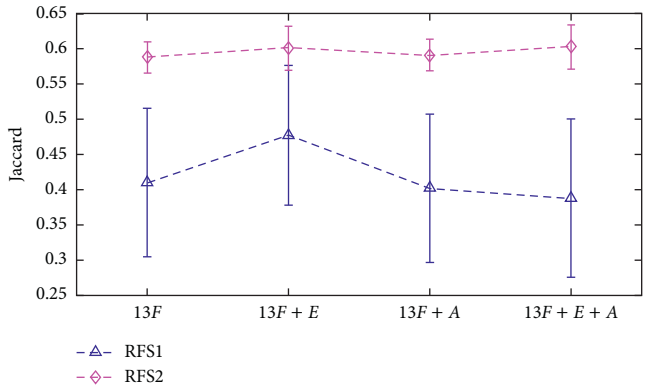

Figure 12: Effects of different image features with or without entropy and anisotropic diffusion.

and deposit autorecognition for auxiliary pathological diagnosis.

Data Availability

The image data used to support the findings of this study are available from the corresponding author upon request.

Conflicts of Interest

The authors declare that there are no conflicts of interest regarding the publication of this article.

Acknowledgments

This work was supported in part by the grants from the National Natural Science Foundation of China (no. 81771916) and the Guangdong Provincial Key Laboratory of Medical Image Processing (no. 2014B030301042). Many thanks are due to Xi Yu, Yuanyuan Liao, Can Xu, Zhenxing Li, and Zitao Zhang, who participated in this study during their graduation project in Southern Medical University and made some contributions.

References

[1] F.-D. Zhou, M.-H. Zhao, W.-Z. Zou et al., "The changing spectrum of primary glomerular diseases within 15 years: a survey of 3331 patients in a single Chinese centre," *Nephrology Dialysis Transplantation*, vol. 24, no. 3, pp. 870–876, 2009.

[2] M. Haas, "A reevaluation of routine electron microscopy in the examination of native renal biopsies," *Journal of the American Society of Nephrology*, vol. 8, no. 1, pp. 70–76, 1997.

[3] M. Santostefano, F. Zanchelliet, A. Zaccaria et al., "The ultrastructural basis of renal pathology in monoclonal gammopathies," *Journal of nephrology*, vol. 18, no. 6, p. 659, 2005.

[4] M. Wagrowska-Danilewicz and M. Danilewicz, "Current position of electron microscopy in the diagnosis of glomerular diseases," *Polish Journal of Pathology*, vol. 58, no. 2, pp. 87–92, 2007.

[5] A. Sementilli, L. A. Moura, and M. F. Franco, "The role of electron microscopy for the diagnosis of glomerulopathies," *Sao Paulo Medical Journal*, vol. 122, no. 3, pp. 104–109, 2004.

[6] G. Osawa, P. Kimmelstiel, and V. Sailing, "Thickness of glomerular basement membranes," *American Journal of Clinical Pathology*, vol. 45, no. 1, pp. 7–20, 1966.

[7] S. Saxela, D. J. Davies, and R. L. G. Kirsner, "Thin basement membranes in minimally abnormal glomeruli," *American Journal of Clinical Pathology*, vol. 43, pp. 32–38, 1990.

[8] J. G. Basta, V. S. Venkataseshan, J. Gil, D. U. Kim, S. H. Dikman, and J. Churg, "Morphometric analysis of glomerular basement membranes (GBM) in thin basement membrane disease (TBMD)," *Clinical Nephrology*, vol. 33, pp. 110–114, 1990.

[9] B. Marquez, I. Zouvani, A. Karagrigoriou et al., "A simplified method for measuring the thickness of glomerular basement membranes," *Ultrastructural Pathology*, vol. 27, no. 6, pp. 409–416, 2003.

[10] S. E. Thomson, S. V. McLennan, P. D. Kirwan et al., "Renal connective tissue growth factor correlates with glomerular basement membrane thickness and prospective albuminuria in a non-human primate model of diabetes: possible predictive marker for incipient diabetic nephropathy," *Journal of Diabetes and Its Complications*, vol. 22, no. 4, pp. 284–294, 2008.

[11] K. Kyriacou, M. Nearchou, I. Zouvani et al., "The many faces of thin basement membrane nephropathy; a population based study," in *Topics in Renal Biopsy and Pathology*, pp. 93–114, IntechOpen, London, UK, 2012.

[12] S. H. Ong, S. T. Giam, R. Sinniah et al., "Adaptive window-based tracking for the detection of membrane structures in kidney electron micrographs," *Machine Vision and Applications*, vol. 6, no. 4, pp. 215–223, 1993.

[13] I. Kamenetsky, R. M. Rangayyan, and H. Benediktsson, "Analysis of the glomerular basement membrane in images of renal biopsies using the split-and-merge method: a pilot study," *Journal of Digital Imaging*, vol. 23, no. 4, pp. 463–474, 2010.

[14] R. M. Rangayyan, I. Kamenetsky, and H. Benediktsson, "Segmentation and analysis of the glomerular basement membrane in renal biopsy samples using active contours: a pilot study," *Journal of Digital Imaging*, vol. 23, no. 3, pp. 323–331, 2010.

[15] H. S. Wu, S. Dikman, and J. Gil, "A semi-automatic algorithm for measurement of basement membrane thickness in kidneys in electron microscopy images," *Computer Methods and Programs in Biomedicine*, vol. 97, no. 3, pp. 223–231, 2010.

[16] H. S. Wu and S. Dikman, "Segmentation and thickness measurement of glomerular basement membranes from electron microscopy images," *Journal of Electron Microscopy*, vol. 59, no. 5, pp. 409–418, 2010.

[17] J. Liu, "Implementation of a semi-automatic tool for analysis of TEM images of kidney samples," Master Thesis, Uppsala University, Uppsala, Sweden, 2012.

[18] L. Breiman, "Random forests," *Machine Learning*, vol. 45, no. 1, pp. 5–32, 2001.

[19] T. K. Ho, "The random subspace method for constructing decision forests," *IEEE Transactions on Pattern Analysis and Machine Intelligence*, vol. 20, no. 8, pp. 832–844, 1998.

[20] T. K. Ho, "Random decision forests," in *Proceedings of 3rd International Conference on Document Analysis and Recognition*, vol. 1, p. 278, Montreal, Canada, August 1995.

[21] A. V. Lebedev, E. Westman, G. J. P. VanWesten et al., "Random Forest ensembles for detection and prediction of Alzheimer's disease with a good between-cohort robustness," *NeuroImage: Clinical*, vol. 6, no. C, pp. 115–125, 2014.

[22] G. Saiprasad, C. I. Chang, N. Safdar et al., "Adrenal gland abnormality detection using random forest classification," *Journal of digital imaging*, vol. 26, no. 5, pp. 891–897, 2013.

[23] D. Mahapatra, "Automatic cardiac segmentation using semantic information from random forests," *Journal of Digital Imaging*, vol. 27, no. 6, pp. 794–804, 2014.

[24] I. Arganda-Carreras, V. Kaynig, C. Rueden et al., "Trainable Weka Segmentation: a machine learning tool for microscopy pixel classification," *Bioinformatics*, vol. 33, no. 15, pp. 75–80, 2017.

[25] E. Frank, M. Hall, G. Holmes et al., "Weka-a machine learning workbench for data mining," in *Data Mining and Knowledge Discovery Handbook*, pp. 1269–1277, 2005.

[26] J. Nayak, B. Naik, and H. S. Behera, "Fuzzy C-means (FCM) clustering algorithm: a decade review from 2000 to 2014," in *Smart Innovation, Systems and Technologies*, vol. 32, pp. 133–149, Springer, New Delhi, India, 2015.

[27] A. Padma and R. Sukanesh, "Segmentation and classification of brain CT images using combined wavelet statistical texture features," *Arabian Journal for Science and Engineering*, vol. 39, no. 2, pp. 767–776, 2014.

[28] B. Tóth, F. Lillo, and J. D. Farmer, "Segmentation algorithm for non-stationary compound Poisson processes," *The European Physical Journal B*, vol. 78, no. 2, pp. 235–243, 2010.

[29] N. M. Noor, J. C. M. Than, O. M. Rijal et al., "Automatic lung segmentation using control feedback system: morphology and texture paradigm," *Journal of Medical Systems*, vol. 39, no. 3, p. 214, 2015.

[30] T. G. Dietterich, "Ensemble Methods in Machine Learning," in *Multiple Classifier Systems, LNCS 1857*, pp. 1–15, Springer, Berlin, Germany, 2000.

[31] T. M. Oshiro, P. S. Perez, and J. A. Baranauskas, "How many trees in a random forest?,"in *Machine Learning and Data Mining in Pattern Recognition. Lecture Notes in Computer Science*, vol. 7376, no. 4, pp. 154–168, Springer, Berlin, Germany, 2012.

[32] S. Lu, Y. Xia, W. Cai, M. Fulham, and D. D. Feng, "Early identification of mild cognitive impairment using incomplete random forest-robust support vector machine and FDG-PET imaging," *Computerized Medical Imaging and Graphics*, vol. 60, pp. 35–41, 2017.

Hindawi
Computational and Mathematical Methods in Medicine
Volume 2019, Article ID 9079840, 14 pages
https://doi.org/10.1155/2019/9079840

Research Article

Minimalistic Approach to Coreference Resolution in Lithuanian Medical Records

Voldemaras Žitkus,[1] Rita Butkienė,[1] Rimantas Butleris,[1] Rytis Maskeliūnas,[1] Robertas Damaševičius,[1] and Marcin Woźniak[2]

[1]*Faculty of Informatics, Kaunas University of Technology, 51386 Kaunas, Lithuania*
[2]*Institute of Mathematics, Silesian University of Technology, 44-100 Gliwice, Poland*

Correspondence should be addressed to Robertas Damaševičius; robertas.damasevicius@ktu.lt

Received 18 January 2019; Accepted 26 February 2019; Published 20 March 2019

Guest Editor: Ka L. Man

Coreference resolution is a challenging part of natural language processing (NLP) with applications in machine translation, semantic search and other information retrieval, and decision support systems. Coreference resolution requires linguistic preprocessing and rich language resources for automatically identifying and resolving such expressions. Many rarer and under-resourced languages (such as Lithuanian) lack the required language resources and tools. We present a method for coreference resolution in Lithuanian language and its application for processing e-health records from a hospital reception. Our novelty is the ability to process coreferences with minimal linguistic resources, which is important in linguistic applications for rare and endangered languages. The experimental results show that coreference resolution is applicable to the development of NLP-powered online healthcare services in Lithuania.

1. Introduction

Digital means of medical informatics, especially when applying natural language processing (NLP), are indispensable in the application of e-health and digitalization of medical records and processes [1]. The use of NLP has proved as a lower-cost alternative to traditional medical methods in many cases such as to forecast stress symptoms and suicide risk in free-text responses sent via a mobile phone [2], or to detect seasonal disease outbreaks by monitoring search engine queries [3], and discovery of healthcare knowledge from social media [4, 5].

With the development of Semantic Web technology, web information retrieval (IR) is changing towards meaning-based IR. The quality of retrieved documents relevant to the user also highly depends on the information extraction (IE) methods applied. In general, IE focuses on automatic extraction of structured information from the unstructured source. Standard document text preprocessing steps used in IE are lexical analysis, morphological analysis, and named entity recognition (NER), which can be complemented by coreference resolution and semantic annotation. The main issue here is the ambiguity and complexity of the natural language, thus making the progress in IE dependent on the evolution of the NLP techniques. While for widely used languages (such as English), the IE-related NLP research has already reached the levels of maturity and practical application on a massive scale (e.g., IBM Watson project) [6], but the resource-poor languages, such as Lithuanian [7], remain an open NLP research field. The baseline application is often steered towards automated concept extraction [8, 9], often in combination with text mining [10, 11].

NER when applied to biomedical texts is a critical step for developing decision support tools for smart healthcare. Examples for it are as follows: drug name recognition (DNR), which recognizes pharmacological substances from biomedical texts and classifies them for discovering drug-drug interactions [12, 13]; biomedical named entity recognition (BNER), which extracts biomedical concepts of interest such as genes and proteins [14]; and medical entity recognition, which is information extraction from unstructured electronic health records [15–17]. Such studies include mapping clinical

descriptions to Systematized Nomenclature of Medicine codes [18] or other medical lexicons. Unstructured texts in the medical domain contain valuable medical information, and there are many errors, such as spelling errors, improper grammatical use, and semantic ambiguities, which hinder data processing and analysis [19]. Structuration of medical domain knowledge using biomedical ontologies and controlled vocabularies provide support for data standardization and interoperability, healthcare administration, and clinical decision support [20]. Rich concepts linked by semantic relationships such as in the Unified Medical Language System (UMLS) contribute to healthcare data integration, pattern mining from EHRs, medical entity recognition in clinical text, and clinical data sharing [21]. The development of online healthcare services as powerful platforms provides users with an opportunity to address health concerns such as improving patient-centered care and supporting self-management. The users consider online healthcare services as a vital source of health information but still need more powerful semantic search engines to arrive at informed decisions on their own health and for more active participation in healthcare processes [22]. However, these services depend greatly upon the support provided by the natural language processing.

Our previous work included the development of the semantic search framework [23] for answering questions presented in structured Lithuanian language, which is based on Semantics of Business Vocabulary and Business Rules (SBVR) language. Our results in [23] showed that there is a strong need to complement the NLP pipeline of semantic search with the coreference resolution. Such coreference resolution tools have not been developed for the Lithuanian language yet, especially for very sector-important digital medical application, as we apply our algorithm to process digital transcripts of a hospital reception. Therefore, the creation of such tools is a prerequisite for further improvement of NLP-supported health-oriented decision making in the Lithuanian language, while the experience gained could be extended to developing semantic search tools for other under-resourced languages as well.

The rest of the paper is structured as follows. In Section 2, we analyse the related works in the coreference resolution field, including the state-of-the-art and the methods proposed for languages which are grammatically similar to Lithuanian. Sections 3 and 4 present the coreference resolution algorithm and its experimental evaluation. Section 5 presents conclusions and discusses future work.

2. Related Works

Machine-learning and rule-based approaches are efficient methods in semantic processing, especially when enhanced with external knowledge and coreference clues derived from the structured document, while often still performing better (in comparison with classic implementations) in coreference resolution when provided with ground truth mentions [24], while further expanded with scaffolding approaches [25]. Unsupervised methods can be applied to large-scale scenarios [26, 27]. Alternatively, a hybrid strategy may be used based on a set of statistical measures and syntactical and semantic information [28]. "Off the shelf" type of IR algorithms can be utilized quite successfully in some of the scenarios, especially with limited focus areas (in a medical sense) [29]. Accuracy can be further improved by analysing trigram frequencies [30] and applying graph-style algorithms [31] in context-sensitive corpus fragments.

In general, the coreference resolution methods can be classified into knowledge rich and knowledge poor. Both methods require large resources such as semantic information, syntactic annotations, or preannotated corpora of hospital transcripts from a hospital reception. Under resourced, rarer languages, like Lithuanian, usually do not have such resources available.

While up-to-date, no research has been performed to solve coreferences in Lithuanian, but many solutions have been proposed for other languages, mostly for English (Table 1). Note that the evaluation results are not directly comparable, as the authors used different corpora.

Considering languages that are more-or-less grammatically similar to Lithuanian (which is one of the Baltic languages), we summarize the related work on Latvian (only other Baltic language) and Slavic languages such as Polish, Russian, and Czech in Table 2.

(i) For Latvian, the only solution is LVCoref [45]. It is a rule-based system that uses an entity-centric model. It focuses on named entity matches (exact matches, acronyms) and uses Hobbs' algorithm for pronouns.

(ii) For Polish, rule-based Ruler [46] for scoring of candidates uses coreferences gender/number and including (removal of nested groups) rules, lemma, and Wordnet rules for nominal expressions and pronoun rule specifically targeting pronouns. BARTEK [47] is an adaptation of BART, which was designed for English, to Polish. Mixed Polish coreferences resolution approach combines neural networks architecture with the sieve-based approach [48].

(iii) For Russian, RU-EVAL-2014 [49] was an evaluation campaign of anaphora and coreferences resolution tools that employed a wide variety of approaches. The evaluation was performed on Russian Coreference Corpus (RuCur). Machine learning approaches [50] were also used.

(iv) For Czech, coreferences are annotated in the tectogrammatical layer of Prague Dependency Treebank (PDT) and their first coreference resolution approach was rule based [51]. At first, all possible candidates are collected and then their list is narrowed down using 8 filters, and then from remaining ones closest to corefering object is selected as antecedent. Nguy et al. [52] adapted two older English language approaches to Czech language and used Decision Tree C5 for the classifier-based approach, while the ranker-based approach employed the averaged perceptron algorithm. Both approaches were trained and evaluated on PTD data with ranker-based approach providing

Table 1: Comparison of coreference resolution approaches.

Method	Foundation	Precision	Recall	$F1$
Hobbs [32]	Syntactic tree with labeled nodes, syntactic rules, selection constraint rules	0.81–0.91	na	na
BFP [33]	Centering theory	0.49–0.90	na	na
Left-right centering [34]	Modified centering theory	0.72–0.81	na	na
Mitkov [35]	POS tagger, antecedent indicators	0.897	na	na
RAP [36]	Salience factors	0.85–0.89	na	na
Xrenner [37]	Syntactic and semantic rules	0.51–0.55	0.49–0.57	0.49–0.56
Probabilistic [38]	Bayesian rule	0.82–0.84	na	na
MARS [39]	Genetic algorithms	0.53–0.84	na	na
Soon et al. [40]	Machine learning (decision tree C5)	0.65–0.69	0.53–0.56	0.62
ILP [41]	Machine learning (logistic classifier)	0.78–0.89	0.47–0.58	0.61–0.68
Wiseman et al. [42]	Deep learning	0.77	0.70	0.73
Lee et al. [43]	Deep learning	0.81	0.73	0.77
Žitnik et al. [44]	Conditional random fields	0.68–0.94	0.30–0.87	0.41–0.87

Table 2: Comparison of coreference resolution methods for Balto-Slavic languages.

Method	Foundation	Precision	Recall	$F1$
LVCoref [45]	Rule based, Hobbs' algorithm	0.69–0.88	0.66–0.80	0.68–0.84
Ruler [46]	Rule based	0.59–0.65	0.50–0.75	0.55–0.69
BARTEK [47]	Machine learning	0.58	0.65	0.61
Mixed [48]	Deep learning, sieve based	0.70	0.68	0.69
RU-sys1 [49]	Rule based, ontology	0.82	0.70	0.76
RU-sys2 [49]	Rule based	0.71	0.58	0.64
RU-sys3 [49]	Rule based	0.63	0.50	0.55
RU-sys4 [49]	Statistical, ontology	0.54	0.51	0.53
RU-sys5 [49]	Machine learning, semantics	0.58	0.42	0.49
RU-sys6 [49]	Decision tree	0.36	0.15	0.21
Khadzhiiskaia and Sysoev [50]	Machine learning	0.84	0.77	0.80
Kučová and Žabokrtský [51]	Rule-based filters	0.60	na	na
CZ classifier [52]	Classifier-based machine learning	0.70–0.76	0.70–0.76	0.70–0.76
CZ ranker [52]	Ranker-based machine learning	0.79	0.79	0.79
Treex CR (Czech, English) [53]	Machine learning	na	na	0.61–0.68
Treex CR (Russian, German) [54]	Machine learning, projection	0.50–0.64	0.15–0.24	0.25–0.34

better results. Treex CR [53] was developed for the Czech language and adapted to English, Russian, and German, although for Russian and German, English coreferences labels were projected, which produced notably lower results [54].

In summary, the rule-based solutions have the advantages of easier adaptability and provide comparable results when good training data are not available as is the case for Lithuania. Many of more advanced solutions cannot be fully adapted for rarer and under-resourced languages due to the lack of available linguistic resources, as is the case with Lithuanian language. For example, BART at the time supported 64 feature extractors, but due to lack of language-specific resources for the Polish language, only 13 could be utilized. The solutions that are not heavy on linguistic resources can be very useful for resource-poor languages in general.

3. A Rule-Based Coreference Resolution: A Lithuanian Case

3.1. Definition and Framework. Coreference resolution (or anaphora) is an expression, the interpretation of which depends on another word or phrase presented earlier in the text (antecedent). For example, "Tom has a backache. He was injured." Here the words "Tom" and "He" refer to the same entity. Without resolving the relationship between these two structures, it would not be possible to determine why Tom has the backache, nor who was injured. In such cases, semantic information would be lost.

Anaphoric objects are expressed with pronouns and cannot be independently interpreted without going back to its antecedent. In this work, such expressions are called coreferences, unless it is required to make a distinction. Usage of such expressions can vary depending on the type and the style of the text. Here we focus on texts from medical-related domains.

The role of coreference resolution in the semantic search framework is to provide additional semantic information after named entity recognition before semantic annotation (Figure 1).

3.2. Conceptual Model of Coreference Resolution. In this chapter, a conceptualization of coreference resolution is presented. A given model, which is expressed as UML class diagram (Figure 2), specifies the concepts playing a certain

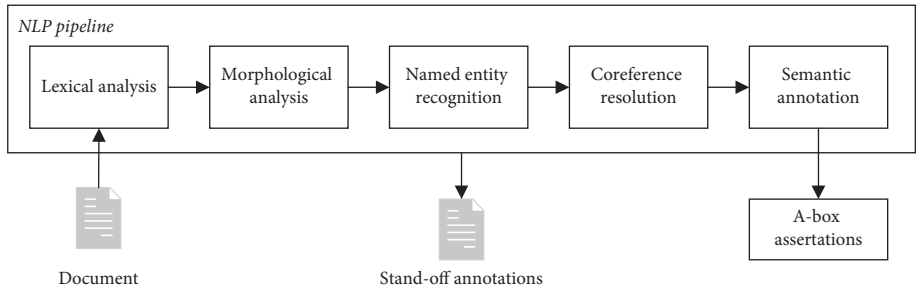

Figure 1: An NLP pipeline of semantic search framework with coreference resolution component.

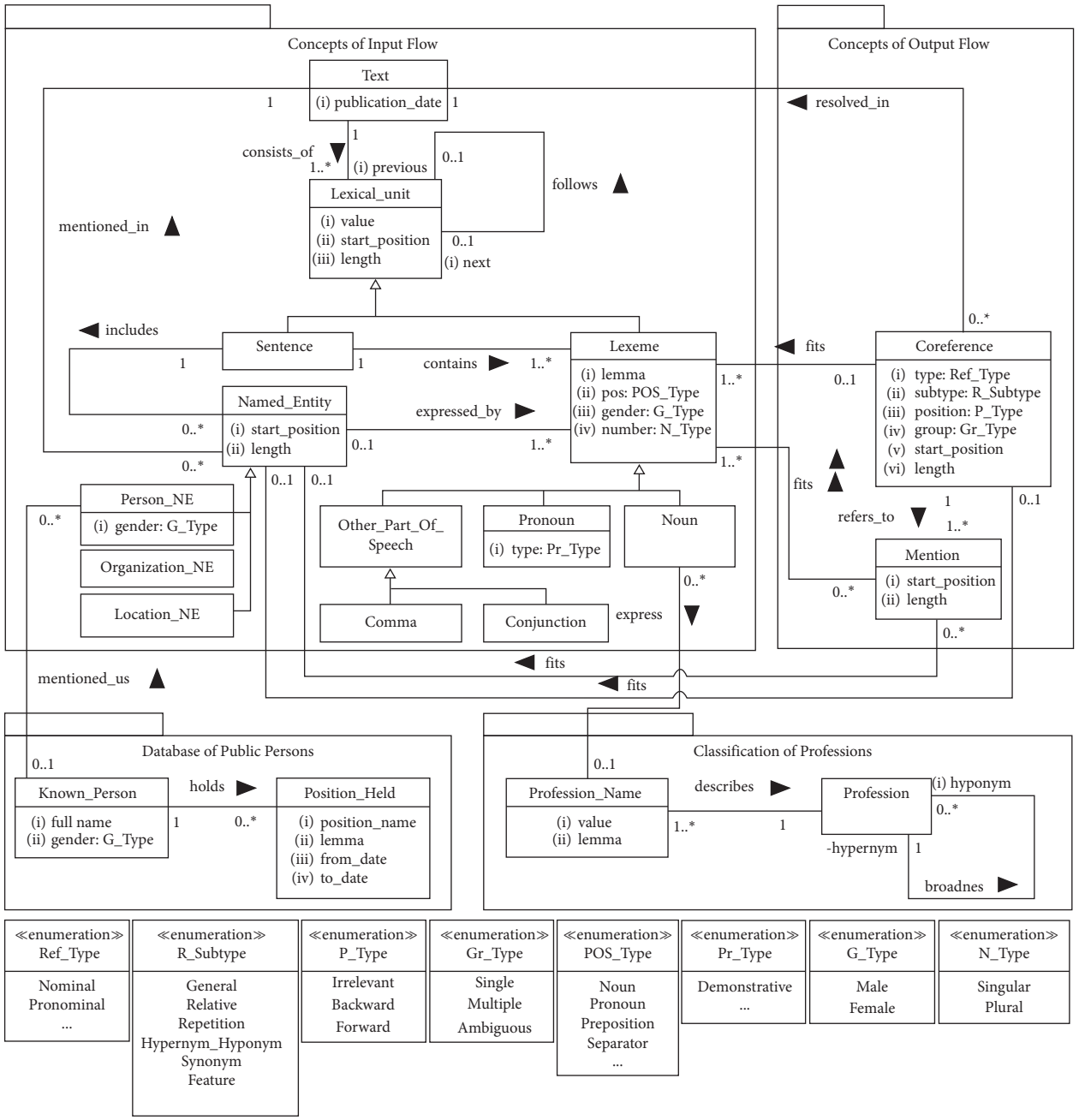

Figure 2: A conceptual model of a coreference resolution domain.

role in the extraction of coreferences of a certain type. The model gives us an understanding of the following:

(i) What features of text, sentence, and word help us recognize the existence of coreference (they are specified in the package Concepts of Input Flow)

(ii) What kind of text preprocessing is required

(iii) What additional resources are required for resolution of certain type coreferences (they are specified in the package Database of Public Persons and Classification of Professions)

For example, from the model provided, it is clear that, before coreference resolution starts, it is important to preprocess text and obtain the following:

(i) A text segmented into sentences and lexemes

(ii) Morphological features of lexemes identified

(iii) Named entities recognized

Text preprocessing itself is not a task of coreference resolution, so it is out of the scope of this paper.

It is worthy to mention that the model is quite abstract, language independent, and technology independent. Therefore, it is applicable not only for Lithuanian but for grammatically similar languages as well. Concepts of this model are used for the formalization of coreference resolution rules in the next section. The concepts are explained in more detail below.

The main concepts of coreference resolution are *Text*, *Lexical_Unit*, and *Named_Entity*. The concept *Text* assumes a textual document whose content should be analysed. Each test has an associated publication date, which is important for solving coreferences. Each text consists of at least one *Lexical_Unit*, which includes paragraphs, sentences, words, and punctuations, classified into the *Sentence* and *Lexeme* categories. *Lexeme* assumes lexical units such as words, punctuations, and numbers. Each lexeme is characterized by a lemma and a part of speech, and some of them (nouns and pronouns) by grammatical gender and number. The lexeme could be specialized by POS category: *Noun*, *Pronoun,* and *Other_Part_Of_Speech*. Special cases of *Other_Part_Of_Speech* are *Comma* and *Conjunction,* which are required for the description of conditions of some coreference resolution rules.

A *Named_Entity* concept defines an object to whom pronouns or certain nouns can refer. NER algorithms usually recognize three types of entities: a person (*Person_NE*), an organization (*Organization_NE*), and a location (*Location_NE*). The named entities of a person type require special attention a person can be mentioned not only using pronouns but also using a position he/she holds (*Position_Held*) and a professional name (*Profession)*. Additional information about a person could help resolving such coreferences more precisely. As an example, source of such information could be a Database of Public Person, which includes *Known_Person*—a well-known person mentioned as *Person_NE* in the text. The output of a coreference resolution algorithm is a *Coreference*—a relationship between coreferents. For each coreference, its type (nominal and pronominal), subtype (relative pronoun and noun repetition), position (points backward, forward, or irrelevant in case of repetitions), and group (is singular, refers to the coreference group or is ambiguous) are specified. Each referent refers at least to one coreferent (a concept *Mention*). Each *Mention* starts at a certain position in the text, is of a certain length, and fits at least one *Lexeme*. Some of them can fit a certain *Named_Entity*.

3.3. Coreference Resolution Algorithms. The decision table with guidelines for the application of the certain resolution algorithm is shown as Figure 3. The conditions are checked consecutively on every lexeme in the text, and, if the condition is satisfied, a corresponding algorithm is activated. For example, if C2 condition is met then immediately A1 algorithm is activated.

For resolution of a specific type of references, we propose the following algorithms:

(i) A1: specific rules resolution algorithm for resolution of certain usage of pronouns

(ii) A2: general pronoun resolution algorithm which focuses on the cases where pronouns refer to nouns (or noun phrases) that are recognized as named entities of "person" class

(iii) A3: PRA (partial, repetition, and acronym) resolution algorithm for resolution of nouns recognized as named entities and their repeated usage in the same text

(iv) A4: HHS (hypernym, hyponym, synonymous) resolution algorithm for resolution of nouns recognized as profession names including their synonyms and hypernyms/hyponyms

(v) A5: feature resolution algorithm for resolution of nouns that represent certain feature (at the moment only public position being held) of the named entity of a person

The coreference resolution starts from the sequential analysis of each lexeme looking for a certain type of pronoun and noun. Depending on identified features of lexeme, a decision about further analysis is taken. The decision table (Figure 3) summarizes conditions for the application of the certain resolution algorithm. The conditions are listed in the upper left quadrant; the decision alternatives are listed in the lower left quadrant. The upper right quadrant shows the possible alternatives for the conditions of the corresponding row. In the upper right quadrant, the answer "na" stands for "not relevant." In the lower right quadrant, "✓" means that the algorithm should be applied and "✗" means that it should not be applied.

The idea is that the pronoun-related coreferences should be solved first sequentially by checking the conditions C1, C2, and C3. Then a noun-related coreference resolution should start by sequentially checking the conditions C4, C6, and C7.

3.4. Formal Description of Coreference Resolution Algorithms. First-order logic (FOL) formulas are employed to define the main conditions the algorithms should check when resolving coreferences. The concepts of the coreference

Conditions	C1: Is a lexeme a pronoun?	Yes			No						Answers
	C2: Does a specific rule exist for this pronoun?	Yes		No	na						
	C3: Was the pronoun resolved by specific rules resolution?	Yes	No	na	na						
	C4: Is a lexeme a noun?	na	na	na	Yes					No	
	C5: Is the noun recognized as a named entity?	na	na	na	Yes	No				na	
	C6: Does the noun exist in profession classification?	na	na	na	na	Yes		No		na	
	C7: Does the noun exist in the knowledge base of public persons?	na	na	na	na	Yes	No	Yes	No	na	
Algorithms	A1: Specific rules resolution	✓		×	×	×	×	×	×	×	Decisions
	A2: General pronoun resolution	×	✓	✓	×	×	×	×	×	×	
	A3: PRA resolution	×	×	×	✓	×	×	×	×	×	
	A4: HHS resolution	×	×	×	×	✓		×	×	×	
	A5: Feature resolution	×	×	×	×	✓	×	✓	×	×	

Figure 3: A decision table for selection of the algorithm. na: not applicable; ✓: the algorithm should be applied; ×: it should not be applied.

resolution model (Figure 2) became the predicates or constants in the FOL formulas: the classes became the unary predicates of the same name as class; the associations between classes—the binary predicates of the same name as association; the attributes of classes—the binary predicates of the same name as attribute plus verb "has" at the beginning; and the literals of enumerations—constants.

The algorithms follow the grammar rules of the Lithuanian language which are based on the analysis of morphological features of lexemes and their order in the sentence and text. Examples of Lithuanian language sentences were translated into English as closely as possible. All proper names were changed to generic abbreviations to comply with GDPR.

3.4.1. A1: Specific Rules Resolution. In some cases, there exists a rather rigid structure for pronoun usage and it can be easily defined by using specific rules, for example,

(i) [LT] Šiandien buvo atėjęs **vyras** [noun], **kuris** [pronoun] skundėsi nugaros skausmu.

[EN] A **man** [noun] **who** [pronoun] had a backache came today.

(ii) [LT] Šiandien buvo atėjęs **vyras** [noun], **su** [preposition] **kuriuo** [pronoun] aptarėme nugaros skausmą.

[EN] A **man** [noun] **with** [preposition] **whom** [pronoun] we discussed a backache came today.

Both examples are similar in their construction: [noun] [comma] [optional preposition] [specific pronoun]. In both cases, pronoun "kuriuo" refers to the noun "vyras." In the first example, we do not have an optional preposition "su," while we have it in the second one.

A condition for the existence of such reference formally is defined as follows:

For every sentence **s** *of text* **t** *and for every "Relative" type pronoun* **p**, *which is contained in the sentence* **s** *and has a start position* **sp1**, *is of length* **ln1**, *follows comma* **c** *or follows prepositional lexeme* **l1**, *which follows comma* **c**, *and for every noun* **l2**, *which has a start position* **sp2**, *is of length* **ln2**, *precedes comma* **c**, *is of the same gender* **g** *and of the same number* **n** *as the pronoun* **p**, *the only one coreference relation* **r**, *which is resolved in text* **t**, *is of "Pronominal" type, "Relative" subtype, "Backward" position and "Single" group between the pronoun* **p** *and the noun* **n**, *its referent starts at position* **sp1** *and has length* **ln1**, *and which fits only one lexeme* **p** *and refers to only one mention* **m**, *which starts at position* **sp2**, *has length* **ln2**, *and fits only one lexeme* **l2**, *exists* (Rule 1).

Rule 1: $\forall$t, s, p, l1, c, l2, g, n, sp1, sp2, ln2. [Text(t) $\wedge$ Sentence(s) $\wedge$ consists_of(t, s) $\wedge$ Pronoun(p) $\wedge$ contains(s, p) $\wedge$ has_type(p, Relative) $\wedge$ has_start_position(p, sp1) $\wedge$ has_length(p, ln1) $\wedge$ Comma(c) $\wedge$ (follows(p, c) $\vee$ (Lexeme(l1) $\wedge$ has_pos(l1, Preposition) $\wedge$ follows(l1, c) $\wedge$ follows(p, l1)) $\wedge$ Noun(l2) $\wedge$ follows(l2, c) $\wedge$ has_gender (p, g) $\wedge$ has_gender (l2, g) $\wedge$ has_number(p, n) $\wedge$ has_number(l2, n) $\wedge$ has_start_position(l2, sp2) $\wedge$ has_length(l2, ln2) $\longrightarrow$ $\exists$!r $\exists$!m. [Coreference(r) $\wedge$ resolved_in(r, t) $\wedge$ has_type(r, Pronominal) $\wedge$ has_subtype(r, Relative) $\wedge$ has_position(r, Backward) $\wedge$ has_ group(r, Single) $\wedge$ has_start_position(r, sp1) $\wedge$ has_length(r, ln1) $\wedge$ fits(r, p) $\wedge$ Mention(m) $\wedge$ refers_to(r, m) $\wedge$ has_start_position(m, sp2) $\wedge$ has_length(m, ln2) $\wedge$ fits(m, l2)]]

The relative pronoun might be plural and refer to multiple singular (or multiple plural) nouns:

(i) [LT] Komisija nerado panašumų tarp **Tomo** [noun], **Lino** [noun], **Petro** [noun] **ir** [conjunction] **Eglės** [noun], **kurių** [pronoun] sužalojimai atrodė panašūs.

[EN] The committee did not find **Tom** [noun], **Linas** [noun], **Peter** [noun] **and** [conjunction] **Eglė** [noun], **who** [pronoun] shared similar injuries.

In this case, a plural pronoun "kurių" is referring to four singular nouns that have different genders. The previous rule would not be able to solve such coreference. For this case, the construction would be: [noun] [comma] [noun] [comma] [noun] [conjunction] [noun] [comma] [optional preposition] [specific pronoun].

For such case, a special condition must be defined:

For every sentence **s** *in text* **t** *and for every "Relative" type pronoun* **p** *of "Plural" number, which is contained in the sentence* **s** *and has a start position* **sp1**, *is of length* **ln1**, *follows comma* **c1** *or follows prepositional lexeme* **l**, *which follows comma* **c1**, *and for every noun* **n1**, *which precedes comma* **c1**, *has a start position* **sp2**, *is of length* **ln2**, *follows conjunction* **j**, *and for every noun* **n2**, *which precedes conjunction* **j**, *has a start position* **sp3**, *is of length* **ln3**, *and for every existing noun* **n3**, *which follows comma* **c2**, *and for every existing noun* **n4**, *which precedes comma* **c2**, *has a start position* **sp4**, *is of length* **ln4**, *the only one coreference relation* **r**, *which is resolved in text* **t**, *is of "Pronominal" type, "Relative" subtype, "Backward" position and "Multiple" group, its referent starts at position* **sp1** *and has length* **ln1**, *fits only one lexeme* **p**, *refers to only one mention* **m1**, *which starts at position* **sp2**, *has length* **ln2**, *and fits noun* **n1**, *refers to only one mention* **m2**, *which starts at position* **sp3**, *has length* **ln3**, *and fits only one noun* **n2**, *and refers at least to one mention* **m3**, *which starts at position* **sp4**, *has length* **ln4,** *and fits noun* **n4**, *exists* (Rule 2).

Rule 2: ∀t, s, p, l, c1, n1, sp1, ln1, sp2, ln2, j, n2, sp3, ln3.[Text(t) ∧ Sentence(s) ∧ consists_of(t, s) ∧ Pronoun(p) ∧ contains(s, p) ∧ has_number(p, Plural) ∧ has_type(p, Relative) ∧ has_start_position(p, sp1) ∧ has_length(p, ln1) ∧ Comma(c1) ∧ (follows(p, c1) ∨ (Lexeme(l) ∧ has_pos(l, Preposition) ∧ follows(p, l) ∧ follows(l, c1)) ∧ Noun(n1) ∧ follows(c1, n1) ∧ has_start_position(n1, sp2) ∧ has_length(n1, ln2) ∧ Conjunction(j) ∧ follows(n1, j) ∧ Noun(n2) ∧ follows(j, n2) ∧ has_start_position(n2, sp3) ∧ has_length(n2, ln3) ∧ (∃n3, c2, n4, sp4, ln4.(Noun(n3) ∧ Comma(c2) ∧ Noun(n4) ∧ follows(n3, c2) ∧ follows(c2, n4) ∧ has_start_position(n4, sp4) ∧ has_length(n4, ln4)) ⟶ ∃!r ∃!m1 ∃!m2 ∃m3. [Coreference(r) ∧ resolved_in(r, t) ∧ has_type(r, Pronominal) ∧ has_subtype(r, Relative) ∧ has_position(r, Backward) ∧ has_ group(r, Multiple) ∧ has_start_position(r, sp1) ∧ has_length(r, ln1) ∧ fits(r, p) ∧ Mention(m1) ∧ refers_to(r, m1) ∧ has_start_position(m1, sp2) ∧ has_length(m1, ln2) ∧ fits(m1, n1) ∧ Mention(m2) ∧ refers_to(r, m2) ∧ has_start_position(m2, sp3) ∧ has_length(m2, ln3) ∧ fits(m2, n2) ∧ Mention(m3) ∧ refers_to(r, m3) ∧ has_start_position(m3, sp4) ∧ has_length(m3, ln4) ∧ fits(m3, n4)]]

Though examples illustrating the certain case of coreference are given in Lithuanian and English only, rules for resolution of such coreferences could be applied for other languages as well. For example, Rule 1 could be successfully applied for coreference resolution in Polish or Russian languages. Let us take the same example of a sentence in Polish and Russian:

[PL] Dzisiaj przychodził mężczyzna [noun], który [pronoun] skarżył się na ból pleców.

[RU] Сегодня причодил мужчина [noun], который [pronoun] жаловался на боль в спине.

We can see that a structure of the sentence (number and order of lexemes) is similar, a pronoun goes after the comma and it refers to a noun, and compatibility of morphological features (gender, number) of noun and pronoun is retained. From the given example, we understand that the coreference relation between pronoun and noun exists and conditions for such existence are the same as specified in Rule 1.

3.4.2. A2: General Purpose Pronoun Resolution. This algorithm focuses on the cases where pronouns refer to nouns (or noun phrases) that are recognized as named entities of "person" class by NER. The algorithm starts from the identification of not demonstrative pronoun. In a given example below, such a pronoun is in the second sentence—"Jis" ("He")

(i) [LT] **Jonas Jonaitis** [person noun phrase] skambino į registratūrą. **Jis** [pronoun] skundėsi galvos skausmu.

[EN] **Jonas Jonaitis** [person noun phrase] called a reception. **He** [pronoun] complained about headache.

If the pronoun is in the relative clause, the algorithm moves backwards analysing words going before the pronoun. In a given example, the pronoun is at the beginning of the sentence, so remaining parts of the sentence are not analysed, and the algorithm moves one sentence backwards.

The conditions for the existence of such reference formally could be defined as three alternatives. The first one describes conditions for reference existing in the same sentence **s1** before pronoun **p**:

For each text's **t** *sentence* **s1** *and pronoun* **p** *not of Demonstrative type that is contained in sentence* **s1** *and has gender* **g,** *number* **n**, *start position* **sp1** *and length of* **ln1**, *and named entity* **e1** *that is in the same sentence* **s1**, *is expressed by lexeme l, and has gender* **g**, *number* **n**, *start position* **sp2** *and is of length* **ln2**, *and is before pronoun* **p** *(***sp2** *is lower than* **sp1**), *but closer to pronoun* **p** *than possible named entities* **e2** *and* **e3** *(***sp2** *higher than* **sp3** *and* **sp4**), *the only one coreference relation* **r**, *which is resolved in text* **t**, *is of "Pronominal" type, "Relative" subtype, "Backward" position and "Single" group between the pronoun* **p** *and the named entity* **e1**, *its referent starts at position* **sp1** *and has length* **ln1**, *and which fits only one pronoun* **p** *and refers to only one mention* **m**, *which starts at position* **sp2**, *has length* **ln2**, *and fits only one named entity* **e1**, *exists* (Rule 3).

Rule 3: ∀t, s1, p, l, e1, g, n, sp1, ln1, sp2, ln2.[Text(t) ∧ Sentence(s1) ∧ consists_of(t, s1) ∧ Pronoun(p) ∧

contains(s1, p) ∧ ¬has_type(p, Demonstrative) ∧ has_gender(p, g) ∧ has_number(p, n) ∧ has_start_position(p, sp1) ∧ has_length(p, ln1) ∧ Person_NE(e1) ∧ includes(s1, e1) ∧ Lexeme(l) ∧ expressed_by(e1, l) ∧ has_gender(e1, g) ∧ has_number(e1, n) ∧ has_start_position(e1, sp2) ∧ has_length(e1, ln2) ∧ sp2<sp1 ∧ ¬(∃e2, e3, sp3, sp4. (e1≠e2 ∧ e1≠e3 ∧ e2≠e3 ∧ Person_NE(e2) ∧ includes(s1, e2) ∧ has_gender(e2, g) ∧ has_number(e2, n) ∧ has_start_position(e2, sp3) ∧ Person_NE(p3) ∧ includes(s1, e3) ∧ has_gender(e3, g) ∧ has_number(e3, n) ∧ has_start_position(e3, sp4) ∧ sp2>sp3 ∧ sp4>sp2)) ⟶ ∃!r ∃!m. [Coreference(r) ∧ resolved_in(r, t) ∧ has_type (r, Pronominal) ∧ has_subtype (r, General) ∧ has_position(r, Backward) ∧ has_group(r, Single) ∧ has_start_position(r, sp1) ∧ has_length(r, ln1) ∧ fits(r, p) ∧ Mention(m) ∧ refers_to(r, t) ∧ has_start_position(m, sp2) ∧ has_length(m, ln2) ∧ fits(m, e1) ∧ fits(m, l)]]

The second alternative describes a case when a pronoun **p** refers to the named entity in the previous sentence **s2**:

For each text's **t** *sentence* **s1, s2**, *where* **s1** *follows* **s2**, *and pronoun* **p** *not of Demonstrative type that is contained in sentence* **s1** *and has gender* **g,** *number* **n**, *start position* **sp1** *and length of* **ln1**, *and named entity* **e1** *that is contained in sentence* **s2**, *is expressed by lexeme l, and has gender* **g**, *number* **n**, *start position* **sp2** *and is of length* **ln2**, *and is closer to pronoun* **p** *than possible named entities* **e2** *and* **e3** *(***sp2** *higher than* **sp3** *and* **sp4**), *the only one coreference relation* **r**, *which is resolved in text* **t**, *is of "Pronominal" type, "Relative" subtype, "Backward" position and "Single" group between the pronoun* **p** *and the named entity* **e1**, *its referent starts at position* **sp1** *and has length* **ln1**, *and which fits only one pronoun* **p** *and refers to only one mention* **m**, *which starts at position* **sp2**, *has length* **ln2**, *and fits only one named entity* **e1**, *exists* (Rule 4).

Rule 4: ∀t, s1, s2, p, l, e1, g, n, sp1, ln1, sp2, ln2.[Text(t) ∧ Sentence(s1) ∧ Sentence(s2) ∧ consists_of(t, s1) ∧ consists_of(t, s2) ∧ follows (s1, s2) ∧ Pronoun(p) ∧ contains(s1, p) ∧ ¬has_type(p, Demonstrative) ∧ has_gender(p, g) ∧ has_number(p, n) ∧ has_start_position(p, sp1) ∧ has_length(p, ln1) ∧ Person_NE(e1) ∧ includes(s2, e1) ∧ Lexeme(l) ∧ expressed_by(e1, l) ∧ has_gender(e1, g) ∧ has_number(e1, n) ∧ has_start_position(e1, sp2) ∧ has_length(e1, ln2) ∧ ¬(∃e2, e3, sp3, sp4. (e1≠e2 ∧ e1≠e3 ∧ e2≠e3 ∧ Person_NE(e2) ∧ includes(s2, e2) ∧ has_gender(e2, g) ∧ has_number(e2, n) ∧ has_start_position(e2, sp3) ∧ Person_NE(p3) ∧ includes(s2, e3) ∧ has_gender(e3, g) ∧ has_number(e3, n) ∧ has_start_position(e3, sp4) ∧ sp2>sp3 ∧ sp4>sp2)) ⟶ ∃!r ∃!m. [Coreference(r) ∧ resolved_in(r, t) ∧ has_type (r, Pronominal) ∧ has_subtype (r, General) ∧ has_position(r, Backward) ∧ has_group(r, Single) ∧ has_start_position(r, sp1) ∧ has_length(r, ln1) ∧ fits(r, p) ∧ Mention(m) ∧ refers_to(r, t) ∧ has_start_position(m, sp2) ∧ has_length(m, ln2) ∧ fits(m, e1) ∧ fits(m, l)]]

The third alternative describes a case when a pronoun **p** in the sentence **s1** refers to the named entity in the sentence **s3**, preceding sentences **s2** and **s1**:

For each text's **t** *sentence* **s1**, **s2**, **s3**, *where* **s1** *follows* **s2** *and* **s2** *follows* **s3**, *and pronoun* **p** *not of Demonstrative type that is contained in sentence* **s1** *and has gender* **g**, *number* **n**, *start position* **sp1** *and length of* **ln1**, *and named entity* **e1** *that is contained in sentence* **s3**, *is expressed by lexeme l, and has gender* **g**, *number* **n**, *start position* **sp2** *and is of length* **ln2**, *and is closer to pronoun* **p** *than possible named entities* **e2** *and* **e3** *(***sp2** *higher than* **sp3** *and* **sp4**), *the only one coreference relation* **r**, *which is resolved in text* **t**, *is of "Pronominal" type, "Relative" subtype, "Backward" position and "Single" group between the pronoun* **p** *and the named entity* **e1**, *its referent starts at position* **sp1** *and has length* **ln1**, *and which fits only one pronoun* **p** *and refers to only one mention* **m**, *which starts at position* **sp2**, *has length* **ln2**, *and fits only one named entity* **e1**, *exists* (Rule 5).

Rule 5: ∀t, s1, s2, s3, p, l, e1, g, n, sp1, ln1, sp2, ln2.[Text(t) ∧ Sentence(s1) ∧ Sentence(s2) ∧ Sentence(s3) ∧ consists_of(t, s1) ∧ consists_of(t, s2) ∧ consists_of(t, s3) ∧ follows (s1, s2) ∧ follows (s2, s3) ∧ Pronoun(p) ∧ contains(s1, p) ∧ ¬has_type(p, Demonstrative) ∧ has_gender(p, g) ∧ has_number(p, n) ∧ has_start_position(p, sp1) ∧ has_length(p, ln1) ∧ Person_NE(e1) ∧ Lexeme(l) ∧ expressed_by(e1, l) ∧ includes(s3, e1) ∧ has_gender(e1, g) ∧ has_number(e1, n) ∧ has_start_position(e1, sp2) ∧ has_length(e1, ln2) ∧ ¬(∃e2, e3, sp3, sp4. (e1≠e2 ∧ e1≠e3 ∧ e2≠e3 ∧ Person_NE(e2) ∧ includes(s3, e2) ∧ has_gender(e2, g) ∧ has_number(e2, n) ∧ has_start_position(e2, sp3) ∧ Person_NE(e3) ∧ includes(s3, e3) ∧ has_gender(e3, g) ∧ has_number(e3, n) ∧ has_start_position(e3, sp4) ∧ sp2>sp3 ∧ sp4>sp2)) ⟶ ∃!r ∃!m. [Coreference(r) ∧ resolved_in(r, t) ∧ has_type (r, Pronominal) ∧ has_subtype (r, General) ∧ has_position(r, Backward) ∧ has_group(r, Single) ∧ has_start_position(r, sp1) ∧ has_length(r, ln1) ∧ fits(r, p) ∧ Mention(m) ∧ refers_to(r, t) ∧ has_start_position(m, sp2) ∧ has_length(m, ln2) ∧ fits(m, e1) ∧ fits(m, l)]]

Another example presents a case when a coreferent of the pronoun "man" (in English, "for me") is in the following sentence:

(i) [LT] Pastebėtina, kad ligoginėse apsilankė 10 mln. pacientų, nepaisant to, kad 2016 m. jų buvo 4% mažiau (apsilankė beveik 9,5 mln.). Tai labiausiai lėmė skaitmeninių paslaugų padidinimas: "Kiek **man** [pronoun] teko analizuoti, padidinus skaitmenines paslaugas tik nedidelė dalis **Lietuvos** [location noun] ligoninių sumažino etatų ar atleido darbuotojus, o tai lėmė nemažą papildomą indėlį į paslaugos kokybę" teigė J. **Jonaitis** [person noun phrase].

[EN] It is noteworthy that the total hospital patient count has reached 10 million, even though in 2016 the number was less than 4% (around 9.5 million patients). This was influenced by the digitization of e-health services. "As far as **I** [pronoun] had analysed, only a small part of **Lithuanian** [location noun] hospitals have reduced their posts or dismissed employees, but digitization of services has led to a

significant additional contribution to the quality of service," said J. **Jonaitis** [person noun phrase].

If the algorithm does not find any named entities moving backwards, it moves back to pronoun and proceeds forward. The algorithm continues moving forward until it locates "J. Jonaitis" entity, which is recognized as a person. Since the gender of the pronoun "man" is ambiguous (it can refer to both female and male persons), only their grammatical numbers are compared. Both are singular; therefore, the algorithm picks "J. Jonaitis" as a postcedent of the corefering object "man." Conditions for the existence of such reference formally could be defined as two alternatives. The first one describes the conditions for reference existing in the same sentence **s1** after pronoun was mentioned:

For each text's **t** *sentence* **s1** *and pronoun* **p** *not of Demonstrative type that is contained in sentence* **s1** *and has gender* **g,** *number* **n**, *start position* **sp1** *and length of* **ln1**, *and named entity* **e1** *that is in the same sentence* **s1**, *is expressed by lexeme l, and has gender* **g**, *number* **n**, *start position* **sp2** *and is of length* **ln2**, *and is after pronoun* **p** *(***sp2** *is higher than* **sp1***), but closer to pronoun* **p** *than possible named entities* **e2** *and* **e3** *(***sp2** *higher than* **sp3** *and* **sp4***), the only one coreference relation* **r**, *which is resolved in text* **t**, *is of "Pronominal" type, "Relative" subtype, "Backward" position and "Single" group between the pronoun* **p** *and the named entity* **e1**, *its referent starts at position* **sp1** *and has length* **ln1**, *and which fits only one pronoun* **p** *and refers to only one mention* **m**, *which starts at position* **sp2**, *has length* **ln2**, *and fits only one named entity* **e1**, *exists* (Rule 6).

Rule 6: ∀t, s1, p, l, e1, g, n, sp1, ln1, sp2, ln2.[Text(t) ∧ Sentence(s1) ∧ consists_of(t, s1) ∧ Pronoun(p) ∧ contains(s1, p) ∧ ¬has_type(p, Demonstrative) ∧ has_gender(p, g) ∧ has_number(p, n) ∧ has_start_position(p, sp1) ∧ has_length(p, ln1) ∧ Person_NE(e1) ∧ includes(s1, e1) ∧ Lexeme(l) ∧ expressed_by(e1, l) ∧ has_gender(e1, g) ∧ has_number(e1, n) ∧ has_start_position(e1, sp2) ∧ has_length(e1, ln2) ∧ sp1<sp2 ∧ ¬(∃e2, e3, sp3, sp4. (e1≠e2 ∧ e1≠e3 ∧ e2≠e3 ∧ Person_NE(e2) ∧ includes(s1, e2) ∧ has_start_position(e2, sp3) ∧ Person_NE(e3) ∧ includes(s1, e3) ∧ has_start_position(e3, sp4) ∧ sp2<sp3 ∧ sp4<sp2)) ⟶ ∃!r ∃!m. [Coreference(r) ∧ resolved_in(r, t) ∧ has_type (r, Pronominal) ∧ has_subtype (r, General) ∧ has_position(r, Forward) ∧ has_group(r, Single) ∧ has_start_position(r, sp1) ∧ has_length(r, ln1) ∧ fits(r, p) ∧ Mention(m) ∧ refers_to(r, t) ∧ has_start_position(m, sp2) ∧ has_length(m, ln2) ∧ fits(m, e1) ∧ fits(m, l)]]

The second alternative describes the case when the pronoun **p** refers to the named entity in the following sentence **s4**:

For each text's **t** *sentence* **s1, s4,** *where* **s4** *follows* **s1**, *and pronoun* **p** *not of Demonstrative type that is contained in sentence* **s1** *and has gender* **g**, *number* **n**, *start position* **sp1** *and length of* **ln1**, *and named entity* **e1** *that is contained in sentence* **s2**, *is expressed by lexeme l, and has gender* **g**, *number* **n**, *start position* **sp2** *and is of length* **ln2**, *and is closer to pronoun* **p** *than possible named entities* **e2** *and* **e3** *(* **sp2** *higher than* **sp3** *and* **sp4** *), the only coreference relation* **r**, *which is resolved in text* **t**, *is of "Pronominal" type, "Relative" subtype, "Backward" position and "Single" group between the pronoun* ***p*** *and the named entity* **e1**, *its referent starts at position* **sp1** *and has length* **ln1**, *and which fits only one pronoun* **p** *and refers to only one mention* **m**, *which starts at position* **sp2**, *has length* **ln2**, *and fits only one named entity* **e1**, *exists* (Rule 7).

Rule 7: ∀t, s1, s2, p, l, e1, g, n, sp1, ln1, sp2, ln2.[Text(t) ∧ Sentence(s1) ∧ Sentence(s2) ∧ consists_of(t, s1) ∧ consists_of(t, s2) ∧ follows (s2, s1) ∧ Pronoun(p) ∧ contains(s1, p) ∧ ¬has_type(p, Demonstrative) ∧ has_gender(p, g) ∧ has_number(p, n) ∧ has_start_position(p, sp1) ∧ has_length(p, ln1) ∧ Person_NE(e1) ∧ includes(s2, e1) ∧ Lexeme(l) ∧ expressed_by(e1, l) ∧ has_gender(e1, g) ∧ has_number(e1, n) ∧ has_start_position(e1, sp2) ∧ has_length(e1, ln2) ∧ ¬(∃e2, e3, sp3, sp4. (e1≠e2 ∧ e1≠e3 ∧ e2≠e3 ∧ Person_NE(e2) ∧ includes(s2, e2) ∧ has_start_position(e2, sp3) ∧ Person_NE(e3) ∧ includes(s2, e3) ∧ has_start_position(e3, sp4) ∧ sp2<sp3 ∧ sp4<sp2)) ⟶ ∃!r ∃!m. [Coreference(r) ∧ resolved_in(r, t) ∧ has_type (r, Pronominal) ∧ has_subtype (r, General) ∧ has_position(r, Forward) ∧ has_group(r, Single) ∧ has_start_position(r, sp1) ∧ has_length(r, ln1) ∧ fits(r, p) ∧ Mention(m) ∧ refers_to(r, t) ∧ has_start_position(m, sp2) ∧ has_length(m, ln2) ∧ fits(m, e1) ∧ fits(m, l)]]

The algorithm ignores demonstrative pronouns because they are often used to refer to entities that are not present in the written text. Such pronouns do not carry any additional semantic information and do not refer to any noun phrase. They are used mostly for syntactic reasons and due to that are usually ignored in coreference resolution.

3.4.3. A3: PRA Resolution. This algorithm is based on exact (or partial) string matches and several rules for acronyms. Once a first named entity that can be matched with an initial named entity is found, then the algorithm stops to keep annotations simple: B ⟶ A, C ⟶ B and D ⟶ C. This allows the formation of the coreference chains linking all mentions of the same entity in a text that can be later reused for semantic analysis, for example,

(i) [LT] **Tomaitis** [named entity] pateko į avariją. Po pietų **Tomaitį** [named entity] išvežė į operacinę.

[EN] **Tomaitis** [named entity] got into a car accident. In the afternoon, **Tomaitis** [named entity] has been taken to a surgery room.

In this example, two mentions of the same entity are made: "Tomaitis" and "Tomaitį." They are of different cases, but their lemmas are identical. A condition for the existence of such reference formally is defined as follows:

For each text's **t** *sentence* **s1** *that includes named entity* **e1**, *that has start position* **sp1** *and is of length* **ln1**, *which is expressed by lexeme* **l1** *that has lemma* **l** *and for each same text's* **t** *sentence* **s2** *that includes named entity* **e2**, *that has a start position* **sp1** *and is of length* **ln1**, *which is expressed by*

lexeme **l2** *that has lemma* **l**, *the only one coreference relation* **r**, *which is resolved in text* **t**, *is of "Nominal" type, "Repetition" subtype, "Irrelevant" position and "Single" group between the noun* **n1** *and the noun* **n2**, *its referent starts at position* **sp1** *and has length* **ln1**, *and which fits only one noun* **n1** *and refers to only one mention* **m**, *which starts at position* **sp2**, *has length* **ln2**, *and fits only one noun* **n2**, *exists* (Rule 8).

Rule 8: ∀t, s1, s2, e1, e2, sp1, ln1, sp2, ln2.[Text(t) ∧ Sentence(s1) ∧ Sentence(s2) ∧ consists_of(t, s1) ∧ consists_of(t, s2) ∧ Named_Entity(e1) ∧ includes(s1, e1) ∧ has_start_position(e1, sp1) ∧ has_length(e1, ln1) ∧ Named_Entity(e2) ∧ includes(s2, e2) ∧ has_start_position(e2, sp2) ∧ has_length(e2, ln2) ∧ e1≠e2 ∧ (∃l1 ∃l2 ∃l.(Lexeme(l1) ∧ Lexeme(l2) ∧ expressed_by(e1, l1) ∧ expressed_by(e2, l2) ∧ has_lemma(l1, l) ∧ has_lemma(l2, l)) ⟶ ∃!r ∃!m. [Coreference(r) ∧ resolved_in(r, t) ∧ has_type (r, Nominal) ∧ has_subtype (r, Repetition) ∧ has_position(r, Irrelevant) ∧ has_group(r, Single) ∧ has_start_position(r, sp1) ∧ has_length(r, ln1) ∧ fits(r, l1) ∧ fits(r, e1) ∧ Mention(m) ∧ refers_to(r, t) ∧ has_start_position(m, sp2) ∧ has_length(m, ln2) ∧ fits(m, l2) ∧ fits(m, e2)]]

Acronym rules vary depending on the type of named entity (currently persons, locations, and organizations are covered).

3.4.4. A4: HHS Resolution. This algorithm is based on profession classification. It attempts to resolve the use of synonyms and hypernyms/hyponyms.

(i) [LT] **Gydytojai** [noun referring to profession] skundžiasi dideliu darbo krūviu. **Chirurgų** [noun referring to profession] darbo krūvis pats didžiausias.

[EN] **Doctors** [noun referring to profession] complain about heavy workload. **Surgeons'** [noun referring to profession] workload is the greatest.

The algorithm determines that "Doctor" in professions classification is a hyponym of "Surgeon," they also agree in gender and number; therefore, the algorithm adds their pair to annotations. Conditions for the existence of such reference formally are defined as follows:

For each text's **t** *sentence* **s1** *that has profession* **p1**, *which is either broader or narrower than profession* **p2**, *name* **v1** *expressing noun* **n1**, *which has gender* **g**, *number* **m**, *start position* **sp1** *and is of length* **ln1**, *and for each same text's* **t** *sentence* **s2** *that has profession* **p2**, *which is either broader or narrower than profession* **p1**, *name* **v2** *expressing noun* **n2**, *which has gender* **g**, *number* **m**, *start position* **sp2** *and is of length* **ln2**, *the only one coreference relation* **r**, *which is resolved in text* **t**, *is of "Nominal" type, "Hypernym_hyponym" subtype, "Irrelevant" position and "Single" group between the noun* **n1** *and the noun* **n2**, *its referent starts at position* **sp1** *and has length* **ln1**, *and which fits only one noun* **n1** *and refers to only one mention* **m**, *which starts at position* **sp2**, *has length* **ln2**, *and fits only one noun* **n2**, *exists* (Rule 9).

Rule 9: ∀t, s1, s2, n1, n2, sp1, ln1, sp2, ln2, v1, v2, p1, p2.[Text(t) ∧ Sentence(s1) ∧ Sentence(s2) ∧ consists_of(t, s1) ∧ consists_of(t, s2) ∧ Noun(n1) ∧ contains(s, n1) ∧ has_start_position(n1, sp1) ∧ has_length(n1, ln1) ∧ Noun(n2) ∧ contains(s2, n2) ∧ has_start_position(n2, sp2) ∧ has_length(n2, ln2) ∧ n1≠n2 ∧ Profession(p1) ∧ Profession(p2) ∧ p1≠p2 ∧ Profession_Name(v1) ∧ Profession_Name(v2) ∧ express(n1, v1) ∧ express(n2, v2) ∧ describes(v1, p1) ∧ describes(v2, p2) ∧ (broadens(p2, p1) ∨ broadens(p1, p2)) ∧ has_gender(n1, g) ∧ has_gender(n2, g) ∧ has_number(n1, n) ∧ has_number(n2, n) ⟶ ∃!r ∃!m. [Coreference(r) ∧ resolved_in(r, t) ∧ has_type (r, Nominal) ∧ has_subtype (r, Hypernym_Hyponym) ∧ has_position(r, Irrelevant) ∧ has_group(r, Single) ∧ has_start_position(r, sp1) ∧ has_length(r, ln1) ∧ fits(r, n1) ∧ Mention(m) ∧ refers_to(r, t) ∧ has_start_position(m, sp2) ∧ has_length(m, ln2) ∧ fits(m, n2)]]

An example of synonym is given as follows:

(i) [LT] J. Jonaitis buvo operacijos **vadovu** [noun referring to profession]. Deja, **vyr. chirurgo** [noun referring to profession] vykdoma operacija buvo nesėkminga.

[EN] From now J. Jonaitis was the **head** surgeon [noun referring to profession] of operation. Unfortunately, the last operation of **chief surgeon** [noun referring to profession] was unsuccessful.

Both "head surgeon" and "chief surgeon" are synonymous; therefore, the condition for the existence of such reference formally could be defined as follows:

For each text's **t** *sentence* **s1** *that has a profession's* **p** *name* **v1**, *which is expressed by noun* **n1** *that has gender* **g**, *number* **m**, *start position* **sp1** *and is of length* **ln1**, *and for each same text's* **t** *sentence* **s2** *that has same profession's* **p** *name* **v2** *expressed by noun* **n2** *that has gender* **g**, *number* **m**, *start position* **sp2** *and is of length* **ln2**, *the only one coreference relation* **r**, *which is resolved in text* **t**, *is of "Nominal" type, "Synonym" subtype, "Irrelevant" position and "Single" group between the noun* **n1** *and the noun* **n2**, *its referent starts at position* **sp1** *and has length* **ln1**, *and which fits only one noun* **n1** *and refers to only one mention* **m**, *which starts at position* **sp2**, *has length* **ln2**, *and fits only one noun* **n2**, *exists* (Rule 10).

Rule 10: ∀t, s1, s2, n1, n2, sp1, ln1, sp2, ln2, v1, v2, p, g, n.[Text(t) ∧ Sentence(s1) ∧ Sentence(s2) ∧ consists_of(t, s1) ∧ consists_of(t, s2) ∧ Noun(n1) ∧ contains(s1, n1) ∧ has_start_position(n1, sp1) ∧ has_length(n1, ln1) ∧ Noun(n2) ∧ contains(s2, n2) ∧ has_start_position(n2, sp2) ∧ has_length(n2, ln2) ∧ n1≠n2 ∧ Profession_name(v1) ∧ Profession_name(v2) ∧ Profession(p) ∧ express(n1, v1) ∧ express(n2, v2) ∧ describes(v1, p) ∧ describes(v2, p) ∧ has_gender(n1, g) ∧ has_gender(n2, g) ∧ has_number(n1, n) ∧ has_number(n2, n) ∧ n1≠n2 ⟶ ∃!r ∃!m. [Coreference(r) ∧ resolved_in(r, t) ∧ has_type (r, Nominal) ∧ has_subtype(r, Synonym) ∧ has_position(r, Irrelevant) ∧ has_group(r, Single) ∧ has_start_position(r, sp1) ∧

has_length(r, ln1) ∧ fits(r, n1) ∧ Mention(m) ∧ refers_to(r, t) ∧ has_start_position(m, sp2) ∧ has_length(m, ln2) ∧ fits(m, n2)]]

3.4.5. A5: Feature Resolution. This algorithm at the time attempts to resolve only those cases when a person is being referred to by his public post (feature) that he holds, other types of features are not currently resolved, for example,

(i) [LT] Ką rekomenduoja S. Suskelis [person noun phrase]? Aptarkime kardiologo [noun referring to held position] siūlomą gydymo planą.

[EN] What does S. Suskelis [person noun phrase] recommend? Let's discuss treatment plan proposed by the cardiologist [noun referring to held position]. Here a noun "cardiologist" is selected, the algorithm moves backwards till it reaches "S. Suskelis" and checks the knowledge base if at the time of the publication of the medical record he has held the position of the cardiologist.. Since "he holds it" the algorithm checks if "S. Suskelis" and "cardiologist" agree in gender and number. They agree, and their pair is added to annotation as a feature reference. A condition for the existence of such reference formally is defined as follows:

For each text's **t** *sentence* **s1** *that has known person* **k**, *who during publication date* **d** *had certain position* **h** *(publication date* **d** *is same or later than position* **h** *start date* **fd** *and same or earlier than position* **h** *end date* **td***), mention as named entity* **e**, *that has a start position* **sp1** *and is of length* **ln1**, *and for each same text's* **t** *sentence* **s2** *mentioned noun* **n**, *that has a start position* **sp2** *and is length* **ln2**, *which is mentioned after named entity* **e** *(noun* **n** *has a higher start position* **sp2** *than named entity's* **sp1***), whose lemma* **l** *matches with position's* **h** *lemma* **l**, *number is Singular and gender g matches known person's* **k** *gender* **g**, *the only one coreference relation* **r**, *which is resolved in text* **t**, *is of "Nominal" type, "Feature" subtype, "Backward" position and "Single" group between the noun* **n** *and the named entity* **e**, *its referent starts at position* **sp2** *and has length* **ln2**, *and which fits only one noun* **n** *and refers to only one mention* **m**, *which starts at position* **sp1**, *has length* **ln1**, *and fits only one named entity* **e**, *exists* (Rule 11).

Rule 11: ∀t, s1, s2, n, k, h, l, d, fd, td, g, sp1, sp2, ln1, ln2.[Text(t) ∧ Sentence(s1) ∧ Sentence(s2) ∧ consists_of(t, s1) ∧ consists_of(t, s2) ∧ Person_NE(e) ∧ includes(s1, e) ∧ Noun(n) ∧ contains(s2, n) ∧ Known_Person(k) ∧ mentioned_as(k, e) ∧ Position_held(h) ∧ holds(k, h) ∧ has_lemma(h, l) ∧ has_lemma(n, l) ∧ has_publication_date(t, d) ∧ has_from_date(h, fd) ∧ has_to_date(h, td) ∧ fd≤d ∧ td≥d ∧ has_gender(k, g) ∧ has_gender(n, g) ∧ has_number(n, Singular) ∧ has_start_position(e, sp1) ∧ has_start_position(n, sp2) ∧ sp1<sp2 ∧ has_length(e, ln1) ∧ has_length(n, ln2) ⟶ ∃!r ∃!m. [Coreference(r) ∧ resolved_in(r, t) ∧ has_type (r, Nominal) ∧ has_subtype (r, Feature) ∧ has_position(r, Backward) ∧ has_group(r, Single) ∧ has_start_position(r, sp2) ∧ has_length(r, ln2) ∧ fits(r, e) ∧ Mention(m) ∧ refers_to(r, t) ∧ has_start_position(m, sp1) ∧ has_length(m, ln1) ∧ fits(m, n)]]

In this case, it is also relevant to track if coreference is pointing backward or forward. We can rewrite the same example and switch a known person with his positions:

(i) [LT] Koks yra mano **šeimos gydytojas** [noun referring to held position]? T. **Tomaitis** [person noun phrase] yra labai patyręs jūsų šeimos gydytojas.

[EN] Who is my **family doctor** [noun referring to held position]? T. **Tomaitis** [person noun phrase] is very experienced doctor assigned to you.

As a result, **sp1** is higher than **sp2** and coreference has different position constant values:

For each text's **t** *sentence* **s1** *that has known person* **k**, *who during publication date* **d** *had certain position* **h** *(publication date* **d** *is same or later than position* **h** *start date* **fd** *and same or earlier than position* **h** *end date* **td***), mention as named entity* **e**, *that has a start position* **sp1** *and is of length* **ln1**, *and for each same text's* **t** *sentence* **s2** *mentioned noun* **n**, *that has a start position* **sp2** *and is length* **ln2**, *which is mentioned after named entity* **e** *(noun* **n** *has a lower start position* **sp2** *than named entity's* **sp1***), whose lemma* **l** *matches with position's* **h** *lemma* **l**, *number is Singular and gender g matches known person's* **k** *gender* **g**, *the only one coreference relation* **r**, *which is resolved in text* **t**, *is of "Nominal" type, "Feature" subtype, "Forward" position and "Single" group between the noun* **n** *and the named entity* **e**, *its referent starts at position* **sp2** *and has length* **ln2**, *and which fits only one noun* **n** *and refers to only one mention* **m**, *which starts at position* **sp1**, *has length* **ln1**, *and fits only one named entity* **e**, *exists* (Rule 12).

Rule 12: ∀t, s1, s2, n, k, h, l, d, fd, td, g, sp1, sp2, ln1, ln2.[Text(t) ∧ Sentence(s1) ∧ Sentence(s2) ∧ consists_of(t, s1) ∧ consists_of(t, s2) ∧ Person_NE(e) ∧ includes(s1, e) ∧ Noun(n) ∧ contains(s2, n) ∧ Known_Person(k) ∧ mentioned_as(k, e) ∧ Position_held(h) ∧ holds(k, h) ∧ has_lemma(h, l) ∧ has_lemma(n, l) ∧ has_publication_date(t, d) ∧ has_from_date(h, fd) ∧ has_to_date(h, td) ∧ fd≤d ∧ td≥d ∧ has_gender(k, g) ∧ has_gender(n, g) ∧ has_number(n, Singular) ∧ has_start_position(e, sp1) ∧ has_start_position(n, sp2) ∧ sp1>sp2 ∧ has_length(e, ln1) ∧ has_length(n, ln2) ⟶ ∃!r ∃!m. [Coreference(r) ∧ resolved_in(r, t) ∧ has_type (r, Nominal) ∧ has_subtype (r, Feature) ∧ has_position(r, Forward) ∧ has_group(r, Single) ∧ has_start_position(r, sp2) ∧ has_length(r, ln2) ∧ fits(r, e) ∧ Mention(m) ∧ refers_to(r, t) ∧ has_start_position(m, sp1) ∧ has_length(m, ln1) ∧ fits(m, n)]]

4. Results and Evaluation

The coreference resolution algorithms and rules presented in Section 3 were implemented as a separate component and integrated into the semantic search framework NLP pipeline

Table 3: Experiment results.

Algorithm	T (actual number of solvable expressions)	F (number of solvable expressions resolved by the algorithm)	C (number of solvable expressions correctly resolved by the algorithm)	R (recall)	P (precision)	$F1$
General purpose (GP)	648	248	202	0.311	0.814	0.451
GP + specific usage rules (SUR)	648	277	223	0.344	0.805	0.482
GP + SUR + PRA	648	330	267	0.412	0.809	0.546
GP + SUR + PRA + HHS	648	343	274	0.422	0.799	0.553
GP + SUR + PRA + HHS + feature	648	371	289	0.446	0.779	0.567

(Figure 1) because it requires lexical, morphological, and NE annotations of the text should be analysed. Solutions for other languages should not follow the same NLP pipeline architecture. But a supply of coreference resolution component with lexical, morphological, and NE information of the text must be ensured.

Coreference resolution for Lithuanian was implemented using Java programming language and JSON data format for annotation storage. But the proposed approach is not technology dependent, and for other languages, it can be implemented on any other platform.

The evaluation was performed by analysing 100 articles that have been preannotated and are available in our Lithuanian Language Coreference Corpus [55], in addition to the transcribed records of medical reception, which we cannot disclose due to the privacy requirements.

For evaluation, we used precision, recall, and $F1$ metrics. Recall R is the ratio of correctly resolved anaphoric expressions C to the total number of anaphoric expressions T. Precision P is the ratio of correctly resolved anaphoric expressions C to the number of resolved anaphoric expressions F. $F1$ is a harmonic mean of P and R:

$$R = \frac{C}{T},$$
$$P = \frac{C}{F}, \quad (1)$$
$$F1 = 2 * \frac{R * P}{\mathrm{R} + \mathrm{P}}.$$

Five experiments were performed with different combinations of coreferencing algorithms presented in Section 3. The results of the experiments are presented in Table 3.

Note the following threats to validity of our results:

(i) The database of public persons must be constantly updated as new information becomes available. Otherwise, recall will get noticeably lower when annotating newer texts.

(ii) In the case where plural pronouns and nouns are used, they are difficult to be identified because of many variations possible that often ignore grammatical compatibility rules.

Linking the named entity to the position held taking into account the date of the publication of the text is limited considering that the text might be published today but written about things that happened in the past. There are no tools, which can identify the timeframe of a certain part of the text.

5. Conclusion

Medical entity recognition and coreferencing are difficult tasks in Lithuanian natural language processing (NLP). We proposed the coreference resolution approach for the Lithuanian language. The coreference resolution algorithm depends on morphological and named entity recognition (NER) annotations and preexisting databases. Due to the proposed approach being detached from specific implementation and rules being formalized, it would not be difficult to adapt it for grammatically similar languages. Our novelty is the ability to process coreferences with minimal linguistic resources, which are very important to consider in linguistic applications for under-resourced and endangered languages. While the proposed method provides encouraging results, when analysing transcribed medical records and other corpora, and they are comparable to the results achieved by other authors applying different resolution approaches on other languages, it has certain limitations: it is domain specific and is able to resolve only a subset of coreference types, while the relatively small dataset was used for experiments. Nevertheless, we hope that our method can contribute to the sustainable development of the NLP-powered online healthcare services in Lithuania.

Data Availability

The dataset used in this research is available upon request.

Conflicts of Interest

The authors declare that they have no conflicts of interest.

References

[1] A. Pomares-Quimbaya, R. A. Gonzalez, S. Quintero et al., "A review of existing applications and techniques for narrative text analysis in electronic medical records," in *Artificial Intelligence*, pp. 1620–1635, Optimizing Medicine Residency Training Programs, Hershey, PA, USA, 2017.

[2] B. L. Cook, A. M. Progovac, P. Chen, B. Mullin, S. Hou, and E. Baca-Garcia, "Novel use of natural language processing (NLP) to predict suicidal ideation and psychiatric symptoms in a text-based mental health intervention in madrid,"

Computational and Mathematical Methods in Medicine, vol. 2016, p. 8, 2016.

[3] J. Ginsberg, M. H. Mohebbi, R. S. Patel, L. Brammer, M. S. Smolinski, and L. Brilliant, "Detecting influenza epidemics using search engine query data," *Nature*, vol. 457, no. 7232, pp. 1012–1014, 2009.

[4] A. Nikfarjam, A. Sarker, K. O'Connor, R. Ginn, and G. Gonzalez, "Pharmacovigilance from social media: mining adverse drug reaction mentions using sequence labeling with word embedding cluster features," *Journal of the American Medical Informatics Association*, vol. 22, pp. 671–681, 2015.

[5] H. Yang and H. Gao, "Toward sustainable virtualized healthcare: extracting medical entities from Chinese online health consultations using deep neural networks," *Sustainability*, vol. 10, no. 9, p. 3292, 2018.

[6] D. Ferrucci, E. Brown, J. Chu-Carroll et al., "Building Watson: an overview of the DeepQA project," *AI magazine*, vol. 31, no. 3, pp. 59–79, 2010.

[7] A. Utka, D. Amilevicius, T. Krilavicius, and D. Vitkute-Adzgauskiene, "Overview of the development of language resources and technologies in Lithuania (2012–2015)," *Frontiers in Artificial Intelligence and Applications*, vol. 289, pp. 12–19, 2016.

[8] M. Kholghi, L. Sitbon, G. Zuccon, and A. Nguyen, "Active learning: a step towards automating medical concept extraction," *Journal of the American Medical Informatics Association*, vol. 23, no. 2, pp. 289–296, 2016.

[9] E. Choi, M. T. Bahadori, E. Searles et al., "Multi-layer representation learning for medical concepts," in *Proceedings of the 22nd ACM SIGKDD International Conference on Knowledge Discovery and Data Mining - KDD'16*, pp. 1495–1504, San Francisco, CA, USA, August 2016.

[10] Y.-M. Kim and D. Delen, "Medical informatics research trend analysis: a text mining approach," *Health Informatics Journal*, vol. 24, no. 4, pp. 432–452, 2018.

[11] M. Simmons, A. Singhal, and Z. Lu, "Text mining for precision medicine: bringing structure to EHRs and biomedical literature to understand genes and health," *Advances in Experimental Medicine and Biology*, vol. 939, pp. 139–166, 2016.

[12] S. Liu, B. Tang, Q. Chen, X. Wang, and X. Fan, "Feature engineering for drug name recognition in biomedical texts: feature conjunction and feature selection," *Computational and Mathematical Methods in Medicine*, vol. 2015, Article ID 913489, 9 pages, 2015.

[13] D. Zeng, C. Sun, L. Lin, and B. Liu, "LSTM-CRF for drug-named entity recognition," *Entropy*, vol. 19, no. 6, p. 283, 2017.

[14] B. Tang, H. Cao, X. Wang, Q. Chen, and H. Xu, "Evaluating word representation features in biomedical named entity recognition tasks," *BioMed Research International*, vol. 2014, Article ID 240403, 6 pages, 2014.

[15] H.-J. Dai, S. Syed-Abdul, C.-W. Chen, and C.-C. Wu, "Recognition and evaluation of clinical section headings in clinical documents using token-based formulation with conditional random fields," *BioMed Research International*, vol. 2015, Article ID 873012, 10 pages, 2015.

[16] J. Liang, X. Xian, X. He et al., "A novel approach towards medical entity recognition in Chinese clinical text," *Journal of Healthcare Engineering*, vol. 2017, Article ID 4898963, 16 pages, 2017.

[17] J. Xu, L. Gan, M. Cheng, and Q. Wu, "Unsupervised medical entity recognition and linking in Chinese online medical text," *Journal of Healthcare Engineering*, vol. 2018, Article ID 2548537, 13 pages, 2018.

[18] S. Doan, M. Conway, T. M. Phuong, and L. Ohno-Machado, "Natural language processing in biomedicine: a unified system architecture overview," in *Methods in Molecular Biology*, pp. 275–294, Springer, New York, NY, USA, 2014.

[19] W. Sun, Z. Cai, Y. Li, F. Liu, S. Fang, and G. Wang, "Data processing and text mining technologies on electronic medical records: a review," *Journal of Healthcare Engineering*, vol. 2018, Article ID 4302425, 9 pages, 2018.

[20] Z. He, C. Tao, J. Bian, M. Dumontier, and W. R. Hogan, "Semantics-powered healthcare engineering and data analytics," *Journal of Healthcare Engineering*, vol. 2017, Article ID 7983473, 3 pages, 2017.

[21] O. Bodenreider, "The unified Medical Language system (UMLS): integrating biomedical terminology," *Nucleic Acids Research*, vol. 32, no. 90001, pp. D267–D270, 2004.

[22] G. Vanagas and R. Klimavičiūtė-Gudauskiene, "Factors affecting electronic health information needs in primary care patients," *Telemedicine and e-Health*, vol. 18, no. 10, pp. 724–728, 2012.

[23] T. Vileiniškis, A. Šukys, and R. Butkienė, "Searching the web by meaning: a case study of Lithuanian news websites," in *Proceedings of the 7th International Joint Conference on Knowledge Discovery, Knowledge Engineering and Knowledge Management: IC3K 2015*, vol. 631, pp. 47–64, Springer, Porto, Portugal, November 2016.

[24] O. Uzuner, A. Bodnari, S. Shen, T. Forbush, J. Pestian, and B. R. South, "Evaluating the state of the art in coreference resolution for electronic medical records," *Journal of the American Medical Informatics Association*, vol. 19, no. 5, pp. 786–791, 2012.

[25] H. Lee, M. Surdeanu, and D. Jurafsky, "A scaffolding approach to coreference resolution integrating statistical and rule-based models," *Natural Language Engineering*, vol. 23, no. 5, pp. 733–762, 2017.

[26] S. Liu, B. Tang, Q. Chen, and X. Wang, "Effects of semantic features on machine learning-based drug name recognition systems: word embeddings vs. Manually constructed dictionaries," *Information*, vol. 6, no. 4, pp. 848–865, 2015.

[27] C. Li, D. Konomis, G. Neubig, P. Xie, C. Cheng, and E. Xing, "Convolutional neural networks for medical diagnosis from admission notes," 2017, https://arxiv.org/abs/1712.02768v1.

[28] H. Ranjan, S. Agarwal, A. Prakash, and S. K. Saha, "Automatic labelling of important terms and phrases from medical discussions," in *Proceedings of the 2017 Conference on Information and Communication Technology (CICT)*, pp. 1–5, Gwalior, India, November 2017.

[29] E. Chiaramello, F. Pinciroli, A. Bonalumi, A. Caroli, and G. Tognola, "Use of "off-the-shelf" information extraction algorithms in clinical informatics: a feasibility study of MetaMap annotation of Italian medical notes," *Journal of Biomedical Informatics*, vol. 63, pp. 22–32, 2016.

[30] J. Dziadek, A. Henriksson, and M. Duneld, "Improving terminology mapping in clinical text with context-sensitive spelling correction," *Studies in Health Technology and Informatics*, vol. 235, pp. 241–245, 2017.

[31] Y. Luo, Ö. Uzuner, and P. Szolovits, "Bridging semantics and syntax with graph algorithms-state-of-the-art of extracting biomedical relations," *Briefings in Bioinformatics*, vol. 18, no. 1, pp. 160–178, 2016.

[32] J. R. Hobbs, "Resolving pronoun references," in *Reading in Natural Language Processing*, B. Grosz, K. Sparck-Jones, and B. Webber, Eds., vol. 99, pp. 339–352, Morgan Kaufmann Publishers, Los Altos, CA, USA, 1986.

[33] J. R. Tetrault, "A corpus-based evaluation of centering and pronoun resolution," *Computational Linguistics*, vol. 27, no. 4, pp. 507–520, 2001.

[34] D. K. Byron, "Resolving pronominal references to abstract entities," in *Proceedings of the 40th Annual Meeting of the Association for Computational Linguistics (ACL)*, pp. 80–87, Philadelphia, PA, USA, July 2002.

[35] R. Mitkov and C. Hallett, "Comparing pronoun resolution algorithms," *Computational Intelligence*, vol. 23, no. 2, pp. 262–297, 2007.

[36] S. Lappin and H. J. Leass, "An algorithm for pronominal anaphora resolution," *Computational Linguistics*, vol. 20, no. 4, pp. 535–561, 1994.

[37] A. Zeldes and S. Zhang, "When annotation schemes change rules help: a configurable approach to coreference resolution beyond ontonotes," in *Proceedings of Workshop on Coreference Resolution Beyond OntoNotes (CORBON 2016)*, pp. 92–101, San Diego, CA, USA, June 2016.

[38] N. Ge, J. Hale, and E. Charniak, "A statistical approach to anaphora resolution," in *Proceedings of the Sixth Workshop on Very Large Corpora*, pp. 161–170, Montreal, Canada, August 1998.

[39] R. Mitkov, R. Evans, and C. Orasan, "A new, fully automatic version of mitkov's knowledge-poor pronoun resolution method," in *Proceedings of the International Conference on Intelligent Text Processing and Computational Linguistics*, pp. 168–186, Springer, Budapest, Hungary, April 2002.

[40] W. M. Soon, H. T. Ng, and D. C. Y. Lim, "A machine learning approach to coreference resolution of noun phrases," *Computational Linguistics*, vol. 27, no. 4, pp. 521–544, 2001.

[41] J. R. Finkel and C. D. Manning, "Enforcing transitivity in coreference resolution," in *Proceedings of the 46th Annual Meeting of the Association for Computational Linguistics on Human Language Technologies: Short Papers*, pp. 45–48, Columbus, OH, USA, June 2008.

[42] S. Wiseman, A. M. Rush, and S. M. Shieber, "Learning global features for coreference resolution," in *Proceedings of Conference of the North American Chapter of the Association for Computational Linguistics: Human Language Technologies*, San Diego, CA, USA, June 2016.

[43] K. Lee, L. He, M. Lewis, and L. Zettlemoyer, "End-to-end neural coreference resolution," in *Proceedings of 2017 Conference on Empirical Methods in Natural Language Processing*, Association for Computational Linguistics, Brussels, Belgium, October–November 2017.

[44] S. Žitnik, L. Šubelj, and M. Bajec, "SkipCor: skip-mention coreference resolution using linear-chain conditional random fields," *PLoS ONE*, vol. 9, no. 6, Article ID e100101, 2014.

[45] A. Znotins and P. Paikens, "Coreference resolution for latvian," in *Proceedings of the 9th International Conference on Language Resources and Evaluation, LREC 2014*, pp. 3209–3213, Reykjavik, Iceland, May 2014.

[46] M. Ogrodniczuk and M. Kopeć, "Rule-based coreference resolution module for polish," in *Proceedings of 8th Discourse Anaphora and Anaphor Resolution Colloquium, DAARC 2011*, pp. 191–200, Faro, Portugal, October 2011.

[47] M. Kopec and M. Ogrodniczuk, "Creating a coreference resolution system for polish," in *Proceedings of the Eighth International Conference on Language Resources and Evaluation (LREC)*, pp. 192–195, Istanbul, Turkey, May 2012.

[48] B. Nitoń, P. Morawiecki, and M. Ogrodniczuk, "Deep neural networks for coreference resolution for Polish," in *Proceedings of the Eleventh International Conference on Language Resources and Evaluation (LREC-2018)*, pp. 395–400, Miyazaki, Japan, May 2018.

[49] S. Toldova, I. Azerkovich, A. Ladygina, A. Roitberg, and M. Vasilyeva, "Error analysis for anaphora resolution in Russian: new challenging issues for anaphora resolution task in a morphologically rich language," in *Proceedings of the Workshop on Coreference Resolution Beyond OntoNotes, CORBON@HLT-NAACL*, pp. 74–83, San Diego, CA, USA, June 2016.

[50] A. Khadzhiiskaia and A. Sysoev, "Coreference resolution for Russian: taking stock and moving forward," in *Proceedings of 2017 Ivannikov ISPRAS Open Conference (ISPRAS)*, pp. 70–75, Moscow, Russia, November–December 2017.

[51] L. Kučová and Z. Žabokrtský, "Anaphora in Czech: large data and experiments with automatic anaphora resolution," in *Text, Speech and Dialogue*, pp. 93–98, Springer, Berlin, Germany, 2005.

[52] G. L. Nguy, V. Novák, and Z. Zabokrtský, "Comparison of classification and ranking approaches to pronominal anaphora resolution in Czech," in *Proceedings of the 10th Annual Meeting of the Special Interest Group on Discourse and Dialogue, SIGDIAL 2009*, pp. 276–285, London, UK, September 2009.

[53] M. Novák, "Coreference resolution system not only for Czech," in *Proceedings of the 17th conference ITAT 2017: Slovenskočeský NLP Workshop (SloNLP 2017)*, Praha, UK, September 2017.

[54] M. Novák, A. Nedoluzhko, and Z. Žabokrtský, "Projection-based coreference resolution using deep syntax," in *Proceedings of the 2nd Workshop on Coreference Resolution Beyond OntoNotes (CORBON 2017)*, pp. 56–64, Valencia, Spain, April 2017.

[55] V. Žitkus, *Lithuanian Coreference Corpus*, CLARIN-LT Digital Library, Lithuania, UK, 2018, http://hdl.handle.net/20.500.11821/19.

Hindawi
Computational and Mathematical Methods in Medicine
Volume 2019, Article ID 4762490, 13 pages
https://doi.org/10.1155/2019/4762490

Research Article

Brain Tissue Segmentation and Bias Field Correction of MR Image Based on Spatially Coherent FCM with Nonlocal Constraints

Jianhua Song[1,2] **and Zhe Zhang**[2]

[1]*College of Physics and Information Engineering, Minnan Normal University, Zhangzhou 363000, China*
[2]*Electronic Engineering College, Heilongjiang University, Harbin 150080, China*

Correspondence should be addressed to Jianhua Song; 98dg_sjh@163.com

Received 27 September 2018; Accepted 11 February 2019; Published 3 March 2019

Guest Editor: Tomas Krilavičius

Influenced by poor radio frequency field uniformity and gradient-driven eddy currents, intensity inhomogeneity (or bias field) and noise appear in brain magnetic resonance (MR) image. However, some traditional fuzzy c-means clustering algorithms with local spatial constraints often cannot obtain satisfactory segmentation performance. Therefore, an objective function based on spatial coherence for brain MR image segmentation and intensity inhomogeneity correction simultaneously is constructed in this paper. First, a novel similarity measure including local neighboring information is designed to improve the separability of MR data in Gaussian kernel mapping space without image smoothing, and the similarity measure incorporates the spatial distance and grayscale difference between cluster centroid and its neighborhood pixels. Second, the objective function with an adaptive nonlocal spatial regularization term is drawn upon to compensate the drawback of the local spatial information. Meanwhile, bias field information is also embedded into the similarity measure of clustering algorithm. From the comparison between the proposed algorithm and the state-of-the-art methods, our model is more robust to noise in the brain magnetic resonance image, and the bias field is also effectively estimated.

1. Introduction

Magnetic resonance image has been widely used in diagnostic imaging for general check-up in clinical application, especially the detection and diagnosis of brain diseases. The volume change for brain tissues often indicates various diseases [1], such as brain tumor, leukoencephalopathy, olivopontocerebellar atrophy (OPCA), etc. Therefore, brain tissue segmentation of MR image has become a very important medical treatment step. However, brain MR image has some lacks such as noise, intensity inhomogeneity, low contrast, the partial volume effect, and so on, which brings serious obstacles to segment the brain MR images. To this end, the multitudinous brain MR image segmentation methods have been put forward by using the theory of fuzzy set, random field, and level set.

Currently, there are two popular methods-based models for medical image segmentation: the random field theory [2–4] and the fuzzy c-means (FCM) algorithm. Random field is density-based unsupervised method where it finds the maximum likelihood estimate of the parameters from a given dataset. However random field algorithm has the disadvantages in high complexity and slow convergence and will drop into local optimization. FCM clustering is another efficient method used in image segmentation because it has robust characteristics for ambiguity and can retain much more information than random field algorithm [5]. Therefore, FCM has been widely applied in different types of image segmentation [6–8]. The neighboring pixels in an image are highly correlated, i.e., the pixels in the immediate neighborhood possess nearly the same feature data. Therefore, the spatial relationship of neighboring pixels is an important characteristic that can be of great aid in imaging segmentation. However, the conventional FCM algorithm does not fully utilize this spatial information. Pedrycz and Waletzky [9] took advantage of the available classified

information and actively applied it as part of their optimization procedures. Szilagyi et al. [10] proposed the enhanced FCM (EnFCM) algorithm to accelerate the image segmentation process in which the pixels of an image are replaced the gray-level histogram and the statistical number and calculation are much smaller than FCM. In order to further reduce the computation time and improve the parameter inflexibility, Cai et al. [11] presented a fast generalized FCM (FGFCM) method, and FGFCM introduced a flexible locality factor S_{ij} incorporating simultaneously both the gray-level difference and spatial distance in a local window. Ji et al. [12] proposed a robust spatially constrained fuzzy c-means (RSCFCM) algorithm for brain MR image segmentation. First, a spatial factor is constructed based on the posterior probabilities and prior probabilities and takes the spatial direction into account. Second, the negative log-posterior is utilized as dissimilarity function by taking the prior probabilities into account.

FCM with spatial constraint and its variants greatly improved the antinoise performance compared with FCM, but when the noise is very serious in the image, the performance of the algorithm may be worse. Therefore, the nonlocal spatial information was often used and incorporated into the distance metric of FCM in recent years [13–16]. Zhao [14] brought in a nonlocal adaptive regularization term in its energy function, and the control factor is adaptive determined to adjust the balance of the objective function. Feng et al. [15] proposed a FCM method with specific nonlocal information for the segmentation of synthetic aperture radar (SAR) image. Ma et al. [16] proposed a modified FGFCM approach by introducing nonlocal constraint term, and local distance metric and nonlocal distance metric are used, respectively, in its objective function. By introducing nonlocal constraint term, the features of image can be used more comprehensively and effectively, and the robustness to noise of FCM-based algorithm is significantly improved. However, there generally exists intensity inhomogeneity in brain MR images. Therefore, it is necessary to further design relevant algorithms to correct the intensity inhomogeneity. Sled et al. designed a set of software package for the estimation of bias field [17], and the characteristic of the method is nonparametric nonuniform intensity normalization or N3 for short; the distribution of the true tissue intensities can be achieved by an iterative method. Tustison et al. [18] improved the N3 algorithm based on modified B-spline approximation and hierarchical optimization algorithm (called N4ITK); N4ITK can also automatically perform without the priori knowledge. Liew and Hong Yan [19] introduced a spatial constraint to a fuzzy cluster method where the inhomogeneity field was modeled by a B-spline surface. The spatial pixel connectivity was implemented by a dissimilarity index, which enforced the connectivity constraint only in the homogeneous areas. Ji et al. proposed the modified possibilistic FCM (MPFCM) algorithm for bias field [20], generalized rough fuzzy c-means (GRFCM) algorithm, [21] and fuzzy local Gaussian mixture model (FLGMM) for brain MR image segmentation [22], respectively. Those methods can estimate bias field and segment the MR images simultaneously.

In this paper, a brain tissue classification and intensity inhomogeneity correction model of MR image based on spatially coherent FCM with nonlocal constraints is proposed. In this model, firstly, both the local constraint term and nonlocal regularization term about brain MR image are incorporated into the objective function, and an adaptive control factor is used to maintain the balance between them. Secondly, the similarity measure is designed in Gaussian kernel mapping space without image filtering, and the detail information and the edge of the image can be preserved well. Meanwhile, bias field model is also embedded into the objective function of clustering algorithm. Therefore, after the intensity inhomogeneity of the MR image is corrected, the segmentation accuracy is improved significantly. Experiments demonstrate that this algorithm can not only effectively estimate the bias field of MR image but also has stronger antinoise ability.

2. Preliminary Theory

2.1. Fuzzy Clustering Algorithms. Let $X = \{x_1, x_2, \ldots, x_N\}$ denote an image with N pixels, where x_k is gray value of the kth pixel in the image. FCM clustering aims at partitioning X into c clusters by minimizing the following objective function:

$$J_{\mathrm{FCM}} = \sum_{i=1}^{c} \sum_{k=1}^{N} u_{ik}^{m} \left\| x_k - v_i \right\|^2, \tag{1}$$

where v_i denotes the ith cluster prototype, u_{ik} denotes the membership degree of x_k belonging to ith cluster and follows $\sum_{i=1}^{c} u_{ik} = 1$, c denotes the number of centers, $\|\cdot\|$ denotes the Euclidean norm, and the parameter m is a weight exponent on each fuzzy membership that determines the amount of fuzziness of the resulting partition.

Ahmed et al. proposed a modification to FCM objective function by introducing a term that allows the labeling of a pixel to be influenced by the labels in its immediate neighborhood [23]. This effect acts as a regularizer and biases the solution toward piecewise homogeneous labeling. It proved useful in segmenting images corrupted by noise. The modified objective function is given by

$$J_{\mathrm{BCFCM}} = \sum_{i=1}^{c} \sum_{k=1}^{N} u_{ik}^{m} \left\| x_k - v_i \right\|^2 + \frac{\alpha}{N_R} \sum_{i=1}^{c} \sum_{k=1}^{N} u_{ik}^{m} \sum_{r \in N_k} \left\| x_r - v_i \right\|^2, \tag{2}$$

where x_r represents the neighbor voxels of x_k and N_R and N_k stand for the number of voxels in the neighborhood of the kth voxel. The parameter α controls the intensity of the neighboring effect. One disadvantage of BCFCM is that the neighborhood labeling is computed in each iteration step, something that is very time consuming.

2.2. Spatially Coherent Fuzzy c-Means Clustering (SCFCM). In view of some drawbacks of standard FCM algorithm, a modified scheme is proposed by Despotović et al. [24]. The similarity measure $D_{ik} = \|x_k - v_i\|^2$ is replaced by $D_{ik}^{*} = (1 - S_{ik})\|x_k - v_i\|^2$ introducing a weight factor S_{ik}, and the objective function is

$$J_{\mathrm{SCFCM}} = \sum_{i=1}^{c} \sum_{k=1}^{N} u_{ik}^{m} (1 - S_{ik}) \left\| x_k - v_i \right\|^2, \tag{3}$$

where S_{ik} is a weight factor including both local spatial information and grayscale difference and is designed as follows:

$$S_{ik} = \frac{\sum_{r\in\Omega_k} u_{ir} a_{kr} d_{kr}^{-1}}{\sum_{r\in\Omega_k} a_{kr} d_{kr}^{-1}}, \tag{4}$$

where Ω_k denotes a local neighboring window around x_k, u_{ir} denotes the membership degree of neighborhood pixels belonging to the ith cluster, $a_{kr} = |x_k - x_r|$ is the absolute intensity difference between the study pixel and its neighbor, $d_{kr} = \sqrt{(p_k - p_r)^2 + (q_k - q_r)^2}$ is the Manhattan distance between the coordinates of pixel x_k and x_r, and (p_k, q_k) and (p_r, q_r) denote the coordinates x_k and x_r in the image, respectively. By minimizing equation (3) by Lagrangian multiplier approach, u_{ik} and v_i can be derived as shown in the following equation:

$$u_{ik} = \frac{\left((1 - S_{ik})\left\|x_k - v_i\right\|^2\right)^{-1/(m-1)}}{\sum_{l=1}^{c}\left((1 - S_{lk})\left\|x_k - v_l\right\|^2\right)^{-1/(m-1)}},$$
$$v_i = \frac{\sum_{k=1}^{N} u_{ik}^m x_k}{\sum_{k=1}^{N} u_{ik}^m}. \tag{5}$$

Compared with the FCM, this algorithm has two advantages: firstly, it enhances the robustness to all kinds of noise. The constraint item of neighborhood information is included into the similarity measure, so as to effectively utilize the local information of the image. Secondly, it considers anisotropic neighborhood information, and more details and edges information can be preserved. However, the influence of bias field for MR images in segmentation algorithm is not mentioned.

2.3. Coherent Local Intensity Clustering Model. Bias field of the MR image usually embodies slowly and smoothly varying for the pixel grayscale of the local region across an image. Meanwhile, in a neighboring local window of the image, bias field can be approximately considered as a constant. Therefore, the most popular model can be described in equation (6) [25]; let Y denote the observed image, b denote the unknown bias field, X denote the true image to be restored, and n denote the additive noise.

$$Y = bX + n. \tag{6}$$

In the observed image, noise n is often assumed to obey Gaussian distribution with zero mean and variance σ_n^2, and the gray level value of the true image approximately takes a constant in a local window. Therefore, the gray level of the observed image can be approximated to obey Gaussian distribution with mean bX and variance σ_n^2. In coherent local intensity clustering (CLIC) model [26], a novel metric introducing spatially coherent local intensity convergence criterion for bias field estimation and image segmentation simultaneously is proposed. A Gaussian kernel weight parameter $K(r-k)$ is introduced into the similarity measure of each pixel gray level x_k and its neighbor pixels x_r, and the objective function of CLIC is

$$J_{\mathrm{CLIC}} = \sum_{i=1}^{c}\sum_{k=1}^{N} u_{ik}^m \sum_{r\in\Omega_k} K(r-k)\left\|x_k - b_r v_i\right\|^2, \tag{7}$$

where $b_r v_i$ is the clustering prototype with bias field in the selective region Ω_k, $K(r-k)$ is the weight of a truncated Gaussian kernel allocated for the intensity x_k, and the weight parameter can be defined as

$$K(y) = \begin{cases} \dfrac{1}{a} e^{-|y|^2/2\sigma^2}, & \text{for } |y| \le \rho, \\ 0, & \text{else}, \end{cases} \tag{8}$$

where σ denotes the standard deviation, a denotes a normalization factor to standardize Gaussian kernel, and ρ denotes a radius to measure the size of the local region.

In the CLIC model, intensity inhomogeneity of the MR image can be effectively corrected and can reduce the misclassification rate, but there are some drawbacks in CLIC. When computing the distance metric between the central pixel and its surrounding pixels in a local region, the model only used the local neighborhood information of the pixel without considering the global structure information of the entire image. As a result, the antinoise performance of this algorithm is unsatisfactory.

3. Proposed Method

The standard FCM algorithm has the shortcoming of being sensitive to noise. Though, the modified FCM algorithms are improved by adding the spatial information, it is difficult to get a satisfied segmentation result for noise robustness. Therefore, an improved FCM approach based on CLIC and SCFCM is proposed; its objective function is constructed according to the local constraint term and global regularization term; the similarity measure including local neighboring information is designed in Gaussian kernel mapping space, and brain tissue classification and intensity inhomogeneity correction can be realized simultaneously.

3.1. Nonlocal Weighted Constraint. In a discrete noisy image $X = \{x_1, x_2, \ldots, x_N\}$, x_k is the kth pixel and y_k is its nonlocal weighted average value. The derivation method of the nonlocal weighted average can be acquired in [27], and the mathematical expression of y_k is

$$y_k = \sum_{l\in w_k^u} w_{kl} x_l, \tag{9}$$

where w_k^u indicates a search region of radius u around x_k, w_{kl} denotes nonlocal weight coefficient depending on similarity measure between x_k and its neighboring pixels x_l in window w_k^u, and w_{kl} satisfies the constraint conditions $0 \le w_{kl} \le 1$ and $\sum_l w_{kl} = 1$. The weight coefficient w_{kl} is computed as follows:

$$w_{kl} = \frac{1}{Z_k} e^{\left(-\left\|x(N_k) - x(N_l)\right\|_{2,\sigma}^2 / h\right)}, \tag{10}$$

where $x(N_k)$ and $x(N_l)$ denote the grayscale vectors in the square neighborhood N_k and N_l of radius s around x_k and

x_l, respectively, and $\|x(N_k) - x(N_l)\|_{2,\sigma}^2$ is the weighted Euclidean distance between $x(N_k)$ and $x(N_l)$; its expression is defined in equation (11). σ is the same as in equation (8), and h denotes a control factor to adjust the variation of the similarity measure w_{kl}.

$$\left\|x(N_k) - x(N_l)\right\|_{2,\sigma}^2 = \sum_{p=1}^{(2s+1)^2} \sigma^p \left(x^p(N_k) - x^p(N_l)\right)^2, \quad (11)$$

where $x^p(N_k)$ is the pth pixel in the grayscale vectors $x(N_k)$ and σ^p is defined as follows:

$$\sigma^p = \sum_{v=\max(d,1)}^{s} \frac{1}{(2v+1)^2 s}, \quad (12)$$

where $y_p = \mathrm{mod}(p, (2s+1))$ and $z_p = \mathrm{floor}(p, (2s+1)) + 1$, (y_p, z_p) denote the coordinates of the pth component in a preselected region and $d = \max(|y_p - s - 1|, |z_p - s - 1|)$.

3.2. Objective Function. In order to correct bias field and classify the brain tissues simultaneously, the modified objective function-incorporated local constraint term and nonlocal regularization term is as follows:

$$J_m = \sum_{i=1}^{c}\sum_{k=1}^{N} u_{ik}^m \sum_{r\in\Omega_k} K(r-k)\left[\alpha_k(1-S_{ik})\left\|x_k - b_k v_i\right\|^2 + (1-\alpha_k)\left\|y_k - b_k v_i\right\|^2\right], \quad (13)$$

where u_{ik} is the membership degree of x_k belonging to the ith cluster, Ω_k denotes a local square region of the radius s around the center x_k, $b_k v_i$ is the ith cluster center in Ω_k, y_k denotes the nonlocal weighted average value of x_k, S_{ik} denotes the weight factor of local neighborhood information in equation (4), and the definitions of $K(r-k)$ and b_k are the same as equation (7). α_k is a trade-off weight factor to adjust the balance of local neighborhood information and nonlocal constraints information, and the definition of parameter α_k is

$$\alpha_k = \frac{1}{1 + \mathrm{var}(x)/(\overline{x})^2}, \quad (14)$$

where $\overline{x}$ denotes the gray level mean of all pixels in the local region Ω_k, and $\mathrm{var}(x)$ denotes the variance of pixel gray values in the same window. The larger the α_k value is, the smaller the influence of the noise is. The factor α_k can be obtained adaptively with the change of the local window Ω_k without being given in advance.

Theorem. *Assume $\sum_{i=1}^{c} u_{ik} = 1, 0 \le u_{ik} \le 1$, and $m > 1$. On the basis of Lagrange multiplier approach, equation (13) is minimized with respect to u_{ik}, v_i and b_k can be derived as shown in the following equation:*

$$u_{ik} = \frac{\sum_{r\in\Omega_k} K\left[\alpha_k(1-S_{ik})\left\|x_k - b_k v_i\right\|^2 + (1-\alpha_k)\left\|y_k - b_k v_i\right\|^2\right]^{-1/(m-1)}}{\sum_{l=1}^{c}\left(\sum_{r\in\Omega_k} K\left[\alpha_k(1-S_{lk})\left\|x_k - b_k v_l\right\|^2 + (1-\alpha_k)\left\|y_k - b_k v_l\right\|^2\right]\right)^{-1/(m-1)}},$$

$$v_i = \frac{\sum_{k=1}^{N}\sum_{r\in\Omega_k} K b_k\left[\alpha_k(1-S_{ik})x_k + (1-\alpha_k)y_k\right]u_{ik}^m}{\sum_{k=1}^{N}\sum_{r\in\Omega_k} K b_k^2(1-\alpha_k S_{ik})u_{ik}^m}, \quad (15)$$

$$b_k = \frac{\sum_{i=1}^{c}\sum_{r\in\Omega_k} K v_i\left[\alpha_k(1-S_{ik})x_k + (1-\alpha_k)y_k\right]u_{ik}^m}{\sum_{i=1}^{c}\sum_{r\in\Omega_k} K v_i^2(1-\alpha_k S_{ik})u_{ik}^m}.$$

Proof. According the method of Lagrange multiplier, equation (13) can be converted to unconstrained optimization problem:

$$L(u_{ik}, v_i, b_k, \lambda_k, \gamma_k) = \sum_{i=1}^{c}\sum_{k=1}^{N} u_{ik}^m \sum_{r\in\Omega_k} \alpha_k K(r-k) \cdot \left[(1-S_{ik})\left\|x_k - b_k v_i\right\|^2 + (1-\alpha_k)\left\|y_k - b_k v_i\right\|^2\right] + \sum_{k=1}^{N}\lambda_k\left[1 - \sum_{i=1}^{c} u_{ik}\right], \quad (16)$$

where λ_k is the Lagrange multiplier of the constraint condition $\sum_{i=1}^{c} u_{ik} = 1$, by computing the partial derivatives of polynomial L in regard to u_{ik} and λ_k, respectively, and set $\partial L/\partial u_{ik} = 0$, $\partial L/\partial \lambda_k = 0$, as shown in the following equation:

$$\frac{\partial L}{\partial u_{ik}} = m u_{ik}^{m-1} \sum_{r\in\Omega_k} K\left[\alpha_k(1-S_{ik})\left\|x_k - b_k v_i\right\|^2 + (1-\alpha_k)\left\|y_k - b_k v_i\right\|^2\right] - \lambda_k = 0, \quad (17)$$

$$\frac{\partial L}{\partial \lambda_k} = 1 - \sum_{i=1}^{c} u_{ik} = 0. \quad (18)$$

The following equation can be obtained by mathematical derivation of equation (17):

$$u_{ik} = \left(\frac{\lambda_k}{m \sum_{r \in \Omega_k} K\left[\alpha_k (1 - S_{ik}) \left\| x_k - b_k v_i \right\|^2 + (1 - \alpha_k) \left\| y_k - b_k v_i \right\|^2 \right]} \right)^{1/m-1}. \tag{19}$$

Substituting equation (19) into equation (17), we obtain the following equation:

$$\left(\frac{\lambda_k}{m} \right)^{1/m-1} = \sum_{i=1}^{c} \left(\sum_{r \in \Omega_k} K\left[\alpha_k (1 - S_{ik}) \left\| x_k - b_k v_i \right\|^2 + (1 - \alpha_k) \left\| y_k - b_k v_i \right\|^2 \right] \right)^{-(1/m-1)}. \tag{20}$$

And then substituting equation (20) into equation (19), the following equation can be obtained:

$$u_{ik} = \frac{\sum_{r \in \Omega_k} K\left[\alpha_k (1 - S_{ik}) \left\| x_k - b_k v_i \right\|^2 + (1 - \alpha_k) \left\| y_k - b_k v_i \right\|^2 \right]^{-(1/m-1)}}{\sum_{l=1}^{c} \left(\sum_{r \in \Omega_k} K\left[\alpha_k (1 - S_{lk}) \left\| x_k - b_k v_l \right\|^2 + (1 - \alpha_k) \left\| y_k - b_k v_l \right\|^2 \right] \right)^{-(1/m-1)}}. \tag{21}$$

Similarly, set $\partial L / \partial v_i = 0$, that is

$$\frac{\partial L}{\partial v_i} = \sum_{k=1}^{N} u_{ik}^m \left(\sum_{r \in \Omega_k} K b_k \left[\alpha_k (1 - S_{ik}) (x_k - b_k v_i) + (1 - \alpha_k) (y_k - b_k v_i) \right] \right) = 0. \tag{22}$$

The following equation can be obtained from equation (22) by mathematical derivation:

$$v_i = \frac{\sum_{k=1}^{N} \sum_{r \in \Omega_k} K b_k \left[\alpha_k (1 - S_{ik}) x_k + (1 - \alpha_k) y_k \right] u_{ik}^m}{\sum_{k=1}^{N} \sum_{r \in \Omega_k} K b_k^2 (1 - \alpha_k S_{ik}) u_{ik}^m}. \tag{23}$$

We adopt the same mathematical derivation process to estimate bias field b_k, for fixed u_{ik} and λ_k, and computing the partial derivative of L with respect to b_k, set $\partial L / \partial b_k = 0$, that is

$$\frac{\partial L}{\partial b_k} = \sum_{i=1}^{c} u_{ik}^m \left(\sum_{r \in \Omega_k} K\left[\alpha_k (1 - S_{ik}) \left(v_i x_k - v_i^2 b_k \right) + (1 - \alpha_k) \left(v_i y_k - v_i^2 b_k \right) \right] \right) = 0, \tag{24}$$

b_k can be obtained from equation (24).

$$b_k = \frac{\sum_{i=1}^{c} \sum_{r \in \Omega_k} K v_i \left[\alpha_k (1 - S_{ik}) x_k + (1 - \alpha_k) y_k \right] u_{ik}^m}{\sum_{i=1}^{c} \sum_{r \in \Omega_k} K v_i^2 (1 - \alpha_k S_{ik}) u_{ik}^m}. \tag{25}$$

The theorem proves to be completed.

Finally, the framework of the proposed algorithm can be summarized in Table 1. □

4. Experimental Results and Analysis

In this section, several classical algorithms for intensity inhomogeneity correction and brain image segmentation are selected as the reference for comparison; bias field estimation and antinoise performance analysis for the brain MR images are the main experimental contents. For the experiments in the following sections, the related parameter values are fuzzy exponential $m = 2$, the stop criterion $\varepsilon = 0.001$, 3×3 neighborhood window, and the radius $u = 10$ of the search window.

4.1. Bias Field Correction

4.1.1. MR Image Database. Intensity inhomogeneity is one of the problems in interfering brain MR image segmentation; in the experiments of bias field correction, the dataset is from a simulated brain database (SBD): BrainWeb [28] in which the brain MR images have three types: T1-, T2-, and proton density- (PD-) weighted 3D data volumes. In Figure 1, the T1-weighted normal brain MR images with $181 \times 217 \times 181$ cubic voxels, 1 mm slice thickness, 40% intensity nonuniformity, and 3% noise are used to test; all the skulls and blood vessels are already stripped ahead of image processing, and the image is segmented into four regions: white matter (WM), gray matter (GM), cerebrospinal fluid (CSF), and background.

4.1.2. Experimental Results. Figure 1 shows the results of bias field correction and segmentation for three brain MR images. Figure 1(a) shows the brain slice images from three different directions: transaxial mode, sagittal mode, and coronal mode. Figure 1(b) shows the estimated bias field, Figure 1(c) shows the final segmentation results, and Figure 1(d) shows the corrected images after removed bias field. Figure 2 shows the histogram comparison of original MR image and bias corrected images corresponding to three images in Figure 2. From Figures 1 and 2, three brain tissues are more homogeneous after bias field correction; each brain tissue approximately obeys Gaussian distribution with different mean and variance, and WM, GM, and CSF can be clearly distinguished. In addition, the histogram distribution of corrected MR image is more reasonable, from which we can see three approximative peaks representing three brain tissues.

Table 1: The basic flow of image segmentation and bias field estimation.

Step 1. Set the number of cluster c, the exponent of fuzziness m, stopping condition of the iteration $\varepsilon > 0$, the radius s of local neighborhood window, and the radius u of search window in equation (11).
Step 2. Set the iteration initial value $t = 0$ and initialize bias field $b_0 = 1$ and the center of cluster $V^1 = \{v_1^1, v_2^1, \ldots, v_c^1\}$.
Step 3. Calculate nonlocal weight coefficient w_{kl}^t in equation (8) and then obtain the nonlocal weighted value y_k^t by equation (7).
Step 4. Update the membership degree u_{ik}^t by equation (14).
Step 5. Update the center of clustering v_i^t by equation (14).
Step 6. Calculate the estimated bias field b_k^t by equation (15).
Step 7. If satisfying $\max\|V^{t+1} - V^t\| < \varepsilon$, then terminate iteration; otherwise, go to step 3 and set $t = t + 1$.

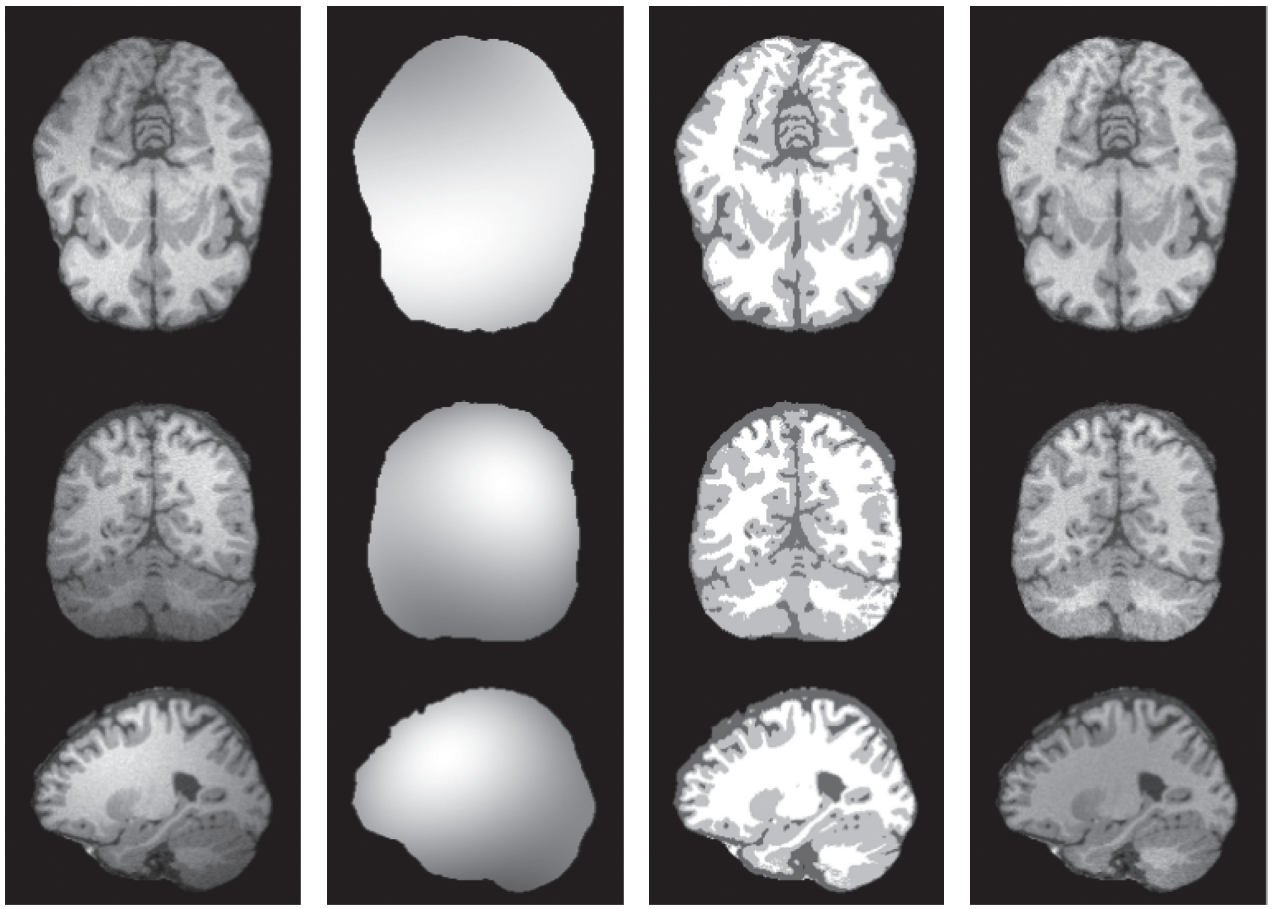

Figure 1: Intensity inhomogeneity correction of brain MR images: (a) original MR images, (b) the estimated bias field, (c) segmentation results, and (d) the corrected MR images.

To further validate the performance of bias field correction, three bias correction algorithms including BCFCM [23], CLIC [26], and N4ITK [18] are chosen as comparative methods, as shown in Figure 3. Figure 3(a) is a T1-weighted transaxial slice of normal brain MR image with 40% spatial inhomogeneity; its slice thickness is 1 mm and the noise level is about 2%. Figures 3(b) and 3(c) are the obtained bias inhomogeneity and the amendatory MR images by BCFCM, CLIC, N4ITK, and our method, respectively. Figure (4) shows the histograms of the image with spatial inhomogeneity and the corrected images in Figure 3. It is can be seen that the distribution of pixel gray level of blue line is more accurate than red dotted line; it indicates that all the algorithms of bias field estimation are more or less effective. However, our method is more reasonable than other three algorithms from Figure 4. Because the histogram normally should have three peaks corresponding to WM, GM, and CSF; the peak value of CSF is minimal according to tissue volume, and the gray level's mean and variance of each tissue are also obviously different.

4.2. Antinoise Performance. In the third experiment, first of all, the 104th transaxial slice of simulated T1-weighted brain MR image with 1 mm slice thickness and 7% Gaussian white noise is used to analyze the robustness to the noise, and we

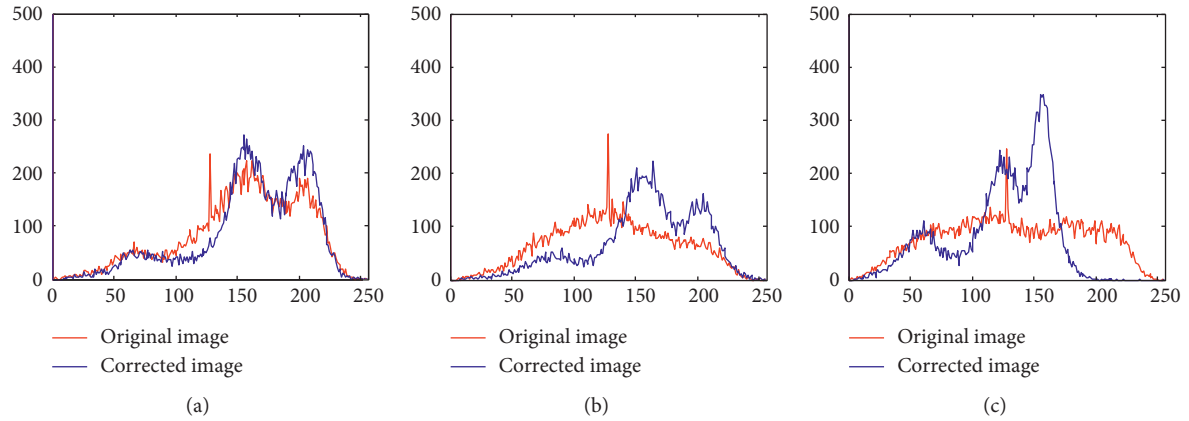

Figure 2: The histogram comparison of original images and corrected images: (a) transaxial slice image, (b) sagittal slice image, and (c) coronal slice image.

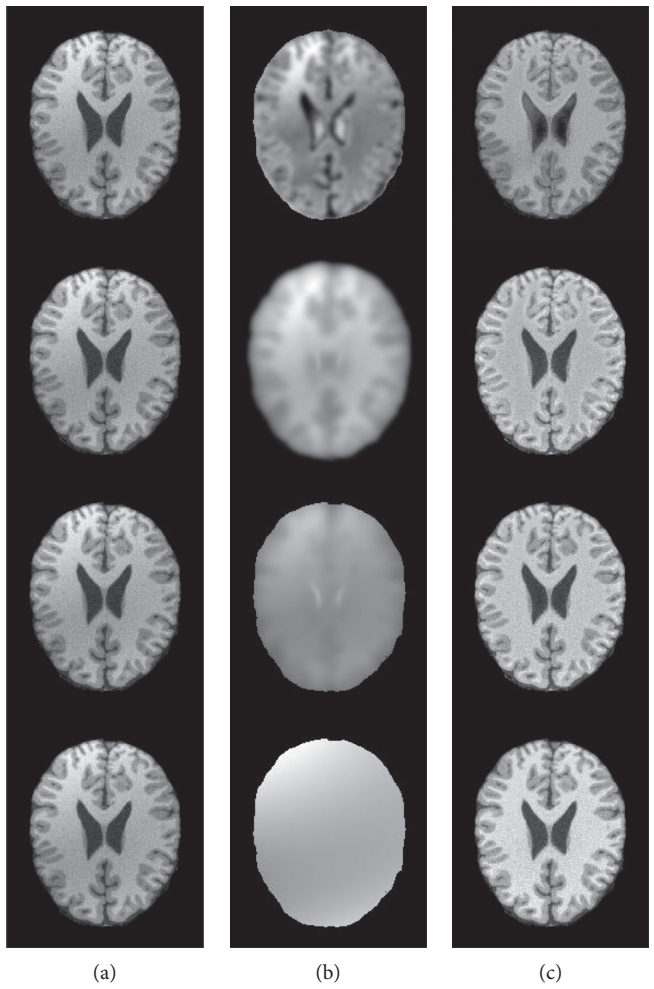

Figure 3: The comparison of bias field estimation by four algorithms: (a) original images, (b) the estimated bias field, and (c) the corrected images.

select four algorithms: standard FCM, BCFCM [23], CLIC [26], and SCFCM [24] as the compared algorithms. The segmentation results are exhibited in Figure 5; Figure 5(a) is a 2D transaxial slice image corrupted by 7% Gaussian noise, and the corresponding classification results by FCM, BCFCM, CLIC, SCFCM, and the proposed method are shown in the Figures 5(b)–5(f), respectively. The segmentation results of FCM, BCFCM, and CLIC are very poor

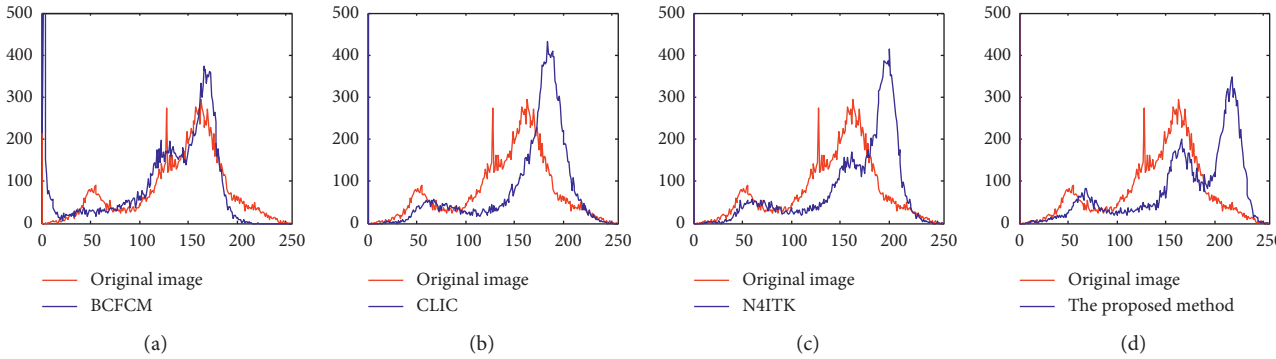

Figure 4: The histogram comparison of original images and corrected images: (a) BCFCM, (b) CLIC, (c) N4ITK, and (d) our method.

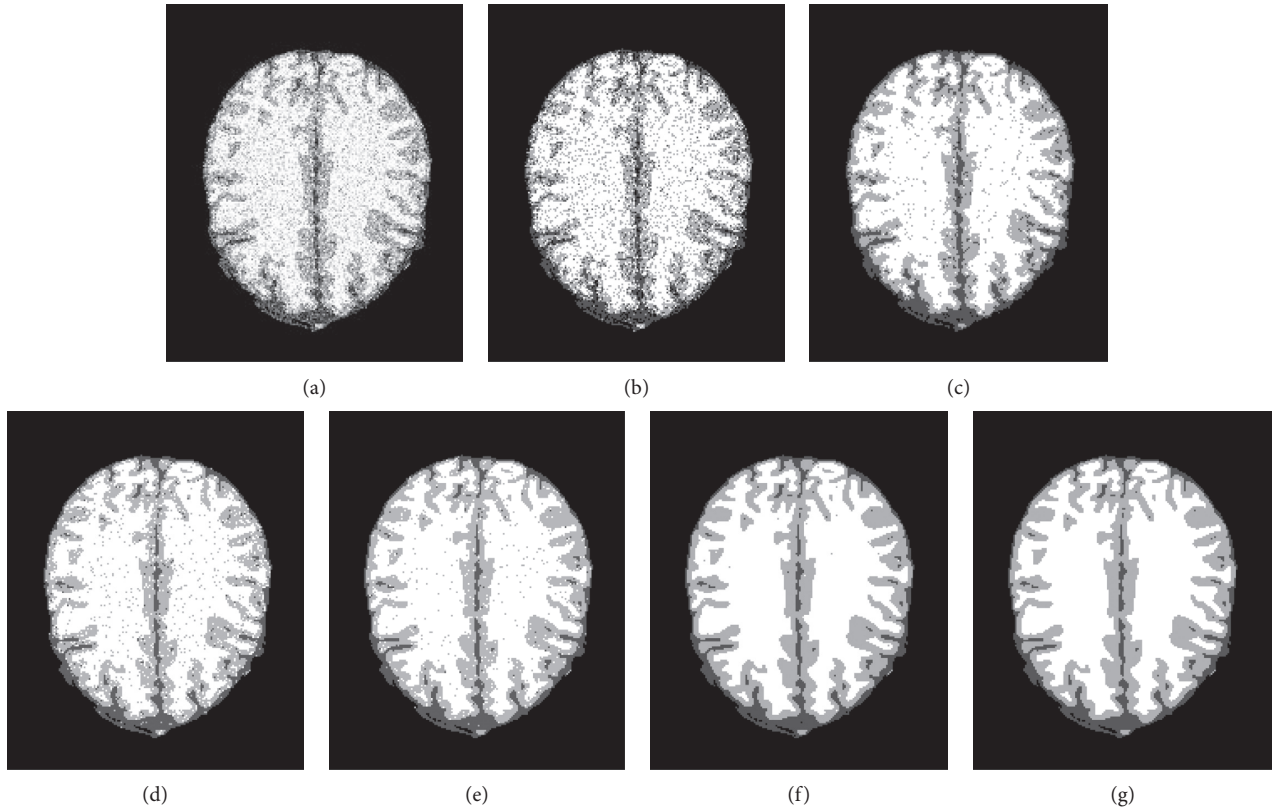

Figure 5: Segmentation results of the 104th transaxial slice by the five algorithms: (a) the noisy MR images, (b) FCM, (c) BCFCM, (d) CLIC, (e) SCFCM, (f) our method, and (g) ground truth.

because many pixels are misclassified; the segmentation result by SCFCM is better than FCM, BCFCM, and CLIC; however, there are still some noisy points that need to be removed. It can be observed that the presented method has more superior segmentation effect than four classical algorithms and can effectively eliminate the influence of the noise. Furthermore, the ability of detail and edge preservation is also compared and analyzed for five algorithms; we select a local region of the MR image to observe by enlarging 3 times, and the detailed images are presented in Figure 6; it is clearly seen that Figure 6(f) is most similar subimage with the ground truth in Figure 6(g), and the vast majority of image details and edge are completely preserved.

In order to further evaluate and compare the antinoise ability of aforementioned five fuzzy clustering algorithms, we choose a brain slice image with 14% additive Gaussian white noise as the test object, as shown in Figure 7. Figure 7(a) is the noisy MR image with bias field, Figures 7(b)–7(f) are the binary images of CSF, WM, and GM after the image is segmented by five algorithms, respectively, and Figure 7(g) is the ground truth. It is clearly seen that the extraction result of each brain tissue of the proposed algorithm significantly outperformed the other algorithms and effectually overcame the disadvantageous defects of intensity inhomogeneity and noise. At the same time, an objective evaluation index JS (Jaccard similarity)

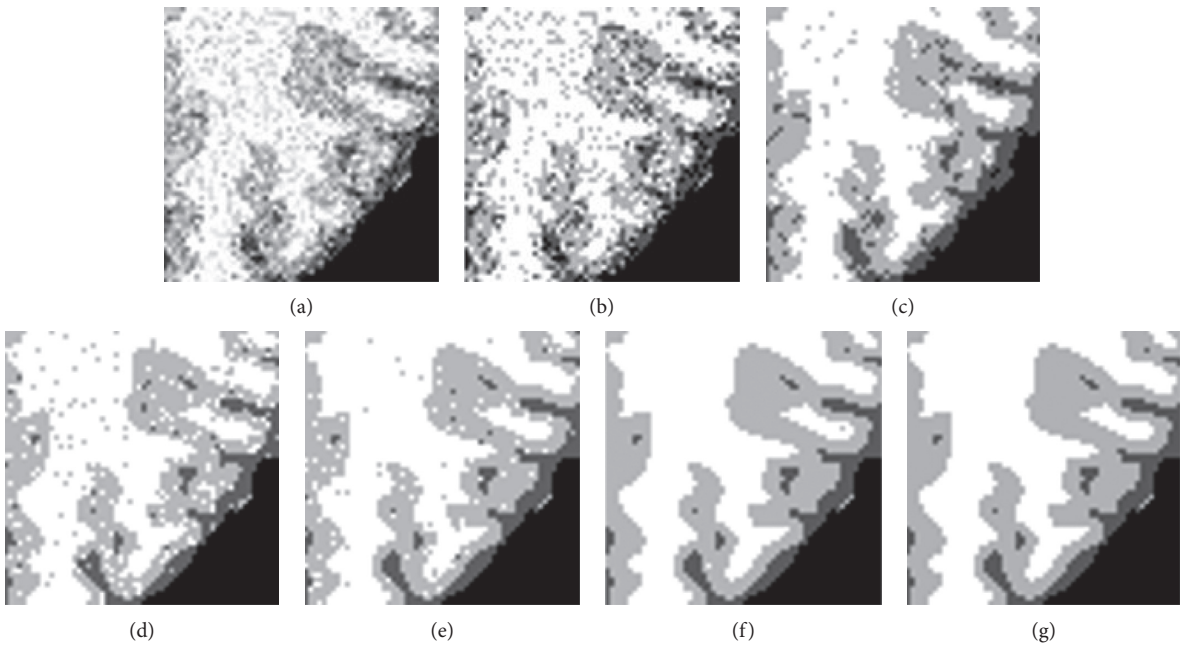

Figure 6: The detailed comparison of the enlarged local region of brain MR image: (a) the noisy MR images, (b) FCM, (c) BCFCM, (d) CLIC, (e) SCFCM, (f) our method, and (g) ground truth.

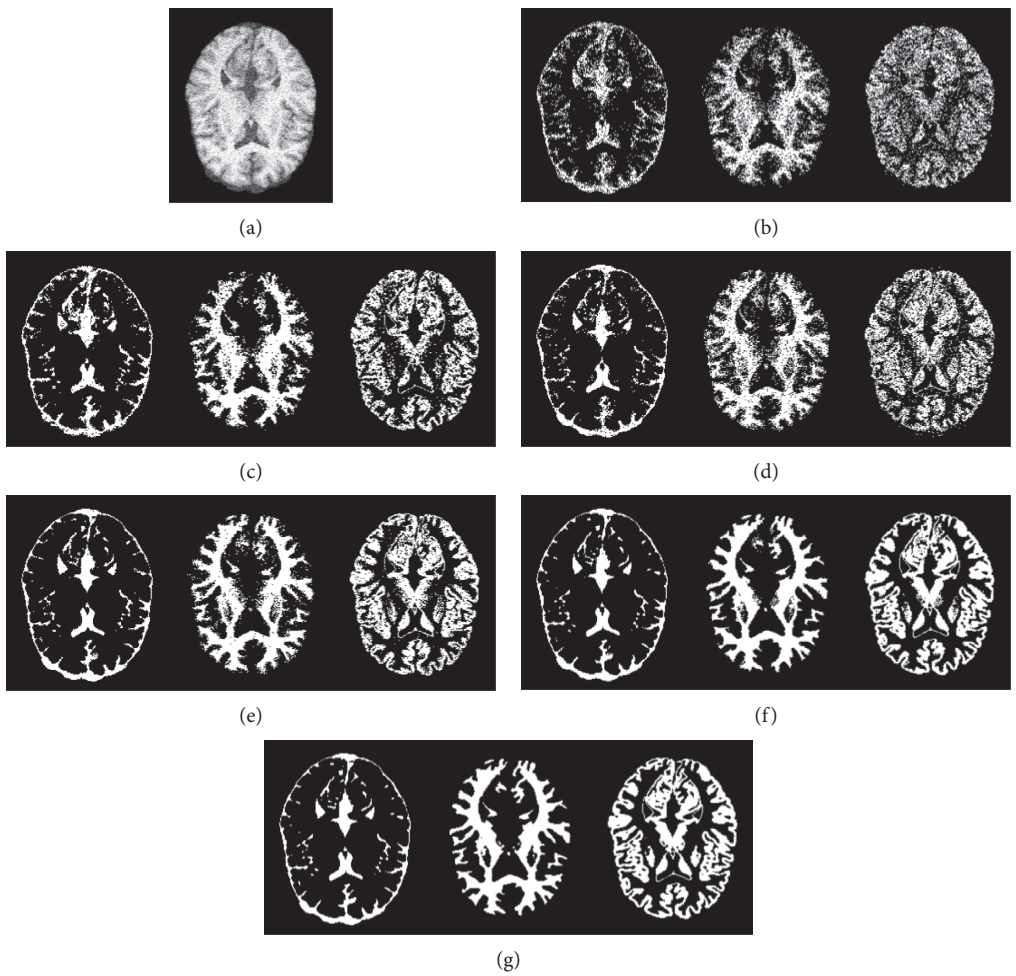

Figure 7: Brain tissue classification results of the five methods on the noisy MR image: (a) original MR image, (b) FCM, (c) BCFCM, (d) CLIC, (e) SCFCM, (f) our method, and (g) ground truth.

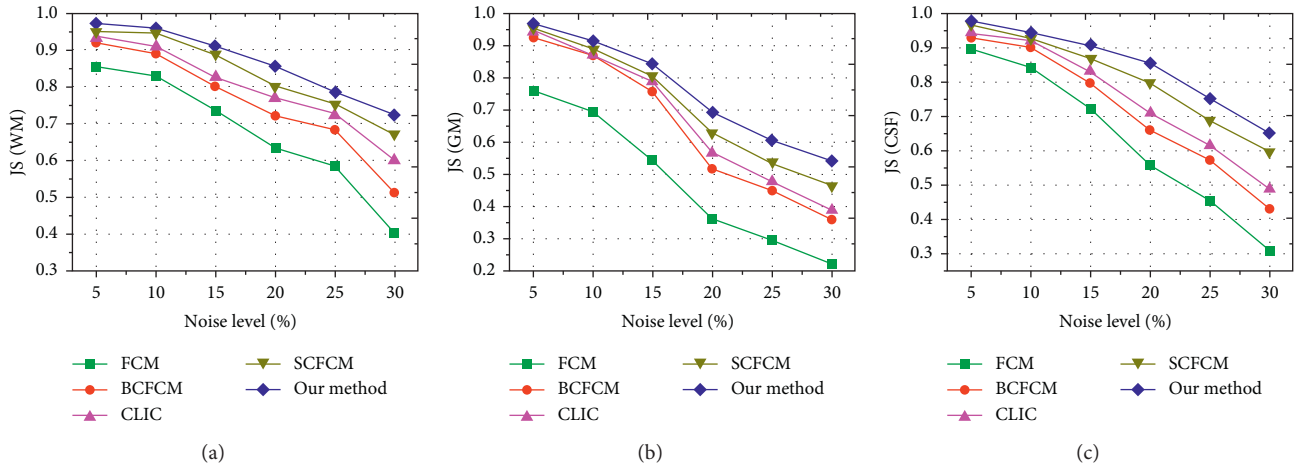

FIGURE 8: JS comparisons of the brain tissue segmentation with different noise level by five algorithms: (a) JS values of WM, (b) JS values of GM, and (c) JS values of CSF.

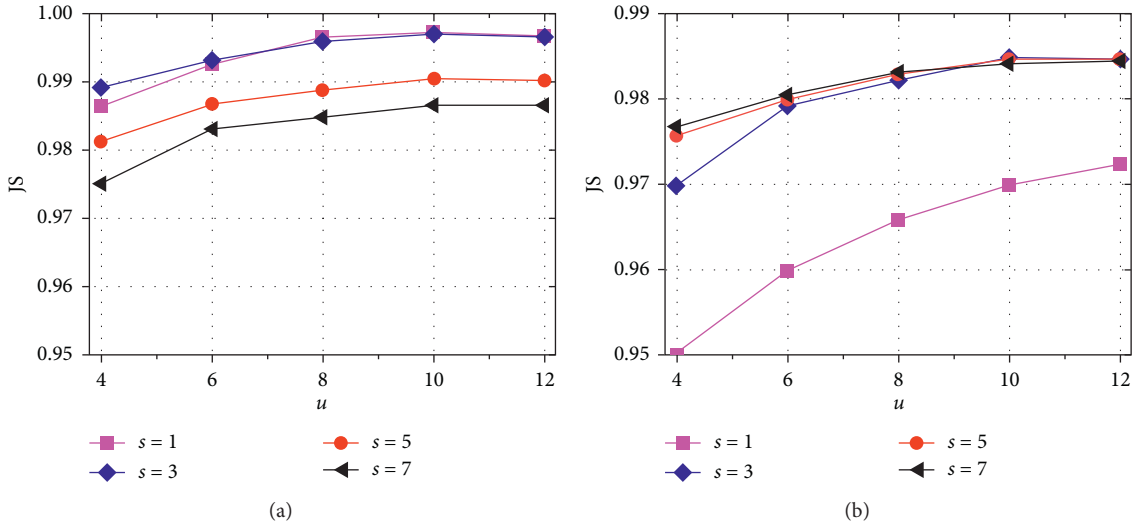

FIGURE 9: JS value under different search window radius u and square neighborhood radius s: (a) curves on the image with 1% noise level and (b) curves on the image with 3% noise level.

[29] is adopted for comparison and quantitative analysis on the different level noise, JS is given as

$$\mathrm{JS}(S_1, S_2) = \frac{|S_1 \cap S_2|}{|S_1 \cup S_2|}, \tag{26}$$

where S_1 represents a set of pixels of the segmented region by a clustering algorithm, S_2 denotes the set of pixels of the corresponding region acquired from the ground truth, $\cap$ denotes the intersection operation, and $\cup$ denotes the union operation. As a quantitative evaluation index, the values of JS belong to the interval of [0, 1], and the higher the JS value is, the better the segmentation performance is. We selected 15 noisy brain MR images with 20% intensity nonuniformity as the experimental objects and the noise level from 5% to 30%. These images are segmented three regions: WM, GM, and CSF by FCM, BCFCM, CLIC, SCFCM, and our method, respectively; JS values comparison results are shown in Figure 8(a)–8(c). It is clearly shown that the presented approach has better matching degree with the ground truth and higher accuracy rate than other four clustering methods.

Then, we evaluate the effect of the search window radius u and the square neighborhood radius s on the performance of the proposed method. Here, we test u and s on the sets {4, 6, 8, 10, 12} and {1, 3, 5, 7}, respectively. In this experiment, the tested images perform 8 independent runs of the algorithm under each pair (u, s), and the noise level is 1% and 3%, respectively. Under each s value, the average JS curve of the algorithm with the increase of u value is shown in Figure 9. It can be found from Figure 9 that the algorithm under $s = 3$ and $u = 10$ can obtain satisfying performance on the noisy images.

In the aforementioned sections, the model is applied in the synthetic brain MR images. Next, this model is also applied to the real clinical images with noise. We selected three normal MR slice images from transaxial, coronal, and

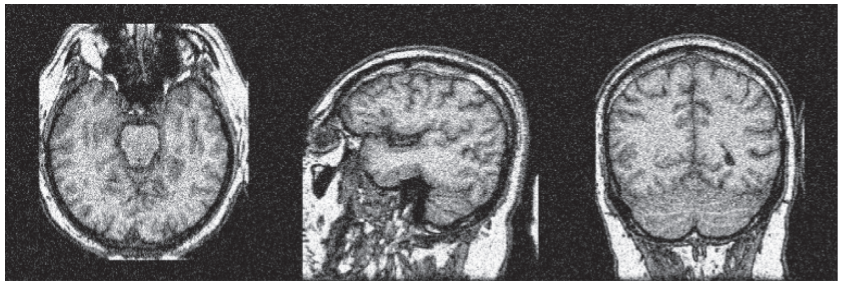

(a)

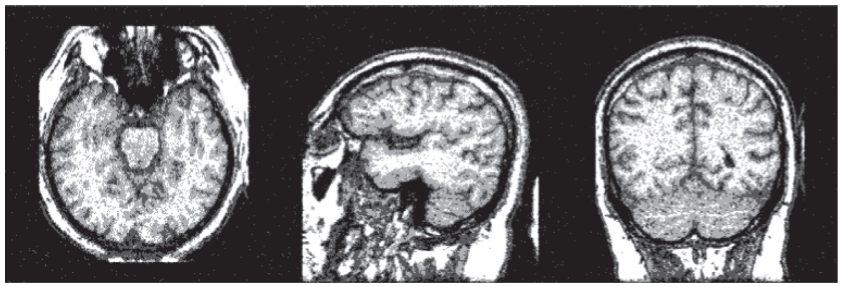

(b)

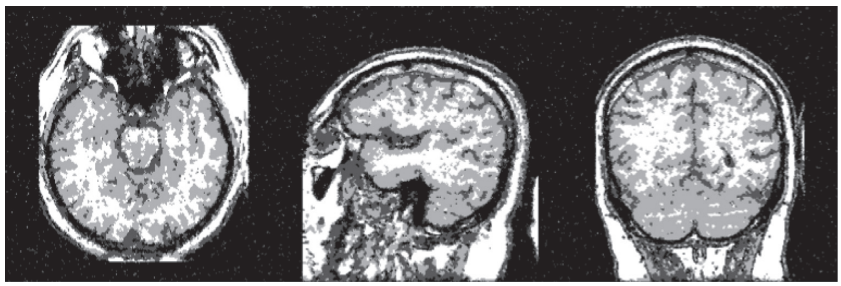

(c)

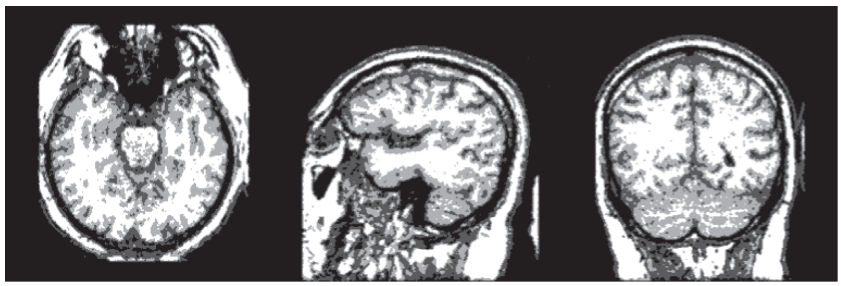

(d)

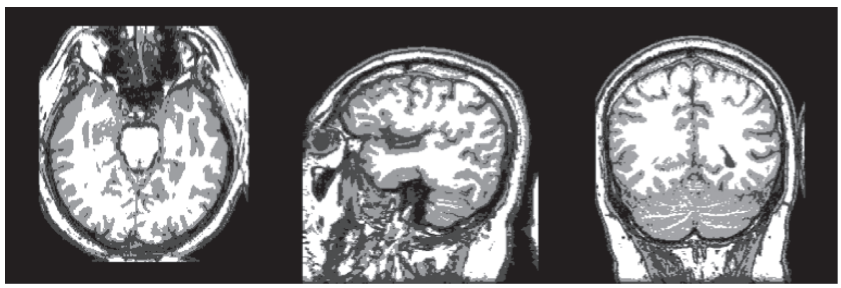

(e)

Figure 10: Experimental results on real MR image: (a) three original images, (b) BCFCM, (c) HMRF-EM, (d) SCFCM, and (e) our method.

sagittal views, and these MR images are obtained from the Whole Brain Atlas clinical MR image database by the Harvard medical school [30]. Figure 10(a) shows three 2D T1-weighted brain MR slice images; the left image is a transaxial slice, the right image is a coronal slice, and the middle image is a sagittal slice. The segmentation results of

brain slice images are given in Figure 10(b)–10(e) by BCFCM, HMRF-EM, SCFCM, and our method, respectively. From the experimental results, it is obvious that the proposed method can effectively segment each brain tissues as well as preserve more detail information of the original MR image. Furthermore, the experimental results of brain tissues in real MR images also further prove the robustness to noise of the proposed method.

5. Conclusion

Brain MR imaging has wide clinical application as an effective medical imaging diagnostic technique; however, the real brain MR images often suffer from some interference such as noise, intensity inhomogeneity, and low contrast. Therefore, a brain tissue classification and nonuniformity field correction scheme in MR images based on spatially coherent FCM with nonlocal constraints is proposed in our study. The available information including local adjacent constraint and nonlocal global information of brain MR image is fully used in our model, and the similarity measure is designed in Gaussian kernel mapping space. Furthermore, the algorithm corrects the bias field of the MR image and improves its antinoise performance. Several experiments on the simulated brain MR images and real brain MR images have demonstrated that the proposed model can effectually overcome the effects of the noise while estimating the bias field existing in brain MR images.

Data Availability

The data used to support the findings of this study are available from the corresponding author upon request.

Conflicts of Interest

The authors declare that there are no conflicts of interest regarding the publication of this paper.

Acknowledgments

This work was partially supported by the Education and Teaching Reform Project of Undergraduate Colleges and Universities in Fujian Province (Grant no. FBJG20180015) and Principal Fund Project of Minnan Normal University (Grant no. KJ18010).

References

[1] S. V. Srinivasan, K. Narasimhan, R. Balasubramaniyam, and S. Rishi Bharadwaj, "Diagnosis and segmentation of brain tumor from MR image," in *Advances in Intelligent Systems and Computing*, pp. 687–693, Springer, Berlin, Germany, 2015.

[2] M. A. Balafar, A. R. Ramli, and S. Mashohor, "Brain magnetic resonance image segmentation using novel improvement for expectation maximizing," *Neurosciences*, vol. 16, no. 3, pp. 242–247, 2011.

[3] J. P. Monaco and A. Madabhushi, "Class-specific weighting for markov random field estimation: application to medical image segmentation," *Medical Image Analysis*, vol. 16, no. 8, pp. 1477–1489, 2012.

[4] M. Xie, J. Gao, C. Zhu, and Y. Zhou, "A modified method for MRF segmentation and bias correction of MR image with intensity inhomogeneity," *Medical & Biological Engineering & Computing*, vol. 53, no. 1, pp. 23–35, 2015.

[5] M. A. Balafar, "Fuzzy C-mean based brain MRI segmentation algorithms," *Artificial Intelligence Review*, vol. 41, no. 3, pp. 441–449, 2014.

[6] Z. Ji, Y. Xia, Q. Chen, Q. Sun, D. Xia, and D. D. Feng, "Fuzzy c-means clustering with weighted image patch for image segmentation," *Applied Soft Computing*, vol. 12, no. 6, pp. 1659–1667, 2012.

[7] J. Aparajeeta, P. K. Nanda, and N. Das, "Modified possibilistic fuzzy C-means algorithms for segmentation of magnetic resonance image," *Applied Soft Computing*, vol. 41, pp. 104–119, 2016.

[8] J. Zheng, D. Zhang, K. Huang, and Y. Sun, "Adaptive image segmentation method based on the fuzzy c-means with spatial information," *IET Image Processing*, vol. 12, no. 5, pp. 785–792, 2018.

[9] W. Pedrycz and J. Waletzky, "Fuzzy clustering with partial supervision," *IEEE Transactions on Systems, Man and Cybernetics, Part B (Cybernetics)*, vol. 27, no. 5, pp. 787–795, 1997.

[10] L. Szilagyi, Z. Benyo, S. M. Szilagyi et al., "MR brain image segmentation using an enhanced fuzzy C-means algorithm," in *Proceedings of International conference of the IEEE engineering in medicine and biology society*, vol. 1, pp. 724–726, Cancun, MX, USA, September 2003.

[11] W. Cai, S. Chen, and D. Zhang, "Fast and robust fuzzy c-means clustering algorithms incorporating local information for image segmentation," *Pattern Recognition*, vol. 40, no. 3, pp. 825–838, 2007.

[12] Z. Ji, J. Liu, G. Cao, Q. Sun, and Q. Chen, "Robust spatially constrained fuzzy c-means algorithm for brain MR image segmentation," *Pattern Recognition*, vol. 47, no. 7, pp. 2454–2466, 2014.

[13] Y. Chen, J. Li, H. Zhang et al., "Non-local-based spatially constrained hierarchical fuzzy C-means method for brain magnetic resonance imaging segmentation," *IET Image Processing*, vol. 10, no. 11, pp. 865–876, 2017.

[14] F. Zhao, "Fuzzy clustering algorithms with self-tuning non-local spatial information for image segmentation," *Neurocomputing*, vol. 106, no. 6, pp. 115–125, 2013.

[15] J. Feng, L. C. Jiao, X. Zhang, M. Gong, and T. Sun, "Robust non-local fuzzy c-means algorithm with edge preservation for SAR image segmentation," *Signal Processing*, vol. 93, no. 2, pp. 487–499, 2013.

[16] J. Ma, D. Tian, M. Gong, and L. Jiao, "Fuzzy clustering with non-local information for image segmentation," *International Journal of Machine Learning and Cybernetics*, vol. 5, no. 6, pp. 845–859, 2014.

[17] J. G. Sled, A. P. Zijdenbos, and A. C. Evans, "A nonparametric method for automatic correction of intensity nonuniformity in MRI data," *IEEE Transactions on Medical Imaging*, vol. 17, no. 1, pp. 87–97, 1998.

[18] N. J. Tustison, B. B. Avants, P. A. Cook et al., "N4ITK: improved N3 bias correction," *IEEE Transactions on Medical Imaging*, vol. 29, no. 6, pp. 1310–1320, 2010.

[19] A. W.-C. Liew and H. Hong Yan, "An adaptive spatial fuzzy clustering algorithm for 3-D MR image segmentation," *IEEE Transactions on Medical Imaging*, vol. 22, no. 9, pp. 1063–1075, 2003.

[20] Z.-X. Ji, Q.-S. Sun, and D.-S. Xia, "A modified possibilistic fuzzy c-means clustering algorithm for bias field estimation and segmentation of brain MR image," *Computerized Medical Imaging and Graphics*, vol. 35, no. 5, pp. 383–397, 2011.

[21] Z. Ji, Q. Sun, Y. Xia, Q. Chen, D. Xia, and D. Feng, "Generalized rough fuzzy c-means algorithm for brain MR image segmentation," *Computer Methods and Programs in Biomedicine*, vol. 108, no. 2, pp. 644–655, 2012.

[22] Z. Ji, Y. Xia, Q. Sun et al., "Fuzzy local Gaussian mixture model for brain MR image segmentation," *IEEE Transactions on Information Technology in Biomedicine*, vol. 16, no. 3, pp. 339–347, 2012.

[23] M. N. Ahmed, S. M. Yamany, N. Mohamed, A. A. Farag, and T. Moriarty, "A modified fuzzy C-means algorithm for bias field estimation and segmentation of MRI data," *IEEE Transactions on Medical Imaging*, vol. 21, no. 3, pp. 193–199, 2002.

[24] I. Despotovic, E. Vansteenkiste, and W. Philips, "Spatially coherent fuzzy clustering for accurate and noise-robust image segmentation," *IEEE Signal Processing Letters*, vol. 20, no. 4, pp. 295–298, 2013.

[25] U. Vovk, F. Pernus, and B. Likar, "A review of methods for correction of intensity inhomogeneity in MRI," *IEEE Transactions on Medical Imaging*, vol. 26, no. 3, pp. 405–421, 2007.

[26] C. Li, C. Xu, A. W. Anderson et al., "MRI tissue classification and bias field estimation based on coherent local intensity clustering: a unified energy minimization framework," in *Proceedings of International Conference on Information Processing in Medical Imaging*, pp. 288–299, Springer-Verlag, Williamsburg, VA, USA, July 2009.

[27] A. Buades, B. Coll, and J. M. Morel, "A non-local algorithm for image denoising," in *Proceedings of IEEE Computer Society Conference on Computer Vision & Pattern Recognition*, pp. 25-26, San Diego, CA, USA, July 2005.

[28] BrainWeb: Simulated Brain Database, 2004, http://brainweb.bic.mni.mcgill.ca/brainweb/.

[29] C. Li, J. C. Gore, and C. Davatzikos, "Multiplicative intrinsic component optimization (MICO) for MRI bias field estimation and tissue segmentation," *Magnetic Resonance Imaging*, vol. 32, no. 7, pp. 913–923, 2014.

[30] A. Keith and M. D. Johnson, The Whole Brain Atlas, http://www.med.harvard.edu/aanlib/.

Hindawi
Computational and Mathematical Methods in Medicine
Volume 2019, Article ID 2123079, 11 pages
https://doi.org/10.1155/2019/2123079

Research Article

Comparing Strategies to Prevent Stroke and Ischemic Heart Disease in the Tunisian Population: Markov Modeling Approach Using a Comprehensive Sensitivity Analysis Algorithm

Olfa Saidi,[1] **Martin O'Flaherty**,[2] **Nada Zoghlami**,[1] **Dhafer Malouche**,[1,3] **Simon Capewell**,[2] **Julia A. Critchley**,[4] **Piotr Bandosz**,[2] **Habiba Ben Romdhane**,[1] **and Maria Guzman Castillo**[2]

[1]*Cardiovascular Epidemiology and Prevention Research Laboratory, Faculty of Medicine of Tunis, University Tunis El Manar, Tunis, Tunisia*
[2]*Department of Public Health and Policy, University of Liverpool, Liverpool, UK*
[3]*National Institute of Statistics and Data Analysis Tunis, Tunis, Tunisia*
[4]*Population Health Research Institute, St George's University of London, London, UK*

Correspondence should be addressed to Olfa Saidi; olfa.saidi@yahoo.fr

Received 25 September 2018; Revised 27 November 2018; Accepted 18 December 2018; Published 29 January 2019

Guest Editor: Giedrius Vanagas

Background. Mathematical models offer the potential to analyze and compare the effectiveness of very different interventions to prevent future cardiovascular disease. We developed a comprehensive Markov model to assess the impact of three interventions to reduce ischemic heart diseases (IHD) and stroke deaths: (i) improved medical treatments in acute phase, (ii) secondary prevention by increasing the uptake of statins, (iii) primary prevention using health promotion to reduce dietary salt consumption. *Methods*. We developed and validated a Markov model for the Tunisian population aged 35–94 years old over a 20-year time horizon. We compared the impact of specific treatments for stroke, lifestyle, and primary prevention on both IHD and stroke deaths. We then undertook extensive sensitivity analyses using both a probabilistic multivariate approach and simple linear regression (metamodeling). *Results*. The model forecast a dramatic mortality rise, with 111,134 IHD and stroke deaths (95% CI 106567 to 115048) predicted in 2025 in Tunisia. The salt reduction offered the potentially most powerful preventive intervention that might reduce IHD and stroke deaths by 27% (−30240 [−30580 to −29900]) compared with 1% for medical strategies and 3% for secondary prevention. The metamodeling highlighted that the initial development of a minor stroke substantially increased the subsequent probability of a fatal stroke or IHD death. *Conclusions*. The primary prevention of cardiovascular disease via a reduction in dietary salt consumption appeared much more effective than secondary or tertiary prevention approaches. Our simple but comprehensive model offers a potentially attractive methodological approach that might now be extended and replicated in other contexts and populations.

1. Background

Cardiovascular diseases (CVDs) cause nearly one-third of all deaths worldwide. 80% of these deaths occur in low-income and middle-income countries. Ischemic heart diseases (IHD) and stroke account for the greatest proportion of CVDs [1–3].

The burden of IHD and stroke is considerable, and they are the first and second leading causes of death, respectively, worldwide [4, 5]. They accounted for 15.2 million deaths (15.0 million to 15.6 million) in 2015 [4]. According to the World Health Organization (WHO), there are 15 million people worldwide who suffer from stroke each year, among them, 5 million die and another 5 million are left permanently disabled, causing a heavy burden for the family and community.

The burden of stroke will increase significantly over the next 20 years, particularly in developing countries [6]. Thus,

the analysis of the effectiveness of health promotion interventions is urgently required for appropriate planning to reduce this burden [7].

Traditional epidemiological study designs cannot address these issues; even clinical trials are usually restricted by inclusion and exclusion criteria and not necessarily generalizable to the entire population [8].

Mathematical modeling overcomes many of these limitations. It plays a crucial role in helping to guide the most effective and cost-effective ways to achieve the goals of health promotion, designed and validated to guide health policies and development strategies at several levels [9, 10].

Briefly, a model is a simplification of a real situation and can encompass a simple, descriptive tool up to systems of mathematical equations [11].

The application of mathematical models in medicine has proved useful and has become more frequent, especially for cardiovascular diseases (CVDs) [12–16] and assessing potential impacts of policies or interventions designed to alter disease trajectories in Tunisia [17, 18].

A commonly used technique is Markov modeling, an approach that models groups of individuals transitioning across specified pathways, informed by transition probabilities [18–20].

Due to the frequent uncertainty of the Markov model's inputs, sensitivity analyses to assess the robustness of the model results are strongly recommended by modeling guidelines. Such uncertainty analyses assess confidence in a chosen course of action and ascertain the value of collecting additional information to better inform the decision [21].

Our study aims (i) to describe a comprehensive Markov model based on both a probabilistic multivariate approach and simple linear regression metamodeling and (ii) using the model to evaluate the effects of increases in uptake of stroke treatments lifestyle changes and primary prevention among the Tunisian population aged 35–94 years old in 2025. We examined three interventions: (a) improved medical treatments in the acute phase, (b) secondary prevention of stroke by increasing the prescribing of statins, and (c) primary prevention aiming to reduce salt intake.

2. Methods

In this study, we describe the development of a Markov IHD and stroke model.

2.1. Definition of Markov Model. Markov models are a type mathematical model based on matrix algebra which describes the transitions a cohort of patients make among a number of mutually exclusive and exhaustive health states during a series of short intervals or cycles. In this model, a patient is always in one of the finite number of health states; events are modeled as transitions from one state to another and contribution of utility to overall prognosis depend on length of time spent in health states [19]. The components of a Markov model are shown below (Figure 1):

(i) States: the set of distinct health states under consideration in the model, together with the possible transitions between them.

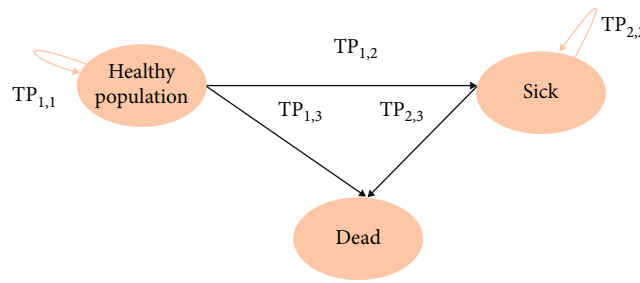

Figure 1: Markov diagram states and transition probabilities (each circle represents a Markov state and arrows indicate transition probabilities).

(ii) Cycle length: the length of time represented by a single stage (or cycle) in a Markov process: Markov models are developed to simulate both short-cycle and long-term processes (e.g., cardiovascular diseases).

(iii) Transition probabilities: the matrix of probabilities of moving between health states from one stage to the next.

2.2. Process of Mathematical Modeling Based on Markov Approach. Before starting the data collection and the calculation, we first defined our model by specifying the different states that can be included based on the literature and expert opinions:

$$S = \{S_1, S_2, \ldots, S_3\}, \text{ set of states in the process.} \quad (1)$$

Having specified the structure of the model in terms of the possible transitions between states, we defined the transition probabilities based on available data.

The transition probability (TP_{ij}) is defined as a conditional probability ($P_t(s_j/s_i)$) of making a transition (moving) from state i to state j during a single cycle (t). Additionally, transition probabilities are stratified by sex and age groups $a_g \in \{c_1, c_2, \ldots, c_g\}$, where $c_1, c_2, \ldots, c_g$ represents a set of age groups [19, 22].

One of the goals of the Markov model is to study the potential effects of some health promotion interventions. We modeled first a baseline scenario and then the intervention scenarios.

For the baseline scenario, we assumed no change will happen during the period "T" of study (20 years) in either the present uptake rates of medical therapies or population level uptakes of specific nutrients.

Based on the model structure in Figure 1, we assume that we will apply three interventions to study their impact on mortality in the future (over the 20 years: from t = year 1 to year 20).

We define a policy $\Pi = (I_0, I_1, I_2, I_3)$ as a set of the health promotion interventions.

I_0 refers the baseline scenario: we assumed no change will happen during 20 years.

I_1: scenario aimed to improve medical treatments in acute phase.

I_2: scenario for secondary prevention.

I_3: scenario for primary prevention.

Starting by the baseline scenario, the process of the Markov model is based on the two first steps below:

Step I. Calculate probabilistic transition probabilities

Probabilistic sensitivity analysis aims to fully evaluate the combination of uncertainty in all model inputs (including transition probabilities) simultaneously on the robustness of model results.

The point estimates in the model can be replaced with probability distributions, where the mean of the distribution reflects the best estimate of the parameter.

In this step, each input parameter (TP_{ij}) is assigned an appropriate statistical distribution, and a Monte Carlo simulation is run multiple times (e.g., 1000). The iteration is stopped when the difference of the outcomes is sufficiently small.

We assume for example that TPs follow the distribution defined by beta (α, β), where α probability distributions are defined on the interval [0, 1] parameterized by two positive shape parameters, denoted by α and β, that appear as exponents of the random variable and control the shape of the distribution [23].

Step II. Calculate the number of people in each state for the baseline scenario

The next step is to define the number of people in each state based on the TPs between states and the number of people in the starting state "healthy people."

In this stage, we define the number of people in each state for the baseline scenario (healthy people (NHP), sick (NS), and deaths (ND)) for all gender and age groups from t = year 1 to year T, given by the following equations:

$$\begin{aligned} \mathrm{NHP}_t &= \mathrm{NHP}_{t-1} \times \left(1 - \sum \mathrm{TP}_{i,j}\right), \\ \mathrm{NS}_t &= \mathrm{NS}_{t-1} + \left(\mathrm{NHP}_{t-1} \times \mathrm{TP}_{1,2}\right), \\ \mathrm{ND}_t &= \mathrm{ND}_{t-1} + \left(\mathrm{NHP}_{t-1} \times \mathrm{TP}_{1,3}\right) + \left(\mathrm{NS}_{t-1} \times \mathrm{TP}_{2,3}\right). \end{aligned} \tag{2}$$

Another indicator can be calculated based on this model, that is, life years gained (LY) defined by the following equation:

$$\mathrm{LY}_t = \mathrm{NHP}_t - \mathrm{ND}_t. \tag{3}$$

The model is then run several times (e.g., 1000 simulations). For each simulation model, parameter values are randomly drawn from each of the distributions, and the expected model outcome is recorded. The 1000 simulations result in a distribution of expected model outcomes (e.g., deaths), which reflects the overall parameter uncertainty in the mode [24].

At the end of the simulation, the mean as well as the lower bound (LB) and upper bound (UB) of 95% confidence interval of the inputs and outputs will be calculated, which correspond to Steps I and II presented in Algorithm 1.

Step III. Calculate the number of people in each state for the interventions scenarios

For the interventions scenarios, the model required a base estimate of risk reduction in deaths and the age effect to calculate policy effectiveness (Π_e^{Ii}) of each intervention.

The policy effectiveness is defined by the following formula:

$$\prod_e^{Ii} = 1 - \left(\mathrm{RR}_i \times a_e\right), \tag{4}$$

where RR_i is the risk reduction associated with the intervention $I_{i(i=1:3)}$ obtained from previous randomized controlled trials and meta-analyses to estimate the reduction in age-specific deaths and a_e represents the age effects for each intervention risk reduction value. Π_e^{Ii} is then used to scale the transition probabilities connected to death states.

In this stage, after recalculating the TPs, we define the number of people in each state (healthy people (NHP^{Ii}), sick (NS^{Ii}), and deaths (ND^{Ii}) for all sex and age groups from t = year 1 to year T for the interventions scenarios I_i, given by the following equations:

$$\begin{aligned} \mathrm{NHP}_t^{li} &= \mathrm{NHP}_{t-1}^{li} \times \left(1 - \mathrm{TP}_{1,2} - \mathrm{TP}_{1,3} \times \prod_e^{Ii}\right), \\ \mathrm{NS}_t^{li} &= \mathrm{NS}_{t-1}^{li} + \left(\mathrm{NHP}_{t-1}^{li} \times \mathrm{TP}_{1,2}\right), \\ \mathrm{ND}_t^{li} &= \mathrm{ND}_{t-1}^{li} + \left(\mathrm{NHP}_{t-1}^{li} \times \mathrm{TP}_{1,3}\right) + \left(\mathrm{NS}_{t-1}^{li} \times \mathrm{TP}_{2,3} \times \prod_e^{Ii}\right), \\ \mathrm{LY}_t^{li} &= \mathrm{NHP}_t^{li} - \mathrm{ND}_t^{li}. \end{aligned} \tag{5}$$

Step IV. Calculate the final outputs (DPPs and LY)

Finally, we calculate the total number of CVD deaths (ischemic stroke and IHD deaths) that could be prevented or postponed (DPPs) and the life years gained (LY) under each specific scenario (equations (6) and (7)), compared to the baseline scenario for all sex and age groups from t = year 1 to year T for the interventions scenarios I_i.

$$\mathrm{DPP}_{s_t}^{li} = \mathrm{ND}_t^{li} - \mathrm{ND}_t^{l0}, \tag{6}$$

$$\mathrm{LY}_{g_t}^{li} = \mathrm{LY}_t^{li} - \mathrm{LY}_t^{l0}. \tag{7}$$

Step V. Linear regression metamodeling

Most current modeling studies are limited to the first four stages and ignore this important step of metamodeling to analyze which model inputs are most influential in affecting the results. The goal of metamodeling was thus to increase the transparency of decision-making analytic models and better communicate their results.

This step is based on the application of a simple linear regression metamodel (LRM) for the optimal policy (Figure 2) [25].

Step I. Calculate probabilistic transition probabilities
for all $k \in \{1\,\text{Male}, 2\,\text{Female}\}$ do
  for all age groups $a_g \in \{c_1, c_2, \ldots, c_g\}$ do
  for $t = 1.....T$ do
    $T_{Pi,j} \longleftarrow \text{beta}(\alpha_{i,j}, \beta_{i,j})$
  end for
  end for
end for
Step II. Calculate the number of people in each state NHP, NS, and ND (Baseline scenario)
for all $k \in \{1\,\text{Male}, 2\,\text{Female}\}$ do
  for all age groups $a_g \in \{c_1, c_2, \ldots, c_g\}$ do
  for $t = 1.....T$ do
    $\text{NHP}_t = \text{NHP}_{t-1} \times (1 - \sum \text{TP}_{i,j})$
    $\text{NS}_t = \text{NS}_{t-1} + (\text{NHP}_{t-1} \times \text{TP}_{1,2})$
    $\text{ND}_t = \text{ND}_{t-1} + (\text{NHP}_{t-1} \times \text{TP}_{1,3}) + (\text{NS}_{t-1} \times \text{TP}_{2,3})$
    $\text{LY}_t = \text{NHP}_t + \text{ND}_t$
  end for
  end for
end for
Step III. Calculate the number of people in each state for the interventions scenarios
for all $k \in \{1\,\text{Male}, 2\,\text{Female}\}$ do
for all age groups $a_g \in \{c_1, c_2, \ldots, c_g\}$ do
  for all intervention $I_i \in \Pi = (I_1, \ldots, I_3)$ do
    $\Pi_e^{Ii} = 1 - (\text{RR}_i \times a_e)$ where RR_{I_i} is the intervention risk reduction value and a_e its age effects
    for $t = 1 \ldots T$
      $\text{NHP}_t^{li} = \text{NHP}_{t-1}^{li} \times (1 - \text{TP}_{1,2} - \text{TP}_{1,3} \times \Pi_e^{Ii})$
      $\text{NS}_t^{li} = \text{NS}_{t-1}^{li} + (\text{NHP}_{t-1}^{li} \times \text{TP}_{1,2})$
      $\text{ND}_t^{li} = \text{ND}_{t-1}^{li} + (\text{NHP}_{t-1}^{li} \times \text{TP}_{1,3}) + (\text{NS}_{t-1}^{li} \times \text{TP}_{2,3} \times \Pi_e^{Ii})$
      $\text{LY}_t^{li} = \text{NHP}_t^{li} - \text{ND}_t^{li}$
    end for
end for
  end for
end for
Step IV. Calculate the final outputs (DPPs and LY)
for all $k \in \{1\,\text{Male}, 2\,\text{Female}\}$ do
  for all age groups $a_g \in \{c_1, c_2, \ldots, c_g\}$ do
  for all intervention $I_i \in \Pi = (I_1, \ldots, I_3)$ do
    $\text{DPP}_{s_t}^{li} = \sum_1^T \text{ND}_t^{li} - \text{ND}_t^{l0}$
    $\text{LY}_{g_t}^{li} = \sum_1^T \text{LY}_t^{li} - \text{LY}_t^{l0}$ end for
  end for
  end for
end for
Step V. Linear regression metamodeling
Calculate the $\beta_{i,j}$ coefficients of the parameters
for all $k \in \{1\,\text{Male}, 2\,\text{Female}\}$ do
  for all age groups $a_g \in \{c_1, c_2, \ldots, c_g\}$ do
    Solve the equation $\text{ND} = \beta_0 + \beta_{i,j}\text{TP}_{i,j} + \varepsilon$
  end for
end for

Algorithm 1: Comprehensive algorithm of the Markov model and of sensitivity analysis.

The original motivation for metamodeling was to define a simpler mathematical relationship between model outputs and inputs than the actual model.

The LRM is defined by the following formula:

$$\text{ND} = \beta_0 + \beta_{i,j}\text{TP}_{i,j} + \varepsilon, \tag{8}$$

where ND is the number of deaths (output of the model); β_0 (the intercept) is the expected outcome when all parameters are set to zero; $\text{TP}_{i,j}$, the transition probabilities (inputs); $\beta_{i,j}$, the other coefficients, are interpreted relative to a 1-unit change in each parameter on the original scales; and ε is the residual term.

Furthermore, the absolute value of the coefficients of the parameters "$\beta_{i,j}$" can be used to rank parameters by their importance: the higher the coefficient is, the more the variable is important and relevant.

The algorithm below summarizes the process with three states that could be generalized to n states depending on the context to study (Algorithm 1).

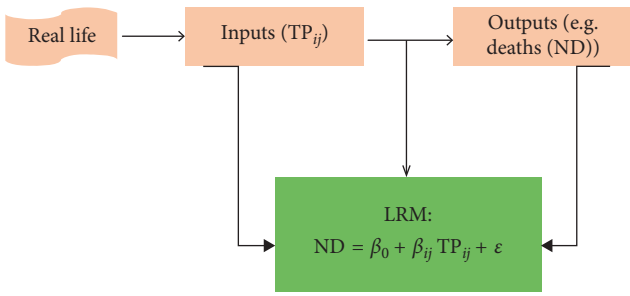

Figure 2: Simple linear regression metamodel (LRM) to summarize the relationship between model inputs and outputs.

2.3. Case Study. The algorithm introduced above has been implemented using R (Version R.3.2.0.) software and applied on Tunisian data. The source codes are available from the authors upon request.

Our model predicts both IHD and stroke deaths in 2025 among the Tunisian population aged 35–94 years old, both men and women, and compares the impact of specific treatments for stroke, lifestyle changes, and primary prevention.

2.4. Model Structure. Data were integrated and analyzed using a closed cohort model based on a Markov approach, with transition probabilities starting from population free of ischemic stroke and moving to health states reflecting the natural history of ischemic stroke [26, 27]. Therefore, the starting states are defined by the size of the population and the number of strokes occurring within this population. The number of persons moving from the starting states to the stroke and death states is estimated by the transition probabilities (Table 9 in the appendix in the supplementary materials).

There are two absorbing states: IHD and stroke deaths and non-IHD and stroke deaths as competing risks for mortality. IHD and stroke have several risk factors in common; increased salt intake is associated with hypertension which is one of the major risk factors for both stroke and IHD. Therefore, any policy aimed at decreasing population level's intake of salt will reduce the risk of both diseases [28].

Potential overlaps between the healthy, minor, major stroke, and deaths are managed by calculating the conditional probabilities of membership. A key element of the model is the calculation of the transition probabilities (TPs), particularly those related to stroke and IHD mortality (Figure 3). The TP calculations are detailed in Table 10 in the Appendix in the supplementary materials.

2.5. Baseline Scenario. In the baseline scenario, we assumed there would be no change over the 20-year model period in the present uptake rates of acute phase medical treatments (thrombolysis, aspirin, and stroke unit) or treatments for secondary prevention following stroke (aspirin, statin, anticoagulants, blood pressure control, and smoking cessation) or treatment and policies for primary prevention (blood pressure control, glucose control, lipid lowering, salt uptake, and smoking cessation).

2.6. Prevention Scenarios. In this paper we evaluated the following three scenarios:

(1) I_1: the first scenario aimed to improve medical treatments in the acute phase: increasing thrombolysis prescribing from 0% to 50% and hospitalization in stroke units from 10% to 100% in Tunisia.

(2) I_2: the second scenario aimed to act on medical treatments after a stroke: increasing the prescribing of statins from 11% to 100% (secondary prevention).

(3) I_3: the third scenario aimed to reduce the consumption of salt by 30%, from 14 grams to 9 grams per day (primary prevention).

Total policy refers to the combined effects of all the three previous strategies: acute treatment + secondary prevention + primary prevention.

2.7. Modeling Policy Effectiveness and Its Impact in Mortality. The model applies the relative risk reduction (RRR), as mentioned in the algorithm above, quantified for each intervention scenario in previous randomized controlled trials and meta-analyses based on international studies (data are detailed in the Appendix in the supplementary materials (Table 8)).

2.8. Data Sources. Published and unpublished data were identified by extensive searches, complemented with specifically designed surveys. Data items included (i) number of stroke patients (minor and major), (ii) uptake of specific medical and surgical treatments, (iii) population data in the initial study year (2005) and (iv) mortality data (after one year (data in 2006) and after 5 years (data in 2010)). Data sources are detailed in Appendixin the supplementary materials.

2.9. Model Outputs. The outputs of this model are the prediction of stroke and IHD deaths prevented or postponed (DPPs) and the life years gained (LY) among the Tunisian population aged 35–94 years old starting from 2005 over a twenty-year time period(to 2025) with and without possible interventions to reduce this mortality.

We modeled all the intervention scenarios to calculate the total number of CVD deaths (ischemic stroke and IHD deaths) that may be prevented or postponed and the LY for each specific scenario compared to the baseline scenario.

3. Results

3.1. Baseline Scenario. In the baseline scenario, the model forecast 111140 [95% CI 106570 to 115050] IHD and ischemic stroke deaths for people aged 35–94 years between 2005 and 2025, including 68890 [95% CI 65730 to 72350] among men and 42250 [95% CI 38840 to 44600] among women.

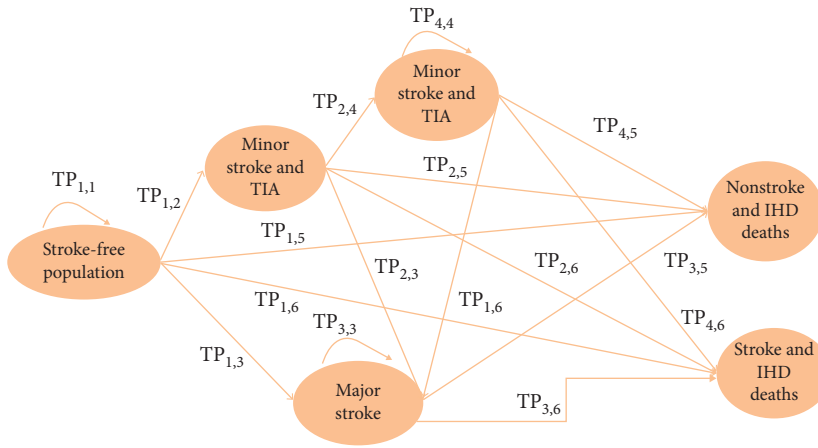

Figure 3: Stroke model structure. TIA: transient ischemic attack; IHD: ischemic heart diseases.

The model estimated that the acute stroke treatment and secondary prevention following stroke would, respectively, prevent 230 [95% CI 200 to 260] deaths due to stroke and IHD and 1920 [95% CI 1830 to 2000] in 2025, whilst primary prevention could prevent 20330 [95% CI 20050 to 20610] cumulative deaths due to stroke and IHD in 2025.

In terms of life years, 150 [95% CI 130 to 180] and 2390 [95% CI 2300 to 2490] would be gained in 2025 by acute stroke treatment and secondary prevention, respectively, whereas for primary prevention (blood pressure control, glucose control, lipid lowering, and smoking cessation), 14590 [95% CI 14350 to 14820] life years would be gained in 2025 (Table 1).

3.2. Scenario Projections

3.2.1. Improvement on Acute Stroke Treatment. If we adopt a strategy to increase thrombolysis uptake from 0% to 50% and stroke units use from 10% to 100%, 600 [95% CI 550 to 650] fewer deaths could be achieved by 2025 (Table 2).

In terms of life years, 370 [95% CI 330 to 410] would be gained in 2025 by increasing thrombolysis uptake (Figure 4).

3.2.2. Improvement on Secondary Prevention. If the uptake of statins for secondary prevention following stroke could be increased from 11% to 100%, 3300 [95% CI 3190 to 3410] fewer deaths could be avoided by 2025 (Table 2).

In terms of life years, 4120 [95% CI 4000 to 4250] would be gained in 2025 (Figure 4).

3.2.3. Food Policies. If the Tunisian government implemented a strategy recommended by the WHO to reduce the daily consumption of salt by 30 % (from 14 g/day to 9 g/day), 30240 [95% CI 29900 to 30580] deaths could be avoided by this scenario in 2025 (Table 2). This results in 20630 [95% CI 20350 to 20910] life year gain by 2025 (Figure 4).

3.3. Linear Regression Metamodeling of the Optimal Policy. The table below shows the results of linear regressing parameters on the stroke and IHD deaths prevented or postponed (DPPs) by the salt reduction intervention. The R^2 is 0.8999, suggesting that 89. 99% of the variance in the model outcomes is explained by our model (Table 3).

Figure 5 shows the five first important parameters based on the absolute value of the coefficients of the parameters. In our case study, the uncertainty of the probability of minor stroke in the first year has the greatest impact on the stroke and IHD deaths estimates associated with salt reduction, followed by the probability of the stroke-free population to die from stroke and IHD causes in the year 1 and the probability of recurrent stroke in ischemic stroke patients after one year. Although the main objective of the meta-regression is to identify the most important parameters of the model, it could also serve to give a rough idea of the size of the effect of each parameter. We know that for each unit increase in the independent variable, our outcome should increase by $\widehat{I}^2$ units. For example, the probability for the stroke-free population to have first stroke in the year 1 has an absolute coefficient of 646.35; this means that for each 10% risk increase in this probability, strokes and IHD will increase by 65 IHD and stroke deaths. However, this should be interpreted with caution since the meta-analysis regression model assumes a linear relationship between outcomes and inputs which is not the case in a Markov model (Figure 5).

4. Discussion

In this study, we have developed a simple but comprehensive Markov model and used it to identify key factors that predict mortality from stroke and IHD in Tunisia in the future, as well as the potential impacts of some medical and health policies.

Different mathematical models have been highly used in medical decision making [19, 29–32], but the technique of metamodeling is less developed in medicine. It has been used to identify the importance of variables that can justify the best medical decisions among pregnant women with deep vein thrombosis [33]. Additionally, linear regression metamodels have also been used in some epidemiological studies [25, 34].

Table 1: Life years and deaths due to stroke and IHD estimations in 2025 keeping the same practices of 2005 by gender.

	Life years [95% CI]	Stroke and IHD deaths [95% CI]
Men		
Acute stroke treatment	80 [70 to 100]	−140 [−170 to −120]
Secondary prevention following stroke	1500 [1420 to 1580]	−1170 [−1240 to −1110]
Primary prevention	12180 [11960 to 12400]	−16760 [−17020 to −16510]
Policy total*	6830 [6700 to 6990]	−8530 [−8710 to −8340]
Women		
Acute stroke treatment	60 [50 to 80]	−80 [−100 to −70]
Secondary prevention following stroke	860 [800 to 920]	−720 [−770 to −670]
Primary prevention	2410 [2310 to 2510]	−3570 [−3690 to −3450]
Policy total*	3730 [3610 to 3850]	−4860 [−5000 to −4720]
Both		
Acute stroke treatment	150 [130 to 1804]	−230 [−260 to −200]
Secondary prevention following stroke	2390 [2300 to 2490]	−1920 [−2000 to −1830]
Primary prevention	14590 [14350 to 14820]	−20330 [−20610 to −20050]
Policy total*	10560 [10360 to 10770]	−13380 [−13610 to −13160]

*Total policy refers to the combined effects of all the three previous strategies: acute treatment + secondary prevention + primary prevention.

Table 2: Life years and deaths due to stroke and IHD by incorporating strategies in 2025 by gender.

	Stroke and IHD deaths [95% CI]
Men	
Acute stroke treatment	−350 [−390 to −310]
Secondary prevention following stroke	−2060 [−2150 to −1970]
Primary prevention	−24500 [−24810 to −24200]
Policy total	−23940 [−24240 to −23640]
Women	
Acute stroke treatment	−220 [−250 to −190]
Secondary prevention following stroke	−1240 [−1310 to −1170]
Primary prevention	−10630 [−10830 to −10430]
Policy total	−17050 [−17300 to −16800]
Both	
Acute stroke treatment	−600 [−650 to −550]
Secondary prevention following stroke	−3300 [−3410 to −3190]
Primary prevention	−30240 [−30580 to −29900]
Policy total*	−40990 [−41390 to −40600]

*Total policy refers to the combined effects of all the three previous strategies: acute treatment + secondary prevention + primary prevention.

This analysis is the first modeling study of stroke and IHD mortality in Tunisia, based on a rigorous and comprehensive modeling approach consisting of three stages:

(i) Apply the Markov model in medical and strategic decision making.

(ii) Provide a probabilistic sensitivity analysis.

(iii) Use a linear regression metamodeling for the optimal policy.

This model has several strengths. First it requires multiple epidemiological national data on ischemic stroke and demographics. In general, the data used in the model were of good quality. However, some assumptions were necessary to fill gaps in the missing information. We made transparent assumptions with clear justification (see Appendix in the supplementary materials).

Another advantage characterizing our approach and differentiating it from the univariate traditional method of deterministic sensitivity analysis is that it allows varying all the parameters of the model simultaneously and thus exploring the whole parameter space. The use of only one-way sensitivity analyses is limited compared with multiway analyses [35].

Furthermore, to increase the transparency of decision-making analytic models, we have used metamodeling in this study by applying a simpler mathematical relationship between model outputs and inputs to analyze which are the most influential inputs on the output.

Our metamodeling approach summarizes the results of the model studied in a transparent way and reveals its important characteristics.

The intercept of the regression result is the expected outcome when all parameters are set to zero. The other coefficients are interpreted relative to a 1-unit change in each parameter on the original scales. For example, in our case, changing the risk of the first minor stroke in the first year from the actual value to 1 increases the number of stroke and IHD deaths by 646 deaths. In addition, the regression coefficients describe the relative importance of the uncertainty in each parameter. And the use of the linear metamodeling regression method can overcome the limitations of other traditional statistical methods [36].

In addition, models often ignore the interaction effect between the input parameters of a model when defining the results. However, in our study, the use of conditional probabilities allows us to take into account interactions in our algorithm.

We also analyzed, in parallel of the deaths prevented or postponed (DPPs), the life years gained according to the different scenarios. Thus, our approach allows interpreting two key indicators in epidemiology via a rigorous and comprehensive mathematical algorithm.

Nevertheless this modeling approach has also some limitations; in fact, a major limitation of our work is that the

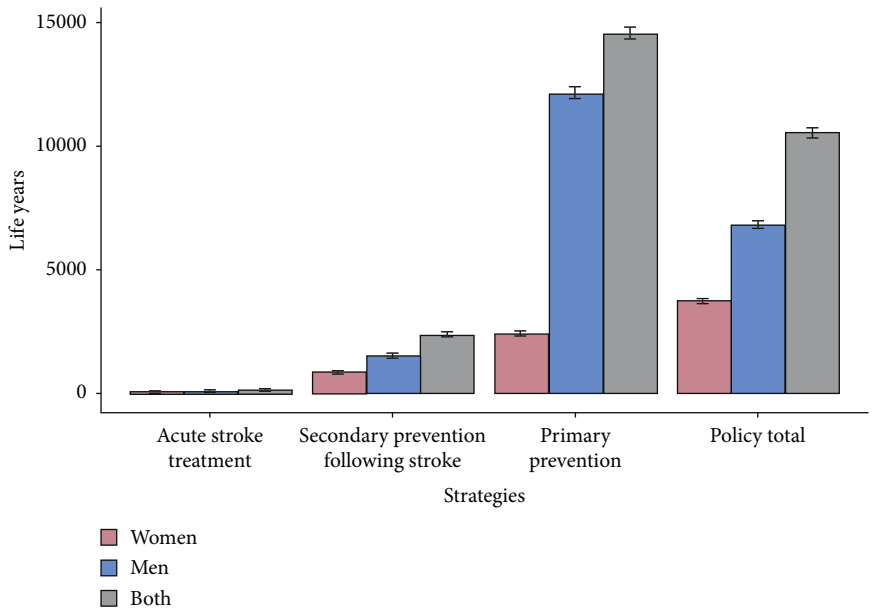

Figure 4: Life years estimations by incorporating strategies by gender in 2025.

Table 3: Regression coefficients from metamodeling on the stroke and IHD deaths by the salt reduction intervention.

Parameters	Dependent variable (Y): stroke and IHD deaths
Intercept	1337.86
$TP_{1,2}$: probability for the stroke-free population to have first stroke in the year 1	646.35
$TP_{1,3}$: probability for the stroke-free population to have first major stroke in the year 1	6.18
$TP_{1,6}$: probability for the stroke-free population to die from stroke and IHD causes in the year 1	38.49
$TP_{1,1}$: probability for population free of stroke	2.45
$TP_{2,3}$: probability of recurrent stroke in ischemic stroke patients after 1 year	13.05
$TP_{2,6}$: probability for the minor stroke patients to die from stroke and IHD causes in the year 1	6.67
$TP_{2,4}$: probability for first minor stroke (1st year) to minor stroke subsequent years	0.45
$TP_{3,3}$: probability of recurrent stroke in ischemic stroke patients after 5 years	−6.49
$TP_{4,6}$: probability for the stroke patients to die from stroke and IHD deaths causes 1 year after first admission	−1.72
$TP_{4,4}$: probability for minor stroke subsequent years	−2.96
$TP_{3,6}$: probability for the major stroke patients to die from stroke and IHD causes	−0.10
Observations	1000
R^2	0.8999

model is a closed cohort, and demographic changes were not considered.

Linear regression is the metamodeling approach most widely used by many researchers for its simplicity and ease of use. Thus, our linear approximation of all input parameters can be considered as a limit, as state-transition models are nonlinear in general. In all metamodeling approaches, the loss of some information is always inevitable [25].

Another limitation of our study is not to consider in the model the costs of the strategies.

In terms of public health, the present modeling study focuses on the future impact of ischemic stroke treatment scenarios and population-level policy interventions on ischemic stroke and IHD deaths and life years gained in Tunisia. The model forecast a dramatic rise in the total cumulative number of IHD and Stroke deaths: by 2025,

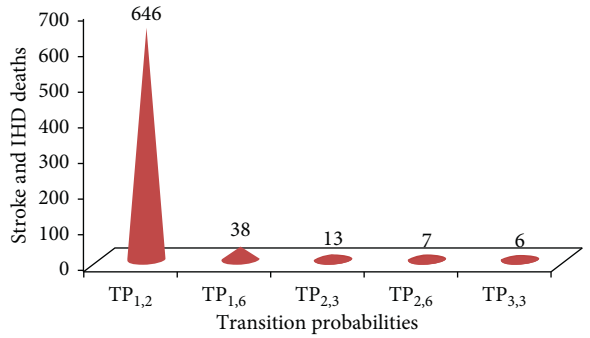

Figure 5: Five first important parameters in the model.

this number was estimated to reach more than 100,000 deaths.

Secondly, the model shows that the rise of thrombolytic treatment and hospitalization in intensive care units of stroke increased statin use for secondary prevention pale in comparison with the salt reduction impact on future deaths (1%, 3% vs 27% deaths prevented by 2025).

The benefits of thrombolytic treatment among patients with acute ischemic stroke are still matter of debate: thrombolytic treatment increases short-term mortality and symptomatic or fatal intracranial haemorrhage but decreases longer term death or dependence [25]. Many studies proved that stroke units have significant benefit to patient outcomes in terms of reducing mortality, morbidity, and improving functional independence. Stroke unit care was also cost effective [37–39].

The substantial effect of salt reduction intervention found in our study is consistent with the literature [40, 41]. High salt intake is associated with significantly increased risks of stroke and total cardiovascular disease ranging from a 14% to 51% increase, depending on salt intake and populations [42–44].

Furthermore, our results are consistent with a modeling study in Tunisia using a different approach. Different strategies for salt reduction were associated with substantial lowering of CVD mortality and were cost saving apart from health promotion [45] and consistent with the Rose hypothesis that the population level strategies are more appropriate in terms of less medicalization [46].

5. Conclusions

The approach presented here is attractive since it is based on a simple comprehensive algorithm to present the results of sensitivity analysis from the Markov model using linear regression metamodeling. This approach can reveal important characteristics of Markov decision process including the base-case results, relative parameter importance, interaction, and sensitivity analyses.

Thus, we recommend using this algorithm for Markov decision process; it can be the object of creation of a complete modeling package in R software and can be extended to other contexts and populations.

In terms of public health, we forecast that absolute numbers of IHD and stroke deaths will increase dramatically in Tunisia over 2005–2025. This Large increase in stroke and IHD mortality in Tunisia needs many actions not only in acute stroke treatment such as implementing more basic and organized stroke units but also in population level primary prevention such as salt reduction in order to manage and treat acute strokes and to alleviate the global burden of these diseases.

Our study highlights the powerful impact of salt reduction on deaths from stroke and IHD. Furthermore, the reducing dietary salt intake across the population appears an effective way of reducing heart disease events and saving substantial costs. This result matches with that of the mathematical model. Indeed our metamodeling highlights that the probability of the first minor stroke among the healthy population has the greatest impact on the stroke and IHD death estimations, which confirms the importance of primary prevention. Prevention is thus the best strategy to fight against stroke and IHD deaths.

Data Availability

Data used are presented in Appendix in the supplementary materials.

Disclosure

The results of the manuscript were presented in the 62nd Annual Scientific Meeting, Society for Social Medicine, University of Strathclyde, Glasgow, on the 5th and 7th of September 2018. The funders had no role in study design, data collection and analysis, decision to publish, or preparation of the manuscript. The MedCHAMPS team had access to all data sources and has the responsibility for the contents of the report. On behalf of EC, FP7 funded MedCHAMPS project (MEDiterranean studies of Cardiovascular Disease and Hyperglycaemia: Analytical Modeling of Population Socio-economic transitions).

Conflicts of Interest

The authors declare that they have no conflicts of interest.

Authors' Contributions

MOF, OS, SC, and JC conceived the idea of the study. OS, DM, and MOF led the project supervised by HBR, JC, and SC. OS, MG, NZ, and PB. assembled the datasets, extracted the data, and populated the models with input. OS, NZ, DM, MG, and MOF wrote the first draft of the paper, and OS, HBR, MOF, SC, and JC finalized the manuscript. All authors contributed to the analysis, intellectual content, critical revisions to the drafts of the paper and approved the final version. HBR is the guarantor.

Acknowledgments

We thank the MedCHAMPS and RESCAPMED advisory group for comments on study design and emerging findings. Particular thanks go to Pat Barker for managing the overall project. We thank also the Tunisian team especially Dr Afef

Skhiri and Dr Olfa Lassoued who participated in data collection and Professor Faycel Hentati for his opinions and comments on the work. We thank Professor K. Bennett for her comments on this paper. This study was funded by the European Community's Seventh Framework Program (FP7/20072013) under grant agreement n223075, the Med-CHAMPS project. MOF was also partially supported by the UK MRC. JC and SC are supported by the UK Higher Education Funding Council.

Supplementary Materials

The supplementary materials submitted contain sources of data and all data used in the model. (*Supplementary Materials*)

References

[1] N. D. Wong, "Epidemiological studies of CHD and the evolution of preventive cardiology," *Nature Reviews Cardiology*, vol. 11, no. 5, pp. 276–289, 2014.

[2] S. Ebrahim and G. D. Smith, "Exporting failure? Coronary heart disease and stroke in developing countries," *International Journal of Epidemiology*, vol. 30, no. 2, pp. 201–5, 2001.

[3] T. A. Gaziano, A. Bitton, S. Anand et al., "Growing epidemic of coronary heart disease in low- and middle-income countries," *Current Problems in Cardiology*, vol. 35, no. 2, pp. 72–115, 2010.

[4] GBD 2015. Mortality and Causes of Death Collaborators, "Global, regional, and national life expectancy, all-cause mortality, and cause-specific mortality for 249 causes of death, 1980–2015: a systematic analysis for the Global Burden of Disease Study 2015," *The Lancet*, vol. 388, no. 10053, pp. 1459–1544, 2016.

[5] G. J. Hankey, "The global and regional burden of stroke," *The Lancet Global Health*, vol. 1, no. 5, pp. e239–e240, 2013.

[6] WHO, "Global burden of stroke," 2015, http://www.who.int/cardiovascular_diseases/en/cvd_atlas_15_burden_stroke.pdf?ua=1.

[7] World Health Organization, "Health promotion," 2018, http://www.who.int/topics/health_promotion/en/.

[8] P. J. Easterbrook, M. C. Doherty, J. H. Perrie, J. L. Barcarolo, and G. O. Hirnschall, "The role of mathematical modelling in the development of recommendations in the 2013 WHO consolidated antiretroviral therapy guidelines," *AIDS*, vol. 28, pp. S85–S92, 2014.

[9] C. J. E. Metcalf, W. J. Edmunds, and J. Lessler, "Six challenges in modelling for public health policy," *Epidemics*, vol. 10, p. 9396, 2015.

[10] M. C. Weinstein, P. G. Coxson, L. W. Williams, T. M. Pass, W. B. Stason, and L. Goldman, "Forecasting coronary heart disease incidence, mortality, and cost: the Coronary Heart Disease Policy Model," *American Journal of Public Health*, vol. 77, no. 11, pp. 1417–1426, 1987.

[11] J. Critchley and S. Capewell, "Why model coronary heart disease?," *European Heart Journal*, vol. 23, no. 2, pp. 110–116, 2002.

[12] G. R. P. Garnett, S. Cousens, T. B. Hallett, R. Steketee, and N. Walker, "Mathematical models in the evaluation of health programmes," *The Lancet*, vol. 378, no. 9790, pp. 515–525, 2011.

[13] M. Ortegon, S. Lim, D. Chisholm, and S. Mendis, "Cost effectiveness of strategies to combat cardiovascular disease, diabetes, and tobacco use in sub-Saharan Africa and South East Asia: mathematical modelling study," *BMJ*, vol. 344, no. 1, p. e607, 2012.

[14] L. C. Leea, G. S. Kassabb, and J. M. Guccionec, "Mathematical modeling of cardiac growth and remodeling," *Wiley Interdisciplinary Reviews: Systems Biology and Medicine*, vol. 8, no. 3, pp. 211–226, 2017.

[15] G. Elena, "Computational and mathematical methods in cardiovascular diseases," *Computational and Mathematical Methods in Medicine*, vol. 2017, Article ID 4205735, 2 pages, 2017.

[16] S. Basu, David Stuckler, S. Vellakkal, and E. Shah, "Dietary salt reduction and cardiovascular disease rates in India: a mathematical model," *PLoS One*, vol. 7, no. 9, 2012.

[17] O. Saidi, N. Ben Mansour, M. O'Flaherty, S. Capewell, J. A. Critchley, and H. B. Romdhane, "Analyzing recent coronary heart disease mortality trends in Tunisia between 1997 and 2009," *PLoS One*, vol. 8, no. 5, Article ID e63202, 2013.

[18] O. Saidi, M. O'Flaherty, N. Ben Mansour et al., "Forecasting Tunisian type 2 diabetes prevalence to 2027: validation of a simple model," *BMC Public Health*, vol. 15, no. 1, p. 104, 2015.

[19] F. A. Sonnenberg and J. R. Beck, "Markov models in medical decision making," *Medical Decision Making*, vol. 13, no. 4, pp. 322–338, 2016.

[20] K. Szmen, B. Unal, S. Capewell, J. Critchley, and M. O'Flaherty, "Estimating diabetes prevalence in Turkey in 2025 with and without possible interventions to reduce obesity and smoking prevalence, using a modeling approach," *International Journal of Public Health*, vol. 60, no. 1, pp. 13–21, 2015.

[21] A. H. Briggs, M. C. Weinstein, E. A. L. Fenwick, J. Karnon, M. J. Sculpher, and A. D. Paltiel, "Model parameter estimation and uncertainty: a report of the ISPOR-SMDM modeling good research practices task force-6," *Value in Health*, vol. 15, no. 6, pp. 835–842, 2012.

[22] M. L. Puterman, *Markov Decision Processes: Discrete Stochastic Dynamic Programming*, Wiley, New York, NY, USA, 2005.

[23] A. Mahanta, "Beta distribution. Kaliabor college," http://www.kaliaborcollege.org/pdf/Mathematical_Excursion_to_Beta_Distribution.pdf.

[24] K. Kuntz, F. Sainfort, M. Butler et al., "Decision and simulation modeling in systematic reviews," Methods Research Report 11(13)-EHC037-EF, AHRQ Publication, Rockville, MA, USA, 2013.

[25] H. Jalal, D. Bryan, F. Sainfort, M. Karen, and Kuntz, "Linear regression metamodeling asa tool to summarize and present simulation model results," *Medical Decision Making*, vol. 33, no. 7, pp. 880–890, 2013.

[26] V. Kapetanakis, F. E. Matthews, and A. van den Hout, "A semi-Markov model for stroke with piecewise-constant hazards in the presence of left, right and interval censoring," *Statistics in Medicine*, vol. 32, no. 4, pp. 697–713, 2012.

[27] C. Eulenburg, S. Mahner, L. Woelber, and K. Wegscheider, "A systematic model specification procedure for an illness-death model without recovery," *PLoS One*, vol. 10, no. 4, Article ID e0123489, 2015.

[28] F. J. He and G. A. MacGregor, "Role of salt intake in prevention of cardiovascular disease: controversies and challenges," *Nature Reviews Cardiology*, vol. 15, no. 6, pp. 371–377, 2018.

[29] J. F. Moxnes and Y. V. Sandbakk, "Mathematical modelling of the oxygen uptake kinetics during whole-body endurance exercise and recovery," *Mathematical and Computer Modelling of Dynamical Systems*, vol. 24, no. 1, pp. 76–86, 2018.
[30] R. B Chambers, "The role of mathematical modeling in medical research: research without patients?," *Ochsner Journal*, vol. 2, no. 4, pp. 218–223, 2000.
[31] F. Achana, J. Alex, D. K. Sutton et al., "A decision analytic model to investigate the cost-effectiveness of poisoning prevention practices in households with young children," *BMC Public Health*, vol. 16, no. 1, p. 705, 2016.
[32] O. Alagoz, H. Hsu, A. J. Schaefer, and M. S. Roberts, "Markov decision processes: a tool for sequential decision making under uncertainty," *Medical Decision Making*, vol. 30, no. 4, pp. 474–483, 2010.
[33] J. F. Merz and M. J. Small, "Measuring decision sensitivity: a combined monte carlo-logistic regression approach," *Medical Decision Making*, vol. 12, no. 3, pp. 189–196, 1992.
[34] P. M. Reis dos Santos and M. Isabel Reis dos Santos, "Using subsystem linear regression metamodels in stochastic simulation," *European Journal of Operational Research*, vol. 196, no. 3, pp. 1031–1040, 2008.
[35] A. Moran, D. Gu, D. Zhao et al., "Future cardiovascular disease in China: Markov model and risk factor scenario projections from the Coronary Heart Disease Policy Model-China," *Circulation: Cardiovascular Quality and Outcomes*, vol. 3, no. 3, pp. 243–252, 2010.
[36] D. Coyle, M. J. Buxton, and B. J. OBrien, "Measures of importance for economic analysis based on decision modeling," *Journal of Clinical Epidemiology*, vol. 56, no. 10, pp. 989–997, 2003.
[37] K. Meisel and B. Silver, "The importance of stroke units," *Medicine and Health, Rhode Island*, vol. 94, no. 12, pp. 376-377, 2011.
[38] P. Langhorne, "Collaborative systematic review of the randomised trials of organised inpatient (stroke unit) care after stroke," *BMJ*, vol. 314, no. 7088, pp. 1151–1159, 1997.
[39] B. J. T. Ao, P. M. Brown, V. L. Feigin, and C. S. Anderson, "Are stroke units cost effective? Evidence from a New Zealand stroke incidence and population-based study," *International Journal of Stroke*, vol. 7, no. 8, pp. 623–630, 2011.
[40] N. Bruce, *The Effectiveness and Costs of Population Interventions to Reduce Salt Consumption*, WHO Library Cataloguing-in-Publication Data, Geneva, Switzerland, 2006, http://www.who.int/dietphysicalactivity/Neal_saltpaper_2006.pdf.
[41] N. Wilson, N. Nghiem, H. Eyles et al., "Modeling health gains and cost savings for ten dietary salt reduction targets," *Nutrition Journal*, vol. 15, no. 1, p. 44, 2016.
[42] D. Klaus, J. Hoyer, and M. Middeke, "Salt restriction for the prevention of cardiovascular disease," *Deutsches Aerzteblatt Online*, vol. 107, no. 26, pp. 457–462, 2010.
[43] J. Tuomilehto, P. Jousilahti, D. Rastenvte et al., "Urinary sodium excretion and cardiovascular mortality in Finland: a prospective study," *The Lancet*, vol. 357, no. 9259, pp. 848–851, 2001.
[44] WHO, "Reducing salt intake," 21-10-2011," 2016, http://www.euro.who.int/en/health-topics/disease-prevention/nutrition/news/news/2011/10/reducing-salt-intake.
[45] H. Mason, A. Shoaibi, R. Ghandour et al., "A cost effectiveness analysis of salt reduction policies to reduce coronary heart disease in four eastern mediterranean countries," *PLoS One*, vol. 9, no. 1, Article ID e84445, 2014.
[46] G. Rose, "Strategy of prevention: lessons from cardiovascular disease," *BMJ*, vol. 282, no. 6279, pp. 1847–1851, 1981.

Hindawi
Computational and Mathematical Methods in Medicine
Volume 2019, Article ID 4059549, 12 pages
https://doi.org/10.1155/2019/4059549

Research Article

The Fractional Differential Model of HIV-1 Infection of $CD4^+$ T-Cells with Description of the Effect of Antiviral Drug Treatment

Bijan Hasani Lichae,[1,2] Jafar Biazar,[3] and Zainab Ayati[4]

[1]*Department of Mathematics, Guilan Science and Research Branch, Islamic Azad University, Rasht, Iran*
[2]*Department of Mathematics, Rasht Branch, Islamic Azad University, Rasht, Iran*
[3]*Department of Applied Mathematics, Faculty of Mathematical Sciences, University of Guilan, P.O. Box 41335-1914, Rasht, Guilan, Iran*
[4]*Department of Engineering Sciences, Faculty of Technology and Engineering East of Guilan, University of Guilan, P.C. 44891-63157, Rudsar-Vajargah, Iran*

Correspondence should be addressed to Jafar Biazar; biazar@guilan.ac.ir

Received 13 June 2018; Revised 11 September 2018; Accepted 17 December 2018; Published 8 January 2019

Guest Editor: Katarzyna Kolasa

In this paper, the fractional-order differential model of HIV-1 infection of $CD4^+$ T-cells with the effect of drug therapy has been introduced. There are three components: uninfected $CD4^+$ T-cells, x, infected $CD4^+$ T-cells, y, and density of virions in plasma, z. The aim is to gain numerical solution of this fractional-order HIV-1 model by Laplace Adomian decomposition method (LADM). The solution of the proposed model has been achieved in a series form. Moreover, to illustrate the ability and efficiency of the proposed approach, the solution will be compared with the solutions of some other numerical methods. The Caputo sense has been used for fractional derivatives.

1. Introduction

Human immunodeficiency virus (HIV) is a retrovirus that causes acquired immunodeficiency syndrome (AIDS) [1]. HIV infects, damages, and reduces $CD4^+$ T-cells. Therefore, it causes to decrease the resistance of immune system [2]. The body becomes more gradually sensitive to infections and loses its safety. AIDS is one the most important and dangerous diseases in our time. According to UNAIDS 2017 annual report, "36.7 million people globally were living with HIV and 1.8 million people became newly infected with HIV and 1 million people died from AIDS-related illnesses in 2016." In spite of the great progress in controlling the disease, no vaccine has been yet discovered for HIV. In the last two decades, a lot of efforts have been made to design and solve mathematical models that have essential rule in analyzing to control and prevent the spread of HIV-related diseases [3–13]. Usually almost all of these mathematical models explain the relation between HIV viruses and uninfected $CD4^+$ cells and the effect of drug therapy to infected cells. Bonhoeffer et al. [4] presented a model for virus dynamics with two components x and y, where x denotes the density of infected cells and y shows the density of virus-producing cells.

The proposed model is as follows:

$$\begin{cases} \dfrac{dx}{dt} = c - \beta x - \gamma xy, \\ \dfrac{dy}{dt} = \gamma xy - dy, \end{cases} \tag{1}$$

where c is the rate of production of infected cells, β is the natural death rate of infected cells, d is the rate of

virus-producing cells' death, and γ is the rate of infection of uninfected cells. This model and many such models were inspired from Anderson's model [14, 15]. Anderson's model is one of the first and the most important models of infectious diseases. Tuckwell and Wan [16] introduced a modified model of equation (1) with three components: uninfected, infected $CD4^+$ T-cells, and density of virions in plasma (x, y, and z, respectively). The presented model with three equations is as follows:

$$\begin{cases} \dfrac{dx}{dt} = s' - \mu x - \beta xz, \\ \dfrac{dy}{dt} = \beta xz - \varepsilon y, \\ \dfrac{dz}{dt} = cy - \gamma z, \end{cases} \tag{2}$$

with the initial conditions $x(0) = k_1, y(0) = k_2$, and $z(0) = k_3$ where s', μ, β, ε, c, and γ are constant coefficients, s' is the rate of creation or production of $CD4^+$ T-cells, μ is the natural death rate, β is the rate of infected $CD4^+$ cells from uninfected $CD4^+$ cells, ε is the rate of virus-producing cells' death, c is the rate of creation of virions viruses by infected cells, and γ is the rate of virus particle death. For the sake of comparison and showing the ability of the proposed approach, we use the parameter values reported in references [6, 16]. The parameter values are as follows: $s' = 0.272$ (day/mm^3), $\mu = 0.00136$ (day/mm^3), $\beta = 0.00027$ (day/virion/mm^3), $\varepsilon = 0.33$ (day/mm^3), $c = 50$ (virion/CLM/day), and $\gamma = 2.0$ (day). The rate of some coefficients will change if drug therapy is not 100% successful. When the drug treatment begins, infected cells which create virus components are affected. If the drug therapy is not effective, a part of infected cells will improve and remaining cells will begin to produce virus [8].

Mathematical modeling of many problems in biology and other branches of sciences appears as differential equations in fractional order. Because the fractional-order differential equations save memory on themselves and are related to fractals [8, 17–19], we prefer to use the fractional-order form of the model (2) as follows:

$$\begin{cases} D^{\alpha_1}(x) = s' - \mu x - \beta xz, \\ D^{\alpha_2}(y) = \beta xz - \varepsilon y, \\ D^{\alpha_3}(z) = cy - \gamma z, \end{cases} \tag{3}$$

with the same initial conditions, where $0 < \alpha_i \leq 1$, $i = 1, 2, 3$. There are some numerical approaches for solving these types of mathematical models. Some of these methods are as follows: homotopy analysis, optimal homotopy asymptotic, homotopy perturbation, Adomian decomposition, and variational iteration [20–30]. In [8], system of fractional equation (3) has been solved by homotopy analysis method (HAM) and generalized Euler method (GEM). In [31], equation (3) has also been solved by homotopy perturbation method (HPM). Adomian [32], introduced a decomposition method (ADM) which is a powerful method to get analytic approximate solution of differential equations. Using Laplace transform method with couple of ADM (LADM) to solve systems of differential equations leads to an effective method that finds many applications in applied mathematics. In this paper, we will solve equation (3) by LADM and will compare the results with the results achieved by generalized Euler, homotopy analysis, homotopy perturbation, and Runge–Kutta methods. The structure of the paper is as follows: in Section 2, we will present a brief review of fractional calculus. In Sections 3 and 4, we will solve the fractional-order HIV-1 model by LADM. In Section 5, the convergence of the method will be discussed. In the last section, we present the conclusion.

2. Fractional Calculus

The purpose of this section is to recall a few preliminaries about what appears in this research.

Definition 2.1. The Riemann–Liouville fractional integral of order α for a function $X : (0, \infty) \longrightarrow R$ is defined as

$$J^{\alpha}X(s) = \frac{1}{\Gamma(\alpha)} \int_0^s (s-t)^{\alpha-1} X(t)dt, \tag{4}$$

where $\alpha\varepsilon(0, \infty)$ (see [33]).

Definition 2.2. The Caputo fractional derivative for a function $X : (0, \infty) \longrightarrow R$ on the closed interval $[0, S]$ is defined as

$$D^{\alpha}X(s) = \frac{1}{\Gamma(m-\alpha)} \int_0^s (s-t)^{m-\alpha-1} X^m(t)dt, \quad m = \lfloor \alpha \rfloor + 1, \tag{5}$$

where α is the integer part of α. Another presentation of the Caputo fractional derivative can be shown as follows (see [33]):

$$D^{\alpha}X(s) = J^{m-\alpha}\left(D^m X(s)\right). \tag{6}$$

Lemma 2.1. *If $\alpha\varepsilon(0, \infty)$ and $m = \alpha + 1$, then the following result holds for fractional calculus:*

$$J^{\alpha}\left[D^{\alpha}X\right](s) = X(s) + \sum_{j=0}^{m-1} \frac{X^j(0)}{j!} s^j. \tag{7}$$

Proof. See [33, 34]. □

Definition 2.3. The Laplace transform of Caputo fractional derivative is defined as follows:

$$\mathscr{L}\{D^{\alpha}X(t)\} = s^{\alpha}Y(s) - \sum_{j=0}^{m-1} s^{\alpha-k-1}X^{j}(0), \quad m-1 < \alpha < m, m \in \mathbb{N}. \tag{8}$$

3. Solution of Model (3)

In this section, LADM has been implemented to solve system of fractional equation (3) with the initial conditions.

We apply Laplace transform on both sides of each equation of equation (3):

$$\begin{cases} L\{D^{\alpha_1}x\} = L\{s' - \mu x - \beta xz\}, \\ L\{D^{\alpha_2}y\} = L\{\beta xz - \varepsilon y\}, \\ L\{D^{\alpha_3}z\} = L\{cy - \gamma z\}, \end{cases} \tag{9}$$

which implies that

$$\begin{cases} s^{\alpha_1}L\{x\} - s^{\alpha_1-1}x(0) = L\{s' - \mu x - \beta xz\}, \\ s^{\alpha_2}L\{y\} - s^{\alpha_2-1}y(0) = L\{\beta xz - \varepsilon y\}, \\ s^{\alpha_3}L\{z\} - s^{\alpha_3-1}z(0) = L\{cy - \gamma z\}. \end{cases} \tag{10}$$

Substitution of the initial conditions in equation (10) and applying inverse Laplace transform results in

$$\begin{cases} x = k_1 + \mathscr{L}^{-1}\left[\dfrac{1}{s^{\alpha_1}}\mathscr{L}\{s' - \mu x - \beta xz\}\right], \\ y = k_2 + \mathscr{L}^{-1}\left[\dfrac{1}{s^{\alpha_2}}\mathscr{L}\{\beta xz - \varepsilon y\}\right], \\ z = k_3 + \mathscr{L}^{-1}\left[\dfrac{1}{s^{\alpha_3}}\mathscr{L}\{cy - \gamma z\}\right]. \end{cases} \tag{11}$$

To apply ADM, let us consider x, y, and z as the following series:

$$\begin{aligned} x &= \sum_{i=0}^{\infty} x_i, \\ y &= \sum_{i=0}^{\infty} y_i, \\ z &= \sum_{i=0}^{\infty} z_i. \end{aligned} \tag{12}$$

To decompose the nonlinear term xz, let us follow an alternate algorithm [35] to get,

$$xz = \sum_{i=0}^{\infty} p_i, \tag{13}$$

where p_i is as the following equation:

$$p_i = \sum_{k=0}^{i} x_k z_{i-k}, \tag{14}$$

substituting equations (12)–(14) into (11) reads

$$\begin{cases} \mathscr{L}(x_0) = \dfrac{k_1}{s}, \\ \mathscr{L}(y_0) = \dfrac{k_2}{s}, \\ \mathscr{L}(z_0) = \dfrac{k_3}{s}, \\ \mathscr{L}(x_1) = \dfrac{s'}{s^{\alpha_1+1}} - \dfrac{\mu}{s^{\alpha_1}}\mathscr{L}(x_0) - \dfrac{\beta}{s^{\alpha_1}}\mathscr{L}(p_0), \\ \mathscr{L}(y_1) = \dfrac{\beta}{s^{\alpha_2}}\mathscr{L}(p_0) - \dfrac{\varepsilon}{s^{\alpha_2}}\mathscr{L}(y_0), \\ \mathscr{L}(z_1) = \dfrac{c}{s^{\alpha_3}}\mathscr{L}(y_0) - \dfrac{\gamma}{s^{\alpha_3}}\mathscr{L}(z_0), \\ \mathscr{L}(x_2) = -\dfrac{\mu}{s^{\alpha_1}}\mathscr{L}(x_1) - \dfrac{\beta}{s^{\alpha_1}}\mathscr{L}(p_1), \\ \mathscr{L}(y_2) = \dfrac{\beta}{s^{\alpha_2}}\mathscr{L}(p_1) - \dfrac{\varepsilon}{s^{\alpha_2}}\mathscr{L}(y_1), \\ \mathscr{L}(z_2) = \dfrac{c}{s^{\alpha_3}}\mathscr{L}(y_1) - \dfrac{\gamma}{s^{\alpha_3}}\mathscr{L}(z_1), \\ \quad\vdots \\ \mathscr{L}(x_{n+1}) = -\dfrac{\mu}{s^{\alpha_1}}\mathscr{L}(x_n) - \dfrac{\beta}{s^{\alpha_1}}\mathscr{L}(p_n), \\ \mathscr{L}(y_{n+1}) = \dfrac{\beta}{s^{\alpha_2}}\mathscr{L}(p_n) - \dfrac{\varepsilon}{s^{\alpha_2}}\mathscr{L}(y_n), \\ \mathscr{L}(z_{n+2}) = \dfrac{c}{s^{\alpha_3}}\mathscr{L}(y_n) - \dfrac{\gamma}{s^{\alpha_3}}\mathscr{L}(z_n). \end{cases} \tag{15}$$

We take inverse Laplace transform on both sides of each equation of equation (15):

$$
\begin{aligned}
x_0 &= k_1,\\
y_0 &= k_2,\\
z_0 &= k_3,\\
x_1 &= \left(s' - \mu x_0 - \beta x_0 z_0\right)\frac{t^{\alpha_1}}{\Gamma(\alpha_1+1)},\\
y_1 &= \left(\beta x_0 z_0 - \varepsilon y_0\right)\frac{t^{\alpha_2}}{\Gamma(\alpha_2+1)},\\
z_1 &= \left(c y_0 - \gamma z_0\right)\frac{t^{\alpha_3}}{\Gamma(\alpha_3+1)},\\
x_2 &= \left\{-(\mu+\beta z_0)\left(s' - \mu x_0 - \beta x_0 z_0\right)\right\}\frac{t^{2\alpha_2}}{\Gamma(2\alpha_2+1)} - \beta x_0\left(c y_0 - \gamma z_0\right)\frac{t^{\alpha_1+\alpha_3}}{\Gamma(\alpha_1+\alpha_3+1)},\\
y_2 &= \beta x_0\left(c y_0 - \gamma z_0\right)\frac{t^{\alpha_2+\alpha_3}}{\Gamma(\alpha_2+\alpha_3+1)} + \beta z_0\left(s' - \mu x_0 - \beta x_0 z_0\right)\frac{t^{\alpha_1+\alpha_2}}{\Gamma(\alpha_1+\alpha_2+1)} - \varepsilon\left(\beta x_0 z_0 - \varepsilon y_0\right)\frac{t^{2\alpha_2}}{\Gamma(2\alpha_2+1)},\\
z_2 &= c\left(\beta x_0 z_0 - \varepsilon y_0\right)\frac{t^{\alpha_2+\alpha_3}}{\Gamma(\alpha_2+\alpha_3+1)} - \gamma\left(c y_0 - \gamma z_0\right)\frac{t^{2\alpha_3}}{\Gamma(2\alpha_3+1)},\\
x_3 &= \beta x_0 c\left(\beta x_0 z_0 - \varepsilon y_0\right)\frac{t^{\alpha_1+\alpha_2+\alpha_3}}{\Gamma(\alpha_1+\alpha_2+\alpha_3+1)} + \beta x_0\gamma\left(c y_0 - \gamma z_0\right)\frac{t^{\alpha_1+2\alpha_3}}{\Gamma(\alpha_1+2\alpha_3+1)} + \beta^2 x_0 z_0\left(c y_0 - \gamma z_0\right)\frac{t^{2\alpha_1+\alpha_2}}{\Gamma(2\alpha_1+\alpha_2+1)}\\
&\quad + \left(s' - \mu x_0 - \beta x_0 z_0\right)\left\{\beta z_0(\mu+z_0) + \mu(\mu+\beta z_0)\right\}\frac{t^{3\alpha_1}}{\Gamma(3\alpha_1+1)} + \beta\left\{\left(c y_0 - \gamma z_0\right)\left(\mu x_0 - \left(s' - \mu x_0 - \beta x_0 z_0\right)\frac{\Gamma(\alpha_1+\alpha_3+1)}{\Gamma(\alpha_1+1)\Gamma(\alpha_3+1)}\right)\right\}\\
&\quad \cdot \frac{t^{2\alpha_1+\alpha_3}}{\Gamma(2\alpha_1+\alpha_3+1)},\\
y_3 &= \left(\beta x_0\left(c\left(\beta x_0 z_0 - \varepsilon y_0\right) - \varepsilon\left(c y_0 - \gamma z_0\right)\right)\right)\frac{t^{2\alpha_2+\alpha_3}}{\Gamma(2\alpha_2+\alpha_3+1)} - \beta x_0\gamma\left(c y_0 - \gamma z_0\right)\frac{t^{\alpha_2+2\alpha_3}}{\Gamma(\alpha_2+2\alpha_3+1)}\\
&\quad - \beta z_0(\mu+\beta z_0)\left(s' - \mu x_0 - \beta x_0 z_0\right)\frac{t^{2\alpha_1+\alpha_2}}{\Gamma(2\alpha_1+\alpha_2+1)} + \beta\left(s' - \mu x_0 - \beta x_0 z_0\right)\frac{\Gamma(\alpha_1+\alpha_3+1)}{\Gamma(\alpha_1+1)\Gamma(\alpha_3+1)}\frac{t^{\alpha_1+\alpha_2+\alpha_3}}{\Gamma(\alpha_1+\alpha_2+\alpha_3+1)}\\
&\quad - \left(\beta^2 x_0 z_0\left(c y_0 - \gamma z_0\right) + \beta z_0\varepsilon\left(s' - \mu x_0 - \beta x_0 z_0\right)\right)\frac{t^{\alpha_1+2\alpha_2}}{\Gamma(\alpha_1+2\alpha_2+1)} + \varepsilon^2\left(\beta x_0 z_0 - \varepsilon y_0\right)\frac{t^{3\alpha_2}}{\Gamma(3\alpha_2+1)},\\
z_3 &= \left(\beta x_0 c\left(c y_0 - \gamma z_0\right) - \gamma c\left(\beta x_0 z_0 - \varepsilon y_0\right)\right)\frac{t^{\alpha_2+2\alpha_3}}{\Gamma(\alpha_2+2\alpha_3+1)} + \gamma^2\left(c y_0 - \gamma z_0\right)\frac{t^{3\alpha_3}}{\Gamma(3\alpha_3+1)}\\
&\quad + \beta z_0 c\left(s' - \mu x_0 - \beta x_0 z_0\right)\frac{t^{\alpha_1+\alpha_2+\alpha_3}}{\Gamma(\alpha_1+\alpha_2+\alpha_3+1)} - \varepsilon c\left(\beta x_0 z_0 - \varepsilon y_0\right)\frac{t^{2\alpha_2+\alpha_3}}{\Gamma(2\alpha_2+\alpha_3+1)}.
\end{aligned}
\tag{16}
$$

We have calculated four terms of the infinite series of x, y, and z as an approximate solution. To get any desired accuracy, one is able to proceed the process and obtain more terms. Finally, the solution of mathematical model can be obtained as follows:

$$
\begin{cases}
x(t) = \displaystyle\sum_{i=0}^{\infty} x_i(t) \approx x_0(t) + x_1(t) + x_2(t) + x_3(t),\\
y(t) = \displaystyle\sum_{i=0}^{\infty} y_i(t) \approx y_0(t) + y_1(t) + y_2(t) + y_3(t),\\
z(t) = \displaystyle\sum_{i=0}^{\infty} z_i(t) \approx z_0(t) + z_1(t) + z_2(t) + z_3(t).
\end{cases}
\tag{17}
$$

4. Numerical Simulation

In this section, constants and initial values are substituted in equation (16) to obtain an approximate solution.

Substituting the following values: $s' = 0.272$ (day/mm^3), $\mu = 0.00136$ (day/mm^3), $\beta = 0.00027$ (day/virion/mm^3), $\varepsilon = 0.33$ (day/mm^3), $c = 50$ (virion/CLM/day), and $\gamma = 2.0$ (day) and the initial conditions $x(0) = 100$, $y(0) = 0$, and $z(0) = 1$ in equation (16), we get,

$$
\begin{aligned}
x_0 &= 100,\\
y_0 &= 0,\\
z_0 &= 1,\\
x_1 &= 0.1090\frac{t^{\alpha_1}}{\Gamma(\alpha_1+1)},\\
y_1 &= 0.0270\frac{t^{\alpha_2}}{\Gamma(\alpha_2+1)},\\
z_1 &= -2.0000\frac{t^{\alpha_3}}{\Gamma(\alpha_3+1)},\\
x_2 &= -0.0001776700\frac{t^{2\alpha 2}}{\Gamma(2\alpha_2+1)} + 0.05400\frac{t^{\alpha_1+\alpha_3}}{\Gamma(\alpha_1+\alpha_3+1)},\\
y_2 &= -0.05400\frac{t^{\alpha_2+\alpha_3}}{\Gamma(\alpha_2+\alpha_3+1)} + 0.0000294300\frac{t^{\alpha_1+\alpha_2}}{\Gamma(\alpha_1+\alpha_2+1)} - 0.0089100\frac{t^{2\alpha_2}}{\Gamma(2\alpha_2+1)},\\
z_2 &= 1.35000\frac{t^{\alpha_2+\alpha_3}}{\Gamma(\alpha_2+\alpha_3+1)} + 4.0000\frac{t^{2\alpha_3}}{\Gamma(2\alpha_3+1)},\\
x_3 &= -0.0364500\frac{t^{\alpha_1+\alpha_2+\alpha_3}}{\Gamma(\alpha_1+\alpha_2+\alpha_3+1)} - 0.10800\frac{t^{\alpha_1+2\alpha_3}}{\Gamma(\alpha_1+2\alpha_3+1)} - 0.0000145800\frac{t^{2\alpha_1+2\alpha_2}}{\Gamma(2\alpha_1+\alpha_2+1)}\\
&\quad + 0.000029711656\frac{t^{3\alpha_1}}{\Gamma(3\alpha_1+1)} - 0.00054\frac{\Gamma(\alpha_1+\alpha_3+1)}{\Gamma(\alpha_1+1)\Gamma(\alpha_3+1)}\frac{t^{2\alpha_1+\alpha_3}}{\Gamma(2\alpha_1+\alpha_3+1)},\\
y_3 &= 0.054270000\frac{t^{2\alpha_2+\alpha_3}}{\Gamma(2\alpha_2+\alpha_3+1)} + 0.10800\frac{t^{\alpha_2+2\alpha_3}}{\Gamma(\alpha_2+2\alpha_3+1)} - 0.000000047971\frac{t^{2\alpha_1+\alpha_2}}{\Gamma(2\alpha_1+\alpha_2+1)}\\
&\quad + 0.0000294300\frac{\Gamma(\alpha_1+\alpha_3+1)}{\Gamma(\alpha_1+1)\Gamma(\alpha_3+1)}\frac{t^{\alpha_1+\alpha_2+\alpha_3}}{\Gamma(\alpha_1+\alpha_2+\alpha_3+1)} + 0.000004868100\frac{t^{\alpha_1+2\alpha_3}}{\Gamma(\alpha_1+2\alpha_3+1)} + 0.0002940300\frac{t^{3\alpha_2}}{\Gamma(3\alpha_2+1)},\\
z_3 &= 0.054270000\frac{t^{\alpha_2+2\alpha_3}}{\Gamma(\alpha_2+2\alpha_3+1)} - 8.0000\frac{t^{3\alpha_3}}{\Gamma(3\alpha_3+1)} + 0.0014715000\frac{t^{\alpha_1+\alpha_2+\alpha_3}}{\Gamma(\alpha_1+\alpha_2+\alpha_3+1)}\\
&\quad - 0.4455000\frac{t^{2\alpha_2+\alpha_3}}{\Gamma(2\alpha_2+\alpha_3+1)}.
\end{aligned}
\tag{18}
$$

Three terms approximations can be written as the following form:

$$
\begin{aligned}
x(t) &= 100 + 0.1090\frac{t^{\alpha_1}}{\Gamma(\alpha_1+1)} - 0.0001776700\frac{t^{2\alpha_2}}{\Gamma(2\alpha_2+1)} + 0.05400\frac{t^{\alpha_1+\alpha_3}}{\Gamma(\alpha_1+\alpha_3+1)} - 0.0364500\frac{t^{\alpha_1+\alpha_2+\alpha_3}}{\Gamma(\alpha_1+\alpha_2+\alpha_3+1)} \\
&\quad - 0.10800\frac{t^{\alpha_1+2\alpha_3}}{\Gamma(\alpha_1+2\alpha_3+1)} - 0.0000145800\frac{t^{2\alpha_1+\alpha_2}}{\Gamma(2\alpha_1+\alpha_2+1)} + 0.000029711656\frac{t^{3\alpha_1}}{\Gamma(3\alpha_1+1)} \\
&\quad - 0.00054\frac{\Gamma(\alpha_1+\alpha_3+1)}{\Gamma(\alpha_1+1)\Gamma(\alpha_3+1)}\frac{t^{2\alpha_1+\alpha_3}}{\Gamma(2\alpha_1+\alpha_3+1)}, \\
y(t) &= 0.0270\frac{t^{\alpha_2}}{\Gamma(\alpha_2+1)} - 0.05400\frac{t^{\alpha_2+\alpha_3}}{\Gamma(\alpha_2+\alpha_3+1)} + 0.0000294300\frac{t^{\alpha_1+\alpha_2}}{\Gamma(\alpha_1+\alpha_2+1)} - 0.0089100\frac{t^{2\alpha_2}}{\Gamma(2\alpha_2+1)} \\
&\quad + 0.054270000\frac{t^{2\alpha_2+\alpha_3}}{\Gamma(2\alpha_2+\alpha_3+1)} + 0.10800\frac{t^{\alpha_2+2\alpha_3}}{\Gamma(\alpha_2+2\alpha_3+1)} - 0.000000047971\frac{t^{2\alpha_1+\alpha_2}}{\Gamma(2\alpha_1+\alpha_2+1)} \\
&\quad + 0.0000294300\frac{\Gamma(\alpha_1+\alpha_3+1)}{\Gamma(\alpha_1+1)\Gamma(\alpha_3+1)}\frac{t^{\alpha_1+\alpha_2+\alpha_3}}{\Gamma(\alpha_1+\alpha_2+\alpha_3+1)} + 0.000004868100\frac{t^{\alpha_1+2\alpha_2}}{\Gamma(\alpha_1+2\alpha_2+1)} \\
&\quad + 0.0002940300\frac{t^{3\alpha_2}}{\Gamma(3\alpha_2+1)}, \\
z(t) &= 1 - 2.0000\frac{t^{\alpha_3}}{\Gamma(\alpha_3+1)} + 1.35000\frac{t^{\alpha_2+\alpha_3}}{\Gamma(\alpha_2+\alpha_3+1)} + 4.0000\frac{t^{2\alpha_3}}{\Gamma(2\alpha_3+1)} + 0.054270000\frac{t^{\alpha_2+2\alpha_3}}{\Gamma(\alpha_2+2\alpha_3+1)} \\
&\quad - 8.0000\frac{t^{3\alpha_3}}{\Gamma(3\alpha_3+1)} + 0.0014715000\frac{t^{\alpha_1+\alpha_2+\alpha_3}}{\Gamma(\alpha_1+\alpha_2+\alpha_3+1)} - 0.4455000\frac{t^{2\alpha_2+\alpha_3}}{\Gamma(2\alpha_2+\alpha_3+1)}.
\end{aligned}
\tag{19}
$$

Let us take α_1, α_2, and α_3 equal to α, so the solution of fractional-order of model (3) is obtained as follows:

$$
\begin{cases}
x(t) = 100 + \dfrac{0.1090t^{\alpha}}{\Gamma(\alpha+1)} + \dfrac{0.0538223300t^{2\alpha}}{\Gamma(2\alpha+1)} - \dfrac{0.1444348683t^{3\alpha}}{\Gamma(3\alpha+1)} - \dfrac{0.00054\Gamma(2\alpha+1)t^{3\alpha}}{\Gamma(3\alpha+1)}, \\
y(t) = \dfrac{0.0270t^{\alpha}}{\Gamma(\alpha+1)} - \dfrac{0.0628805700t^{2\alpha}}{\Gamma(2\alpha+1)} + \dfrac{0.1625688501t^{3\alpha}}{\Gamma(3\alpha+1)} + \dfrac{0.0000294300\Gamma(2\alpha+1)t^{3\alpha}}{\Gamma(3\alpha+1)}, \\
z(t) = 1 - \dfrac{2.0000t^{\alpha}}{\Gamma(\alpha+1)} + \dfrac{5.35000t^{2\alpha}}{\Gamma(2\alpha+1)} - \dfrac{8.389758500t^{3\alpha}}{\Gamma(3\alpha+1)}.
\end{cases}
\tag{20}
$$

For $\alpha_1 = \alpha_2 = \alpha_3 = 1$, the solution of equation (3) will be as follows:

$$
\begin{cases}
x(t) = 100 + 0.1090t + 0.02691116500t^2 - 0.02425247806t^3, \\
y(t) = 0.0270t - 0.03144028500t^2 + 0.02710461836t^3, \\
z(t) = 1 - 2.0000t + 2.6750000t^2 - 1.398293083t^3.
\end{cases}
\tag{21}
$$

In Tables 1–3, one can compare the approximate solution of fractional-order of model (3) with the results of GEM, HAM, RK4 in [8], and HPM in [31] using traditional order $\alpha = 1$. The results of LADM are more accurate than the results obtained by other methods.

Figures 1–3 show the results for different values of α, and the results can be compared.

Table 1: Numerical results of $x(t)$ (uninfected CD4$^+$ T-cells).

t	LADM	GEM	HPM	HAM	RK4
0	100	100	100	100	100
0.2	100.023	100.023	100.023	100.023	100.023
0.4	100.046	100.047	100.047	100.047	100.047
0.6	100.070	100.071	100.071	100.071	100.071
0.8	100.092	100.097	100.097	100.096	100.097
1.0	100.112	100.122	100.123	100.122	100.122

Table 2: Numerical results of $y(t)$ (infected CD4$^+$ T-cells).

t	LADM	GEM	HPM	HAM	RK4
0	0	0	0	0	0
0.2	0.00436	0.00434	0.00434	0.00434	0.00434
0.4	0.00750	0.00715	0.00721	0.00714	0.00715
0.6	0.01074	0.00908	0.00934	0.00909	0.00908
0.8	0.01336	0.01049	0.01117	0.01063	0.01049
1.0	0.01866	0.01161	0.01276	0.01194	0.01161

Table 3: Numerical results of $z(t)$ (density of virions in plasma).

t	LADM	GEM	HPM	HAM	RK4
0	1	1	1	1	1
0.2	0.69581	0.69030	0.69071	0.69059	0.69070
0.4	0.53851	0.51152	0.51208	0.51237	0.51190
0.6	0.46097	0.41069	0.41394	0.40994	0.41103
0.8	0.39607	0.35656	0.37749	0.35148	0.35684
1.0	0.27671	0.33053	0.42419	0.32869	0.33073

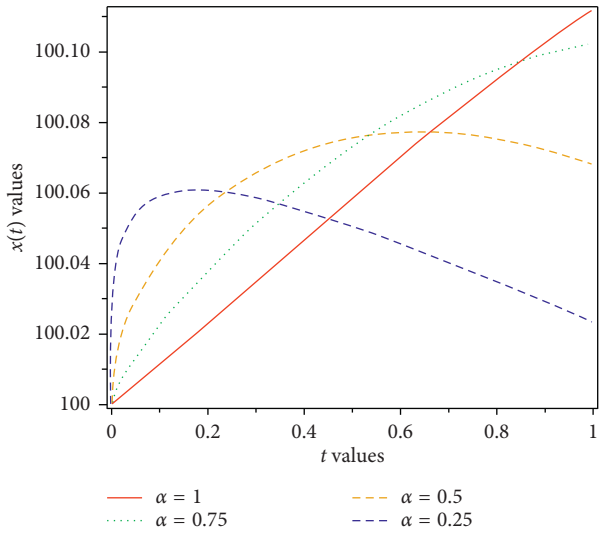

Figure 1: Dynamics of uninfected CD4$^+$ T-cells for various values of α.

5. Convergence Analysis of the Method

In this section, convergence of the proposed method, using the idea presented in [36], is studied.

Consider the following functional equation:

$$F(v(t)) = g(t), \tag{22}$$

where F is a functional operator and can be decomposed as $F = D^\alpha + R + N$ and g is a known function.

D^α is a Caputo fractional derivative operator, R is a linear operator, and N is a nonlinear analytic operator, respectively. So equation (22) can be written as follows:

$$D^\alpha(v(t)) = g(t) - R(v(t)) - N(v(t)). \tag{23}$$

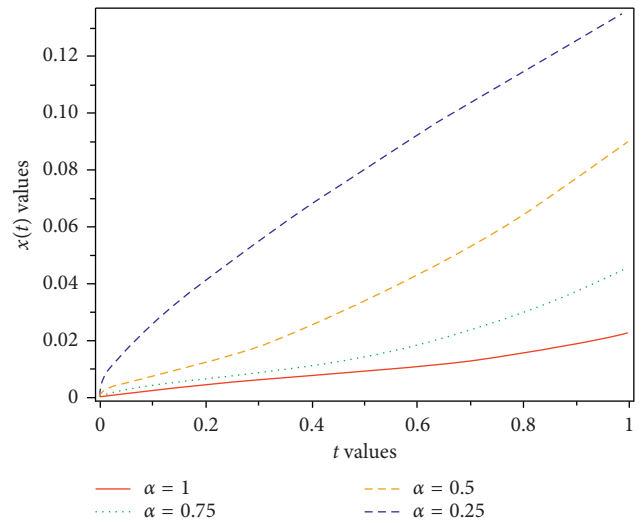

FIGURE 2: Dynamics of infected CD4$^+$ T-cells for various values of α.

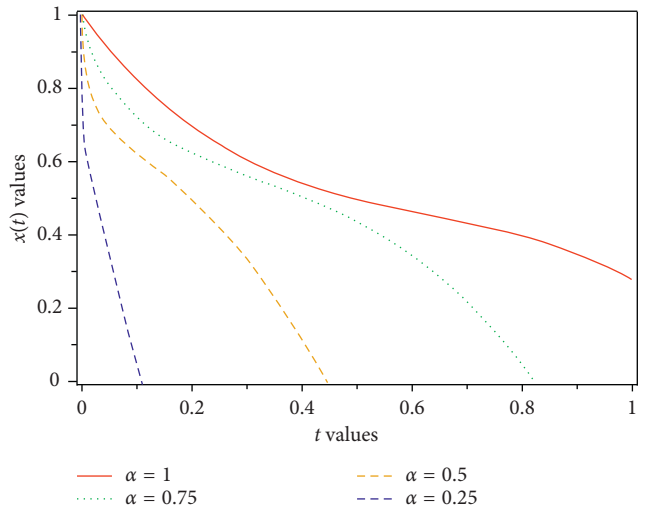

FIGURE 3: Dynamics of density of virions in plasma for various values of α.

The goal is to find a function $v(t)$ satisfying equation (22). By applying the Laplace transform on both sides of equation (23) reads

$$\mathscr{L}\{D^{\alpha}(v(t))\} = \mathscr{L}\{g(t) - R(v(t)) - N(v(t))\}. \tag{24}$$

By using definition (2.3), equation (23) can be written as follows:

$$\mathscr{L}\{v(t)\} = \frac{v(0)}{s} + \frac{\mathscr{L}\{g(t)\}}{s^{\alpha}} - \frac{\mathscr{L}\{R(v(t))\}}{s^{\alpha}} - \frac{\mathscr{L}\{N(v(t))\}}{s^{\alpha}}, \tag{25}$$

by considering $v(0) = v_0$ and using inverse of Laplace transform on both sides of equation (25) results in

$$\mathscr{L}^{-1}\{\mathscr{L}\{v(t)\}\} = \mathscr{L}^{-1}\left\{\frac{v(0)}{s} + \frac{\mathscr{L}\{g(t)\}}{s^{\alpha}} - \frac{\mathscr{L}\{R(v(t))\}}{s^{\alpha}} - \frac{\mathscr{L}\{N(v(t))\}}{s^{\alpha}}\right\}, \tag{26}$$

which implies that

$$v(t) = v_0 + \mathscr{L}^{-1}\left\{\frac{\mathscr{L}\{g(t)\}}{s^{\alpha}}\right\} - \mathscr{L}^{-1}\left\{\frac{\mathscr{L}\{R(v(t))\}}{s^{\alpha}}\right\} - \mathscr{L}^{-1}\left\{\frac{\mathscr{L}\{N(v(t))\}}{s^{\alpha}}\right\}. \tag{27}$$

By implementing ADM and assuming the solution $v(t)$ as an infinite series say, $v(t) = \sum_{n=0}^{\infty} v_n(t)$, and writing the nonlinear term based on Adomian polynomials such as

$$N(v(t)) = \sum_{n=0}^{\infty} p_n(v_0(t), v_1(t), \ldots, v_n(t)), \tag{28}$$

where

$$p_n(v_0(t), v_1(t), \ldots, v_n(t)) = \frac{1}{\Gamma(n+1)} \frac{d^n}{d\lambda^n} \left\{ N_{\lambda}\left(\sum_{i=0}^{n} v_i(t)\lambda^i \right) \right\}_{\lambda=0}. \tag{29}$$

Equation (27) can be written as the following form:

$$\sum_{n=0}^{\infty} v_n(t) = v_0 + \mathscr{L}^{-1}\left\{\frac{\mathscr{L}\{g(t)\}}{s^\alpha}\right\} - \mathscr{L}^{-1}\left\{\frac{\mathscr{L}\{R(\sum_{n=0}^{\infty} v_n(t))\}}{s^\alpha}\right\} - \mathscr{L}^{-1}\left\{\frac{\mathscr{L}\{\sum_{n=0}^{\infty} p_n(v_0(t), v_1(t), \ldots, v_n(t))\}}{s^\alpha}\right\}. \tag{30}$$

So, we have

$$\sum_{n=0}^{\infty} v_n(t) = v_0 + \mathscr{L}^{-1}\left\{\frac{\mathscr{L}\{g(t)\}}{s^\alpha}\right\} - \sum_{n=0}^{\infty}\mathscr{L}^{-1}\left\{\frac{\mathscr{L}\{R(v_n(t))\}}{s^\alpha}\right\} - \sum_{n=0}^{\infty}\mathscr{L}^{-1}\left\{\frac{\mathscr{L}\{p_n(v_0(t), v_1(t), \ldots, v_n(t))\}}{s^\alpha}\right\}. \tag{31}$$

From which we can define

$$\begin{cases} v_0(t) = v_0, \\ v_1(t) = \mathscr{L}^{-1}\left\{\frac{\mathscr{L}\{g(t)\}}{s^\alpha}\right\} - \mathscr{L}^{-1}\left\{\frac{\mathscr{L}\{R(v_0(t))\}}{s^\alpha}\right\} - \mathscr{L}^{-1}\left\{\frac{\mathscr{L}\{p_0(v_0(t))\}}{s^\alpha}\right\}, \\ v_2(t) = -\mathscr{L}^{-1}\left\{\frac{\mathscr{L}\{R(v_1(t))\}}{s^\alpha}\right\} - \mathscr{L}^{-1}\left\{\frac{\mathscr{L}\{p_1(v_0(t), v_1(t))\}}{s^\alpha}\right\}, \\ \vdots \\ v_{n+1}(t) = -\mathscr{L}^{-1}\left\{\frac{\mathscr{L}\{R(v_n(t))\}}{s^\alpha}\right\} - \mathscr{L}^{-1}\left\{\frac{\mathscr{L}\{p_n(v_0(t), v_1(t), \ldots, v_n(t))\}}{s^\alpha}\right\}. \end{cases} \tag{32}$$

Theorem 5.1. *LADM for equation (21) with the solution (19) is equivalent to*

$$\begin{aligned} s_n(t) &= v_0(t) + v_1(t) + \ldots + v_n(t), \\ s_0(t) &= v_0(t). \end{aligned} \tag{33}$$

By using the following iterative scheme:

$$s_{n+1}(t) = v_0 + \mathscr{L}^{-1}\left\{\frac{\mathscr{L}\{g(t)\}}{s^\alpha}\right\} - \mathscr{L}^{-1}\left\{\frac{\mathscr{L}\{R(s_n(t))\}}{s^\alpha}\right\} - \mathscr{L}^{-1}\left\{\frac{\mathscr{L}\{N(s_n(t))\}}{s^\alpha}\right\}, \tag{34}$$

where

$$N\left(\sum_{i=0}^{n} v_i(t)\right) = \sum_{i=0}^{n} p_i(v_0(t), v_1(t), \ldots, v_i(t)), \quad n = 0, 1, 2, \ldots. \tag{35}$$

Proof. For $n = 0$, from equation (33):

$$\begin{aligned} s_1(t) &= v_0 + \mathscr{L}^{-1}\left\{\frac{\mathscr{L}\{g(t)\}}{s^\alpha}\right\} - \mathscr{L}^{-1}\left\{\frac{\mathscr{L}\{R(s_0(t))\}}{s^\alpha}\right\} - \mathscr{L}^{-1}\left\{\frac{\mathscr{L}\{N(s_0(t))\}}{s^\alpha}\right\} \\ &= v_0 + \mathscr{L}^{-1}\left\{\frac{\mathscr{L}\{g(t)\}}{s^\alpha}\right\} - \mathscr{L}^{-1}\left\{\frac{\mathscr{L}\{R(v_0(t))\}}{s^\alpha}\right\} - \mathscr{L}^{-1}\left\{\frac{\mathscr{L}\{p_0(v_0(t))\}}{s^\alpha}\right\}. \end{aligned} \tag{36}$$

Then, by assumption of equation (33), we have

$$v_1(t) = \mathscr{L}^{-1}\left\{\frac{\mathscr{L}\{g(t)\}}{s^\alpha}\right\} - \mathscr{L}^{-1}\left\{\frac{\mathscr{L}\{R(v_0(t))\}}{s^\alpha}\right\} - \mathscr{L}^{-1}\left\{\frac{\mathscr{L}\{p_0(v_0(t))\}}{s^\alpha}\right\}, \tag{37}$$

for $n = 1$:

$$\begin{aligned} s_2(t) &= v_0 + \mathscr{L}^{-1}\left\{\frac{\mathscr{L}\{g(t)\}}{s^\alpha}\right\} - \mathscr{L}^{-1}\left\{\frac{\mathscr{L}\{R(s_1(t))\}}{s^\alpha}\right\} - \mathscr{L}^{-1}\left\{\frac{\mathscr{L}\{N(s_1(t))\}}{s^\alpha}\right\} \\ &= v_0 + \mathscr{L}^{-1}\left\{\frac{\mathscr{L}\{g(t)\}}{s^\alpha}\right\} - \mathscr{L}^{-1}\left\{\frac{\mathscr{L}\{R(v_0(t) + v_1(t))\}}{s^\alpha}\right\} - \mathscr{L}^{-1}\left\{\frac{\mathscr{L}\{p_0(v_0(t)) + p_1(v_0(t), v_1(t))\}}{s^\alpha}\right\} \\ &= v_0(t) + v_1(t) - \mathscr{L}^{-1}\left\{\frac{\mathscr{L}\{R(v_1(t))\}}{s^\alpha}\right\} - \mathscr{L}^{-1}\left\{\frac{\mathscr{L}\{p_1(v_0(t), v_1(t))\}}{s^\alpha}\right\}. \end{aligned} \tag{38}$$

We know that $s_2(t) = v_0(t) + v_1(t) + v_2(t)$, so we obtain

$$v_2(t) = -\mathscr{L}^{-1}\left\{\frac{\mathscr{L}\{R(v_1(t))\}}{s^\alpha}\right\} - \mathscr{L}^{-1}\left\{\frac{\mathscr{L}\{p_1(v_0(t), v_1(t))\}}{s^\alpha}\right\}. \tag{39}$$

By strong induction, let us have

$$v_{k+1}(t) = -\mathscr{L}^{-1}\left\{\frac{\mathscr{L}\{R(v_k(t))\}}{s^\alpha}\right\} - \mathscr{L}^{-1}\left\{\frac{\mathscr{L}\{p_k(v_0(t), v_1(t), \ldots, v_k(t))\}}{s^\alpha}\right\}, \quad k = 1, 2, \ldots, n-1, \tag{40}$$

and prove the following for $k = n$,

$$\begin{aligned} s_{n+1}(t) &= v_0 + \mathscr{L}^{-1}\left\{\frac{\mathscr{L}\{g(t)\}}{s^\alpha}\right\} - \mathscr{L}^{-1}\left\{\frac{\mathscr{L}\{R(s_n(t))\}}{s^\alpha}\right\} \\ &\quad - \mathscr{L}^{-1}\left\{\frac{\mathscr{L}\{N(s_n(t))\}}{s^\alpha}\right\} \\ &= v_0 + \mathscr{L}^{-1}\left\{\frac{\mathscr{L}\{g(t)\}}{s^\alpha}\right\} - \mathscr{L}^{-1}\left\{\frac{\mathscr{L}\{R(\sum_{k=0}^{n} v_k(t))\}}{s^\alpha}\right\} \\ &\quad - \mathscr{L}^{-1}\left\{\frac{\mathscr{L}\{\sum_{k=0}^{n} p_k(v_0(t), v_1(t), \ldots, v_k(t))\}}{s^\alpha}\right\} \\ &= v_0 + \mathscr{L}^{-1}\left\{\frac{\mathscr{L}\{g(t)\}}{s^\alpha}\right\} - \sum_{k=0}^{n}\mathscr{L}^{-1}\left\{\frac{\mathscr{L}\{R(v_k(t))\}}{s^\alpha}\right\} \\ &\quad - \sum_{k=0}^{n}\mathscr{L}^{-1}\left\{\frac{\mathscr{L}\{p_k(v_0(t), v_1(t), \ldots, v_k(t))\}}{s^\alpha}\right\} \\ &= v_0(t) + v_1(t) + \ldots v_n(t) - \mathscr{L}^{-1}\left\{\frac{\mathscr{L}\{R(v_n(t))\}}{s^\alpha}\right\} \\ &\quad - \mathscr{L}^{-1}\left\{\frac{\mathscr{L}\{p_n(v_0(t), v_1(t), \ldots, v_n(t))\}}{s^\alpha}\right\}. \end{aligned} \tag{41}$$

Then, from equation (33), we derive

$$v_{n+1}(t) = -\mathscr{L}^{-1}\left\{\frac{\mathscr{L}\{R(v_n(t))\}}{s^\alpha}\right\} - \mathscr{L}^{-1}\left\{\frac{\mathscr{L}\{p_n(v_0(t), v_1(t), \ldots, v_n(t))\}}{s^\alpha}\right\}. \tag{42}$$

This entails the statement is true and the theorem is proved. □

Theorem 5.2. *Let X be a Banach space.*

(i) $\sum_{i=0}^{\infty} v_i(t)$ resulted from equation (31), convergence to $s \in X$, if $\exists\ c \in [0, 1)$, s.t $(\forall\ n \in \mathbb{N} \Longrightarrow \|v_{n+1}\| \le c\ \|v_n\|)$,

(ii) $s(t) = \sum_{i=0}^{\infty} v_i(t)$ satisfies in

$$s(t) = v_0 + \mathscr{L}^{-1}\left\{\frac{\mathscr{L}\{g(t)\}}{s^\alpha}\right\} - \mathscr{L}^{-1}\left\{\frac{\mathscr{L}\{R(s(t))\}}{s^\alpha}\right\} - \mathscr{L}^{-1}\left\{\frac{\mathscr{L}\{N(s(t))\}}{s^\alpha}\right\}. \tag{43}$$

Proof.

$$\|s_{n+1} - s_n\| = \|v_{n+1}\| \le c\|v_n\| \le c^2\|v_{n-1}\| \le \ldots \le c^{n+1}\|v_0\|. \tag{44}$$

$\forall n, m \in \mathbb{N}, n \ge m$, we have

$$\begin{aligned} \|s_n - s_m\| &= \|(s_n - s_{n-1}) + (s_{n-1} - s_{n-2}) + \ldots + (s_{m+1} - s_m)\| \\ &\le \|s_n - s_{n-1}\| + \|s_{n-1} - s_{n-2}\| + \ldots + \|s_{m+1} - s_m\| \\ &\le c^n\|v_0\| + c^{n-1}\|v_0\| + \ldots + c^{m+1}\|v_0\| \\ &\le \left(c^n + c^{n-1} + \ldots + c^{m+1}\right)\|v_0\| \\ &\le c^{m+1}\left(1 + c + c^2 + \ldots + c^n + \ldots\right) \le \frac{c^{m+1}}{1-c}\|v_0\|. \end{aligned} \tag{45}$$

This means that $\lim_{n,m\longrightarrow\infty} \|s_n - s_m\| = 0$, therefore, $\{s_n\}$ is a Cauchy sequence in the Banach space of X and is convergent. So, $\exists\ s\ \epsilon\ X$, s.t $\lim_{n\longrightarrow\infty} s_n = s$.

From equation (33), we derive

$$\begin{aligned} \lim_{n\longrightarrow\infty} s_n(t) &= v_0 + \mathscr{L}^{-1}\left\{\frac{\mathscr{L}\{g(t)\}}{s^\alpha}\right\} \\ &\quad - \mathscr{L}^{-1}\left\{\frac{\mathscr{L}\left\{\lim_{n\longrightarrow\infty} R(s_n(t))\right\}}{s^\alpha}\right\} \\ &\quad - \mathscr{L}^{-1}\left\{\frac{\mathscr{L}\left\{\lim_{n\longrightarrow\infty} N(s_n(t))\right\}}{s^\alpha}\right\} \\ &= v_0 + \mathscr{L}^{-1}\left\{\frac{\mathscr{L}\{g(t)\}}{s^\alpha}\right\} \\ &\quad - \mathscr{L}^{-1}\left\{\frac{\mathscr{L}\left\{\lim_{n\longrightarrow\infty} R(\sum_{k=0}^{n} v_k(t))\right\}}{s^\alpha}\right\} \\ &\quad - \mathscr{L}^{-1}\left\{\frac{\mathscr{L}\left\{\lim_{n\longrightarrow\infty} N(\sum_{k=0}^{n} v_k(t))\right\}}{s^\alpha}\right\} \\ &= v_0 + \mathscr{L}^{-1}\left\{\frac{\mathscr{L}\{g(t)\}}{s^\alpha}\right\} \\ &\quad - \mathscr{L}^{-1}\left\{\frac{\mathscr{L}\left\{\lim_{n\longrightarrow\infty} \sum_{k=0}^{n} R(v_k(t))\right\}}{s^\alpha}\right\} \\ &\quad - \mathscr{L}^{-1}\left\{\frac{\mathscr{L}\left\{\lim_{n\longrightarrow\infty} \sum_{k=0}^{n} p_k(v_0(t), v_1(t), \ldots, v_k(t))\right\}}{s^\alpha}\right\} \\ &= v_0 + \mathscr{L}^{-1}\left\{\frac{\mathscr{L}\{g(t)\}}{s^\alpha}\right\} \\ &\quad - \mathscr{L}^{-1}\left\{\frac{\mathscr{L}\{\sum_{k=0}^{\infty} R(v_k(t))\}}{s^\alpha}\right\} \\ &\quad - \mathscr{L}^{-1}\left\{\frac{\mathscr{L}\{\sum_{k=0}^{\infty} p_k(v_0(t), v_1(t), \ldots, v_k(t))\}}{s^\alpha}\right\}, \end{aligned} \tag{46}$$

From equation (35), we have

$$N\left(\sum_{i=0}^{\infty} v_i(t)\right) = \sum_{i=0}^{\infty} p_i\left(v_0(t), v_1(t), \ldots, v_i(t)\right), \quad n = 0, 1, 2. \ldots. \tag{47}$$

So,

$$\begin{aligned} s(t) &= v_0 + \mathscr{L}^{-1}\left\{\frac{\mathscr{L}\{g(t)\}}{s^\alpha}\right\} - \mathscr{L}^{-1}\left\{\frac{\mathscr{L}\{R\left(\sum_{k=0}^{\infty} v_k(t)\right)\}}{s^\alpha}\right\} \\ &\quad - \mathscr{L}^{-1}\left\{\frac{\mathscr{L}\{N\left(\sum_{k=0}^{\infty} v_k(t)\right)\}}{s^\alpha}\right\} \\ &= v_0 + \mathscr{L}^{-1}\left\{\frac{\mathscr{L}\{g(t)\}}{s^\alpha}\right\} - \mathscr{L}^{-1}\left\{\frac{\mathscr{L}\{R(s(t))\}}{s^\alpha}\right\} \\ &\quad - \mathscr{L}^{-1}\left\{\frac{\mathscr{L}\{N(s(t))\}}{s^\alpha}\right\}. \end{aligned} \tag{48}$$

□

Lemma 5.1. *Equation (43) is equivalent to equation (22).*

Proof. By using Laplace transform on both sides of equation (43) reads to

$$\begin{aligned} \mathscr{L}(s(t)) &= \mathscr{L}(v_0) + \frac{\mathscr{L}\{g(t)\}}{s^\alpha} - \frac{\mathscr{L}\{R(s(t))\}}{s^\alpha} - \frac{\mathscr{L}\{N(s(t))\}}{s^\alpha} \\ &= \frac{v(0)}{s} + \frac{\mathscr{L}\{g(t)\}}{s^\alpha} - \frac{\mathscr{L}\{R(s(t))\}}{s^\alpha} - \frac{\mathscr{L}\{N(s(t))\}}{s^\alpha} \\ &= \frac{s^{\alpha-1}v(0)}{s^\alpha} + \frac{\mathscr{L}\{g(t)\}}{s^\alpha} - \frac{\mathscr{L}\{R(s(t))\}}{s^\alpha} - \frac{\mathscr{L}\{N(s(t))\}}{s^\alpha}, \end{aligned} \tag{49}$$

so we can write

$$\begin{aligned} s^\alpha \mathscr{L}(s(t)) - s^{\alpha-1}v(0) &= \mathscr{L}\{g(t)\} - \mathscr{L}\{R(s(t))\} \\ &\quad - \mathscr{L}\{N(s(t))\}. \end{aligned} \tag{50}$$

In virtue of definition 2.3 and linearity of the Laplace transform, equation (50) can be written as the follows:

$$\mathscr{L}\{D^\alpha s(t)\} = \mathscr{L}\{g(t) - R(s(t)) - N(s(t))\}. \tag{51}$$

By applying the inverse of Laplace transform on both sides of equation (51), we derive

$$D^\alpha s(t) = g(t) - R(s(t)) - N(s(t)). \tag{52}$$

Considering $v(t) = s(t)$, one gets equation (22). So, the solution of equation (43) is the same as the solution of equation (22). □

6. Conclusion

In this paper, a fractional-order model of HIV-1 with three components has been introduced. When $\alpha \longrightarrow 1$, then $D^\alpha x(t) \longrightarrow Dx(t)$; therefore, the fractional-order of presented model reduces to traditional model. By applying Laplace transform and Adomian decomposition method, or LADM for short, which is a strong approach to compute numerical solution of fractional differential equations, we gain an approximate solution of the proposed model. The accuracy of the proposed approach has made it a reliable method. We have calculated four terms of the infinite series of x, y, and z as an approximate solution. The result of LADM has been compared with the results of some other methods such as GEM, HAM, RK4 [8], and HPM [31]. The results are presented in Tables 1–3. Figures 1–3, show that the uninfected $CD4^+$ T-cells, x, infected $CD4^+$ T-cells, y, and density of virions in plasma, z, depend on the various values of α, the various values of the parameters, and the time fractional derivative. A comparison of the approximate solutions shows that LADM can work more accurate than other methods. Convergence of the proposed method is studied. Because of the fact that obtaining the exact solution for system of fractional equation is difficult or impossible, we would like to suggest such an easy and reliable approach for further research, in the future.

Data Availability

Data used to support this study are available at DOI: https://doi.org/10.1038/sj.icb.7100056. These prior studies (and datasets) are cited at relevant places within the text as references [6, 8, 16].

Disclosure

This research did not receive specific funding, but has resulted from a Ph.D. program, by Mr. Bijan Hasani Lichaee, under supervision of Prof. Jafar Biazar and cosupervision of Dr. Zainab Ayati.

Conflicts of Interest

The authors declare that they have no conflicts of interest.

References

[1] R. Weiss, "How does HIV cause AIDS?," *Science*, vol. 260, no. 5112, pp. 1273–1279, 1993.

[2] D. C. Douek, M. Roederer, and R. A. Koup, "Emerging concepts in the immunopathogenesis of AIDS," *Annual Review of Medicine*, vol. 60, no. 1, pp. 471–484, 2009.

[3] A. V. Herz, S. Bonhoeffer, R. M. Anderson, R. M. May, and M. A. Nowak, "Viral dynamics in vivo: limitations on estimates of intracellular delay and virus decay," *Proceedings of the National Academy of Sciences*, vol. 93, no. 14, pp. 7247–7251, 1996.

[4] S. Bonhoeffer, J. M. Coffin, and M. A. Nowak, "Human immunodeficiency virus drug therapy and virus load," *Journal of Virology*, vol. 71, no. 4, pp. 3275–3278, 1997.

[5] R. V. Culshaw and S. Ruan, "A delay-differential equation model of HIV infection of $CD4^+$ T-cells," *Mathematical biosciences*, vol. 165, no. 1, pp. 27–39, 2000.

[6] H. C. Tuckwell and F. Y. M. Wan, "On the behavior of solutions in viral dynamical models," *BioSystems*, vol. 73, no. 3, pp. 157–161, 2004.

[7] C. Lv and Z. Yuan, "Stability analysis of delay differential equation models of HIV-1 therapy for fighting a virus with another virus," *Journal of Mathematical Analysis and Applications*, vol. 352, no. 2, pp. 672–683, 2009.

[8] A. A. M. Arafa, S. Z. Rida, and M. Khalil, "The effect of antiviral drug treatment of human immunodeficiency virus type 1 (HIV-1) described by a fractional order model," *Applied Mathematical Modelling*, vol. 37, no. 4, pp. 2189–2196, 2013.

[9] A. A. M. Arafa, S. Z. Rida, and M. Khalil, "Fractional modeling dynamics of HIV and CD4+ T-cells during primary infection," *Nonlinear biomedical physics*, vol. 6, no. 1, p. 1, 2012.

[10] Y. Yan and C. Kou, "Stability analysis for a fractional differential model of HIV infection of $CD4^+$ T-cells with time delay," *Mathematics and Computers in Simulation*, vol. 82, no. 9, pp. 1572–1585, 2012.

[11] L. Wang and M. Y. Li, "Mathematical analysis of the global dynamics of a model for HIV infection of $CD4^+$ T cells," *Mathematical Biosciences*, vol. 200, no. 1, pp. 44–57, 2006.

[12] A. S. Perelson, D. E. Kirschner, and R. De Boer, "Dynamics of HIV infection of $CD4^+$ T cells," *Mathematical Biosciences*, vol. 114, no. 1, pp. 81–125, 1993.

[13] J. Biazar, "Solution of the epidemic model by Adomian decomposition method," *Applied Mathematics and Computation*, vol. 173, no. 2, pp. 1101–1106, 2006.

[14] R. M. Anderson and R. M. May, "Population biology of infectious diseases: part I," *Nature*, vol. 280, no. 5721, pp. 361–367, 1979.

[15] R. M. May and R. M. Anderson, "Population biology of infectious diseases: part II," *Nature*, vol. 280, no. 5722, pp. 455–461, 1979.

[16] H. C. Tuckwell and F. Y. M. Wan, "Nature of equilibria and effects of drug treatments in some simple viral population dynamical models," *IMA Journal of Mathematical Control and Information*, vol. 17, no. 4, pp. 311–327, 2000.

[17] N. Heymans and J.-C. Bauwens, "Fractal rheological models and fractional differential equations for viscoelastic behavior," *Rheologica Acta*, vol. 33, no. 3, pp. 210–219, 1994.

[18] M. Giona and H. E. Roman, "Fractional diffusion equation on fractals: one-dimensional case and asymptotic behaviour," *Journal of Physics A: Mathematical and General*, vol. 25, no. 8, pp. 2093–2105, 1999.

[19] F. B. Tatom, "The relationship between fractional calculus and fractals," *Fractals*, vol. 3, no. 1, pp. 217–229, 1995.

[20] S. J. Liao, *The proposed homotopy analysis technique for the solution of nonlinear problems*, Ph.D. thesis, Shanghai Jiao Tong University, Shanghai, China, 1992.

[21] V. S. Ertürk, Z. M. Odibat, and S. Momani, "An approximate solution of a fractional order differential equation model of human T-cell lymphotropic virus I (HTLV-I) infection of $CD4^+$ T-cells," *Computers and Mathematics with Applications*, vol. 62, no. 3, pp. 996–1002, 2011.

[22] Y. Ding and H. Ye, "A fractional-order differential equation model of HIV infection of $CD4^+$ T-cells," *Mathematical and Computer Modelling*, vol. 50, no. 3-4, pp. 386–392, 2009.

[23] F. Haq, K. Shah, G. U. Rahman et al., "Numerical solution of fractional order smoking model via laplace Adomian decomposition method," *Alexandria Engineering Journal*, vol. 57, no. 2, pp. 1061–1069, 2017.

[24] M. Merdan, A. Gökdoğan, and A. Yildirim, "On the numerical solution of the model for HIV infection of $CD4^+$ T cells," *Computers and Mathematics with Applications*, vol. 62, no. 1, pp. 118–123, 2011.

[25] Y. Khan, H. Vazquez-Leal, and Q. Wu, "An efficient iterated method for mathematical biology model," *Neural Computing and Applications*, vol. 23, no. 3-4, pp. 677–682, 2013.

[26] Ş. Yüzbaşı, "A numerical approach to solve the model for HIV infection of $CD4^+$ T cells," *Applied Mathematical Modelling*, vol. 36, no. 12, pp. 5876–5890, 2012.

[27] M. Ghoreishi, A. M. Ismail, and A. Alomari, "Application of the homotopy analysis method for solving a model for HIV infection of $CD4^+$ T-cells," *Mathematical and Computer Modelling*, vol. 54, no. 11-12, pp. 3007–3015, 2011.

[28] A. Atangana and E. F. D. Goufo, "On the mathematical analysis of Ebola hemorrhagic fever: deathly infection disease in West African countries," *BioMed Research International*, vol. 2014, Article ID 261383, 7 pages, 2014.

[29] M. Y. Ongun, "The Laplace adomian decomposition method for solving a model for HIV infection of $CD4^+$ T cells," *Mathematical and Computer Modelling*, vol. 53, no. 5-6, pp. 597–603, 2011.

[30] A. A. M. Arafa, S. Rida, and M. Khalil, "A fractional-order model of HIV infection with drug therapy effect," *Journal of the Egyptian Mathematical Society*, vol. 22, no. 3, pp. 538–543, 2014.

[31] M. Merdan and T. Khan, "Homotopy perturbation method for solving viral dynamical model," *CÜ Fen-Edebiyat Fakültesi, Fen Bilimleri Dergisi*, vol. 31, pp. 65–77, 2010.

[32] G. Adomian, *Nonlinear Stochastic Systems Theory and Applications to Physics*, Springer Science & Business Media, Vol. 46, Springer Science & Business Media, Berlin, Germany, 1988.

[33] K. Diethelm, *The Analysis of Fractional Differential Equations: An Application-Oriented Exposition using Differential Operators of Caputo Type*, Springer, Berlin, Germany, 2010.

[34] A. A. Kilbas, H. M. Srivastava, and J. J. Trujillo, *Preface*, Elsevier, New York City, NY, USA, 2006.

[35] J. Biazar, E. Babolian, G. Kember, A. Nouri, and R. Islam, "An alternate algorithm for computing Adomian polynomials in special cases," *Applied Mathematics and Computation*, vol. 138, no. 2-3, pp. 523–529, 2003.

[36] Z. Ayati and J. Biazar, "On the convergence of Homotopy perturbation method," *Journal of the Egyptian Mathematical Society*, vol. 23, no. 2, pp. 424–428, 2015.

Hindawi
Computational and Mathematical Methods in Medicine
Volume 2018, Article ID 4091497, 8 pages
https://doi.org/10.1155/2018/4091497

Research Article

Control of Blood Glucose for Type-1 Diabetes by Using Reinforcement Learning with Feedforward Algorithm

Phuong D. Ngo,[1] **Susan Wei**,[2] **Anna Holubová**,[3] **Jan Muzik**,[3] **and Fred Godtliebsen**[1]

[1]*UiT The Arctic University of Norway, Tromsø, Norway*
[2]*The University of Melbourne, Australia*
[3]*Czech Technical University, Prague, Czech Republic*

Correspondence should be addressed to Phuong D. Ngo; phuong.ngo@uit.no

Received 9 August 2018; Revised 18 November 2018; Accepted 28 November 2018; Published 30 December 2018

Guest Editor: Ka L. Man

Background. Type-1 diabetes is a condition caused by the lack of insulin hormone, which leads to an excessive increase in blood glucose level. The glucose kinetics process is difficult to control due to its complex and nonlinear nature and with state variables that are difficult to measure. *Methods*. This paper proposes a method for automatically calculating the basal and bolus insulin doses for patients with type-1 diabetes using reinforcement learning with feedforward controller. The algorithm is designed to keep the blood glucose stable and directly compensate for the external events such as food intake. Its performance was assessed using simulation on a blood glucose model. The usage of the Kalman filter with the controller was demonstrated to estimate unmeasurable state variables. *Results*. Comparison simulations between the proposed controller with the optimal reinforcement learning and the proportional-integral-derivative controller show that the proposed methodology has the best performance in regulating the fluctuation of the blood glucose. The proposed controller also improved the blood glucose responses and prevented hypoglycemia condition. Simulation of the control system in different uncertain conditions provided insights on how the inaccuracies of carbohydrate counting and meal-time reporting affect the performance of the control system. *Conclusion*. The proposed controller is an effective tool for reducing postmeal blood glucose rise and for countering the effects of external known events such as meal intake and maintaining blood glucose at a healthy level under uncertainties.

1. Introduction

Type-1 diabetes is a chronic condition that is characterized by an excessive increase in blood glucose level because the pancreas does not produce insulin hormone due to the autoimmune destruction of pancreatic beta cells. High blood glucose can lead to both acute and chronic complications and eventually result in failure of various organs.

Until today, there are many challenges in control of the blood glucose in type-1 diabetes. One of them is that the glucose kinetics process is complex, nonlinear, and only approximately known [1]. There are also many external known and unknown factors that affect the blood glucose level such as food intakes, physical activities, stress, and hormone changes. Generally, it is difficult to predict and quantify those factors and disturbances.

By using control theories, various studies have been conducted to design a control system for patients with type-1 diabetes. For example, Marchetti et al. [2], derived an improved proportional-integral-derivative controller for blood glucose control. Soylu et al. [3] proposed a Mamdani type fuzzy control strategy for exogenous insulin infusion. Model predictive control has also been widely used in type-1 diabetes and artificial pancreas development [4, 5]. Recently, together with the development of artificial intelligence and machine learning, reinforcement learning (RL) has emerged as a data-driven method to control unknown nonlinear systems [6, 7] and has been used as a long-term management tool for chronic diseases [8, 9]. The biggest advantage of RL compared to other methods is that the algorithm depends only on interactions with the system and does not require a well represented model of the environment. This especially

makes RL well suited for type-1 diabetes since the modelling process of the insulin-kinetic dynamics is complex and requires invasive measurements on the patient or must be fit through a large dataset. Hence, by using RL as the control algorithm, the modelling process can be bypassed, which makes the algorithm not susceptible to any modelling error.

In diabetes, controlling of blood glucose require actions that are made at specific instance throughout the day in terms of insulin doses or food intakes. The actions are based on the current observable states of the patients (e.g., blood glucose measurement and heart rate). The effectiveness of the actions is calculated by how far the measured blood glucose value is compared to the healthy level. In RL, an agent makes decision based on the current state of the environment. The task of the algorithm is to maximize a cumulative reward function or to minimize a cumulative cost function. Based on these similarities in the decision-making process between a human being and a RL agent, RL may be key to the development of an artificial pancreas system.

When dealing with meal disturbances, modelling of glucose ingestion is the norm as well as the first step in designing a controller for disturbance rejection [10]. Feed-forward control was proven to be an effective tool to improve disturbance rejection performance [11, 12]. In control system theory, feed-forward is the term that describes a controller that utilizes the signal obtained when there is a (large) deviation from the model. Compared to feed-back control, where action is only taken after the output has moved away from the setpoint, the feed-forward architecture is more proactive since it uses the disturbance model to suggest the time and size of control action. Furthermore, building a meal disturbance model is simpler and requires less data to fit than finding the insulin-glucose kinetics. Based on the model, necessary changes in insulin actions can be calculated to compensate for the effects of carbohydrate on the blood glucose level.

A challenge in the control of the blood glucose is the lack of real-time measurement techniques. With the development of continuous glucose measurement sensors, blood glucose level can be measured and provided to the controller in minute intervals. However, blood glucose value alone is usually not enough to describe the states of the system for control purpose. Therefore, an observer is needed to estimate other variables in the state space from the blood glucose measurement. In this paper, the Kalman filter was chosen for that purpose since it can provide an optimal estimation of the state variables when the system is subjected to process and measurement noises [13, 14].

Vrabie et al. [15] established methodologies to obtain optimal adaptive control algorithms for dynamical systems with unknown mathematical models by using reinforcement learning. Based on that, Ngo et al. [16] proposed a reinforcement learning algorithm for updating basal rates in patients with type-1 diabetes. This paper completes the framework for blood glucose control with both basal and bolus insulin doses. The framework includes the reinforcement learning algorithm, the feed-forward controller for compensating food intake and the Kalman filter for estimating unmeasurable state variables during the control process. This paper also conducts simulations under uncertain information to evaluate the robustness of the proposed controller.

2. Methods

2.1. Problem Formulation. The purpose of our study is to design an algorithm to control the blood glucose in patients with type-1 diabetes by the means of changing the insulin concentration. The blood glucose metabolism is a dynamic system in which the blood glucose changing over time as the results of many factors such as food intake, insulin doses, physical activities, and stress level. The learning process of RL is based on the interaction between a decision-making agent and its environment, which will lead to an optimal action policy that results in desirable states [17]. The RL framework for type-1 diabetes includes the following elements:

(i) The state vector at time instance k consists of the states of the patient:

$$\mathbf{x}_k = \left[\, g(k) - g_{\mathrm{d}}(k) \;\; \chi(k) \,\right]^T, \tag{1}$$

where $g(k)$ and $g_{\mathrm{d}}(k)$ the are measured and desired blood glucose levels, respectively, and $\chi(k)$ is the interstitial insulin activity (defined in the appendix).

(ii) The control variable (insulin action) u_k, which is part of the total insulin i_k (a combination of the basal and the bolus insulin (Figure 1)):

$$i_k = u_{\mathrm{basal}}(k) + u_{\mathrm{bolus}}(k) = u_k + u_{\mathrm{basal}}(0) + u_{\mathrm{bolus}}(k), \tag{2}$$

where $u_{\mathrm{basal}}(k)$ and $u_{\mathrm{bolus}}(k)$ are the basal and bolus at time instance k, respectively.

(iii) The cost received one time-step later as a consequence of the action. In this paper, the cost was calculated by the following quadratic function:

$$r_{k+1} = \mathbf{x}_k^T \mathbf{Q} \mathbf{x}_k + u_k^T R u_k, \tag{3}$$

where $\mathbf{Q} = \begin{bmatrix} 1 & 0 \\ 0 & 0.1 \end{bmatrix}$ and $R = 0.01$. Each element in matrix $\mathbf{Q}$ and the value of R indicate the weighting factors of the cost function. The element in the first row and the first column of $\mathbf{Q}$ has the highest value, which corresponds to the weighting of the difference between the measured blood glucose and the prescribed healthy value. Since our ultimate goal is to reduce this difference, the factor of this measurement should have the largest value in the cost function. The element in the second row and second column of $\mathbf{Q}$ corresponds to the weighting of the interstitial insulin activity. The value of R indicates the weighting factor of the action (basal update). Minimizing the cost function, therefore, becomes the problem of minimizing the difference

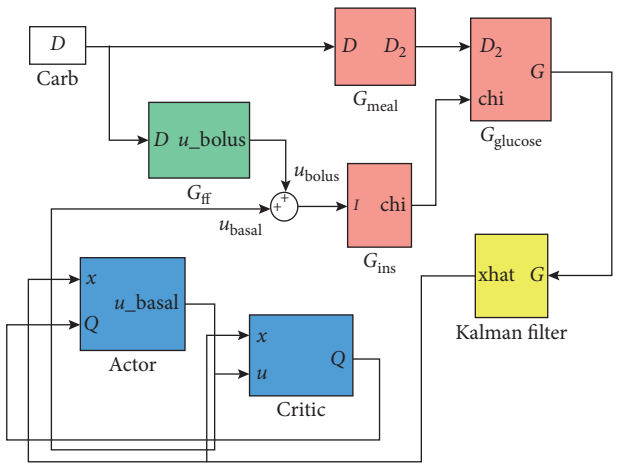

Figure 1: Control system diagram.

between the measured blood glucose and the desired value, the interstitial insulin activity, and the change in basal insulin.

At time instance $k+1$, a sequence of observations would be $\mathbf{x}_k$, u_k, r_{k+1}, $\mathbf{x}_{k+1}$ and u_{k+1}. Based on this observation, the agent receives information about the state of the patient and chooses an insulin action. The body reacts to this action and transitions to a new state. This determines the cost of the action.

For the control design purpose, the blood glucose model (Appendix) was divided into three submodels: the meal (G_{meal}), the insulin (G_{ins}), and the glucose kinetics (G_{glucose}). The controller has three main components: the actor, the critic, and the feedforward algorithm. The actor is used to estimate the action-value function, the critic's task is to obtain optimal basal insulin, and the feedforward algorithm is used to propose the bolus insulin profile for disturbance compensation (food intake). The purpose of the Kalman filter is to estimate unmeasurable states of the patient.

2.2. Basal Update by Actor and Critic. When the patient is in a fasting condition, the controller only needs to change the basal insulin level through the actor and the critic. Based on the current state $\mathbf{x}_k$, the actor proposes an insulin action u_k through the policy $\pi: u_k = \pi(\mathbf{x}_k)$. The updated basal rate is obtained from u_k as follows:

$$u_{\text{basal}} = u_k + u_{\text{basal}}(0). \tag{4}$$

After each action, the patient transforms into a new state, and the cost associated with the previous action can be calculated using equation (3). The action-value function (Q-function) of action u is defined as the accumulation of cost when the controller takes action $u_k = u$ at time instance k and then continues following policy $\pi(\mathbf{x}_{k+1})$:

$$Q_k^\pi(\mathbf{x}, u) = \mathbb{E}_\pi\left\{\sum_{i=0}^{\infty} \gamma^i r_{k+i+1} \mid \mathbf{x}_k = \mathbf{x}, u_k = u\right\}, \tag{5}$$

where γ (with $0 < \gamma \leq 1$) is the discount factor that indicates the weighting of future cost in the action-value function.

The action-value function depends on the current state and the next action. It was shown that the action-value function satisfies the following recursive equation (Bellman equation) [15, 17]:

$$Q_k^\pi(\mathbf{x}, u) = r_k + \gamma Q_{k+1}^\pi(\mathbf{x}, u). \tag{6}$$

Since the state space and action space are infinite, function approximation was used in this paper for estimation of the Q-function. In this case, the Q-function was approximated as a quadratic function of vectors $\mathbf{x}_k$ and u_k:

$$Q_k^\pi(\mathbf{x}, u) \approx \mathbf{z}_k^T \mathbf{P} \mathbf{z}_k, \tag{7}$$

where the symmetric and positive definite matrix $\mathbf{P}$ is called the kernel matrix and contains the parameters that need to be estimated. Vector $\mathbf{z}_k$ is the combined vector of $\mathbf{x}_k$ and u_k:

$$\mathbf{z} = \begin{bmatrix} \mathbf{x}_k^T & u_k^T \end{bmatrix}^T. \tag{8}$$

With Kronecker operation, the approximated Q-function can be expressed as a linear combination of the basis function $\Phi(\mathbf{z}_k) = \mathbf{z}_k \otimes \mathbf{z}_k$:

$$Q_k^\pi(\mathbf{x}, u) \approx \mathbf{z}_k^T \mathbf{P} \mathbf{z}_k = \mathbf{w}^T(\mathbf{z}_k \otimes \mathbf{z}_k) = \mathbf{w}^T \Phi(\mathbf{z}_k), \tag{9}$$

where $\mathbf{w}$ is the vector that contains elements of $\mathbf{P}$ and $\otimes$ is the Kronecker product.

By substituting $Q_k^\pi(\mathbf{x}, u)$ in equation (6) by $\mathbf{w}^T \Phi(\mathbf{z}_k)$ and using the policy iteration method with the least square algorithm [15], elements of vector $\mathbf{w}$ can be estimated. Matrix $\mathbf{P}$ can then be obtained from $\mathbf{w}$ using the Kronecker transformation.

By decomposing the kernel matrix $\mathbf{P}$ into smaller matrices $\mathbf{P}_{\mathbf{xx}}$, $\mathbf{P}_{\mathbf{x}u}$, $\mathbf{P}_{u\mathbf{x}}$, and $\mathbf{P}_{uu}$, the approximated Q-function can be written as follows:

$$Q_k^\pi(\mathbf{x}, u) = \frac{1}{2}\begin{bmatrix} \mathbf{x}_k \\ u_k \end{bmatrix}^T \mathbf{P} \begin{bmatrix} \mathbf{x}_k \\ u_k \end{bmatrix} = \frac{1}{2}\begin{bmatrix} \mathbf{x}_k \\ u_k \end{bmatrix}^T \begin{bmatrix} \mathbf{P}_{\mathbf{xx}} & \mathbf{P}_{\mathbf{x}u} \\ \mathbf{P}_{u\mathbf{x}} & \mathbf{P}_{uu} \end{bmatrix} \begin{bmatrix} \mathbf{x}_k \\ u_k \end{bmatrix}. \tag{10}$$

The current policy is improved with actions that minimize the Q-function $Q_k^\pi(\mathbf{x}, u)$. This can be done by first taking the partial derivative of the Q-function and then solving $\partial Q_k^\pi(\mathbf{x}, u)/\partial u = 0$. The optimal solution can thereafter be obtained as follows [15]:

$$u_k = -\mathbf{P}_{uu}^{-1} \mathbf{P}_{u\mathbf{x}} \mathbf{x}_k. \tag{11}$$

With that, the update of basal insulin is

$$u_{\text{basal}} = -\mathbf{P}_{uu}^{-1} \mathbf{P}_{u\mathbf{x}} \mathbf{x}_k + i_{\text{be}}, \tag{12}$$

where i_{be} is the equilibrium basal plasma insulin concentration.

2.3. Bolus Update by Feedforward Algorithm. When the patient consumes meals, in addition to the basal insulin, the controller calculates and applies boluses to compensate for the rise of blood glucose as the results of carbohydrate in the food. The feedforward algorithm first predicts how much blood glucose level will rise and then suggests a bolus profile

to counter the effects of the meal. The starting time of the bolus doses was also calculated by the algorithm based on the meal intake model.

Since the meal intake model (equations (A.1) and (A.2)) and the insulin model (equation (A.4)) are linear time-invariant (LTI) models, they can be transformed from state space equations into transfer functions as follows:

$$G_{\text{meal}}(s) = \frac{D_2(s)}{D(s)} = \mathbf{C}_{\text{meal}}\left(s\mathbf{I} - \mathbf{A}_{\text{meal}}\right)^{-1}\mathbf{B}_{\text{meal}} = \frac{A_G}{\left(s\tau_D + 1\right)^2},$$

$$G_{\text{ins}}(s) = \frac{D_2(s)}{D(s)} = \mathbf{C}_{\text{ins}}\left(s\mathbf{I} - \mathbf{A}_{\text{ins}}\right)^{-1}\mathbf{B}_{\text{ins}} = \frac{p_3}{s + p_2}, \tag{13}$$

where

$$\begin{aligned}
\mathbf{A}_{\text{meal}} &= \begin{bmatrix} -1/\tau_D & 0 \\ 1/\tau_D & -1/\tau_D \end{bmatrix}, \\
\mathbf{B}_{\text{meal}} &= \begin{bmatrix} A_G \\ 0 \end{bmatrix}, \\
\mathbf{C}_{\text{meal}} &= \begin{bmatrix} 0 & 1/\tau_D \end{bmatrix}, \\
\mathbf{A}_{\text{ins}} &= -p_2, \\
\mathbf{B}_{\text{ins}} &= p_3, \\
\mathbf{C}_{\text{ins}} &= 1.
\end{aligned} \tag{14}$$

Descriptions and values of τ_D, p_2, and p_3 are shown in Tables 1 and 2. The transfer function from the meal intake $D(s)$ to the blood glucose level $g(s)$ can be calculated as

$$F(s) = \frac{g(s)}{D(s)} = \left(G_{\text{meal}}(s) + G_{\text{ff}}(s)G_{\text{ins}}(s)\right)G_{\text{glucose}}(s). \tag{15}$$

In order to compensate for the meal, the gain of the open loop system $F(s)$ must be made as small as possible. Hence, the feedforward transfer function was chosen such that $G_{\text{meal}}(s) + G_{\text{ff}}(s)G_{\text{ins}}(s) \longrightarrow 0$, which leads to

$$G_{\text{ff}}(s) = -G_{\text{meal}}(s)G_{\text{ins}}^{-1}(s) = \frac{-A_G\left(s + p_2\right)}{p_3\left(\tau_D s + 1\right)^2}. \tag{16}$$

The meal compensation bolus in s-domain can be calculated from the feedforward transfer function:

$$u_{\text{bolus}}(s) = G_{\text{ff}}(s)D(s) = \frac{-A_G\left(s + p_2\right)}{p_3\left(\tau_D s + 1\right)^2}D(s). \tag{17}$$

Hence, the feedforward action becomes the output of the following dynamic system, which can be solved easily using any ordinary differential equation solver:

$$\begin{aligned}
&p_3\tau_D^2\ddot{u}_{\text{bolus}}(t) + 2p_3\tau_D\dot{u}_{\text{bolus}}(t) + p_3u_{\text{bolus}}(t) \\
&\quad = -A_G\left(\dot{D}(t) + p_2D(t)\right).
\end{aligned} \tag{18}$$

2.4. Kalman Filter for Type-1 Diabetes System. Since the interstitial insulin activity, the amounts of glucose in compartments 1 and 2 cannot be measured directly during implementation, Kalman filter was used to provide an estimation of the state variables from the blood glucose level. The discretized version of the type-1 diabetes system can be written in the following form:

$$\begin{aligned}
\mathbf{x}_K(k+1) &= \mathbf{A}_K\mathbf{x}_K(k) + \mathbf{B}_K\mathbf{u}_K(k) + \mathbf{H}_Kw(k), \\
y_K(k) &= \mathbf{C}_K\mathbf{x}_K(k) + v(k),
\end{aligned} \tag{19}$$

where $\mathbf{x}_K(k) = \begin{bmatrix} D_1 & D_2 & g(k) - g_{\text{d}}(k) & \chi(k) \end{bmatrix}^T$, $\mathbf{u}_K(k) = \begin{bmatrix} D(k) & i(k) \end{bmatrix}^T$, and matrices $\mathbf{A}_K$, $\mathbf{B}_K$, $\mathbf{C}_K$ are linearized coefficient matrices of the model:

$$\begin{aligned}
\mathbf{A}_K &= \begin{bmatrix} -1/\tau_D & 0 & 0 & 0 \\ 1/\tau_D & -1/\tau_D & 0 & 0 \\ 0 & 1/\tau_D & -p_1 - g_{\text{d}} & 0 \\ 0 & 0 & 0 & -p_2 \end{bmatrix}, \\
\mathbf{B}_K &= \begin{bmatrix} A_G & 0 \\ 0 & 0 \\ 0 & 0 \\ 0 & p_3V \end{bmatrix}, \\
\mathbf{C}_K &= \begin{bmatrix} 0 & 0 & 1 & 0 \end{bmatrix},
\end{aligned} \tag{20}$$

matrix $\mathbf{H}_K$ is the noise input matrix: $\mathbf{H}_K = \begin{bmatrix} 0 & 0 & 0 & p_3V \end{bmatrix}^T$, the output value $y_K(k) = g(k) - g_{\text{d}}(k)$ is the measured blood glucose deviation from the desired level, $w(k)$ is the insulin input noise, and $v(k)$ is the blood glucose measurement noise with zero-mean Gaussian distribution. The variances of $w(k)$ and $v(k)$ are assumed to be as follows:

$$\begin{aligned}
E\left(w^2(k)\right) &= R_w, \\
E\left(v^2(k)\right) &= R_v.
\end{aligned} \tag{21}$$

Table 1: Parameters and constants of the insulin-glucose kinetics model.

Name	Description	Value
p_1	Glucose effectiveness	$0.2\,\text{min}^{-1}$
p_2	Insulin sensitivity	$0.028\,\text{min}^{-1}$
p_3	Insulin rate of clearance	$10^{-4}\,\text{min}^{-1}$
A_G	Carbohydrate bioavailability	$0.8\,\text{min}^{-1}$
τ_D	Glucose absorption constant	10 min
V	Plasma volume	2730 g
i_{be}	Equilibrium basal plasma insulin concentration	$7.326\,\mu$IU/ml

Table 2: Variables of the insulin-glucose kinetics model.

Name	Description	Unit
D	Amount of CHO intake	mmol/min
D_1	Amount of glucose in compartment 1	mmol
D_2	Amount of glucose in compartment 2	mmol
$g(t)$	Plasma glucose concentration	mmol/l
$\chi(t)$	Interstitial insulin activity	min^{-1}
$i(t)$	Plasma insulin concentration	μIU/ml

Based on the discretized model, a Kalman filter was implemented through the following equation:

$$\hat{\mathbf{x}}(k+1 \mid k) = \mathbf{A}_k \cdot \hat{\mathbf{x}}(k \mid k-1) + \mathbf{B}_k \cdot \mathbf{u}_K(k) + \mathbf{L}[y(k) - \mathbf{C} \cdot \hat{\mathbf{x}}(k \mid k-1)], \tag{22}$$

where $\hat{\mathbf{x}}(k+1 \mid k)$ denotes the estimation of $\mathbf{x}(k+1)$ based on measurements available at time k. The gain $\mathbf{L}$ is the steady-state Kalman filter gain, which can be calculated by

$$\mathbf{L} = \mathbf{M}\mathbf{C}^T\left(\mathbf{C}\mathbf{M}\mathbf{C}^T + R_v\right)^{-1}, \tag{23}$$

where $\mathbf{M}$ is the solution of the corresponding algebraic Riccati equation [13, 14, 18]:

$$\mathbf{M} = \mathbf{A}\mathbf{M}\mathbf{A}^T + \mathbf{B}R_w B - \mathbf{A}\mathbf{M}\mathbf{C}^T\left(\mathbf{C}\mathbf{M}\mathbf{C}^T + \mathbf{R}\right)^{-1}\mathbf{C}\mathbf{M}\mathbf{A}^T. \tag{24}$$

By assuming the noise variances to be $R_w = R_v = 0.01$, the Kalman filter gain was calculated from equation (23) as

$$\mathbf{L} = \begin{bmatrix} 0 & 0 & 8.32 \cdot 10^{-4} & -6.40 \cdot 10^{-7} \end{bmatrix}. \tag{25}$$

2.5. Simulation Setup. First, a pretraining of the algorithm was conducted on the type-1 diabetes model in the scenario where the patient is in a fasting condition (without food intake). The purpose of the pretraining simulation is to obtain an initial estimation of the action-value function for the algorithm. The learning process was conducted by repeating the experiment multiple times (episodes). Each episode starts with an initial blood glucose of 90 mg/dL and ends after 30 minutes. The objective of the algorithm is to search and explore actions that can drive the blood glucose to its target level of 80 mg/dL.

By using the initial estimation of the action-value function, the controller was then tested in the daily scenario with food intake. Comparisons were made between the proposed reinforcement learning with the feedforward (RLFF) controller, the optimal RL (ORL) controller [15], and the proportional-integral-derivative (PID) controller. The ORL was designed with the same parameters and pretrained in the same scenario as with the RLFF. The PID controller gains were chosen, which produces a similar blood glucose settling time as the RLFF:

$$u_k = K_p\left(g(k) - g_{\mathrm{d}}(k)\right) + K_i \sum_k \left(g(k) - g_{\mathrm{d}}(k)\right) + K_d\left(g(k) - g(k-1)\right), \tag{26}$$

where

$$\begin{aligned} K_p &= 1, \\ K_i &= 0.001, \\ K_d &= 0.01. \end{aligned} \tag{27}$$

In order to understand the effects of different food types on the controlled system, two sets of simulations were conducted for food that has slow and fast glucose absorption rates while containing a similar amount of carbs. Absorption rates in the simulations are characterized by parameter τ_D from the model, where $\tau_D = 50$ corresponds to food with a slow absorption rate and $\tau_D = 10$ corresponds to food with a fast absorption rate. The amount of carbohydrate (CHO) per meal can be found in Figure 2.

Next, the performance of the proposed controller was evaluated under uncertainties of meal information. Two cases of uncertainties were considered: uncertain CHO estimation case and uncertain meal-recording time. In the uncertain CHO estimation, the estimated CHO information that provided to the controller was assumed to be a normal distribution with a standard deviation of 46% from the correct carbohydrate value shown in Figure 2. The standard deviation value was used based on the average adult estimates and the computerized evaluations by the dietitian [19]. For the uncertain meal-recording time, the estimated meal starting time is assumed to be a normal distribution with a standard deviation of two minutes from the real starting time. This standard deviation value was randomly selected because systematic research on the accuracy of meal-time recording for patients with type-1 diabetes could not be found. For each case, multiple simulations were conducted in the same closed-loop system with its corresponding random variables. From the obtained results, the mean and standard deviation for blood glucose responses at each time point will be calculated and analyzed.

3. Results

After pretraining in the no-meal scenario, the Q-function was estimated as follows:

$$Q_k^{\pi}(\mathbf{x}, u) = \begin{bmatrix} \mathbf{x}_k^T & u_k^T \end{bmatrix} \begin{bmatrix} 4.454 \cdot 10^2 & -8.870 \cdot 10^4 & -0.084 \\ -8.870 \cdot 10^4 & 3.538 \cdot 10^7 & 33.630 \\ -0.084 & 33.630 & 0.010 \end{bmatrix} \cdot \begin{bmatrix} \mathbf{x}_k \\ u_k \end{bmatrix}. \tag{28}$$

The initial basal policy was obtained from the initial Q-function and equation (12):

$$u_{\mathrm{basal}}(k) = 8.86\left(g(k) - 80\right) - 3534.11\chi(k) + 7.326. \tag{29}$$

The initial estimation of the Q-function and the initial basal policy were used for subsequent testing simulations of the control algorithm.

During the simulation with correct meal information, blood glucose responses of the RLFF, the ORL, and the PID are shown in Figures 3 and 4. The insulin concentration during the process can also be found in Figures 5 and 6. With slow-absorption food, the fluctuation range of blood glucose was approximately ±30 mg/dL for all three controllers from the desired value (Figure 3). However, with fast absorption glucose meals, the fluctuation range of the postmeal blood glucose level was within ±40 mg/dL with the RLFF compared to ±60 mg/dL with the ORL and is significantly smaller than the fluctuation range ±80 mg/dL of the PID (Figure 4).

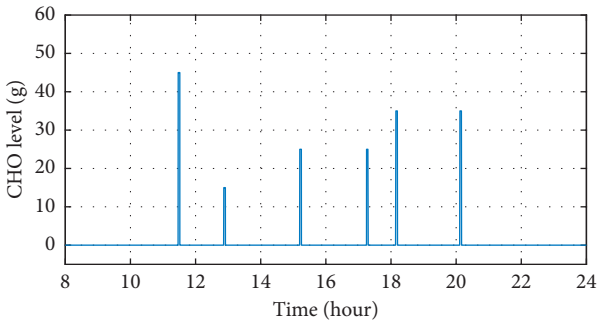

Figure 2: CHO consumed throughout the day.

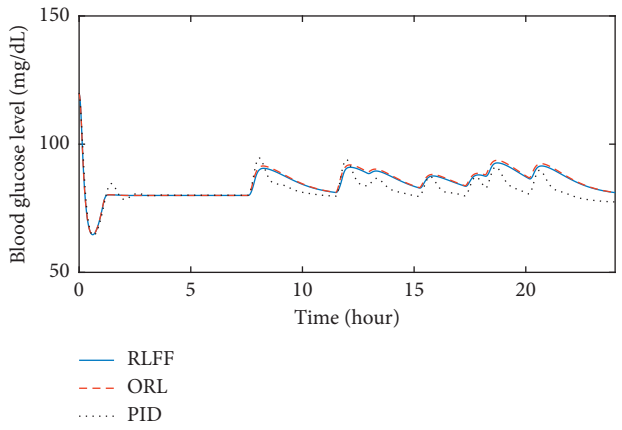

Figure 3: Comparison of the blood glucose responses in the nominal condition for slow glucose absorption food.

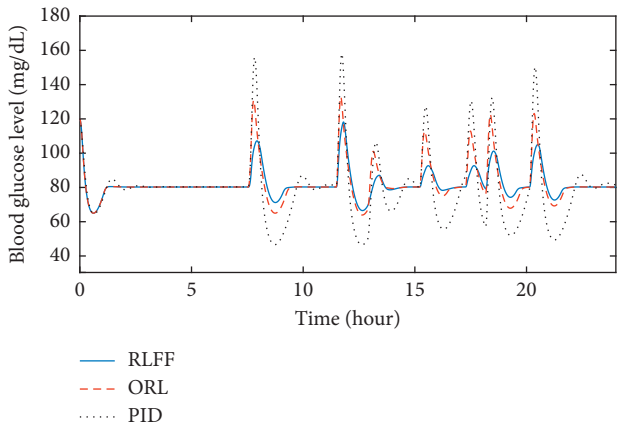

Figure 4: Comparison of the blood glucose responses in the nominal condition for fast glucose absorption food.

Figures 7 and 8 show the blood glucose variation under uncertain meal time and CHO counting. The upper and lower bounds in shaded areas show the mean blood glucose value plus and minus the standard deviation for each instance. Under uncertain meal information, the upper bound was kept to be smaller than 40 mg/dL from the desired blood glucose value for fast glucose absorption food and 15 mg/dL for slow glucose absorption food. The lower bound is smaller than 15 mg/dL from the desired value for

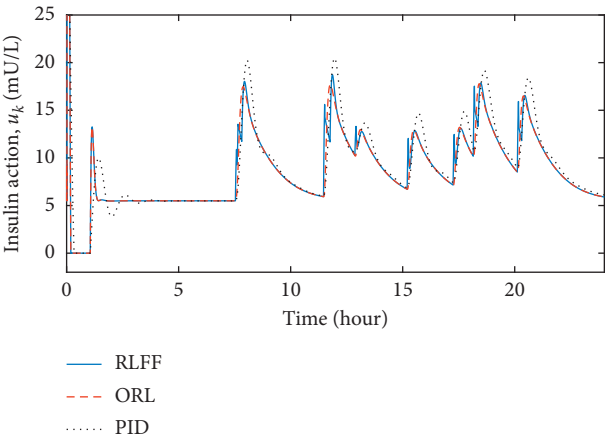

Figure 5: Comparison of insulin concentrations in the nominal condition for slow glucose absorption food.

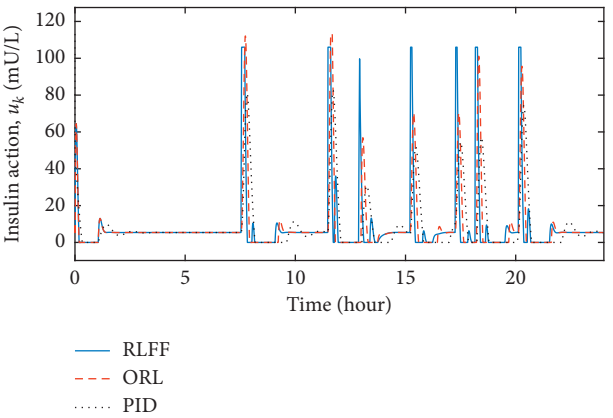

Figure 6: Comparison of insulin concentrations in the nominal condition for fast glucose absorption food.

fast glucose absorption food and 5 mg/dL for slow glucose absorption food.

4. Discussion

The controller has shown its capability to reduce the rise of postmeal blood glucose in our simulations. It can be seen in Figures 3 and 4 that three controllers were able to stabilize the blood glucose. However, when using the RLFF, the added bolus makes the insulin responses much faster when there is a change in blood glucose level, which reduces the peak of the postmeal glucose rise by approximately 30 percent compared to the ORL and 50 percent compared to the PID in the fast-absorption case. It can also be seen that the undershoot blood glucose (the distance between the lowest blood glucose and the desired blood glucose value) of the PID controller is much larger than that of the RLFF and the ORL. The RLFF has the smallest glucose undershoot among the three controllers. Low blood glucose value (hypoglycemia) can be very dangerous for patients with type-1 diabetes. Therefore, simulation results show the advantage of using RLFF in improving safety for patients. In general, with the feedforward algorithm, the proposed algorithm is an

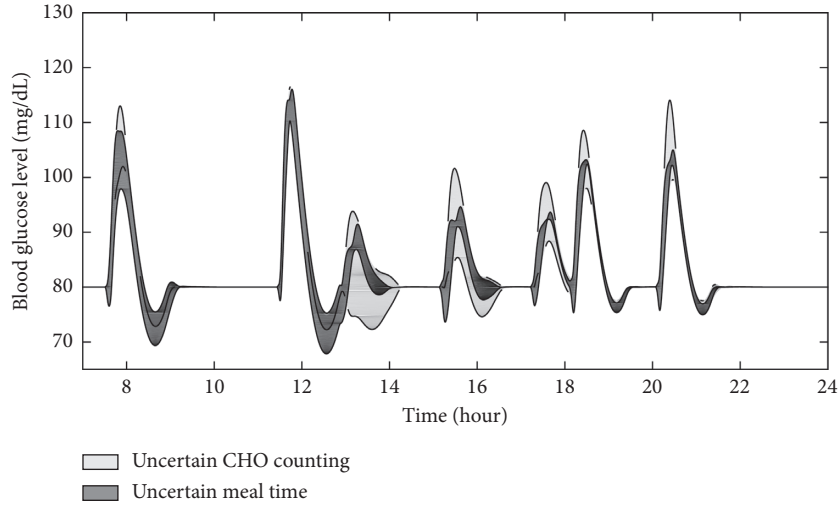

Figure 7: Blood glucose responses under uncertainties for fast glucose absorption food.

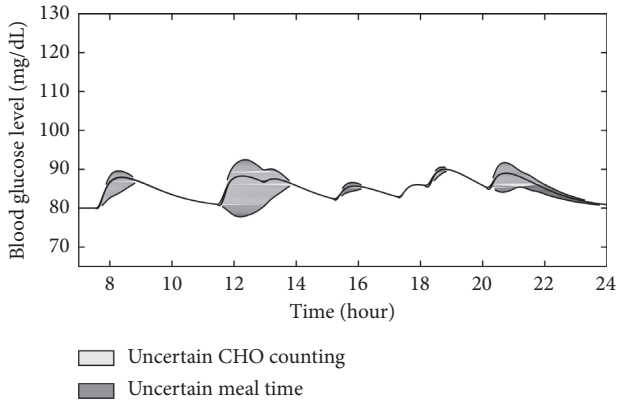

Figure 8: Blood glucose responses under uncertainties for slow glucose absorption food.

effective tool for countering the effects of external events such as meal intake.

Among uncertainties, carb counting created more effect on the variation of the blood glucose than meal-time recording, especially with slow absorbing food. The uncertainty in recording meal time may also lead to larger undershot of blood glucose below the desired level as can be seen in Figure 7. Following the same trend as previous simulations, the fluctuation range of the blood glucose with slow absorbing food is smaller than the fluctuation range with fast glucose absorbing food. In general, the control algorithm kept the blood glucose at the healthy level although uncertainties affect the variation of the responses. However, an accurate carbohydrate counting and accurate meal-time recording method are still important for the purpose of blood glucose control in order to completely avoid the chance of getting hypoglycemia.

5. Conclusion

The paper proposes a blood glucose controller based on reinforcement learning and feedforward algorithm for type-1 diabetes. The controller regulates the patient's glucose level using both basal and bolus insulin. Simulation results of the proposed controller, the optimal reinforcement learning, and the PID controller on a type-1 diabetes model show that the proposed algorithm is the most effective algorithm. The basal updates can stabilize the blood glucose, and the bolus can reduce the glucose undershoot and prevent hypoglycemia. Comparison of the blood glucose variation under different uncertainties provides understandings of how the accuracy of carbohydrate estimation and meal-recording time can affect the closed-loop responses. The results show that the control algorithm was able to keep the blood glucose at a healthy level although uncertainties create variations in the blood glucose responses.

Appendix

Blood Glucose Model

In this paper, the insulin-glucose process was used as the subject in our simulations. The model is described by the following equations [20–23]:

$$\frac{dD_1(t)}{dt} = A_G D(t) - \frac{D_1(t)}{\tau_D}, \tag{A.1}$$

$$\frac{dD_2(t)}{dt} = \frac{D_1(t)}{\tau_D} - \frac{D_2(t)}{\tau_D}, \tag{A.2}$$

$$\frac{dg(t)}{dt} = -p_1 g(t) - \chi(t) g(t) + \frac{D_2(t)}{\tau_D}, \tag{A.3}$$

$$\frac{d\chi(t)}{dt} = -p_2 \chi(t) + p_3 V\left(i(t) - u_{\mathrm{be}}\right), \tag{A.4}$$

where variable descriptions and parameter values are given in Tables 1 and 2. In this model, the inputs are the amount of CHO intake D and the insulin concentration $i(t)$. The output of the model is the blood glucose concentration $g(t)$. It is assumed that the blood glucose is controlled by using an

insulin pump, and there is no delay between the administered insulin and the plasma insulin concentration.

Abbreviations

RL: Reinforcement learning
RLFF: Reinforcement learning with feedforward algorithm
ORL: Optimal reinforcement learning
PID: Proportional-integral-derivative
LTI: Linear time-invariant
CHO: Carbohydrate.

Data Availability

The data used to support the findings of this study are available from the corresponding author upon request.

Conflicts of Interest

The authors declare no conflicts of interest.

Acknowledgments

The research has been funded by financial support from Tromsø Forskningsstiftelse. The publication charges for this article have been funded by a grant from the publication fund of UiT, the Arctic University of Norway.

References

[1] Q. Wang, P. Molenaar, S. Harsh et al., "Personalized state-space modeling of glucose dynamics for type 1 diabetes using continuously monitored glucose, insulin dose, and meal intake," *Journal of Diabetes Science and Technology*, vol. 8, no. 2, pp. 331–345, 2014.

[2] G. Marchetti, M. Barolo, L. Jovanovic, H. Zisser, and D. E. Seborg, "An improved PID switching control strategy for type 1 diabetes," *IEEE Transactions on Biomedical Engineering*, vol. 55, no. 3, pp. 857–865, 2008.

[3] S. Soylu, K. Danisman, I. E. Sacu, and M. Alci, "Closed-loop control of blood glucose level in type-1 diabetics: a simulation study," in *Proceedings of International Conference on Electrical and Electronics Engineering (ELECO)*, pp. 371–375, Bursa, Turkey, November 2013.

[4] D. Boiroux, A. K. Duun-Henriksen, S. Schmidt et al., "Overnight glucose control in people with type 1 diabetes," *Biomedical Signal Processing and Control*, vol. 39, pp. 503–512, 2018.

[5] H. Lee and B. W. Bequette, "A closed-loop artificial pancreas based on model predictive control: human-friendly identification and automatic meal disturbance rejection," *Biomedical Signal Processing and Control*, vol. 4, no. 4, pp. 347–354, 2009.

[6] M. K. Bothe, L. Dickens, K. Reichel et al., "The use of reinforcement learning algorithms to meet the challenges of an artificial pancreas," *Expert Review of Medical Devices*, vol. 10, no. 5, pp. 661–673, 2014.

[7] M. De Paula, L. O. Ávila, and E. C. Martínez, "Controlling blood glucose variability under uncertainty using reinforcement learning and Gaussian processes," *Applied Soft Computing*, vol. 35, pp. 310–332, 2015.

[8] C. J. C. H. Watkins and P. Dayan, "Technical note: Q-learning," in *Reinforcement Learning*, pp. 55–68, vol. 292Springer US, Boston, MA, USA, 1992.

[9] J. Pineau, M. G. Bellemare, A. J. Rush, A. Ghizaru, and S. A. Murphy, "Constructing evidence-based treatment strategies using methods from computer science," *Drug and Alcohol Dependence*, vol. 88, no. S2, pp. S52–S60, 2007.

[10] K. Lunze, T. Singh, M. Walter, M. D. Brendel, and S. Leonhardt, "Blood glucose control algorithms for type 1 diabetic patients: a methodological review," *Biomedical Signal Processing and Control*, vol. 8, no. 2, pp. 107–119, 2013.

[11] S. P. Bhattacharyyta, "Disturbance rejection in linear systems," *International Journal of Systems Science*, vol. 5, no. 7, pp. 633–637, 1974.

[12] H. Zhong, L. Pao, and R. de Callafon, "Feedforward control for disturbance rejection: model matching and other methods," in *Proceedings of 24th Chinese Control and Decision Conference (CCDC)*, pp. 3528–3533, Taiyuan, China, May 2012.

[13] F. Lewis, *Optimal Estimation*, John Wiley & Sons, Inc., Hoboken, NJ, USA, 1986.

[14] G. F. Franklin, J. D. Powell, and M. L. Workman, *Digital Control of Dynamic Systems*, Addison-Wesley, Boston, MA, USA, 2nd edition, 1990.

[15] D. Vrabie, K. G. Vamvoudakis, and F. L. Lewis, *Optimal Adaptive Control and Differential Games by Reinforcement Learning Principles*, Institution of Engineering and Technology, vol. 81, 1st edition, 2012.

[16] P. D. Ngo, S. Wei, A. Holubova, J. Muzik, and F. Godtliebsen, "Reinforcement-learning optimal control for type-1 diabetes," in *Proceedings of 2018 IEEE EMBS International Conference on Biomedical & Health Informatics (BHI)*, pp. 333–336, Las Vegas, NV, USA, March 2018.

[17] R. Sutton and A. Barto, *Reinforcement Learning: An Introduction*, MIT Press, Cambridge, MA, USA, 1st edition, 1998.

[18] MathWorks, *MATLAB Optimization Toolbox: User's Guide (r2018a)*, MathWorks, Natick, MA, USA, 2018.

[19] A. S. Brazeau, H. Mircescu, K. Desjardins et al., "Carbohydrate counting accuracy and blood glucose variability in adults with type 1 diabetes," *Diabetes Research and Clinical Practice*, vol. 99, no. 1, pp. 19–23, 2013.

[20] R. N. Bergman, Y. Z. Ider, C. R. Bowden, and C. Cobelli, "Quantitative estimation of insulin sensitivity," *American Journal of Physiology-Endocrinology and Metabolism*, vol. 236, no. 6, p. E667, 1979.

[21] R. Hovorka, V. Canonico, L. J. Chassin et al., "Nonlinear model predictive control of glucose concentration in subjects with type 1 diabetes," *Physiological Measurement*, vol. 25, no. 4, pp. 905–920, 2004.

[22] M. E. Wilinska, L. J. Chassin, H. C. Schaller, L. Schaupp, T. R. Pieber, and R. Hovorka, "Insulin kinetics in type-1 diabetes: continuous and bolus delivery of rapid acting insulin," *IEEE Transactions on Biomedical Engineering*, vol. 52, no. 1, pp. 3–12, 2005.

[23] A. Mösching, *Reinforcement Learning Methods for Glucose Regulation in Type 1 Diabetes*, Ecole Polytechnique Federale de Lausanne, Lausanne, Switzerland, 2016.

Hindawi
Computational and Mathematical Methods in Medicine
Volume 2018, Article ID 6287913, 13 pages
https://doi.org/10.1155/2018/6287913

Research Article

Evaluation of the Feasibility of Screening Tau Radiotracers Using an Amyloid Biomathematical Screening Methodology

Ying-Hwey Nai[1,2] **and Hiroshi Watabe**[1,2]

[1]*Division of Radiation Informatics for Medical Imaging, Graduate School of Biomedical Engineering, Tohoku University, Sendai, Japan*
[2]*Division of Radiation Protection and Safety Control, Cyclotron and Radioisotope Center, Tohoku University, Sendai, Japan*

Correspondence should be addressed to Hiroshi Watabe; hwatabe@tohoku.ac.jp

Received 16 August 2018; Revised 6 November 2018; Accepted 21 November 2018; Published 19 December 2018

Guest Editor: Giedrius Vanagas

The purpose of this study is to evaluate the feasibility of extending a previously developed amyloid biomathematical screening methodology to support the screening of tau radiotracers during compound development. 22 tau-related PET radiotracers were investigated. For each radiotracer, in silico MLogP, V_x, and in vitro K_D were input into the model to predict the in vivo K_1, k_2, and BP_{ND} under healthy control (HC), mild cognitive impaired (MCI), and Alzheimer's disease (AD) conditions. These kinetic parameters were used to simulate the time activity curves (TACs) in the target regions of HC, MCI, and AD and a reference region. Standardized uptake value ratios (SUVR) were determined from the integrated area under the TACs of the target region over the reference region within a default time window of 90–110 min. The predicted K_1, k_2, and BP_{ND} values were compared with the clinically observed values. The TACs and SUVR distributions were also simulated with population variations and noise. Finally, the clinical usefulness index (CUI) ranking was compared with clinical comparison results. The TACs and SUVR distributions differed for tau radiotracers with lower tau selectivity. The CUI values ranged from 0.0 to 16.2, with 6 out of 9 clinically applied tau radiotracers having CUI values higher than the recommend CUI value of 3.0. The differences between the clinically observed TACs and SUVR results showed that the evaluation of the clinical usefulness of tau radiotracer based on single target binding could not fully reflect in vivo tau binding. The screening methodology requires further study to improve the accuracy of screening tau radiotracers. However, the higher CUI rankings of clinically applied tau radiotracers with higher signal-to-noise ratio supported the use of the screening methodology in radiotracer development by allowing comparison of candidate radiotracers with clinically applied radiotracers based on SUVR, with respect to binding to a single target.

1. Introduction

Alzheimer's disease (AD) is a progressive neurodegenerative disorder defined by histopathological features such as senile plaques and neurofibrillary tangles (NFT), and clinical symptoms such as memory loss and reduced executive functions [1]. The yearly number of AD cases is increasing worldwide, leading to an increased cost of care for dementia patients. Positron emission tomography (PET) using amyloid and tau radiotracers can measure the amyloid and tau loads, in terms of standardized uptake values ratio (SUVR), and their distributions in a subject's brain from static PET images. Since abnormal accumulation of amyloid and tau in the brain occurs before clinical symptoms appear, the imaging of these precursors can support differential diagnosis and early intervention to increase the success rate of treating AD or slow down the rate of dementia. As such, the 2018 National Institute on Aging-Alzheimer's Association (NIA-AA) research framework includes not only symptomatic stages of AD, but also biomarker classification involving amyloid, tau, and neurodegeneration AT(N) biomarkers [2]. The new framework will be able to identify subjects at risk for AD for suitable and early treatment, in particular, preclinical AD subjects (classified as A+T−(N−) or A+T+(N+)), who are not cognitively impaired but have abnormal amyloid and tau protein deposits [2].

Despite active efforts since 2000 to develop amyloid and tau-targeting PET radiotracers to assist in the diagnosis of AD and to support AD drug development, there are few radiotracers that have made it into clinical studies and displayed good clinical efficacy. In conventional radiotracer and drug development, poor bench-to-bedside translation often results due to the differences between in vitro and in vivo conditions. Similarly, animal models, especially rodents, are often poor predictors of human physiology and treatment response and have been reported to be incorrect in approximately one out of three cases [3]. Although larger animals (e.g., pigs and primates) show closer physiology to that of human, they are still in-prefect human models and are costly for high-throughput screening compared to rodents. These issues lead to high attrition rates in drug and radiotracer development. Biomathematical simulation can complement high-throughput screening by allowing simultaneous and rapid evaluation of many candidate radiotracers [4–6].

Compared to amyloid radiotracers, the development of a successful tau radiotracer encounters additional challenges due to the tau phenotypes. Tau proteins have six isoforms, which differ in the number of exons (0, 1, 2) on the acidic region and the number of repeats (3 repeats (3R) or 4R) in the repeat-domain regions [7]. The different isoforms undergo several posttranslational modifications, leading to various ultrastructural conformations, which will affect the binding of tau radiotracers. In addition, they also need to discriminate between the paired helical filament (PHF) tau from other β-sheet structured aggregates such as amyloid-beta (Aβ) and α-synuclein. Although the tau protein is larger than the Aβ protein, the tau binding sites are present in smaller concentrations compared to the Aβ binding sites by 5–20 folds; hence, the selectivity of tau over other β-sheet structured aggregates needs to be high to ensure accurate quantification. Moreover, as tau proteins exist intracellularly, tau radiotracers not only need to cross the blood-brain barrier (BBB), they also need to be able to cross the cell membrane [8].

Existing clinically applied tau radiotracers showed some limitations. [^{11}C]PBB3 has high binding selectivity to tau over Aβ, but it is difficult to synthesize as it will undergo photoisomerization [9]. Moreover, it is rapidly metabolized in the plasma, and its polar metabolite is shown to cross the blood-brain barrier and enter into the brain [10]. The short half-life of carbon-11 has also prompted the development of fluorinated PBB3 compounds ([^{18}F]AM-PBB3 and [^{18}F]PM-PBB3) and other tau radiotracers so that they can be used in hospitals without dedicated cyclotron facilities. [^{18}F]T808 (also known as [^{18}F]AV-680) exhibits defluorination, which will affect the quantitative analysis of PET images especially for regions near the skull [11]. Some THK compounds (Tohoku University, Japan) showed differences in the uptake due to the enantiomeric properties of the compounds [12]. A serious confounding factor facing the development of tau radiotracers is off-target brain binding, which might affect the quantitative analysis of the PET images as observed in [^{11}C]PBB3, [^{18}F]THK5351, and [^{18}F]flortaucipir (also known as [^{18}F]AV1451 or [^{18}F]T807) [13–15]. [^{18}F]MK6240 was reported to have reduced off-target binding but further evaluation was still required [16].

We have previously developed an amyloid biomathematical screening methodology to support the screening of candidate amyloid radiotracers during compound development [4, 5]. The screening methodology predicts the standardized uptake values ratios (SUVRs) of different subject conditions of a radiotracer and then compares the clinical usefulness of multiple radiotracers simultaneously in discriminating the subject conditions using a clinical usefulness index (CUI). The CUI was developed to objectively evaluate the clinical usefulness of a radiotracer, based on its binding capability to a single target of interest, in terms of SUVR. The SUVR is a semiquantitative parameter that generalizes the complicated behaviors of tau radiotracers. SUVR is also generally preferred for diagnosis of patients in amyloid and tau imaging; hence, the clinical data are more readily available for comparison. Thus, we chose SUVR over other kinetic parameters such as nondisplaceable binding potential (BP_{ND}, unitless).

In this study, we evaluate the feasibility of extending the amyloid-validated screening methodology to support the development of tau PET radiotracers, where more challenges like off-target binding exist. This is the first in silico method investigated, which uses the physicochemical and pharmacological properties of the compounds to support tau PET radiotracers developments. 22 PET radiotracers reported to bind to tau proteins were investigated, including 9 clinically applied and tau-focused radiotracers, namely, [^{18}F]THK523, [^{18}F]THK5105, [^{18}F]THK5117, [^{18}F]THK5317, [^{18}F]THK5351, [^{18}F]flortaucipir, [^{18}F]T808, [^{11}C]PBB3 and [^{18}F]MK6240, and 3 clinically applied but non-tau-focused radiotracers, specifically [^{18}F]Lansoprazole, [^{11}C]Astemizole, and [^{18}F]FDDNP.

2. Materials and Methods

An overview of the amyloid biomathematical methodology is described briefly, followed by the screening of tau PET radiotracers using the biomathematical methodology. The details of the methodology are found in somewhere [4, 5].

2.1. Biomathematical Screening Methodology. The screening methodology was based on a simplified 1-tissue-compartment model (1TCM), with the assumption that the radiotracers cross the blood-brain barrier (BBB) by passive diffusion. It consists of four main parts (Figure 1).

2.2. Generation of Physicochemical and Pharmacological Parameters. A total of three inputs were required for each radiotracer: in silico molecular volume and lipophilicity as represented by McGowan Volume (V_x, cm^3/mol/100), Moriguchi LogP (MLogP, unitless), and an in vitro dissociation constant (K_D, nM) (Table 1). V_x and MLogP were generated based on the chemical structure of the radiotracer using commercial software, dproperties (Talete, Italy). K_D values were extracted from the literature, measured via binding assays, using synthetic tau or human brain homogenates. MLogP was used to derive the free fractions of

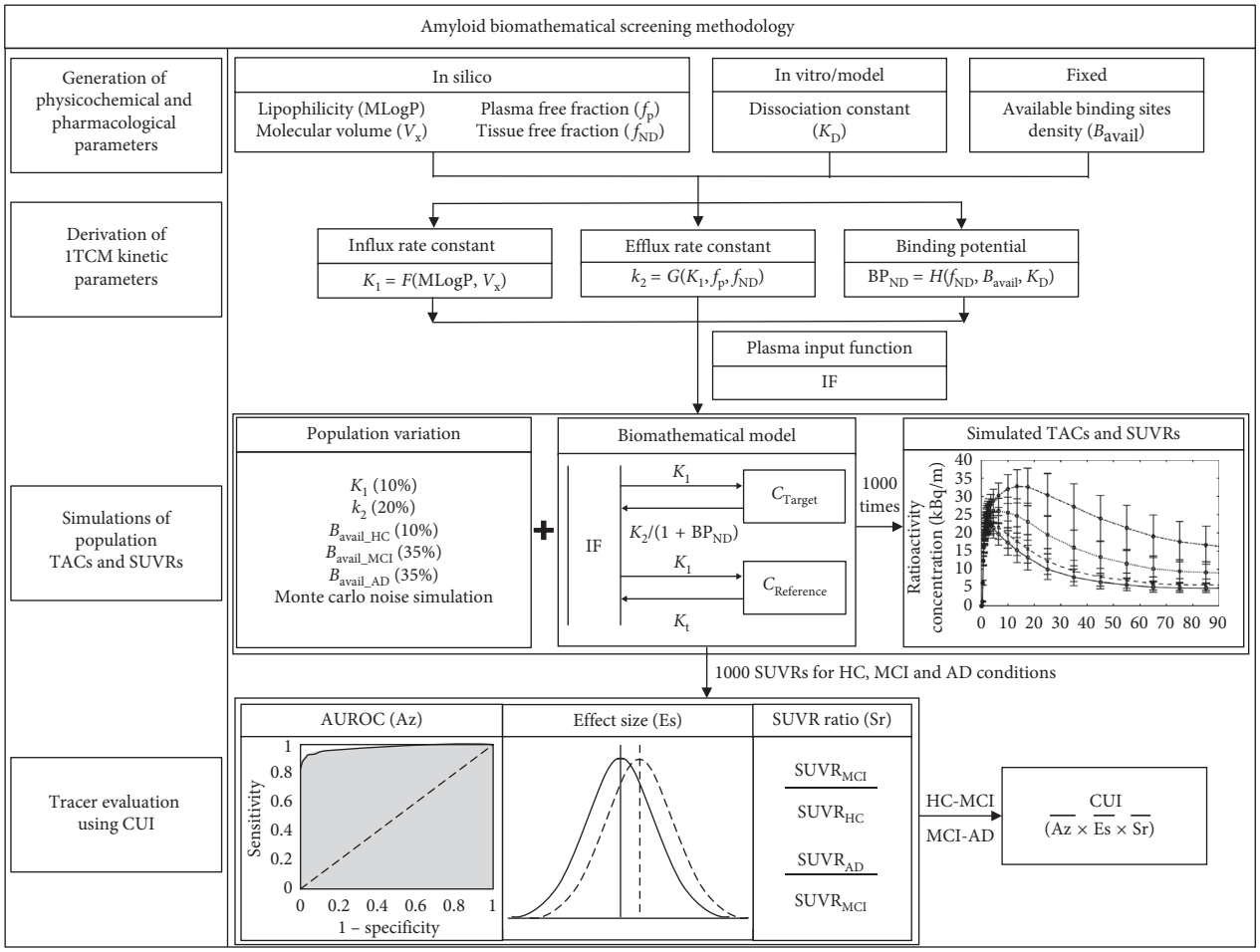

Figure 1: Overview of amyloid biomathematical screening methodology.

the radiotracer in tissues (f_{ND}, unitless) and in plasma (f_P, unitless) from the following relationships [4]:

$$f_{ND} = 7.717e^{-1.634 \cdot MLogP},$$
$$f_P = 0.936 \cdot f_{ND}^{0.600}. \quad (1)$$

The list of 22 tau radiotracers and their respective inputs are shown in Table 1. The K_D values that were utilized for simulations are given in bold for human brain homogenates, and italicized for synthetic tau, if available for comparison.

2.3. Derivation of 1TCM Kinetic Parameters. The influx rate constant (K_1, mL/cm^3/min) was derived using the modified Renkin and Crone equation, using compound-specific permeability (P, cm/min), with fixed values of capillary surface area (S = 150 cm^2/cm^3 of brain) and perfusion (f = 0.6 mL/cm^3/min) as follows [4, 6]:

$$K_1 = f\left(1 - e^{-PS/f}\right). \quad (2)$$

The compound-specific permeability was derived from the simplified Lanevskij's permeability model, with MLogP and V_x as inputs [4, 6]:

$$P = 10^{-0.121\,(MLogP\ -2.298)^2\ -2.544\log\left(V_x^{1/3}\right)-2.525}. \quad (3)$$

The efflux rate constant (k_2, min^{-1}) can be derived using K_1, f_P, and f_{ND} at equilibrium:

$$k_2 = \frac{f_{ND}}{f_P} \cdot K_1. \quad (4)$$

The in vivo nondisplaceable binding potential (BP_{ND}, unitless) was determined using Mintun's equation with B_{avail}, f_{ND}, and K_D:

$$BP_{ND} = f_{ND} \cdot \frac{B_{avail}}{K_D}. \quad (5)$$

The available tau-binding sites (B_{avail}, nM) were measured using enzyme-linked immunosorbent assay (ELISA). The total amount of tau fibrils (B_{avail}, nM) in the frontal lobes, parietal lobes, and hippocampus in HC and AD were 1.5 and 16.0 nM, respectively [29], assuming a tau molecular weight of 78,928 Da (https://www.phosphosite.org).

2.4. Simulations of Population Time Activity Curves (TACs) and SUVRs. The predicted K_1, k_2, and BP_{ND} were used to

Table 1: In silico MLogP and V_x and in vitro K_D of 22 tau-related PET radiotracers. K_D values employed for simulations are given in bold (measured using brain homogenates) and italicized (measured using synthetic tau).

Radiotracers	MLogP	V_x	K_D	References for K_D
[^{18}F]THK523	3.19	2.11	*1.67*$^{\alpha}$	[17]
			1.99$^{\alpha}$	[18]
			86.5	[19]
[^{18}F]THK5105	3.08	2.59	*1.45*$^{\alpha}$	[19]
			2.63	
[^{18}F]THK5116	2.62	2.31	**106**$^{\&}$	[12]
[^{18}F]THK5117	2.85	2.45	**2.65**$^{\$}$	[20]
[^{18}F]THK5125	3.08	2.59	**10.2**	[12]
[^{18}F]THK5129	2.48	2.55	**3.14**	[12]
[^{18}F]THK5151	2.25	2.41	**7.07**	[12]
[^{18}F]THK5287	1.94	2.55	**2.60**	[12]
[^{18}F]THK5307	1.71	2.41	**5.60**	[12]
[^{18}F]THK5317	2.85	2.45	**9.40**$^{\&}$	[21]
[^{18}F]THK5351	2.25	2.41	**2.90**	[15]
[^{18}F]THK5451	2.25	2.41	**28.0**	[12]
[^{18}F]flortaucipir	1.95	1.86	**14.6**$^{\#}$	[22]
[^{18}F]T808	3.64	2.23	**22.0**$^{\#}$	[11]
[^{11}C]PBB3	2.34	2.31	*2.50*$^{\alpha}$	[10]
			6.30	[23]
[^{18}F]FDDNP	2.89	2.31	*36.7*$^{\alpha}$	[18]
[^{18}F]FPPDB	2.87	3.15	**44.8**	[24]
[^{11}C]NML	1.98	2.51	*0.700*$^{\alpha}$	[25]
[^{18}F]Lansoprazol	1.75	2.37	*3.30*$^{\alpha}$	[25]
			>**3998**$^{\delta}$	[11]
[^{11}C]Astemizole	4.63	3.56	**13.4**	[26]
			1.86$^{\alpha}$	
			>3998$^{\delta}$	[11]
[^{18}F]MK6240	2.49	1.96	**0.260**$^{\beta}$	[27]
[^{18}F]JNJ64349311 ([^{18}F]JNJ311)	2.07	1.83	**7.90**$^{\delta}$	[28]

Units: MLogP (unitless), V_x (cm^3/mol/100), K_D (nM). $^{\$}$Averaged K_D values (2.2, 3.1) for tau in AD brain homogenates of temporal and hippocampus. $^{\beta}$Averaged K_D values 0.14, 0.30, 0.25, 0.24, and 0.38 for tau in AD brain homogenates of frontal and entorhinal cortex of 5 AD. $^{\alpha}K_D$ values are measured using synthetic tau (K18Δ280K) $^{\&}K_i$ values measured using AD brain homogenates with THK5105 as competitor $^{\delta}K_i$ values measured using AD brain homogenates with T808 as competitor. $^{\#}K_D$ values measured using AD brain via autoradiography.

simulate the TACs in the target regions of HC, MCI, and AD and a reference region, with a fixed arterial input function (IF):

$$C_{\text{Target}}(t) = K_1 \cdot e^{-k_2/(1+\text{BP}_{\text{ND}})\cdot t} \otimes \text{IF}(t),$$
$$C_{\text{Reference}}(t) = K_1 \cdot e^{-k_2 \cdot t} \otimes \text{IF}(t). \quad (6)$$

An input function with similar kinetics to that observed in tau imaging with a fast uptake and washout is required to reflect tau kinetics. For our simulations, a fixed arterial input function was applied with fast kinetics that was derived by averaging the metabolite-corrected arterial plasma input functions of 6 HC subjects injected with [^{11}C]BF227 [30].

The same K_1 and k_2 scaling factors of 1.23 and 1.15, respectively, were introduced to account for the differences between the predicted and in vivo values [5]. The scaling factor of BP_{ND} was modified from 0.39 to 1.0 because there were few reported values to determine the appropriate scaling factor. Monte Carlo simulations were applied to generate 1000 TACs in both target and reference regions with 3% noise, to reflect the noise in PET data, and the population variation, by varying K_1 and k_2 by 10% and 20%, respectively [5, 6]. The variations in the tau fibrils in HC and AD were determined as 10% and 35%, respectively, using the ratio of the summed standard deviation to the mean value [29]. The amount of soluble tau in HC, MCI, and AD was reported, but since they did not correlate well with the amount of phosphorylated tau, these values could not be used [31]. In our simulations, the total amount of tau fibrils in MCI was assumed to be the mean of that in HC and AD, with the same amount of variation of 35%, as used for the amyloid simulations [5].

1000 noisy TACs in both target and reference regions were generated by computer simulations with noise. In our simulation, the target region refers to a brain region with varying concentrations of phosphorylated tau depending on subject conditions (e.g., temporal lobe) and a reference is a brain region devoid of phosphorylated tau (e.g., cerebellum). 1000 SUVRs of each subject condition of HC, MCI, and AD were determined from the ratio of the areas under the TACs of the target regions in HC, MCI, and AD and that of the reference region within a chosen time window. For our simulations, a default time window of 90–110 min was selected as the predicted TACs of HC, MCI, and AD appeared to reach a quasi-steady-state in this time window for almost all 9 clinically applied tau radiotracers (Supplementary 2). To evaluate the efficacy of fixed time windows, SUVRs were also determined using the literature-reported time windows for the 9 clinically applied radiotracers.

2.5. Tracer Evaluation Using CUI. Az, Es, and Sr are the area under the receiver operating characteristics curve, effect size, and SUVR ratios, respectively. The 1000 SUVR simulated under the subject conditions of HC, MCI, and AD were used to determine Az, Es, and Sr for conditions-pairs of HC-MCI and MCI-AD. CUI was then derived from the product of the averaged Az ($\overline{\text{Az}}$), Es ($\overline{\text{Es}}$), and Sr ($\overline{\text{Sr}}$) of conditions-pairs of HC-MCI and MCI-AD with equal weightage applied:

$$\text{CUI} = \overline{\text{Az}} \times \overline{\text{Es}} \times \overline{\text{Sr}}. \quad (7)$$

The simulated TACs and the predicted SUVR were compared to the clinical data of 9 clinically applied tau radiotracers. The predicted K_1, k_2 and BP_{ND} values were compared with the clinically observed values where applicable. Finally, the list of 22 tau radiotracers (Table 1) was evaluated using CUI. We previously developed a MATLAB-based program, RSwCUI, (Ver. 2014b, The MathWorks, US) [5], to support the screening of amyloid radiotracers based on the proposed amyloid biomathematical screening methodology. The program was used for the evaluation of tau radiotracers in this study.

3. Results

Figure 2 shows the simulated TACs for the target regions of HC, MCI, and AD and reference regions of 9 clinically applied tau radiotracers. In general, the clinically observed TACs of THK compounds of the reference region had higher peaks and faster washout in the cerebellum than the target regions [15,32–35], while the peaks of the simulated TACs of the reference region were always lower than that of the target regions (Figures 2(a)–2(e)). The simulated TACs of [^{11}C]PBB3 (Figure 2(f)) were close to that observed clinically in AD in the nonbinding and low-, middle-, and high-binding regions [10]. The simulated TACs of [^{18}F]flortaucipir (Figure 2(g)) had slightly sharper peaks and faster washout compared to the clinically observed TACs for both HC and AD [36]. Unlike the THK compounds, the peaks of the clinically observed TACs of the target regions of [^{18}F]flortaucipir were higher than that of the reference region, which was also observed in the simulated TACs [36]. The predicted TACs of [^{18}F]T808 for both the reference and the target regions of HC, MCI, and AD conditions completely overlapped with each other (Figure 2(h)). The clinically observed TACs of [^{18}F]T808 appeared close to that of [^{18}F]flortaucipir, but with smaller differences between the subject conditions. However, the simulated TACs showed complete overlapped between the HC and AD conditions with a slower uptake and washout [37]. The predicted TACs of both target and reference regions of [^{18}F]MK6240 showed similar fast uptake but slower washout than clinically observed TACs [16].

Table 2 compares the predicted and clinically-reported values of K_1, k_2, and BP_{ND} of five clinically applied tau radiotracers with reported kinetic parameters. For [^{18}F]flortaucipir, the predicted K_1 and k_2 values of 0.256 and 0.199, respectively, were relatively close to the reported averaged cerebellar K_1 and k_2 values of 0.26 and 0.17, respectively [36]. The predicted k_2 value of [^{18}F]THK5351 was 0.140, which was higher than the clinically observed value of 0.115, with a difference of 21.7% [38]. However, unlike [^{18}F]flortaucipir where both K_1 and k_2 values were determined using the two-tissue-compartment model with a variable fraction [36], the reported k_2 value of [^{18}F]THK5351 was an apparent rate constant from reference region to plasma, which was determined using the simplified reference tissue model (SRTM) [38].

The predicted k_2 value of [^{18}F]THK5317 of 0.087 was close to the literature-reported value of 0.09, even though K_1 of [^{18}F]THK5317 value differed of [^{18}F]THK5317 from the clinically observed value with a difference of −39% [39]. The predicted BP_{ND} values of 0.125 and 8.13 were very different from the clinically observed values of 0.60 and 5.11 in AD for [^{18}F]THK5317 [39] and [^{18}F]MK6240 [16]. The predicted BP_{ND} value was fairly close to that of [^{11}C]PBB3 [10]. The predicted K_1 of [^{18}F]MK6240 was close to the clinically observed K_1 value with 2.50% difference but the predicted k_2 value yielded greater difference of about 40% [16].

Table 3 shows the predicted SUVR values obtained using the default time window and literature-reported time window of 90–110 min, and the clinically observed SUVR for 10, 10, and 9 clinically applied tau radiotracers. The differences in the SUVRs predicted using both time windows were very small for both HC and AD. The predicted SUVR for HC was always greater than 1.0, but the clinically observed SUVR values were less than 1.0 for some radiotracers. In general, the clinically observed SUVR for HC and AD were greater than the predicted SUVR determined using the literature-reported time window, except for [^{11}C]PBB3 and [^{18}F]MK6240, where the predicted SUVR for HC and AD were greater.

The correlations between the predicted and highest clinically observed SUVR for AD were similar with coefficients of determination, R^2 of 0.90 and 0.89, respectively, using the literature-reported time window and the default time window (Figure 3). However, the good correlation was driven by [^{18}F]MK6240, which had the highest predicted and clinically observed SUVR. Poor correlation was observed after removing [^{18}F]THK5351 and [^{18}F]MK6240. The small difference between the predicted SUVR using the default and clinical-reported time window, and the value of R^2, showed that the default time window of 90–110 min was suitable for predicting the SUVR of the tau radiotracers (Figure 3).

The simulated SUVR distribution of [^{18}F]THK523 across HC, MCI, and AD conditions substantially overlapped each other (Figure 4(a)). However, the clinically observed SUVR distribution of [^{18}F]THK523 differed across different regions of interest, with HC− (PIB-negative) having the smallest spread and smallest values, HC+ (PIB-positive) having a relatively large spread and values ranging between that of HC− and AD, and AD subjects having the largest values and a nearly similar spread as HC+ [30]. For [^{11}C]PBB3, [^{18}F]THK5117, and [^{18}F]flortaucipir, the clinically observed SUVR distributions were generally larger for AD than HC for all regions of interest analyzed, in terms of the spread and absolute values [14, 34, 40]. The trend of the

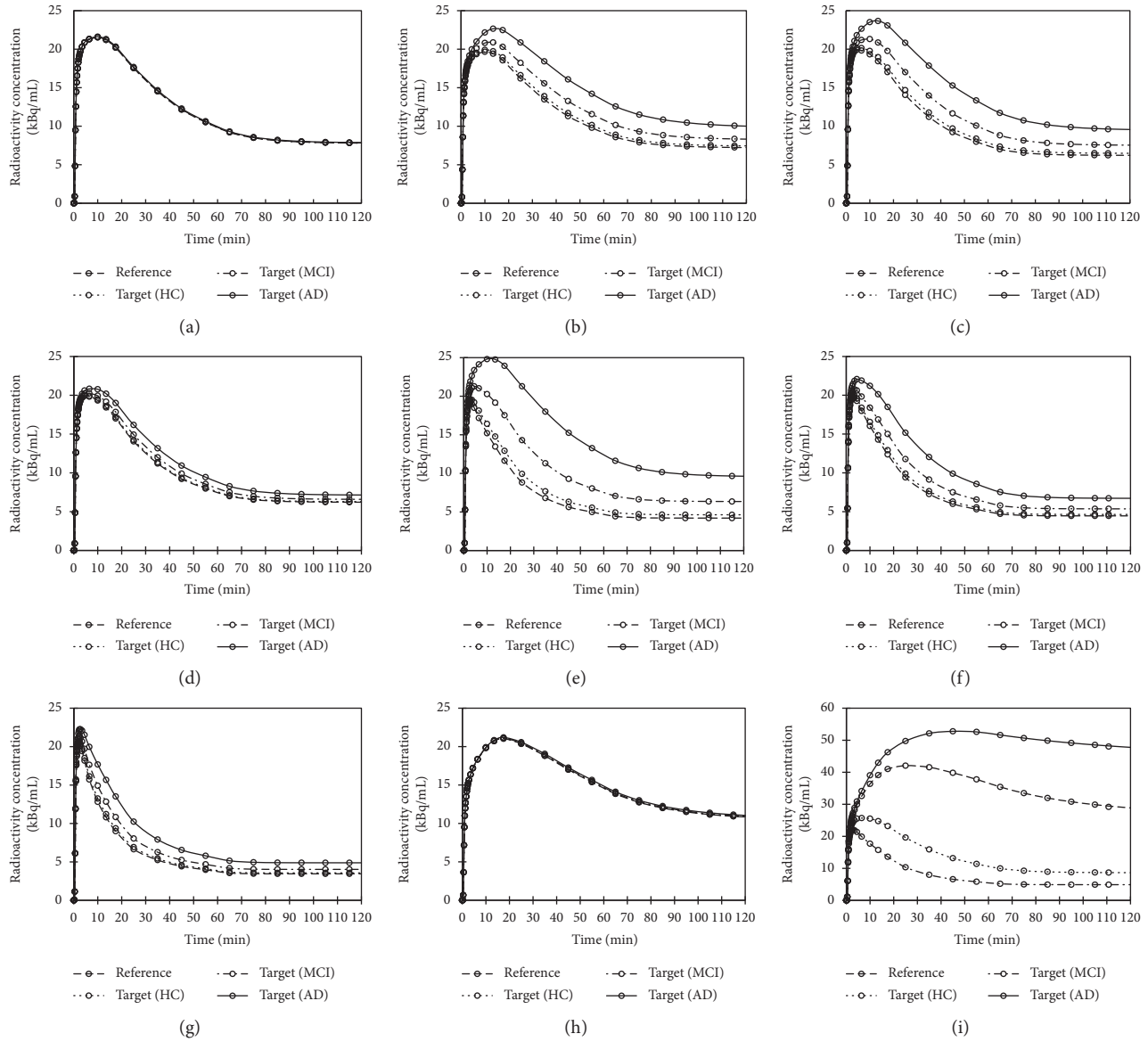

Figure 2: Simulated TACs of target regions of HC, MCI, and AD and reference regions for (a) [^{18}F]THK523, (b) [^{18}F]THK5105, (c) [^{18}F]THK5117, (d) [^{18}F]THK5317, (e) [^{18}F]THK5351, (f) [^{11}C]PBB3, (g) [^{18}F]flortaucipir, (h) [^{18}F]T808, and (i) [^{18}F]MK6240 from 0–120 min.

simulated SUVR population distribution was close to that observed clinically for HC and AD conditions (Figures 4(b)–4(d)). This supported the use of 35%, 35% and 10% variations in B_{avail} for population simulations.

Figure 5 shows the CUI distribution of 22 tau-related radiotracers. Among the clinically applied tau radiotracers, [^{18}F]MK6240 was ranked first, followed by [^{18}F]THK5351, [^{18}F]THK5117, [^{11}C]PBB3, [^{18}F]flortaucipir, [^{18}F]THK5317, [^{18}F]FDDNP, [^{18}F]T808, and [^{18}F]THK523, based on the K_{D} values measured using AD brain homogenates. For candidate radiotracers, [^{18}F]THK5287 was ranked first based on the K_{D} values measured using AD brain homogenates, while [^{11}C]NML was ranked first based on the K_{D} values measured using heparin-induced tau polymer (HITP) (Table 1). The CUI values generated using the K_{D} values for the synthetic tau were higher than those of the brain homogenates as the K_{D} values measured using synthetic tau were smaller (Table 1). The ranking of the CUI values generated using the K_{D} values measured with synthetic tau and brain homogenates differed for [^{18}F]THK523, [^{18}F]THK5105, and [^{11}C]PBB3. 10 out of 16 tau radiotracers had CUI values higher than the recommend CUI value of 3.0, where the results were simulated using K_{D} values measured with human brain homogenates. Apart from [^{18}F]THK523, [^{18}F]THK5317, [^{18}F]T808, and [^{18}F]FDDNP, the other 6 clinically applied tau radiotracers yielded high CUI values. The CUI values ranged from about 0.0 to 16.2, which ranged wider than that for amyloid.

4. Discussion

In this paper, we evaluated the feasibility of extending a previously developed amyloid biomathematical screening

Table 2: Comparison of predicted and clinically observed K_1, k_2, and BP_{ND} values of four clinically applied tau radiotracers.

Radiotracers	Parameters	Literature			Predicted values	% diff
		Region	Clinically observed values	References		
[^{18}F]flortaucipir	K_1	Cerebellum excluding vermis	0.26	[36]	0.256	−1.54
	k_2		0.17		0.199	17.1
[^{18}F]THK5351 (*S*-enantiomer of [^{18}F] THK5151)	$k_2'^{\ddagger}$	Target$^{\beta}$	0.115	[38]	0.140	21.7
[^{18}F]THK5317 (*S*-enantiomer of [^{18}F] THK5117)	K_1	Target$^{\delta}$	0.33	[35]	0.202	−38.8
	k_2		0.09		0.087	−3.33
	BP_{ND} (AD)*	Putamen	0.60	[39]	0.125	−79.2
[^{11}C]PBB3	BP_{ND} (AD)¶	High-binding cortical regions	0.37	[10]	0.427	15.4
[^{18}F]MK6240	K_1	Posterior cingulate cortex	0.246	[16]	0.252	2.50
	k_2		0.099		0.138	39.2
	BP_{ND}§		5.11		8.13	59.2

$^{\beta}$Target ROIs: anterior cingulate, brainstem, caudate nucleus, eroded white matter, entorhinal cortex, frontal cortex, fusiform gyrus, hippocampus, inferior temporal cortex, lingual gyrus, middle temporal gyrus, occipital cortex, pallidum, parahippocampal gyrus, parietal cortex, posterior cingulate, precuneus, putamen, thalamus. $^{\delta}$Target ROIs: thalamus, putamen, hippocampus, amygdala, parietal cortex, frontal cortex, sensory motor cortex, occipital cortex, midbrain, entorhinal cortex, and temporal cortex. *BP_{ND} = DVR-1, where DVR was determined using reference Logan, averaged from 4 prodromal AD. ¶BP_{ND} determined using $MRTM_0$. §BP_{ND} determined using k_3/k_4 using 2T4CM in 7 symptomatic individuals classified as MCI and AD. ‡k_2' optimized from fitting all target ROIs using SRTM with cerebellum as the reference region.

Table 3: Comparison of predicted (literature-reported and default time window of 90–110 min) and clinically observed SUVR (highest SUVR in AD) of HC and AD conditions.

Clinically applied radiotracers	Predicted SUVR						Clinically observed SUVR		
	Default		Literature		Highest in AD		Regions	Time window (min)	References
	HC	AD	HC	AD	HC	AD			
[^{18}F]THK523	1.00	1.01	1.00	1.01	0.96	1.81	ITL	60–90	[32]
[^{18}F]THK5105	1.03	1.34	1.03	1.35	1.41	1.52	PU	90–100	[33]
[^{18}F]THK5117	1.04	1.47	1.05	1.56	1.57	1.77	PU	50–60	[34]
[^{18}F]THK5317	1.01	1.13	1.01	1.14	—	—	—	—	—
[^{18}F]THK5351	1.10	2.11	1.11	2.38	2.14	2.98	HIP	50–60	[15]
[^{18}F]flortaucipir	1.03	1.35	1.03	1.35	1.17	2.19	ITL	80–100	[40]
[^{18}F]T808	1.00	1.02	1.00	1.02	0.94	1.52	LTL	80–100	[35]
[^{11}C]PBB3	1.04	1.43	1.05	1.55	0.85	1.42	Global$^{\#}$	30–50	[10]
[^{18}F]FDDNP	1.00	1.03	1.00	1.04	1.24	1.37	ACG	45–55	[41]
[^{18}F]MK6240	1.78	9.94	1.78	9.93	—	~5*	PRE	90–110	[16]

ITL = inferior temporal lobe, LTL = lateral temporal lobe, PU = putamen, PAR = parietal lobe, HIP = hippocampus, ACG = anterior posterior cingulate, PRE = precuneus. $^{\#}$Global = cerebral cortex for HC and high binding ROI for AD. *SUVR is approximated from the plot, taking the highest SUVR in AD.

methodology to support the screening of candidate tau radiotracers during compound development. 22 clinically applied and candidate tau-related radiotracers were thus used to investigate the CUI ranking of clinically applied and candidate tau radiotracers.

4.1. Comparison of Simulated TACs and SUVR Distribution. The simulated TACs were very different from the clinically observed TACs of [^{18}F]THK523 and [^{18}F]T808, but were only slightly different for that of [^{18}F]THK5117, [^{18}F] THK5351, [^{18}F]flortaucipir, [^{11}C]PBB3, and [^{18}F]MK6240 (Figure 2). The simulated SUVR distributions were different for [^{18}F]THK523 but were similar to the clinically observed results under HC and AD conditions for [^{18}F]THK5117, [^{18}F]flortaucipir, and [^{11}C]PBB3 (Figure 4). Both the predicted and clinically observed SUVR values were less than 1.0 in HC for some radioligands, especially those with a lower selectivity for tau (e.g., [^{18}F]THK523). The clinically observed SUVR of AD is much higher than that of HC. However, there is little difference in the predicted SUVR for [^{18}F]THK523. This shows that the predictions were less accurate for tau compounds with a lower selectivity for the target. Poor predictions might be due to binding to other β-sheet structured proteins or off-target sites shown in the clinical data, whereas the predicted values showed the binding of the radiotracers to only the target site. Non-specific binding in white matter may also lead to spill-over into the surrounding cortical regions, leading to higher clinically observed SUVRs. The issue of non-specific binding

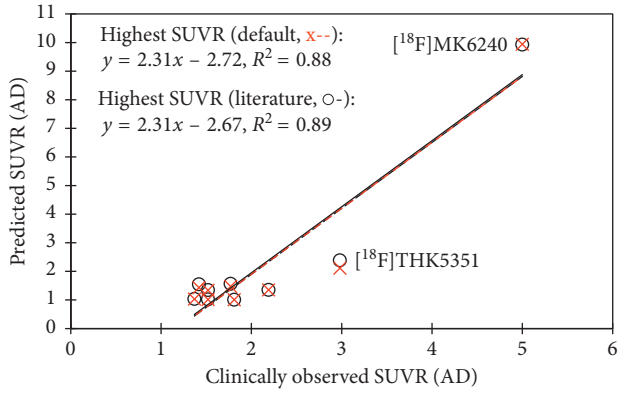

Figure 3: Correlations of clinically observed and predicted SUVR values using literature-stated time window (o-) and default time window (x--).

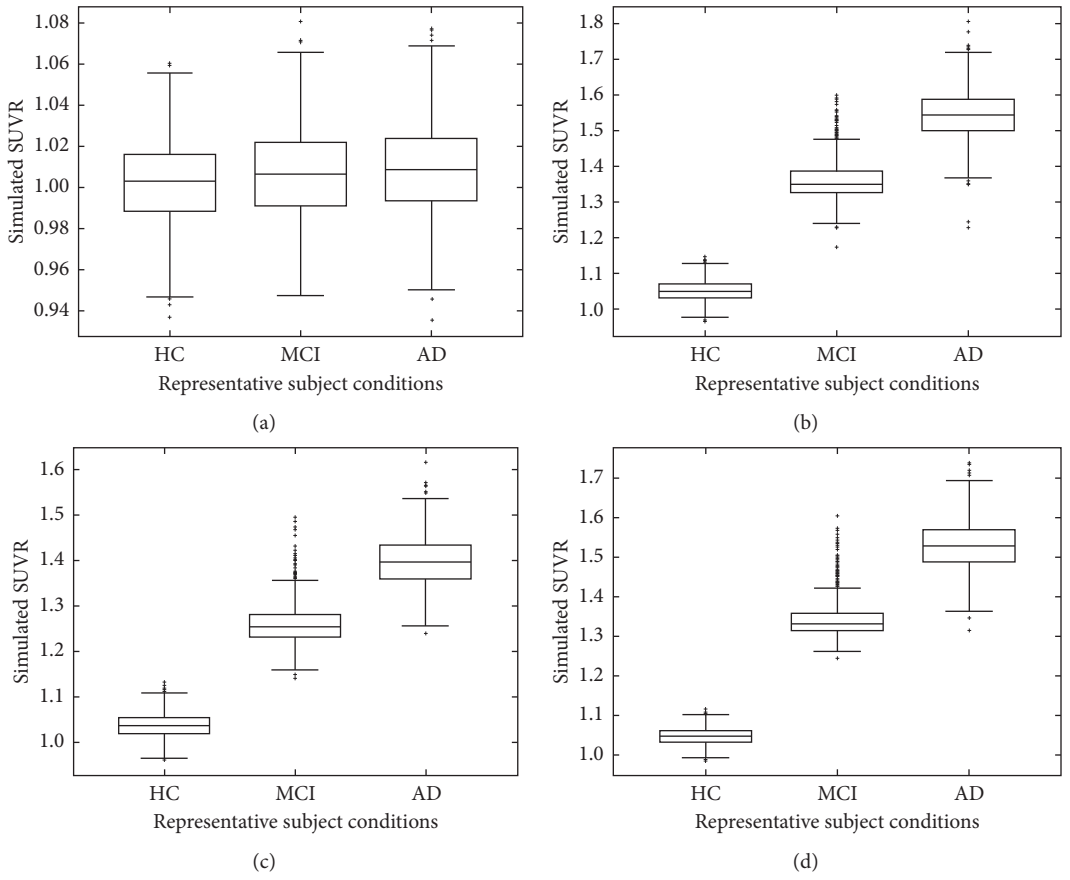

Figure 4: Simulated SUVR distributions of (a) [18F]THK523, (b) [18F]THK5117, (c) [18F]flortaucipir, (d) [11C]PBB3.

is more apparent for tau radiotracers with lower tau-binding selectivity, such as [18F]THK523 and [18F]THK5117 (Table 2).

4.2. Comparison of Predicted 1TCM and SUVR. The prediction for the K_1 and k_2 values of the tau radiotracers appeared to work well in racemic compounds (e.g., [18F]flortaucipir), but not as well for enantiomeric compounds like [18F]THK5351 and [18F]THK5317, which are S-enantiomers of [18F]THK5151 and [18F]THK5117 respectively (Table 2). The predictions for BP_{ND} were generally poor for the three clinically-reported tau radiotracers (Table 2). This may be due to the use of a simplified 1TCM for prediction, even though 2TCM was reported to be more suitable for many clinically applied tau radiotracers. The simplified 1TCM was selected even though 2TCM is more accurate for modeling tau kinetics as the prediction of a larger number of microparameters may be difficult to estimate reliably. Moreover, the 1TCM worked reasonably

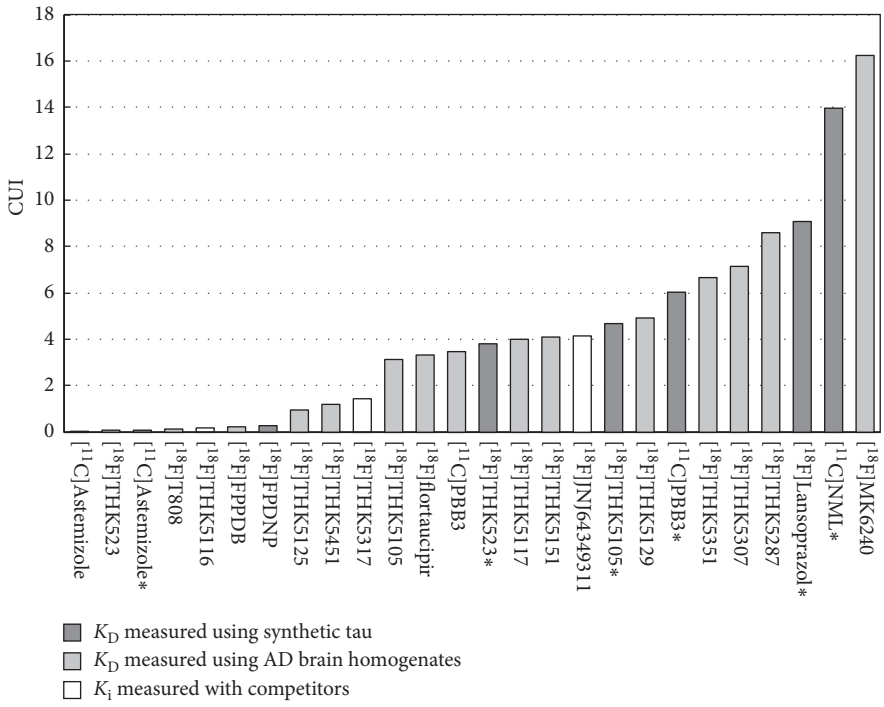

Figure 5: CUI distributions of 22 tau-related PET radiotracers.

well in predicting the kinetics of the amyloid radiotracers, even though 2TCM was reported to be more suitable [5]. Other possible reasons for the poorer BP_{ND} predictions included differences in binding to the plasma proteins due to the enantiomeric properties of the radiotracers [42], metabolites crossing the BBB for [^{11}C]PBB3 [10], binding of tau radiotracers to other similar β-sheet structures (Aβ and α--synuclein), or off-target binding in target regions of interest [13–15]. The predicted 1TCM parameters and SUVR, as well as the simulated TACs and SUVR distribution, were compared to clinically observed data where applicable. However, we were limited by the small number of reported kinetic parameters and SUVR values to fully assess the amyloid biomathematical model for screening tau radiotracers.

The predicted and highest clinicallyobserved SUVR data for AD correlated well using fixed time window of 90–110 min and the literature-reported time window with R^2 values of 0.88 and 0.89 respectively, for 9 clinically applied tau radiotracers (Figure 3). However, the results were driven mostly by [^{18}F]MK6240. Some of the clinically applied tau radiotracers ([^{18}F]THK523, [^{18}F]THK5351 and [^{18}F]flortaucipir) did not have high selectivity for tau, which may have contributed to smaller predicted values as the predicted values were based on binding to a single target site but the off-target binding or specific binding to other β-sheet structures (e.g., amyloid) may yield higher clinical SUVR values. The predicted TACs of [^{18}F]T808 exhibited a much slower clearance compared to the clinically observed kinetics, which resulted in a large difference between the predicted and clinically observed SUVR. This may be due to the poor predictive ability of in silico parameters for [^{18}F]T808, which has a unique chemical structure.

4.3. Comparison of Tau Radiotracers with CUI. The CUI value of [^{18}F]flortaucipir was large while the CUI value of [^{18}F]T808 was very small and does not appear to be a promising clinical tau radiotracer. Similarly, [^{18}F]THK523 also yielded a small CUI value, even though studies showed that it could be applied clinically. [^{18}F]THK523, [^{18}F]Lansoprazole, and [^{11}C]Astemizole yielded small CUI values using the K_D values measured using human brain homogenates, which differed greatly from that measured using synthetic tau. K_D or K_i values measured using AD brain homogenates were very different from those measured using heparin-induced tau polymer (HITP) (Table 1). This is because HITP is composed of only 3R and/or 4R, and hence may not undergo the same phosphorylation process as human tau [19, 43]. On the other hand, the K_D or K_i values of amyloid radiotracers measured using synthetic tau and AD brain homogenates did not differ greatly [5]. The huge difference in the K_D values measured using human brain homogenates and synthetic tau were much greater for [^{18}F]THK523 than for [^{18}F]THK5105 (Table 1). This might also indicate the binding preferences of [^{18}F]THK523 to certain tau-binding sites available on synthetic tau, that were fewer in numbers in human brain homogenates. Therefore, it is important to determine the binding affinity of tau radiotracers to different subtypes of tau protein and other β-sheet structures such as Aβ and α-synuclein.

[^{18}F]THK5351 yielded higher clinically observed SUVR than [^{18}F]THK5117 in the same AD patients, with lower white matter binding [15]. [^{18}F]THK5351 was also reported to have a higher signal-to-noise ratio (SNR), and a lower non-specific binding in white matter than [^{18}F]THK5105 and [^{18}F]THK5117 [8]. Similarly, the CUI value of [^{18}F]

THK5351 was higher than [^{18}F]THK5105 and [^{18}F]THK5117. [^{11}C]PBB3, [^{18}F]flortaucipir, and [^{18}F]THK5105 have nearly similar CUI values (Figure 5), but the difference in the clinically observed SUVR values between HC and AD were greatest in [^{18}F]flortaucipir, followed by [^{11}C]PBB3 then [^{18}F]THK5105 (Table 3). This difference may be attributed to the tau subtypes that [^{11}C]PBB3 is binding. [^{18}F]THK5351 and [^{18}F]flortaucipir was reported to bind to the same targets but with different affinities, while [^{11}C]PBB3 seems to bind to a different tau subtype [44]. If the tau subtype that [^{11}C]PBB3 binds to is of a lower concentration in subject, the clinical SUVR will become smaller. The difference between the clinically observed results and CUI ranking showed that the evaluation of the clinical usefulness of tau radiotracer based on binding to a single target could not reflect the actual in vivo binding in subjects. High tau selectivity and off-target binding affect the comparison of the in vivo binding of tau radiotracers, which are less prominent in amyloid radiotracers. Despite the differences in CUI rankings, the clinically applied tau radiotracers had CUI values above the recommended value especially for those with high SNR. Thus, the screening methodology can still provide confidence in the decision-making of moving candidate radiotracers for clinical studies.

4.4. Limitations of Screening Methodology. Few measurements of tau concentration in postmortem human brains using ELISA have been reported, and these values are very different [17, 29, 45, 46]. In addition, these reported tau concentrations were mostly measured using normal-aged control and AD brains, with very little data on the tau concentration in MCI. As such, the simulated SUVR distribution might not reflect the clinically observed MCI result. Moreover, the input function of the amyloid radiotracer [^{11}C]BF227 was used for simulations. Thus far, the input functions of only three clinically applied tau radiotracers of [^{11}C]PBB3 [10], [^{18}F]flortaucipir [36], and [^{18}F]MK6240 [16] have been reported. The arterial input functions of these radiotracers were similar in HC and AD, with a fast uptake and a fast washout, and the shape of the curves was similar to that of [^{11}C]BF227 as used in the simulation. Although the shape of the input function of these two radiotracers was similar to that of [^{11}C]BF227, the shape of the arterial input function might be different for other tau radiotracers. Thus, we evaluated the effect of the input function on the outcome using four different input functions with fast kinetics for HC and AD subjects injected with [^{11}C]BF227 or [^{18}F]FACT, with areas under the input function curves from 0 to 120 min of 536 (default), 649, 434, and 306 (kBq/mL) min. The % COV of the predicted SUVR was less than 7.0 for all conditions and radiotracers, while %COV of the CUI was less than 7.0 for all except the poor radiotracers, namely, [^{18}F]FDDNP, [^{18}F]FPPDB, and [^{11}C]Astemizole. This showed that the results would not be changed significantly using input functions with similar kinetics. However, there were also issues with metabolites crossing the BBB (e.g., [^{11}C]PBB3), but the amyloid biomathematical screening methodology could not be used to predict the possibility of metabolites crossing this barrier.

Off-target binding was observed in some clinically applied tau radiotracers. [^{18}F]flortaucipir was reported to show specific binding in the midbrain, vessels, iron-associated regions (e.g., basal ganglia), substantia nigra, calcifications in the choroid plexus, and leptomeningeal melanin [13]. [^{11}C]PBB3 was reported to accumulate in the venous sinuses, basal ganglia, and thalamus, while its fluorinated compounds showed off-target binding in the choroid plexus [14, 44]. [^{18}F]THK5351 was reported to bind to monoamine oxidase B (MAO-B), which is highly expressed throughout the brain, and thus, its tau binding data needs to be corrected for MAO-B binding [47]. [^{18}F]MK6240 was reported to have reduced off-target binding on the whole but showed off-target binging in regions such as the retina, substantia nigra, ethmoid sinus, and dura matter [16]. Depending on the region of off-target binding, the effects may not limit PET quantification due to little or no anatomical overlap of the target regions of interest (ROIs) with off-target regions. Accurate PET quantification is also less affected if the radiotracer has high target selectivity or if the concentrations of the off-target binding sites are much lower compared to that of the target [48]. Off-target binding may be one of the contributing factors that led to the observed differences between simulation and the clinical data of tau PET radiotracers. The possibility of binding to off-targets is difficult to predict, and systematic screening is required to determine the binding of the candidate compound to a wide range of proteins. This will increase the time and cost of compound screening. The amyloid biomathematical screening methodology could not predict off-target binding, and the inclusion of multiple binding sites appeared to be required for tau radiotracers to correct for this issue.

4.5. Feasibility of Extending to the Screening of Tau Radiotracers. To date, the comparison of multiple tau radiotracers has been performed via in vitro competition binding assays in human brain sections, using human AD brain homogenates [11, 12] or by means of preclinical imaging [38]. There is a lack of consideration of the possible in vivo kinetics of the radiotracers during development, which may lead to poor clinical performance [4–6]. The use of in silico data can support predictions of tracer kinetics and increases confidence in clinical translation, in addition to facilitating radiotracer comparisons. The weak SUVR correlation was obtained between the predicted and clinically observed SUVR results, mostly due to the small SUVR values for tau radiotracers with poorer tau selectivity. However, there are very few reported kinetic parameters to assess the limitations of the screening methodology. The TACs, SUVR distribution, and CUI rankings differed primarily for tau radiotracers with low selectivity to tau. This showed that the evaluation of the clinical usefulness of tau radiotracer based on binding to a single target could not fully reflect the actual in vivo binding in subjects since they also exhibited binding preferences to nontarget sites. Thus, it is not feasible to

directly apply the amyloid biomathematical screening methodology to tau radiotracers due to the increased complexity of evaluating the binding of tau radiotracers, namely, target-binding, off-target binding, and non-specific binding. More work is required to improve the accuracy of predicting the clinical usefulness of tau radiotracers by including possible binding to other β-sheet structures or off-target sites. However, the high CUI values generated for clinically applied tau radiotracers with high SNR showed that the screening methodology could be used to increase confidence in decision-making when choosing candidate radiotracers for further evaluation.

5. Conclusions

The predicted TACs, SUVR, and CUI ranking differed for some clinically applied tau radiotracers, especially those with lower selectivity for tau. This showed that the evaluation of the clinical usefulness of tau radiotracer based on binding to a single target could not reflect the actual in vivo tau binding in subjects due to more challenges in evaluating the in vivo binding of tau radiotracers, such as off-target binding and high tau selectivity, compared to amyloid radiotracers. The inclusion of possible binding to other β-sheet structures or off-target sites and the binding affinities to different target sites would improve the accuracy of the prediction. From our results, clinically applied tau radiotracers with higher SNR, such as [^{18}F]MK6240 and [^{18}F]THK5351, had higher CUI rankings. This supported the use of the screening methodology in radiotracer development by allowing comparison of candidate radiotracers with clinically-applied radiotracers based on SUVR, with respect to binding to a single target. Our results will hopefully provide some insights to guide the development of in silico models in supporting the development of tau radiotracers.

Data Availability

The program (RSwCUI) used for TACs simulation and CUI evaluation can be download from http://www.rim.cyric.tohoku.ac.jp/software/CUI-Software. The predicted $K1$, $k2$, and BP_{ND} values in HC and AD of 9 clinically applied tau-related radiotracers are provided in the interest of readers and are included within the supplementary information file.

Conflicts of Interest

The authors declare that there are no conflicts of interest regarding the publication of this paper.

Acknowledgments

This study was supported by Grants-in-Aid for Scientific Research (B) (no. 17H04118) from the Ministry of Education, Culture, Sports, Science and Technology (MEXT), Japanese Government.

Supplementary Materials

Supplementary 1. Table 1: Predicted $K1$, $k2$, and BP_{ND} values in HC and AD of 9 clinically applied tau-related radiotracers.

Supplementary 2. Figure 1: Quasi-steady-state of TACs of HC (gray), MCI (blue), and AD (orange) conditions of 9 clinically applied tau radiotracers from 0 to 120 min. The box highlighted the time window of 90 to 110 min, which was applied as the default time window for simulating SUVRs.

References

[1] R. J. Perrin, A. M. Fagan, and D. M. Holtzman, "Multimodal techniques for diagnosis and prognosis of Alzheimer's disease," *Nature*, vol. 461, no. 7266, pp. 916–922, 2009.

[2] C. R. Jack, D. A. Bennett, K. Blennow et al., "NIA-AA Research Framework: toward a biological definition of Alzheimer's disease," *Alzheimer's and Dementia*, vol. 14, no. 4, pp. 535–562, 2018.

[3] R. C. Garner and G. Lappin, "Commentary," *British Journal of Clinical Pharmacology*, vol. 61, no. 4, pp. 367–370, 2006.

[4] Y. Arakawa, Y. Nai, M. Shidahara et al., "Prediction of the clinical SUV ratio in amyloid PET imaging using a biomathematic modeling approach toward the efficient development of a radioligand," *Journal of Nuclear Medicine*, vol. 58, no. 8, pp. 1285–1292, 2017.

[5] Y. H. Nai, M. Shidahara, C. Seki, and H. Watabe, "Biomathematical screening of amyloid radiotracers with clinical usefulness index," *Alzheimer's and Dementia: Translational Research & Clinical Interventions*, vol. 3, no. 4, pp. 542–552, 2017.

[6] Q. Guo, M. Brady, and R. N. Gunn, "A biomathematical modeling approach to central nervous system radioligand discovery and development," *Journal of Nuclear Medicine*, vol. 50, no. 10, pp. 1715–1723, 2009.

[7] L. Buée, T. Bussière, V. Buée-Scherrer, A. Delacourte, and P. R. Hof, "Tau protein isoforms, phosphorylation and role in neurodegenerative disorders11These authors contributed equally to this work," *Brain Research Reviews*, vol. 33, no. 1, pp. 95–130, 2000.

[8] V. L. Villemagne, M. T. Fodero-Tavoletti, C. L. Masters, and C. C. Rowe, "Tau imaging: early progress and future directions," *Lancet Neurology*, vol. 14, no. 1, pp. 114–124, 2015.

[9] H. Hashimoto, K. Kawamura, N. Igarashi et al., "Radiosynthesis, photoisomerization, biodistribution, and metabolite analysis of 11C-PBB3 as a clinically useful PET probe for imaging of tau pathology," *Journal of Nuclear Medicine*, vol. 55, no. 9, pp. 1532–1538, 2014.

[10] Y. Kimura, M. Ichise, H. Ito et al., "PET quantification of tau pathology in human brain with 11C-PBB3," *Journal of Nuclear Medicine*, vol. 56, no. 9, pp. 1359–1365, 2015.

[11] L. Declercq, S. Celen, J. Lecina et al., "Comparison of new tau PET-tracer candidates with [^{18}F]T808 and [^{18}F]T807," *Molecular Imaging*, vol. 15, article 153601211562492, 2016.

[12] T. Tago, S. Furumoto, N. Okamura et al., "Preclinical evaluation of [^{18}F]THK-5105 enantiomers: effects of chirality on its effectiveness as a tau imaging radiotracer," *Molecular Imaging and Biology*, vol. 18, no. 2, pp. 258–266, 2015.

[13] V. J. Lowe, G. Curran, P. Fang et al., "An autoradiographic evaluation of AV-1451 Tau PET in dementia," *Acta Neuropathologica Communications*, vol. 4, no. 1, 2016.

[14] M. Maruyama, H. Shimada, T. Suhara et al., "Imaging of tau pathology in a tauopathy mouse model and in Alzheimer patients compared to normal controls," *Neuron*, vol. 79, no. 6, pp. 1094–1108, 2013.

[15] R. Harada, N. Okamura, S. Furumoto et al., "^{18}F-THK5351: a novel PET radiotracer for imaging neurofibrillary pathology in alzheimer disease," *Journal of Nuclear Medicine*, vol. 57, no. 2, pp. 208–214, 2015.

[16] T. A. Pascoal, M. Shin, M. S. Kang et al., "In vivo quantification of neurofibrillary tangles with [^{18}F]MK-6240," *Alzheimer's Research and Therapy Internet*, vol. 10, no. 1, 2018.

[17] M. T. Fodero-Tavoletti, N. Okamura, S. Furumoto et al., "^{18}F-THK523: a novel in vivo tau imaging ligand for Alzheimer's disease," *Brain*, vol. 134, no. 4, pp. 1089–1100, 2011.

[18] R. Harada, N. Okamura, S. Furumoto et al., "Comparison of the binding characteristics of [^{18}F]THK-523 and other amyloid imaging tracers to Alzheimer's disease pathology," *European Journal of Nuclear Medicine and Molecular Imaging*, vol. 40, no. 1, pp. 125–132, 2012.

[19] N. Okamura, S. Furumoto, R. Harada et al., "Novel ^{18}F-labeled arylquinoline derivatives for noninvasive imaging of tau pathology in Alzheimer disease," *Journal of Nuclear Medicine*, vol. 54, no. 8, pp. 1420–1427, 2013.

[20] L. Lemoine, L. Saint-Aubert, A. Marutle et al., "Visualization of regional tau deposits using 3H-THK5117 in Alzheimer brain tissue," *Acta Neuropathologica Communications*, vol. 3, no. 1, p. 40, 2015.

[21] T. Tago, *Development of PET probes for imaging of tau pathology in Alzheimer's disease*, Ph.D. Thesis, Graduate School of Pharmaceutical Sciences, Tohoku University, Sendai, Japan, 2016.

[22] C.-F. Xia, J. Arteaga, G. Chen et al., "[^{18}F]T807, a novel tau positron emission tomography imaging agent for Alzheimer's disease," *Alzheimer's and Dementia*, vol. 9, no. 6, pp. 666–676, 2013.

[23] M. Ono, N. Sahara, K. Kumata et al., "Distinct binding of PET ligands PBB3 and AV-1451 to tau fibril strains in neurodegenerative tauopathies," *Brain*, vol. 12, p. aww339, 2017.

[24] K. Matsumura, M. Ono, H. Kimura et al., "^{18}F-Labeled phenyldiazenyl benzothiazole for in vivo imaging of neurofibrillary tangles in alzheimer's disease brains," *ACS Medicinal Chemistry Letters*, vol. 3, no. 1, pp. 58–62, 2011.

[25] M. V. Fawaz, A. F. Brooks, M. E. Rodnick et al., "High affinity radiopharmaceuticals based upon lansoprazole for PET imaging of aggregated tau in Alzheimer's disease and progressive supranuclear palsy: synthesis, preclinical evaluation, and lead selection," *ACS Chemical Neuroscience*, vol. 5, no. 8, pp. 718–730, 2014.

[26] L. E. Rojo, J. Alzate-Morales, I. N. Saavedra, P. Davies, and R. B. Maccioni, "Selective interaction of lansoprazole and astemizole with tau polymers: potential new clinical use in diagnosis of Alzheimer's disease," *Journal of Alzheimer's Disease*, vol. 19, no. 2, pp. 573–589, 2010.

[27] E. D. Hostetler, A. M. Walji, Z. Zeng et al., "Preclinical characterization of 18F-MK-6240, a promising PET tracer for in vivo quantification of human neurofibrillary tangles," *Journal of Nuclear Medicine*, vol. 57, no. 10, pp. 1599–1606, 2016.

[28] F. J. R. Rombouts, J. I. Andrés, M. Ariza et al., "Discovery of N-(Pyridin-4-yl)-1,5-naphthyridin-2-amines as potential tau pathology PET tracers for Alzheimer's disease," *Journal of Medicinal Chemistry*, vol. 60, no. 4, pp. 1272–1291, 2017.

[29] M. Herrmann, S. Golombowski, K. Kräuchi et al., "ELISA-quantitation of phosphorylated tau protein in the Alzheimer's disease brain," *European Neurology*, vol. 42, no. 4, pp. 205–210, 1999.

[30] M. Shidahara, H. Watabe, M. Tashiro et al., "Quantitative kinetic analysis of PET amyloid imaging agents [^{11}C]BF227 and [^{18}F]FACT in human brain," *Nuclear Medicine and Biology*, vol. 42, no. 9, pp. 734–744, 2015.

[31] P. Han, G. Serrano, T. G. Beach et al., "A quantitative analysis of brain soluble tau and the tau secretion factor," *Journal of Neuropathology and Experimental Neurology*, vol. 76, no. 1, pp. 44–51, 2017.

[32] V. L. Villemagne, S. Furumoto, M. T. Fodero-Tavoletti et al., "In vivo evaluation of a novel tau imaging tracer for Alzheimer's disease," *European Journal of Nuclear Medicine and Molecular Imaging*, vol. 41, no. 5, pp. 816–826, 2014.

[33] N. Okamura, S. Furumoto, M. T. Fodero-Tavoletti et al., "Non-invasive assessment of Alzheimer's disease neurofibrillary pathology using [^{18}F]-THK5105 PET," *Brain*, vol. 137, no. 6, pp. 1762–1771, 2014.

[34] R. Harada, N. Okamura, S. Furumoto et al., "[^{18}F]THK-5117 PET for assessing neurofibrillary pathology in Alzheimer's disease," *European Journal of Nuclear Medicine and Molecular Imaging*, vol. 42, no. 7, pp. 1052–1061, 2015.

[35] M. Jonasson, A. Wall, K. Chiotis et al., "Tracer kinetic analysis of (S)-^{18}F-THK5117 as a PET tracer for assessing tau pathology," *Journal of Nuclear Medicine*, vol. 57, no. 4, pp. 574–581, 2016.

[36] D. W. Wooten, N. J. Guehl, E. E. Verwer et al., "Pharmacokinetic evaluation of the tau PET radiotracer ^{18}F-T807 (^{18}F-AV-1451) in human subjects," *Journal of Nuclear Medicine*, vol. 58, no. 3, pp. 484–491, 2016.

[37] D. T. Chien, A. K. Szardenings, S. Bahri et al., "Early clinical PET imaging results with the novel PHF-tau radioligand [F18]-T808," *Journal of Alzheimer's Disease*, vol. 38, no. 1, pp. 171–184, 2014.

[38] S. N. Lockhart, S. L. Baker, N. Okamura et al., "Dynamic PET measures of tau accumulation in cognitively normal older adults and alzheimer's disease patients measured using [^{18}F] THK-5351," *PLoS One*, vol. 11, no. 6, Article ID e0158460, 2016.

[39] K. Chiotis, L. Saint-Aubert, I. Savitcheva et al., "Imaging in-vivo tau pathology in Alzheimer's disease with THK5317 PET in a multimodal paradigm," *European Journal of Nuclear Medicine and Molecular Imaging*, vol. 43, no. 9, pp. 1686–1699, 2016.

[40] K. A. Johnson, A. Schultz, R. A. Betensky et al., "Tau positron emission tomographic imaging in aging and early Alzheimer disease," *Annals of Neurology*, vol. 79, no. 1, pp. 110–119, 2015.

[41] C. Tauber, E. Beaufils, C. Hommet et al., "Brain [^{18}F]FDDNP binding and glucose metabolism in advanced elderly healthy subjects and alzheimer's disease patients," *Journal of Alzheimer's Disease*, vol. 36, no. 2, pp. 311–320, 2013.

[42] T. Itoh, Y. Saura, Y. Tsuda, and H. Yamada, "Stereoselectivity and enantiomer-enantiomer interactions in the binding of ibuprofen to human serum albumin," *Chirality*, vol. 9, no. 7, pp. 643–649, 1997.

[43] M. Ariza, H. C. Kolb, D. Moechars, F. Rombouts, and J. I. Andrés, "Tau positron emission tomography (PET) imaging: past, present, and future," *Journal of Medicinal Chemistry*, vol. 58, no. 11, pp. 4365–4382, 2015.

[44] L. Lemoine, P. G. Gillberg, M. Svedberg et al., "Comparative binding properties of the tau PET tracers THK5117, THK5351, PBB3, and T807 in postmortem Alzheimer brains," *Alzheimer's Research and Therapy*, vol. 9, no. 1, p. 96, 2017.

[45] E. B. Mukaetova-Ladinska, Z. Abdel-All, E. S. Mugica et al., "Tau proteins in the temporal and frontal cortices in patients with vascular dementia," *Journal of Neuropathology and Experimental Neurology*, vol. 74, no. 2, pp. 148–157, 2015.

[46] R. Hashimoto, Y. Nakamura, I. Tsujio, H. Tanimukai, T. Kudo, and M. Takeda, "Quantitative analysis of neurofilament proteins in Alzheimer brain by enzyme linked immunosorbent assay system," *Psychiatry and Clinical Neurosciences*, vol. 53, no. 5, pp. 587–591, 1999.

[47] K. P. Ng, T. A. Pascoal, S. Mathotaarachchi et al., "Monoamine oxidase B inhibitor, selegiline, reduces ^{18}F-THK5351 uptake in the human brain," *Alzheimer's Research and Therapy*, vol. 9, no. 1, p. 25, 2017.

[48] G. C. Van de Bittner, E. L. Ricq, and J. M. Hooker, "A philosophy for CNS radiotracer design," *Accounts of Chemical Research*, vol. 47, no. 10, pp. 3127–3134, 2014.

Hindawi
Computational and Mathematical Methods in Medicine
Volume 2018, Article ID 1981627, 10 pages
https://doi.org/10.1155/2018/1981627

Research Article

Continuous Blood Pressure Estimation Based on Two-Domain Fusion Model

Qian Wang,[1,2] Yajie Xu ,[2] Guoqiang Zeng,[1] and Mingshan Sun [2]

[1]*College of Nuclear Technology and Automation Engineering, Chengdu University of Technology, Chengdu 610051, Sichuan, China*
[2]*Medical Imaging Department, Suzhou Institute of Biomedical Engineering and Technology, Chinese Academy of Sciences, Suzhou 215163, Jiangsu, China*

Correspondence should be addressed to Yajie Xu; xuyj@sibet.ac.cn

Received 17 September 2018; Accepted 6 November 2018; Published 16 December 2018

Guest Editor: Ka L. Man

Blood pressure (BP) is one of the indispensable elements of physiological health characteristics and a significant indicator for predicting and diagnosing hypertension and cardiovascular diseases. This paper proposes a two-domain fusion model to estimate BP continuously from pulse wave acquired with a pressure sensor. *Method*. The optimal external pressure applied on the pressure sensor is first determined in order to capture pulse wave in the radial artery. The captured pulse wave is then processed in both the time and frequency domains via filtering and fast Fourier transform. Finally, a set of features are extracted from these two domains and input into a neural network along with blood pressure values measured by a commercial sphygmomanometer for training. The model is then tested on new data for accuracy evaluation. *Results*. The proposed two-domain fusion method achieved a high degree of accuracy in measuring blood pressure.

1. Introduction

According to the American Journal of Medicine, between 1990 and 2015, the rate of blood pressure (BP) greater than 140 mmHg rose from 17307/100000 to 20526/100000 and the associated mortality rate from 97.9/100000 to 106.3/100000 [1]. Admittedly, abnormal BP can cause a burden on the heart, which increases the risk of cardiovascular diseases [2, 3]. The traditional way of measuring blood pressure is to place a cuff on the upper arm and then detect changes in the pressure inside the cuff during inflation and deflation to obtain systolic blood pressure (SBP) and diastolic blood pressure (DBP). However, this method can hinder the circulation of blood and is not intended for continuous BP measurement.

In recent years, great progress has been made in noninvasive continuous BP measurement. A study found an inverse correlation between BP and the pulse transit time (PTT) [4, 5]. But this method requires an additional electrocardiogram (ECG) module, which brings complexity and inconvenience to portable blood pressure measurement. Wu et al. only used ECG signal to estimate BP. They took 6 features of the ECG and calculated the time between the relevant features. Two sets of ECG signal containing 4 time periods were combined and input into a neural network for training to get the BP. However, this model cannot simultaneously derive the BP and is significantly different compared with the target value [6]. Secondly, PTT has a significant correlation with systolic blood pressure but little relationship with diastolic blood pressure [7]. Xu et al. used PTT and photoplethysmogram (PPG) parameters to estimate blood pressure. They defined PTT as the different time between the R wave of ECG and the following pulse peak of PPG. They took the pulse wave amplitude, PTT, pulse wave period, and area as the parameters to send to a feed-forward back propagation neural network for training. Although the error could be within 5 mmHg, calibration was required before getting the output

[8]. Luo et al. fabricated a low-power (3 nW) piezoresistive sensor (PS) device and measured BP using a single parameter PTT but also required clinical calibration of the initial values [9].

With the advancement of sensor technology, piezoelectric sensors nowadays become sensitive enough to reveal the pulse wave morphological features. However, during their use, piezoelectric sensors require an external force to balance the pressure between the probe and soft tissue [10]. In order to find the right amount of force applied to each individual, this paper proposes a method to use body mass index (BMI) to quantify the balance and find a suitable pressure for everyone. This will be explained in the third part of this paper.

Our goal is to develop a stable, efficient continuous blood pressure measurement system that requires no user calibration, to be used by patients with hypertension, cardiovascular, or other diseases for continuous BP monitoring. The paper is organized as follows: in Section 2, the background on propagation of pulse wave is given. In Section 3, a two-domain fusion model and its use with artificial neural networks (ANN) are elaborated. Section 4 shows experimental results, and Section 5 provides a discussion and conclusion on this proposed method.

2. Background

Figure 1 shows pulse wave and blood propagation. When the cardiac ejection is completed, the central aorta forms a wave (#1), which is rebounded and generates a rebound wave (#2) when it propagates to the first reflection site (the arterial node between thoracic aorta and renal arteries). The rebound wave will be rebounded again, producing a wave (#3) when the wave (#1) gets to the second reflection site (the arterial node between abdominal aorta and iliac arteries). Finally, both of the rebound waves (#2 and #3) will superimpose on the main wave with a certain time delay and then propagate along the blood vessel to the radial artery or fingertip artery [11].

As shown in Figure 2, the features of the pulse wave mainly include (b)–(g). The (b)–(e) points correspond to the pulse wave's starting point, main peak, trough point, and the peak produced by the superposition between the first rebound wave (#2) and the main wave (#1). Points f and g are formed by the superposition between the second rebound wave (#3) and the main wave (#1). Note that in a young person with good blood vessel elasticity, the rebound wave can be weak and it can be submerged in the main wave and not visible in the waveform.

In order to accurately identify the characteristic points of the pulse wave, the pulse wave needs to be acquired with high signal-to-noise ratio (SNR) and without distortion. The detection of pulse wave feature points is shown below in the next section.

3. Methods

3.1. Pulse Wave Detection. There are two mainstream methods for pulse wave detection. One is photoplethysmogram (PPG), and the other is to apply a piezoelectric sensor (PS) in the radial artery. In PPG, light is emitted from a photodiode through a fingertip, a wrist, or the like, and the blood inside the artery absorbs the light and causes a change in the light intensity, so that a change in the amount of blood can be detected, therefore the pulse wave is obtained. The pulse wave signal in PPG is weak, and its SNR acquired by this method is generally not high. In addition, if a patient has arterial occlusion, tissue edema and blood clots, arrhythmia, or weak peripheral circulation, this method will show considerable deviations. While in PS, a pressure sensor is applied to the skin above the radial artery and records the pulse directly. The signal often has better SNR. Because one is an indirect measure and the other is a direct measure, the waveform characteristics collected by the two are different, and we have found that PS offers a lot of more details, thus more information, in its pulse waveform than in PPGs.

Figures 3(a) and 3(b) are pulse waves from a 25-year-old with arrhythmia, collected by PPG and PS, respectively. In Figure 3(a), all the peaks except the main peak are all submerged due to the irregular heart beating. In comparison, there are three peaks in addition to the main peak clearly visible in Figure 3(b). Figures 3(c) and 3(d) are the normal PPG and PS waveform from a 26-year-old female. It can be seen that although the PPG can detect the pulse wave (note the 2nd peak is submerged), the ratio between the 3rd peak and the main peak is bigger than expected. The PS on the other hand has a better representation for the true pulse wave. Therefore, we will use PS as the method of pulse wave measurement for our study.

3.2. Optimal Pressure for Piezoresistive Sensor. As for the pressure sensor for blood waveform measurement, we choose Honeywell 1865 Series (Honeywell, Fort Mill, USA). It is a piezoresistive sensor that employs a solid-state piezopressure transducer mounted in a plastic package and offers high resolution using its Wheatstone bridge strain gauge design. It is designed to accurately collect tiny biological signals with good linearity, high test accuracy, and fast response. It is used here to accurately detect the pressure change caused by pulsation.

The sensor is applied on top of the radial artery with a certain external pressure to obtain the pulse wave by detecting the beat of the superficial artery on the surface of the skin. In actual measurements, the pressure applied to a same person can be different at different times, resulting in a difference in waveforms for the same individual and possibly errors in BP estimation. We thus need to find a constant and optimal pressure applied onto the sensor for each individual. Unfortunately, the research on this problem is still relatively muted. We will thus address this issue first before we move onto our two-domain fusion model.

Since the external force applied to the sensor is mainly to counter the pressure from the elasticity of the soft tissue, we hypothesize that the optimal pressure for an individual is dependent on the individual's physical measures such as height or obesity. We have thus done a lot of experiments to show this indeed is the case. When a force is applied to the detection unit and varied from small to large, the soft tissue

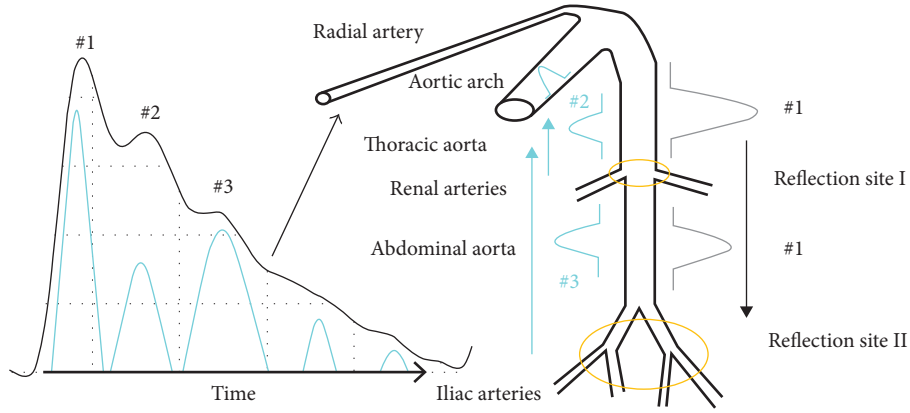

Figure 1: Relationship between pulse and BP.

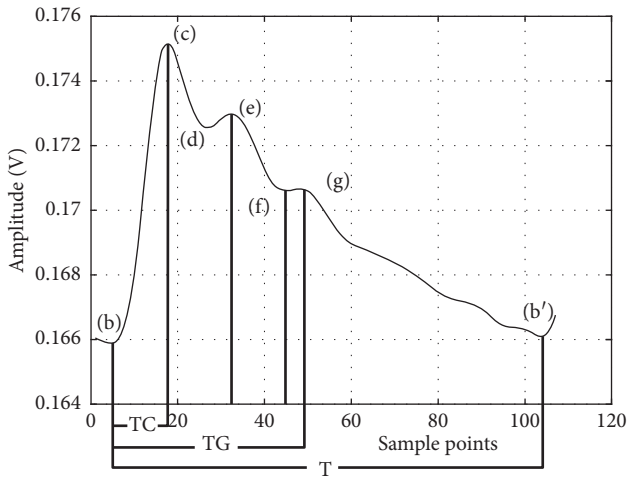

Figure 2: Standard pulse wave and characteristic points.

under the sensor probe forms a force field. If the pressure of the sensor probe and the arterial wall of the radial artery are in close equilibrium, the shape and features of the pulse wave are the most conspicuous. Correspondingly, we define the pressure that produces the most detail of the pulse wave as the optimal pressure (OP) for capturing pulse wave. Admittedly, if you want to get different OP for different people, you need to rely on some indicator to quantify the soft tissue thickness above the radial artery. For this reason, we select the body mass index (BMI).

Figure 4(a) shows the piezoresistive sensor used in this article. It is equipped with a homemade casing and probe (the contact point or the tip) and signal processing board. Figures 4(b)–4(d) are pulse waves at the pressures 2.3 N, 3.8 N, and 14 N, respectively. At 2.3 N, the amplitude of the pulse wave is small, and the features are not clear. On the contrary, the pulse and its features are obvious at 3.8 N. Then at 14 N, the pulse wave is distorted with severe baseline shift and waveform overlapping. In order to get the OP, we collected pulse waves for each person at different external pressures. The steps are as follows:

Step 1. Find the place where the radial artery beats the most. Place the sensor probe on it.

Step 2. Place a piezoelectric film (Tekscan A201, Boston, USA) between the probe and the skin, adjust the wrist band so the average pressure reading is 2 N, and store 20 sets of pressure value in 500 ms cycles. Then, withdraw the piezoelectric film and measure the pulse wave at this time.

Step 3. Reinsert the piezoelectric film at the end of each measurement. Increase the pressure by 0.5 N and repeat step 2. Stop when the pressure reaches 14 N.

Step 4. Find a set of pulse waves with ideal amplitude and features and use median filter to fit the baseline of the corresponding pressure measured by the film.

Step 5. Find the value with the largest difference between the pressure value and the baseline and record the value of the baseline at this time.

Step 6. Repeat the above steps for 30 people and then use the BMI and the baseline values obtained in step 5 to perform a 3rd order polynomial fit to get the OP curve, where BMI is determined by the following equation:

$$\mathrm{BMI} = \frac{\mathrm{weight\,(Kg)}}{\mathrm{height\,(m)}^2}. \tag{1}$$

In Figure 5(b), when the BMI is less than 24, the OP curve is basically linear. It exhibits a saturation trend when the BMI goes beyond 24. Admittedly, the BMI of more than 24 is considered overweight in China [12]. So, we can come to a conclusion: when the BMI is lower than 24, the OP curve is linear with BMI. The OP is then determined by the following equation:

$$\mathrm{OP} = -0.0114 * \mathrm{BMI}^3 + 0.7302 * \mathrm{BMI}^2 - 15.0889 * \mathrm{BMI} + 104.4144. \tag{2}$$

3.3. Two-Domain Fusion Model. After the pulse wave is acquired, we now move to the two-domain model. The analysis and decomposition of pulse waves so far in the literature were essentially in a single domain, that is, either in

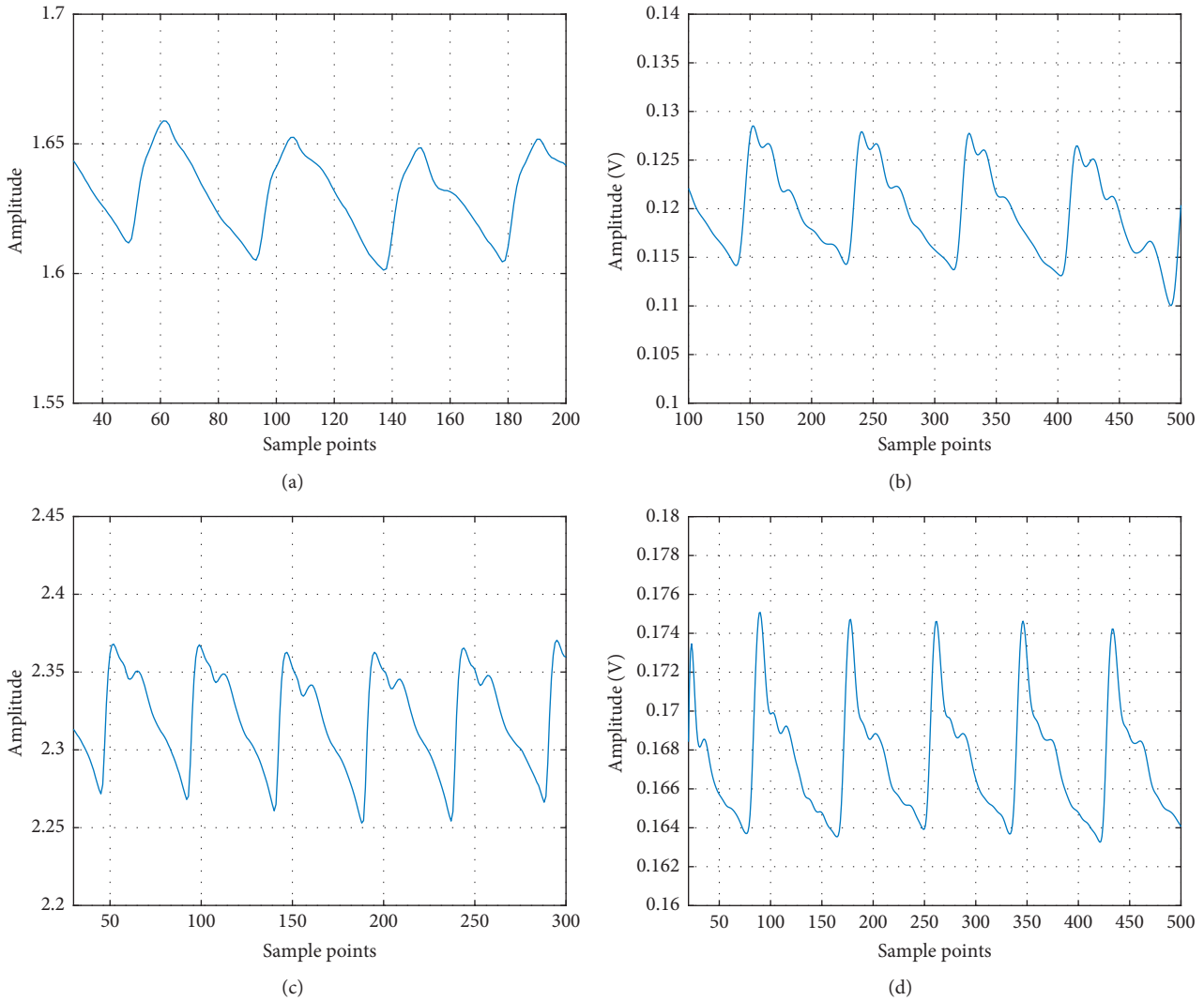

Figure 3: Pulse waves captured by PS and PPG. (a) PPG with arrhythmia. (b) PS with arrhythmia. (c) Normal PPG. (d) Normal PS.

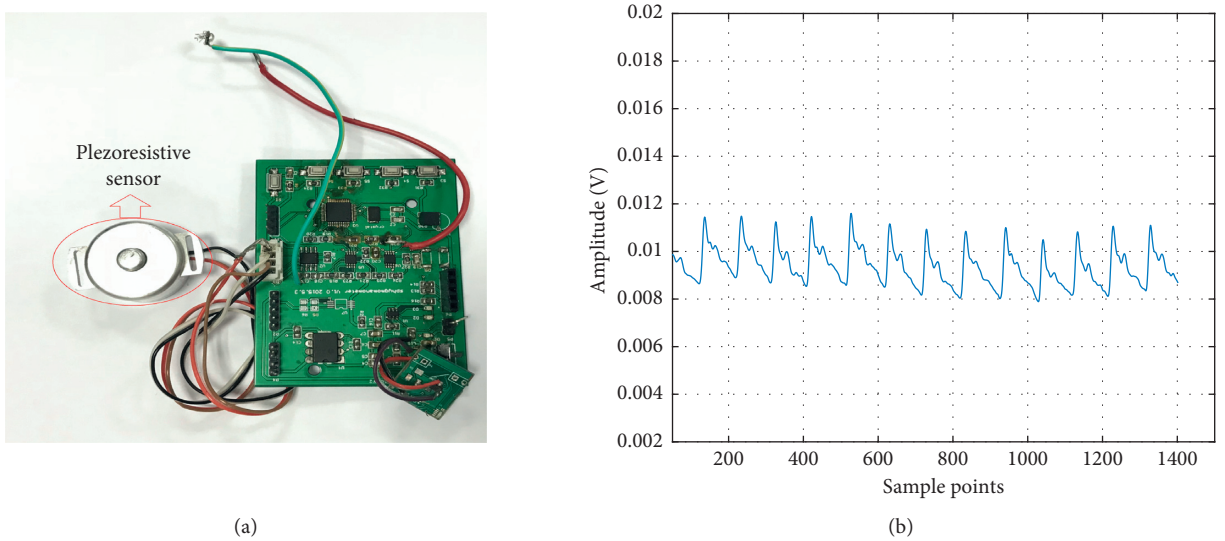

Figure 4: Continued.

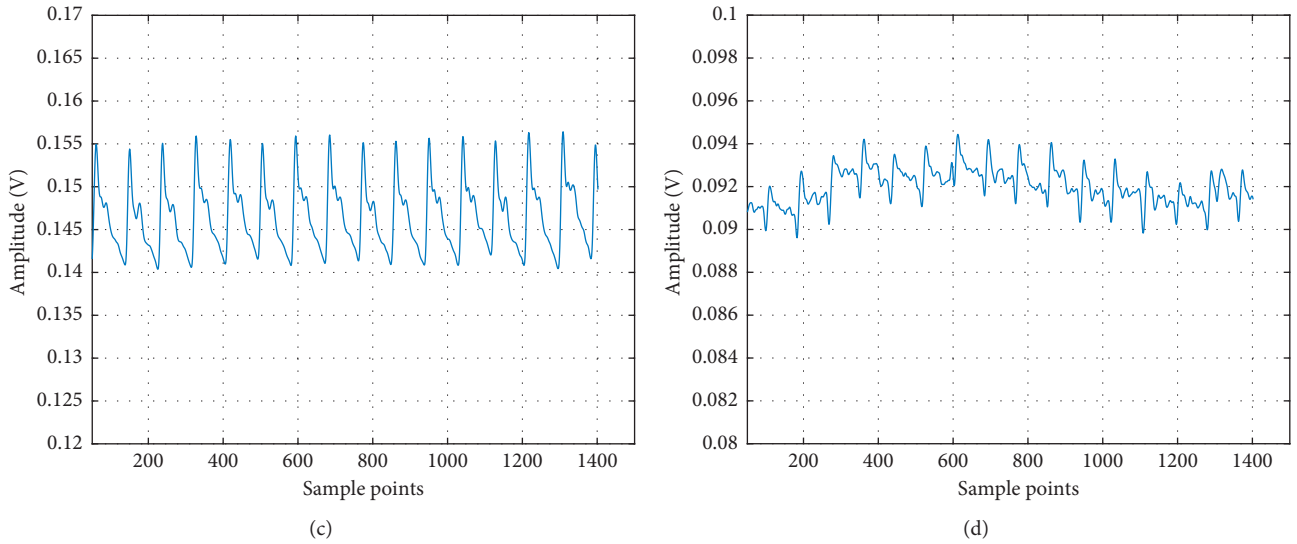

Figure 4: Pulse wave with different pressure. (a) Piezoresistive sensor. (b) Pulse wave at 2.3 N. (c) Pulse wave at 3.8 N. (d) Pulse wave at 14 N.

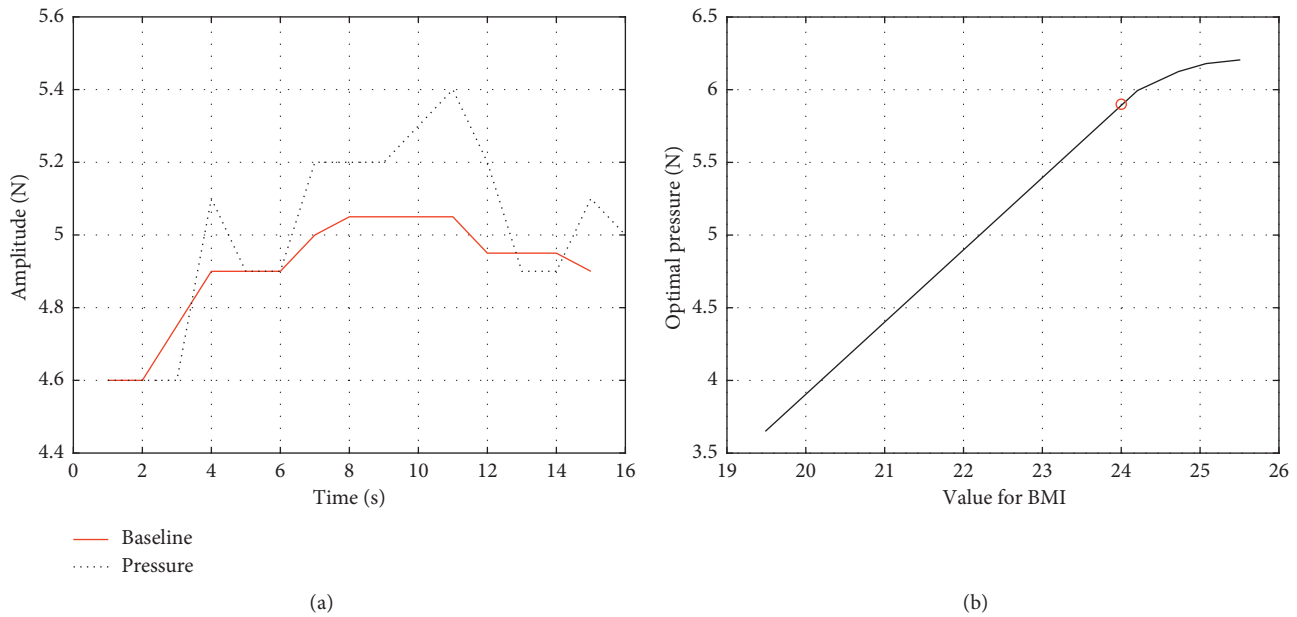

Figure 5: The pressure baseline and OP vs. BMI curve. (a) Baseline of pressure fitted with median filter. (b) Third-order polynomial fitting for optimal pressure of capturing pulse wave.

the time domain or in the frequency domain. Millasseau et al. have obtained a generalized transfer function (GTF) by the fast Fourier transform to analyze PPG and peripheral pressure pulse. They found that GTF is not only suitable for normotensive and hypertensive subjects, even adding few nitroglycerin (NTG, 500 mg sublingually) to the blood [13]. However, they only studied the peripheral pressure pulse analysis but nothing for blood pressure estimation. Xing et al. have decomposed the pulse wave in the frequency domain and found that the blood pressure has a high correlation with the amplitude of the fast Fourier transform and that the phase also has a good correlation in the low frequency part [14].

In the time domain, each morphological point of the pulse wave can be related to physiological features that are in turn related to the elasticity of the arteries and the ability of the heart to contract. One can derive blood pressure based on these characteristics. In Figure 6, the wave will be decomposed into 7 features in the time domain.

In order to prevent confusion in the identification of periodic features of several pulse waves, we extract features only in a single pulsation period and then identify other features in other pulsation period the same way.

At each systole, the amount of cardiac ejection is different. The blood is transmitted through the arterial wave and ultimately reflected in the amplitude of the systolic peak

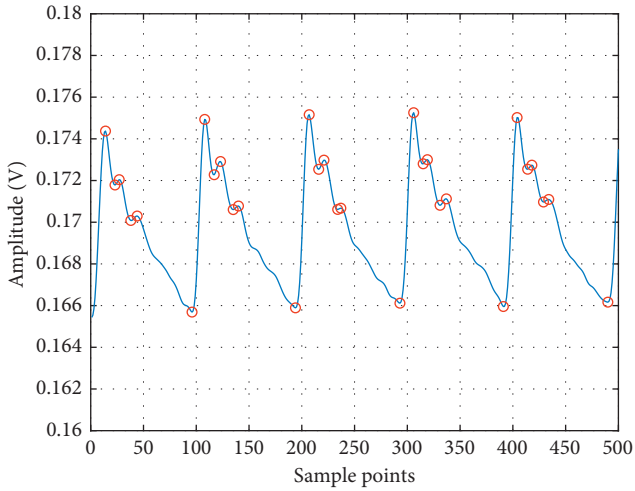

Figure 6: Feature points in the pulse wave in the time domain.

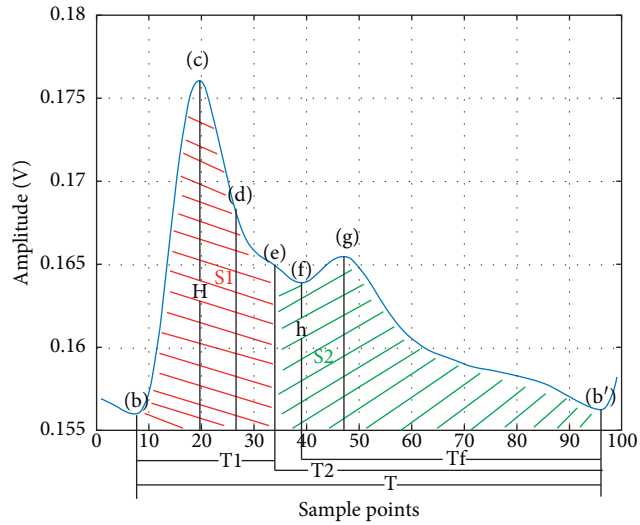

Figure 7: Illustration of time features.

[15]. Peripheral resistance will change with the diameter of the artery and the viscosity of the blood, affecting the pulse wave [16]. If the elasticity of the distal end of the blood vessel is higher, the peak of the rebounding wave will be relatively lower, and the position superimposed on the main peak will change the ratio of the area between the systolic and diastolic points, which in turn affects the blood pressure [17, 18]. Furthermore, vascular elasticity has an influence on the PTT. The ratio of time between the main peak and other peaks can be different if arteriosclerosis, tissue edema, and clots are found out in the body [19]. The time domain focuses on features from a single beat, such as the ratio of each peak within one pulse wave, while the beat-to-beat variations will be taken into consideration in the frequency domain. Figure 7 and Table 1 show the area of S1 (cardiac systole) and S2 (cardiac diastole) and other relevant parameters in the time domain.

In the frequency domain, as shown in Figure 8, there are substantial amplitude components at 0.3 Hz, 1.2 Hz, 2.4 Hz, 4.8 Hz, etc., after the fast Fourier transform (FFT) of the pulse wave, but the amplitude decays rapidly even almost submerge after 10 Hz. In this case, 0.3 Hz should be the frequency of breathing, 1.2 Hz is the heart rate, and the others are the multiple of the heart rate. It can be concluded that the main components of the pulse wave in the frequency domain are superimposed by the multiples or harmonics of the frequency of the heart rate and the frequency near the heart rate. The amplitude component corresponding to the frequency in the frequency domain of the pulse wave corresponds to the energy scale of each frequency. In order to improve accuracy and stability, this paper performs the FFT on five complete pulsation cycles for better frequency sampling. The features in the frequency domain are the amplitudes and corresponding phases of the first three characteristic peaks and are listed in Table 2. As for the other points, their amplitudes are smaller and may be interfered with the pulse wave noise.

The features from both domains are concatenated together and processed, combining the high precision of time domain and the stability of frequency domain into a better dual-domain fusion model. Experimental details are given below.

Table 1: Features extracted in time domain.

Parameter	Definition
FC	The ratio between h and H
Sss	The ratio between S1 and S1 plus S2
Sds	The ratio between S2 and S1 plus S2
Tft	The ratio between Tf and T
Tst	The ratio between T1 and T
SL	The max slope between b and c

3.4. Implementation. After fitting and obtaining OP for each people according to their BMI, a group of subjects underwent measurement of pulse wave in the morning, afternoon, and evening for 3 days. In addition, each measurement is accompanied by BP obtained by a commercial medical upper-arm sphygmomanometer (Yuwell 670B, Jiangsu, China). Both the features of pulse wave and BP are fed into a neural network for supervised learning. The process flow is shown in Figure 9 and is described below.

Step 1. Collect real-time pulse wave data and then shape and filter to pulse wave.

Step 2. Decompose the pulse wave in the time and frequency domains.

Step 3. Reconstruct and fuse features in the time and frequency domains.

Step 4. Perform the mean shift and normalization with the recombined features.

Step 5. Send the processed features to the neural network to obtain SBP and DBP.

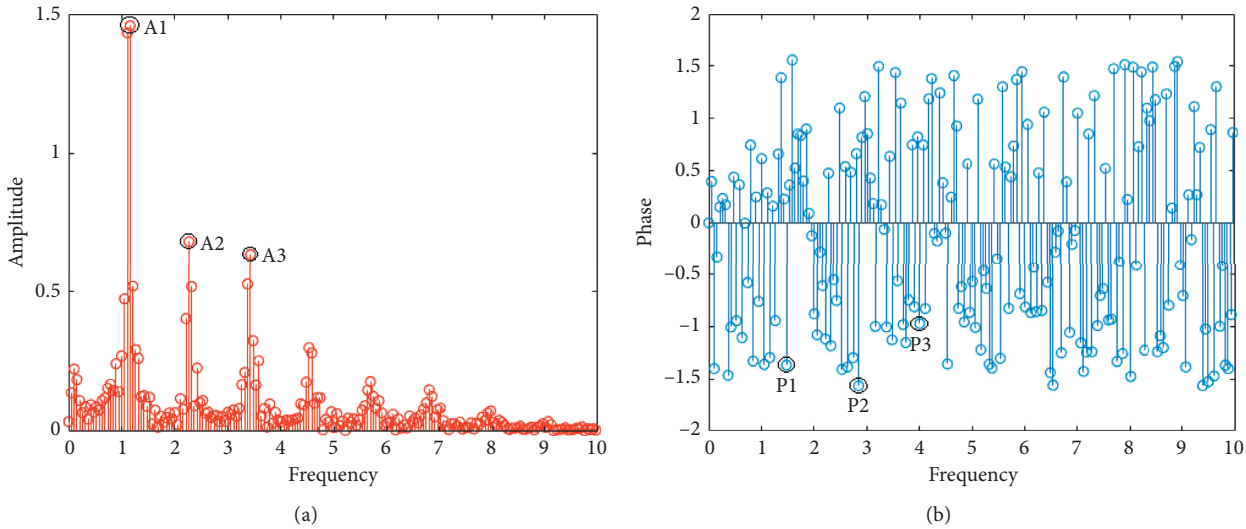

Figure 8: Illustration of frequency features. (a) FFT amplitude of pulse wave. (b) FFT phase of pulse wave.

Table 2: Features extracted in frequency domain.

Parameter	Definition
A1	The amplitude of first peak
A2	The amplitude of second peak
A3	The amplitude of third peak
P1	The phase of first peak
P2	The phase of second peak
P3	The phase of third peak

Note in the two-domain fusion model, the fusion is done in the input level of the neural network. We first exact features from the time and the frequency domains separately to form two vectors and then combine them into one data matrix to feed into the neural network for training. An additional label matrix records the true blood pressure measured by the commercial sphygmomanometer to serve as the training target. The neural network then iterates through the combined feature data, from which the weight corresponding to each feature is generated. The final trained model will contain coefficients for all time and frequency features, thus achieving the two-domain fusion.

In this paper, the quasi-Newton method is adopted for better convergence speed of the training. The neural network is a feed-forward back propagation ANN with 12 input points, 30 nodes in single hidden layer, and 2 output nodes. All 12 inputs of the network are the features extracted from the time domain and the frequency domain. The major superiorities of this type of network are as follows: (1) it is robust. Error in one input does little damage to the other inputs. (2) It can be proved mathematically that a three-layer network can approximate any continuous nonlinear relationship with arbitrary precision. (3) It has a strong self-adaptive learning ability and outputs adaptive learning contents to the weights of networks [8, 20]. In order to verify the training results, the data are randomly divided into 70%, 15%, and 15%, used for training, verification, and testing of the neural network, respectively. The structure of ANN is shown in Figure 10, where x_1 to x_n are the spatial and frequency features listed in Tables 1 and 2.

In addition, the number of hidden layer nodes of the neural network is quantitatively analyzed to study the effectiveness after the number of hidden layer neurons has been increased. The results show that there is very little increase in accuracy when there are more than 30 hidden layer nodes. Furthermore, for the accuracy to increase by 0.01 mmHg, the training time goes up an order of magnitude by a network with a hidden layer of 50 neurons. Thus, we have chosen to use the aforementioned parameters for the ANN.

4. Experiment Results

A total of 30 volunteers have participated in the experiment, and a total of 1231 pulse wave data were measured. In order to improve the accuracy and stability of blood pressure estimation, we collected the pulse waves in a single cycle. Besides, we built a threshold matrix to prevent any parameters, such as period and amplitude, exceeding the threshold range, upon which the data are considered abnormal and discarded. The training and fitting results of BP are shown in Figure 11.

The training automatically stopped after the about 200 iterations when the verification error became minimal. The total errors were within ±2 mmHg according to the error histogram (Figure 11(d)). In order to verify the performance of the model, we used the 15% data previously put aside and tested it. It is found that the output and target values show a highly linear correlation.

In addition, we also compared our model results with that of the traditional single-domain model. The performance of the single-domain model is inferior to that of our two-domain model. As shown in Figure 12, the error is ±3 mmHg and ±9 mmHg in the time domain and the frequency domain, respectively.

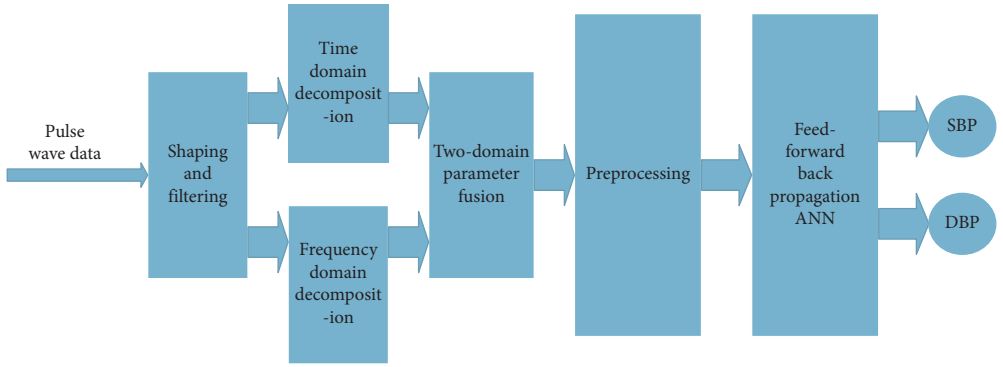

Figure 9: System structure.

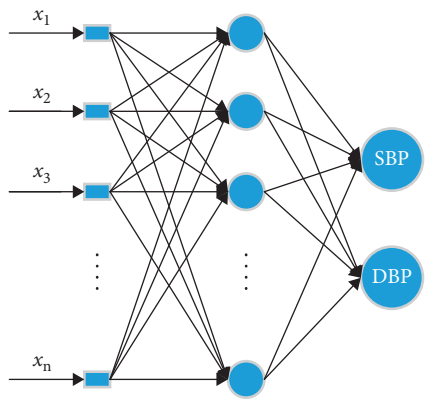

Figure 10: Structure of ANN.

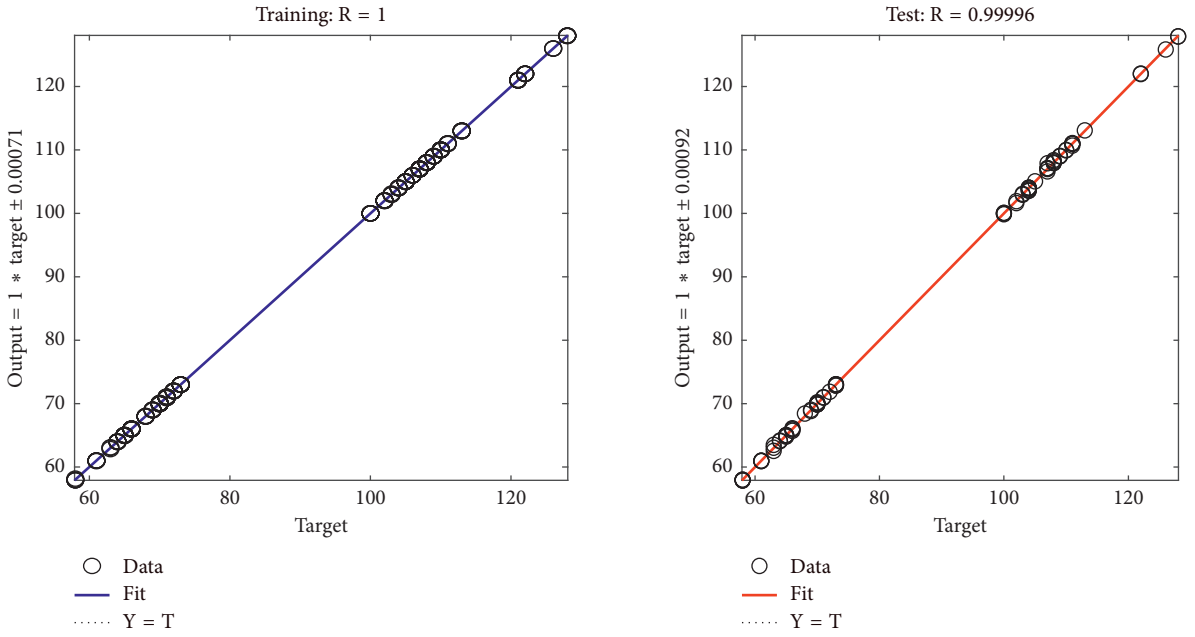

(a) (b)

Figure 11: Continued.

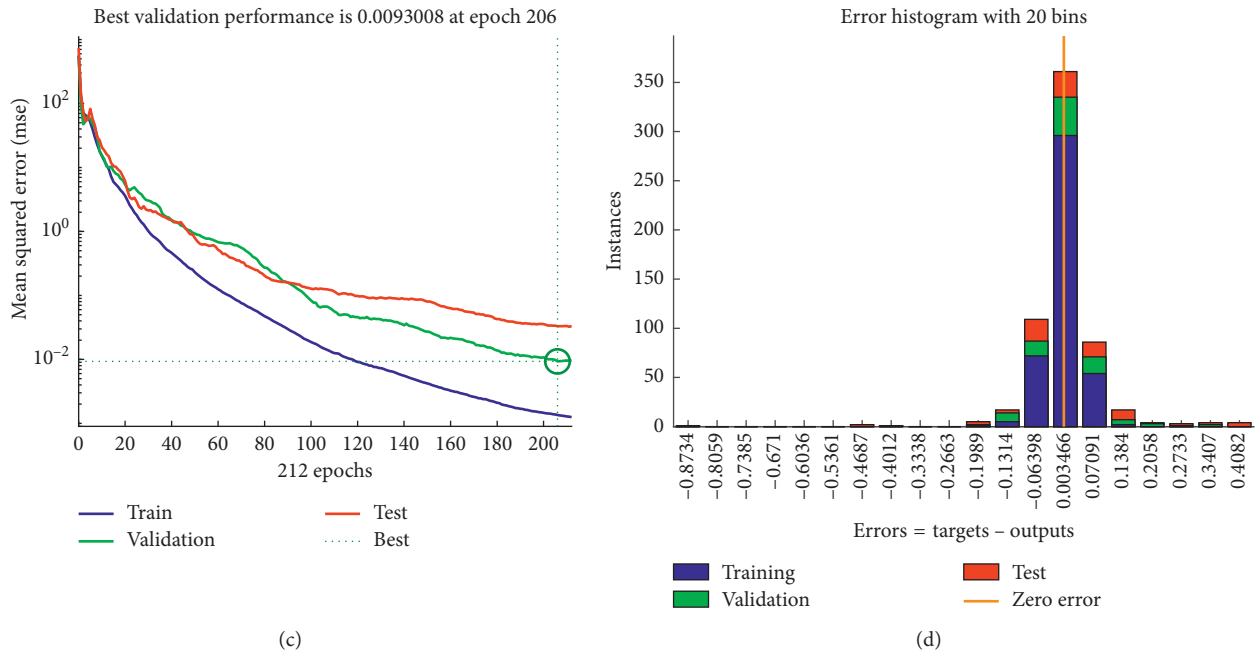

Figure 11: Two-domain model result. (a) Training error. (b) Testing error. (c) Iterations of ANN. (d) Two-domain error.

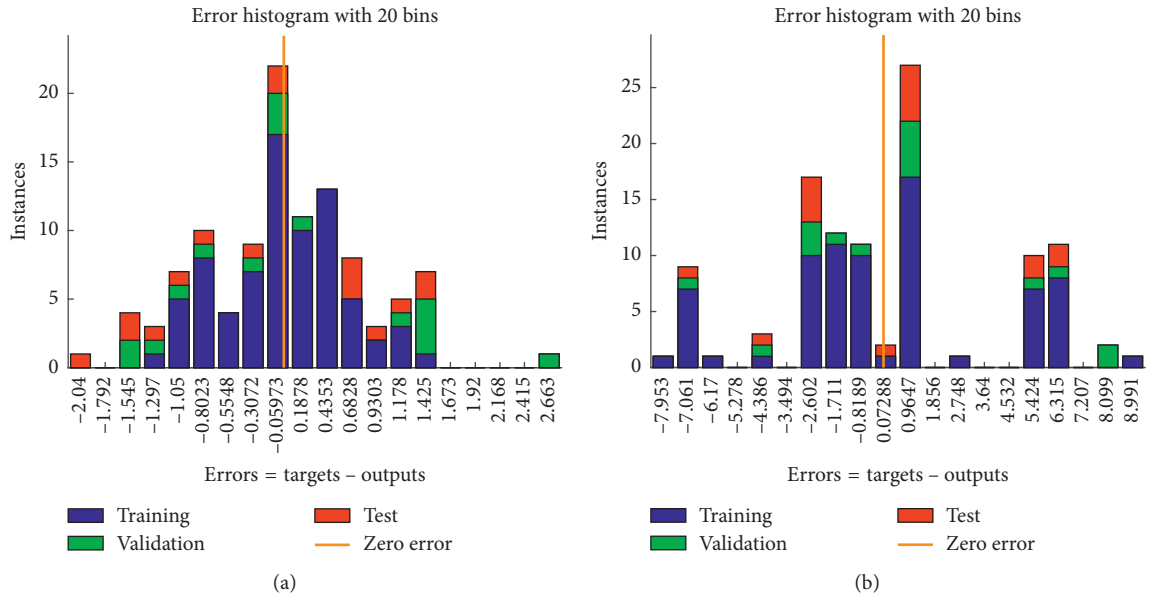

Figure 12: Errors of single-domain model. (a) Error of time domain. (b) Error of frequency.

5. Discussion and Conclusion

Experiments show that piezoresistive sensors can very well detect the features of the pulse wave under complex factors such as arrhythmia and are superior to PPG. There exists an optimal restraint pressure for the piezoresistive sensor, and it can be related back to the BMI for different people.

Considering the fact that the time domain model is unstable when measuring pulse wave data but has a high-accuracy contribution to BP and that the frequency domain model is stable in decomposing pulse waves, the two-domain model proposed in this paper not only retains the high accuracy of the time domain model but also integrates the stability of the frequency domain model. Experiments on the time and frequency domains and two domains combined were done and compared. The results show that the continuous blood pressure estimation based on the two-domain model can give BP with higher accuracy and stability than a single-domain model does.

There are limitations to this study, however. For example, the training and testing sample size is still small and not diverse enough. Subjects were not divided into training

and testing groups, i.e., data from all subjects were mixed together and then divided for training and testing, which could introduce internal correlation. In addition, the features we choose to extract and use may not be the best to represent the underlying mechanisms of BP, and the number of features may not be the best. In the future, we will continue to optimize the feature selection in both the time and frequency domains and plan to enlarge the sample space and amend the method of data splitting for a more rigid evaluation study.

Data Availability

The datasets generated and analyzed during the current study are available from the corresponding author upon reasonable request, without breaching participant confidentiality.

Conflicts of Interest

The authors declare that they have no conflicts of interest regarding the publication of this manuscript.

Acknowledgments

This study was supported in part by Grant 11805263 from NSFC, Grant 2018K058B from Jiangsu Post-Doctoral Funds, and the 5th 333 Project of Jiangsu Province of China.

References

[1] M. H. Forouzanfar, P. Liu, G. A. Roth et al., "Global burden of hypertension and systolic blood pressure of at least 110 to 115 mmHg," *JAMA*, vol. 317, no. 2, pp. 165–182, 2017.

[2] S. Lewington, R. Clarke, N. Qizilbash, R. Peto, R. Collins, and Prospective Studies Collaboration, "Age-specific relevance of usual blood pressure to vascular mortality: a meta-analysis of individual data for one million adults in 61 prospective studies," *Lancet*, vol. 360, no. 9349, pp. 1903–1913, 2002.

[3] R. Agarwal, J. E. Bills, T. J. W. Hecht, and R. P. Light, "Role of home blood pressure monitoring in overcoming therapeutic inertia and improving hypertension control: a systematic review and meta-analysis," *Hypertension*, vol. 57, no. 1, pp. 29–38, 2011.

[4] L. A. Geddes, M. H. Voelz, C. F. Babbs, J. D. Bourland, and W. A. Tacker, "Pulse transit time as an indicatoro of arterial blood pressure," *Psychophysiology*, vol. 18, no. 1, pp. 71–74, 1981.

[5] Y. Choi, Q. Zhang, and S. Ko, "Noninvasive cuffless blood pressure estimation using pulse transit time and Hilbert-Huang transform," *Computers and Electrical Engineering*, vol. 39, no. 1, pp. 103–111, 2013.

[6] C. M. Wu, C. Y. Chuang, Y. J. Chen, and S. C. Chen, "A new estimate technology of non-invasive continuous blood pressure measurement based on electrocardiograph," *Advances in Mechanical Engineering*, vol. 8, no. 6, article 168781401665368, 2016.

[7] M. F. O'Rourke, "Time domain analysis of the arterial pulse in clinical medicine," *Medical and Biological Engineering and Computing*, vol. 47, no. 2, pp. 119–129, 2009.

[8] Z. Xu, J. Liu, X. Chen, Y. Wang, and Z. Zhao, "Continuous blood pressure estimation based on multiple parameters from eletrocardiogram and photoplethysmogram by Back-propagation neural network," *Computers in Industry*, vol. 89, no. 5, pp. 50–59, 2017.

[9] N. Luo, W. Dai, C. Li et al., "Flexible piezoresistive sensor patch enabling ultralow power cuffless blood pressure measurement," *Advanced Functional Materials*, vol. 26, no. 8, pp. 1178–1187, 2016.

[10] J. Li, "Pulse wave analysis under different pressure," Master's thesis, Yanshan University, Qinhuangdao, China, 2015.

[11] M. C. Baruch, D. E. R. Warburton, S. S. D. Bredin, A. Cote, D. W. Gerdt, and C. M. Adkins, "Pulse decomposition analysis of the digital arterial pulse during hemorrhage simulation," *Nonlinear Biomedical Physics*, vol. 5, no. 1, p. 1, 2015.

[12] B. Zhou, "The obesity standard of Chinese people," *Popular medicine*, vol. 206, p. 7, 2002.

[13] S. C. Millasseau, F. G. Guigui, R. P. Kelly et al., "Noninvasive assessment of the digital volume pulse," *Hypertension*, vol. 36, no. 6, pp. 952–956, 2000.

[14] X. Xing and M. Sun, "Optical blood pressure estimation with photoplethysmography and FFT-based neural networks," *Biomedical Optics Express*, vol. 7, no. 8, pp. 3007–3020, 2016.

[15] Z. Yuan, X. Huang, and F. Fan, "Analysis of photoplethysmogram on different positions of 253 normal adults," *Journal Hunan College of Traditional Chinese Medicine*, vol. 20, no. 3, pp. 1–3, 2000.

[16] M. Elgendi, "On the analysis of fingertip photoplethysmogram signals," *Current Cardiology Reviews*, vol. 8, no. 1, pp. 14–25, 2012.

[17] M. Saito, M. Matsukawa, T. Asada, and Y. Watanabe, "Noninvasive assessment of arterial stiffness by pulse wave analysis," *IEEE Transactions on Ultrasonics, Ferroelectrics, and Frequency Control*, vol. 59, no. 11, pp. 2411–2419, 2012.

[18] P. Shi, S. Hu, Y. Zhu, J. Zheng, Y. Qiu, and P. Y. S. Cheang, "Insight into the dicrotic notch in photoplethysmographic pulses from the finger tip of young adults," *Journal of Medical Engineering & Technology*, vol. 33, no. 8, pp. 628–633, 2009.

[19] H. Lax, A. W. Feinberg, and B. M. Cohen, "Studies of the arterial pulse wave," *Journal of Chronic Diseases*, vol. 3, no. 6, pp. 618–631, 1956.

[20] S. C. Gao, P. Wittek, L. Zhao, and W. J. Jiang, "Data-driven estimation of blood pressure using the photoplethysmographic signals," in *Proceedings of 2016 38th Annual International Conference of the IEEE Engineering in Medicine and Biology Society (EMBC)*, Orlando, FL, USA, August 2016.

Hindawi
Computational and Mathematical Methods in Medicine
Volume 2018, Article ID 7325938, 9 pages
https://doi.org/10.1155/2018/7325938

Research Article

Some Similarity Measures of Neutrosophic Sets Based on the Euclidean Distance and Their Application in Medical Diagnosis

Donghai Liu,[1] **Guangyan Liu**,[1] **and Zaiming Liu**[2]

[1]*Department of Mathematics, Hunan University of Science and Technology, Xiangtan, Hunan 411201, China*
[2]*Department of Mathematics, Central South University, Changsha, Hunan 410075, China*

Correspondence should be addressed to Donghai Liu; donghailiu@126.com

Received 6 July 2018; Revised 25 September 2018; Accepted 23 October 2018; Published 28 November 2018

Guest Editor: Tomas Krilavičius

Similarity measure is an important tool in multiple criteria decision-making problems, which can be used to measure the difference between the alternatives. In this paper, some new similarity measures of single-valued neutrosophic sets (SVNSs) and interval-valued neutrosophic sets (IVNSs) are defined based on the Euclidean distance measure, respectively, and the proposed similarity measures satisfy the axiom of the similarity measure. Furthermore, we apply the proposed similarity measures to medical diagnosis decision problem; the numerical example is used to illustrate the feasibility and effectiveness of the proposed similarity measures of SVNSs and IVNSs, which are then compared to other existing similarity measures.

1. Introduction

The concept of fuzzy set (FS) $A = \{\langle x_i, u_A(x_i)\rangle | x_i \in X\}$ in $X = \{x_1, x_2, \ldots, x_n\}$ was proposed by Zadeh [1], where the membership degree $u_A(x_i)$ is a single value between zero and one. The FS has been widely applied in many fields, such as medical diagnosis, image processing, supply decision-making [2–4], and so on. In some uncertain decision-making problems, the degree of membership is assumed not exactly as a numerical value but as an interval. Hence, Zadeh [5] proposed the interval-valued fuzzy set (IVFS). However, the FS and IVFS only have the membership degree, and they cannot describe the nonmembership degree of the element belonging to the set. For example, in the national entrance examination for postgraduate, a panel of ten professors evaluated the admission of a student; five professors considered the student can be accepted, three professors disapproved of his or her admission, and two professors remained neutral. In this case, the FS and IVFS cannot represent such information. In order to solve this problem, Atanassov et al. [6] proposed the intuitionistic fuzzy set (IFS) $E = \{\langle x_i, u_E(x_i), v_E(x_i)\rangle | x_i \in X\}$, where $u_E(x_i)(0 \le u_E(x_i) \le 1)$ and $v_E(x_i)(0 \le v_E(x_i) \le 1)$ represent the membership degree and nonmembership degree, respectively, and the indeterminacy-membership degree $\pi_E(x_i) = 1 - u_E(x_i) - v_E(x_i)$. The IFS is more effective to deal with the vague information than the FS and IVFS. Then, the information about the admission of the student can be represented as an IFS $E = 0.5,\ 0.3,\ 0.2$, where $0.5, 0.3,$ and 0.2 stand for the membership degree, nonmembership degree, and indeterminacy-membership degree, respectively. However, the IFS also have limitation in expressing the decision information. For example, three groups of experts evaluate the benefits of the stock, a group of experts thinks the possibility of the stock that will be profitable is 0.6, the second group of experts thinks the possibility of loss is 0.3, the third group of experts is not sure whether the stock that will be profitable is 0.4. In this case, the IFS cannot express such information because $0.6 + 0.3 + 0.4 > 1$. Therefore, Wang et al. [7] proposed a single-valued neutrosophic set (SVNS) $N = \{\langle x_i, T_N(x_i), I_N(x_i), F_N(x_i)\rangle | x_i \in X\}$, where $T_N(x_i), I_N(x_i)$ and $F_N(x_i)$ represent the degree of the truth-membership, indeterminacy-membership, and falsity-membership, respectively, and they belong to $[0, 1]$. So, the information about the benefits of the stock can be represented as $N = 0.6,\ 0.4,\ 0.3$. However, due to the uncertainty of the decision-making environment in multiple criteria decision-making problems, the single numerical value

cannot meet the needs of evaluating information. Then, Wang [8] defined the interval-valued neutrosophic set (IVNS) based on the SVNS, which used the interval to describe truth membership degree, indeterminacy membership degree, and falsity membership degree, respectively. Since the neutrosophic set was proposed, there have been some researchers focusing on this subject [9–12].

On the other hand, similarity measure is an important tool in multiple criteria decision-making problems, which can be used to measure the difference between the alternatives. Many studies about the similarity measure are obtained. For example, Beg et al. [13] proposed a similarity measure of FSs based on the concept of ϵ – fuzzy transitivity and discussed the degree of transitivity of different similarity measures. Song et al. [14] considered the similarity measure of IFSs and proposed corresponding distance measure between intuitionistic fuzzy belief functions. Majumdar and Samanta [15] proposed a similarity measure between SVNSs based on the membership degree.

In addition, cosine similarity measure is also an important similarity measure, and it can be defined as the inner product of two vectors divided by the product of their lengths. There are some scholars who study the cosine similarity measures [16–21]. For example, Ye [16] proposed the cosine similarity measure and weighted cosine similarity measure of IVFSs with risk preference, and they were applied to the supplier selection problem. Then, Ye [17] proposed the cosine similarity measure of IFSs and applied it to medical diagnosis and pattern recognition. Furthermore, Ye [18] defined the cosine similarity measure of SVNSs and IVNSs, but when the SVNSs $N_1 \neq N_2$, $\cos(N_1, N_2) = 1$ (the example can be seen in Section 3). Furthermore, Ye [19] proposed the improved cosine similarity measures of SVNSs and IVNSs based on cosine function.

In this paper, we propose a new method to construct the similarity measures of SVNSs, which is based on the existing similarity measure proposed by Majumdar and Samanta [15] and Ye [18], respectively. They play an important role in practical application, especially in pattern recognition, medical diagnosis, and so on. Furthermore, we will propose the corresponding similarity measures of IVNSs.

The rest of the paper is organized as follows. In Section 2, the basic definition and some properties about SVNS and IVNS are given. In Section 3, we proposed a method to construct the new similarity measures of SVNSs and IVNSs, respectively. In Section 4, we apply the proposed new similarity measures to medical diagnosis problems, the numerical examples are used to illustrate the feasibility and effectiveness of the proposed similarity measures, which are then compared to other existing similarity measures. Finally, the conclusions and future studies are discussed in Section 5.

2. Preliminaries

In this section, we give some basic knowledge about the SVNS and the IVNS. Some existing distance measures are also introduced, which will be used in the next section.

2.1. SVNS

Definition 1. Given a fixed set $X = \{x_1, x_2, \ldots, x_n\}$ [7], the SVNS N in X is defined as follows:

$$N = \left\{\langle x_i, T_N(x_i), I_N(x_i), F_N(x_i)\rangle \middle| x_i \in X\right\}, \quad (1)$$

where the function $T_N(x_i) : X \longrightarrow [0,1]$ defines the truth-membership degree, the function $I_N(x_i) : X \longrightarrow [0,1]$ defines indeterminacy-membership degree, and the function $F_N(x_i) : X \longrightarrow [0,1]$ defines the falsity-membership degree, respectively. For any SVNS N, it holds that $0 \leq T_N(x_i) + I_N(x_i) + F_N(x_i) \leq 3 \ (\forall x_i \in X)$.

For any two SVNSs $N_1 = \{\langle x_i, T_{N_1}(x_i), I_{N_1}(x_i), F_{N_1}(x_i)\rangle | x_i \in X\}$ and $N_2 = \{\langle x_i, T_{N_2}(x_i), I_{N_2}(x_i), F_{N_2}(x_i)\rangle | x_i \in X\}$, the following properties are satisfied:

(1) $N_1 \subseteq N_2$ if and only if $T_{N_1}(x_i) \leq T_{N_2}(x_i)$, $I_{N_1}(x_i) \geq I_{N_2}(x_i)$, and $F_{N_1}(x_i) \geq F_{N_2}(x_i)$

(2) $N_1 = N_2$ if and only if $N_1 \subseteq N_2$ and $N_2 \subseteq N_1$

2.2. IVNS

Definition 2. Given a fixed set $X = \{x_1, x_2, \ldots, x_n\}$ [8], the IVNS N' on X is defined as follows:

$$N' = \left\{\left\langle x_i, \left[T^L_{N'}(x_i), T^U_{N'}(x_i)\right], \left[I^L_{N'}(x_i), I^U_{N'}(x_i)\right], \left[F^L_{N'}(x_i), F^U_{N'}(x_i)\right]\right\rangle \middle| x_i \in X\right\}, \quad (2)$$

where $T_{N'}(x_i) = [T^L_{N'}(x_i), T^U_{N'}(x_i)]$, $I_{N'}(x_i) = [I^L_{N'}(x_i), I^U_{N'}(x_i)]$, and $F_{N'}(x_i) = [F^L_{N'}(x_i), F^U_{N'}(x_i)]$ represent the truth-membership function, the indeterminacy-membership function, and the falsity-membership function, respectively. For any $x_i \in X$, it holds that $T_{N'}(x_i), I_{N'}(x_i), F_{N'}(x_i) \subseteq [0,1]$ and $0 \leq T^U_{N'}(x_i) + I^U_{N'}(x_i) + F^U_{N'}(x_i) \leq 3$.

For any two IVNSs $N'_1 = \{\langle x_i, [T^L_{N'_1}(x_i), T^U_{N'_1}(x_i)], [I^L_{N'_1}(x_i), I^U_{N'_1}(x_i)], [F^L_{N'_1}(x_i), F^U_{N'_1}(x_i)]\rangle | x_i \in X\}$ and $N'_2 = \{\langle x_i, [T^L_{N'_2}(x_i), T^U_{N'_2}(x_i)], [I^L_{N'_2}(x_i), I^U_{N'_2}(x_i)], [F^L_{N'_2}(x_i), F^U_{N'_2}(x_i)]\rangle | x_i \in X\}$, the following properties are satisfied:

(1) $N'_1 \subseteq N'_2$ if and only if $T^L_{N'_1}(x_i) \leq T^L_{N'_2}(x_i), T^U_{N'_1}(x_i) \leq T^U_{N'_2}(x_i), I^L_{N'_1}(x_i) \geq I^L_{N'_2}(x_i), I^U_{N'_1}(x_i) \geq I^U_{N'_2}(x_i), F^L_{N'_1}(x_i) \geq F^L_{N'_2}(x_i)$, and $F^U_{N'_1}(x_i) \geq F^U_{N'_2}(x_i)$

(2) $N'_1 = N'_2$ if and only if $N'_1 \subseteq N'_2$ and $N'_2 \subseteq N'_1$

Remark 1. When $T^L_{N'_1}(x_i) = T^U_{N'_1}(x_i), I^L_{N'_1}(x_i) = I^U_{N'_1}(x_i), F^L_{N'_1}(x_i) = F^U_{N'_1}(x_i)$, the IVNS N'_1 is reduced to the SVNS N_1.

2.3. Existing Distance Measures between SVNSs and IVNSs

Definition 3. Let $N_1 = \{\langle x_i, T_{N_1}(x_i), I_{N_1}(x_i), F_{N_1}(x_i)\rangle | x_i \in X\}$ and $N_2 = \{\langle x_i, T_{N_2}(x_i), I_{N_2}(x_i), F_{N_2}(x_i)\rangle | x_i \in X\}$ be any two SVNSs in $X = \{x_1, x_2, \ldots, x_n\}$ [15]; then, the Euclidean distance between SVNSs N_1 and N_2 is defined as follows:

$$D_{\mathrm{SVNS}}(N_1, N_2) = \sqrt{\frac{\sum_{i=1}^{n}\left[\left(T_{N_1}(x_i) - T_{N_2}(x_i)\right)^2 + \left(I_{N_1}(x_i) - I_{N_2}(x_i)\right)^2 + \left(F_{N_1}(x_i) - F_{N_2}(x_i)\right)^2\right]}{3n}}. \tag{3}$$

Definition 4. Let $N_1' = \{\langle x_i, [T^L_{N_1'}(x_i), T^U_{N_1'}(x_i)], [I^L_{N_1'}(x_i), I^U_{N_1'}(x_i)], [F^L_{N_1'}(x_i), F^U_{N_1'}(x_i)]\rangle | x_i \in X\}$ and $N_2' = \{\langle x_i, [T^L_{N_2'}(x_i), T^U_{N_2'}(x_i)], [I^L_{N_2'}(x_i), I^U_{N_2'}(x_i)], [F^L_{N_2'}(x_i), F^U_{N_2'}(x_i)]\rangle | x_i \in X\}$ be any two IVNSs in $X = \{x_1, x_2, \ldots, x_n\}$ [22]; the Euclidean distance between IVNSs N_1' and N_2' is defined as follows:

$$D_{\mathrm{IVNS}}(N_1', N_2') = \sqrt{\frac{\sum_{i=1}^{n}\left[\left(T^L_{N_1'}(x_i) - T^L_{N_2'}(x_i)\right)^2 + \left(T^U_{N_1'}(x_i) - T^U_{N_2'}(x_i)\right)^2 + \left(I^L_{N_1'}(x_i) - I^L_{N_2'}(x_i)\right)^2 + \left(I^U_{N_1'}(x_i) - I^U_{N_2'}(x_i)\right)^2 + \left(F^L_{N_1'}(x_i) - F^L_{N_2'}(x_i)\right)^2 + \left(F^U_{N_1'}(x_i) - F^U_{N_2'}(x_i)\right)^2\right]}{6n}}. \tag{4}$$

Next, we propose a new method to construct the similarity measures of SVNSs and IVNSs based on the Euclidean distance measure.

3. Several New Similarity Measures

The similarity measure is a most widely used tool to evaluate the relationship between two sets. The following axiom about the similarity measure of SVNSs (or IVNSs) should be satisfied:

Lemma 1. *Let $X = \{x_1, x_2, \ldots, x_n\}$ be the universal set [18] if the similarity measure $S(N_1, N_2)$ between SVNSs (or IVNSs) N_1 and N_2 satisfies the following properties:*

(1) $0 \le S(N_1, N_2) \le 1$

(2) $S(N_1, N_2) = 1$ if and only if $N_1 = N_2$

(3) $S(N_1, N_2) = S(N_2, N_1)$.

Then, the similarity measure $S(N_1, N_2)$ is a genuine similarity measure.

3.1. The New Similarity Measures between SVNSs. To introduce the new similarity measure between SVNSs, we first review the similarity measure $S_{1\mathrm{SVNS}}$ between N_1 and N_2 defined by Majumdar et al. [15], which is given as follows:

Definition 5. Let $X = \{x_1, x_2, \ldots, x_n\}$ be a universal set [15], for any two SVNSs $N_1 = \{\langle x_i, T_{N_1}(x_i), I_{N_1}(x_i), F_{N_1}(x_i)\rangle | x_i \in X\}$ and $N_2 = \{\langle x_i, T_{N_2}(x_i), I_{N_2}(x_i), F_{N_2}(x_i)\rangle | x_i \in X\}$; the similarity measure of SVNSs between N_1 and N_2 is defined as follows:

$$S_{1\mathrm{SVNS}}(N_1, N_2) = \frac{\sum_{i=1}^{n}\left(\min\left(T_{N_1}(x_i), T_{N_2}(x_i)\right) + \min\left(I_{N_1}(x_i), I_{N_2}(x_i)\right) + \min\left(F_{N_1}(x_i), F_{N_2}(x_i)\right)\right)}{\sum_{i=1}^{n}\left(\max\left(T_{N_1}(x_i), T_{N_2}(x_i)\right) + \max\left(I_{N_1}(x_i), I_{N_2}(x_i)\right) + \max\left(F_{N_1}(x_i), F_{N_2}(x_i)\right)\right)}. \tag{5}$$

It is already known that the similarity measure $S_{1\mathrm{SVNS}}$ defined by Majumdar et al. [15] satisfies the properties in Lemma 1. It is proposed based on the membership degree; in this section, we adopt the various methods for calculating the similarity measure between neutrosophic sets.

Firstly, we propose a new method to construct a new similarity measure of SVNSs, which is based on the similarity measure proposed by Majumdar et al. [15] and the Euclidean distance; it can be defined as follows:

Definition 6. Let $X = \{x_1, x_2, \ldots, x_n\}$ be a universal set, for any two SVNSs $N_1 = \{x_i, T_{N_1}(x_i), I_{N_1}(x_i), F_{N_1}(x_i) | x_i \in X\}$ and $N_2 = \{x_i, T_{N_2}(x_i), I_{N_2}(x_i), F_{N_2}(x_i) | x_i \in X\}$; a new similarity measure $S^*_{1\mathrm{SVNS}}(N_1, N_2)$ is defined as follows:

$$S^*_{1\mathrm{SVNS}}(N_1, N_2) = \frac{1}{2}\left(S_{1\mathrm{SVNS}}(N_1, N_2) + 1 - D_{\mathrm{SVNS}}(N_1, N_2)\right). \tag{6}$$

The proposed similarity measure of SVNSs satisfies the following Theorem 1.

Theorem 1. *The similarity measure $S^*_{1SVNS}(N_1, N_2)$ between $N_1 = \{\langle x_i, T_{N_1}(x_i), I_{N_1}(x_i), F_{N_1}(x_i)\rangle | x_i \in X\}$ and $N_2 = \{\langle x_i, T_{N_2}(x_i), I_{N_2}(x_i), F_{N_2}(x_i)\rangle | x_i \in X\}$ satisfies the following properties:*

(1) $0 \le S^*_{1\mathrm{SVNS}}(N_1, N_2) \le 1$

(2) $S^*_{1\mathrm{SVNS}}(N_1, N_2) = 1$ if and only if $N_1 = N_2$

(3) $S^*_{1\mathrm{SVNS}}(N_1, N_2) = S^*_{1\mathrm{SVNS}}(N_2, N_1)$

Proof.

(1) Because $D_{\mathrm{SVNS}}(N_1, N_2)$ is an Euclidean distance measure, obviously, $0 \le D_{\mathrm{SVNS}}(N_1, N_2) \le 1$. Furthermore, according to Proposition 4.2.2 by Majumdar et al. [15], we know $0 \le S_{1\mathrm{SVNS}}(N_1, N_2) \le 1$. Then, $0 \le 1/2\,(S_{1\mathrm{SVNS}}(N_1, N_2) + 1 - D_{\mathrm{SVNS}}(N_1, N_2)) \le 1$, i.e., $0 \le S^*_{1\mathrm{SVNS}}(N_1, N_2) \le 1$.

(2) If $S^*_{1\mathrm{SVNS}}(N_1, N_2) = 1$, we have $S_{1\mathrm{SVNS}}(N_1, N_2) + 1 - D_{\mathrm{SVNS}}(N_1, N_2) = 2$, that is, $S_{1\mathrm{SVNS}}(N_1, N_2) = 1 + D_{\mathrm{SVNS}}(N_1, N_2)$. Because $D_{\mathrm{SVNS}}(N_1, N_2)$ is the Euclidean distance measure, $0 \le D_{\mathrm{SVNS}}(N_1, N_2) \le 1$. Furthermore, $0 \le S_{1\mathrm{SVNS}}(N_1, N_2) \le 1$ is obtained in Proposition 4.2.2 [15], then $S_{1\mathrm{SVNS}}(N_1, N_2) = 1$ and $D_{\mathrm{SVNS}}(N_1, N_2) = 0$ should be established at the same time. If the Euclidean distance measure $D_{\mathrm{SVNS}}(N_1, N_2) = 0$, $N_1 = N_2$ is obvious. According to Proposition 4.2.2 by Majumdar et al. [15], when $S_{1\mathrm{SVNS}}(N_1, N_2) = 1$, $N_1 = N_2$; so, if $S^*_{1\mathrm{SVNS}}(N_1, N_2) = 1$, $N_1 = N_2$ is obtained.

On the other hand, when $N_1 = N_2$, according to formulae (3) and (5) $D_{\mathrm{SVNS}}(N_1, N_2) = 0$ and $S_{1\mathrm{SVNS}}(N_1, N_2) = 1$ are obtained respectively. Furthermore, we can get $S^*_{1\mathrm{SVNS}}(N_1, N_2) = 1$.

(3) $S^*_{1\mathrm{SVNS}}(N_1, N_2) = S^*_{1\mathrm{SVNS}}(N_2, N_1)$ is straightforward.

From Theorem 1, we know the proposed new similarity measure $S^*_{1\mathrm{SVNS}}(N_1, N_2)$ is a genuine similarity measure.

On the other hand, cosine similarity measure is also an important similarity measure. In 2014, Ye [18] proposed a cosine similarity measure between SVNSs as follows: □

Definition 7. Let $\mathrm{X} = \{x_1, x_2, \ldots, x_n\}$ be a universal set [18], for any two SVNSs $N_1 = \{\langle x_i, T_{N_1}(x_i), I_{N_1}(x_i), F_{N_1}(x_i)\rangle | x_i \in X\}$ and $N_2 = \{\langle x_i, T_{N_2}(x_i), I_{N_2}(x_i), F_{N_2}(x_i)\rangle | x_i \in X\}$, the cosine similarity measure between N_1 and N_2 is defined as follows:

$$S_{2\mathrm{SVNS}}(N_1, N_2) = \frac{1}{n}\sum_{i=1}^{n} \frac{T_{N_1}(x_i)T_{N_2}(x_i) + I_{N_1}(x_i)I_{N_2}(x_i) + F_{N_1}(x_i)F_{N_2}(x_i)}{\sqrt{T^2_{N_1}(x_i) + I^2_{N_1}(x_i) + F^2_{N_1}(x_i)}\sqrt{T^2_{N_2}(x_i) + I^2_{N_2}(x_i) + F^2_{N_2}(x_i)}}. \tag{7}$$

From Example 1, we know the cosine similarity measure defined by Ye [18] does not satisfy Lemma 1.

Example 1. For two SVNSs $N_1 = x$, 0.4, 0.2, 0.6 and $N_2 = x$, 0.2, 0.1, 0.3, we can easily know $N_1 \neq N_2$. But using formula (7) to calculate the cosine similarity measure $S_{2\mathrm{SVNS}}(N_1, N_2)$, we have $S_{2\mathrm{SVNS}}(N_1, N_2) = 1$. That is to say, when $N_1 \neq N_2$, $S_{2\mathrm{SVNS}}(N_1, N_2) = 1$, which means the cosine similarity measure $S_{2\mathrm{SVNS}}(N_1, N_2)$ defined by Ye [18] does not satisfy the necessary condition of property 2 in Lemma 1; thus, it is not a genuine similarity measure. Furthermore, Ye [19] proposed the improved cosine similarity measures of SVNS based on the cosine similarity measure proposed by Ye [18], which overcomes its shortcoming.

In this paper, we go on proposing another new similarity measure of SVNSs based on the cosine similarity measure proposed by Ye [18] and the Euclidean distance D_{SVNS}. It considers the similarity measure not only from the point of view of algebra but also from the point of view of geometry, which can be defined as:

Definition 8. Let $X = \{x_1, x_2, \ldots, x_n\}$ be a universal set, for any two SVNSs $N_1 = \{\langle x_i, T_{N_1}(x_i), I_{N_1}(x_i), F_{N_1}(x_i)\rangle | x_i \in X\}$ and $N_2 = \{\langle x_i, T_{N_2}(x_i), I_{N_2}(x_i), F_{N_2}(x_i)\rangle | x_i \in X\}$; a new similarity measure $S^*_{2\mathrm{SVNS}}(N_1, N_2)$ is defined as follows:

$$S^*_{2\mathrm{SVNS}}(N_1, N_2) = \frac{1}{2}\left(S_{2\mathrm{SVNS}}(N_1, N_2) + 1 - D_{\mathrm{SVNS}}(N_1, N_2)\right). \tag{8}$$

Remark 2. Using formula (8) to calculate Example 1 again, for two SVNSs $N_1 = x$, 0.4, 0.2, 0.6 and $N_2 = x$, 0.2, 0.1, 0.3, we have $S^*_{2\mathrm{SVNS}}(N_1, N_2) = 0.8920$. We can see that the proposed new similarity measure $S^*_{2\mathrm{SVNS}}(N_1, N_2)$ overcomes the shortcoming of cosine similarity measure $S_{2\mathrm{SVNS}}(N_1, N_2)$ defined by Ye [18].

Theorem 2. *The similarity measure $S^*_{2\mathrm{SVNS}}(N_1, N_2)$ between $N_1 = \{\langle x_i, T_{N_1}(x_i), I_{N_1}(x_i), F_{N_1}(x_i)\rangle | x_i \in X\}$ and $N_2 = \{\langle x_i, T_{N_2}(x_i), I_{N_2}(x_i), F_{N_2}(x_i)\rangle | x_i \in X\}$ satisfies the following properties:*

(1) $0 \le S^*_{2\mathrm{SVNS}}(N_1, N_2) \le 1$

(2) $S^*_{2\mathrm{SVNS}}(N_1, N_2) = 1$ if and only if $N_1 = N_2$

(3) $S^*_{2\mathrm{SVNS}}(N_1, N_2) = S^*_{2\mathrm{SVNS}}(N_2, N_1)$

Proof. The proof of the properties (1) and (3) are similar to Theorem 1; here, we only give the proof of property (2).

If $S^*_{2\mathrm{SVNS}}(N_1, N_2) = 1$, we have $S_{2\mathrm{SVNS}}(N_1, N_2) + 1 - D_{\mathrm{SVNS}}(N_1, N_2) = 2$, i.e., $S_{2\mathrm{SVNS}}(N_1, N_2) = 1 + D_{\mathrm{SVNS}}(N_1, N_2)$. Because $D_{\mathrm{SVNS}}(N_1, N_2)$ is the Euclidean distance measure, $0 \le D_{\mathrm{SVNS}}(N_1, N_2) \le 1$. According to the property of $S_{2\mathrm{SVNS}}(N_1, N_2)$ in Ye [18], $0 \le S_{2\mathrm{SVNS}}(N_1, N_2) \le 1$; then, $S_{2\mathrm{SVNS}}(N_1, N_2) = 1$ and $D_{\mathrm{SVNS}}(N_1, N_2) = 0$ should be held at the same time. When $S_{2\mathrm{SVNS}}(N_1, N_2) = 1$, we have $T_{N_1}(x_i) = k \cdot T_{N_2}(x_i)$, $I_{N_1}(x_i) = k \cdot I_{N_2}(x_i)$, and $F_{N_1}(x_i) = k \cdot F_{N_2}(x_i)$ (k is a constant). When $D_{\mathrm{SVNS}}(N_1, N_2) = 0$, we have $N_1 = N_2$. Then $N_1 = N_2$ is obtained.

On the other hand, according to formulae (3) and (7), if $N_1 = N_2$, $D_{\mathrm{SVNS}}(N_1, N_2) = 0$ and $S_{2\mathrm{SVNS}}(N_1, N_2) = 1$ are obtained, respectively; then we can get $S^*_{2\mathrm{SVNS}}(N_1, N_2) = 1$.

Thus, $S^*_{2\mathrm{SVNS}}(N_1, N_2)$ satisfies all the properties in Theorem 2. □

3.2. Some New Similarity Measures between IVNSs. In some situations, it is difficult to provide the truth-membership degree, false-membership degree, and indeterminate-membership degree with a precise numerical value; Wang [8] used the interval numbers to express the related membership degrees. Furthermore, Broumi et al. [22] proposed the corresponding similarity measure of IVNSs based on the similarity measure S_{1SVNS} proposed by Majumdar et al. [15].

Definition 9. Let $X = \{x_1, x_2, \ldots, x_n\}$ be a universal set, for any two IVNSs $N_1' = \{\langle x_i, [T^L_{N_1'}(x_i), T^U_{N_1'}(x_i)], [I^L_{N_1'}(x_i), I^U_{N_1'}(x_i)], [F^L_{N_1'}(x_i), F^U_{N_1'}(x_i)]\rangle | x_i \in X\}$ and $N_2' = \{\langle x_i, [T^L_{N_2'}(x_i) T^U_{N_2'}(x_i)], [I^L_{N_2'}(x_i), I^U_{N_2'}(x_i)], [F^L_{N_2'}(x_i), F^U_{N_2'}(x_i)]\rangle | x_i \in X\}$ [22]; the similarity measure between IVNSs N_1' and N_2' is defined as follows:

$$S_{1IVNS}(N_1', N_2') = \frac{\sum_{i=1}^{n}\left\{\min\left(T^L_{N_1'}(x_i), T^L_{N_2'}(x_i)\right) + \min\left(T^U_{N_1'}(x_i), T^U_{N_2'}(x_i)\right) + \min\left(I^L_{N_1'}(x_i), I^L_{N_2'}(x_i)\right) + \min\left(I^U_{N_1'}(x_i), I^U_{N_2'}(x_i)\right) + \min\left(F^L_{N_1'}(x_i), F^L_{N_2'}(x_i)\right) + \min\left(F^U_{N_1'}(x_i), F^U_{N_2'}(x_i)\right)\right\}}{\sum_{i=1}^{n}\left\{\max\left(T^L_{N_1'}(x_i), T^L_{N_2'}(x_i)\right) + \max\left(T^U_{N_1'}(x_i), T^U_{N_2'}(x_i)\right) + \max\left(I^L_{N_1'}(x_i), I^L_{N_2'}(x_i)\right) + \max\left(I^U_{N_1'}(x_i), I^U_{N_2'}(x_i)\right) + \max\left(F^L_{N_1'}(x_i), F^L_{N_2'}(x_i)\right) + \max\left(F^U_{N_1'}(x_i), F^U_{N_2'}(x_i)\right)\right\}}. \tag{9}$$

Remark 3. If $T^L_{N_j'}(x_i) = T^U_{N_j'}(x_i), I^L_{N_j'}(x_i) = I^U_{N_j'}(x_i), F^L_{N_j'}(x_i) = F^U_{N_j'}(x_i)\,(j = 1, 2)$, then the similarity measure $S_{1IVNS}(N_1', N_2')$ is reduced to the similarity measure $S_{1SVNS}(N_1, N_2)$.

Similarly to Section 3.1, we propose a corresponding similarity measure between IVNSs, which is based on the similarity measure $S_{1IVNS}(N_1', N_2')$ and the Euclidean distance $D_{IVNS}(N_1', N_2')$ defined in Definition 4.

Definition 10. Let $X = \{x_1, x_2, \ldots, x_n\}$ be a universal set, for any two IVNSs $N_1' = \{x_i, [T^L_{N_1'}(x_i), T^U_{N_1'}(x_i)], [I^L_{N_1'}(x_i), I^U_{N_1'}(x_i)], [F^L_{N_1'}(x_i), F^U_{N_1'}(x_i)] | x_i \in X\}$ and $N_2' = \{x_i, [T^L_{N_2'}](x_i), T^U_{N_2'}(x_i)], [I^L_{N_2'}(x_i), I^U_{N_2'}(x_i)], [F^L_{N_2'}(x_i), F^U_{N_2'}(x_i)] | x_i \in X\}$; a new similarity measure $S^*_{1IVNS}(N_1', N_2')$ is defined as follows:

$$S^*_{1IVNS}(N_1', N_2') = \frac{1}{2}\left(S_{1IVNS}(N_1', N_2') + 1 - D_{IVNS}(N_1', N_2')\right). \tag{10}$$

The proposed similarity measure also satisfies Theorem 3.

Theorem 3. *The similarity measure $S^*_{1IVNS}(N_1', N_2')$ satisfies the following properties:*

(1) $0 \le S^*_{1IVNS}(N_1', N_2') \le 1$

(2) $S^*_{1IVNS}(N_1', N_2') = 1$ *if and only if* $N_1' = N_2'$

(3) $S^*_{1IVNS}(N_1', N_2') = S^*_{1IVNS}(N_2', N_1')$

Proof. The proof is similar to Theorem 1; hence, we omit it here.

Next, we will use the same method to define the similarity measure $S^*_{2IVNS}(N_1', N_2')$ between IVNS, which is based on the cosine similarity measure $S_{2IVNS}(N_1', N_2')$ proposed by Ye [21] (Definition 11) and the Euclidean distance $D_{IVNS}(N_1', N_2')$ defined in formula (4). □

Definition 11. Let $X = \{x_1, x_2, \ldots, x_n\}$ be a universal set, for any two IVNSs $N_1' = \{\langle x_i, [T^L_{N_1'}(x_i), T^U_{N_1'}(x_i)], [I^L_{N_1'}(x_i), I^U_{N_1'}(x_i)], [F^L_{N_1'}(x_i), F^U_{N_1'}(x_i)]\rangle | x_i \in X\}$ and $N_2' = \{\langle x_i, [T^L_{N_2'}(x_i), T^U_{N_2'}(x_i)], [I^L_{N_2'}(x_i), I^U_{N_2'}(x_i)], [F^L_{N_2'}(x_i), F^U_{N_2'}(x_i)]\rangle | x_i \in X\}$; the cosine similarity measure $S^*_{2IVNS}(N_1', N_2')$ is defined as follows [21]:

$$S_{2IVNS}(N_1', N_2') = \frac{1}{n}\sum_{i=1}^{n} \cdot \frac{T^L_{N_1'}(x_i)T^L_{N_2'}(x_i) + T^U_{N_1'}(x_i)T^U_{N_2'}(x_i) + I^L_{N_1'}(x_i)I^L_{N_2'}(x_i) + I^U_{N_1'}(x_i)I^U_{N_2'}(x_i) + F^L_{N_1'}(x_i)F^L_{N_2'}(x_i) + F^U_{N_1'}(x_i)F^U_{N_2'}(x_i)}{\sqrt{\left(T^L_{N_1'}(x_i)\right)^2 + \left(T^U_{N_1'}(x_i)\right)^2 + \left(I^L_{N_1'}(x_i)\right)^2 + \left(I^U_{N_1'}(x_i)\right)^2 + \left(F^L_{N_1'}(x_i)\right)^2 + \left(F^U_{N_1'}(x_i)\right)^2}\sqrt{\left(T^L_{N_2'}(x_i)\right)^2 + \left(T^U_{N_2'}(x_i)\right)^2 + \left(I^L_{N_2'}(x_i)\right)^2 + \left(I^U_{N_2'}(x_i)\right)^2 + \left(F^L_{N_2'}(x_i)\right)^2 + \left(F^U_{N_2'}(x_i)\right)^2}}. \tag{11}$$

Example 2. For two IVNSs $N_1' = x, [0.3, 0.4], [0.2, 0.3], [0.4, 0.5]$ and $N_2' = x, [0.6, 0.8], [0.4, 0.6], [0.8, 1]$, according to formula (11), we have $S_{2IVNS}(N_1', N_2') = 1$, but $N_1' \neq N_2'$. In this case, the necessary condition of (2) in Lemma 1 is not satisfied. Therefore, the cosine similarity measure $S_{2IVNS}(N_1', N_2')$ proposed by Ye [22] is not a genuine similarity measure. Motivated by this, we will propose a new similarity measure $S^*_{2IVNS}(N_1', N_2')$ based on $S_{2IVNS}(N_1', N_2')$ and the Euclidean distance measure $D_{IVNS}(N_1', N_2')$ as follows:

Definition 12. Let $X = \{x_1, x_2, \ldots, x_n\}$ be a universal set, for any two IVNSs $N_1' = \{\langle x_i, [T^L_{N_1'}(x_i), T^U_{N_1'}(x_i)], [I^L_{N_1'}(x_i), I^U_{N_1'}(x_i)], [F^L_{N_1'}(x_i), F^U_{N_1'}(x_i)]\rangle | x_i \in X\}$ and $N_2' = \{\langle x_i, [T^L_{N_2'}(x_i), T^U_{N_2'}(x_i)], [I^L_{N_2'}(x_i), I^U_{N_2'}(x_i)], [F^L_{N_2'}(x_i), F^U_{N_2'}(x_i)]\rangle | x_i \in X\}$;

a new similarity measure $S^*_{2\text{IVNS}}(N_1', N_2')$ can be defined as follows:

$$S^*_{2\text{IVNS}}(N_1', N_2') = \frac{1}{2}\left(S_{2\text{IVNS}}(N_1', N_2') + 1 - D_{\text{IVNS}}(N_1', N_2')\right). \tag{12}$$

Remark 4. In Example 2, when $N_1' \neq N_2'$, the similarity measure $S_{2\text{IVNS}}(N_1', N_2') = 1$, this is inconsistent with the real decision problems. But, using formula (12) to calculate it again, we have $S^*_{2\text{IVNS}}(N_1', N_2') = 0.8185$. Obviously, the proposed similarity measure $S^*_{2\text{IVNS}}(N_1', N_2')$ can rectify the existing cosine similarity measure $S_{2\text{IVNS}}(N_1', N_2')$ defined by Ye [22].

Theorem 4. *The similarity measure $S^*_{2IVNS}(N_1', N_2')$ satisfies the following properties:*

(1) $0 \leq S^*_{2\text{IVNS}}(N_1', N_2') \leq 1$

(2) $S^*_{2\text{IVNS}}(N_1', N_2') = 1$ if and only if $N_1' = N_2'$

(3) $S^*_{2\text{IVNS}}(N_1', N_2') = S^*_{2\text{IVNS}}(N_2', N_1')$

Proof. The proof is similar to Theorem 2, we also omit it here.

In the next section, we will apply the proposed new similarity measures to medical diagnosis decision problem; numerical examples are also given to illustrate the application and effectiveness of the proposed new similarity measures. □

4. Applications of the Proposed Similarity Measures

4.1. The Proposed Similarity Measures between SVNSs for Medical Diagnosis. We first give a numerical example about a medical diagnosis (adapted from Ye [19]) to illustrate the feasibility of the proposed new similarity measures $S^*_{1\text{SVNS}}$ and $S^*_{2\text{SVNS}}$ between SVNSs.

Example 3. Consider a medical diagnosis decision problem; suppose a set of diagnoses $Q = \{Q_1\,(\text{viral fever}), Q_2\,(\text{malaria}), Q_3\,(\text{typhoid}), Q_4\,(\text{gastritis}), Q_5\,(\text{stenocardia})\}$ and a set of symptoms $S = \{S_1\,(\text{fever}), S_2\,(\text{headache}), S_3\,(\text{stomach pain}), S_4\,(\text{cough}), S_5\,(\text{chestpain})\}$. Assume a patient P_1 has all the symptoms in the process of diagnosis, the SVNS evaluate information about P_1 is

$$\begin{aligned} P_1\,(\text{Patient}) = \{&\langle S_1, 0.8, 0.2, 0.1\rangle, \langle S_2, 0.6, 0.3, 0.1\rangle, \\ &\langle S_3, 0.2, 0.1, 0.8\rangle, \langle S_4, 0.6, 0.5, 0.1\rangle, \\ &\langle S_5, 0.1, 0.4, 0.6\rangle\}. \end{aligned} \tag{13}$$

The diagnosis information $Q_i\,(i = 1, 2, \ldots, 5)$ with respect to symptoms $S_i\,(i = 1, 2, \ldots, 5)$ also can be represented by the SVNSs, which is shown in Table 1.

By applying formulae (6) and (8), we can obtain the similarity measure values $S^*_{1\text{SVNS}}(P_1, Q_i)$ and $S^*_{2\text{SVNS}}(P_1, Q_i)$; the results are shown in Table 2.

From the above two similarity measures $S^*_{1\text{SVNS}}$ and $S^*_{2\text{SVNS}}$, we can conclude that the diagnoses of the patient P_1 are all malaria (Q_2). The proposed two similarity measures $S^*_{1\text{SVNS}}$ and $S^*_{2\text{SVNS}}$ produce the same results as Ye [19], which means the proposed similarity measures are feasible and effective.

Table 1: The relation between the diagnosis and the symptom for SVNS decision information.

	S_1	S_2	S_3	S_4	S_5
Q_1	<0.4, 0.6, 0.0>	<0.3, 0.2, 0.5>	<0.1, 0.3, 0.7>	<0.4, 0.3, 0.3>	<0.1, 0.2, 0.7>
Q_2	<0.7, 0.3, 0.0>	<0.2, 0.2, 0.6>	<0.0, 0.1, 0.9>	<0.7, 0.3, 0.0>	<0.1, 0.1, 0.8>
Q_3	<0.3, 0.4, 0.3>	<0.6, 0.3, 0.1>	<0.2, 0.1, 0.7>	<0.2, 0.2, 0.6>	<0.1, 0.0, 0.9>
Q_4	<0.1, 0.2, 0.7>	<0.2, 0.4, 0.4>	<0.8, 0.2, 0.0>	<0.2, 0.1, 0.7>	<0.2, 0.1, 0.7>
Q_5	<0.1, 0.1, 0.8>	<0.0, 0.2, 0.8>	<0.2, 0.0, 0.8>	<0.2, 0.0, 0.8>	<0.8, 0.1, 0.1>

We can calculate the similarity measures $S^*_{1\text{SVNS}}(P_1, Q_i)$ and $S^*_{2\text{SVNS}}(P_1, Q_i)\,(i = 1, 2, \ldots, 5)$, and then the diagnoses of the patient P_1 can be classified by $R_j = \arg\max_{1\leq i\leq 5}\{S^*_{j\text{SVNS}}(P_1, Q_i)\}\,(j = 1, 2)$.

Table 2: The similarity measures between P_1 and Q_i.

	Q_1	Q_2	Q_3	Q_4	Q_5
$S^*_{1\text{SVNS}}(P_1, Q_i)$	0.6663	**0.7188**	0.5387	0.4594	0.4336
$S^*_{2\text{SVNS}}(P_1, Q_i)$	0.8223	**0.8378**	0.6377	0.5500	0.4881

4.2. The Proposed Similarity Measures between IVNSs for Medical Diagnosis. We know if the doctor examines the patient two or three times a day, then the interval values of multiple inspections for the patient are obtained. In this section, we will apply the proposed similarity measures $S^*_{1\text{IVNS}}$ and $S^*_{2\text{IVNS}}$ to medical diagnosis, the example is also adapted from Ye [19].

Example 4. Let us reconsider Example 3, assume a patient P_2 has all the symptoms, which can be expressed by the following IVNS information.

$$\begin{aligned} P_2\,(\text{Patient}) = \{&\langle S_1, [0.3, 0.5], [0.2, 0.3], [0.4, 0.5]\rangle, \\ &\langle S_2, [0.7, 0.9], [0.1, 0.2], [0.1, 0.2]\rangle, \\ &\langle S_3, [0.4, 0.6], [0.2, 0.3], [0.3, 0.4]\rangle, \\ &\langle S_4, [0.3, 0.6], [0.1, 0.3], [0.4, 0.7]\rangle, \\ &\langle S_5, [0.5, 0.8], [0.1, 0.4], [0.1, 0.3]\rangle\}. \end{aligned} \tag{14}$$

The same way as Example 3 in Ye [19], the diagnosis information of SVNSs Q_i with respect to symptoms $S_i\,(i = 1, 2, \cdots, 5)$ are transformed into IVNSs, which are shown in Table 3.

By applying formulae (10) and (12), we obtain the similarity measure values $S^*_{1\text{IVNS}}(P_2, Q_i)$ and $S^*_{2\text{IVNS}}(P_2, Q_i)$, the results are shown in Table 4.

From the two similarity measure values in Table 4, we can see that the patient P_2 suffers from typhoid (Q_3); the diagnosis results are the same as shown by Ye [19].

Table 3: The relation between the diagnosis and the symptom for IVNS decision information.

	S_1	S_2	S_3	S_4	S_5
Q_1	<[0.4, 0.4], [0.6, 0.6], [0.0, 0.0]>	<[0.3, 0.3], [0.2, 0.2], [0.5, 0.5]>	<[0.1, 0.1], [0.3, 0.3], [0.7, 0.7]>	<[0.4, 0.4], [0.3, 0.3], [0.3, 0.3]>	<[0.1, 0.1], [0.2, 0.2], [0.7, 0.7]>
Q_2	<[0.7, 0.7], [0.3, 0.3], [0.0, 0.0]>	<[0.2, 0.2], [0.2, 0.2], [0.6, 0.6]>	<[0.0, 0.0], [0.1, 0.1], [0.9, 0.9]>	<[0.7, 0.7], [0.3, 0.3], [0.0, 0.0]>	<[0.1, 0.1], [0.1, 0.1], [0.8, 0.8]>
Q_3	<[0.3, 0.3], [0.4, 0.4], [0.3, 0.3]>	<[0.6, 0.6], [0.3, 0.3], [0.1, 0.1]>	<[0.2, 0.2], [0.1, 0.1], [0.7, 0.7]>	<[0.2, 0.2], [0.2, 0.2], [0.6, 0.6]>	<[0.1, 0.1], [0.0, 0.0], [0.9, 0.9]>
Q_4	<[0.1, 0.1], [0.2, 0.2], [0.7, 0.7]>	<[0.2, 0.2], [0.4, 0.4], [0.4, 0.4]>	<[0.8, 0.8], [0.2, 0.2], [0.0, 0.0]>	<[0.2, 0.2], [0.1, 0.1], [0.7, 0.7]>	<[0.2, 0.2], [0.1, 0.1], [0.7, 0.7]>
Q_5	<[0.1, 0.1], [0.1, 0.1], [0.8, 0.8]>	<[0.0, 0.0], [0.2, 0.2], [0.8, 0.8]>	<[0.2, 0.2], [0.0, 0.0], [0.8, 0.8]>	<[0.2, 0.2], [0.0, 0.0], [0.8, 0.8]>	<[0.8, 0.8], [0.1, 0.1], [0.1, 0.1]>

We can calculate the similarity measures $S^*_{1\mathrm{IVNS}}(P_2, Q_i)$ and $S^*_{2\mathrm{IVNS}}(P_2, Q_i)(i = 1, 2, \cdots, 5)$, and the diagnosis of the patient P_2 can be classified by $R_j = \arg\max_{1\le i\le 5}\{S^*_{j\mathrm{IVNS}}(P_2, Q_i)\}\ (j = 1, 2)$.

Table 4: The similarity measures between P_2 and Q_i.

	Q_1	Q_2	Q_3	Q_4	Q_5
$S^*_{1\mathrm{IVNS}}(P_2, Q_i)$	0.5783	0.4610	**0.6273**	0.5772	0.5401
$S^*_{2\mathrm{IVNS}}(P_2, Q_i)$	0.6804	0.5729	**0.7503**	0.7061	0.6734

4.3. Comparative Analyses of Existing Similarity Measures. To illustrate the effectiveness of the proposed similarity measures for medical diagnosis, we will apply the existing similarity measures of SVNSs and IVNSs for comparative analyses.

At first, we introduce the existing similarity measures between SVNSs as follows:

Let $N_1 = \{\langle x_i, T_{N_1}(x_i), I_{N_1}(x_i), F_{N_1}(x_i)\rangle \mid x_i \in X\}$ and $N_2 = \{x_i, T_{N_2}(x_i), I_{N_2}(x_i), F_{N_2}(x_i) \mid x_i \in X\}$ be two SVNSs in $X = \{x_1, x_2, \ldots, x_n\}$, the existing similarity measures between N_1 and N_2 are defined as follows:

(1) Broumi et al. [23] proposed the similarity measure $\mathrm{SM}_{\mathrm{SVNS}}$:

$$\mathrm{SM}_{\mathrm{SVNS}}(N_1, N_2) = 1 - D_{\mathrm{SVNS}}(N_1, N_2). \tag{15}$$

(2) Şahin and Ahmet [24] proposed the similarity measure $\mathrm{SD}_{\mathrm{SVNS}}$:

$$\mathrm{SD}_{\mathrm{SVNS}}(N_1, N_2) = \frac{1}{1 + D_{\mathrm{SVNS}}(N_1, N_2)}. \tag{16}$$

(3) Ye [19] proposed the improved cosine similarity measures $\mathrm{SC}_{1\mathrm{SVNS}}$ and $\mathrm{SC}_{2\mathrm{SVNS}}$:

$$\mathrm{SC}_{1\mathrm{SVNS}}(N_1, N_2) = \frac{1}{n}\sum_{i=1}^{n}\cos\left[\frac{\pi\cdot\max\left(\left|T_{N_1}(x_i) - T_{N_2}(x_i)\right|, \left|I_{N_1}(x_i) - I_{N_2}(x_i)\right|, \left|F_{N_1}(x_i) - F_{N_2}(x_i)\right|\right)}{2}\right], \tag{17}$$

$$\mathrm{SC}_{2\mathrm{SVNS}}(N_1, N_2) = \frac{1}{n}\sum_{i=1}^{n}\cos\left[\frac{\pi\left(\left|T_{N_1}(x_i) - T_{N_2}(x_i)\right| + \left|I_{N_1}(x_i) - I_{N_2}(x_i)\right| + \left|F_{N_1}(x_i) - F_{N_2}(x_i)\right|\right)}{6}\right]. \tag{18}$$

(4) Yang et al. [25] proposed the similarity measure $\mathrm{SY}_{\mathrm{SVNS}}(N_1, N_2)$:

$$\mathrm{SY}_{\mathrm{SVNS}}(N_1, N_2) = \frac{\mathrm{SC}_{\mathrm{SVNS}}(N_1, N_2)}{\mathrm{SC}_{\mathrm{SVNS}}(N_1, N_2) + D_{\mathrm{SVNS}}(N_1, N_2)}. \tag{19}$$

Example 3′. We apply formulae (5), (7), and (15)–(19) to calculate Example 5 again; the similarity measure values between P_1 and $Q_i(i = 1, 2, \ldots, 5)$ are shown in Table 5.

As we can see from Table 5, the patient P_1 is still assigned to malaria (Q_2), and the results are same as the proposed similarity measures in this paper, which means the proposed similarity measures are feasible and effective.

Next, we introduce the existing similarity measures between IVNSs as follows:

Let $N_1' = \{\langle x_i, [T^L_{N_1'}(x_i), T^U_{N_1'}(x_i)], [I^L_{N_1'}(x_i), I^U_{N_1'}(x_i)], [F^L_{N_1'}(x_i), F^U_{N_1'}(x_i)]\rangle | x_i \in X\}$ and $N_2' = \{x_i, [T^L_{N_2'}(x_i), T^U_{N_2'}(x_i)], [I^L_{N_2'}(x_i), I^U_{N_2'}(x_i)], [F^L_{N_2'}(x_i), F^U_{N_2'}(x_i)] | x_i \in X\}$ be two IVNSs in $X = \{x_1, x_2, \ldots, x_n\}$, the existing similarity measures between N_1' and N_2' are defined as follows:

(1) Broumi et al. [23] proposed the similarity measure $\mathrm{SM}_{\mathrm{IVNS}}$:

$$\mathrm{SM}_{\mathrm{IVNS}}(N_1', N_2') = 1 - D_{\mathrm{IVNS}}(N_1', N_2'). \tag{20}$$

(2) Şahin and Ahmet [24] proposed the similarity measure $\mathrm{SD}_{\mathrm{IVNS}}$:

$$\mathrm{SD}_{\mathrm{IVNS}}(N_1', N_2') = \frac{1}{1 + D_{\mathrm{IVNS}}(N_1', N_2')}. \tag{21}$$

Table 5: Comparisons of different similarity measure between SVNSs.

	Q_1	Q_2	Q_3	Q_4	Q_5
SM_{SVNS} [23]	0.7941	**0.8094**	0.4568	0.5851	0.5517
SD_{SVNS} [24]	0.8293	**0.8399**	0.6480	0.7067	0.6905
SC_{1SVNS} [22]	0.8942	**0.8976**	0.8422	0.6102	0.5607
SC_{2SVNS} [22]	0.9443	**0.9571**	0.9264	0.8214	0.7650
SY_{SVNS} [25]	0.8128	**0.8248**	0.6079	0.5953	0.5557
S_{1SVNS} [15]	0.5385	**0.6282**	0.6206	0.3336	0.3154
S_{2SVNS} [18]	0.8505	**0.8661**	0.8185	0.5148	0.4244

Table 6: Comparisons of different similarity measures between IVNSs.

	Q_1	Q_2	Q_3	Q_4	Q_5
SM_{IVNS} [23]	0.6833	0.5844	**0.7265**	0.6923	0.6596
SD_{IVNS} [24]	0.7595	0.7064	**0.7852**	0.7647	0.7460
SC_{1IVNS} [22]	0.7283	0.6079	**0.7915**	0.7380	0.7157
SC_{2IVNS} [22]	0.8941	0.8459	**0.9086**	0.9056	0.8797
SY_{IVNS} [25]	0.6969	0.5939	**0.8429**	0.7057	0.6777
S_{1IVNS} [22]	0.4733	0.3376	**0.5209**	0.4620	0.4205
S_{2IVNS} [21]	0.6775	0.5613	**0.7741**	0.7198	0.6872

(3) Broumi and Smarandache [22] proposed the improved cosine similarity measures SC_{1SVNS} and SC_{2SVNS}:

$$\begin{aligned} SC_{1IVNS}(N_1', N_2') = \frac{1}{n}\sum_{i=1}^{n}\cos\frac{\pi}{4}\Bigg[&\max\left(\left|T^L_{N_1'}(x_i) - T^L_{N_2'}(x_i)\right|, \left|I^L_{N_1'}(x_i) - I^L_{N_2'}(x_i)\right|, \left|F^L_{N_1'}(x_i) - F^L_{N_2'}(x_i)\right|\right) \\ &+ \max\left(\left|T^U_{N_1'}(x_i) - T^U_{N_2'}(x_i)\right|, \left|I^U_{N_1'}(x_i) - I^U_{N_2'}(x_i)\right|, \left|F^U_{N_1'}(x_i) - F^U_{N_2'}(x_i)\right|\right)\Bigg], \end{aligned} \tag{22}$$

$$\begin{aligned} SC_{2IVNS}(N_1', N_2') = \frac{1}{n}\sum_{i=1}^{n}\cos\frac{\pi}{12}\Big(&\left|T^L_{N_1'}(x_i) - T^L_{N_2'}(x_i)\right| + \left|I^L_{N_1'}(x_i) - I^L_{N_2'}(x_i)\right| + \left|F^L_{N_1'}(x_i) - F^L_{N_2'}(x_i)\right| \\ &+ \left|T^U_{N_1'}(x_i) - T^U_{N_2'}(x_i)\right| + \left|I^U_{N_1'}(x_i) - I^U_{N_2'}(x_i)\right| + \left|F^U_{N_1'}(x_i) - F^U_{N_2'}(x_i)\right|\Big). \end{aligned} \tag{23}$$

(4) Yang et al. [25] proposed the similarity measure $SY_{SVNS}(N_1', N_2')$:

$$SY_{IVNS}(N_1', N_2') = \frac{SC_{IVNS}(N_1', N_2')}{SC_{IVNS}(N_1', N_2') + D_{IVNS}(N_1', N_2')}. \tag{24}$$

Example 4′. Applying formulae (9), (11), and (20)–(24) to calculate Example 6 again, the similarity measure values between P_2 and Q_i $(i = 1, 2, \ldots, 5)$ are shown in Table 6.

The results of Table 6 show that the patient P_2 should be assigned to typhoid (Q_3), they are same as the proposed similarity measures S^*_{1IVNS} and S^*_{2IVNS} in the paper, which means the proposed methods are feasible and effective.

The proposed similarity measures in the paper have some advantages in solving multiple criteria decision-making problems. They are constructed based on the existing similarity measures and Euclidean distance, which not only satisfy the axiom of the similarity measure but also consider the similarity measure from the points of view of algebra and geometry. Furthermore, they can be applied more widely in the field of decision-making problems.

5. Conclusions

The similarity measure is widely used in multiple criteria decision-making problems. This paper proposed a new method to construct the similarity measures combining the existing cosine similarity measure and the Euclidean distance measure of SVNSs and IVNSs, respectively, which are based on the above existing similarity measures and the Euclidean distance measure. And, the similarity measures are proposed not only from the points of view of algebra and geometry but also satisfy the axiom of the similarity measure. Furthermore, we apply the proposed similarity measures to medical diagnosis decision problems, and the numerical example is used to illustrate the feasibility and effectiveness of the proposed similarity measure, which are then compared to other existing similarity measures. In future research, we will focus on studying the similarity measure between linguistic neutrosophic set and the application of the proposed similarity measures of neutrosophic sets, such as pattern recognition, supplier selection, and so on.

Data Availability

The data used to support the findings of this study are included within the article.

Conflicts of Interest

The authors declare no conflicts of interest regarding the publication for the paper.

Acknowledgments

This research is fully supported by a grant by the National Natural Science Foundation of Hunan (2017JJ2096 and 2018JJ3137), the National Natural Science Foundation of

China (11501191), the National Social Science Foundation of China (15BTJ028), the Outstanding Youth Project of Hunan Education Department (1713092), and Major Projects of the National Social Science Foundation of China (17ZDA046).

References

[1] L. A. Zadeh, "Fuzzy sets," *Information and Control*, vol. 8, no. 3, pp. 338–353, 1965.

[2] S. K. De, R. Biswas, and A. R. Roy, "Multicriteria decision making using intuitionistic fuzzy set theory," *Journal of Fuzzy Mathematics*, vol. 6, no. 4, pp. 591–629, 1998.

[3] N. H. Phuong and V. V. Thang, "Case based reasoning for medical diagnosis using fuzzy set theory," *International Journal of Biomedical Soft Computing and Human Sciences*, vol. 5, pp. 1–7, 2000.

[4] O. J. Tobias and R. Seara, "Image segmentation by histogram thresholding using fuzzy sets," *IEEE Transactions on Image Processing*, vol. 11, no. 12, pp. 1457–1465, 2002.

[5] L. A. Zadeh, "The concept of a linguistic variable and its application to approximate reasoning," *Information Science*, vol. 8, no. 3, pp. 199–249, 1974.

[6] K. T. Atanassov and P. Rangasamy, "Intuitionistic fuzzy sets," *Fuzzy Sets and Systems*, vol. 20, no. 1, pp. 87–96, 1986.

[7] H. Wang, F. Smarandache, Y. Zhang et al., "Single valued neutrosophic sets," *Review of the Air Force Academy*, vol. 3, no. 1, pp. 33–39, 2013.

[8] H. Wang, "Interval neutrosophic sets and logic: theory and applications in computing," *Computer Science*, vol. 65, no. 4, pp. 1–99, 2005.

[9] J. Ye, "Multiple attribute group decision-making method with completely unknown weights based on similarity measures under single valued neutrosophic environment," *Journal of Intelligent and Fuzzy Systems*, vol. 27, pp. 2927–2935, 2014.

[10] I. Arockiarani and I. R. Sumathi, "Some results on interval valued Fuzzy neutrosophic soft set," *International Journal of Innovative Research and Studies*, vol. 3, no. 5, pp. 386–405, 2014.

[11] A. Mukherjee and S. Sarkar, "Several similarity measures of neutrosophic soft sets and its application in real life problems," *Annals of Pure and Applied Mathematics*, vol. 7, no. 1, pp. 1–6, 2014.

[12] J. Ye, "Similarity measures between interval neutrosophic sets and their applications in multicriteria decision-making," *Journal of Intelligent and Fuzzy Systems*, vol. 26, no. 1, pp. 165–172, 2014.

[13] Beg, Ismat, Ashraf et al., "Similarity measures for fuzzy sets," *Applied and Computational Mathematics*, vol. 8, no. 2, pp. 192–202, 2009.

[14] Y. Song, X. Wang, and H. Zhang, "A distance measure between intuitionistic fuzzy belief functions," *Knowledge-Based Systems*, vol. 86, pp. 288–298, 2015.

[15] P. Majumdar and S. K. Samanta, "On similarity and entropy of neutrosophic sets," *Journal of Intelligent and Fuzzy Systems*, vol. 26, no. 3, pp. 1245–1252, 2013.

[16] J. Ye, "Multicriteria decision-making method based on cosine similarity measures between interval- valued fuzzy sets with risk preference," *Economic Computation and Economic Cybernetics Studies and Research*, vol. 50, no. 4, pp. 205–215, 2016.

[17] J. Ye, "Cosine similarity measures for intuitionistic fuzzy sets and their applications," *Mathematical and Computer Modelling*, vol. 53, no. 1, pp. 91–97, 2011.

[18] J. Ye, "Vector similarity measures of simplified neutrosophic sets and their application in multicriteria decision making," *International Journal of Fuzzy Systems*, vol. 16, no. 2, pp. 204–211, 2014.

[19] J. Ye, "Improved cosine similarity measures of simplified neutrosophic sets for medical diagnoses," *Artificial Intelligence In Medicine*, vol. 63, no. 3, pp. 171–179, 2015.

[20] D. Liu, X. Chen, and D. Peng, "Interval-valued intuitionistic fuzzy ordered weighted cosine similarity measure and its application in investment decision-making," *Complexity*, vol. 2017, article 1891923, 11 pages, 2017.

[21] D. Liu, X. Chen, and D. Peng, "The intuitionistic fuzzy linguistic cosine similarity measure and its application in pattern recognition," *Complexity*, vol. 2018, no. 1, pp. 1–11, 2018.

[22] S. Broumi and F. Smarandache, "New distance and similarity measures of interval neutrosophic sets," in *Proceedings of International Conference on Information Fusion*, pp. 1–7, IEEE, Salamanca, Spain, July 2014.

[23] S. Broumi and F. Smarandache, "Several similarity measures of neutrosophic sets," *Neutrosophic Sets and Systems*, vol. 1, no. 1, pp. 54–62, 2013.

[24] R. Şahin and K. Ahmet, *On Similarity and Entropy of Neutrosophic Soft Sets*, vol. 29Amsterdam, Netherlands, 2014.

[25] Y. Yang, R. Zhang, and J. Guo, "A multi-attribute decision-making approach based on hesitant neutrosophic sets," *Fuzzy Systems and Mathematics*, vol. 31, no. 2, pp. 114–122, 2017.

Hindawi
Computational and Mathematical Methods in Medicine
Volume 2018, Article ID 4253928, 12 pages
https://doi.org/10.1155/2018/4253928

Research Article

Computational Prediction of the Combined Effect of CRT and LVAD on Cardiac Electromechanical Delay in LBBB and RBBB

Aulia K. Heikhmakhtiar and Ki M. Lim

Department of IT Convergence Engineering, Kumoh National Institute of Technology, Gumi 39177, Republic of Korea

Correspondence should be addressed to Ki M. Lim; kmlim@kumoh.ac.kr

Received 17 May 2018; Revised 3 September 2018; Accepted 25 October 2018; Published 14 November 2018

Guest Editor: Ka L. Man

Two case reports showed that the combination of CRT and LVAD benefits the end-stage heart failure patients with prolonged QRS interval significantly. In one of the reports, the patient had the LVAD removed due to the recovery of the heart function. However, the quantification of the combined devices has yet to be conducted. This study aimed at computationally predicting the effects of CRT-only or combined with LVAD on electromechanical behaviour in the failing ventricle with left bundle branch blocked (LBBB) and right bundle branch blocked (RBBB) conditions. The subjects are normal sinus rhythm, LBBB, RBBB, LBBB with CRT-only, RBBB with CRT-only, LBBB with CRT + LVAD, and RBBB with CRT + LVAD. The results showed that the CRT-only shortened the total electrical activation time (EAT) in the LBBB and RBBB conditions by 20.2% and 17.1%, respectively. The CRT-only reduced the total mechanical activation time (MAT) and electromechanical delay (EMD) of the ventricle under LBBB by 21.3% and 10.1%, respectively. Furthermore, the CRT-only reduced the contractile adenosine triphosphate (ATP) consumption by 5%, increased left ventricular (LV) pressure by 6%, and enhanced cardiac output (CO) by 0.2 L/min under LBBB condition. However, CRT-only barely affects the ventricle under RBBB condition. Under the LBBB condition, CRT + LVAD increased LV pressure and CO by 10.5% and by 0.9 L/min, respectively. CRT + LVAD reduced ATP consumption by 15%, shortened the MAT by 23.4%, and shortened the EMD by 15.2%. In conclusion, we computationally predicted and quantified that the CRT + LVAD implementation is superior to CRT-only implementation particularly in HF with LBBB condition.

1. Introduction

Heart failure (HF) plays a major role in the number of death worldwide [1]. Thus, the study of heart diseases including cardiac arrhythmia, which progressively leads to HF condition, is very important. Two types of cardiac therapy devices are commonly used to treat patients with cardiac disease: cardiac resynchronization therapy (CRT) and left ventricular assist device (LVAD). CRT is considered as a valuable treatment for patients with dyssynchrony HF with QRS interval >120 ms and left ventricular ejection fraction (EF) <35% [2, 3]. A number of studies showed significant benefits of using CRT. CRT synchronizes systolic function [4–6], restores heart structure [7, 8], and improves symptoms and the quality of life of the patients identified by the improvement of exercise endurance [3, 8–12]. However, 30% of patients with HF failed to benefit from the CRT [9]. Hu et al. [13] described that three major responses could be obtained from the CRT treatment: resynchronization of the intraventricular contraction, efficient ventricular preloading by a properly timed atrial contraction, and reduction of mitral regurgitation. One of the study findings was that resynchronization of the intraventricular contraction itself did not necessarily lead to stroke work improvement. However, the synchronization of the atrioventricular firing time was essential.

LVAD supports the ventricular pumping via mechanical unloading for weakened heart. LVAD was initially used as a bridge to transplantation for patients with end-stage disease [14, 15]. However, because the availability of heart donors is very limited, LVAD is now used as destination therapy as it lasts for years [16–18]. LVAD reverses the

damaged ventricle and recovers myocardial functionalities by repairing left ventricular (LV) mass [19, 20], heart chamber size [20, 21], improves mitral filling [22], and induces cardiomyocyte hypertrophy regression [21, 22]. The use of LVAD also increased the quality of life of the patients [23–25]. Previously, we observed the effect of LVAD on the electromechanical delay (EMD) under mild and severe HF conditions [26]. The results showed that the LVAD not only increased the EF but also shortened the EMD under the mild HF and even better under severe HF conditions. The comparison study of the symptomatic relief of CRT and LVAD by Delgado et al. concluded that the use of both devices could synergistically improve cardiac functions for severe HF treatment [27].

In 2011, a case report article stated that the CRT supported the restoration of end-stage HF in a 15-year-old patient who underwent LVAD implantation [28]. The CRT shortened the septal to posterior wall motion delay from 146 ms to 104 ms, and overall, it backed up the hemodynamic improvements. After such improvement, the patient successfully had the LVAD removed. In another case report article, the CRT and LVAD cooperatively restored the cardiac functions of a 62-year-old patient who had cardiogenic shock and left bundle branch block (LBBB) [29]. The report stated that the combination of CRT and LVAD performed a profound treatment on the weakening heart under LBBB condition. It recovered the heart hypertrophy, and the EF was increased. Based on these reports, we conducted a computational modelling which combined the CRT and LVAD to the failing ventricle with LBBB and RBBB in order to understand the mechanism of the two devices combined to provide such improvement to the heart.

To the best of our knowledge, a computational study that quantifies the effect of combined CRT and LVAD has yet to be conducted. This study aims at predicting, computationally with an electromechanical failing ventricles model, the effects of CRT alone and the combination of CRT and LVAD treatment in patients with LBBB or right bundle branch block (RBBB). We used a well-developed electromechanical ventricular model which had been used to observe different heart conditions, including the prolonged EMD in the dyssynchrony HF condition [30], mechanoelectrical feedback on scroll wave stability [31], and spontaneous arrhythmia in acute regional ischemia [32]. Recently, by using similar electromechanical coupling model, our group revealed the effect of KCNQ1 S140G mutation on arrhythmogenesis and pumping performance [33]. We used computational methods to overcome the measurement limitations and risks of the experimental study. We analyzed seven HF diseases and therapies: (i) normal sinus rhythm, (ii) LBBB, (iii) LBBB with CRT alone (LBBB + CRT), (iv) LBBB with CRT and LVAD combination (LBBB + CRT + LVAD), (v) RBBB, (vi) RBBB with CRT alone (RBBB + CRT), and (vii) RBBB with combined CRT and LVAD (RBBB + CRT + LVAD) conditions.

2. Materials and Methods

We followed an existing well-developed electromechanical failing ventricle model with the fibers and laminar sheet structures based on diffusion tensor magnetic resonance imaging [34–37]. In this study, our electromechanical model was coupled with circulatory systems and LVAD models similarly as Lim et al. with additional Purkinje networks compartment to simulate LBBB and RBBB conditions [38]. The electromechanical model consisted of electrophysiological and myofilament dynamics model coupled by Ca^{2+} transient. The LVAD function included the circulatory systems, which connected to the 3D ventricular mechanics. Figure 1 shows a full schematic of the system we used in this study.

The electrical component was a failing ventricular mesh with 241,725 nodes and 1,298,751 tetrahedron elements. The electrical mesh has the characteristics of realistic heart compartment, which consists of endocardial, midmyocardial, and epicardial cells following the ten Tusscher et al. human ventricular tissue model [39]. The line mesh type representing Purkinje networks was mapped onto a 3D ventricle chamber as well at the endocardial region (Figure 2(c)).

The Purkinje networks induced the electrical activation sequences of sinus rhythm (normal), LBBB, and RBBB (Figure 2(c)). The CRT pacing site of the LBBB was placed at the LV free-wall, while the CRT pacing site of the RBBB was placed at the RV endocardial apex as shown in Figure 2(b). The electrical stimulation was first induced at the root node of Purkinje fiber model, which propagates to the terminals, hence stimulating the ventricular tissue. The electrical propagation in the Purkinje can be described by solving a one-dimensional wave propagation equation and triggered the ventricular activation [40].

The electrical propagation signal represents an ion exchange across the myocyte as described by ten Tusscher et al. [39]. The electrophysiological phenomenon for the single cell can be described as follows:

$$\frac{dV}{dt} = \frac{-I_{\text{ion}} + I_{\text{stim}}}{C_{\text{m}}}, \tag{1}$$

where V represents the voltage difference of intracellular and extracellular, t represents time, I_{ion} represents the sum of all transmembrane ionic currents, I_{stim} represents the current if an external stimulus is applied, and C_{m} represents the cell capacitance per unit of surface area. I_{ion} consists of major ionic current as follows:

$$\begin{aligned} I_{\text{ion}} = {} & I_{\text{Na}} + I_{\text{K1}} + I_{\text{to}} + I_{\text{Kr}} + I_{\text{Ks}} + I_{\text{CaL}} + I_{\text{NaCa}} + I_{\text{NaK}} \\ & + I_{\text{pCa}} + I_{\text{pK}} + I_{\text{bCa}} + I_{\text{bNa}}, \end{aligned} \tag{2}$$

where I_{Na} is fast inward Na^+ current, I_{K1} is inward rectifier K1 current, I_{to} is transient outward K^+ current, I_{Kr} is rapid

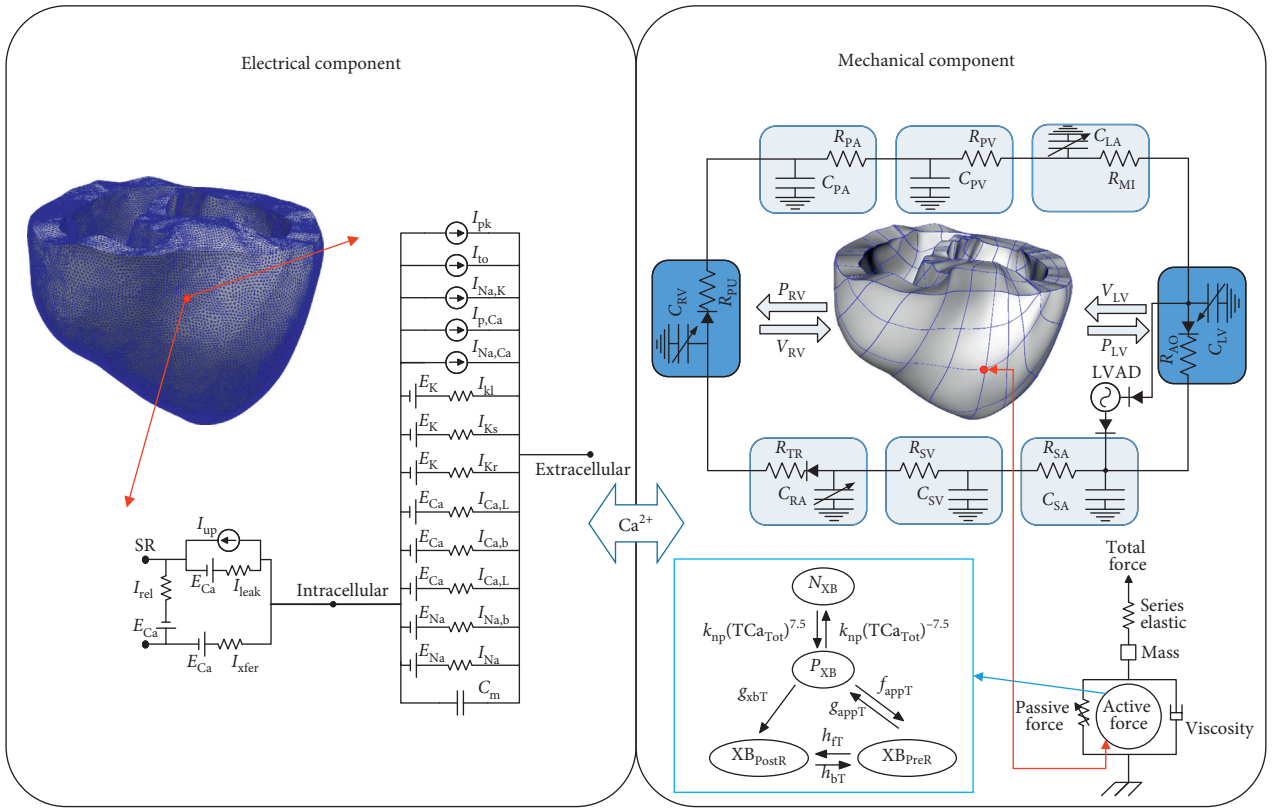

FIGURE 1: Schematics of the electrical and mechanical elements coupled with transient calcium. Electrical element: it represents the currents, pumps, and exchanger of the ten Tusscher ionic model as explained in equation (1). Mechanical element: a schematic diagram of the finite-element ventricular mechanical model coupled with the circulatory and LVAD models. P_{RV}, RV pressure; V_{RV}, RV volume; P_{LV}, LV pressure; V_{LV}, LV volume; R_{PA}, pulmonary artery resistance; C_{PA}, pulmonary artery compliance; R_{PV}, pulmonary vein resistance; C_{PV}, pulmonary vein compliance; R_{MI}, mitral valve resistance; C_{LA}, left atrium compliance; R_{AO}, aortic valve resistance; R_{SA}, systemic artery resistance; C_{SA}, systemic artery compliance; R_{SV}, systemic vein resistance; C_{SV}, systemic vein compliance; R_{TR} tricuspid valve resistance; C_{RA}, right atrium compliance; R_{PU}, pulmonary valve resistance.

delayed rectifier K^+ current, I_{Ks} is slow delayed rectifier K^+ current, I_{CaL} is L-type inward Ca^{2+} current, I_{NaCa} is Na^+/Ca^{2+} exchanger current, I_{NaK} is the Na^+/K^+ pump current, I_{pCa} and I_{pK} are sarcoplasmic plateau Ca^{2+} and K^+ currents, I_{bCa} is background Ca^{2+} current, and $I_{Na,b}$ is background Na^+ current.

To represent the electrical propagation through the conduction in 3D spatial, the cardiac tissue in this case could be described by the combination of the Equation (1) with the cellular resistivity (ρ) and surface-to-volume ratio (S) in x, y, and z directions, respectively. This phenomenon can be described by the following partial differential equation:

$$\frac{dV}{dt} = \frac{-I_{ion} + I_{stim}}{C_m} + \frac{1}{\rho_x S_x C_m}\frac{\partial^2 V}{\partial x^2} + \frac{1}{\rho_y S_y C_m}\frac{\partial^2 V}{\partial y^2} + \frac{1}{\rho_z S_z C_m}\frac{\partial^2 V}{\partial z^2}. \quad (3)$$

The mathematical equation for calcium dynamics for coupling the electromechanical simulation was also described by ten Tusscher et al. [39]:

$$I_{leak} = V_{leak}\left(Ca_{sr} - Ca_i\right),$$

$$I_{up} = \frac{V_{maxup}}{1 + K_{up}^2/Ca_i^2},$$

$$I_{rel} = \left(a_{rel}\frac{Ca_{sr}^2}{b_{rel}^2 + Ca_{sr}^2} + C_{rel}\right)dg,$$

$$Ca_{ibufc} = \frac{Ca_i \times Buf_c}{Ca_i + K_{bufc}},$$

$$\frac{dCa_{itotal}}{dt} = \frac{-I_{Cal} + I_{bCa} + I_{pCa} - 2I_{NaCa}}{2V_c F} + I_{leak} - I_{up} + I_{rel},$$

$$Ca_{srbufsr} = \frac{Ca_{sr} \times Buf_{sr}}{Ca_{sr} + K_{bufsr}},$$

$$\frac{dCa_{stotal}}{dt} = \frac{V_C}{V_{sr}}\left(-I_{leak} + I_{up} - I_{rel}\right), \quad (4)$$

where I_{leak} represents the calcium released from the sarcoplasmic reticulum (SR) into the cell. I_{up} represents the

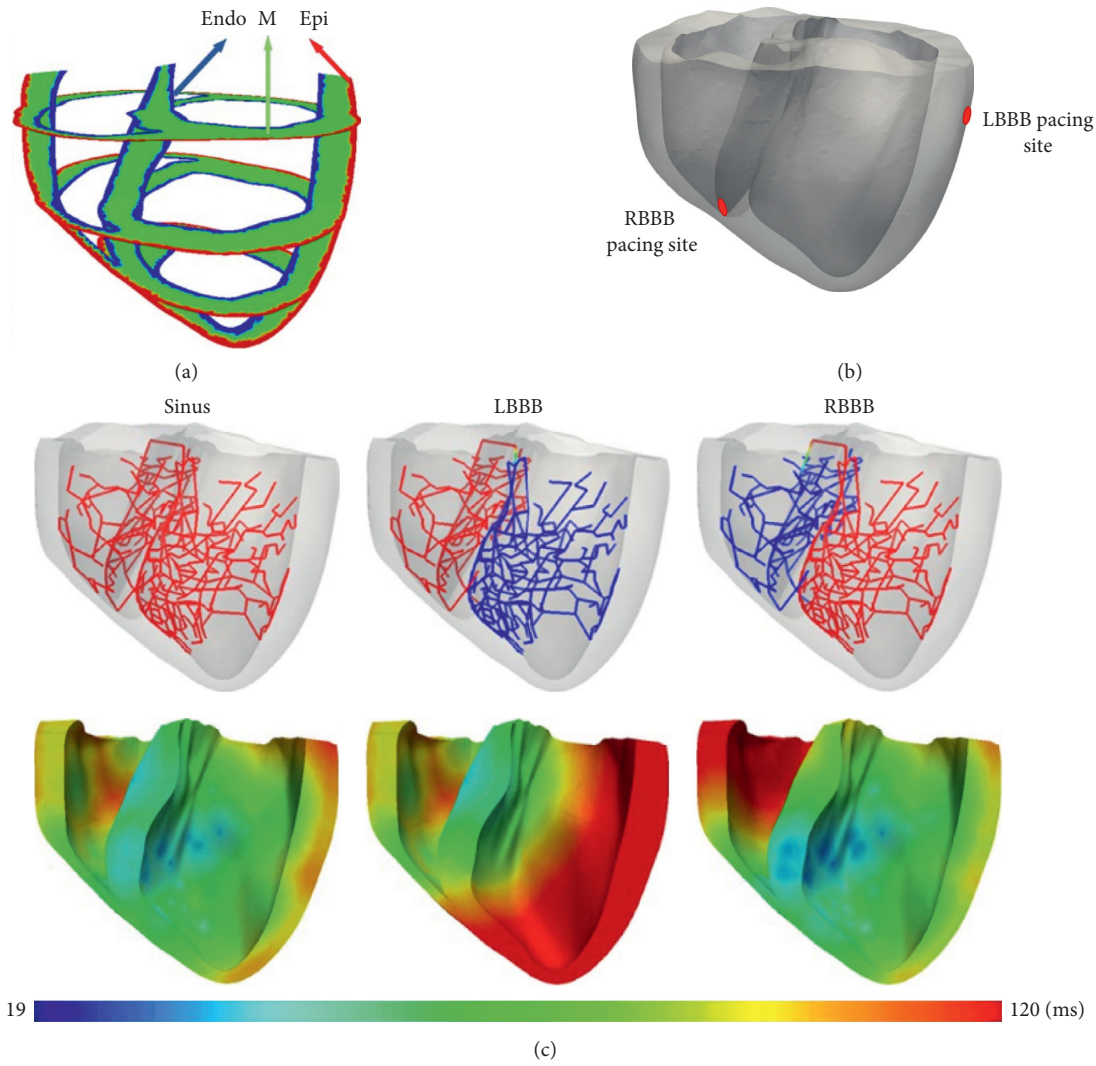

FIGURE 2: (a) The heterogeneous mesh that has the characteristics of endocardial, midmyocardial, and epicardial cells. (b) The CRT pacing site for the LBBB heart was placed on the LV free-wall, while that for the RBBB heart was placed inside the RV at the bottom of the septum. (c) The electrical propagation by the Purkinje network in the sinus, LBBB, and RBBB conditions. The electrical activation by the Purkinje networks is indicated in red. In sinus pacing, the Purkinje network delivers the electrical signal to its terminals. In the LBBB condition, the Purkinje network delivered the signal only to the right network in the RV area. In the RBBB condition, the Purkinje network delivered the signal only to the left network in the LV area. CRT, cardiac resynchronization therapy; LBBB, left bundle branch block; LV, left ventricular; RBBB, right bundle branch block; RV, right ventricular.

calcium pumping to restore the calcium again back to the SR. I_{rel} represents the calcium-induced calcium release current, d is the activation gate of I_{rel}, which was the same with I_{CaL}. Ca_{itotal} is the total calcium inside the cell, which consists of Ca_{ibufc}, the calcium buffer inside the cell, and Ca_i, the free calcium inside the cell. Accordingly, the $Ca_{srtotal}$ is the sum of calcium in the SR, which includes $Ca_{srbufsr}$, the calcium buffer, and Ca_{sr}, the free calcium inside the SR.

A Ca^{2+} transient serves as an input to the cell myofilament model representing the generation of active tension within each myocyte in which an ODE set and multiple algebraic equations describe Ca^{2+} binding to troponin C, cooperatively between regulatory proteins, and cross-bridge cycling. Ventricular contraction results from the active tension generation represented by the myofilament dynamics model described by Rice et al. [41]. Ventricular deformation is described by the equations of passive cardiac mechanics, with the myocardium being orthotropically hyperelastic, and nearly incompressible material with passive properties defined by an exponential strain-energy function. Simultaneous solutions of the myofilament model equations to those representing passive cardiac mechanics on the finite-element mesh constitute cardiac contraction. Considering the isometric contraction, we assumed that the sarcomere length (SL) is 0 at the initial value, $dSL/dt = 0$. To measure the isotonic contraction, the SL is solved using the following ordinary differential equation (ODE):

$$\frac{d}{dt}SL = \frac{\text{Integral}_{\text{Force}} + (\text{SL}_0 - \text{SL}) \times \text{viscosity}}{\text{mass}}, \quad (5)$$

the viscosity and mass are described in Figure 1 at the mechanical compartment, and $\text{Integral}_{\text{Force}}$ is the sum of the normalized force integrated toward time:

$$\text{Integral}_{\text{Force}} = \int_0^t \left(F_{\text{active}}(x) + F_{\text{passive}}(x) - F_{\text{preload}} - F_{\text{afterload}}(x)\right) dt, \quad (6)$$

where the $F_{\text{active}}(x)$ is the active force and the $F_{\text{passive}}(x)$ is the passive force. F_{preload} is the constant force at the resting length of the initial sarcomere length, and $F_{\text{afterload}}$ is the force during the isotonic or isometric contraction. Thus, $F_{\text{afterload}}$ is expressed as follows:

$$F_{\text{afterload}}(x) = \text{KSE} \times (x - \text{SL}_0). \quad (7)$$

We calculated the ATP consumption by integrating the myofilament model in one cycle proposed by Rice et al. from each node [41]. In the myofilament model, the ATP consumption rate (E) is the outcome of cross-bridge detachment rate (g_{xbT}) and the single overlap fraction of thick filaments ($\text{SOVF}_{\text{Thick}}$):

$$E = g_{xbT} \times \text{SOVF}_{\text{Thick}}. \quad (8)$$

To construct an integrated model of an LVAD-implanted cardiovascular system, we added a compartment of LVAD function between LV and systemic arteries in the circulatory system based on Kerckhoffs et al. [42] as described previously by Lim et al. [38]. Briefly, the LVAD component was modelled as a flow generator with a specific mean flow rate of 3 L/min. Constant-flow conditions were used to simulate the continuous LVAD with the inlet at the LV apex and the outlet at the ascending aorta.

For the simulation protocol, first we simulated the electrical model with the Purkinje delivering the signal representing sinus rhythm, LBBB, or RBBB until the steady state was achieved. We set the conduction velocity by 60 cm/s and the basic cycle length by 600 ms. Here, we incorporated the dyssynchrony HF conditions (LBBB and RBBB) using CRT-alone or combined CRT and LVAD. We then used Gaussian point for the interpolation of transient Ca^{2+} from the electrical simulation as the input to the mechanical simulation. To model the HF condition, we multiplied the constant of passive scaling in the strain-energy function by 5 times to stiffen the myocardium. The mechanical model was simulated for 20 seconds to reach the steady state. We compared the ATP consumption rates and tension activation during end-systolic volume (ESV) and the strain during end-diastolic volume (EDV) by integrating the information of them from each node. EMD was defined as the time interval between mechanical activation time (MAT) and electrical activation time (EAT). MAT was identified when the local strain was shortened to 10% before its maximum, while EAT was identified when the myocyte started to depolarize, which in our case was −50 mV [30].

3. Results and Discussion

3.1. Electrophysiological Simulation Results. Figure 3 shows the membrane potential propagation in the normal sinus rhythm (sinus), LBBB, LBBB + CRT, LBBB + CRT + LVAD, RBBB, RBBB + CRT, and RBBB + CRT + LVAD conditions. The electrical wavelength almost covered the whole ventricle tissue at 100 ms in the sinus condition, and the EAT in the sinus condition was 120 ms (Table 1). The EAT in the LBBB condition was 173 ms, which was the longest among other cases. CRT shortened the EAT in the LBBB condition to 138 ms, which was close to that in the sinus condition. In the RBBB heart, the EAT was 164 ms. CRT shortened the EAT in the RBBB heart to 136 ms, which was close to the sinus condition as well.

Figure 4 shows the calcium activation sequences. The calcium activation sequence followed the electrical activation sequence for each case. Compared to the membrane potential, which deactivated after 450 ms, the Ca^{2+} deactivation occurred at 250 ms. CRT fastened the Ca^{2+} activation throughout the ventricle in the LBBB condition but insignificantly in the RBBB condition due to the CRT pacing site.

3.2. Cardiac Mechanics Simulation Results. Figure 5 shows the 3D ATP consumption rate, tension, and strain transmural distribution in the sinus, LBBB, LBBB + CRT, LBBB + CRT + LVAD, RBBB, RBBB + CRT, and RBBB + CRT + LVAD conditions. We pick one node at the LV free-wall as representative to compare the values of them. Overall, the ATP consumption rate and tension in the LBBB condition had the highest values, 3.3 and 3.5 times larger than those in the normal sinus condition, respectively. However, the CRT decreased the ATP consumption rate and tension in the LBBB condition to be 6% and 7% lower than those in the normal sinus condition. Furthermore, CRT and LVAD reduced the ATP consumption rate and tension in the LBBB condition to 10% and 12% lower than those in the normal sinus condition, respectively. The ATP consumption rate and tension in the RBBB condition were 8% and 9% higher than those in the control condition. The CRT reduced the ATP consumption rate and tension by 4% and 5%, respectively. CRT and LVAD reduced the ATP consumption rate and tension by 9% and 11% in the RBBB condition, respectively. The strain under the LBBB condition was 80 times larger than that in the normal condition (notified by major red region in the LV free-wall). The CRT reduced the strain in the LBBB 56 times lower than that in the normal sinus condition. CRT significantly restored the total strain under the LBBB condition with the pacing site at the LV free-wall. However, under LBBB + CRT + LVAD, the total strain was only eight times lower than that in the sinus condition. The continuous LVAD altered the overall strain in the ventricles. The total strain in the RBBB condition was 84 times larger than that in the normal condition. In the RBBB + CRT model, the strain activation was 122 times larger. In the RBBB + CRT + LVAD model, the strain

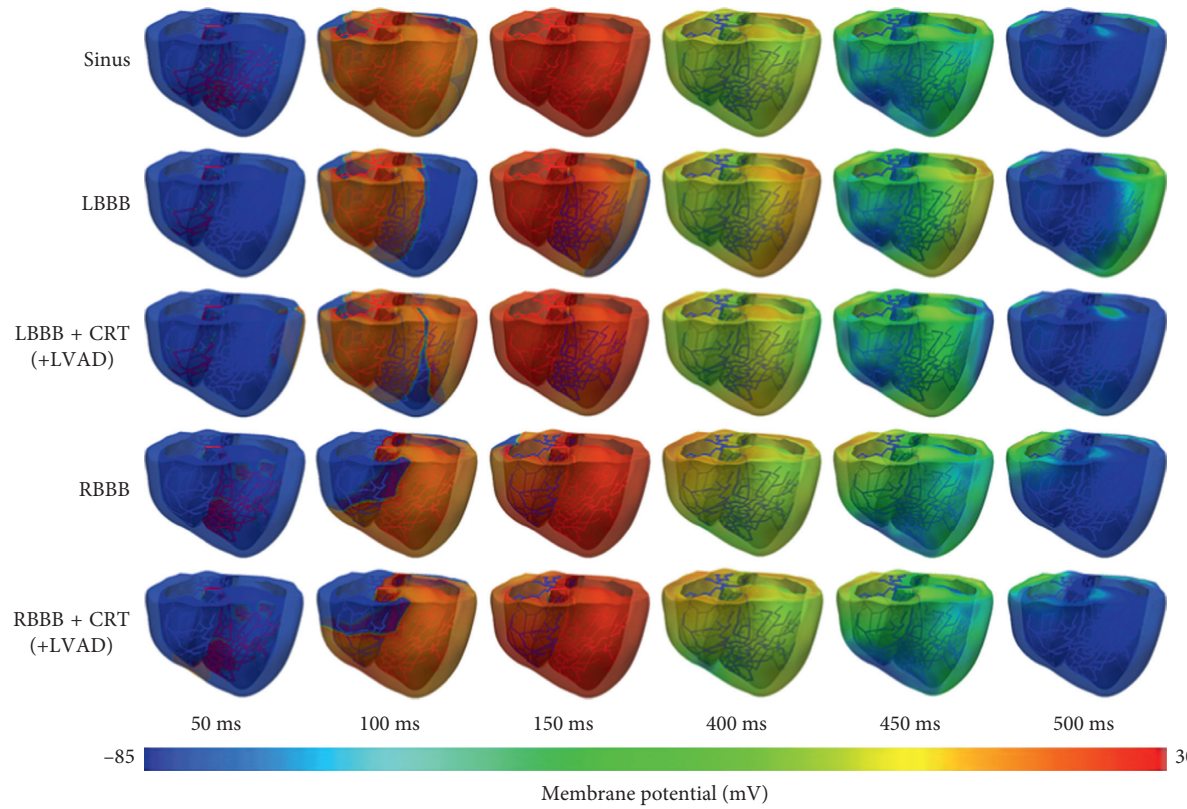

Figure 3: The membrane potential propagation of the sinus pacing, LBBB, LBBB + CRT, RBBB, and RBBB + CRT models. For the LBBB + CRT + LVAD and RBBB + CRT + LVAD models, we used the same electrical activation sequence as the LBBB + CRT and RBBB + CRT models, respectively, because the LVAD was incorporated into the mechanical computation. LBBB, left bundle branch block; CRT, cardiac resynchronization therapy; RBBB, right bundle branch block; LVAD, left ventricular assist device.

Table 1: Hemodynamic responses under normal, LBBB, LBBB + CRT, LBBB + CRT + LVAD, RBBB, RBBB + CRT, and RBBB + CRT + LVAD models.

Condition	EDV (mL)	ESV (mL)	CO (L/min)	EF (%)	Longest EAT (ms)	Average MAT (ms)	Average EMD (ms)
Normal sinus rhythm	88	55	3.4	38	120	157	78
LBBB	90	60	3	33.4	173	188	79
LBBB + CRT	89	57	3.2	36	138	148	71
LBBB + CRT + LVAD	—	—	3.9	—	138	144	67
RBBB	87	54	3.4	38	164	162	80
RBBB + CRT	88	55	3.4	38	136	157	81
RBBB + CRT + LVAD	—	—	4	—	136	155	79

activation was 23 times lower than that in the normal condition.

Figure 6(a) shows the LV pressure-volume (PV) loop diagram in the sinus, LBBB, LBBB + CRT, LBBB + CRT + LVAD, RBBB, RBBB + CRT, and RBBB + CRT + LVAD conditions. The LV PV-loop in the normal sinus rhythm condition was the same as those in the RBBB and RBBB + CRT conditions. The EDV in the three conditions was 88 mL, ESV was 54.5 mL, and EF was 38%. The LBBB condition had the highest EDV and ESV of 90 mL and 60 mL, respectively. The stroke volume (SV) and EF were 30 mL and 33.4%, respectively. CRT increased the EF up to 36% in the LBBB condition. The EDV, ESV, and SV in the LBBB + CRT condition were 89 mL, 57 mL, and 32 mL, respectively. We did not quantify the EF in models in which LVAD model was incorporated because the PV-loop of the LV was altered due to the LVAD implementation. However, the CO was presented to compare the effects of CRT-alone and combined CRT and LVAD. The complete EDV, ESV, CO, EF, MAT, and EMD data in all conditions are provided in Table 1.

Figure 6(b) shows the LV and systemic artery pressures coloured in black and red lines, respectively. In the normal sinus condition, the peak LV pressure was 148 mmHg. The LV pressure peaked at 358 ms, and the aortic valve was opened for 96 ms. In the LBBB condition, the LV peak pressure was 132.5 mmHg. The LV peak pressure time was prolonged to 407 ms, and the aortic valve was opened for 100 ms. The LV peak pressure in the LBBB + CRT condition

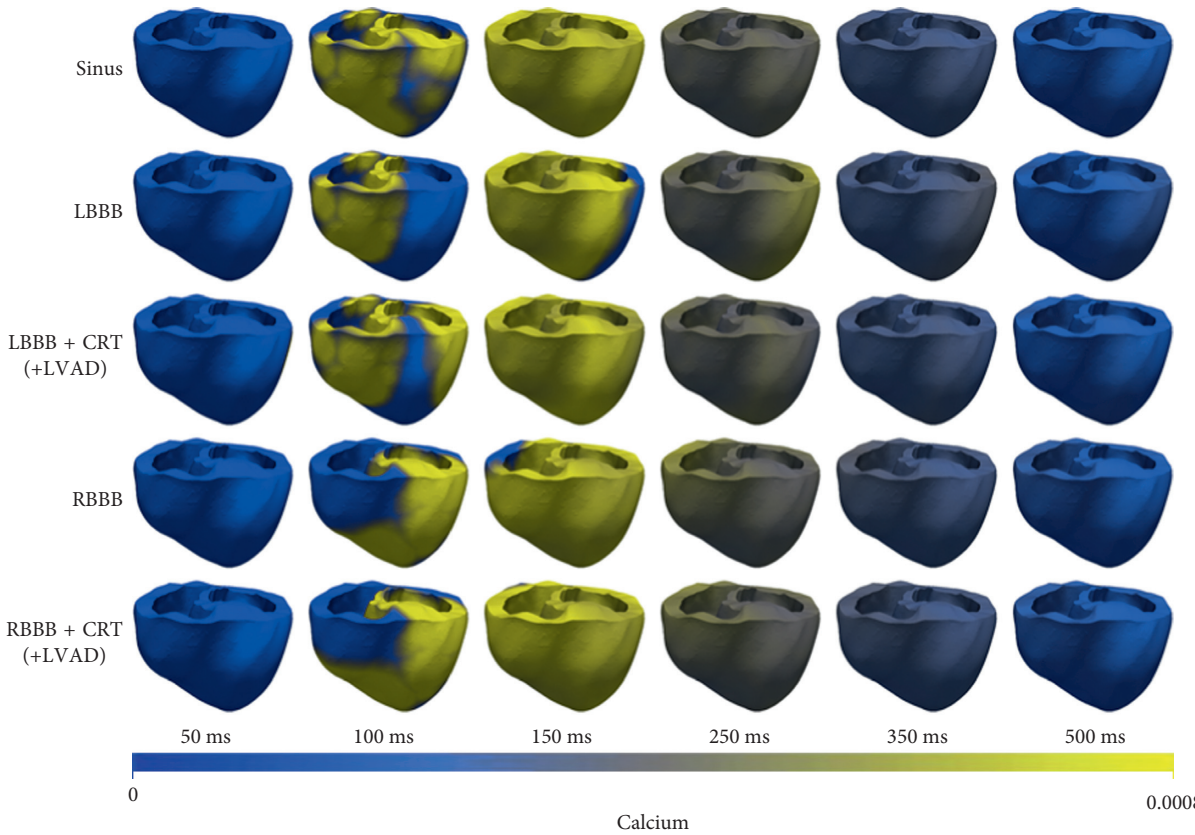

Figure 4: The Ca^{2+} propagation sequence following the membrane potential activation sequence in all cases. LBBB, left bundle branch block; CRT, cardiac resynchronization therapy; LVAD, left ventricular assist device; RBBB, right bundle branch block.

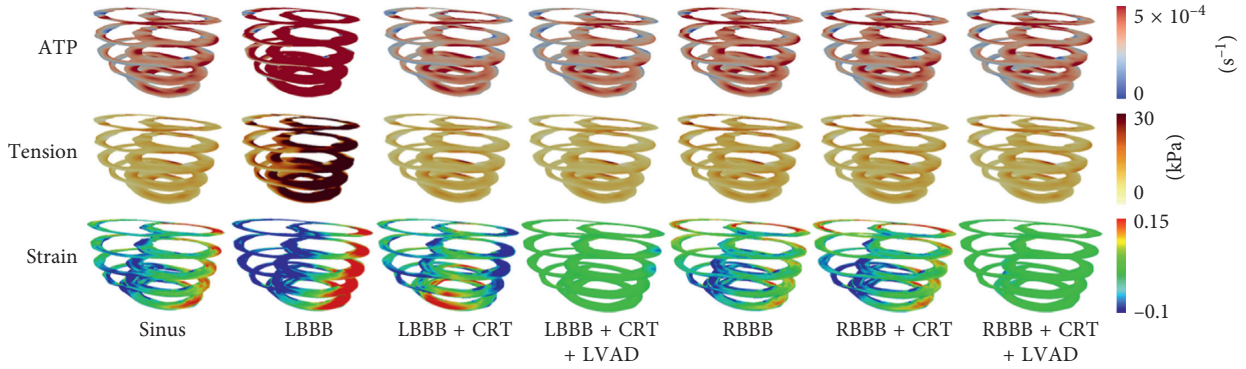

Figure 5: The 3D transmural distribution of ATP, tension, and strain in all cases. The snapshot for the ATP and tension was taken at the end-systolic volume, while the strain snapshot was taken at the end-diastolic volume time. ATP, adenosine triphosphate; LBBB, left bundle branch block; CRT, cardiac resynchronization therapy; LVAD, left ventricular assist device; RBBB, right bundle branch block.

was increased to 141 mmHg. The LV peak pressure time was shortened to 364 ms, and the aortic valve was opened for 96 ms. In the LBBB + CRT + LVAD condition, the peak LV pressure was 148 mmHg, the same as that in the normal condition, the LV peak pressure time was 363 ms, and the aortic valve was opened for 62 ms. The combination of CRT and LVAD restored the LV peak pressure and LV peak pressure time in the LBBB condition better than CRT alone. In the RBBB and RBBB + CRT conditions, the LV peak pressures and LV peak pressure time were the same at 148 mmHg and 353 ms, respectively, and the aortic valve was opened for 96 ms, the same as that in the normal condition. The reason was that the electrical activation of the LV was not altered in the RBBB condition. In the RBBB + CRT + LVAD condition, the peak LV pressure and LV peak pressure time were increased to 155 mmHg and 350 ms, respectively, and the aortic valve was opened for 63 ms. This finding shows that the combined CRT and LVAD increased the LV pressure and systemic artery more than the CRT-only implementation.

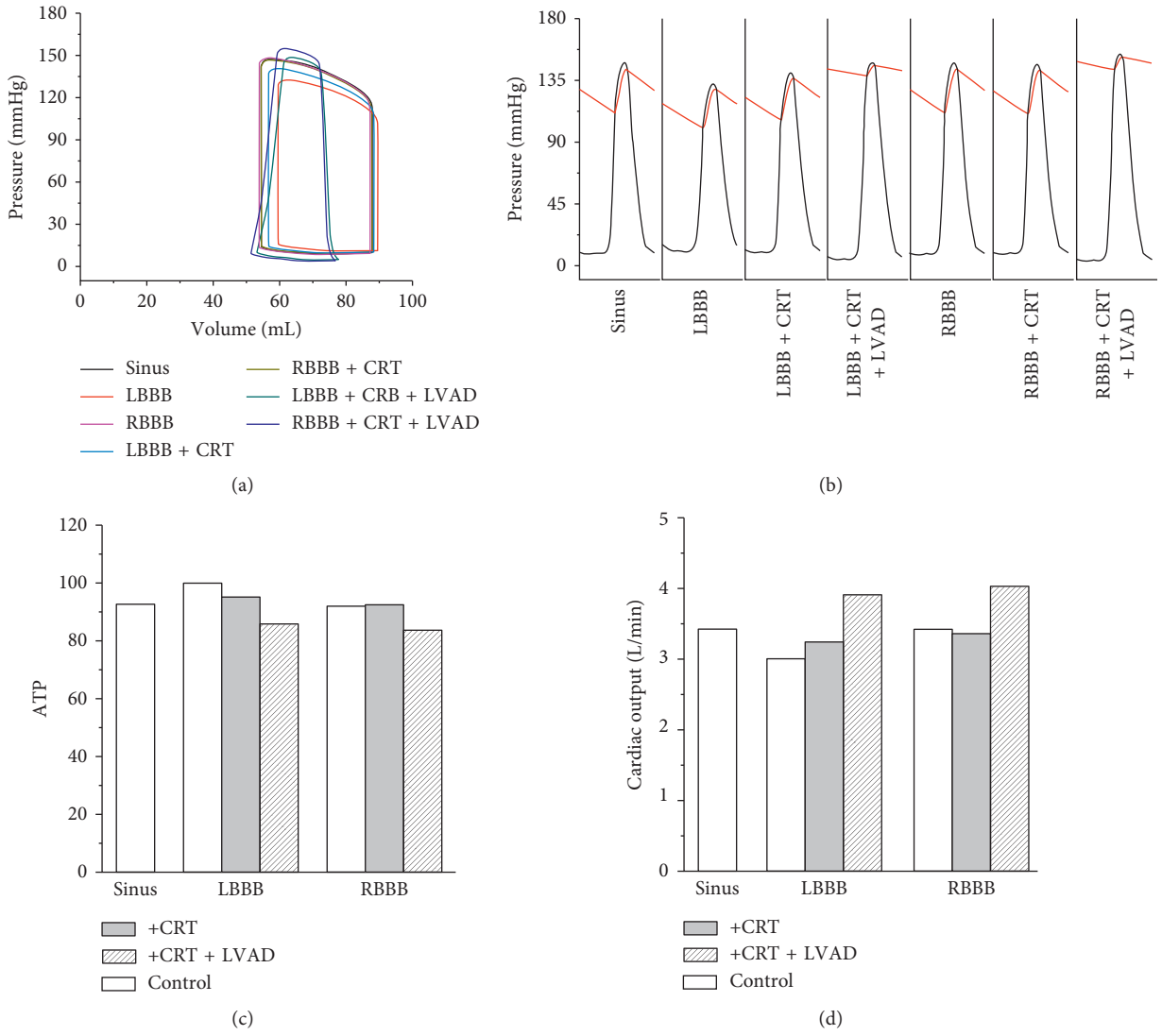

Figure 6: (a) LV pressure-volume loop, (b) LV pressure and aortic pressure, (c) ATP consumption rate, and (d) cardiac output of all cases. LV, left ventricular; LBBB, left bundle branch block; CRT, cardiac resynchronization therapy; LVAD, left ventricular assist device; RBBB, right bundle branch block; ATP, adenosine triphosphate.

Figure 6(c) shows the overall ATP consumption rate from one cycle of steady state. In the normal sinus condition, the ATP consumption rate was 93 s^{-1}. The ATP consumption rate in LBBB condition was the highest at 100 s^{-1}. CRT reduced the ATP consumption rate in the LBBB condition by 5%, while CRT and LVAD reduced the ATP consumption rate by 15%. In the RBBB and RBBB + CRT conditions, the ATP consumption rates were the same as that in the normal condition, 93 s^{-1}. However, with CRT and LVAD support, the ATP consumption rate in the RBBB condition was decreased by 16% to 84 s^{-1}.

Figure 6(d) shows the CO of the seven subjects. CRT increased the CO slightly in the LBBB condition but not in the RBBB condition. With the combination of CRT and LVAD, the CO of the LBBB and RBBB conditions was significantly increased (Table 1).

Figure 7(a) shows the 3D contour of EAT, MAT, and EMD, while Figure 7(b) shows the MAT and EMD of all cases. As shown in Figure 7(a), the activation sequence of MAT and EMD was identical to the EAT. The MAT and EMD values in the normal condition were 157 and 78 ms, respectively. In the LBBB condition, the MAT and EMD values were the greatest at 188 ms and 79 ms, respectively. CRT shortened the MAT and EMD to 148 ms and 71 ms in the LBBB condition. Furthermore, the MAT and EMD in the LBBB condition were further shortened with the combined CRT and LVAD to 144 and 67 ms, respectively. This finding showed that combination of CRT and LVAD performed better than CRT alone despite having the same EAT. In the RBBB condition, the MAT and EMD values were 162 and 80 ms, respectively. In the RBBB + CRT condition, the mean MAT and EMD values were reduced slightly to 157 and 81 ms, respectively. In the RBBB + CRT + LVAD condition, the mean MAT and EMD values were reduced to 155 and 79 ms (close to the control condition), respectively. In the RBBB condition, CRT alone only slightly affected the electrical and

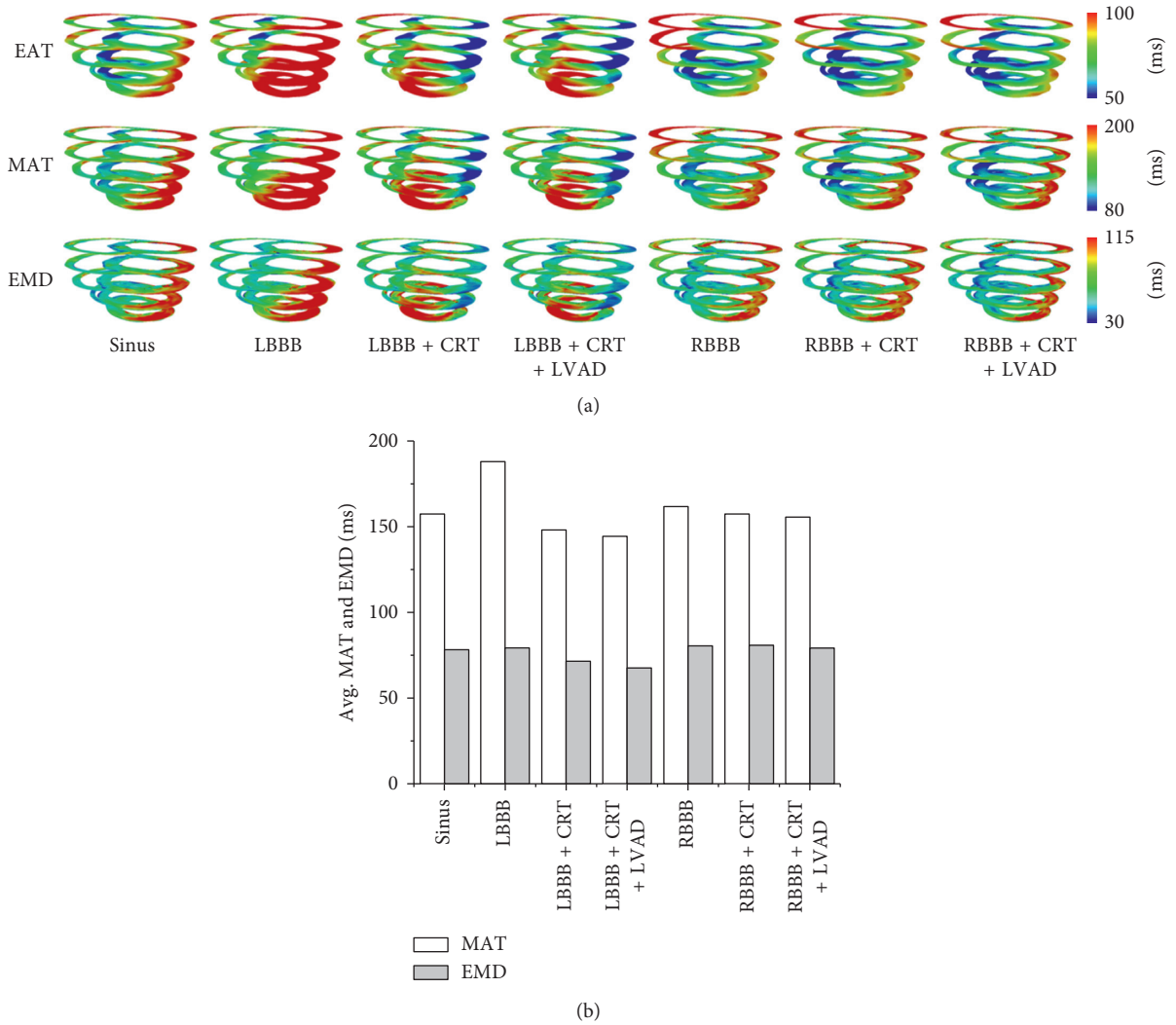

Figure 7: (a) Three-dimensional contour distribution of the EAT, MAT, and EMD and (b) the mean MAT and EMD values in all cases. EAT, electrical activation time; MAT, mechanical activation time; EMD, electromechanical delay; LBBB, left bundle branch block; CRT, cardiac resynchronization therapy; LVAD, left ventricular assist device; RBBB, right bundle branch block.

mechanical responses. However, CRT + LVAD increased CO in the RBBB condition significantly as expected.

In general, we performed a simulation and analyzed seven cardiac diseases and therapy conditions by using an electromechanical ventricular model incorporated with a circulatory systems, CRT, and LVAD models. The models including normal sinus rhythm, LBBB, LBBB + CRT, LBBB + CRT + LVAD, RBBB, RBBB + CRT, and RBBB + CRT + LVAD. The major findings of this study are as follows:

(1) CRT shortened the longest EAT by 20.2% in the LBBB condition and 17.1% in the RBBB condition. CRT shortened EMD by 10.1% in the LBBB condition but did not shorten EMD in the RBBB condition.

(2) Combination of CRT and LVAD treatment shortened EMD more than CRT alone in the LBBB condition (15.2%) and shortened EMD in the RBBB condition (1.3%).

(3) CRT reduced the ATP consumption by 5% as well as the tension and strain in the LBBB condition. CRT also slightly increased the LV peak pressure by 6% and increased the CO by 0.2 L/min in the LBBB condition. However, CRT-alone did not affect these mechanical responses in the RBBB condition.

(4) Combination of CRT and LVAD reduced the ATP consumption by 15% in the LBBB condition and by 16% in the RBBB condition. It also increased the LV pressure by 10.5% in the LBBB condition and 5.7% in the RBBB condition as well as the CO up to 4 L/min for both conditions, a degree greater than that in the control condition.

The pacing site at the tissue greatly affected synchronization. Placement at the LV free-wall showed faster activation throughout the chamber since the signal propagated evenly from the midway between the base and apex throughout the LV tissue. However, the pacing site at the RV

endocardial apex showed a longer activation time for the electrical signal to propagate to the base.

In the RBBB condition, the electrical activation of the LV chamber was the same as normal sinus despite the electrical activation alteration in the RV. This is the major factor why the mechanical responses of the LV (LV PV-loop, LV pressure, and CO) were also the same as that in normal sinus rhythm. Even the CRT implementation in the RBBB condition did not affect the mechanical responses of the LV chamber. However, we observed significant improvement in CO in the RBBB + CRT + LVAD condition. CRT and LVAD also reduced the ATP consumption and tension and increased the LV and aortic pressure in the RBBB condition.

CRT-alone did not fully restore the mechanical responses under the LBBB condition to normal despite the resynchronization of the EAT, which shortened the MAT and EMD to back normal. On the contrary, the use of combined CRT and LVAD reduced the energy consumption (indicated by the ATP consumption rate), tension, increased the LV pressure, and produced CO by 18% more than that in the HF with sinus rhythm condition. In addition, the LVAD did not fully assist the blood distribution in the LBBB or RBBB condition.

The computational method allowed us to predict the electromechanical phenomenon in the dyssynchrony heart which underwent CRT and LVAD treatment. It is hardly possible to observe some parameters including ATP consumption, tension, MAT, and EMD from the patient's heart of that condition in experimental procedure. This study quantified the electrical activation and hemodynamic responses in several dyssynchrony HF combined with CRT-only, and CRT and LVAD, which has never been conducted previously. As for the clinical impact, the results of this study can be used as reference to generally predict the effect of the combination of CRT and LVAD devices to the HF patients with LBBB. Though, there are some parameters need to be consider deeply by the cardiologist expert.

This computational study has several limitations that need to be addressed. The study did not follow the standard biventricular pacing method [43]. Instead, we used only one CRT pacing site: the RV endocardial apex (for the RBBB condition) or the LV lateral wall (for the LBBB condition). The LV pacing site was not placed at the optimal position as described before [44]. We did not observe or describe the RV mechanical responses in the RBBB condition; instead, we showed the LV responses only. We used LVAD instead of a right ventricular assist device to support the RBBB condition. Because of our limitations, we did not validate the results of our simulation with experimental data. In addition, we did not describe long-term effects such as recovery of cardiac functions by the combined CRT and LVAD, as previously described [28, 29].

4. Conclusions

In conclusion, although CRT-alone shortened the MAT and EMD to more than normal in the LBBB condition, the mechanical responses in the LBBB condition were not restored to normal. The combined CRT and LVAD shortened the MAT and EMD more than CRT-alone, restored the hemodynamic, and produced a greater CO than normal in the LBBB and RBBB conditions. Using the combined system, LVAD contributed to the MAT reduction by mechanical unloading, shortened the EMD, reduced ATP consumption, and reduced tension, which contributes to the recovery of the heart shape and function. In short, we computationally predicted and quantified that the CRT + LVAD implementation is superior to CRT-only implementation particularly in HF with the LBBB condition.

Data Availability

The methods and results data used to support the findings of this study are included within the article.

Conflicts of Interest

The authors declare that they have no conflicts of interest.

Acknowledgments

This research was partially supported by the MSIT (Ministry of Science, ICT), under the ITRC support program (IITP-2018-2014-0-00639) and and Global IT Talent Support Program (IITP-2017-0-01811) supervised by the IITP, and NRF under basic engineering research project (2016R1D1A1B0101440) and the EDISON (NRF-2011-0020576) Programs.

References

[1] D. Lloyd-Jones, R. Adams, M. Carnethon et al., "Heart disease and stroke statistics—2009 update: a report from the American Heart Association Statistics Committee and Stroke Statistics Subcommittee," *Circulation*, vol. 119, no. 3, pp. e21–e181, 2009.

[2] C. Linde, C. Leclercq, S. Rex et al., "Long-term benefits of biventricular pacing in congestive heart failure: results from the MUltisite STimulation in cardiomyopathy (MUSTIC) study," *Journal of the American College of Cardiology*, vol. 40, no. 1, pp. 111–118, 2002.

[3] J. B. Young, W. T. Abraham, A. L. Smith et al., "Combined cardiac resynchronization and implantable cardioversion defibrillation in advanced chronic heart failure: the MIRACLE ICD Trial," *JAMA*, vol. 289, no. 20, pp. 2685–2694, 2003.

[4] M. Kawaguchi, T. Murabayashi, B. J. Fetics et al., "Quantitation of basal dyssynchrony and acute resynchronization from left or biventricular pacing by novel echo-contrast variability imaging," *Journal of the American College of Cardiology*, vol. 39, no. 12, pp. 2052–2058, 2002.

[5] G. S. Nelson, R. D. Berger, B. J. Fetics et al., "Left ventricular or biventricular pacing improves cardiac function at diminished energy cost in patients with dilated cardiomyopathy and left bundle-branch block," *Circulation*, vol. 102, no. 25, pp. 3053–3059, 2000.

[6] P. Søgaard, W. Y. Kim, H. K. Jensen et al., "Impact of acute biventricular pacing on left ventricular performance and volumes in patients with severe heart failure," *Cardiology*, vol. 95, no. 4, pp. 173–182, 2001.

[7] A. Auricchio, C. Stellbrink, S. Sack et al., "Long-term clinical effect of hemodynamically optimized cardiac

resynchronization therapy in patients with heart failure and ventricular conduction delay," *Journal of the American College of Cardiology*, vol. 39, no. 12, pp. 2026–2033, 2002.

[8] M. G. S. J. Sutton, T. Plappert, K. E. Hilpisch et al., "Sustained reverse left ventricular structural remodeling with cardiac resynchronization at one year is a function of etiology quantitative doppler echocardiographic evidence from the Multicenter InSync Randomized Clinical Evaluation (MIRACLE)," *Circulation*, vol. 113, no. 2, pp. 266–272, 2006.

[9] W. T. Abraham, W. G. Fisher, A. L. Smith et al., "Cardiac resynchronization in chronic heart failure," *New England Journal of Medicine*, vol. 346, no. 24, pp. 1845–1853, 2002.

[10] S. Cazeau, C. Leclercq, T. Lavergne et al., "Effects of multisite biventricular pacing in patients with heart failure and intraventricular conduction delay," *New England Journal of Medicine*, vol. 344, no. 12, pp. 873–880, 2001.

[11] J. G. Cleland, J.-C. Daubert, E. Erdmann et al., "The effect of cardiac resynchronization on morbidity and mortality in heart failure," *New England Journal of Medicine*, vol. 352, no. 15, pp. 1539–1549, 2005.

[12] A. J. Moss, W. J. Hall, D. S. Cannom et al., "Cardiac-resynchronization therapy for the prevention of heart-failure events," *New England Journal of Medicine*, vol. 361, no. 14, pp. 1329–1338, 2009.

[13] Y. Hu, V. Gurev, J. Constantino, and N. Trayanova, "Efficient preloading of the ventricles by a properly timed atrial contraction underlies stroke work improvement in the acute response to cardiac resynchronization therapy," *Heart Rhythm*, vol. 10, no. 12, pp. 1800–1806, 2013.

[14] R. John, F. Kamdar, K. Liao et al., "Improved survival and decreasing incidence of adverse events with the HeartMate II left ventricular assist device as bridge-to-transplant therapy," *Annals of Thoracic surgery*, vol. 86, no. 4, pp. 1227–1235, 2008.

[15] D. Casarotto, T. Bottio, A. Gambino, L. Testolin, and G. Gerosa, "The last to die is hope: prolonged mechanical circulatory support with a Novacor left ventricular assist device as a bridge to transplantation," *Journal of Thoracic and Cardiovascular Surgery*, vol. 125, no. 2, pp. 417-418, 2003.

[16] M. A. Daneshmand, K. Rajagopal, B. Lima et al., "Left ventricular assist device destination therapy versus extended criteria cardiac transplant," *Annals of Thoracic Surgery*, vol. 89, no. 4, pp. 1205–1210, 2010.

[17] E. J. Birks, "Left ventricular assist devices," *Heart*, vol. 96, no. 1, pp. 63–71, 2010.

[18] E. A. Rose, A. C. Gelijns, A. J. Moskowitz et al., "Long-term use of a left ventricular assist device for end-stage heart failure," *New England Journal of Medicine*, vol. 345, no. 20, pp. 1435–1443, 2001.

[19] G. T. Altemose, V. Gritsus, V. Jeevanandam, B. Goldman, and K. B. Margulies, "Altered myocardial phenotype after mechanical support in human beings with advanced cardiomyopathy," *Journal of heart and lung transplantation: The Official Publication of the International Society for Heart Transplantation*, vol. 16, no. 7, pp. 765–773, 1997.

[20] H. R. Levin, M. C. Oz, J. M. Chen et al., "Reversal of chronic ventricular dilation in patients with end-stage cardiomyopathy by prolonged mechanical unloading," *Circulation*, vol. 91, no. 11, pp. 2717–2720, 1995.

[21] A. Barbone, M. C. Oz, D. Burkhoff, and J. W. Holmes, "Normalized diastolic properties after left ventricular assist result from reverse remodeling of chamber geometry," *Circulation*, vol. 104, no. 1, pp. I-229–I-232, 2001.

[22] S. Nakatani, P. M. McCarthy, K. Kottke-Marchant et al., "Left ventricular echocardiographic and histologic changes: impact of chronic unloading by an implantable ventricular assist device," *Journal of the American College of Cardiology*, vol. 27, no. 4, pp. 894–901, 1996.

[23] K. L. Grady, P. Meyer, A. Mattea et al., "Improvement in quality of life outcomes 2 weeks after left ventricular assist device implantation," *Journal of Heart and Lung Transplantation*, vol. 20, no. 6, pp. 657–669, 2001.

[24] F. D. Pagani, L. W. Miller, S. D. Russell et al., "Extended mechanical circulatory support with a continuous-flow rotary left ventricular assist device," *Journal of the American College of Cardiology*, vol. 54, no. 4, pp. 312–321, 2009.

[25] M. S. Slaughter, J. G. Rogers, C. A. Milano et al., "Advanced heart failure treated with continuous-flow left ventricular assist device," *New England Journal of Medicine*, vol. 361, no. 23, pp. 2241–2251, 2009.

[26] A. K. Heikhmakhtiar, A. J. Ryu, E. B. Shim et al., "Influence of LVAD function on mechanical unloading and electromechanical delay: a simulation study," *Medical and Biological Engineering and Computing*, vol. 56, no. 5, pp. 911–921, 2017.

[27] R. M. Delgado and B. Radovancevic, "Symptomatic relief: left ventricular assist devices versus resynchronization therapy," *Heart Failure Clinics*, vol. 3, no. 3, pp. 259–265, 2007.

[28] J. Muratsu, M. Hara, I. Mizote et al., "The impact of cardiac resynchronization therapy in an end-stage heart failure patient with a left ventricular assist device as a bridge to recovery," *International Heart Journal*, vol. 52, no. 4, pp. 246-247, 2011.

[29] H. Keilegavlen, J. E. Nordrehaug, S. Faerestrand et al., "Treatment of cardiogenic shock with left ventricular assist device combined with cardiac resynchronization therapy: a case report," *Journal of Cardiothoracic Surgery*, vol. 5, no. 1, p. 1, 2010.

[30] J. Constantino, Y. Hu, A. C. Lardo, and N. A. Trayanova, "Mechanistic insight into prolonged electromechanical delay in dyssynchronous heart failure: a computational study," *American Journal of Physiology-Heart and Circulatory Physiology*, vol. 305, no. 8, pp. H1265–H1273, 2013.

[31] Y. Hu, V. Gurev, J. Constantino, J. D. Bayer, and N. A. Trayanova, "Effects of mechano-electric feedback on scroll wave stability in human ventricular fibrillation," *PLoS One*, vol. 8, no. 4, Article ID e60287, 2013.

[32] X. Jie, V. Gurev, and N. Trayanova, "Mechanisms of mechanically induced spontaneous arrhythmias in acute regional ischemia," *Circulation Research*, vol. 106, no. 1, pp. 185–192, 2010.

[33] K. M. Lim and D. U. Jeong, "Influence of the KCNQ1 S140G mutation on human ventricular arrhythmogenesis and pumping performance: simulation study," *Frontiers in Physiology*, vol. 9, p. 926, 2018.

[34] V. Gurev, T. Lee, J. Constantino, H. Arevalo, and N. A. Trayanova, "Models of cardiac electromechanics based on individual hearts imaging data," *Biomechanics and Modeling in Mechanobiology*, vol. 10, no. 3, pp. 295–306, 2011.

[35] J. Provost, V. Gurev, N. Trayanova, and E. E. Konofagou, "Mapping of cardiac electrical activation with electromechanical wave imaging: an in silico–in vivo reciprocity study," *Heart Rhythm*, vol. 8, no. 5, pp. 752–759, 2011.

[36] N. A. Trayanova, "Whole-heart modeling: applications to cardiac electrophysiology and electromechanics," *Circulation Research*, vol. 108, no. 1, pp. 113–128, 2011.

[37] N. A. Trayanova and J. J. Rice, "Cardiac electromechanical models: from cell to organ," *Frontiers in Physiology*, vol. 2, p. 43, 2011.

[38] K. M. Lim, J. Constantino, V. Gurev et al., "Comparison of the effects of continuous and pulsatile left ventricular-assist

devices on ventricular unloading using a cardiac electromechanics model," *Journal of Physiological Sciences*, vol. 62, no. 1, pp. 11–19, 2012.

[39] K. ten Tusscher, D. Noble, P. Noble, and A. Panfilov, "A model for human ventricular tissue," *American Journal of Physiology-Heart and Circulatory Physiology*, vol. 286, no. 4, pp. H1573–H1589, 2004.

[40] O. Berenfeld and J. Jalife, "Purkinje-muscle reentry as a mechanism of polymorphic ventricular arrhythmias in a 3-dimensional model of the ventricles," *Circulation Research*, vol. 82, no. 10, pp. 1063–1077, 1998.

[41] J. J. Rice, F. Wang, D. M. Bers, and P. P. De Tombe, "Approximate model of cooperative activation and crossbridge cycling in cardiac muscle using ordinary differential equations," *Biophysical Journal*, vol. 95, no. 5, pp. 2368–2390, 2008.

[42] R. C. Kerckhoffs, M. L. Neal, Q. Gu et al., "Coupling of a 3D finite element model of cardiac ventricular mechanics to lumped systems models of the systemic and pulmonic circulation," *Annals of Biomedical Engineering*, vol. 35, no. 1, pp. 1–18, 2007.

[43] J. B. Shea and M. O. Sweeney, "Cardiac resynchronization therapy a patient's guide," *Circulation*, vol. 108, no. 9, pp. e64–e66, 2003.

[44] Y. Hu, V. Gurev, J. Constantino, and N. Trayanova, "Optimizing cardiac resynchronization therapy to minimize ATP consumption heterogeneity throughout the left ventricle: a simulation analysis using a canine heart failure model," *Heart Rhythm*, vol. 11, no. 6, pp. 1063–1069, 2014.